



HAL
open science

Theoretical and experimental study of organometallic transition metal nanoclusters and nanoparticles

Jianyu Wei

► **To cite this version:**

Jianyu Wei. Theoretical and experimental study of organometallic transition metal nanoclusters and nanoparticles. Inorganic chemistry. Université Rennes 1, 2022. English. NNT : 2022REN1S050 . tel-03908475

HAL Id: tel-03908475

<https://theses.hal.science/tel-03908475v1>

Submitted on 20 Dec 2022

HAL is a multi-disciplinary open access archive for the deposit and dissemination of scientific research documents, whether they are published or not. The documents may come from teaching and research institutions in France or abroad, or from public or private research centers.

L'archive ouverte pluridisciplinaire **HAL**, est destinée au dépôt et à la diffusion de documents scientifiques de niveau recherche, publiés ou non, émanant des établissements d'enseignement et de recherche français ou étrangers, des laboratoires publics ou privés.

THESE DE DOCTORAT DE

L'UNIVERSITE DE RENNES 1

ECOLE DOCTORALE N° 596

Matière, Molécules, Matériaux

Spécialité : *Chimie inorganique*

Par

Jianyu WEI

Etude théorique et expérimentale de nanoclusters et nanoparticules organométalliques de métaux de transition

Thèse présentée et soutenue à Rennes le 12 septembre 2022

Unité de recherche : Institut des Sciences chimiques de Rennes – UMR 6226

Thèse N° :

Rapporteurs avant soutenance :

Mme Hélène GERARD

Professeure, Sorbonne Université, Paris

M. Romuald POTEAU

Professeur, Université Toulouse 3 – Paul Sabatier, Toulouse

Composition du Jury :

Président : M. Didier ASTRUC

Professeur émérite, Université de Bordeaux, Bordeaux

Examineurs : M. Alvaro MUÑOZ-CASTRO

Professeur, Universidad Autónoma de Chile, Santiago, Chili

Dir. de thèse : M. Jean-François HALET

Directeur de recherche, CNRS–Saint-Gobain–NIMS, Tsukuba, Japon

Co-dir. de thèse : M. Jean-Yves SAILLARD

Professeur émérite, Université de Rennes 1, Rennes

Invité(s)

Membre invitée : Mme Samia KAHLAL

Maîtresse de conférences, Université de Rennes 1, Rennes

ACKNOWLEDGEMENTS

It is a genuine pleasure to express my deep sense of thanks and gratitude to my supervisors, Dr. Samia Kahlal, Prof. Jean-François Halet, Prof. Jean-Yves Saillard and Prof. Didier Astruc, for their continuous support, invaluable ideas, help, advice and encouragement throughout the past four years. They help me in all the time of research and writing of this thesis, and without whom I would not have succeeded.

I would also like to thank all the members of the Chimie Théorique Inorganique (CTI) team in the Institut des Sciences Chimiques de Rennes (ISCR), for their help in both of my scientific and daily life. I expressed my special thanks to our engineer, Dr. Rémi Marchal, who supported me to solve lots of technical problems which occurred in my study and research. I also expressed my sincere gratitude to our administrative and financial assistant, Mme Véronique Mallegol-Legrand, who took care of my registration and administration processes during my PhD work.

I should also like to thank my friends and colleagues belonging to CTI group in ISCR, Rennes and CSH group in ISM, Bordeaux, for their concern and help. Thanks to M. Xiaoyang Che, Mme Qi Wang, M. Franck Gam, M. Vincent Montigaud, M. Vincent Delmas, Mme Alicia Lecomte, M. Isaac Chantrenne and M. Hao Liang in the CTI group in Rennes. Thanks to Mme Wenjuan Wang, Mme Naixin Kang, Mme Qiuxia Zhao and Mme Yue Liu in the CSH group in Bordeaux.

My sincere thank also goes to our good friends and collaborators, Prof. Alvaro Muñoz-Castro and Dr. Desmond MacLeod Carey in Chile, for their ideas, support and help which provided me a chance to communicate and connect with the overseas chemistry world. I'd like to also thank Profs. Jean-René Hamon and Philippe Hapiot from ISCR, for their suggestions and help in part of my experimental work.

I am extremely grateful to my girlfriend, Dr. Xiaojiao Yang, for her love, patience and understanding.

Finally, I'd like to express my deep thanks to my parents, for their love, prayers, caring and sacrifices for educating and preparing me for my future.

Last but not least, it should be stressed that this work in Rennes and Bordeaux could not have occurred without the support of the China Scholarship Council, which I warmly acknowledge for the allowance of a full PhD scholarship.

Table of Contents

Résumé de la thèse en français	7
General Introduction	15
Chapter 1	23
Bonding Models in Cluster Compounds	23
1.1 Introduction	25
1.2 The <i>Spherical Jellium Model</i> and <i>Superatom Concept</i>	26
1.3 Application of <i>Superatom Concept</i> in Group-11 Nanoclusters.....	31
1.3.1 Pseudo-spherical Nanoclusters	31
1.3.2 Non-spherical Nanoclusters	38
1.3.2.1 Unconventional Electron Counts Stabilized by Lowering of Symmetry.....	38
1.3.2.2 Assemblies of <i>Superatoms (Supermolecules)</i>	40
1.4 References	43
Chapter 2	55
Towards the Formation of N-Heterocyclic Carbene-Protected Gold Clusters of Various Nuclearities. A Comparison with Their Phosphine-Protected Analogs from DFT Calculations	55
2.1 Introduction.....	57
2.2 Computational Details	59
2.3 Results and Discussion.....	60
2.3.1 Structures and Bonding Modes	60
2.3.2 Bonding Energies Analysis.....	69
2.3.3 Optical Properties.....	70
2.4 Conclusions.....	74
2.5 References	74
2.6 Annex	81
Chapter 3	87
Insight into the Stability, Electronic and Optical Properties of N-Heterocyclic Carbene Analogues of Halogen/Phosphine Protected Au ₁₃ <i>Superatomic Clusters</i>	87
3.1 Introduction.....	89
3.2 Computational Details	91
3.3 Results and Discussion.....	92
3.4 Conclusions.....	99

3.5 References.....	100
3.6 Annex	109
Chapter 4	115
Ligand-Induced Cuboctahedral versus Icosahedral Core Isomerism within Eight- Electron Heterocyclic-Carbene-Protected Gold Nanoclusters	115
4.1 Introduction.....	117
4.2 Computational Details	118
4.3 Results and Discussion.....	119
4.4 Conclusion	124
4.5 References.....	124
4.6 Annex	131
Chapter 5	137
On Heteronuclear Isoelectronic Alternatives to $[\text{Au}_{13}(\text{dppe})_5\text{Cl}_2]^{3+}$: Electronic and Optical Properties of the 18-electron $\text{Os}@\text{[Au}_{12}(\text{dppe})_5\text{Cl}_2]$ Cluster from DFT Computations	137
5.1 Introduction.....	139
5.2 Computational Details	141
5.3 Results and Discussion.....	142
5.4 Conclusion	148
5.5 References.....	149
5.6 Annex	158
Chapter 6	161
From 8- to 18-cluster electrons Superatoms. Investigation of the Ligand-Protected $\text{W}@\text{Au}_{12}(\text{dppe})_6$ Cluster Displaying Distinctive Electronic and Optical Properties	161
6.1 Introduction.....	163
6.2 Computational Details	165
6.3 Results and Discussion.....	165
6.4 Conclusions.....	173
6.5 References.....	173
6.6 Annex	183
Chapter 7	187
Elucidating the Electronic Structure of the Ligated Cuboctahedral Palladium Cluster $[\text{Pd}_{13}(\mu_4\text{-C}_7\text{H}_7)_6]^{2+}$	187
7.1 Introduction.....	189

7.2 Computational Details	191
7.3 Results and Discussion.....	191
7.4 Conclusion	197
7.5 References.....	198
7.6 Annex	204
Chapter 8	209
Theoretical Analysis of the Mackay Icosahedral Cluster Pd₅₅(PⁱPr₃)₁₂(μ₃-CO)₂₀: An	
Open-shell 20-electron <i>Superatom</i>	209
8.1 Introduction.....	211
8.2 Computational Details	213
8.3 Results and Discussion.....	213
8.4 Conclusion	221
8.5 References.....	222
8.6 Annex	228
Chapter 9	231
Looking at Platinum Carbonyl Nanoclusters as <i>Superatoms</i>.....	
9.1 Introduction.....	233
9.2 Computational Details	234
9.3 Results and Discussion.....	235
9.3.1 Decorated 8-electron <i>Superatoms</i> and Related Species.....	235
9.3.1.1 Experimentally Characterized Species	235
9.3.1.2 The Hypothetical <i>D</i> _{5h} [Pt ₁₃ (μ-CO) ₅ (CO) ₁₂] ²⁻ Model: The Versatile Role of “Additional” Bridging Ligands.....	240
9.3.1.3 Non-spherical Clusters Related to the <i>D</i> _{5h} [Pt ₁₃ (μ-CO) ₅ (CO) ₁₂] ²⁻ Model: [Pt ₁₄ (μ-CO) ₆ (CO) ₁₂] ⁴⁺ and [Pt ₁₅ (μ-CO) ₈ (CO) ₁₁] ⁴⁺	241
9.3.2 Assemblies of Individual <i>Superatoms</i>	242
9.3.2.1 Experimentally Characterized Species	242
9.3.2.2 Hypothetical Models.....	247
9.3.3 Other Clusters with 3D Architectures.....	249
9.3.3.1 Pseudo-spherical Species	249
9.3.3.2 Non-pseudo-spherical Species	250
9.4 Conclusion	252
9.5 References.....	253

9.6 Annex	263
Chapter 10	289
Synthesis and Characterizations of Ferrocenylalkylthiolates Protected Gold	
Nanoparticles.....	289
10.1 Introduction.....	291
10.2 Results and Discussion.....	292
10.3 Conclusion	295
10.4 Experimental Section.....	295
10.5 References.....	300
Conclusion and Perspectives.....	305
Publications related to this work.....	313

Résumé de la thèse en français

Les nanoclusters métalliques (MNC) de composition exacte ont suscité de grands intérêts de recherche ces dernières années en raison de leur structure géométrique bien définie et de leurs propriétés physiques et chimiques particulières.¹⁻³ D'une part, les MNC peuvent être utilisés comme éléments de base pour construire des nanomatériaux de structures et propriétés bien définies.⁴ D'autre part, ils présentent un intérêt propre dans divers domaines d'application, tels que la catalyse,³ la nanomédecine,⁵ les capteurs,⁶ ou encore la photonique...⁷ Dans la grande famille des nanoclusters, ceux constitués de métaux nobles sont parmi les espèces les plus populaires et ce, depuis le 19^{ème} siècle.¹⁻³ Il existe de nombreuses techniques de synthèse et de caractérisation qui ont été développées par les chimistes expérimentateurs pour ces nanoclusters.^{1-3,8} En parallèle, les théoriciens ont également fait beaucoup d'efforts pour comprendre la liaison, la stabilité, la structure électronique et les propriétés associées des MNC.⁹⁻¹¹

Le travail rapporté dans cette thèse porte principalement sur l'étude théorique en méthode de la fonctionnelle de la densité (DFT), de la stabilité, de la structure et des propriétés optiques des nanoclusters stables des éléments des groupes 10 et 11 protégés par des ligands. Le manuscrit de thèse comporte dix chapitres. Il commence par un examen complet des modèles de liaison dans les clusters (chapitre 1), suivi d'une série d'études théoriques systématiques sur les nanoclusters d'or stabilisés par des ligands (chapitres 2, 3 et 4), les clusters superatomiques d'or dopés par un seul hétéroatome (chapitres 5 et 6), les nanoclusters de métaux du groupe 11 (Pd, Pt) stabilisés par des ligands (chapitres 7, 8 et 9), et quelques études expérimentales sur des nanoparticules d'or de grande taille protégées par des monocouches (chapitre 10).

Dans le chapitre 1, sont brièvement passés en revue le développement des règles de comptage d'électrons des composés clusters, y compris la théorie des paires d'électrons de squelette dans les polyèdres (PSEPT, également connue sous le nom de règles de Wade-Mingos),^{12,13} la théorie du tenseur harmonique de surface (TSH)¹⁴ et le concept de superatome.¹⁵⁻¹⁶ Ce dernier, basé sur le modèle du jellium sphérique¹⁷, est décrit en détail puisqu'il est utilisé dans tous les travaux rapportés dans cette thèse. L'équation de Schrödinger abordée dans le concept de superatome a d'abord été illustrée. Ensuite, deux jalons historiques, qui montrent comment ce concept de base peut être appliqué, à la fois aux clusters nus et protégés par des ligands dans la chimie de l'aluminium, ont également été analysés. Enfin, quelques exemples typiques d'applications du concept de superatome dans la chimie des nanoclusters métalliques protégés par des ligands sont présentés.

Dans le chapitre 2, nous avons étudié une série de nanoclusters d'or protégés par des ligands de type carbènes N-hétérocyclique (NHC) ($\text{Au}_n\text{-C}$) de différentes nucléarités ($n = 6-13$), qui

dérivent des clusters d'or stabilisés par des phosphines (**Au_n-P**), bien connus et caractérisés expérimentalement. Les séries **Au_n-P** et **Au_n-C** présentent des stabilités et des caractéristiques structurales similaires. Les ligands NHC se révèlent même un peu plus fortement liés au noyau d'or (de quelques kcal/mol par ligand) que les phosphines. L'étude des propriétés optiques des deux séries à l'aide de calculs TD-DFT indique des similitudes dans la nature et les énergies des transitions optiques UV-vis et, par conséquent, des formes relativement similaires des spectres simulés, avec une tendance générale au décalage vers le bleu quand on passe de **Au_n-P** à **Au_n-C**. Le comportement en fluorescence observé expérimentalement pour certaines des espèces **Au_n-P** devrait également se produire pour leurs analogues **Au_n-C**, ainsi qu'à d'autres nanoclusters protégés par un ligand carbène. Nos résultats montrent qu'il devrait être possible de stabiliser des clusters d'or avec des ligands NHC, offrant de nouvelles briques de construction pour la conception de matériaux nanostructurés aux propriétés variées.

Dans le chapitre 3, nous étendons les recherches à une série hypothétique de clusters superatomiques à 8 électrons Au₁₃ et M₄Au₉ (M = Cu, Ag) protégés par des NHC. Leurs analogues protégés par des phosphines et connus expérimentalement, ont également été étudiés pour comparaison. Nos résultats montrent que le remplacement des phosphines par des ligands NHC conduit à des structures et stabilités électroniques similaires, mais des propriétés optiques quelque peu différentes. Ces résultats soutiennent la possibilité de synthèse de nouvelles cibles mettant en valeur des ligands NHC sur des espèces de taille moyenne basées sur le cœur icosaédrique Au₁₃ bien connu. Ces espèces hypothétiques semblent être des modèles intéressants en tant que motifs de construction dans des matériaux nanostructurés aux propriétés ajustées, qui encouragent l'exploration expérimentale dans les clusters superatomiques homo- et hétérométalliques.

Dans le chapitre 4, nous montrons que les ligands NHC peuvent non seulement stabiliser efficacement le noyau superatomique Au₁₃, mais peuvent également induire l'isomérisation du noyau du cluster cible. La modification structurale contrôlée de clusters d'or protégés par des ligands est abordée par une variation appropriée de la taille et de la forme des ligands NHC. Les calculs DFT montrent que le noyau Au₁₃ de [Au₁₃(NHC)₈Br₄]⁺ peut être façonné en un icosaèdre et/ou un cuboctaèdre (ce dernier jusqu'ici inédit) en fonction de l'effet stérique émanant des bras latéraux du ligand NHC. En conséquence, les propriétés du cluster peuvent être modifiées, encourageant une exploration plus poussée sur l'isomérisation contrôlée du noyau dans la chimie des nanoclusters d'or.

Dans le chapitre 5, nous discutons comment le dopage des atomes hétérométalliques peut affecter la liaison, la structure électronique et les propriétés optiques des clusters

superatomiques icosaédriques centrés de type $M@Au_{12}$. Nous explorons à l'aide de calculs DFT la possibilité de substituer l'atome d'or central dans le cluster classique $[Au_{13}(dppe)_5Cl_2]^{3+}$ par un atome d'osmium. Bien que $[Au_{13}(dppe)_5Cl_2]^{3+}$ et $[Os@Au_{12}(dppe)_5Cl_2]$ aient le même nombre total d'électrons, nous montrons qu'ils ne sont pas isoélectroniques dans le formalisme du modèle du superatome, étant respectivement à 8 et 18 électrons. Il en résulte qu'ils présentent des structures similaires mais des comportements optiques significativement différents (UV/visible et dichroïsme circulaire). Des résultats similaires sont obtenus pour $M = Ru$ et Fe . Les propriétés d'émission indiquent un certain décalage vers le rouge de l'émission $T_1 \rightarrow S_1$ par rapport à $[Au_{13}(dppe)_5Cl_2]^{3+}$, associée à une distorsion équatoriale du noyau $Au_{12}Cl_2$ à l'état T_1 . Ces résultats suggèrent qu'une exploration expérimentale plus poussée des différentes espèces dopées dérivant du noyau $Au_{12}Cl_2$ devrait être encouragée.

Dans le chapitre 6, nous complétons l'étude de superatomes $M@Au_{12}$ ($M =$ hétérométal) en envisageant le dopage du cluster modèle $[Au_{13}dppm_6]^{5+}$ caractérisé expérimentalement avec un hétérométal des groupes 11 à 6 (Au, Pt, Ir, Os, Re et W). Le cluster $[WAu_{12}dppm_6]$ a été étudié en détail. Nos résultats montrent des différences fondamentales entre les clusters à 8 et à 18 électrons (*ce*), conduisant à des modèles différents dans leur structure électronique, leurs spectres optiques et le rôle de la sphère des ligands dans la stabilité globale du cluster. Le caractère des orbitales frontières varie de 1P/1D dans le cas 8-*ce* à un 1D/ligand dans les espèces 18-*ce*, permettant un transfert de charge efficace vers les ligands ; ce qui présente un intérêt pour les applications d'injection d'électrons et d'absorbeurs noirs. Les propriétés de l'état excité sont également revisités, montrant différentes variations de structure géométrique et électronique entre les espèces 8- et 18-*ce*. Les espèces à 18 électrons présentent des alternatives utiles pour obtenir différentes propriétés dans des motifs structuraux connexes.

Dans le chapitre 7, nous menons une étude théorique sur un nanocluster de palladium cuboctaédrique à 13 atomes $[Pd_{13}(\mu_4-C_7H_7)_6]^{2+}$. Auparavant, aucune règle générale de comptage d'électrons ne permettait de rationaliser la stabilité d'une telle architecture. Les résultats indiquent que la liaison dans ce cluster peut être décrite à partir d'un noyau $[Pd_{13}]^{2-}$ interagissant avec une enveloppe de ligands $[Tr_6]^{4+}$ ($Tr = C_7H_7$) partiellement réduite. Les interactions orbitales entre les deux fragments sont fortes, du fait notamment de la très forte capacité acceptrice des ligands. La liaison Pd–Pd (de force modérée) résulte en partie, de l'occupation de la combinaison en phase fortement liante des orbitales 5s (Pd) (niveau jellium 1S). Ce cas particulier nous a fourni quelques inspirations pour les études suivantes présentées dans les chapitres 8 et 9.

Dans le chapitre 8, nous montrons que le concept de superatome peut être utilisé pour rationaliser la liaison et la structure électronique des nanoclusters organométalliques du palladium. Comme illustration, nous avons analysé le cluster icosaédrique très typique de Mackay $\text{Pd}_{55}(\text{P}^i\text{Pr}_3)_{12}(\mu_3\text{-CO})_{20}$, rapporté par le groupe de Dahl en 2016. Les résultats révèlent qu'il peut être considéré comme un superatome régulier avec un nombre d'électrons "magique" de 20, et associé à la configuration $1\text{S}^2 1\text{P}^6 1\text{D}^{10} 2\text{S}^2$. Sa nature à couche ouverte résulte d'une occupation partielle des niveaux non-superatomiques de type $4d$ localisés au cœur du noyau Pd_{55} . Cela montre que le modèle de superatome peut être utilisé pour rationaliser la liaison et la stabilité des clusters sphériques de métaux du groupe 10 protégés par des ligands, et ceci malgré leur nombre apparent d'électrons qui est égal à 0. Nous pensons que les deux autres nanoclusters de palladium de plus grande taille, à savoir le cluster multisphérique à trois couches métalliques $\text{Pd}_{145}(\text{CO})_x(\text{PEt}_3)_{30}$ ($x \approx 60$), et le cluster Pd/Pt à quatre couches $\text{Pd}_{164-x}\text{Pt}_x(\mu_{12}\text{-Pt})(\text{CO})_{72}(\text{PPh}_3)_{20}$ ($x \approx 7$) sont aussi des superatomes caractérisés par (au moins approximativement) un compte d'électrons "magique", ces électrons occupant des états $5s(\text{Pd})$ ou $6s(\text{Pt})$ et résultant d'un transfert depuis les états $4d(\text{Pd})$ ou $5d(\text{Pt})$.

Dans le chapitre 9, nous cherchons à compléter une image générale du modèle superatomique dans la chimie des clusters du groupe 10. Nous avons étudié une série de nanoclusters organométalliques du platine caractérisés expérimentalement. Bien que la chimie des nanoclusters de platine protégés par des ligands carbonyles soit bien établie, leur mode de liaison reste mal compris. Dans la plupart d'entre eux, l'état d'oxydation moyen du Pt est nul ou légèrement négatif ; ce qui conduit à la configuration moyenne apparente $5d^{10} 6s^\varepsilon$ ($\varepsilon = 0$ ou très petit) et à la conclusion apparente que la liaison métal–métal ne peut pas provenir de la couche $5d$ qui est complètement remplie, ni des orbitales $6s$ qui sont vides (ou presque vides). Cependant, les calculs DFT montrent en fait que dans le cas de ces espèces, la configuration moyenne réelle est $5d^{10-x} 6s^x$, ce qui fournit à l'ensemble du cluster un nombre total important d'électrons $6s$, qui assurent la liaison métal–métal en peuplant les combinaisons liantes. Le croisement de niveaux associé à ce transfert d'électrons, qui n'existe pas dans les clusters Pt_n nus, est induit par la couche de ligands, dont le rôle n'est donc pas anodin vis-à-vis de la liaison métal–métal. Cette configuration moyenne ("excitée") est à mettre en parallèle avec celle des métaux du groupe 11 ($nd^{10} (n + 1)s^x$). Les calculs montrent que la liaison métal–métal dans la plupart de ces nanoclusters de platine peut être rationalisée à l'aide des concepts de superatomes et de supermolécules, de la même manière que pour les nanoclusters du groupe 11. Nos études

ont exploré les limites du concept de superatome, ce qui nous a permis de faire le pont entre la chimie des clusters du groupe 10 et celle du groupe 11.

Enfin, nous rapportons dans le chapitre 10 des travaux expérimentaux sur des nanoparticules d'or protégées par des monocouches. Nous décrivons la synthèse de ligands 6-(amidoferrocényl)hexanethiol (FcSH) ainsi que celle de AuNP stabilisées par FcSH (**FcSH-AuNP**). Les composés **FcSH-AuNP** synthétisés ont été caractérisés par spectroscopie UV-vis et microscopie électronique à transmission. Les propriétés redox des **FcSH-AuNP** ont également été étudiées en voltamétrie cyclique. Les résultats montrent que le ligand 6-(amidoferrocényl)hexanethiol peut stabiliser des AuNP ultrafins avec une très bonne stabilité et une bonne monodispersité. Les **FcSH-AuNP** synthétisés présentent une taille moyenne ultrafine de 2 nm, ce qui est inférieur à celle des AuNP protégés par un ligand mixte alkylthiolate et ferrocénylalkylthiolate rapportés précédemment. La raison possible est que l'effet stérique des groupes ferrocényle terminaux inhibe la croissance ultérieure du noyau métallique. Les **FcSH-AuNP** montrent une large bande de plasmon à 500 nm en raison de la courte distance entre les particules. Un signal clair dans leurs voltamogrammes cycliques a pu être enregistré, encourageant le fait que les espèces **FcSH-AuNP** pourraient être utilisées dans la conception d'électrodes dérivées pour les applications de détection.

Références

- 1 Jin, R.; Li, G.; Sharma, S.; Li, Y.; Du, X. Toward active-site tailoring in heterogeneous catalysis by atomically precise metal nanoclusters with crystallographic structures. *Chem. Rev.* **2020**, *121*, 567–648.
- 2 Kang, X.; Li, Y.; Zhu, M.; Jin, R. Atomically precise alloy nanoclusters: syntheses, structures, and properties. *Chem. Soc. Rev.* **2020**, *49*, 6443–6514.
- 3 Du, Y.; Sheng, H.; Astruc, D.; Zhu, M. Atomically precise noble metal nanoclusters as efficient catalysts: a bridge between structure and properties. *Chem. Rev.* **2019**, *120*, 526–622.
- 4 Chakraborty, P.; Nag, A.; Chakraborty, A.; Pradeep, T. Approaching materials with atomic precision using supramolecular cluster assemblies. *Acc. Chem. Res.* **2018**, *52*, 2–11.
- 5 Tao, Y.; Li, M.; Ren, J.; Qu, X. Metal nanoclusters: novel probes for diagnostic and therapeutic applications. *Chem. Soc. Rev.* **2015**, *44*, 8636–8663.
- 6 Shang, L.; Xu, J.; Nienhaus, G.U. Recent advances in synthesizing metal nanocluster-based nanocomposites for application in sensing, imaging and catalysis. *Nano Today* **2019**, *28*, 100767.

- 7 Zhang, B.; Wang, Z.; Zhang, C.; Wu, H.; Dang, S.; Du, J.; Song, Y.; Zhang, H.; Liu, J.; Nie, G. Gold Nanocluster-Modified Titanium Nitride for Ultrafast Photonics Applications. *Adv. Electron. Mater.* **2021**, *7*, 2000954.
- 8 Zeng, C.; Jin, R. Gold nanoclusters: size-controlled synthesis and crystal structures. *Gold Clusters, Colloids and Nanoparticles I* **2014**, 87–115.
- 9 Weerawardene, K. D. M.; Häkkinen, H.; Aikens, C. M. Connections between theory and experiment for gold and silver nanoclusters. *Annu. Rev. Phys. Chem.* **2018**, *69*, 205–229.
- 10 Häkkinen, H. Electronic shell structures in bare and protected metal nanoclusters. *Adv. Phys-X* **2016**, *1*, 467–491.
- 11 Fernando, A.; Weerawardene, K. D. M.; Karimova, N. V.; Aikens, C. M. Quantum mechanical studies of large metal, metal oxide, and metal chalcogenide nanoparticles and clusters. *Chem. Rev.* **2015**, *115*, 6112–6216.
- 12 Wade, K. The structural significance of the number of skeletal bonding electron-pairs in carboranes, the higher boranes and borane anions, and various transition-metal carbonyl cluster compounds. *J. Chem. Soc. Chem. Commun.* **1971**, 792–793.
- 13 Mingos, D. M. P.; Wales, D. J. *Introduction to cluster chemistry*. Prentice Hall: **1990**.
- 14 Stone, A. J. A new approach to bonding in transition metal clusters: theory. *Mol. Phys.* **1980**, *41*, 1339–1354.
- 15 Walter, M.; Akola, J.; Lopez-Acevedo, O.; Jadzinsky, P. D.; Calero, G.; Ackerson, C. J.; Whetten, R. L.; Grönbeck, H.; Häkkinen, H. A unified view of ligand-protected gold clusters as superatom complexes. *Proc. Natl. Acad. Sci. U. S. A.* **2008**, *105*, 9157–9162.
- 16 Häkkinen, H. Atomic and electronic structure of gold clusters: understanding flakes, cages and superatoms from simple concepts. *Chem. Soc. Rev.* **2008**, *37*, 1847–1859.
- 17 Knight, W.; Clemenger, K.; de Heer, W. A.; Saunders, W. A.; Chou, M.; Cohen, M. L. Electronic shell structure and abundances of sodium clusters. *Phys. Rev. Lett.* **1984**, *52*, 2141.

General Introduction

Atom-precise metal nanoclusters (MNCs) have raised great research interests in recent years due to their well-defined geometric structure and distinct physical and chemical properties.¹⁻³ On one hand, MNCs can be used as building blocks to construct large three dimensional nanomaterials with well-defined structures and properties.⁴ On the other hand, MNCs have their own interests involved in various application fields including catalysis,³ nanomedicine,⁵ sensing⁶ and photonics.⁷ Among the big MNCs family, coinage metal nanoclusters are among the most popular species which have been widely investigated since the 19th century.¹⁻³ There are a lot of synthesis and characterization techniques that have been developed by experimental chemists for these nanoclusters.^{1-3,8} In parallel, theoreticians also made a lot of efforts to understand the bonding, stability, electronic structure and related properties of MNCs.⁹⁻¹¹

The work reported in this thesis deals principally with the investigation by density functional theory (DFT) calculations of the stability, structure and optical properties of ligand-protected group-10 and group-11 stable nanoclusters. The thesis manuscript is divided in ten chapters. It begins with a comprehensive review on the bonding models for cluster compounds (Chapter 1), followed by a series of systematic theoretical studies on ligated gold nanoclusters (Chapter 2 to Chapter 4), single atom alloyed *superatomic* clusters (Chapter 5 and Chapter 6), ligated group-11 (Pd, Pt) nanoclusters (Chapter 7 to Chapter 9), and some experimental studies on large-sized monolayer protected gold nanoparticles (Chapter 10).

In Chapter 1, the development of the electron counting rules of the cluster compounds, including *Polyhedral Skeletal Electron Pair Theory* (PSEPT, also known as Wade-Mingos rules),^{12,13} *Tensor Surface Harmonic* (TSH) theory¹⁴ and *superatom* concept,¹⁵⁻¹⁶ were briefly reviewed. Among them, the *superatom* concept, based on the *spherical jellium* model,¹⁷ was described in details since it was used in all the work reported in this thesis. The Schrödinger equation addressed in the *superatom* concept was firstly illustrated. Then, two historical milestones, which shows how this basic concept can be applied to both bare and ligated clusters in aluminium chemistry, were also mentioned. Finally, some typical examples of the applications of *superatom* concept in ligated metal nanocluster chemistry were introduced.

In Chapter 2, we investigated a series of N-heterocyclic carbene (NHC) protected gold nanoclusters (**Au_n-C**) with different nuclearity ($n = 6 - 13$), which derived from the well-known experimentally-characterized phosphine-stabilized gold clusters (**Au_n-P**). Both the **Au_n-P** and **Au_n-C** series exhibit similar stabilities and structural features. The NHC ligands are found to be even slightly more strongly bonded to the gold core (by a few kilocalories per mole per ligand) than phosphines. Investigation of the optical properties of both series using TD-DFT calculations indicates similarities in the nature and energies of the UV-vis optical transitions

and, consequently, relatively similar shapes of the simulated spectra, with a general blue-shift tendency when going from $\text{Au}_n\text{-P}$ to $\text{Au}_n\text{-C}$. The fluorescence behavior observed experimentally for some of the $\text{Au}_n\text{-P}$ species is expected to occur also for their $\text{Au}_n\text{-C}$ analogues, which can be extended to other carbene-ligand-protected nanoclusters. Our results show that it should be possible to stabilize gold clusters with NHC ligands, in relation to the seminal Au_{13} -ligand-protected core, offering novel building blocks for the design of nanostructured materials with various properties.

In Chapter 3, we extend the investigations on a series hypothetical 8-electron NHC protected Au_{13} and M_4Au_9 ($\text{M} = \text{Cu}, \text{Ag}$) *superatomic* clusters, their corresponded experimentally characterized phosphine protected analogues were also studied for the comparison. Our results show that replacing phosphine by NHC ligands in Au_{13} (M_4Au_9) series results in a similar electronic structure and stability but somewhat different optical properties. These findings support the feasible obtention of novel targets for explorative synthetic efforts featuring NHC ligands on medium-sized species based on the recurrent Au_{13} icosahedral core. The hypothetical species appear to be interesting templates for building blocks in nanostructured materials with tuned properties, which encourage experimental exploration of ligand versatility in homo- and heterometallic superatomic clusters.

In Chapter 4, We shown that NHC ligands not only can effeciently stabilize *superatomic* Au_{13} core, but also can induce the core isomerization of the target cluster. The controlled structural modification of ligand-protected gold clusters is evaluated by a proper variation of the size and shape NHC ligands. DFT calculations show that the Au_{13} core of $[\text{Au}_{13}(\text{NHC})_8\text{Br}_4]^+$ can be shaped into an icosahedron and/or a so far unexpected cuboctahedron depending on the sterical effect inferred by the NHC ligand side arms. As a result, the cluster properties can be modified, encouraging further exploration on controlled core isomerization in ligated gold cluster chemistry.

In Chapter 5, we have shown how heterometal atom doping effects the bonding, electronic structure and optical properties of the well-known centered icosahedral $\text{M}@\text{Au}_{12}$ *superatomic* clusters. We explore by means of density functional theory calculations the possibility of doping the central gold atom in the classical $[\text{Au}_{13}(\text{dppe})_5\text{Cl}_2]^{3+}$ cluster (**1**) by Os. Although both $[\text{Au}_{13}(\text{dppe})_5\text{Cl}_2]^{3+}$ and $[\text{Os}@\text{Au}_{12}(\text{dppe})_5\text{Cl}_2]$ have the same total number of electrons, we show that they are not isoelectronic within the formalism of the *superatom* model, being respectively an 8- and an 18-electron species. It results that they exhibit similar structures but present significantly different optical behaviors (ultraviolet/visible and circular dichroism). Similar results are obtained for the Ru and Fe relatives. Emission properties indicate some

redshift of the T1→S1 decay with respect to $[\text{Au}_{13}(\text{dppe})_5\text{Cl}_2]^{3+}$, involving an equatorial distortion of the $\text{Au}_{12}\text{Cl}_2$ core in the T1 state, rather than the axial distortion afforded by **1**. The sizable highest occupied molecular orbital–lowest unoccupied molecular orbital gaps found for the three doped species suggest that further experimental exploration of different stable doped species derived from the ligand-protected $\text{Au}_{12}\text{Cl}_2$ core should be encouraged.

In Chapter 6, based on an experimentally characterized di-phosphine ligated $[\text{Au}_{13}\text{dppm}_6]^{5+}$ model cluster, we completed the story of heterometal atom doped $\text{M}@\text{Au}_{12}$ *superatoms*, by evaluation of the group 11 to 6 dopant elements (Au, Pt, Ir, Os, Re, W). The $\text{WAu}_{12}\text{dppm}_6$ cluster was described in details. Our results expose fundamental differences between 8- and 18-electron clusters (*ce*), leading to different patterns in their electronic structure, optical spectra, and role of the protecting-ligand shell in the overall cluster stability. The character of frontier orbitals varies from 1P/1D in the 8-*ce* case to a 1D/ligand in 18-*ce* species, enabling an efficient charge transfer towards the ligands of interest for electron-injection and black absorbers applications. Excited-state properties are also revisited, showing different geometrical and electronic structure variations between 8- and 18-*ce* species. Moreover, evaluation of group 11 to 6 dopant elements, exhibits a breaking point where the *nd*-dopant orbitals are able to overlap to Au_{12} -cage orbitals leading to a populated *superatomic* 1D-shell, and hence, resulting in species that can be considered as 18-*ce* clusters. Thus, 18-*ce* derivatives obtained as doped counterparts of homometallic gold clusters can introduce useful alternatives to achieve different properties in related structural motifs, which can be further explored owing to their extension of the well-established versatility of current gold nanoclusters.

In Chapter 7, we carried out a theoretical study on a rare 13-atom cuboctahedral palladium nanocluster $[\text{Pd}_{13}(\mu_4\text{-C}_7\text{H}_7)_6]^{2+}$, since no general electron counting rules could be perfectly applied for such group-10 cluster chemistry. Results indicate that the bonding in this cluster can be described from the formal starting point of a $[\text{Pd}_{13}]^{2-}$ core interacting with a partly reduced $[\text{Tr}_6]^{4+}$ ligand shell. The orbital interactions between the two fragments are strong, owing in particular to the very strong accepting ability of the surrounding ligands. The (moderate) Pd–Pd bonding character is in part due to the occupation of the strongly bonding in-phase combination of the 5s(Pd) orbitals (the 1S *jellium* level) and for another part from through-bond interactions. This special case provides us some inspirations in the following studies in chapter 8 and chapter 9.

In Chapter 8, we shown firstly that *superatom* concept can be used to rationalize the bonding and electronic structure of organometallic palladium nanoclusters. We analyzed a very typical

spherical Mackay icosahedral cluster $\text{Pd}_{55}(\text{PiPr}_3)_{12}(\mu_3\text{-CO})_{20}$, reported by Dahl's group in 2016. Results reveal that it can be considered as a regular *superatom* with a “magic” electron count of 20, characterized by a $1\text{S}^2 1\text{P}^6 1\text{D}^{10} 2\text{S}^2$ *jellium* configuration. Its open shell nature is associated with partial occupation of *non-jellium*, *4d*-type, levels located on the interior of the Pd_{55} kernel. This shows that the *superatom* model can be used to rationalize the bonding and stability of spherical ligated group 10 clusters, despite their apparent 0-electron count. We believe that the other two larger-sized palladium nanoclusters contains interior two-shell icosahedral Mackay-type geometries, namely the three-shell 145-metal-atom $\text{Pd}_{145}(\text{CO})_x(\text{PEt}_3)_{30}$ ($x \approx 60$) cluster compound, and the Pd-Pt four-shell 165-metal-atom $\text{Pd}_{164-x}\text{Pt}_x(\mu_{12}\text{-Pt})(\text{CO})_{72}(\text{PPh}_3)_{20}$ ($x \approx 7$) cluster, are indeed *superatoms* characterized by (at least approximately) “magic” electron counts, these electrons occupying $5s(\text{Pd})$ or $6s(\text{Pt})$ states and resulting from electron transfer from $4d(\text{Pd})$ or $5d(\text{Pt})$ states.

In Chapter 9, we aimed to complete a general picture of the bonding pattern and electronic structure of group-10 cluster chemistry. A series of experimentally characterized platinum carbonyl nanoclusters we investigated. Although the chemistry of carbonyl-protected platinum nanoclusters is well established, their bonding mode remains poorly understood. In most of them, the average Pt oxidation state is zero or slightly negative, leading to the apparent average configuration $5d^{10} 6s^\varepsilon$ ($\varepsilon = 0$ or very small) and the apparent conclusion that metal–metal bonding cannot arise from the completely filled $5d$ shell nor from the empty (or almost empty) $6s$ orbitals. However, DFT calculations show in fact that in these species the actual average configuration is $5d^{10-x} 6s^x$, which provides to the whole cluster a significant total number of $6s$ electrons that ensures metal–metal bonding. This (“excited”) average configuration is to be related to that of coinage metals in ligated group-11 nanoclusters ($nd^{10} (n + 1)s^x$). Calculations show that metal–metal bonding in most of these platinum nanoclusters can be rationalized within the concepts of *superatoms* and *supermolecules*, in a similar way as for group-11 nanoclusters. The “excited” $5d^{10-x} 6s^x$ configuration results from a level crossing between $5d$ combinations and $6s$ combinations, the former transferring their electrons to the latter. This level crossing, which does not exist in the bare Pt_n clusters, is induced by the ligand shell, the role of which being thus not innocent with respect to metal–metal bonding. Our studies explored the frontier of *superatom* concept, which paved the road between the group-10 and group-11 cluster chemistry.

Finally, in Chapter 10, we report some experimental work on monolayer protected gold nanoparticles. We present the synthesis of 6-(amidoferrocenyl)hexanethiol (**FcSH**) ligands as

well as **FcSH** stabilized AuNPs (**FcSH-AuNPs**). The synthesized **FcSH-AuNPs** were characterized by UV-Vis spectroscopy and transmission electron microscopy. Indeed, the redox properties of **FcSH-AuNPs** were also investigated by cyclic voltammetry technique. The results show that the 6-(amidoferrocenyl)hexanethiol ligand could stabilize ultrafine AuNPs with very good stability and mono-dispersity. The synthesized **FcSH-AuNPs** show an ultrafine average size of 2 nm which is smaller than that of the previous reported mixed alkylthiolate and ferrocenylalkylthiolate ligand-protected AuNPs. The possible reason is that the large steric effect of the terminal ferrocenyl groups inhibits the further growth of the gold metallic kernel. **FcSH-AuNPs** show a broad plasmon band at 500 nm because of the short distance between particles. A clear signal in their cyclic voltammograms could be recorded, encouraging the fact that **FcSH-AuNPs** could be used in the design of derivatized electrode for sensing applications.

References

- 18 Jin, R.; Li, G.; Sharma, S.; Li, Y.; Du, X. Toward active-site tailoring in heterogeneous catalysis by atomically precise metal nanoclusters with crystallographic structures. *Chem. Rev.* **2020**, *121*, 567–648.
- 19 Kang, X.; Li, Y.; Zhu, M.; Jin, R. Atomically precise alloy nanoclusters: syntheses, structures, and properties. *Chem. Soc. Rev.* **2020**, *49*, 6443–6514.
- 20 Du, Y.; Sheng, H.; Astruc, D.; Zhu, M. Atomically precise noble metal nanoclusters as efficient catalysts: a bridge between structure and properties. *Chem. Rev.* **2019**, *120*, 526–622.
- 21 Chakraborty, P.; Nag, A.; Chakraborty, A.; Pradeep, T. Approaching materials with atomic precision using supramolecular cluster assemblies. *Acc. Chem. Res.* **2018**, *52*, 2–11.
- 22 Tao, Y.; Li, M.; Ren, J.; Qu, X. Metal nanoclusters: novel probes for diagnostic and therapeutic applications. *Chem. Soc. Rev.* **2015**, *44*, 8636–8663.
- 23 Shang, L.; Xu, J.; Nienhaus, G.U. Recent advances in synthesizing metal nanocluster-based nanocomposites for application in sensing, imaging and catalysis. *Nano Today* **2019**, *28*, 100767.
- 24 Zhang, B.; Wang, Z.; Zhang, C.; Wu, H.; Dang, S.; Du, J.; Song, Y.; Zhang, H.; Liu, J.; Nie, G. Gold Nanocluster-Modified Titanium Nitride for Ultrafast Photonics Applications. *Adv. Electron. Mater.* **2021**, *7*, 2000954.
- 25 Zeng, C.; Jin, R. Gold nanoclusters: size-controlled synthesis and crystal structures. *Gold Clusters, Colloids and Nanoparticles I* **2014**, 87–115.

- 26 Weerawardene, K. D. M.; Häkkinen, H.; Aikens, C. M. Connections between theory and experiment for gold and silver nanoclusters. *Annu. Rev. Phys. Chem.* **2018**, *69*, 205–229.
- 27 Häkkinen, H. Electronic shell structures in bare and protected metal nanoclusters. *Adv. Phys-X* **2016**, *1*, 467–491.
- 28 Fernando, A.; Weerawardene, K. D. M.; Karimova, N. V.; Aikens, C. M. Quantum mechanical studies of large metal, metal oxide, and metal chalcogenide nanoparticles and clusters. *Chem. Rev.* **2015**, *115*, 6112–6216.
- 29 Wade, K. The structural significance of the number of skeletal bonding electron-pairs in carboranes, the higher boranes and borane anions, and various transition-metal carbonyl cluster compounds. *J. Chem. Soc. Chem. Commun.* **1971**, 792–793.
- 30 Mingos, D. M. P.; Wales, D. J. *Introduction to cluster chemistry*. Prentice Hall: **1990**.
- 31 Stone, A. J. A new approach to bonding in transition metal clusters: theory. *Mol. Phys.* **1980**, *41*, 1339–1354.
- 32 Walter, M.; Akola, J.; Lopez-Acevedo, O.; Jadzinsky, P. D.; Calero, G.; Ackerson, C. J.; Whetten, R. L.; Grönbeck, H.; Häkkinen, H. A unified view of ligand-protected gold clusters as superatom complexes. *Proc. Natl. Acad. Sci. U. S. A.* **2008**, *105*, 9157–9162.
- 33 Häkkinen, H. Atomic and electronic structure of gold clusters: understanding flakes, cages and superatoms from simple concepts. *Chem. Soc. Rev.* **2008**, *37*, 1847–1859.
- 34 Knight, W.; Clemenger, K.; de Heer, W. A.; Saunders, W. A.; Chou, M.; Cohen, M. L. Electronic shell structure and abundances of sodium clusters. *Phys. Rev. Lett.* **1984**, *52*, 2141.

Chapter 1

Bonding Models in Cluster Compounds

1.1 Introduction

Atomically precise nanoclusters are currently a hot topic in nanoscience due to their distinct chemical and physical properties.¹⁻⁵ Their molecule-like and size-dependent properties, as well as the well-defined structures, provide opportunities to design building blocks for new nanomaterials with controllable structure and properties.⁶⁻¹⁰ In nanocluster synthesis, surface ligands play a crucial role.¹¹⁻¹³ On one hand, they stabilize the highly reactive metal surface of clusters. On the other hand, they also strongly influence the physical and chemical properties of the whole clusters. Thanks to the advanced single-crystal X-ray crystallographic techniques,¹⁴ lots of cluster compounds with detailed structure information have been reported,¹⁵⁻¹⁹ Indeed, these atom-precise structures can provide us ideas on the deeply understanding of the bonding mode and structure evolution pattern of more complicated nanomaterials, which can accelerate the design and discovery of new species.

In addition to experimental studies, nanoclusters have also attracted the interest of the theoreticians. A large number of investigations have been in turn concentrated on the relationship between their geometries, electronic structures and relative stabilities.²⁰⁻²⁷ For boranes, carboranes and main group and/or transition organometallic clusters, the geometrical structures have been systemically rationalized by a set of simple rules such as the *Polyhedral Skeletal Electron Pair Theory* (PSEPT), also known as the Wade-Mingos rules,²⁸⁻³⁰ which account for the relationship between the skeletal structure and its total number of skeletal electrons pairs. The foundations of this PSEPT theory were then underpinned by Stone with the *Tensor Surface Harmonic* (TSH) theory.³¹⁻³⁴ In short, TSH theory is related to the problem of an electron gas constrained to remain *over* the surface of a sphere, and this is why the original rules apply only to hollow pseudo-spherical (*closo*, *nido*, *arachno*...) clusters, although PSEPT is able to extend them to other cluster families³⁵ through *aufbau* processes based on capping and condensation principles.²⁸⁻³⁰

In the case of non-hollow, compact pseudo-spherical clusters, one has to rely on a somewhat different conceptual model, the so-called *spherical jellium* model,³⁶ which is based on the problem of an electron gas constrained to remain *inside* a sphere. Although well known within the physics community³⁷ for a long time, the *jellium* model is not so familiar to chemists. It was initially used to interpret mass spectrometry experiments on sodium Na_n clusters and other alkali clusters,³⁶ which exhibited particular abundance for specific numbers of alkali atoms ($n = 2, 8, 20, 40...$), which were called “magic numbers”.^{36, 38-40} The *jellium* model views a cluster

of atoms as a single large pseudo-atom with electron shell closings for 2, 8, 18, 20, 34, 40, 58, etc. electrons. This model was subsequently adapted to gold phosphine clusters by Mingos *et al.* in the 1980s.⁴¹⁻⁴⁸ In the 1990s, the relationships between the *jellium* model and the TSH theory were also used to interpret the geometries of clusters derived from *ab initio* calculations.^{49,50}

1.2 The *Spherical Jellium Model and Superatom Concept*

The *spherical jellium* model³⁶ provides the simplest approximation for the ionic background in the case of clusters, in which the detailed spatial distribution of the ions is replaced by a uniform positive charge distribution. Based on this qualitative model, the concept of *superatom*, which mimics the chemistry of the large three-dimensional cluster compounds with simple atoms, was developed.^{36, 51-55}

The Hamiltonian operator for a polyelectronic atom is recalled on the left side of Figure 1. The solutions of the Schrödinger equation for such a spherical system are polyelectronic functions that can be written on the basis of simple mono-electronic functions, the so-called atomic orbitals, which are the product of a spherical harmonic and a radial function. In the case of a molecule (middle of Figure 1), several nuclei (Z_p) are present. Thus, the spherical symmetry is broken and the polyelectronic solutions of the Schrödinger equation can no longer be written on the basis of atomic orbitals, all of them centered on the same nucleus. However, in the very specific case of a pseudo-spherical close-packed (compact) arrangement of the nuclei, the approximation of replacing the dense cloud of nuclei point charges by a smoothed (average) uniform positive potential of radial symmetry, $v(r)$, can be made (Figure 1, right side). This is the *spherical jellium* approximation. Thus, the resulting approximate Hamiltonian somewhat resembles that of the polyelectronic atom. Both reflect the spherical symmetry of their respective systems, and have their electron/nucleus (nuclei) interactions described by a radial potential. It follows that, as for the polyelectronic atom case, the solutions of the Schrödinger equation resulting from the *spherical jellium* approximation can be written on the basis of mono-electronic functions which are the product of a spherical harmonic and a radial function (Figure 1). These $\Psi_{n,l,m}$ functions are called “*jellium orbitals*” in the following sections. Their S, P, D, F... designation for $l = 0, 1, 2, 3, \dots$, respectively, was coined by Mingos *et al.* in the beginning of the 1980s.⁵⁶ Three important remarks should be made at this point.

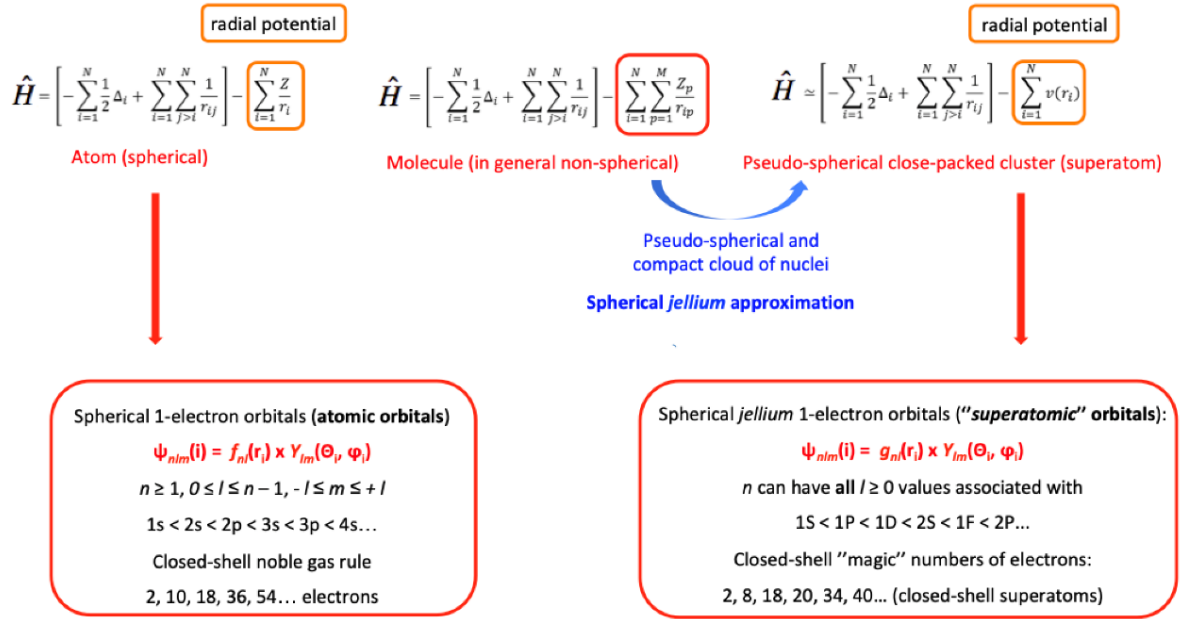


Figure 1. Main features of the spherical *jellium* approximation and *superatom* concept.

(i) It is important to keep in mind that the *spherical jellium* approximation is based on the assumption of pseudo-spherical symmetry *and* cluster compactness. Both conditions have to be satisfied simultaneously. Applying such a model to non-spherical clusters and/or to clusters with hollow cages is likely to lead to erroneous conclusions. In some cases, however, clusters with lower symmetries can be treated from the point of view of Jahn-Teller-distorted spheres.

(ii) Although the Hamiltonian operator of the polyelectronic atom and that of the *spherical jellium* approximation have related expressions, they differ by the nature of their radial potential. In the atomic case, it is in $1/r$, whereas in the *spherical jellium* formalism it is generally approximated to a rounded square potential, i.e., having a certain value inside the sphere, another one outside and some continuous function connecting these two regions (Woods-Saxon potential).⁵⁷ The *jellium* orbitals thus differ from the atomic orbitals by their radial functions. In particular, their principal number n conventionally starts at $n = 1$, regardless of the associated value of the angular momentum number l . The shell level ordering $1S < 1P < 1D < 2S < 1F < 2P < 1G < 2D < 1H \dots$ is rather independent of the mathematical expression and parameterization given to the radial potential $v(r)$. It is thus largely independent from the cluster nature, in the same way as the $1s < 2s < 2p < 3s < 3p \dots$ shell ordering in polyelectronic atoms is quasi-independent from the atom nature.

(iii) Since the *jellium* approximation consists of replacing the atomic nuclei by an average potential, there are no nuclei, no atoms, thus no atomic orbitals within the framework of this

approximation. Thus, the *jellium* orbitals are not combinations of atomic orbitals. In fact, the S, P, D, F... *jellium* orbitals have similar shapes as *s, p, d, f...* atomic orbitals, except that they expand significantly over a much larger space, that is within a volume of the order of magnitude of the cluster sphere. Nowadays in cluster chemistry, the *spherical jellium* approximation model is most often used at a qualitative level for the purpose of electron counting (see below). Modern quantum chemical calculations — usually performed at the density functional theory (DFT) level — are based on the linear combination of atomic orbitals (LCAO) approach. The question, which arises after such calculations is to identify among all the computed molecular (Kohn-Sham) orbitals (MOs), those that would have been obtained from quantitative calculations assuming the *spherical jellium* approximation, i.e., the *jellium* orbitals. Indeed, regular LCAO calculations on a given cluster will provide an orbital spectrum containing much more MOs than that corresponding to the *jellium orbitals*, such as those associated with atomic cores or ligand orbitals for instance. The DFT-computed orbital diagram of a bare centered icosahedral $I_h [Ag_{13}]^{5+}$ cluster is shown as an example in Figure 2, with its lowest *jellium* orbitals lying among and above the non-*jellium* 4d (Ag) combinations.²⁵

The chemical parentage in terms of their shell electronic structures and associated one-electron orbitals between polyelectronic atoms and clusters that can be described within this framework has been largely deepened at the turn of the last century, leading to the word of *superatom* to designate the latter species,^{51, 54, 58-61} their *jellium* orbitals being often referred as *superatomic orbitals*. As for any molecule, chemical stability (viability⁶²) of a *superatom* is expected to be reached when it will satisfy the closed-shell requirement with a significant HOMO–LUMO gap. The following configurations result from the successive filling of *jellium shells*:

$1S^2$ (2 electrons)

$1S^2 1P^6$ (8 electrons)

$1S^2 1P^6 1D^{10}$ (18 electrons)

$1S^2 1P^6 1D^{10} 2S^2$ (20 electrons)

$1S^2 1P^6 1D^{10} 2S^2 1F^{14}$ (34 electrons)

$1S^2 1P^6 1D^{10} 2S^2 1F^{14} 2P^6$ (40 electrons)

$1S^2 1P^6 1D^{10} 2S^2 1F^{14} 2P^6 1G^{18}$ (58 electrons)

etc.

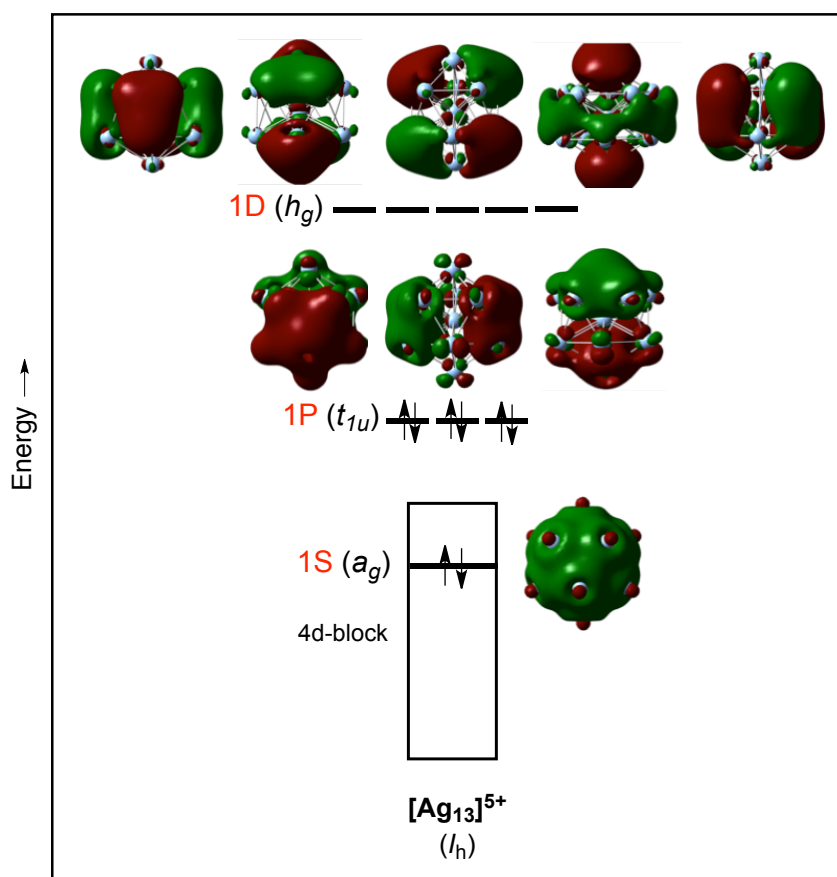


Figure 2. DFT-computed MO diagram of $I_h[Ag_{13}]^{5+}$ ($1S^2 1P^6$ configuration). Note that the $1S$ orbital is buried within the block of the *non-jellium* $4d$ combinations.²⁵

The closed-shell *jellium* electron numbers (2, 8, 18, 20, 34, 40, 58...) are referred to as the so-called “magic numbers” which provide the *superatom* with chemical stability. The similarity with the noble gas configurations (2, 10, 18, 36, 54... electrons), which confers stability to a neutral or ionic atom, is obvious.

Before addressing electron counting in specific late transition-metal clusters, let us illustrate our purpose with two historical milestones of the basic concepts. Both have been taken from aluminium cluster chemistry and show how the *superatom* concept can be applied to both bare and ligated cluster species. The first one concerns $[Al_{13}]^-$, which adopts the close-packed centered icosahedral structure $Al@Al_{12}$ (Figure 3, left), a common motif in *superatom* chemistry. Its peculiar stability was first recognised by Castleman and colls. from mass spectrometry experiments.⁵⁸ This bare cluster, which possesses $(13 \times 3) + 1 = 40$ valence electrons was shown by Khanna and Jena⁶³ to be a closed-shell *superatom* of *jellium* configuration $1S^2 1P^6 1D^{10} 2S^2 1F^{14} 2P^6$. The same authors computed the electron affinity of the neutral Al_{13} species (outer configuration $2P^5$) to show that it was comparable to that of a halogen,⁶⁰ and defined this cluster as a *superhalogen*.⁶⁴ The second example is the large ligated

$\text{Al}_{50}\text{Cp}^*_{12}$ compound ($\text{Cp}^* = \eta^5\text{-C}_5\text{Me}_5$), synthesized by Schnöckel and co-workers.⁶⁵ This cluster exhibits a rather compact pseudo-spherical structure (Figure 3, right) consisting of an inner Al_8 square antiprism encapsulated within an Al_{30} icosidodecahedron, the 12 pentagonal faces of which are capped by AlCp^* units (onion-like structure $\text{Al}_8@ \text{Al}_{30}@ (\text{AlCp}^*)_{12}$). Assuming the Cp^* ligands to be formally anionic, one is left with $(50 \times 3) - 12 = 138$ aluminium electrons, which is a *superatom* magic number. Indeed, DFT calculations performed later on by Clayborne *et al.* confirmed the $1\text{S}^2 1\text{P}^6 1\text{D}^{10} 2\text{S}^2 1\text{F}^{14} 2\text{P}^6 1\text{G}^{18} 2\text{D}^{10} 1\text{H}^{22} 3\text{S}^2 2\text{F}^{14} 3\text{P}^6 1\text{I}^{26}$ *superatomic* configuration, secured by a surprisingly large HOMO–LUMO gap.⁶⁶ Other *superatom* examples can be found in the rich metalloid-type chemistry developed by Schnöckel and collaborators.⁶⁷

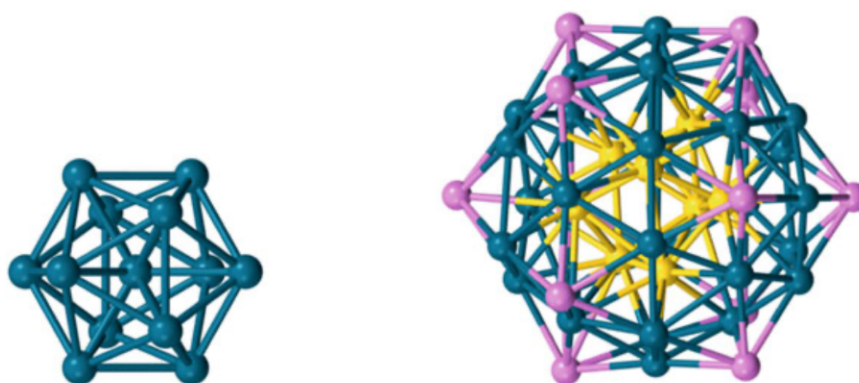


Figure 3. Structural arrangement of bare $[\text{Al}_{13}]^-$ (left) and $\text{Al}_{50}\text{Cp}^*_{12}$ [described as $\text{Al}_8@ \text{Al}_{30}@ (\text{AlCp}^*)_{12}$] (right) aluminium *superatoms*. Yellow, blue and pink spheres are Al atoms of the Al_8 , Al_{30} and Al_{12} shells, respectively. Surrounding Cp^* groups are omitted for clarity.²⁵

Some time ago, Mingos⁶⁸⁻⁷² and Teo⁷³ showed that this *jellium* model could also be particularly effective for understanding the structure and closed-shell electronic configuration of the large class of spherical or near-spherical ligated inorganic gold clusters. This is mostly due to the fact that in these species the metal–metal bonding is principally ensured by the $6s$ (Au) orbitals, whereas the participation of the occupied $5d$ (Au) ones can be neglected. Today, the *superatom* model is largely employed in the field of ligand-protected noble metal nanoclusters (not only gold, but also other coinage metals^{52-53, 74}). Recently, it has been also used to rationalize the bonding and stability of spherical ligated group-10 nanoclusters, despite the apparent zero-electron count for some of them (see Chapters 7-9 in this manuscript).^{25, 75-77} Some specific examples are discussed in the following sections.

1.3 Application of *Superatom* Concept in Group-11 Nanoclusters

1.3.1 Pseudo-spherical Nanoclusters

Among the group-11 metal triad, gold is certainly the most widely encountered in ligated nanocluster chemistry. In fact, as said above, the pioneering work in this field started in the eighties, with substantial contributions from Mingos' ⁶⁸⁻⁷² and Teo's ⁷³ groups. But the booming of gold cluster and nanocluster chemistry really started at the beginning of this century, in particular (but not only) with the general use of thiolate ligands as metal core-protecting ligands. ^{7, 78-84} In terms of structure rationalization, the major contributions have come from Häkkinen and co-workers who have shown that the stability of these species can be interpreted within the framework of the *superatom* concept. ^{52-53, 85} This unified view of ligand-protected gold clusters applies as well to the silver and copper nano-species which were characterized subsequently.

Bare $[M_n]^{x+}$ *superatomic* cations have little chance to be isolated as classical salts in a regular chemistry laboratory, not only because they usually bear an unrealistically large cationic charge, but also because there is an accepting radial (*sp*) orbital on each of the atoms occupying the vertices of its surface metal shell. For reaching chemical stability, the *superatomic* $[M_n]^{x+}$ core needs to be stabilized by a (sometimes complex) outer shell constituted of ligands and possibly additional metal centers. This is illustrated below with a few examples having the same 8-electron $[M_{13}]^{5+}$ ($M = Au, Ag$) icosahedral core, namely $[Au_{13}(dppm)_6]^{5+}$ ($dppm = 1,1$ -bis(diphenylphosphino)methane), ⁸⁶ $[Au_{13}(PMe_2Ph)_{10}Cl_2]^{3-}$, ⁷⁰ $[Au_{25}(SR)_{18}]^-$ ⁸⁷⁻⁸⁹ and $[Ag_{21}\{S_2P(OR)_2\}_{12}]^+$. ⁹⁰

On a bare $[Au@Au_{12}]^{5+}$ *superatom*, there are twelve accepting orbitals, one on each of the twelve atoms occupying the icosahedron vertices. The presence of these accepting orbitals creates unsaturation at the icosahedron surface, that needs to be released by bringing twelve two-electron terminal ligands on it. This condition is achieved in $[Au_{13}(dppm)_6]^{5+}$, ⁸⁶ where each of the twelve outer metal atoms is linked to a phosphine group (Figure 4, left). It is however not always easy to isolate highly charged cations such as $[Au_{13}(dppm)_6]^{5+}$, and balancing as much as possible the $[Au_{13}]^{5+}$ positive charge by using (at least in part) anionic ligands (halides for example), should be more appropriate. It turns out that the first ever isolated ligand-protected icosahedral gold *superatom* was $[Au_{13}(PMe_2Ph)_{10}Cl_2]^{3-}$ which consists of a $[Au_{13}]^{5+}$ core protected (passivated) by two (formally anionic) chlorides and twelve neutral phosphines (Figure 4, right). This historical cluster was isolated as its hexafluorophosphate salt by Mingos

in the early 1980's.⁷⁰ Since then, several $[\text{Au}_{13}\text{L}_{12-n}\text{X}_n]^{(5-x)-}$ (L = neutral two-electron ligand; X = halogen; $n = 2-6$) clusters have been isolated.^{70, 91-97}

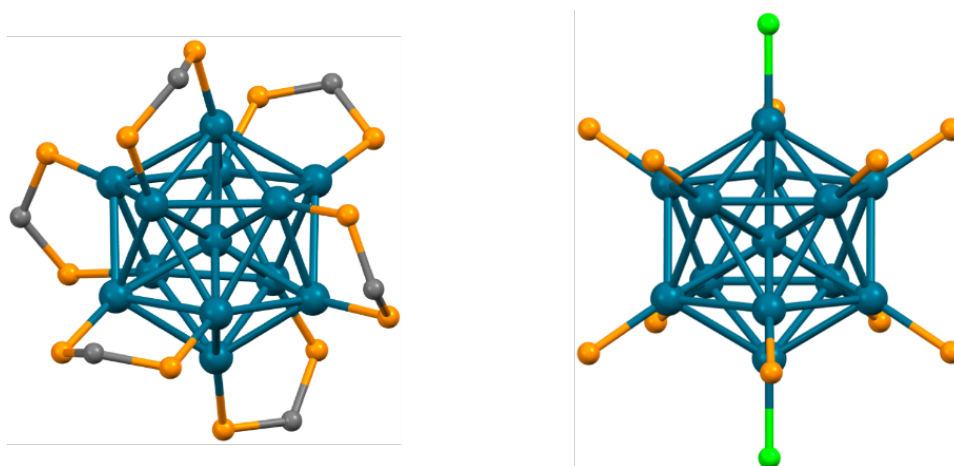


Figure 4. Structural arrangement of $[\text{Au}_{13}(\text{dppm})_6]^{5+}$ (left) and $[\text{Au}_{13}(\text{PMe}_2\text{Ph})_{10}\text{Cl}_2]^{3-}$ (right). H, Me and Ph groups are omitted for clarity. Atoms forming the *superatomic* icosahedral $[\text{M}_{13}]^{5+}$ core are in blue. Outer C, P and Cl atoms are in grey, orange and green, respectively.

More complex passivating outer shells are usually found in the chemistry of chalcogenolate-protected Au and Ag *superatoms*. Such compounds are usually prepared by reducing Au(III), Au(I) or Ag(I) salts (with sodium borohydride, for example) in the presence of chalcogenolates, usually thiolates (SR^-). Thus, the reaction medium is rich in M(0), M(I) and thiolates (SR^-), favoring the formation of mixed-valent $[\text{M}_n]^{x+}$ *superatomic* kernels that are seeking for the unsaturation release by coordinating thiolates. One can imagine, for example, that an $[\text{Au}_{13}]^{5+}$ icosahedral kernel, could readily coordinate twelve terminal thiolates to satisfy this unsaturation. Now, one is left with a tentative $[\text{Au}_{13}(\text{SR})_{12}]^{7-}$ composition. The negative charge is not realistic and needs to be balanced by additional positively charged components. The medium is rich in Au(I) cations, and because thiolates are prone to make two S-M bonds ($\mu_2\text{-SR}$), one could imagine extra (6, 7 or 8?) Au(I) atoms that would bridge the 12 sulfur atoms of $[\text{Au}_{13}(\text{SR})_{12}]^{7+}$. It turns out that the terminal thiolates are much too far apart for satisfying such a condition. In fact, supplementary S'R thiolates are enlisted to make $[\text{Au(I)-S'(R)-Au(I)}]^+$ units that bridge the 12 sulfur atoms terminally bonded to the icosahedron (here, the prime symbol labels sulfurs non-attached to the icosahedron). There are six $[\text{Au(I)-S'(R)-Au(I)}]^+$ extra units that bridge six S...S pairs of the 12 sulfur atoms in $[\text{Au}_{13}(\text{SR})_{12}]^{7+}$. They make S-Au-S'-Au-S staples that are clipped onto the 12 gold atoms. In these staples, the Au(I) metals are linearly coordinated, making locally stable 14-electron metal centers. In fact, they cap 12 among the 20 triangular

faces of the icosahedron, but the corresponding interactions, rather weak and largely of metallophilic nature, can be neglected, at least in first approximation. Thus, with one $[\text{Au}_{13}]^{5+}$ *superatomic* core and an outer shell made of 12 $\text{SR}^- + 6 \text{S}'\text{R}^-$ ligands and 12 additional Au^+ metal atoms, the final composition $[\text{Au}_{25}(\text{SR})_{18}]^-$ satisfy the unsaturation of all its components, together with approaching electroneutrality. The ideal symmetry of the whole $[\text{Au}_{25}(\text{SR})_{18}]^-$ cluster is S_6 .

We continue now with an icosahedral $[\text{Ag}_{13}]^{5+}$ *superatomic* core and a dithiophosphate-rich medium. $[\text{S}_2\text{P}(\text{OR})_2]^-$ dithiophosphates (dtp^-) are bidentate dithiolato ligands which bear a single anionic charge. Since dtp ligands ($\text{S}\dots\text{S} \sim 3.4 \text{ \AA}$) cannot bind to two icosahedral Ag neighbors ($\text{Ag}-\text{Ag} \sim 2.8 \text{ \AA}$), one is left with the $[\text{Ag}_{13}(\text{dtp})_{12}]^{7-}$ intermediate composition. Assuming that each sulfur atom seeks for the donation of two lone pairs, there are still $12 + 2 \times 12 = 36$ sulfur lone pairs available for complexation by extra $\text{Ag}(\text{I})$ atoms. $\text{Ag}(\text{I})$ likes trigonal planar coordination, but the spatial constraints do not allow the formation of such 12 peripheral 16-electron centers by the addition of 12 supplementary $\text{Ag}(\text{I})$ ions, which moreover would push the cluster charge to the large value of +5. Rather, only 8 additional $\text{Ag}(\text{I})$ ions are allowed to coordinate sulfur lone pairs in a trigonal planar mode, leaving 12 (among 36) uncoordinated sulfur lone pairs in the cluster final composition $[\text{Ag}_{21}(\text{dtp})_{12}]^+$ of modest cationic charge. The possibility of exchange between complexed and non-complexed lone pairs allows the occurrence of isomery by changing the outer shell topology, without perturbing significantly the $[\text{Ag}_{13}]^{5+}$ core. So far, structures of T_d , C_3 and C_1 symmetry have been isolated with different dithiophosphates and dithioselenates.^{81, 98-101} In certain conditions, some of these species can lose one of their outer Ag^+ cations leading to the $[\text{Ag}_{20}(\text{dtp})_{12}]$ species, which satisfy perfect neutrality, but to the detriment of losing three $\text{Ag}(\text{I})-\text{S}$ bonds.¹⁰² Generalizing the above examples, and at the risk of oversimplifying, chemically stable, isolable inorganic group-11 metal *superatoms* can be conceptually described as made of two components:

(i) The compact pseudo-spherical M_x ($\text{M} = \text{Cu}, \text{Ag}, \text{Au}$) cluster core, which is the *superatomic* part of the nano-molecules. Most often, the average oxidation state of M in the core is comprised between 0 and +I ($[\text{M}_x]^{m+}$, $0 \leq m < x$). If it was +I for all M atoms, then they all would have an $nd^{10}(n+1)s^0$ configuration and hardly any $\text{M}-\text{M}$ bonding would be possible since all the d orbital combinations would be formally occupied. Thus $(n+1)s$ valence electrons are needed for ensuring $\text{M}-\text{M}$ bonding, but not too many to avoid filling antibonding $(n+1)s$ combinations. This is why the M average oxidation state is generally slightly higher than zero. Thus, in the case of group-11 clusters, the number of metallic $(n+1)s$ electrons can be identified as the number of *jellium* electrons (sometimes called *free* electrons), i.e., those responsible for

cluster bonding.^{69, 103} Consistently, in a first approximation, the combinations of the metallic ($n + 1$) s AOs can be identified as counterpart MOs of *jellium* (or *superatomic*) orbitals, independently from their occupation number. Of course, these ($n + 1$) s combinations afford some mixing with metallic occupied nd and vacant ($n + 1$) p AOs, but as far as electron counting is concerned, the ($n + 1$) s combinations of the metallic core can be considered as corresponding to *jellium* orbitals. In many cases, a simple 3-dimensional Hückel calculation of the $[M_x]^{m+}$ core (i.e., considering isotropic s orbitals) can provide the favored *superatomic jellium* configuration. At this point, it is easy to understand why in the $[M_x]^{m+}$ core the M average oxidation state cannot be lower than zero. With $M(0)$ atoms, $x/2 =$ half of the ($n + 1$) s combinations are occupied. This is the limit case where the number of bonding and antibonding ($n + 1$) s combinations are equal. In general, in close-packed spherical systems the number of bonding combinations is lower than $x/2$, all the other ones being antibonding.

(ii) The peripheral protecting (passivating) ligand shell. As a whole, its total formal charge is generally negative to compensate the formal cationic charge of the metal core. This negative charge comes generally from ligands that are considered as formally anionic from the point of view of oxidation states, i.e., hydrides (H^-), halogenides (X^-), thiolates (SR^-), alkynyls (CCR^-), etc. Neutral ligands such as phosphines or N-heterocyclic carbenes (NHCs) can also be present. The metal atoms that belong to the $[M_x]^{m+}$ *superatomic* core and that lie on its interface, are generally bonded to one ligand. An important point to notice is that, as far as thiolates are present, in many cases the peripheral protecting “ligand” shell contains also supplementary metal centers (see above). These metal atoms can be considered as being in their +I oxidation state. They are generally only weakly bonded to the $[M_x]^{m+}$ *superatomic* core (mainly *via* metallophilic interactions) and strongly bonded to two or three sulfur atoms, making the so-called “staples”. Their role is to satisfy the nucleophilic demand of extra sulfur lone pairs and/or to participate to the total charge balance, owing to the fact that the charge of an isolable inorganic molecule is most often equal or close to zero.

Thus, the structure and chemical composition of such atom-precise nanoclusters is the result of a non-trivial compromise between M–M bonding within the *superatomic* core, M–ligand bonding, charge balance and steric requirements. To illustrate this complexity, we go back to the structures and electron counts of the two related nanocluster species discussed above,, namely $[Au_{25}(SR)_{18}]^-$ ($R = CH_2CH_2Ph$,⁸⁸ Me ⁸⁹) and $[Ag_{21}[S_2P(OR)_2]_{12}]^+$ ($R = ^iPr$ ⁹⁰) (Figure 5). The *superatomic* cores of both clusters are similar, i.e., exhibiting a close-packed centered icosahedral M_{13} ($M@M_{12}$) arrangement ($M = Ag, Au$) of ideal I_h symmetry, with a formal charge of +5. These $[M_{13}]^{5+}$ cores are 8-electron *superatoms* with $1S^2 1P^6$ closed-shell

configuration (see Figure 2). It is of note that combining 13 *s*-type AOs in I_h symmetry leads to 4 bonding MOs ($a_g + t_{1u}$) and 9 antibonding MOs ($h_g^* + a_g^* + t_{2u}^*$). Thus, the most favored closed-shell electron number for such a system is 8. The 1S, 1P, 1D and 2S *jellium* orbitals can be identified as the a_g , t_{1u} , h_g^* and a_g^* combinations, respectively, whereas the t_{2u}^* level can be associated with a part of the seven-fold 1F manifold (the number of *jellium* orbitals is infinite, while that of the $(n + 1)s$ combinations is not). As said above, the peripheral shell of $[\text{Au}_{25}(\text{SR})_{18}]^-$ is composed of 18 formally anionic thiolate ligands and 12 formally cationic gold atoms, leading to the global composition $[\text{Au}_{12}(\text{SR})_{18}]^{6-}$ for the protecting shell. Each peripheral Au(I) atom is bonded to two sulfur atoms in an approximately linear coordination, making a local stable 14-electron center. With the sulfur atoms they are bonded to, these peripheral metal atoms form “–S–Au–S–Au–S–” staples that are clipped onto the central icosahedral Au_{13} core, making each of its 12 Au vertices radially bonded to one sulfur atom (see Figure 5). From a structural point of view, the 12 outer Au(I) centers are capping 12 of the 20 icosahedral faces of the Au_{13} core, *via* weak interactions being mainly of aurophilic nature.

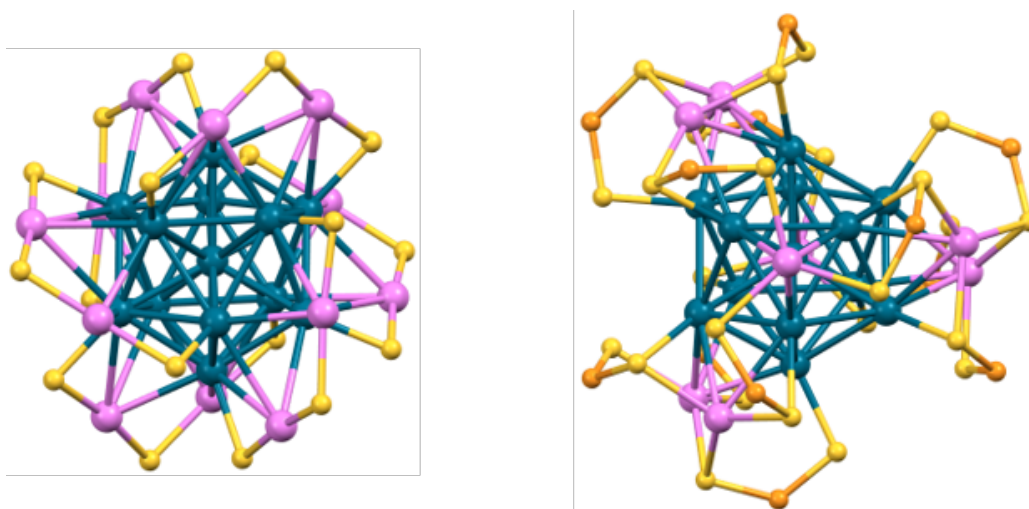


Figure 5. Structural arrangement of $[\text{Au}_{25}(\text{SR})_{18}]^-$ ($\text{R} = \text{CH}_2\text{CH}_2\text{Ph}$, Me) (left) and $[\text{Ag}_{21}\{\text{S}_2\text{P}(\text{OR})_2\}_{12}]^+$ ($\text{R} = {}^i\text{Pr}$) (right). R and OR groups are omitted for clarity. Atoms forming the *superatomic* icosahedral $[\text{M}_{13}]^{5+}$ core are in blue. Outer M(I), S and P atoms are in purple, yellow and orange, respectively.²⁵

The peripheral shell of $[\text{Ag}_{21}\{\text{S}_2\text{P}(\text{OR})_2\}_{12}]^+$ is composed of 12 formally mono-anionic dithiophosphate ($\text{dtp} = \text{S}_2\text{P}(\text{OR})_2$) ligands and 8 peripheral formally cationic silver atoms, leading to the global composition $[\text{Ag}_8\{\text{S}_2\text{P}(\text{OR})_2\}_{12}]^{4+}$ for the protecting shell. Each of these peripheral Ag(I) atoms is bonded to three sulfur atoms in an approximately planar trigonal coordination, making local stable 16-electron centers. These 8 peripheral Ag(I) atoms are

capping in a *metallophilic* bonding fashion 8 out of the 20 icosahedral faces of the Ag_{13} icosahedral core. Finally, each of the 12 Ag atoms of the icosahedral core is radially mono-coordinated to a sulfur atom. The orbital diagram of the $[\text{Ag}_{21}\{\text{S}_2\text{PH}_2\}_{12}]^+$ model used to mimic $[\text{Ag}_{21}\{\text{S}_2\text{P}(\text{OR})_2\}_{12}]^+$ is shown in Figure 6. A comparison with that of its $[\text{Ag}_{13}]^{5+}$ core (Figure 2) indicates that the peripheral shell does not destroy the *superatomic* nature of the cluster.⁹⁰

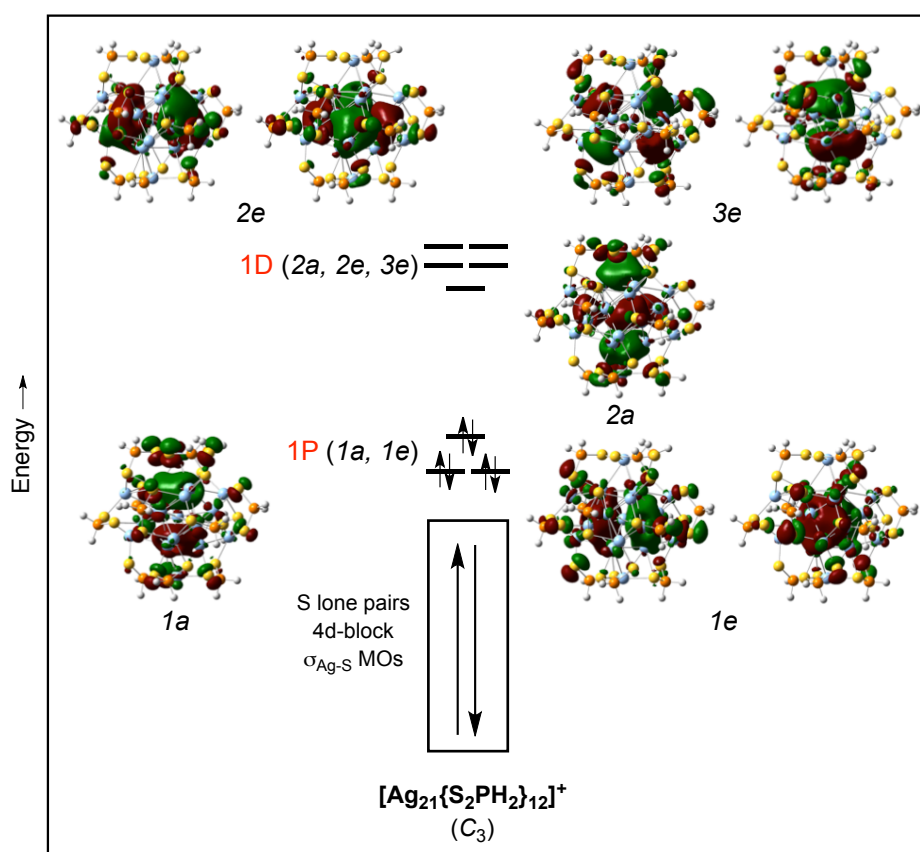


Figure 6. DFT-computed MO diagram of the model $[\text{Ag}_{21}\{\text{S}_2\text{PH}_2\}_{12}]^+$ of C_3 symmetry. MO plots correspond to the 1P ($1a + 1e$) and 1D ($2a + 2e + 3e$) *jellium* (*superatomic*) orbitals. See Figure 3 for a comparison with $I_h[\text{Ag}_{13}]^{5+}$.²⁵

Thus, although being related through their 8-electron *superatomic* nature, $[\text{Au}_{25}(\text{SR})_{18}]^-$ and $[\text{Ag}_{21}\{\text{S}_2\text{P}(\text{OR})_2\}_{12}]^+$ differ substantially by their peripheral protecting shells due to the different nature of their ligands. Although both thiolate and dtp ligands are formally mono-anions, they differ from their number of coordinating S centers (one vs. two) and by their space occupancy (assuming similar R groups, one dtp ligand is less bulky than two thiolate ones). The two clusters differ also from the preference of Au(I) for a linear coordination and Ag(I) for a trigonal coordination. It is also noteworthy that the peripheral shells are subject to potential

isomerism,^{89, 102, 104-105} leading to different topologies, all of them maintaining the major bonding features discussed above.

Apart from the singularity of their peripheral protecting shell, group-11 nanoclusters are most often easy to identify with respect to the nature of their *superatomic* core and their *jellium* electron count. A few selected examples are provided in Table 1. To this list, one could add the bare (non-ligated) neutral Au₂₀ cluster of tetrahedral symmetry,¹⁰⁶ which illustrates the Au(0) lowest limit case of metal oxidation state. This gas phase species is of course metastable with respect to aggregation.

Table 1. Selected examples of structurally characterized closed-shell homometallic group 11 *superatomic* clusters.

Compound	<i>Jellium</i> electron number	<i>Jellium</i> configuration	<i>Superatomic</i> core
[Cu ₁₃ {S ₂ CNR ₂ } ₆ (CCR') ₄] ⁺ ₁₀₁	2 (13 – 6 – 4 – 1)	1S ²	[Cu ₁₃] ¹¹⁺ centered cuboctahedron
[Cu ₂₅ H ₂₂ (PR ₃) ₁₂] ⁺ ₁₀₇	2 (25 – 22 – 1)	1S ²	[Cu ₁₃] ¹¹⁺ centered icosahedron
[Au ₁₃ (PR ₃) ₁₀ Cl ₂] ³⁺ ₇₀	8 (13 – 2 – 3)	1S ² 1P ⁶	[Au ₁₃] ⁵⁺ centered icosahedron
[Ag ₄₄ (SR) ₃₀] ⁴⁻ ₁₀₈	18 (44 – 30 + 4)	1S ² 1P ⁶ 1D ¹⁰	icosahedral [Ag ₁₂ @Ag ₂₀] ¹⁴⁺
[Ag ₄₆ (PR ₃) ₈ (SR) ₂₄] ²⁺ ₁₀₉	20 (46 – 24 – 2)	1S ² 1P ⁶ 1D ¹⁰ 2S ²	fcc-related [Ag ₃₈] ¹⁸⁺
Au ₆₈ (SR) ₃₄ ¹¹⁰	34 (68 – 34)	1S ² 1P ⁶ 1D ¹⁰ 2S ² 1F ¹⁴	[Au ₁₉ @Au ₃₀] ¹⁵⁺ Marks-decahedron
Au ₁₀₂ (SR) ₄₄ ¹¹¹	58 (102 – 44)	1S ² 1P ⁶ 1D ¹⁰ 2S ² 1F ¹⁴ 2P ⁶ 1G ¹⁸	[Au ₈₀] ²²⁺ Marks-decahedron-like

Very large ligand-protected Au and Ag clusters have been so far structurally characterized (up to more than 300 metal atoms).¹¹¹⁻¹¹⁸ Such huge species do not always obey the “magic” *jellium* electron number rule. Several reasons can be invoked to explain these exceptions.

(i) The cluster shape is not spherical enough for the strict application of the *spherical jellium* approximation. However, in some cases, the electron count can be rationalized from the point of view of the removal of *jellium* shell degeneracies by specific geometries with lower symmetry.

(ii) The cluster charge is not always precisely known. In particular, it can be difficult to clearly identify in the X-ray structure the (possibly disordered) small counter-ions in the vicinity of the huge nanocluster. One could remark for example that the X-ray characterized

$\text{Ag}_{211}(\text{SR})_{71}(\text{PPh}_3)_6\text{Cl}$ (139 electrons)¹¹² when computed as a cationic species, presents a significant HOMO–LUMO gap for the 138-electron count, which is by the way (and perhaps accidentally), a “magic” electron number.

(iii) When the metal core increases in size, the favored HOMO–LUMO gap tends to decrease, leading to a ‘metallic’ situation over a certain size limit.¹¹⁹⁻¹²⁰ In other words, the *superatomic jellium* levels start to coalesce developing a *band structure*. This limit is not clear-cut, since it depends on several parameters such as the metal and ligand nature and the intimate structure of the core. The metallic or near-metallic situation is often accompanied with a plasmonic behavior. For example, $\text{Au}_{246}(\text{SR})_{80}$ has been reported to be non-metallic with a small band gap, based on UV/Vis and femtosecond transient absorption spectroscopic as well as electrochemical measurements.¹¹⁶ Later, the same authors found a non-metallic–to–metallic transition when going from $\text{Au}_{246}(\text{SR})_{80}$ to $\text{Au}_{279}(\text{SR})_{84}$ with nascent surface plasmonic resonance.¹¹⁷ Similarly, calculations on the structurally related $[\text{Ag}_{136}(\text{SR})_{64}\text{Cl}_3]^-$ and $\text{Ag}_{374}(\text{SR})_{113}\text{Br}_2\text{Cl}_2$ nanoclusters have shown that the former exhibits a significant HOMO–LUMO gap, whereas it is closed for the latter. On the other hand, both show plasmonic behaviour.¹¹⁸

1.3.2 Non-spherical Nanoclusters

1.3.2.1 Unconventional Electron Counts Stabilized by Lowering of Symmetry

In the same way as simple transition-metal complexes can afford Jahn-Teller distortion away from ideal symmetry when their electron count deviates from that satisfying the *effective atomic number* (EAN) rule, *superatoms* can also distort away from sphericity when their *jellium* electron count is not equal to a *superatom* closed-shell *magic* number. In such cases, simple oblate (flattening) or prolate (elongating) distortions come obviously to mind. The 6-electron $\text{MAu}_{24}(\text{SR})_{18}$ (M = Pd, Pt) species constitute nice examples of oblate distorted structures. Indeed, their structure is related to the 8-electron di-anionic forms $[\text{MAu}_{24}(\text{SR})_{18}]^{2-}$ which are isoelectronic and isostructural to the homometallic $[\text{Au}_{25}(\text{SR})_{18}]^-$ cluster.⁸⁸⁻⁸⁹ Whereas the centered icosahedral $[\text{M}@\text{Au}_{12}]^{4+}$ *superatomic* core in the dianions adopts a regular icosahedral shape, their neutral six-electron counterparts exhibit a flattened centered icosahedral $[\text{M}@\text{Au}_{12}]^{6+}$ core.¹²¹⁻¹²² This oblate distortion was first predicted by DFT calculations¹²¹ and later proven by X-ray diffraction measurements.¹²² It causes a two-below-one splitting of the three nearly degenerate 1P HOMOs in the undistorted core (of idealized t_{1u} symmetry; see Figure 2), thus opening a HOMO–LUMO gap which allows stabilizing the *non-magic* 6-

electron $1S^2 1P^4$ closed-shell configuration (Figure 7). However, both the flattening distortion and HOMO–LUMO gap are moderate, indicative of some cluster frustration with respect to not reaching the *magic* 8-electron count.⁴¹⁻⁴⁸

Clusters with structures much farther away from sphericity can still sometimes be described as distorted *superatoms* with unconventional *jellium* configuration. This is the case for example of the very prolate 6-electron cluster $[Cu_{10}Zn_2](mesitylene)_6(Cp^*)_2$, the *jellium* configuration of which was shown by DFT calculations to be $1S^2 1P^2 2S^2$.¹²³ It should be noted that oblate or prolate distortions are not necessary for inducing removal of *jellium* shell degeneracy. The sphere is more symmetrical than any finite (even “pseudo”-spherical) molecular object. A typical example is the 12-electron $Au_{36}(SR)_{24}$ cluster, which possesses a tetrahedral Au_{28} core. In T_d symmetry, the 1D shell splits into two components (e below t_2), leading to the closed-shell configuration $1S^2 1P^6 1D_e^4$.¹²⁴ In this particular case, the deviation away from sphericity is sufficiently large for inducing a degeneracy splitting that is strong enough to favor an unconventional electron count. This is of course, not a general case.

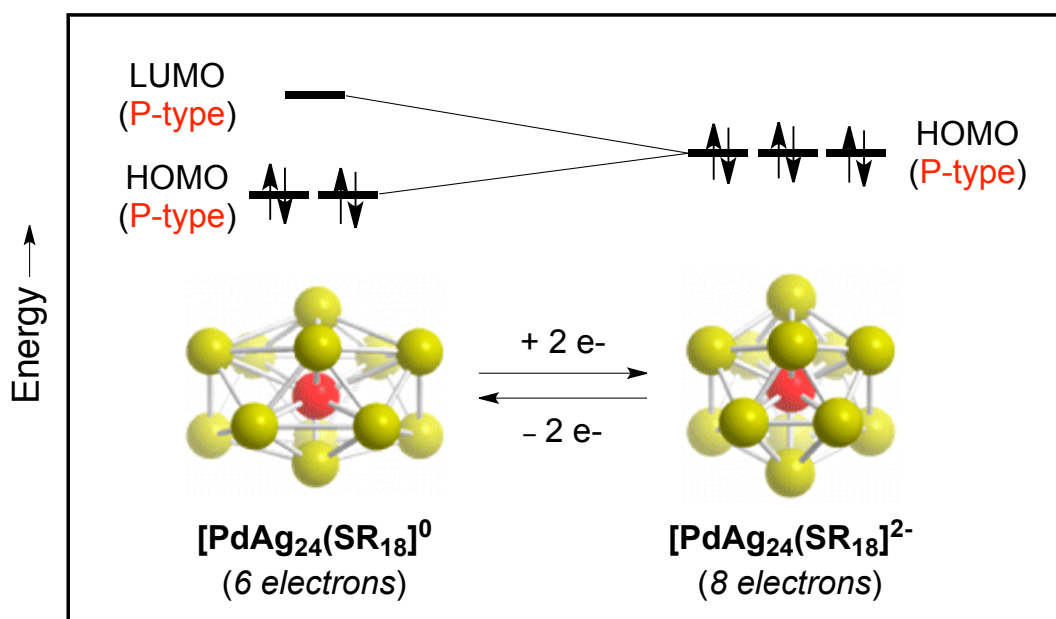


Figure 7. Jahn-Teller distortion associated with the stabilization of the 6-electron cluster $Pd@Au_{12}(SR)_{18}$.¹²¹

There are also a few cases that still escape from any general electron counting scheme that could be related in a simple way to the *spherical jellium* model, as exemplified by the very nice oblate 30-electron cluster $[Au_8Ag_{57}(Dppp)_4(C_8H_{11}S)_{32}Cl_2]^+$ ($Dppp=1,3$ -bis(diphenylphosphino)propane).¹²⁵ DFT calculations found the closed-shell *jellium*

configuration $1S^2 1P^6 1D^8 2S^2 2P^4 1F^4 1G^4$, which suggests an intermediate situation between the spherical (3D) and planar (2D) *jellium* approximations.¹²⁶

1.3.2.2 Assemblies of *Superatoms* (*Supermolecules*)

There is a rapid growing family of definitely non-spherical group-11-rich nanoclusters where the structure can be described as resulting from the assembly of several pseudo-spherical (mainly icosahedral) basis units. Teo and co-workers noticed it a long time ago and proposed the concept of *clusters of clusters* for its rationale.^{127,128} In fact, in many cases it is possible to describe such assemblies of pseudo-spherical *superatomic* units as “*supermolecules*”,⁸³ in the same way as one looks at molecules as being composed of electron-sharing atoms with electron counts related the bond order, i.e., to the degree of fusion between the atoms/*superatoms*.^{5, 129-136}

With respect to gold-rich clusters made of two fused centered icosahedra, Mingos elegantly proposed in 2015¹²⁹ to extend the Mulliken’s *united atom* model used for diatomics¹³⁷⁻¹⁴⁰ to clusters to show the analogy between their total *jellium* electron numbers and the valence electron counts of stable main-group diatomic orbitals. Indeed, fusion of polyhedra provides the equivalent of compression (i.e., bond order) for simple diatomic molecules.¹²⁹ The major conceptual developments of what he called a *united cluster* approach are illustrated for a series of homo- and heterometallic nanoclusters in Table 2 and Figure 8. Consider first the closed-shell $Au_{38}(SR)_{24}$ cluster for example.¹⁴¹ Its total number of *jellium* ($6s$ (Au)) electrons is $38 - 24 = 14$. These 14 *jellium* electrons are associated to the $[Au_{23}]^{9+}$ core of the cluster made of two $Au@Au_{12}$ icosahedra that share a triangular face (see Table 2 and Figure 8). The other 15 Au atoms are peripheral Au(I) centers, mainly bonded to sulfur atoms and belonging to the protecting shell, together with the 24 formally anionic thiolate ligands. The analogy with the 14-electron closed-shell F_2 molecule is straightforward. It can be shown in turn that in the bare $[Au_{23}]^{9+}$ core, the combinations of the $6s$ (Au) orbitals can be described as combinations of the *superatomic* (or *jellium*) $1S$ and $1P$ orbitals of the two individuals icosahedral *superatoms*, in the same way as the $2s$ and $2p$ AOs of fluorine combine in F_2 , leading to the same $1\sigma_g^2 1\sigma_u^2 \pi_u^4 2\sigma_g^2 \pi_g^4 2\sigma_u^0$ electron configuration. Such *supermolecular* orbitals can still be identified in the entire $Au_{38}(SR)_{24}$ cluster.

An important parameter affecting the *supermolecule* electron count is its degree of fusion (vertex-sharing, face-sharing or interpenetrating) in a similar way as the bond order does for main group molecules.¹²⁹ For example, $[Au_{17}Ag_2(NO_3)_9(PMe_2Ph)_{10}]^+$ ¹⁴² has an $[Au_{17}Ag_2]^{9+}$ core made of two interpenetrating icosahedra (Table 2 and Figure 8) and its *jellium* electron

count is similar to the electron count of the triply bonded N_2 molecule. On the other hand, the much less compact $[Au_{13}Ag_{12}]^{9+}$ core in $[Au_{13}Ag_{12}Br_8(Ptol_3)_{10}]^+$ ¹³⁵ consists of two icosahedra sharing one vertex and its *jellium* electron count is that of a van der Waals $(Ne)_2$ molecule (bond order = 0) (Table 2 and Figure 8). To the best of our knowledge, no intermediate 12-electron bis-icosahedral *supermolecule* with an open-shell configuration analogous to that of O_2 has been reported so far. Interestingly however, Tsukuda and co-workers reported recently the 12-electron $MM'Au_{36}(SR)_{24}$ species ($M, M' = Pd, Pt$) which exhibits an $[MM'Au_{21}]^{9+}$ core made of two centered icosahedra sharing one face.¹⁴³ However, its structure is somewhat C_{2v} Jahn-Teller distorted, resulting in a splitting of the *superatomic* π_g level and a $\pi_g(x)^2 \pi_g(y)^0$ closed-shell situation.

Table 2. Mingos' analogy between diatomic molecules and group-10 clusters made of two fused centered icosahedra.

Diatomic molecule	N_2	O_2	F_2	$(Ne)_2$
Number of electrons	$10 = 2 \times 8 - 6$	$12 = 2 \times 8 - 4$	$14 = 2 \times 8 - 2$	$16 = 2 \times 8$
Bond order	3	2 (Triplet states)	1	0 (van der Waals)
Example of analogous cluster	$[Au_{17}Ag_2(NO_3)_9(PMe_2Ph)_{10}]^+$ ¹⁴²	So far unknown	$Au_{38}(SR)_{24}$ ¹⁴¹	$[Au_{13}Ag_{12}Br_8(Ptol_3)_{10}]^+$ ¹³⁵
Electron configuration ^a	$1\sigma_g^2 1\sigma_u^2 \pi_u^4 2\sigma_g^2 \pi_g^0 2\sigma_u^0$	$1\sigma_g^2 1\sigma_u^2 \pi_u^4 2\sigma_g^2 \pi_g^2 2\sigma_u^0$	$1\sigma_g^2 1\sigma_u^2 \pi_u^4 2\sigma_g^2 \pi_g^4 2\sigma_u^0$	$1\sigma_g^2 1\sigma_u^2 \pi_u^4 2\sigma_g^2 \pi_g^4 2\sigma_u^2$
Core structure ^b	interpenetrated $2 \times 13 - 5 - 1 - 1 = 19$ atoms $[Au_{17}Ag_2]^{9+}$		face-sharing $2 \times 13 - 3 = 23$ atoms $[Au_{23}]^{9+}$	edge-sharing $2 \times 13 - 1 = 25$ atoms $[Au_{13}Ag_{12}]^{9+}$

^a The energy ordering of the occupied levels is arbitrary. ^b Encapsulated and shared atoms are in green and red, respectively.

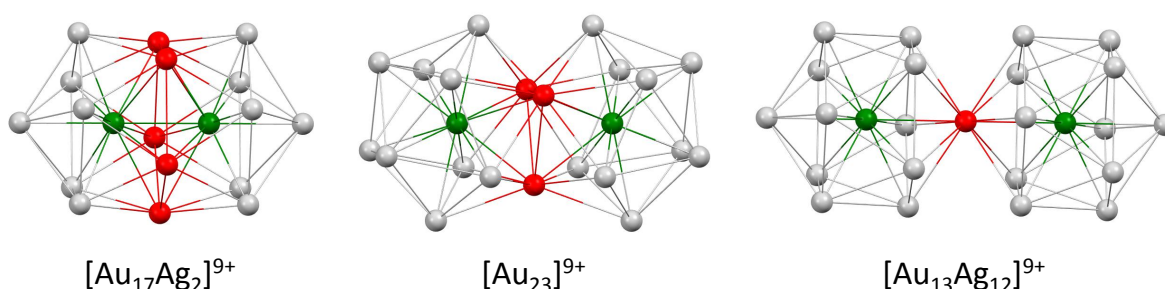


Figure 8. Core structures of some clusters resulting from the condensation of centered icosahedral clusters *via* vertex sharing ($[Au_{13}Ag_{12}Br_8(Ptol_3)_{10}]^+$, right), face sharing ($Au_{38}(SR)_{24}$, middle), and interpenetration ($[Au_{17}Ag_2(NO_3)_9(PMe_2Ph)_{10}]^+$, left). Encapsulated and shared atoms are in green and red, respectively.

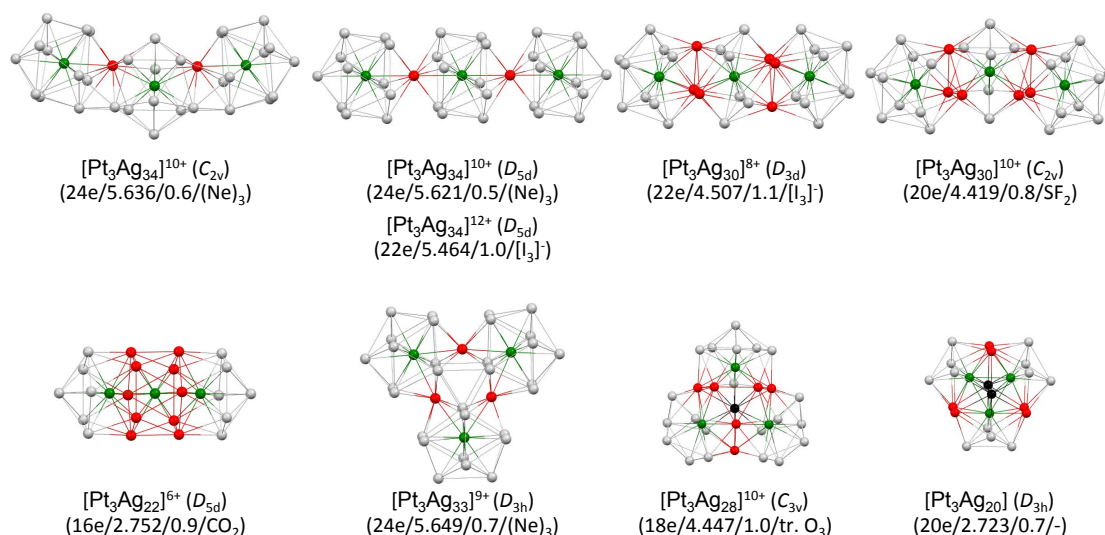


Figure 9. Stable closed-shell assemblies made of three fused icosahedra.¹²⁶ Pt atoms are in green, and silver atoms in red and black are shared between two and three icosahedra, respectively. Electron count, $d_{\text{Pt-Pt}}$ (Å), HOMO–LUMO gap (eV), and *isolobal* molecule are given in brackets.

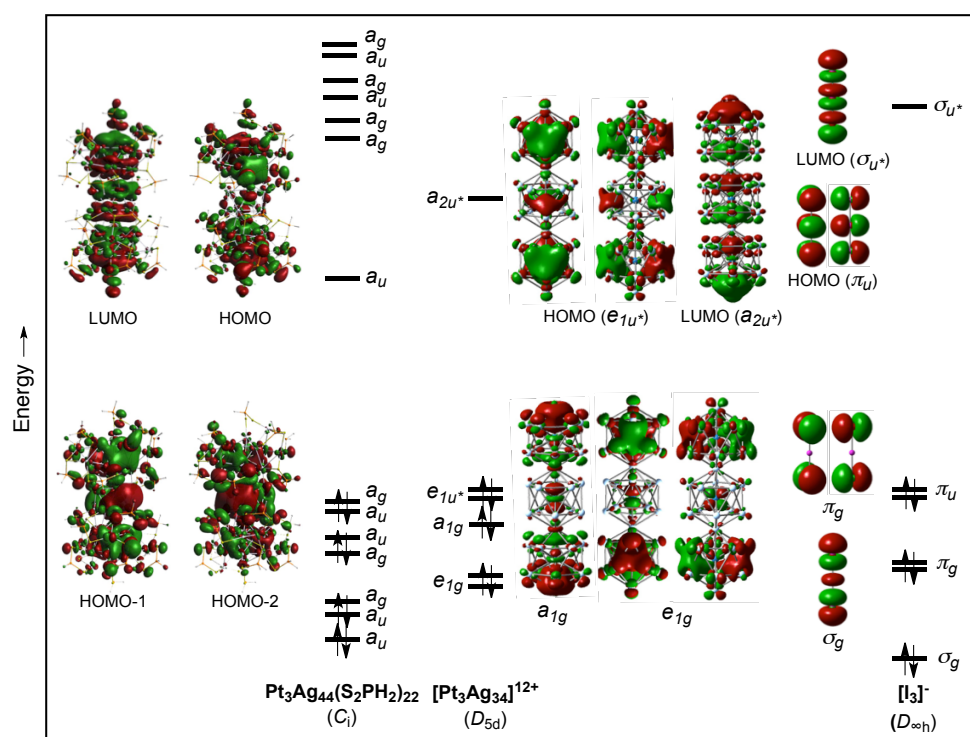


Figure 10. DFT-computed MO diagrams of $\text{Pt}_3\text{Ag}_{44}(\text{dtp})_{22}$, its 22-electron $[\text{Pt}_3\text{Ag}_{34}]^{12+}$ core and $[\text{I}_3]^-$. Note that the MO diagram of the ligated cluster $\text{Pt}_3\text{Ag}_{44}(\text{dtp})_{22}$ is comparable to that of the bare cluster $[\text{Pt}_3\text{Ag}_{34}]^{12+}$ with (minor) additional orbital mixing/splitting due to lower symmetry.¹⁰⁰

Such a molecular analogy, which is in a way a variation of the well-known *isolobal* analogy¹⁴⁴⁻¹⁴⁵ can be extended to assemblies made of more than two *superatoms*. This is illustrated in Figure 9 for instance for some cluster *supermolecular* cores that are computed to be *isolobal* to simple triatomic molecules.¹²⁶ It is noteworthy that the fusion of icosahedra allows non-linear “bond” angles between them upon “hybridization” requirement similarly as in polyatomic molecules. Indeed, some nanoclusters containing such cluster cores have already been characterized, as exemplified with Pt₃Ag₄₄(dtp)₂₂ which contains a [Pt₃Ag₃₄]¹²⁺ *supermolecular* assembly *isolobal* to the [I₃]⁻ anion, as shown in Figure 10.¹⁰⁰

It is likely that the library of *supermolecules* made of the assembly of more than two *superatomic* (mostly but not exclusively icosahedral) subunits, will develop in the next future. Stable *supermolecules* analogous to unknown or unstable molecules (such as cyclic O₃^{75, 126}) could be designed. However, the *isolobal* analogy between assemblies of atoms and *superatoms* should not be pushed too far. There are obvious differences (among them the presence of 1D *superatomic* orbitals¹⁴⁶), which can add up when the number of considered atoms/*superatoms* increases. Closed-shell non-spherical group 11 nanoclusters exist, the complex structures of which has not been yet rationalized on the basis of simple electron counting rules, even those made from fused icosahedral units.¹²⁶

1.4 References

- 1 Chakraborty, P.; Nag, A.; Chakraborty, A.; Pradeep, T. Approaching materials with atomic precision using supramolecular cluster assemblies. *Acc. Chem. Res.* **2018**, *52*, 2–11.
- 2 Ghosh, A.; Mohammed, O. F.; Bakr, O. M. Atomic-level doping of metal clusters. *Acc. Chem. Res.* **2018**, *51*, 3094–3103.
- 3 Hossain, S.; Niihori, Y.; Nair, L. V.; Kumar, B.; Kurashige, W.; Negishi, Y. Alloy clusters: Precise synthesis and mixing effects. *Acc. Chem. Res.* **2018**, *51*, 3114–3124.
- 4 Ferrari, P.; Vanbuel, J.; Janssens, E.; Lievens, P. Tuning the reactivity of small metal clusters by heteroatom doping. *Acc. Chem. Res.* **2018**, *51*, 3174–3182.
- 5 Chakraborty, I.; Pradeep, T. Atomically precise clusters of noble metals: emerging link between atoms and nanoparticles. *Chem. Rev.* **2017**, *117*, 8208–8271.
- 6 Jin, R.; Li, G.; Sharma, S.; Li, Y.; Du, X. Toward active-site tailoring in heterogeneous catalysis by atomically precise metal nanoclusters with crystallographic structures. *Chem. Rev.* **2020**, *121*, 567–648.
- 7 Kang, X.; Li, Y.; Zhu, M.; Jin, R. Atomically precise alloy nanoclusters: syntheses, structures, and properties. *Chem. Soc. Rev.* **2020**, *49*, 6443–6514.

- 8 Yang, J.; Jin, R. New advances in atomically precise silver nanoclusters. *ACS Mater. Lett.* **2019**, *1*, 482–489.
- 9 Higaki, T.; Li, Q.; Zhou, M.; Zhao, S.; Li, Y.; Li, S.; Jin, R. Toward the tailoring chemistry of metal nanoclusters for enhancing functionalities. *Acc. Chem. Res.* **2018**, *51*, 2764–2773.
- 10 Du, Y.; Sheng, H.; Astruc, D.; Zhu, M. Atomically precise noble metal nanoclusters as efficient catalysts: a bridge between structure and properties. *Chem. Rev.* **2019**, *120*, 526–622.
- 11 Zhang, B.; Chen, J.; Cao, Y.; Chai, O. J. H.; Xie, J. Ligand Design in Ligand-Protected Gold Nanoclusters. *Small* **2021**, *17*, 2004381.
- 12 Kang, X.; Zhu, M. Transformation of atomically precise nanoclusters by ligand-exchange. *Chem. Mater.* **2019**, *31*, 9939–9969.
- 13 Yan, J.; Teo, B. K.; Zheng, N. Surface chemistry of atomically precise coinage–metal nanoclusters: from structural control to surface reactivity and catalysis. *Acc. Chem. Res.* **2018**, *51*, 3084–3093.
- 14 Li, Y.; Jin, R. Seeing ligands on nanoclusters and in their assemblies by X-ray crystallography: Atomically precise nanochemistry and beyond. *J. Am. Chem. Soc.* **2020**, *142*, 13627–13644.
- 15 Zeng, C.; Jin, R. Gold nanoclusters: size-controlled synthesis and crystal structures. *Gold Clusters, Colloids and Nanoparticles I* **2014**, 87–115.
- 16 Negishi, Y. Metal-nanocluster science and technology: my personal history and outlook. *Phys. Chem. Chem. Phys.* **2022**, *24*, 7569–7594.
- 17 Chen, L.; Black, A.; Parak, W. J.; Klinke, C.; Chakraborty, I. Metal nanocluster-based devices: Challenges and opportunities. *Aggregate* **2021**, e132.
- 18 Kang, X.; Zhu, M. Structural isomerism in atomically precise nanoclusters. *Chem. Mater.* **2020**, *33*, 39–62.
- 19 Kawawaki, T.; Imai, Y.; Suzuki, D.; Kato, S.; Kobayashi, I.; Suzuki, T.; Kaneko, R.; Hossain, S.; Negishi, Y. Atomically precise alloy nanoclusters. *Chem. Eur. J.* **2020**, *26*, 16150–16193.
- 20 Xu, W. W.; Zeng, X. C.; Gao, Y. Application of electronic counting rules for ligand-protected gold nanoclusters. *Acc. Chem. Res.* **2018**, *51*, 2739–2747.
- 21 Weerawardene, K. D. M.; Häkkinen, H.; Aikens, C. M. Connections between theory and experiment for gold and silver nanoclusters. *Annu. Rev. Phys. Chem.* **2018**, *69*, 205–229.
- 22 Häkkinen, H. Electronic shell structures in bare and protected metal nanoclusters. *Adv.*

- Phys-X* **2016**, *1*, 467–491.
- 23 Aikens, C. M. Electronic and geometric structure, optical properties, and excited state behavior in atomically precise thiolate-stabilized noble metal nanoclusters. *Acc. Chem. Res.* **2018**, *51*, 3065–3073.
 - 24 Fernando, A.; Weerawardene, K. D. M.; Karimova, N. V.; Aikens, C. M. Quantum mechanical studies of large metal, metal oxide, and metal chalcogenide nanoparticles and clusters. *Chem. Rev.* **2015**, *115*, 6112–6216.
 - 25 Gam, F.; Wei, J.; Kahlal, S.; Saillard, J.-Y.; Halet, J.-F. Electron Counting in Ligated High Nuclearity Late Transition Metal Clusters. *Struct. Bond.* **2021**, *188*, 69–102.
 - 26 Saillard, J.-Y.; Halet, J.-F. Structure and bonding patterns in large molecular ligated metal clusters. *Struct. Bond.* **2016**, *169*, 157–179.
 - 27 Frapper, G.; Halet, J.-F. Rationalising and predicting the structure and bonding of bare and ligated transition metal clusters and nanoparticles. *Computational Materials Discovery* **2018**, 320–351.
 - 28 Wade, K. The structural significance of the number of skeletal bonding electron-pairs in carboranes, the higher boranes and borane anions, and various transition-metal carbonyl cluster compounds. *J. Chem. Soc. Chem. Commun.* **1971**, 792–793.
 - 29 Mingos, D. M. P.; Wales, D. J. *Introduction to cluster chemistry*. Prentice Hall: **1990**.
 - 30 Fehlner, T.; Halet, J.-F.; Saillard, J.-Y. *Molecular clusters: a bridge to solid-state chemistry*. Cambridge University Press: **2007**.
 - 31 Stone, A. J. A new approach to bonding in transition metal clusters: theory. *Mol. Phys.* **1980**, *41*, 1339–1354.
 - 32 Stone, A. J. New approach to bonding in transition-metal clusters and related compounds. *Inorg. Chem.* **1981**, *20*, 563–571.
 - 33 Stone, A. J.; Alderton, M. A new model of structure and bonding in the boron hydrides. *Inorg. Chem.* **1982**, *21*, 2297–2302.
 - 34 Stone, A. J. The bonding in boron and transition-metal cluster compounds. *Polyhedron* **1984**, *3*, 1299–1306.
 - 35 Mingos, D. M. P.; Lin, Z. A theoretical analysis of high-nuclearity metal carbonyl clusters. *J. Chem. Soc. Dalton Trans.* **1988**, 1657–1664.
 - 36 Knight, W.; Clemenger, K.; de Heer, W. A.; Saunders, W. A.; Chou, M.; Cohen, M. L. Electronic shell structure and abundances of sodium clusters. *Phys. Rev. Lett.* **1984**, *52*, 2141.
 - 37 Goeppert Mayer, M.; Jensen, J. H. D. *Elementary Theory of Nuclear Shell Structure*. New

- York/London: John Wiley & Sons/Chapman & Hall: **1955**.
- 38 Ekardt, W. Size-dependent photoabsorption and photoemission of small metal particles. *Phys. Rev. B* **1985**, *31*, 6360.
- 39 Ekardt, W. Collective multipole excitations in small metal particles: Critical angular momentum l_{cr} for the existence of collective surface modes. *Phys. Rev. B* **1985**, *32*, 1961.
- 40 De Heer, W. A. The physics of simple metal clusters: experimental aspects and simple models. *Rev. Mod. Phys.* **1993**, *65*, 611.
- 41 Wales, D. J.; Mingos, D. M. P. Splitting of cluster orbitals. *Inorg. Chem.* **1989**, *28*, 2748–2754.
- 42 Lin, Z.; Slee, T.; Mingos, D., A structural jellium model of cluster electronic structure. *Chem. Phys.* **1990**, *142*, 321–334.
- 43 Lin, Z.; Kanter, R. P.; Mingos, D. M. P. Closed-shell electronic requirements for condensed clusters of the group 11 elements. *Inorg. Chem.* **1991**, *30*, 91–95.
- 44 Mingos, D. M. P. Theoretical analyses and electron counting rules for high nuclearity clusters. *J. Chem. Soc. Chem. Commun.* **1985**, 1352–1354.
- 45 Johnston, R. L.; Mingos, D. M. P. A group theoretical paradigm for describing the skeletal molecular orbitals of cluster compounds. Part 1. Deltahedral clusters. *J. Chem. Soc. Dalton Trans.* **1987**, 647–656.
- 46 Johnston, R. L.; Mingos, D. M. P. A group theoretical paradigm for describing the skeletal molecular orbitals of cluster compounds. Part 2. Bispherical clusters. *J. Chem. Soc. Dalton Trans.* **1987**, 1445–1456.
- 47 Mingos, D. M. P.; Slee, T.; Lin, Z. Bonding models for ligated and bare clusters. *Chem. Rev.* **1990**, *90*, 383–402.
- 48 Johnston, R. L. *Atomic and molecular clusters*. CRC Press: **2002**.
- 49 Wales, D. J.; Mingos, D. M. P.; Slee, T.; Lin, Z. Clusters in inorganic and molecular beam chemistry. some unifying principles. *Acc. Chem. Res.* **1990**, *23*, 17–22.
- 50 Johnston, R. L. Mathematical cluster chemistry. *Structural and Electronic Paradigms in Cluster Chemistry* **1997**, 1–34.
- 51 Luo, Z.; Castleman, A. W. Special and general superatoms. *Acc. Chem. Res.* **2014**, *47*, 2931–2940.
- 52 Walter, M.; Akola, J.; Lopez-Acevedo, O.; Jadzinsky, P. D.; Calero, G.; Ackerson, C. J.; Whetten, R. L.; Grönbeck, H.; Häkkinen, H. A unified view of ligand-protected gold clusters as superatom complexes. *Proc. Natl. Acad. Sci. U. S. A.* **2008**, *105*, 9157–9162.
- 53 Häkkinen, H. Atomic and electronic structure of gold clusters: understanding flakes, cages

- and superatoms from simple concepts. *Chem. Soc. Rev.* **2008**, *37*, 1847–1859.
- 54 Castleman Jr, A.; Khanna, S. Clusters, superatoms, and building blocks of new materials. *J. Phys. Chem. C* **2009**, *113*, 2664–2675.
- 55 Jena, P. Beyond the periodic table of elements: The role of superatoms. *J. Phys. Chem. Lett.* **2013**, *4*, 1432–1442.
- 56 Hall, K. P.; Theoblad, B. R.; Gilmour, D. I.; Mingos, D. M. P.; Welch, A. J. Synthesis and structural characterization of $[\text{Au}_9\{\text{P}(p\text{-C}_6\text{H}_4\text{OMe})_3\}_8](\text{BF}_4)_3$; a cluster with a centred crown of gold atoms. *J. Chem. Soc. Chem. Commun.* **1982**, 528–530.
- 57 Woods, R. D.; Saxon, D. S. Diffuse surface optical model for nucleon-nuclei scattering. *Phys. Rev.* **1954**, *95*, 577.
- 58 Leuchtner, R.; Harms, A.; Castleman Jr, A. Thermal metal cluster anion reactions: Behavior of aluminum clusters with oxygen. *J. Chem. Phys.* **1989**, *91*, 2753–2754.
- 59 Khanna, S.; Jena, P. Assembling crystals from clusters. *Phys. Rev. Lett.* **1992**, *69*, 1664.
- 60 Jena, P.; Khanna, S.; Rao, B. Designing clusters as superelements. *Surf. Rev. Lett.* **1996**, *3*, 993–999.
- 61 Bergeron, D.; Roach, P.; Castleman Jr, A.; Jones, N.; Khanna, S. Al cluster superatoms as halogens in polyhalides and as alkaline earths in iodide salts. *Science* **2005**, *307*, 231–235.
- 62 Hoffmann, R.; Schleyer, P. v. R.; Schaefer III, H. F. Predicting molecules—more realism, please! *Angew. Chem. Int. Ed.* **2008**, *47*, 7164–7167.
- 63 Khanna, S.; Jena, P. Atomic clusters: Building blocks for a class of solids. *Phys. Rev. B* **1995**, *51*, 13705.
- 64 Bergeron, D. E.; Castleman Jr, A. W.; Morisato, T.; Khanna, S. N. Formation of Al_{13}F^- : Evidence for the superhalogen character of Al_{13} . *Science* **2004**, *304*, 84–87.
- 65 Vollet, J.; Hartig, J. R.; Schnöckel, H. $\text{Al}_{50}\text{C}_{120}\text{H}_{180}$: a pseudofullerene shell of 60 carbon atoms and 60 methyl groups protecting a cluster core of 50 aluminum atoms. *Angew. Chem. Int. Ed.* **2004**, *43*, 3186–3189.
- 66 Clayborne, P. A.; Lopez-Acevedo, O.; Whetten, R. L.; Grönbeck, H.; Häkkinen, H. The $\text{Al}_{50}\text{Cp}^*_{12}$ Cluster – A 138-Electron Closed Shell ($L = 6$) Superatom. *Eur. J. Inorg. Chem.* **2011**, *17*, 2649–2652.
- 67 Schnöckel, H. Structures and properties of metalloid Al and Ga clusters open our eyes to the diversity and complexity of fundamental chemical and physical processes during formation and dissolution of metals. *Chem. Rev.* **2010**, *110*, 4125–4163.
- 68 Mingos, D. M. P. Molecular-orbital calculations on cluster compounds of gold. *J. Chem.*

- Soc. Dalton Trans.* **1976**, 1163–1169.
- 69 Mingos, D. M. P. Gold cluster compounds. *Gold Bull.* **1984**, *17*, 5–12.
- 70 Briant, C. E.; Theobald, B. R.; White, J. W.; Bell, L. K.; Mingos, D. M. P.; Welch, A. J. Synthesis and X-ray structural characterization of the centred icosahedral gold cluster compound $[\text{Au}_{13}(\text{PMe}_2\text{Ph})_{10}\text{Cl}_2](\text{PF}_6)_3$; the realization of a theoretical prediction. *J. Chem. Soc. Chem. Commun.* **1981**, 201–202.
- 71 Briant, C. E.; Hall, K. P.; Mingos, D. M. P. Structural characterisation of two crystalline modifications of $[\text{Au}_9\{\text{P}(\text{C}_6\text{H}_4\text{OMe-}i>p\text{)}_3\}_8](\text{NO}_3)_3$: the first example of skeletal isomerism in metal cluster chemistry. *J. Chem. Soc. Chem. Commun.* **1984**, 290–291.
- 72 Mingos, D. M. P. Structural and bonding issues in clusters and nano-clusters. *Struc. Bond.* **2014**, *162*, 1–65.
- 73 Teo, B. K. A perspective on the science of clusters. *J. Clust. Sci.* **2014**, *25*, 5–28.
- 74 Häkkinen, H. Theoretical studies of gold nanoclusters in various chemical environments: when the size matters. *From gold nanoparticles for physics, chemistry and biology* **2012**, *9*, 233–272.
- 75 Wei, J.; Marchal, R.; Astruc, D.; Kahlal, S.; Halet, J.-F.; Saillard, J.-Y. Looking at platinum carbonyl nanoclusters as superatoms. *Nanoscale* **2022**, *14*, 3946–3957.
- 76 Wei, J.; Kahlal, S.; Halet, J.-F.; Saillard, J.-Y. Elucidating the electronic structure of the ligated cuboctahedral palladium cluster $[\text{Pd}_{13}(\mu_4\text{-C}_7\text{H}_7)_6]^{2+}$. *J. Clust. Sci.* **2019**, *30*, 1227–1233.
- 77 Wei, J.; Marchal, R.; Astruc, D.; Saillard, J. Y.; Halet, J. F.; Kahlal, S. Theoretical analysis of the Mackay icosahedral cluster $\text{Pd}_{55}(\text{PiPr}_3)_{12}(\mu_3\text{-CO})_{20}$: An open-shell 20-electron superatom. *Chem. Eur. J.* **2020**, *26*, 5508–5514.
- 78 Jin, R.; Zeng, C.; Zhou, M.; Chen, Y. Atomically precise colloidal metal nanoclusters and nanoparticles: fundamentals and opportunities. *Chem. Rev.* **2016**, *116*, 10346–10413.
- 79 Yao, Q.; Chen, T.; Yuan, X.; Xie, J. Toward total synthesis of thiolate-protected metal nanoclusters. *Acc. Chem. Res.* **2018**, *51*, 1338–1348.
- 80 Sakthivel, N. A.; Dass, A. Aromatic thiolate-protected series of gold nanomolecules and a contrary structural trend in size evolution. *Acc. Chem. Res.* **2018**, *51*, 1774–1783.
- 81 Sharma, S.; Chakrahari, K. K.; Saillard, J.-Y.; Liu, C. W. Structurally precise dichalcogenolate-protected copper and silver superatomic nanoclusters and their alloys. *Acc. Chem. Res.* **2018**, *51*, 2475–2483.
- 82 Kang, X.; Zhu, M. Tailoring the photoluminescence of atomically precise nanoclusters. *Chem. Soc. Rev.* **2019**, *48*, 2422–2457.

- 83 Omoda, T.; Takano, S.; Tsukuda, T. Toward controlling the electronic structures of chemically modified superatoms of gold and silver. *Small* **2021**, *17*, 2001439.
- 84 Mingos, D. M. P. Historical Introduction to Gold Colloids, Clusters and Nanoparticles. *Struct. Bond.* **2014**, *161*, 1–47.
- 85 Häkkinen, H. Electronic structure: shell structure and the superatom concept. In *Frontiers of Nanoscience*, Elsevier: **2015**; Vol. 9, pp 189–222.
- 86 Van der Velden, J.; Vollenbroek, F.; Bour, J.; Beurskens, P.; Smits, J.; Bosnian, W. Gold clusters containing bidentate phosphine ligands. Preparation and X-Ray structure investigation of $[\text{Au}_5(\text{dppmH})_3(\text{dppm})](\text{NO}_3)_2$ and $[\text{Au}_{13}(\text{dppmH})_6](\text{NO}_3)_n$. *Rec. Trav. Chim. Pays Bas* **1981**, *100*, 148–152.
- 87 Zhu, M.; Aikens, C. M.; Hollander, F. J.; Schatz, G. C.; Jin, R. Correlating the crystal structure of a thiol-protected Au_{25} cluster and optical properties. *J. Am. Chem. Soc.* **2008**, *130*, 5883–5885.
- 88 Heaven, M. W.; Dass, A.; White, P. S.; Holt, K. M.; Murray, R. W. Crystal structure of the gold nanoparticle $[\text{N}(\text{C}_8\text{H}_{17})_4][\text{Au}_{25}(\text{SCH}_2\text{CH}_2\text{Ph})_{18}]$. *J. Am. Chem. Soc.* **2008**, *130*, 3754–3755.
- 89 Akola, J.; Walter, M.; Whetten, R. L.; Häkkinen, H.; Grönbeck, H. On the structure of thiolate-protected Au_{25} . *J. Am. Chem. Soc.* **2008**, *130*, 3756–3757.
- 90 Dhayal, R. S.; Liao, J. H.; Liu, Y. C.; Chiang, M. H.; Kahlal, S.; Saillard, J. Y.; Liu, C. $[\text{Ag}_{21}\{\text{S}_2\text{P}(\text{O}i\text{Pr})_2\}_{12}]^+$: An Eight-Electron Superatom. *Angew. Chem. Int. Ed.* **2015**, *127*, 3773–3777.
- 91 Shichibu, Y.; Konishi, K. HCl-Induced Nuclearity Convergence in Diphosphine-Protected Ultrasmall Gold Clusters: A Novel Synthetic Route to “Magic-Number” Au_{13} Clusters. *Small* **2010**, *6*, 1216–1220.
- 92 Hall, K. P.; Mingos, D. M. P. Homo-and heteronuclear cluster compounds of gold. *Prog. Inorg. Chem.* **1984**, *32*, 237–325.
- 93 Narouz, M. R.; Takano, S.; Lummis, P. A.; Levchenko, T. I.; Nazemi, A.; Kaappa, S.; Malola, S.; Yousefalizadeh, G.; Calhoun, L. A.; Stamplecoskie, K. G. Robust, highly luminescent Au_{13} superatoms protected by N-heterocyclic carbenes. *J. Am. Chem. Soc.* **2019**, *141*, 14997–15002.
- 94 Shen, H.; Xiang, S.; Xu, Z.; Liu, C.; Li, X.; Sun, C.; Lin, S.; Teo, B. K.; Zheng, N. Superatomic Au_{13} clusters ligated by different N-heterocyclic carbenes and their ligand-dependent catalysis, photoluminescence, and proton sensitivity. *Nano Res.* **2020**, *13*,

- 1908–1911.
- 95 Royston, C.; Mingos, D. M. P. Synthesis and characterization of the centred icosahedral cluster series $[\text{Au}_9\text{M}^{\text{IB}}_4\text{Cl}_4(\text{PMePh}_2)_8][\text{C}_2\text{B}_9\text{H}_{12}]$, where $\text{M}^{\text{IB}} = \text{Au}, \text{Ag}$ or Cu . *J. Chem. Soc. Dalton Trans.* **1996**, 491–500.
- 96 Shichibu, Y.; Suzuki, K.; Konishi, K. Facile synthesis and optical properties of magic-number Au_{13} clusters. *Nanoscale* **2012**, *4*, 4125–4129.
- 97 Yang, L.; Cheng, H.; Jiang, Y.; Huang, T.; Bao, J.; Sun, Z.; Jiang, Z.; Ma, J.; Sun, F.; Liu, Q. In situ studies on controlling an atomically-accurate formation process of gold nanoclusters. *Nanoscale* **2015**, *7*, 14452–14459.
- 98 Chiu, T.-H.; Liao, J.-H.; Gam, F.; Chantrenne, I.; Kahlal, S.; Saillard, J.-Y.; Liu, C. All-selenolate-protected eight-electron platinum/silver nanoclusters. *Nanoscale* **2021**, *13*, 12143–12148.
- 99 Liao, J. H.; Chang, H. W.; Fang, C. S.; Liu, C. *T*-symmetric 40-nucleus silver clusters assembled by hetero-anions. *J. Chin. Chem. Soc.* **2020**, *67*, 2163–2170.
- 100 Chiu, T.-H.; Liao, J.-H.; Gam, F.; Chantrenne, I.; Kahlal, S.; Saillard, J.-Y.; Liu, C. Homoleptic Platinum/Silver Superatoms Protected by Dithiolates: Linear Assemblies of Two and Three Centered Icosahedra Isolobal to Ne_2 and I^{3-} . *J. Am. Chem. Soc.* **2019**, *141*, 12957–12961.
- 101 Chakrahari, K. K.; Liao, J. H.; Kahlal, S.; Liu, Y. C.; Chiang, M. H.; Saillard, J. Y.; Liu, C. $[\text{Cu}_{13}\{\text{S}_2\text{CN}^n\text{Bu}_2\}_6(\text{acetylide})_4]^+$: A Two-Electron Superatom. *Angew. Chem. Int. Ed.* **2016**, *128*, 14924–14928.
- 102 Dhayal, R. S.; Lin, Y. R.; Liao, J. H.; Chen, Y. J.; Liu, Y. C.; Chiang, M. H.; Kahlal, S.; Saillard, J.-Y.; Liu, C. $[\text{Ag}_{20}\{\text{S}_2\text{P}(\text{OR})_2\}_{12}]$: a superatom complex with a chiral metallic core and high potential for isomerism. *Chem. Eur. J.* **2016**, *22*, 9943–9947.
- 103 Mingos, D. M. P.; Johnston, R. L. Theoretical models of cluster bonding. *Struct. Bond.* **1987**, *68*, 29–87.
- 104 Yan, J.; Zhang, J.; Chen, X.; Malola, S.; Zhou, B.; Selenius, E.; Zhang, X.; Yuan, P.; Deng, G.; Liu, K. Thiol-stabilized atomically precise, superatomic silver nanoparticles for catalysing cycloisomerization of alkynyl amines. *Nat. Sci. Rev.* **2018**, *5*, 694–702.
- 105 Kalenius, E.; Malola, S.; Matus, M. F.; Kazan, R.; Bürgi, T.; Häkkinen, H. Experimental confirmation of a topological isomer of the ubiquitous $\text{Au}_{25}(\text{SR})_{18}$ cluster in the gas phase. *J. Am. Chem. Soc.* **2021**, *143*, 1273–1277.
- 106 Li, J.; Li, X.; Zhai, H.-J.; Wang, L.-S. Au_{20} : a tetrahedral cluster. *Science* **2003**, *299*, 864–

867.

- 107 Nguyen, T.-A. D.; Jones, Z. R.; Goldsmith, B. R.; Buratto, W. R.; Wu, G.; Scott, S. L.; Hayton, T. W. A Cu₂₅ nanocluster with partial Cu(0) character. *J. Am. Chem. Soc.* **2015**, *137*, 13319–13324.
- 108 Yang, H.; Wang, Y.; Huang, H.; Gell, L.; Lehtovaara, L.; Malola, S.; Häkkinen, H.; Zheng, N. All-thiol-stabilized Ag₄₄ and Au₁₂Ag₃₂ nanoparticles with single-crystal structures. *Nat. Commun.* **2013**, *4*, 1–8.
- 109 Chai, J.; Yang, S.; Lv, Y.; Chen, T.; Wang, S.; Yu, H.; Zhu, M. A unique pair: Ag₄₀ and Ag₄₆ nanoclusters with the same surface but different cores for structure–property correlation. *J. Am. Chem. Soc.* **2018**, *140*, 15582–15585.
- 110 Dass, A. Mass spectrometric identification of Au₆₈(SR)₃₄ molecular gold nanoclusters with 34-electron shell closing. *J. Am. Chem. Soc.* **2009**, *131*, 11666–11667.
- 111 Jadzinsky, P. D.; Calero, G.; Ackerson, C. J.; Bushnell, D. A.; Kornberg, R. D. Structure of a thiol monolayer-protected gold nanoparticle at 1.1 Å resolution. *science* **2007**, *318*, 430–433.
- 112 Liu, J. Y.; Alkan, F.; Wang, Z.; Zhang, Z. Y.; Kurmoo, M.; Yan, Z.; Zhao, Q. Q.; Aikens, C. M.; Tung, C. H.; Sun, D. Different silver nanoparticles in one crystal: Ag₂₁₀(iPrPhS)₇₁(Ph₃P)₅Cl and Ag₂₁₁(iPrPhS)₇₁(Ph₃P)₆Cl. *Angew. Chem. Int. Ed.* **2019**, *58*, 195–199.
- 113 Hu, F.; Li, J. J.; Guan, Z. J.; Yuan, S. F.; Wang, Q. M. Formation of an Alkynyl-Protected Ag₁₁₂ Silver Nanocluster as Promoted by Chloride Released In Situ from CH₂Cl₂. *Angew. Chem. Int. Ed.* **2020**, *59*, 5312–5315.
- 114 Higaki, T.; Liu, C.; Zhou, M.; Luo, T.-Y.; Rosi, N. L.; Jin, R. Tailoring the structure of 58-electron gold nanoclusters: Au₁₀₃S₂(S-Nap)₄₁ and its implications. *J. Am. Chem. Soc.* **2017**, *139*, 9994–10001.
- 115 Lei, Z.; Li, J. J.; Wan, X. K.; Zhang, W. H.; Wang, Q. M. Isolation and Total Structure Determination of an All-Alkynyl-Protected Gold Nanocluster Au₁₄₄. *Angew. Chem. Int. Ed.* **2018**, *130*, 8775–8779.
- 116 Zhou, M.; Zeng, C.; Song, Y.; Padelford, J. W.; Wang, G.; Sfeir, M. Y.; Higaki, T.; Jin, R. On the Non-Metallicity of 2.2 nm Au₂₄₆(SR)₈₀ Nanoclusters. *Angew. Chem. Int. Ed.* **2017**, *129*, 16475–16479.
- 117 Higaki, T.; Zhou, M.; Lambright, K. J.; Kirschbaum, K.; Sfeir, M. Y.; Jin, R., Sharp transition from nonmetallic Au₂₄₆ to metallic Au₂₇₉ with nascent surface plasmon resonance. *J. Am. Chem. Soc.* **2018**, *140*, 5691–5695.

- 118 Yang, H.; Wang, Y.; Chen, X.; Zhao, X.; Gu, L.; Huang, H.; Yan, J.; Xu, C.; Li, G.; Wu, J. Plasmonic twinned silver nanoparticles with molecular precision. *Nat. Commun.* **2016**, *7*, 1–8.
- 119 Malola, S.; Häkkinen, H. How many gold atoms make gold metal? *Europhysics News* **2015**, *46*, 23–26.
- 120 Chakraborty, I.; Erusappan, J.; Govindarajan, A.; Sugi, K.; Udayabhaskararao, T.; Ghosh, A.; Pradeep, T. Emergence of metallicity in silver clusters in the 150 atom regime: a study of differently sized silver clusters. *Nanoscale* **2014**, *6*, 8024–8031.
- 121 Kwak, K.; Tang, Q.; Kim, M.; Jiang, D.-e.; Lee, D. Interconversion between superatomic 6-electron and 8-electron configurations of $M@Au_{24}(SR)_{18}$ clusters ($M = Pd, Pt$). *J. Am. Chem. Soc.* **2015**, *137*, 10833–10840.
- 122 Suyama, M.; Takano, S.; Nakamura, T.; Tsukuda, T., Stoichiometric Formation of Open-Shell $[PtAu_{24}(SC_2H_4Ph)_{18}]^-$ via Spontaneous Electron Proportionation between $[PtAu_{24}(SC_2H_4Ph)_{18}]^{2-}$ and $[PtAu_{24}(SC_2H_4Ph)_{18}]^0$. *J. Am. Chem. Soc.* **2019**, *141*, 14048–14051.
- 123 Schütz, M.; Muhr, M.; Freitag, K.; Gemel, C.; Kahlal, S.; Saillard, J.-Y.; Da Silva, A. C.; Da Silva, J. L.; Fässler, T. F.; Fischer, R. A. Contrasting structure and bonding of a copper-rich and a zinc-rich intermetalloid Cu/Zn cluster. *Inorg. Chem.* **2020**, *59*, 9077–9085.
- 124 Zeng, C.; Qian, H.; Li, T.; Li, G.; Rosi, N. L.; Yoon, B.; Barnett, R. N.; Whetten, R. L.; Landman, U.; Jin, R. Total structure and electronic properties of the gold nanocrystal $Au_{36}(SR)_{24}$. *Angew. Chem. Int. Ed.* **2012**, *51*, 13114–13118.
- 125 Jin, S.; Zhou, M.; Kang, X.; Li, X.; Du, W.; Wei, X.; Chen, S.; Wang, S.; Zhu, M. Three-dimensional Octameric Assembly of Icosahedral M_{13} Units in $[Au_8Ag_{57}(Dppp)_4(C_6H_{11}S)_{32}Cl_2]Cl$ and its $[Au_8Ag_{55}(Dppp)_4(C_6H_{11}S)_{34}][BPh_4]_2$ Derivative. *Angew. Chem. Int. Ed.* **2020**, *59*, 3891–3895.
- 126 Gam, F.; Liu, C.; Kahlal, S.; Saillard, J.-Y. Electron counting and bonding patterns in assemblies of three and more silver-rich superatoms. *Nanoscale* **2020**, *12*, 20308–20316.
- 127 Teo, B. K.; Zhang, H.; Shi, X. Cluster of clusters: a modular approach to large metal clusters. Structural characterization of a 38-atom cluster $[(p-Tol_3P)_{12}Au_{18}Ag_{20}Cl_{14}]$ based on vertex-sharing triicosahedra. *J. Am. Chem. Soc.* **1990**, *112*, 8552–8562.
- 128 Teo, B. K.; Shi, X.; Zhang, H. Cluster of clusters. Structure of a novel gold-silver cluster $[(Ph_3P)_{10}Au_{13}Ag_{12}Br_8](SbF_6)$ containing an exact staggered-eclipsed-staggered metal configuration. Evidence of icosahedral units as building blocks. *J. Am. Chem. Soc.* **1991**, *113*, 4329–4331.
- 129 Mingos, D. M. P. Structural and bonding patterns in gold clusters. *Dalton Trans.* **2015**, *44*,

- 6680–6695.
- 130 Saito, S.; Ohnishi, S. Stable $(\text{Na}_{19})_2$ as a giant alkali-metal–atom dimer. *Phys. Rev. Lett.* **1987**, *59*, 190.
- 131 Cheng, L.; Yang, J. Communication: New insight into electronic shells of metal clusters: Analogues of simple molecules. *J. Chem. Phys.* **2013**, *138*, 141101.
- 132 Sun, Z.-M.; Xiao, H.; Li, J.; Wang, L.-S. $\text{Pd}_2@ \text{Sn}_{18}^{4+}$: Fusion of two endohedral stannaspherenes. *J. Am. Chem. Soc.* **2007**, *129*, 9560–9561.
- 133 Jena, P.; Sun, Q. Superatomic clusters: design rules and potential for building blocks of materials. *Chem. Rev.* **2018**, *118*, 5755–5870.
- 134 Muñoz-Castro, A. Single, double, and triple intercluster bonds: analyses of $\text{M}_2\text{Au}_{36}(\text{SR})_{24}$ ($\text{M} = \text{Au}, \text{Pd}, \text{Pt}$) as 14-, 12- and 10- ve superatomic molecules. *Chem. Commun.* **2019**, *55*, 7307–7310.
- 135 Teo, B. K.; Keating, K. Novel triicosahedral structure of the largest metal alloy cluster: hexachlorododecakis (triphenylphosphine)-gold-silver cluster $[(\text{Ph}_3\text{P})_{12}\text{Au}_{13}\text{Ag}_{12}\text{Cl}_6]^{m+}$. *J. Am. Chem. Soc.* **1984**, *106*, 2224–2226.
- 136 Liu, L.; Li, P.; Yuan, L.-F.; Cheng, L.; Yang, J. From isosuperatoms to isosupermolecules: new concepts in cluster science. *Nanoscale* **2016**, *8*, 12787–12792.
- 137 Strickler, S. Molecular spectra and molecular structure. Volume 3, electronic spectra and electronic structure of polyatomic molecules (Herzberg, Gerhard). *J. Chem. Educ.* **1967**, *44*, A760.
- 138 Mulliken, R. S. Electronic structures of polyatomic molecules and valence. II. General considerations. *Phys. Rev.* **1932**, *41*, 49–71.
- 139 Mulliken, R. S. Electronic structures of polyatomic molecules and valence. II. Quantum theory of the double bond. *Phys. Rev.* **1932**, *41*, 751–758.
- 140 Mulliken, R. S. Electronic structures of polyatomic molecules and valence. *Phys. Rev.* **1932**, *40*, 55–62.
- 141 Qian, H.; Eckenhoff, W. T.; Zhu, Y.; Pintauer, T.; Jin, R. Total structure determination of thiolate-protected Au_{38} nanoparticles. *J. Am. Chem. Soc.* **2010**, *132*, 8280–8281.
- 142 Nunokawa, K.; Ito, M.; Sunahara, T.; Onaka, S.; Ozeki, T.; Chiba, H.; Funahashi, Y.; Masuda, H.; Yonezawa, T.; Nishihara, H. A new 19-metal-atom cluster $[(\text{Me}_2\text{PhP})_{10}\text{Au}_{12}\text{Ag}_7(\text{NO}_3)_9]$ with a nearly staggered–staggered M_5 ring configuration. *Dalton Trans.* **2005**, 2726–2730.
- 143 Ito, E.; Takano, S.; Nakamura, T.; Tsukuda, T. Controlled Dimerization and Bonding Scheme of Icosahedral $\text{M}@ \text{Au}_{12}$ ($\text{M} = \text{Pd}, \text{Pt}$) Superatoms. *Angew. Chem. Int. Ed.* **2021**,

- 60, 645–649.
- 144 Elian, M.; Chen, M. M.; Mingos, D. M. P.; Hoffmann, R. Comparative bonding study of conical fragments. *Inorg. Chem.* **1976**, *15*, 1148–1155.
- 145 Hoffmann, R. Building bridges between inorganic and organic chemistry (Nobel Lecture). *Angew. Chem. Int. Ed.* **1982**, *21*, 711–724.
- 146 Muñoz-Castro, A. Triple 1D \equiv 1D superatomic bonding. Au₂₂(dppo)₆ as a Π^4 - and Δ^2 -triply bonded cluster based on Au₁₁ assembled units. *Phys. Chem. Chem. Phys.* **2020**, *22*, 1422–1426.

Chapter 2

Towards the Formation of N-Heterocyclic Carbene-Protected Gold Clusters of Various Nuclearities. A Comparison with Their Phosphine-Protected Analogs from DFT Calculations

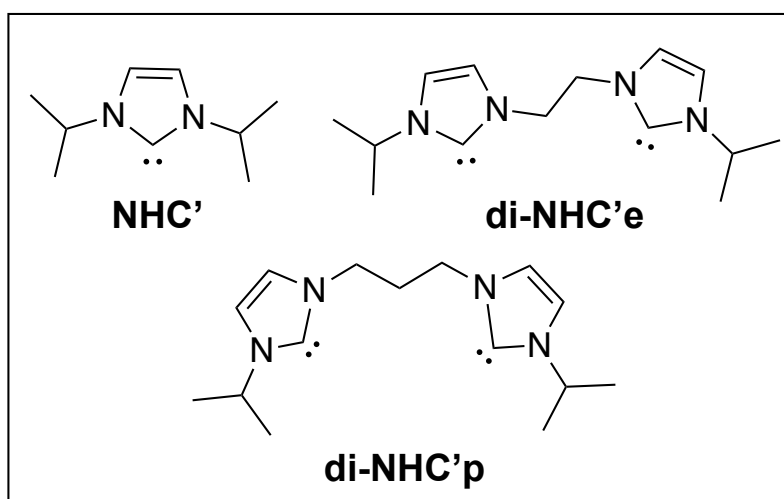
2.1 Introduction

Ligated atom-precise gold nanoclusters (AuNCs) are currently the subject of considerable interest.¹⁻⁷ On one side, they represent the lowest size limit of gold nanoparticles (AuNPs), with, in addition, ideal mono-dispersity. They constitute thus interesting models for fundamentally understanding the numerous properties of potential technological interest of larger AuNPs.¹⁻¹⁶ On the other side, AuNCs have also their own intrinsic interest, due to their specific properties associated with their delocalized 6s electrons. The field of their various chemical, biochemical, physicochemical and physical properties is as large as their extremely rich structural chemistry.¹⁻⁷ Numerous theoretical and experimental research efforts have contributed to the rationalization of their structure and stability towards the design of novel noble-metal nanostructures.¹⁷⁻³¹ It appears obvious that the role played by the AuNC ligand shell is decisive in the stabilization of a given structure for a given electron count. Ligands do not only play the role of passivating the metal core surface, but can also have significant influence on the AuNC structure and properties. Thus, introducing new ligands in the synthetic chemistry of AuNCs is of prime interest, in particular for tuning their optical properties.

From this view point, it is worth noting that N-heterocyclic carbenes (NHCs) have been very recently introduced as new protecting ligands of gold clusters.^{6,32-37} In particular, Crudden and coworkers synthesized NHC-protected Au₁₃ *superatoms* that exhibit large photoluminescent quantum yields.^{33,34} It turns out that one of us recently published a Density Functional Theory (DFT) investigation on the effect of substituting the diphosphine ligands by NHCs in the well-known [Au₁₃(dppe)₅Cl₂]³⁺ cluster (dppe = diphenylphosphinethane).³⁸ It was found that the substitution does not substantially modify the AuNC stability, but significantly affects the optical properties. Thus, NHCs appear to be an interesting alternative to their phosphine *isobal* analogs, allowing increasing cluster versatility, owing to the electronic variability of NHCs, which range from strong to weak donor ligands.³⁹⁻⁴³

As a continuation of our first work,³⁸ this chapter shown a comprehensive DFT investigation on the substitution of phosphines by NHCs in a series of small and medium size phosphine-protected AuNCs. The analysis is mainly focused on the substitution-induced changes on the structural arrangement, electronic structure and optical (including emissive) properties. The chosen AuNCs phosphine reference series (see Table 1) is composed of the experimentally characterized [Au₆(dppp)₄]²⁺ (**Au₆-P**),^{44,45} [Au₈(dppp)₄]²⁺ (**Au₈-P**),⁴⁶ [Au₈(dppp)₄Cl₂]²⁺ (**Au₈Cl₂-P**),⁴⁶ [Au₉(PPh₃)₈]³⁺ (**Au₉-P**),^{47,48} [Au₁₁(dppe)₆]³⁺ (**Au₁₁-P**),⁴⁹ [Au₁₁(PPh₃)₈Cl₂]⁺ (**Au₁₁Cl₂-P**),^{50,51} and [Au₁₃(dppe)₅Cl₂]³⁺ (**Au₁₃Cl₂-P**)⁵² (dppp = diphenylphosphinepropane).

These compounds were chosen because they offer a reasonable range of nuclearity (from 6 to 13), structure types and *superatom* electron counts (from 4 to 8 – 5*d* electrons are not considered). Some of them have diphosphines, whereas others have simple phosphines. Some bear chloride ligands whereas the others are homoleptic. Moreover, photoluminescence data are available for most of them.^{46,47,52,53} The hypothetical $[\text{Au}_{13}(\text{PPh}_3)_9\text{Cl}_3]^{2+}$ (**Au₁₃Cl₃-P**) compound, which is the phosphine counterpart of several recently characterized NHC derivatives $[\text{Au}_{13}(\text{NHC})_9\text{Cl}_3]^{2+}$ was added to this series.³³ Thus, we believe that the variety of these compounds makes this series a good reference sampling for investigating the changes occurring upon substituting the phosphine ligands by NHC homologs. These homologs were designed by substituting the mono-phosphines by the mono-carbene N,N'-diisopropylimidazolidenyl ligands (noted NHC' in the followings, see Scheme 1), taken from the literature.³² The dppe and dppp diphosphine ligands were substituted by their NHC analogs, namely 1,3-bis{N-isopropylimidazolidenyl}ethane (di-NHC'e) and 1,3-bis{N-isopropylimidazolidenyl}propane (di-NHC'p), respectively (Scheme 1). These carbenes are representative of standard NHCs and exhibit realistic steric volume. Thus, the computed NHC clusters are: $[\text{Au}_6(\text{di-NHC}'\text{p})_4]^{2+}$ (**Au₆-C**), $[\text{Au}_8(\text{di-NHC}'\text{p})_4]^{2+}$ (**Au₈-C**), $[\text{Au}_8(\text{di-NHC}'\text{p})_4\text{Cl}_2]^{2+}$ (**Au₈Cl₂-C**), $[\text{Au}_9(\text{NHC}')_8]^{3+}$ (**Au₉-C**), $[\text{Au}_{11}(\text{di-NHC}'\text{e})_6]^{3+}$ (**Au₁₁-C**), $[\text{Au}_{11}(\text{NHC}')_8\text{Cl}_2]^+$ (**Au₁₁Cl₂-C**), $[\text{Au}_{13}(\text{di-NHC}'\text{e})_5\text{Cl}_2]^{3+}$ (**Au₁₃Cl₂-C**), and $[\text{Au}_{13}(\text{NHC}')_9\text{Cl}_3]^{2+}$ (**Au₁₃Cl₃-C**).



Scheme 1. NHC ligands considered in the calculations.

Table 1. Structurally characterized phosphine-protected AuNCs from which models were considered in our calculations.

Compound	Abbreviation	Number of 6s (Au) electrons	Structure of the Au _n core	Ref.
[Au ₆ (dppp) ₄] ²⁺	Au₆-P	4	edge-bridged tetrahedron	44, 45
[Au ₈ (dppp) ₄] ²⁺	Au₈-P	6	edge-sharing tri-tetrahedron	46
[Au ₈ (dppp) ₄ Cl ₂] ²⁺	Au₈Cl₂-P	4	bicapped edge-sharing bi-tetrahedron	46
[Au ₉ (PPh ₃) ₈] ³⁺	Au₉-P	6	bicapped centered chair	47, 48
[Au ₁₁ (dppe) ₆] ³⁺	Au₁₁-P	8	doubly-bridged bicapped centered chair	49
[Au ₁₁ (PPh ₃) ₈ Cl ₂] ⁺	Au₁₁Cl₂-P	8	incomplete centered icosahedron	50,51
[Au ₁₃ (dppe) ₅ Cl ₂] ³⁺	Au₁₃Cl₂-P	8	centered icosahedron	52
[Au ₁₃ (PPh ₃) ₉ Cl ₃] ²⁺	Au₁₃Cl₃-P^a	8	centered icosahedron	33

(a) Structure modeled from that of Crudden's NHC derivative [Au₁₃(NHC)₉Cl₃]²⁺.³³

2.2 Computational Details

Geometry optimizations were carried out at the Density Functional Theory (DFT) level⁵⁴ with the addition of Grimme's D3 empirical corrections⁵⁵ in order to take into account dispersion effects. The Amsterdam Density Functional code⁵⁶ (ADF2017), incorporating the relativistic scalar corrections via the ZORA Hamiltonian was used.⁵⁷ The all-electron triple- ζ -Slater basis set plus a polarization function (STO-TZP),⁵⁸ were used, together with the Becke-Perdew (BP86)^{59,60} exchange-correlation functional. This functional was chosen for its good performance in reproducing cluster ground state geometries and its reasonable CPU time demand.¹⁹ An energy convergence criterion of 5×10^{-5} Hartree and a radial convergence criterion of 5×10^{-3} Å were employed. All the optimized structures were confirmed as true minima on their potential energy surface by analytical vibration frequency calculations. All the computed species have a closed-shell ground state. The Gaussian16 package⁶¹ was used to calculate natural atomic orbital (NAO) populations and Wiberg bond indices (WBI) using the ADF-optimized geometries with its NBO6.0 module,⁶² with the Def2-SVP⁶³ basis set and the BP86 functional. In order to reduce computational efforts, the Gaussian16 package was also used for calculating the UV-Vis optical transitions by time-dependent density functional theory⁶⁴ (TD-DFT) calculations, using the Def2-SVP⁶³ basis set (which includes effective core potentials accounting for scalar relativistic effects) and the B3LYP functional.⁶⁵ The choice of this functional was made after having tested several of them, namely B3LYP,⁶⁵ BP86,^{59,60} and LB94,⁶⁶ with respect to the experimental spectra of the phosphine-protected AuNCs listed in Table 1. Similar trends were found for the three functionals, but the B3LYP-computed optical

transitions were found to be in the closest quantitative agreement with experiment. The UV-Vis spectra were simulated from the computed TD-DFT transition energies and their oscillator strength by using the SWizard program,⁶⁷ each transition being associated with a Gaussian function of half-height width equal to 3000 cm^{-1} , a value that best reproduces experimental spectra. To calculate the fluorescence emission wavelengths, the geometry of the excited singlet states was optimized at the TD-DFT/B3LYP level with the Gaussian16 program. To compute the phosphorescence emission wavelengths, the geometry of the triplet state was calculated at the DFT/BP86 level with ADF2017 and its energy and that of the ground state were recalculated for this geometry as single points at the B3LYP level with Gaussian16. To compute the energy differences between the singlet and triplet excited states, the ADF optimized triplet excited geometries were re-calculated via single point calculations using Gaussian 16.

2.3 Results and Discussion

2.3.1 Structures and Bonding Modes

The geometries of the phosphine-protected AuNCs (**Au_n-P**) and their NHC homologs (**Au_n-C**) were optimized and compared. The formers are found to be in good agreement with their corresponding X-ray structures.^{33,44,46,47,49,51,52} Together with those of their NHC homologs (**Au_n-C**), they are shown in Figure 1. Their corresponding MO diagrams are represented in the form of density-of-states (DOS) plots in Figures S1-S6 (Annex). They all exhibit similar features, with the $5d(\text{Au})$ states contributing mainly to the large band below the HOMO and the $6s/6p(\text{Au})$ to the lowest unoccupied states. As examples, those of the smallest **Au₆-X** and the largest **Au₁₃Cl₂-X** species ($X = \text{P}, \text{C}$) are shown in Figure 2. The HOMOs and LUMOs of the computed **Au_n-P** and **Au_n-C** species are pictured in Figures S7 and S8 (Annex), respectively.

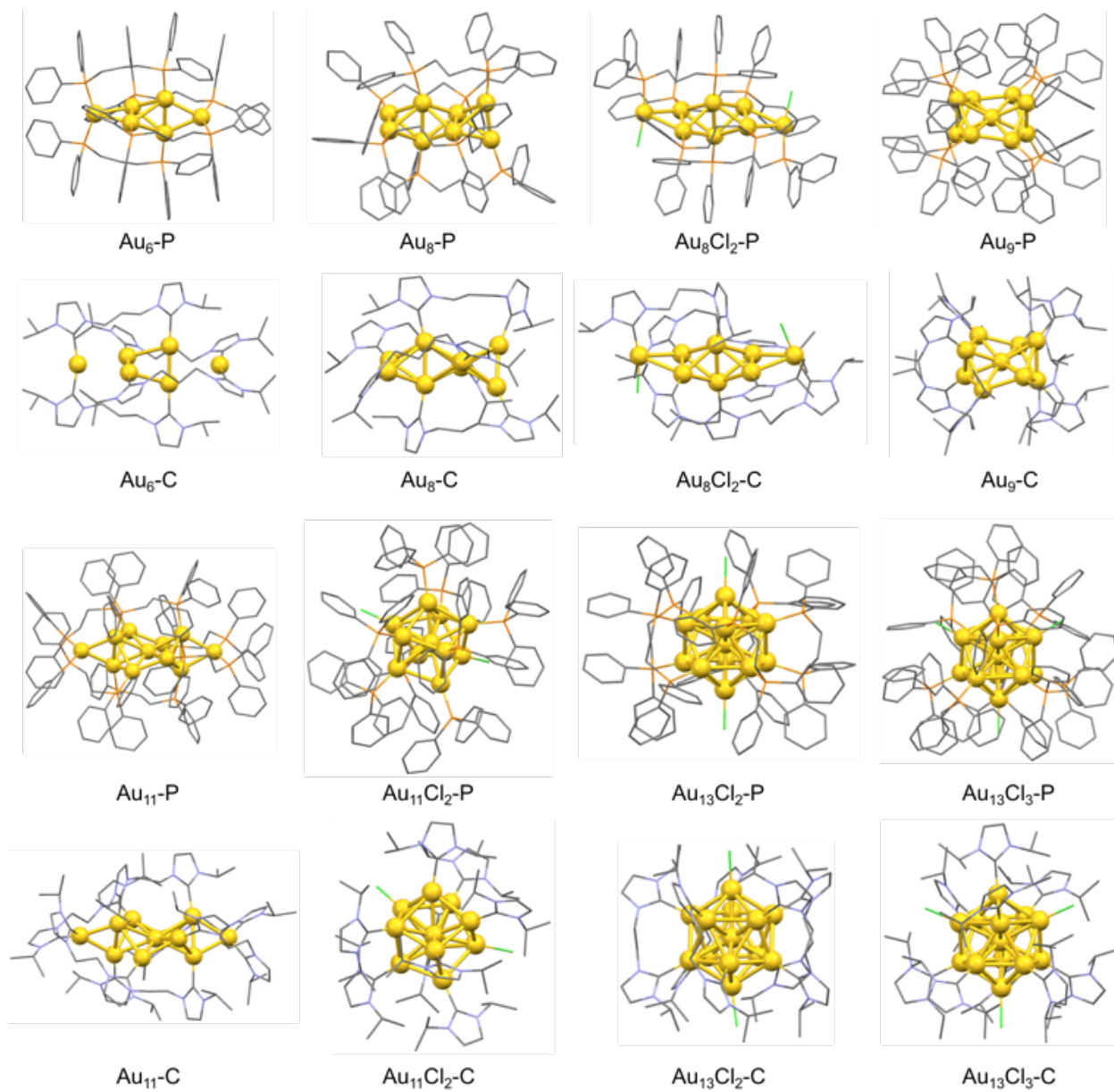


Figure 1. Optimized geometries of the computed Au_n-X clusters ($X = P, C$).

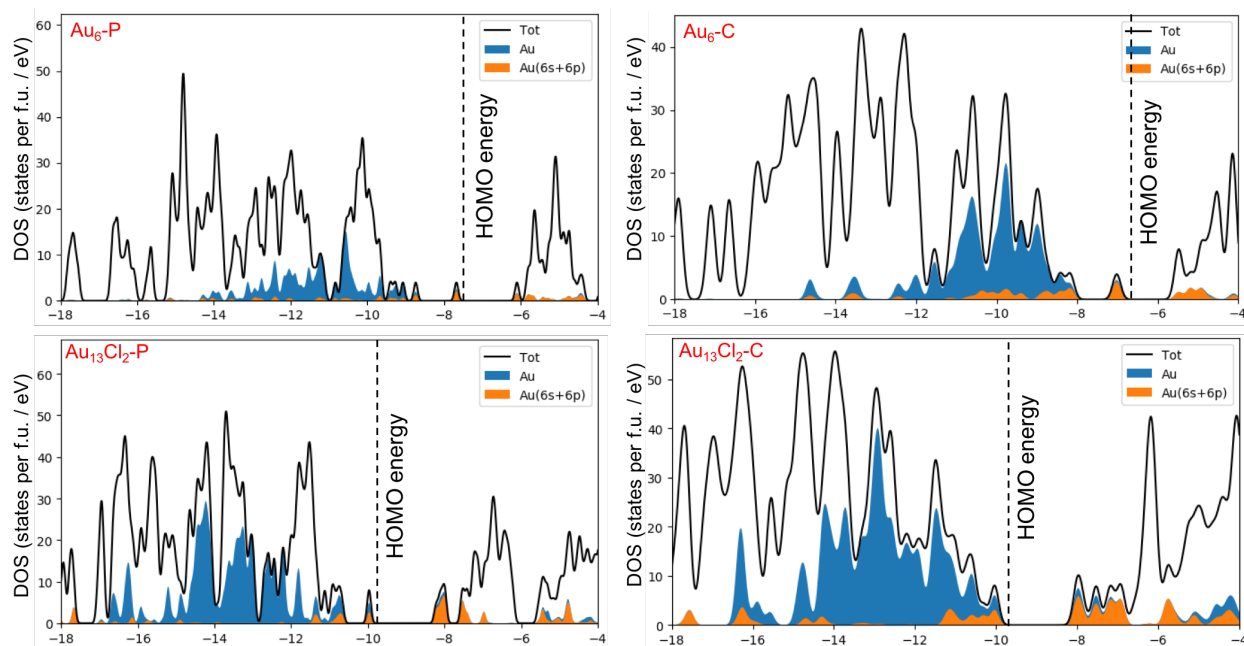


Figure 2. Density of states of $\text{Au}_6\text{-X}$ (top) and $\text{Au}_{13}\text{Cl}_2\text{-X}$ (bottom) ($X = \text{P}, \text{C}$). Gaussian full width at half maximum: 0.05 eV. The dotted line corresponds to the energy of the HOMO.

The core structure of $\text{Au}_6\text{-P}$ consists of an edge-bridged tetrahedron (Figure 1). Whereas its X-ray structure is of S_4 symmetry, its DFT-optimized geometry was found to be slightly distorted into D_2 symmetry. In a first approximation, the computed data given in Table 2 are consistent with a view of $\text{Au}_6\text{-P}$ made of two $\text{R}_3\text{P-Au(0)-Au(0)-PR}_3$ sub-systems (each containing a 2 electron/2-center bond) and two $\text{R}_3\text{P-Au(I)-PR}_3$ units. In both fragment types, the 14-electron gold centers adopt the (approximately) linear ‘ ML_2 ’ coordination mode expected to favor its stability for this particular electron count.⁶⁸ This is confirmed by the nature of the HOMO (b_1) and HOMO-1 (a) of $\text{Au}_6\text{-P}$, which can be described as the out-of-phase and in-phase combinations, respectively, of the $\sigma(\text{Au-Au})$ bonding orbitals of the two $\text{R}_3\text{P-Au(0)-Au(0)-PR}_3$ moieties (Figure S7, Annex). These orbitals, of large $6s/6p$ character, are moderately delocalized on the $\text{R}_3\text{P-Au(I)-PR}_3$ fragments, suggesting that the 4 electrons remain principally located on the two short Au-Au bonds of the Au_4 tetrahedron, as also confirmed by the much smaller Wiberg bond indices of the other Au-Au contacts (Table 2). It thus can be concluded that these longer Au-Au contacts are largely the result of metallophilic interactions. The LUMO (a) is also of important $6s/6p$ character and has significant localization on the two bridging Au atoms. $\text{Au}_6\text{-C}$ differs from $\text{Au}_6\text{-P}$ in the fact that each of its two L-Au(0)-Au(0)-L and two L-Au(I)-L fragments are even less interacting with the others (see data in Table 2), so that they

can be considered as almost independent from each other. Nevertheless, the HOMO (b_1) and HOMO-1 (a) of **Au₆-C** are similar to their **Au₆-P** counterparts (Figure S8, Annex). The LUMO and LUMO+1 are ligand-based levels. Although localized in part on the bridging Au atoms, the LUMO is different from the LUMO of **Au₆-P**. The LUMO+2 (a), mainly localized on the outer Au atoms, is the counterpart of the **Au₆-P** LUMO.

Table 2. Relevant computed data for the $[\text{Au}_6\text{L}_4]^{2+}$ clusters (L = dppp (**Au₆-P**) and L = di-NHC'p (**Au₆-C**)). Au_t and Au_b designate the atoms of the central tetrahedron and the bridging atoms, respectively. Experimental interatomic distances of **Au₆-P** are provided for comparison.

		Au₆-P exp ⁴⁴ (S_4)	Au₆-P (D_2)	Au₆-C (D_2)
Distance (Å) [WBI] ^a	Au _t -Au _t	2.630 × 2 2.923 × 2 2.923 × 2 av. 2.825	2.630 [0.302] × 2 2.861 [0.032] × 2 2.972 [0.023] × 2 av. 2.821 [0.119]	2.561 [0.462] × 2 3.178 [0.019] × 2 3.390 [0.011] × 2 av. 3.043 [0.164]
	Au _b -Au _t	2.798 × 4	2.790 [0.090] × 4	3.601 [0.013] × 4
	Au-L	av. 2.378	av. 2.332 [0.391]	av. 2.069 [0.441]
HOMO-LUMO gap (eV)			1.58	1.53
NAO ^b charge	Au _t		-0.02 × 4	-0.04 × 4
	Au _b		+0.27 × 2	+0.42 × 2
	L		+0.39 × 4	+0.33 × 4

^aWiberg bond index. ^bNatural atomic orbital.

The core structure of **Au₈-P** consists of three edge-sharing linearly arranged tetrahedra (Figure 1). Its ideal symmetry is S_4 , whereas after relaxation its symmetry is lowered to C_2 . It can be described as made of four quasi-linear L-Au-Au-L units packed perpendicularly along a common pseudo- S_4 axis in a staggered fashion. The shortest Au-Au distances are those within these L-Au-Au-L fragments. The favored electron count for an Au₄ tetrahedron is 2,⁶⁹ so it is expected that the 6 electrons of **Au₈-P** are delocalized over the three tetrahedra. This is supported by the Au-Au WBIs given in Table 3 that are all significant, contrarily to the case of **Au₆-P** (Table 2). A more detailed analysis of their disparity and examination of the NAO charges tend to favor the view of a 2-electron central tetrahedron $[\text{Au}_4(\text{PR}_3)_4]^{2+}$ interacting in a moderate but significant covalent way with two linear R₃P-Au(0)-Au(0)-PR₃ units. The HOMO (a) and HOMO-1 (b), of large 6s/6p character, can be associated with the two outer Au(0)-Au(0) bonding pairs, partly delocalized on the central tetrahedron (Figure S7, Annex). It was not possible to identify a unique orbital associated with the third bonding pair, because

of orbital mixing, but several *5d*-type levels present some non-negligible *6s/6p* bonding character within the central tetrahedron. The LUMO and LUMO+1, both of *b* symmetry, are *6s/6p* Au–Au antibonding orbitals.

As for the Au₆ systems described above, substituting the phosphines in **Au₈-P** by NHC ligands tends to reinforce the Au–Au bonding in the four R₃P–Au–Au–PR₃ units and weakens somewhat the other Au–Au contacts, but the effect is not as strong as in the Au₆ systems. The HOMO and HOMO-1 of **Au₈-C** are the counterparts of those of **Au₈-P**. The LUMO+2 and LUMO of **Au₈-C** are the counterparts of the LUMO and LUMO+1 of **Au₈-P** (Figure S8, Annex). As for the Au₆ systems, a slightly smaller HOMO-LUMO gap is computed when phosphines are substituted by NHC ligands.

Table 3. Relevant computed data for [Au₈L₄]²⁺ clusters (L = dppp (**Au₈-P**) and L = di-NHC’p (**Au₈-C**)). Experimental interatomic distances of **Au₈-P** are provided for comparison.

		Au₈-P exp ⁴⁶ (<i>S</i> ₄)	Au₈-P (<i>C</i> ₂)	Au₈-C (<i>C</i> ₂)
Distance (Å) [WBI]	Au _t –Au _t (center)	min. 2.630 max. 2.896 av. 2.785	min. 2.687 [0.213] max. 2.887 [0.086] av. 2.790 [0.135]	min. 2.649 [0.268] max. 3.083 [0.074] av. 2.842 [0.151]
	Au _t –Au _t (outer)	min. 2.607 max. 2.854 av. 2.795	min. 2.646 [0.302] max. 2.866 [0.064] av. 2.812 [0.108]	min. 2.640 [0.331] max. 3.096 [0.038] av. 2.864 [0.115]
	Au–L	av. 2.304	av. 2.314 [0.381]	av. 2.067 [0.399]
HOMO-LUMO gap (eV)			1.79	1.67
NAO charge (av.)	Au (center)		+0.10 x 4	+0.17 x 4
	Au (outer)		–0.01 x 4	+0.06 x 4
	L		+0.41 x 4	+0.27 x 4

The structural arrangement of the **Au₈Cl₂-P** cluster differs from that of **Au₈-P** (Figure 1). It exhibits a core made of two edge-sharing tetrahedra capped on both sides by two nearly linear R₃P–Au_b–Cl units. Its ideal symmetry is *D*_{2h}, but DFT computations found it slightly distorted into *C*₁ after relaxation. This is a 4-electron species, and the NAO charge distribution (Table 4) indicates that the two bridging atoms can be considered as Au_b(I) centers. The 4 electrons can thus be associated with the bi-tetrahedron, where they are predominantly located on the R₃P–Au_m–Au_m–PR₃ and R₃P–Au_s–Au_s–PR₃ bonds, as shown by the corresponding WBIs. This is in line with the composition and shape of the HOMO and HOMO-1 (Figure S7, Annex) orbitals of **Au₈Cl₂-P**, which are associated with these 4 electrons. The LUMO and LUMO+1 are *6s/6p* in composition associated with the bridging Au_b atoms and the bi-tetrahedron, respectively (Figure S7, Annex). Compound **Au₈Cl₂-C** has similar arrangement and electronic structure as

its phosphine homolog (Figure S8, Annex). When going from **Au₈Cl₂-P** to **Au₈Cl₂-C**, a strengthening of the R₃PAu–AuPR₃ bond and some weakening of the other Au–Au bonds is observed, a tendency already noted in the previous clusters, but less pronounced in the present systems. In contrast with the previous Au₆ and Au₈ systems, a larger HOMO-LUMO gap is computed when phosphine ligands are substituted by NHC ligands.

Table 4. Relevant computed data for [Au₈Cl₂L₄]²⁺ clusters (L = dppp (**Au₈Cl₂-P**) and L = di-NHC’p (**Au₈Cl₂-C**)). Experimental interatomic distances of **Au₈Cl₂-P** are provided for comparison. Au_m and Au_s designate the middle and side atoms of the bi-tetrahedron, respectively, and Au_b the bridging atoms.

		Au₈Cl₂-P exp ⁴⁶ (<i>D</i> _{2h})	Au₈Cl₂-P (<i>C</i> ₁)	Au₈Cl₂-C (<i>C</i> ₁)
Distance (Å) [WBI]	Au _m –Au _m	2.648	av. 2.676 [0.196]	av. 2.667 [0.230]
	Au _s –Au _s	av. 2.654	av. 2.692 [0.244]	av. 2.691 [0.273]
	Au _m –Au _s	av. 2.821	av. 2.849 [0.089]	av. 2.878 [0.093]
	Au _s –Au _b	av. 3.026	av. 2.960 [0.042]	av. 3.034 [0.032]
	Au–L	av. 2.302	av. 2.311 [0.441]	av. 2.062 [0.449]
	Au–Cl	av. 2.289	av. 2.348 [0.394]	av. 2.346 [0.423]
HOMO-LUMO gap (eV)			1.87	2.03
NAO charge (av.)	Au _m		+0.14 x 2	+0.22 x 2
	Au _s		+0.05 x 4	+0.12 x 4
	Au _b		+0.30 x 2	+0.37 x 2
	L		+0.49 x 4	+0.35 x 4
	Cl		–0.52 x 2	–0.54 x 2

The 6-electron **Au₉-P** cluster that we investigated (Figure 1) is generally described as a bicapped centered chair,^{47,48} that is, a centered Au₆ chair-like ring with two opposite vertices capped by two supplementary gold atoms. It has an isomer exhibiting a centered crown,⁷⁰ which is not discussed here. The whole structure of **Au₉-P** is of ideal *D*₂ symmetry. Analysis of the data in Table 5 and its Kohn-Sham orbitals allows us to describe **Au₉-P** as an oblate-distorted *superatom*, with corresponding 1S² 1P⁴ closed-shell electron configuration. The HOMO (*b*₂) and the HOMO-1 (*b*₁) are the P_x and P_y orbitals, whereas the LUMO+1 is the P_z counterpart (Figure S7, Annex). The LUMO is the D_{x²-y²} orbital. The electronic structure of **Au₉-C** is the same as that of **Au₉-P**, except the LUMO and LUMO+1, which are inverted in energy (Figure S8, Annex). Again, a small strengthening of the Au–Au bonding is noted when going from **Au₉-P** to **Au₉-C**. Comparable HOMO-LUMO gaps are computed for both species.

Table 5. Relevant computed data for $[\text{Au}_9\text{L}_8]^{3+}$ clusters (L = PPh₃ (**Au₉-P**) and L = NHC' (**Au₉-C**)). Experimental interatomic distances of **Au₉-P** are provided for comparison. Au_c and Au_p designate the unique central and the eight peripheral atoms, respectively.

		Au₉-P exp ⁴⁷ (<i>D</i> ₂)	Au₉-P (<i>D</i> ₂)	Au₉-C (<i>D</i> ₂)
Distance (Å) [WBI]	Au _c -Au _p	av. 2.692	av. 2.717 [0.132]	av. 2.729 [0.144]
	Au _p -Au _p	av. 2.834	av. 2.842 [0.096]	av. 2.888 [0.099]
	Au-L	av. 2.281	av. 2.294 [0.441]	av. 2.043 [0.460]
HOMO-LUMO gap (eV)			1.54	1.50
NAO charge (av.)	Au _c		-0.05	-0.05
	Au _p		+0.08	+0.16
	L		+0.30	+0.22

The 8-electron **Au₁₁-P** cluster (Figure 1) can be viewed as resulting from the bridging of the **Au₉-P** metal core on two opposite sides (along the *y* axis) by two supplementary Au(PPh₃)₂ units. It has two more electrons than **Au₉-P** that are located in a kind of 1D_y² HOMO, resulting in the prolate 1S² 1P⁴ 1D² closed-shell configuration. Its LUMO can be tentatively described as a 2P_y level (Figure S7, Annex). **Au₁₁-C** has comparable geometry (Table 6) and electronic structure (Figure S8, Annex).

Table 6. Relevant computed data for $[\text{Au}_{11}\text{L}_6]^{3+}$ clusters (L = dppe (**Au₁₁-P**) and L = di-NHC'e (**Au₁₁-C**)). Experimental interatomic distances of **Au₁₁-P** are provided for comparison. Au_c, Au_p and Au_b designate the unique central, the eight peripheral atoms and the two bridging atoms, respectively.

		Au₁₁-P exp ⁴⁹ (<i>C</i> ₂)	Au₁₁-P (<i>C</i> ₂)	Au₁₁-C (<i>C</i> ₂)
Distance (Å) [WBI]	Au _c -Au _p	av. 2.746	av. 2.745 [0.101]	av. 2.828 [0.110]
	Au _p -Au _p	av. 2.859	av. 2.878 [0.104]	av. 2.973 [0.109]
	Au _b -Au _p	av. 2.801	av. 2.773 [0.126]	av. 2.814 [0.158]
	Au-L	av. 2.319	av. 2.317 [0.420]	av. 2.087 [0.388]
HOMO-LUMO gap (eV)			1.40	1.49
NAO charge (av.)	Au _c		-0.16	-0.18
	Au _p		+0.03	+0.12
	Au _b		+0.29	+0.48
	L		+0.39	+0.21

Finally, the last three phosphine clusters of the series (Table 1), namely **Au₁₁Cl₂-P**, **Au₁₃Cl₂-P** (already theoretically studied previously)⁷¹ and **Au₁₃Cl₃-P** (Figure 1), are more compact, exhibiting a centered icosahedral core (incomplete in the case of **Au₁₁Cl₂-P**). The somewhat

distorted icosahedra display rather homogeneous Au_c-Au_p distances (Table 7). They are all regular 8-electron pseudo-spherical *superatoms* with $1S^2 1P^6$ configuration. The HOMOs and LUMOs are of 1P and 1D nature, respectively (Figure S7, Annex). Their NHC counterparts, **Au₁₁Cl₂-C**, **Au₁₃Cl₂-C**, and **Au₁₃Cl₃-C** exhibit quite similar features (Table 7 and Figure S8, Annex).

Hence, besides the already characterized NHC-protected as protecting ligands for Au₆ and Au₁₃ clusters,^{32,33} carbene ligands appear to be able to stabilize gold clusters of any size. Thus, size-dependent properties related to cluster core nuclearity can be explored, in addition to the versatility shown by NHC's characteristics ranging from strong to weak donor ligands.⁴⁰

Table 7. Relevant computed data for $[\text{Au}_{11}\text{Cl}_2\text{L}_8]^+$ clusters (L = PPh₃ (**Au₁₁Cl₂-P**) and L = NHC' (**Au₁₁Cl₂-C**)); $[\text{Au}_{13}\text{Cl}_2\text{L}_5]^{3+}$ clusters (L = dppe (**Au₁₃Cl₂-P**) and L = di-NHC'e (**Au₁₃Cl₂-C**)); $[\text{Au}_{13}\text{Cl}_3\text{L}_9]^{2+}$ clusters (L = PPh₃ (**Au₁₃Cl₃-P**) and L = NHC' (**Au₁₃Cl₃-C**)). Experimental interatomic distances are provided for comparison. Au_c and Au_p designate the central and peripheral atoms, respectively.

		Au₁₁Cl₂-X (C₁)			Au₁₃Cl₂-X (C₁)			Au₁₃Cl₃-X (C₁)		
		Au₁₁Cl₂-P exp ⁵¹	Au₁₁Cl₂-P	Au₁₁Cl₂-C	Au₁₃Cl₂-P exp ⁵²	Au₁₃Cl₂-P	Au₁₃Cl₂-C	Au₁₃Cl₃-C exp ³³	Au₁₃Cl₃-P	Au₁₃Cl₃-C
Distance (Å) [WBI]	Au _c -Au _p	av. 2.687	av. 2.702 [0.140]	av. 2.718 [0.155]	av. 2.764	av. 2.773 [0.121]	av. 2.787 [0.135]	av. 2.768	av. 2.801 [0.119]	av. 2.800 [0.131]
	Au _p -Au _p	av. 2.954	av. 2.877 [0.072]	av. 3.019 [0.069]	av. 2.906	av. 2.916 [0.063]	av. 2.930 [0.063]	av. 2.911	av. 2.946 [0.065]	av. 2.945 [0.066]
	Au _p -Cl	av. 2.357	av. 2.388 [0.322]	av. 2.422 [0.285]	av. 2.351	av. 2.348 [0.381]	av. 2.355 [0.384]	av. 2.352	av. 2.381 [0.324]	av. 2.394 [0.316]
	Au-L	av. 2.289	av. 2.288 [0.411]	av. 2.042 [0.429]	av. 2.289	av. 2.289 [0.664]	av. 2.036 [0.448]	av. 2.051	av. 2.313 [0.440]	av. 2.047 [0.442]
HOMO-LUMO gap (eV)			1.89	1.91		1.74	2.02		1.90	2.13
NAO charge (av.)	Au _c		-0.22	-0.24		-0.32	-0.33		-0.27	-0.27
	Au _p		+0.10	+0.16		+0.15	+0.21		+0.15	+0.21
	Cl		-0.60	-0.63		-0.55	-0.57		-0.57	-0.61
	L		+0.17	+0.12		+0.54	+0.39		+0.24	+0.17

2.3.2 Bonding Energies Analysis

A more quantitative comparison of the thermodynamic stability of the investigated phosphine and NHC species can be performed from the comparison of the energies of interaction between the ligands and the metal core, but also from the evaluation of the energy cost associated with the distortion afforded by the metal core upon complexation. To this end, we optimized the geometries of the bare $[\text{Au}_n]^{x+}$ core of the investigated species, obtained after removal of the neutral phosphine (or NHC) and anionic chloride (if any) ligands. Interestingly, these optimized bare ionic metal cores maintain the structure that they adopt in the $\text{Au}_n\text{-P}$, $\text{Au}_n\text{Cl}_m\text{-P}$ experimental structures (see Figure S9 and S10, Annex). Apart from the icosahedral $[\text{Au}_{13}]^{5+}$ core,⁷² there is no certainty that such configurations are global minima,⁷³ but at least they are local minima, as ascertained by vibrational frequency analyses. Consistently, they all present a significant HOMO-LUMO gap (> 1 eV), except that of $[\text{Au}_8]^{2+}$ (0.39 eV), perhaps due to its low compacity. Interestingly, the two optimized $[\text{Au}_{11}]^{3+}$ structures differ by a substantial energy difference of 1.07 eV at the expense of the less compact one. The energy cost afforded by the bare metal cores to prepare their structure to bonding with ligands (E_{Prep}) is given in Table 8. It is computed as the difference between the energy of the $[\text{Au}_n]^{x+}$ core as it is in the optimized $\text{Au}_n\text{-X}$ or $\text{Au}_n\text{Cl}_m\text{-X}$ species and that of the free $[\text{Au}_n]^{x+}$. Most of these values are small, consistently with the moderate change of the metal configuration upon complexation. The exception of $\text{Au}_6\text{-C}$ can be explained by its structural difference with its $\text{Au}_6\text{-P}$ counterpart (see above). That of the two $[\text{Au}_{11}]^{3+}$ cores constitute also an exception, but they show similar E_{Prep} values for both phosphine and NHC clusters. Thus, except for the $\text{Au}_6\text{-X}$ ($\text{X} = \text{P}, \text{C}$) clusters, the E_{Prep} values of the phosphine and NHC couples are very similar.

The bonding energy ($E_{\text{Bond.}}$) of the neutral phosphine or NHC ligand sphere to the $[\text{Au}_n]^{x+}$ or $[\text{Au}_n\text{Cl}_m]^{(x-m)+}$ fragments in the $\text{Au}_n\text{-X}$ or $\text{Au}_n\text{Cl}_m\text{-X}$, respectively, was computed according to $E_{\text{bond.}} = E(\text{Au}_n\text{-X}) - E([\text{Au}_n]^{x+}) - E(\text{neutral ligand sphere})$ or $E_{\text{bond.}} = E(\text{Au}_n\text{Cl}_m\text{-X}) - E([\text{Au}_n\text{Cl}_m]^{(x-m)+}) - E(\text{neutral ligand sphere})$, respectively. In these equations, all the considered (frozen) fragment structures were taken from the $\text{Au}_n\text{-X}$ or $\text{Au}_n\text{Cl}_m\text{-X}$ optimized geometries. It is clear from Table 8 that the NHCs are more strongly bonded than their phosphine analogues in all the investigated systems. The difference is not very large, but significant (a few eVs). Even taking into account the E_{Prep} destabilizing component, the difference remains in favor of stronger NHC bonding. When this difference is normalized to one phosphine/carbene function, it is found to lie within a range of 4-7 kcal/mol (E_{Prep} -corrected in the case of $\text{Au}_6\text{-X}$ couple), except for the $\text{Au}_{13}\text{Cl}_3\text{-X}$ system where it is a bit higher (10 kcal/mol).

Table 8. Energetic data associated with cluster bonding (all values in eV). $E_{Prep.}$ = energy cost afforded by the bare $[Au_n]^{x+}$ metal core to go from its equilibrium structure to that it adopts in the Au_n-X or Au_nCl_m-X cluster. $E_{bond.} = E(Au_n-X) - E([Au_n]^{x+}) - E(\text{neutral ligand sphere})$ or $E_{bond.} = E(Au_nCl_m-X) - E([Au_nCl_m]^{(x-m)+}) - E(\text{neutral ligand sphere})$. Neutral ligands = phosphines or NHCs. All fragment structures taken from the Au_n-X or Au_nCl_m-X optimized geometries.

Compound	Corresponding optimized metal core ^a	X = P $E_{Prep.}$ (metal core)	X = C $E_{Prep.}$ (metal core)	X = P $E_{Bond.}$	X = C $E_{Bond.}$
Au_6-X	$[Au_6]^{2+} (D_2)$	0.19	2.85	-24.97	-29.25
Au_8-X	$[Au_8]^{2+} (C_2)$	0.38	0.32	-26.88	-28.70
Au_8Cl_2-X	$[Au_8]^{4+} (D_{2h})$	0.21	0.23	-29.59	-31.36
Au_9-X	$[Au_9]^{3+} (D_{2h})$	0.09	0.15	-33.78	-35.86
$Au_{11}-X$	$[Au_{11}]^{3+} (C_2, \Delta E = 1.07^b)$	1.09	1.24	-39.68	-41.53
$Au_{11}Cl_2-X$	$[Au_{11}]^{3+} (C_2, \Delta E = 0.00^b)$	1.02	1.00	-25.01	-27.23
$Au_{13}Cl_2-X$	$[Au_{13}]^{5+} (I_h)$	0.49	0.40	-40.04	-42.58
$Au_{13}Cl_3-X$		0.38	0.33	-33.67	-37.32

^a See Figure S9; ^b Relative energies between $[Au_{11}]^{3+}$ isomers.

2.3.3 Optical Properties

The UV-Vis absorption spectra of the computed clusters were simulated (see Computational Details above). They are gathered in Figure 3 and the major computed electronic transition energies associated with are given in Table 9, together with corresponding experimental λ_{max} values taken from the literature where available.^{33,44-53} Although spin orbit corrections were not considered in our calculations, a good match was obtained between the computed excitation energies and the available experimental λ_{max} values, in particular for the low-energy transitions. This agreement provides confidence in the reliability of our results, retaining small deviations (0.07 to 0.32 eV) within the method error.¹⁹ Going from L = phosphine to L = NHC does not change importantly the nature and the energies of the optical transitions of a given cluster and consequently the shape of its simulated spectrum. A general blue-shift tendency is observed when going from L = phosphine to L = NHC, except for the low-energy absorption band of Au_9-X (Figure 3) in agreement with the smaller HOMO-LUMO gaps computed for the later over all. Indeed, in the Au_6-P to $Au_{11}-P$ series, the lowest energy band is associated with a HOMO→LUMO transition of metal-to-metal charge transfer (MMCT) nature (Table 9). A transition involving orbitals of the same nature is found for the homologous Au_6-C to $Au_{11}-C$ series, although in the cases of Au_6-C and Au_9-C it is a HOMO→LUMO+2 transition, which

is mainly responsible. In the pseudo-spherical $\text{Au}_{11}\text{Cl}_2\text{-X}$ to $\text{Au}_{13}\text{Cl}_3\text{-X}$ ($\text{X} = \text{P}, \text{C}$) series, the low-energy band is associated to MMCT $1\text{P} \rightarrow 1\text{D}$ transitions.

In the two $\text{Au}_6\text{-X}$ and $\text{Au}_{11}\text{-X}$ ($\text{X} = \text{P}, \text{C}$) series the major transitions of higher energy are mainly of $5d(\text{Au}) \rightarrow \text{ligand}$ character, sometimes mixed with some $5d(\text{Au}) \rightarrow 6s/6p(\text{Au})$ character. In the pseudo-spherical $\text{Au}_{11}\text{Cl}_2\text{-X}$ and $\text{Au}_{13}\text{Cl}_3\text{-X}$ ($\text{X} = \text{P}, \text{C}$) series, the high-energy transitions are mainly of $5d(\text{Au}) \rightarrow 1\text{D}$ character. Note that similar results were theoretically obtained for $\text{Au}_{13}\text{Cl}_2\text{-P}$.⁷¹

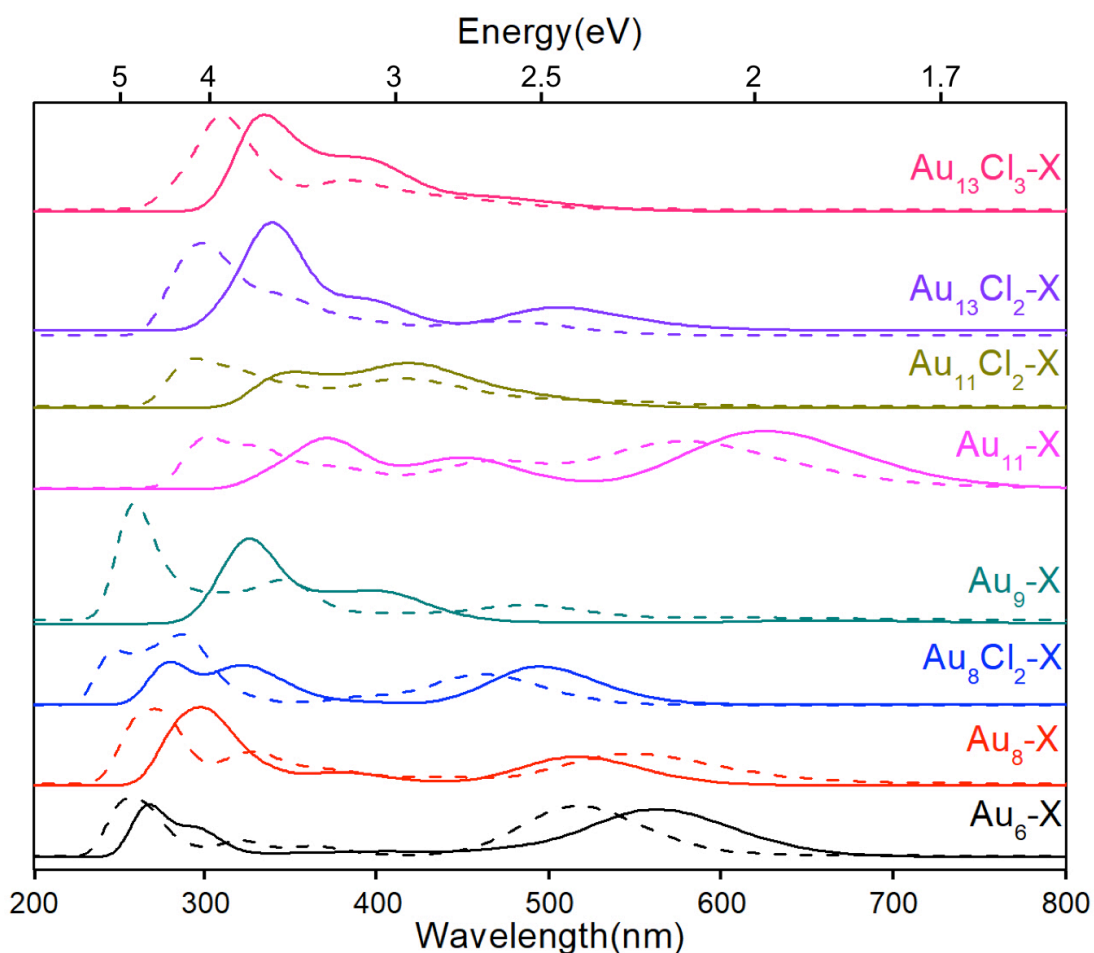


Figure 3. Simulated UV-Vis absorption spectra for computed $\text{Au}_n\text{-P}$ (solid line) and $\text{Au}_n\text{-C}$ (dotted line) clusters.

In order to get an idea of the emission wavelength change when going from phosphine- to NHC-protected species, we have computed the corresponding transitions assuming both fluorescence and phosphorescence behavior. The emission energies were calculated by TD-DFT as vertical transitions between the optimized singlet excited state and the ground state (see

Computational Details). They are given in Table 10, together with the experimental data available for the $\text{Au}_n\text{-P}$ series^{46,47,52,53} and $\text{Au}_{13}\text{Cl}_3\text{-C}$.³³ A reasonably good agreement is found between the experimental and TD-DFT values, giving us confidence in the computed data. When comparing the two $\text{Au}_n\text{-P}$ and $\text{Au}_n\text{-C}$ series, similar values are obtained, except for the $\text{Au}_6\text{-X}$ homologues for which the large difference in their emission wavelength can be related to the significant difference in their structure (see below). In any case, no systematic tendency (blue- or red-shifting) is found when going from $\text{Au}_n\text{-P}$ to $\text{Au}_n\text{-C}$, which is attributable to size-dependent and core-composition effects exhibited by the respective cluster core along the series.

Table 9. Major TD-DFT computed UV-Vis excitation energies. Bold values are associated with the more intense absorption bands in the simulated spectra shown in Figure 3. Available experimental λ_{max} values are reported for comparison.

Compound	Absorption λ (nm)			Major character of the low-energy band (X = P, C)
	Exp. ^a	X = P	X = C	
$\text{Au}_6\text{-X}$	587, 432, 326 ⁴⁵	564 , 417, 299, 272	517 , 363, 321, 262	$\text{Au}_t \rightarrow \text{Au}_b$
$\text{Au}_8\text{-X}$	590 (sh), 520, 308 ⁴⁶	516 , 390, 304	538 , 322, 277	$\text{Au}_{\text{outer}} \rightarrow \text{Au}_{\text{center}}$
$\text{Au}_8\text{Cl}_2\text{-X}$	508, 390, 322 ⁴⁶	494 , 327 , 281	460 , 298 , 277	$\text{Au}_{m+s} \rightarrow \text{Au}_b$
$\text{Au}_9\text{-X}$	443, 375 (Sh), 352 (sh), 314 ⁴⁷	404, 332	488 , 347 , 262	$1\text{P}_x \rightarrow 1\text{D}_{x^2-y^2}$
$\text{Au}_{11}\text{-X}$	663, 471 (sh), 390, 316 ⁴⁹	625 , 445, 370	573 , 472, 326	$1\text{D}_{y^2} \rightarrow 2\text{P}_y$
$\text{Au}_{11}\text{Cl}_2\text{-X}$	416, 312, 240 ⁵¹	426 , 353	416 , 298	$1\text{P} \rightarrow 1\text{D}$
$\text{Au}_{13}\text{Cl}_2\text{-X}$	493, 359, 304 (sh) ⁵²	505, 390, 340	470, 408, 354, 307	$1\text{P} \rightarrow 1\text{D}$
$\text{Au}_{13}\text{Cl}_3\text{-X}$	490, 420, 330 ³³	466, 391, 329	434, 376, 304	$1\text{P} \rightarrow 1\text{D}$

^aX = P except for $\text{Au}_{13}\text{Cl}_3\text{-X}$, for which X = C.³³

The phosphorescence emission energies were computed as vertical transitions between the triplet state in its equilibrium geometry and the singlet state in the same geometry. The results are given in Table 11. To our knowledge, no experimental evidence of phosphorescence has been reported for the known compounds. As in the case of fluorescence, the results do not show any general trend when going from phosphine- to NHC-protected clusters. Most of the computed transition energies are within the near-IR and IR range, which probably explains why phosphorescence is disfavored with respect to thermal relaxation, with perhaps the exception of $\text{Au}_{13}\text{Cl}_2\text{-X}$, $\text{Au}_{13}\text{Cl}_3\text{-X}$ and $\text{Au}_8\text{Cl}_2\text{-X}$ (X = P, C).

Table 10. TD-DFT computed hypothetical fluorescence emission energies.

Compound	E_{emission}	Compound	E_{emission}
Au₆-P	2.24 eV (552 nm)	Au₆-C	1.25 eV (992 nm)
Au₈-P	1.81 eV (683 nm) Non-luminescent ⁵³	Au₈-C	1.75 eV (707 nm)
Au₈Cl₂-P	2.08 eV (595 nm) Exp. 2.07 eV (597 nm) ⁴⁶	Au₈Cl₂-C	2.62 eV (473 nm)
Au₉-P	1.39 eV (891 nm) Exp. 2.14 eV, 1.45 eV (579 nm, 853 nm) ⁴⁷	Au₉-C	1.52 eV (814 nm)
Au₁₁-P	1.85 eV (670 nm)	Au₁₁-C	1.82 eV (683 nm)
Au₁₁Cl₂-P	1.62 eV (764 nm) Non-luminescent ⁵³	Au₁₁Cl₂-C	1.86 eV (667 nm)
Au₁₃Cl₂-P	1.75 eV (709 nm) Exp. 1.62 eV (766 nm) ⁵²	Au₁₃Cl₂-C	1.72 eV (720 nm)
Au₁₃Cl₃-P	1.76 eV (705 nm)	Au₁₃Cl₃-C	1.71 eV (723 nm) Exp. 1.59 – 1.70 eV (730-780 nm) ³³

Table 11. DFT-computed hypothetical phosphorescence emission.

Compound	E_{emission}	Compound	E_{emission}
Au₆-P	1.46 eV (849 nm)	Au₆-C	1.13 eV (1097 nm)
Au₈-P	0.68 eV (1823 nm)	Au₈-C	0.85 eV (1458 nm)
Au₈Cl₂-P	1.70 eV (729 nm)	Au₈Cl₂-C	1.82 eV (681 nm)
Au₉-P	1.09 eV (1137 nm)	Au₉-C	0.40 eV (3099 nm)
Au₁₁-P	1.37 eV (904 nm)	Au₁₁-C	1.02 eV (1215 nm)
Au₁₁Cl₂-P	1.01 eV (1227 nm)	Au₁₁Cl₂-C	0.81 eV (1530 nm)
Au₁₃Cl₂-P	1.40 eV (885 nm)	Au₁₃Cl₂-C	1.41 eV (879 nm)
Au₁₃Cl₃-P	1.45 eV (855 nm)	Au₁₃Cl₃-C	1.50 eV (826 nm)

Going from **Au₆-P** to **Au₆-C**, a red shift in the fluorescence emission wavelength is found, which is also observed to a lesser extent in the **Au₈-P/Au₈-C** counterparts. Interestingly, a blue shift is found in the case of the chlorine-derivatives **Au₈Cl₂-P/Au₈Cl₂-C**, which is also observed for the **Au₁₁-P/Au₁₁-C** and **Au₁₁Cl₂-P/Au₁₁Cl₂-C** pairs. A blue shift in the emission is also calculated for the **Au₉-P/Au₉-C** pair, depicting strong differences with the **Au₆**, **Au₈**, and **Au₁₁** cores. Hence, different cluster cores retain different behavior when NHC's ligands are included, increasing the versatility of the properties.

Finally, we would like to make some comments about the energy difference between the first excited singlet and triplet states (Table S1). These gaps range 1.9-3.3 eV and 0.7-1.8 eV for the **Au_n-P** and **Au_n-C** series, respectively. Although these values are not accurate due to the way they were calculated (see Computational Details), two general trends can be noted. The

first one is that within each series, this gap increases with the nuclearity. The second one is that it is much larger for $\text{Au}_n\text{-P}$ than for their $\text{Au}_n\text{-C}$ counterparts, whatever n . The particularly large gap computed for the $\text{Au}_n\text{-P}$ derivatives disfavors the intersystem crossing, also in agreement with the non-observation of phosphorescence in this experimentally characterized series. From this point of view, the $\text{Au}_n\text{-C}$ series appears more capable for enabling intersystem crossing and possible phosphorescence.

2.4 Conclusions

The hypothetical NHC-protected gold clusters we have calculated exhibit similar structural chemistry as their experimentally characterized phosphine-protected analogs. The similarities in bond distances and Wiberg bond indices are indicative of analogous thermodynamic stability. This is confirmed by the evaluation of the Au-P and Au-C bonding energies in these species, the latter being even slightly stronger than the former by a few kcal/mol. This is in phase with what is known from the few NHC-protected gold clusters known so far.^{32-34,36} The comparable HOMO-LUMO gaps are also indicative of comparable kinetic stability. Their optical properties are also likely to be quite similar, the NHC derivatives being however more prone to exhibit phosphorescence behavior. Our results show the feasibility to achieve variable-sized stable NHC-protected gold clusters with properties related to their parent phosphine-protected species. This allows further evaluation of size-dependent properties, which in addition, takes advantage of the versatility in the electronic properties of the NHC's family, ranging from strong to weak donor ligands.

2.5 References

- 1 Qian, H.; Jin, R. Controlling nanoparticles with atomic precision: The case of $\text{Au}_{144}(\text{SCH}_2\text{CH}_2\text{Ph})_{60}$. *Nano Lett.* **2009**, *9*, 4083–4087.
- 2 Levi-Kalisman, Y.; Jadzinsky, P. D.; Kalisman, N.; Tsunoyama, H.; Tsukuda, T.; Bushnell, D. A.; Kornberg, R. D. Synthesis and characterization of $\text{Au}_{102}(p\text{-MBA})_{44}$ nanoparticles. *J. Am. Chem. Soc.* **2011**, *133*, 2976–2982.
- 3 Qian, H.; Zhu, M.; Wu, Z.; Jin, R. Quantum sized gold nanoclusters with atomic precision. *Acc. Chem. Res.* **2012**, *45*, 1470–1479.
- 4 Tsukuda, T. Optical properties of ultra-small gold nanostructures. *Springer Series in Chemical Physics (Progress in Photon Science)*. **2017**, *115*, 205–218.
- 5 Kang, X.; Chong, H.; Zhu, M. $\text{Au}_{25}(\text{SR})_{18}$: the captain of the great nanocluster ship. *Nanoscale* **2018**, *10*, 10758–10834.

- 6 Tang, Q.; Hu, G.; Fung, V.; Jiang, D. Insights into interfaces, stability, electronic properties, and catalytic activities of atomically precise metal nanoclusters from first principles. *Acc. Chem. Res.* **2018**, *51*, 2793–2802.
- 7 Pei, Y.; Wang, P.; Ma, Z.; Xiong, L. Growth-rule-guided structural exploration of thiolate-protected gold nanoclusters. *Acc. Chem. Res.* **2019**, *52*, 23–33.
- 8 Daniel, M. C.; Astruc, D. Gold nanoparticles: assembly, supramolecular chemistry, quantum-size-related properties, and applications toward biology, catalysis, and nanotechnology. *Chem. Rev.* **2004**, *104*, 293–346.
- 9 Tsukuda, T.; Tsunoyama, H.; Sakurai, H. Aerobic oxidations catalyzed by colloidal nanogold. *Chem. Asian J.* **2011**, *6*, 736–748.
- 10 Zhu, Y.; Qian, H.; Jin, R. Catalysis opportunities of atomically precise gold nanoclusters. *J. Mater. Chem.* **2011**, *21*, 6793–6799.
- 11 Kwak, K.; Kumar, S. S.; Lee, D. Selective determination of dopamine using quantum-sized gold nanoparticles protected with charge selective ligands. *Nanoscale*. **2012**, *4*, 4240–4246.
- 12 Sakai, N.; Tatsuma, T. Photovoltaic properties of glutathione-rotected gold clusters adsorbed on TiO₂ electrodes. *Adv. Mater.* **2010**, *22*, 3185–3188.
- 13 Wu, Z.; Wang, M.; Yang, J.; Zheng, X.; Cai, W.; Meng, G.; Qian, H.; Wang, H.; Jin, R. Well-defined nanoclusters as fluorescent nanosensors: A case study on Au₂₅(SG)₁₈. *Small*. **2012**, *8*, 2028–2035.
- 14 Murray, R. W. Nanoelectrochemistry: metal nanoparticles, nanoelectrodes, and nanopores. *Chem. Rev.* **2008**, *108*, 2688–2720.
- 15 Galloway, J. M.; Bramble, J. P.; Rawlings, A. E.; Burnell, G.; Evans, S. D.; Staniland, S. S. Biotemplated magnetic nanoparticle arrays. *Small* **2012**, *8*, 204–208.
- 16 Du, Y.; Sheng, H.; Astruc, D.; Zhu, M. Atomically precise noble metal nanoclusters as efficient catalysts: A bridge between structure and properties. *Chem. Rev.* **2020**, *120*, 526–622.
- 17 Yao, Q.; Chen, T.; Yuan, X.; Xie, J. Toward total synthesis of thiolate-protected metal nanoclusters. *Acc. Chem. Res.* **2018**, *51*, 1338–1348.
- 18 Sakthivel, N. A.; Dass, A. Aromatic thiolate-protected series of gold nanomolecules and a contrary structural trend in size evolution. *Acc. Chem. Res.* **2018**, *51*, 1774–1783.
- 19 Aikens, C. M. Electronic and geometric structure, optical properties, and excited state behavior in atomically precise thiolate-stabilized noble metal nanoclusters. *Acc. Chem. Res.* **2018**, *51*, 3065–3073.

- 20 Ghosh, A.; Mohammed, O. F.; Bakr, O. M. Atomic-level doping of metal clusters. *Acc. Chem. Res.* **2018**, *51*, 3094–3103.
- 21 Hossain, S.; Niihori, Y.; Nair, L. V.; Kumar, B.; Kurashige, W.; Negishi, Y. Alloy clusters: Precise synthesis and mixing effects. *Acc. Chem. Res.* **2018**, *51*, 3114–3124.
- 22 Harb, M.; Rabilloud, F.; Simon, D. Structural, electronic, magnetic and optical properties of icosahedral silver–nickel nanoclusters. *Phys. Chem. Chem. Phys.* **2010**, *12*, 4246–4254.
- 23 Yu, C.; Schira, R.; Brune, H.; Issendorff, B. V.; Rabilloud, F.; Harbich, W. Optical properties of size selected neutral Ag clusters: electronic shell structures and the surface plasmon resonance. *Nanoscale* **2018**, *10*, 20821–20827.
- 24 Zhang, Q.-F.; Chen, X.; Wang, L.-S. Toward solution syntheses of the tetrahedral Au₂₀ pyramid and atomically precise gold nanoclusters with uncoordinated sites. *Acc. Chem. Res.* **2018**, *51*, 2159–2168.
- 25 Cook, A. W.; Hayton, T. W. Case studies in nanocluster synthesis and characterization: Challenges and opportunities. *Acc. Chem. Res.* **2018**, *51*, 2456–2464.
- 26 Lei, Z.; Wan, X.-K.; Yuan, S. F.; Guan, Z.-J.; Wang, Q. M. Alkynyl approach toward the protection of metal nanoclusters. *Acc. Chem. Res.* **2018**, *51*, 2465–2474.
- 27 Sharma, S.; Chakrahari, K. K.; Saillard, J.-Y.; Liu, C. W. Structurally precise dichalcogenolate-protected copper and silver superatomic nanoclusters and their alloys. *Acc. Chem. Res.* **2018**, *51*, 2475–2483.
- 28 Higaki, T.; Li, Q.; Zhou, M.; Zhao, S.; Li, Y.; Li, S.; Jin, R. Toward the tailoring chemistry of metal nanoclusters for enhancing functionalities. *Acc. Chem. Res.* **2018**, *51*, 2764–2773.
- 29 Tang, Q.; Hu, G.; Fung, V.; Jiang, D. Insights into interfaces, stability, electronic properties, and catalytic activities of atomically precise metal nanoclusters from first principles. *Acc. Chem. Res.* **2018**, *51*, 2793–2802.
- 30 Konishi, K.; Iwasaki, M.; Shichibu, Y. Phosphine-ligated gold clusters with core+exo geometries: Unique properties and interactions at the ligand-cluster interface. *Acc. Chem. Res.* **2018**, *51*, 3125–3133.
- 31 Yan, J.; Teo, B. K.; Zheng, N. Surface chemistry of atomically precise coinage–metal nanoclusters: from structural control to surface reactivity and catalysis. *Acc. Chem. Res.* **2018**, *51*, 3084–3093.
- 32 Ube, H.; Zhang, Q.; Shionoya, M. A carbon-centered hexagold (I) cluster supported by N-heterocyclic carbene ligands. *Organometallics* **2018**, *37*, 2007–2009.
- 33 Narouz, M. R.; Takano, S.; Lummis, P. A.; Levchenko, T. I.; Nazemi, A.; Kaappa, S.; Malola, S.; Yousefalizadeh, G.; Calhoun, L. A.; Stampelcoskie, K. G.; Häkkinen, H.;

- Tsukuda, T.; Crudden, C. M. Robust, highly luminescent Au₁₃ superatoms protected by N-heterocyclic carbenes. *J. Am. Chem. Soc.* **2019**, *141*, 14997–15002.
- 34 Narouz, M. R.; Osten, K. M.; Unsworth, P. J.; Man, R. W. Y.; Salorinne, K.; Takano, S.; Tomihara, R.; Kaappa, S.; Malola, S.; Dinh, C. T.; Padmos, J. D.; Ayoo, K.; Garrett, P. J.; Nambo, M.; Horton, J. H.; Sargent, E. H.; Häkkinen, H.; Tsukuda, T.; Crudden, C. M. N-heterocyclic carbene-functionalized magic-number gold nanoclusters. *Nat. Chem.* **2019**, *11*, 419–425.
- 35 Tang, Q.; Jiang, D. Comprehensive view of the ligand-gold interface from first principles. *Chem. Mater.* **2017**, *29*, 6908–6915.
- 36 Shen, H.; Deng, G.; Kaappa, S.; Tan, T.; Han, Y.; Malola, S.; Lin, S.; Teo, B. K.; Häkkinen, H.; Zheng, N. Highly robust but surface-active: An N-heterocyclic carbene-stabilized Au₂₅ nanocluster. *Angew. Chem. Int. Ed.* **2019**, *58*, 17731–17735.
- 37 Jiang, L.; Zhang, B.; Médard, G.; Seitsonen, A. P.; Haag, F.; Allegretti, F.; Reichert, J.; Kuster, B.; Bartha, J. V.; Papageorgiou, A. C. N-heterocyclic carbenes on close-packed coinage metal surfaces: bis-carbene metal adatom bonding scheme of monolayer films on Au, Ag and Cu. *Chem. Sci.* **2017**, *8*, 8301–8308.
- 38 Muñoz-Castro, A. Potential of N-heterocyclic carbene derivatives from Au₁₃(dppe)₅Cl₂ gold superatoms. Evaluation of electronic, optical and chiroptical properties from relativistic DFT. *Inorg. Chem. Front.* **2019**, *6*, 2349–2358.
- 39 Tolman, C. A. Steric effects of phosphorus ligands in organometallic chemistry and homogeneous catalysis. *Chem. Rev.* **1977**, *77*, 313–348.
- 40 Munz, D. Pushing Electrons-which carbene ligand for which application? *Organometallics* **2018**, *37*, 275–289.
- 41 Gusev, D. G.; Peris, E. The Tolman electronic parameter (TEP) and the metal–metal electronic communication in ditopic NHC complexes. *Dalton Trans.* **2013**, *42*, 7359–7364.
- 42 Arduengo, A. J.; Bertrand, G. Carbenes introduction. *Chem. Rev.* **2009**, *109*, 3209–3210.
- 43 Nelson, D. J.; Nolan, S. P. Quantifying and understanding the electronic properties of N-heterocyclic carbenes. *Chem. Soc. Rev.* **2013**, *42*, 6723.
- 44 van der Velden, J. W. A.; Bour, J. J.; Steggerda, J. J.; Beurskens, P. T.; Roseboom, M.; Noordik, J. H. Gold clusters. Tetrakis [1, 3-bis (diphenylphosphino) propane] hexagold dinitrate: preparation, x-ray analysis, and gold-197 Moessbauer and phosphorus-31 {proton} NMR spectra. *Inorg. Chem.* **1982**, *21*, 4321–4324.
- 45 Shichibu, Y.; Konishi, K. Electronic properties of [core+exo]-type gold clusters: Factors affecting the unique optical transitions. *Inorg. Chem.* **2013**, *52*, 6570–6575.

- 46 Kamei, Y.; Shichibu, Y.; Konishi, K. Generation of small gold clusters with unique geometries through cluster - to - cluster transformations: Octanuclear clusters with edge-sharing gold tetrahedron motifs. *Angew. Chem. Int. Ed.* **2011**, *50*, 7442–7445.
- 47 Wen, F.; Englert, U.; Gutrath, B.; Simon, U. Crystal structure, electrochemical and optical properties of $[\text{Au}_9(\text{PPh}_3)_8](\text{NO}_3)_3$. *Eur. J. Inorg. Chem.* **2008**, *1*, 106–111.
- 48 van der Velden, J. W. A.; Bour, J. J.; Bosman, W. P.; Noordik, J. H.; Beurskens, P. T. The electrochemical preparation of $[\text{Au}_9(\text{PPh}_3)_8]^+$. A comparative study of the structures and properties of $[\text{Au}_9(\text{PPh}_3)_8]^+$ and $[\text{Au}_9(\text{PPh}_3)_8]^{3+}$. *Recl. Trav. Chim. Pays-Bas* **1984**, *103*, 13–16.
- 49 Shichibu, Y.; Kamei, Y.; Konishi, K. Unique [core+two] structure and optical property of a dodeca-ligated undecagold cluster: critical contribution of the exo gold atoms to the electronic structure. *Chem. Commun.* **2012**, *48*, 7559–7561.
- 50 Shichibu, Y.; Negishi, Y.; Tsukuda, T.; Teranishi, T. Large-scale synthesis of thiolated Au_{25} clusters via ligand exchange reactions of phosphine-stabilized Au_{11} clusters. *J. Am. Chem. Soc.* **2005**, *127*, 13464–13465.
- 51 McKenzie, L. C.; Zaikova, T. O.; Hutchison, J. E. Structurally similar triphenylphosphine-stabilized undecagolds, $\text{Au}_{11}(\text{PPh}_3)_7\text{Cl}_3$ and $[\text{Au}_{11}(\text{PPh}_3)_8\text{Cl}_2]\text{Cl}$, exhibit distinct ligand exchange pathways with glutathione. *J. Am. Chem. Soc.* **2014**, *136*, 13426–13435.
- 52 Shichibu, Y.; Konishi, K. HCl-Induced nuclearity convergence in diphosphine-protected ultrasmall gold clusters: A novel synthetic route to “Magic-Number” Au_{13} clusters. *Small* **2010**, *6*, 1216–1220.
- 53 Konishi, K. Phosphine-coordinated pure-gold clusters: diverse geometrical structures and unique optical properties/responses. *Struct. Bond. (Gold Clusters, Colloids and Nanoparticles I)* **2014**, *161*, 49–86.
- 54 Parr, R.G.; Yang, W. *Density-Functional Theory of Atoms and Molecules*. **1994**, Oxford University Press, UK.
- 55 Grimme, S. Semiempirical GGA-type density functional constructed with a long-range dispersion correction. *J. Comput. Chem.* **2006**, *27*, 1787–1799.
- 56 a) te Velde, G.; Bickelhaupt, F. M.; van Gisbergen, S. J. A.; Guerra, C. F.; Baerends, E. J.; Snijders, J. G.; Ziegler, T. Chemistry with ADF. *J. Comput. Chem.* **2001**, *22*, 931–967; b) ADF2016, SCM, Theoretical Chemistry, Vrije Universiteit: Amsterdam, The Netherlands; <http://www.scm.com>.
- 57 van Lenthe, E.; Baerends, E. J.; Snijders, J. G. Relativistic total energy using regular approximations. *J. Chem. Phys.* **1994**, *101*, 9783–9792.

- 58 Lenthe, E. V.; Baerends, E. J. Optimized Slater-type basis sets for the elements 1–118. *J. Comput. Chem.* **2003**, *24*, 1142–1156.
- 59 Becke, A. D. Density-functional exchange-energy approximation with correct asymptotic behavior. *Phys. Rev. A* **1988**, *38*, 3098–3100.
- 60 Perdew, J. P. Density-functional approximation for the correlation energy of the inhomogeneous electron gas. *Phys. Rev. B* **1986**, *33*, 8822–8824.
- 61 Frisch, M. J.; Trucks, G. W.; Schlegel, H. B.; Scuseria, G. E.; Robb, M. A.; Cheeseman, J. R.; Scalmani, G.; Barone, V.; Petersson, G. A.; Nakatsuji, H.; Li, X.; Caricato, M.; Marenich, A. V.; Bloino, J.; Janesko, B. G.; Gomperts, R.; Mennucci, B.; Hratchian, H. P.; Ortiz, J. V.; Izmaylov, A. F.; Sonnenberg, J. L.; Williams-Young, D.; Ding, F.; Lipparini, F.; Egidi, F.; Goings, J.; Peng, B.; Petrone, A.; Henderson, T.; Ranasinghe, D.; Zakrzewski, V. G.; Gao, J.; Rega, N.; Zheng, G.; Liang, W.; Hada, M.; Ehara, M.; Toyota, K.; Fukuda, R.; Hasegawa, J.; Ishida, M.; Nakajima, T.; Honda, Y.; Kitao, O.; Nakai, H.; Vreven, T.; Throssell, K.; Montgomery, J. A., Jr.; Peralta, J. E.; Ogliaro, F.; Bearpark, M. J.; Heyd, J. J.; Brothers, E. N.; Kudin, K. N.; Staroverov, V. N.; Keith, T. A.; Kobayashi, R.; Normand, J.; Raghavachari, K.; Rendell, A. P.; Burant, J. C.; Iyengar, S. S.; Tomasi, J.; Cossi, M.; Millam, J. M.; Klene, M.; Adamo, C.; Cammi, R.; Ochterski, J. W.; Martin, R. L.; Morokuma, K.; Farkas, O.; Foresman, J. B.; Fox, D. J. *Gaussian16*, Gaussian, Inc.: Wallingford, CT, **2016**.
- 62 Glendening, E. D.; Badenhoop, J. K.; Reed, A. E.; Carpenter, J. E.; Bohmann, J. A.; Morales, C. M.; Weinhold, F. NBO 6.0. Theoretical Chemistry Institute, University of Wisconsin (Madison, WI, **2001**, <http://nbo6.chem.wisc.edu>).
- 63 Weigend F.; Ahlrichs, R. Balanced basis sets of split valence, triple zeta valence and quadruple zeta valence quality for H to Rn: Design and assessment of accuracy. *Phys. Chem. Chem. Phys.* **2005**, *7*, 3297–3305.
- 64 Runge, E.; Gross, E. K. U. Density-functional theory for time-dependent systems. *Phys. Rev. Lett.* **1984**, *52*, 997–1000.
- 65 Stephens, P. J.; Devlin, F. J.; Chabalowski, C. F.; Frisch, M. J. Ab Initio calculation of vibrational absorption and circular dichroism spectra using density functional force fields. *J. Phys. Chem.* **1994**, *98*, 11623–11626.
- 66 van Leeuwen, R.; Baerends, E. J. Exchange-correlation potential with correct asymptotic behavior. *Phys. Rev. A* **1994**, *49*, 2421–2431.
- 67 Gorelsky, S. I. *SWizard* program. Revision 4.5, <http://www.sg-chem.net>.

- 68 Albright, T. A.; Burdett, J. K.; Whangbo, M. H. *Orbital Interactions in Chemistry*. 2nd Ed. John Wiley & Sons Inc., Hoboken, New Jersey, **2013**.
- 69 Mingos, D. M. P.; Wales, D. J. *Introduction to Cluster Chemistry*. Prentice-Hall. Englewood Cliffs, **1990**.
- 70 Briant, C. E.; Hall, K. P.; Mingos, D. M. P. Structural characterisation of two crystalline modifications of $[\text{Au}_9\{\text{P}(\text{C}_6\text{H}_4\text{OMe-p})_3\}_8](\text{NO}_3)_3$: The first example of skeletal isomerism in metal cluster chemistry. *J. Chem. Soc., Chem. Commun.* **1984**, 5, 290–292.
- 71 Weerawardene, K. L. D. M.; Pandeya, P.; Zhou, M.; Chen, Y.; Jin R.; Aikens, C. M. Luminescence and electron dynamics in atomically precise nanoclusters with eight superatomic electrons. *J. Am. Chem. Soc.* **2019**, 141, 18715–18726.
- 72 Gam, F.; Paez-Hernandez, D.; Arratia-Perez, R.; Liu, C. W.; Kahlal, S.; Saillard, J. Y.; Muñoz-Castro, A. Coinage Metal Superatomic Cores: Insights into Their Intrinsic Stability and Optical Properties from Relativistic DFT Calculations. *Chem. Eur. J.*, **2017**, 23, 11330–11337.
- 73 Results obtained from a non-exhaustive search for low-energy isomers of the $[\text{Au}_n]^{x+}$ systems are provided in Figure S18.

2.6 Annex

Table S1. Computed energy difference between the first excited singlet and triplet states ($\Delta E_{S1-T1} = E_{S1} - E_{T1}$).

Compound	ΔE_{S1-T1}	Compound	ΔE_{S1-T1}
Au ₆ -P	1.91 eV	Au ₆ -C	0.71 eV
Au ₈ -P	1.86 eV	Au ₈ -C	0.96 eV
Au ₈ Cl ₂ -P	2.49 eV	Au ₈ Cl ₂ -C	0.74 eV
Au ₉ -P	2.47 eV	Au ₉ -C	0.91 eV
Au ₁₁ -P	2.74 eV	Au ₁₁ -C	1.84 eV
Au ₁₁ Cl ₂ -P	3.60 eV	Au ₁₁ Cl ₂ -C	1.05 eV
Au ₁₃ Cl ₂ -P	3.08 eV	Au ₁₃ Cl ₂ -C	1.50 eV
Au ₁₃ Cl ₃ -P	3.25 eV	Au ₁₃ Cl ₃ -C	1.32 eV

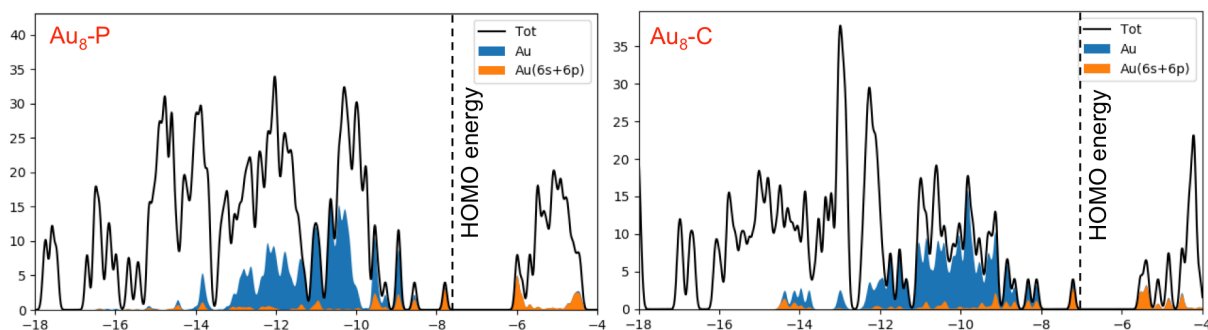


Figure S1. Density of states of Au₈-X (X = P, C).

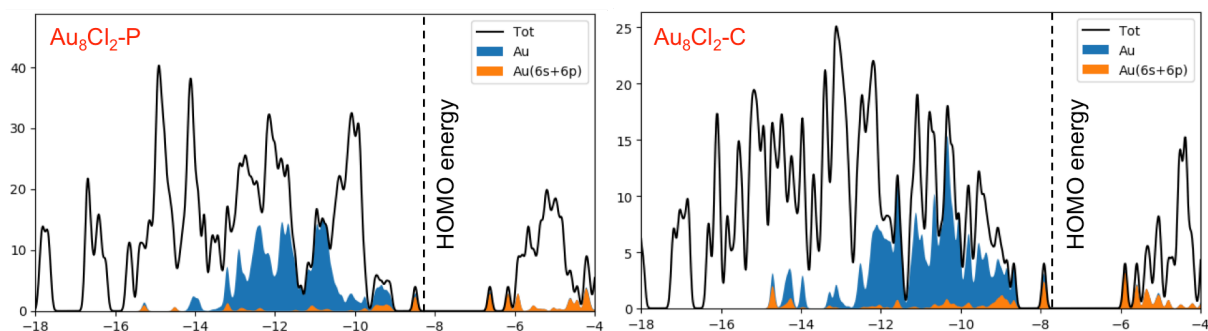


Figure S2. Density of states of Au₈Cl₂-X (X = P, C).

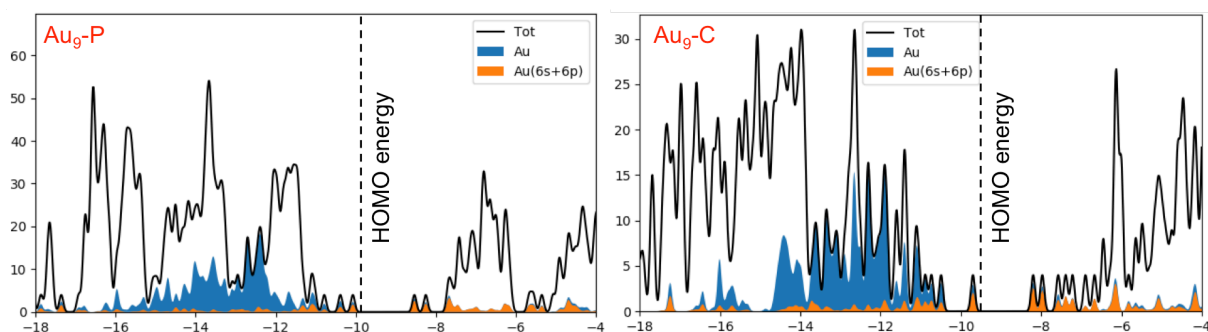


Figure S3. Density of states of $\text{Au}_9\text{-X}$ ($X = \text{P}, \text{C}$).

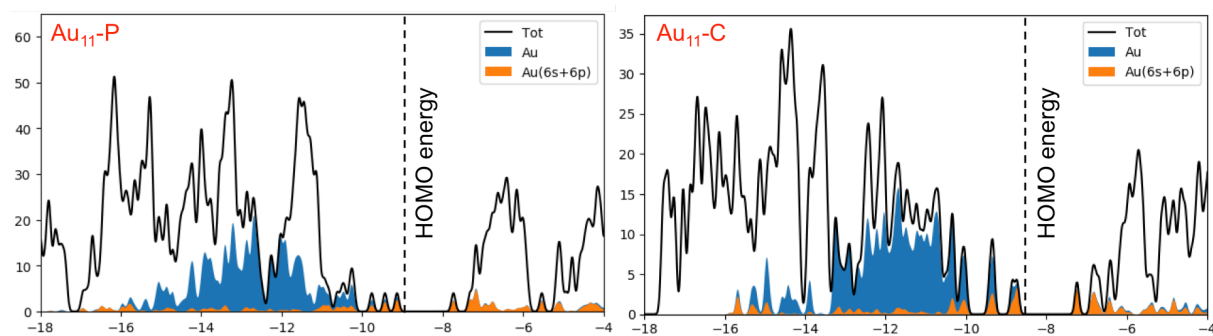


Figure S4. Density of states of $\text{Au}_{11}\text{-X}$ ($X = \text{P}, \text{C}$).

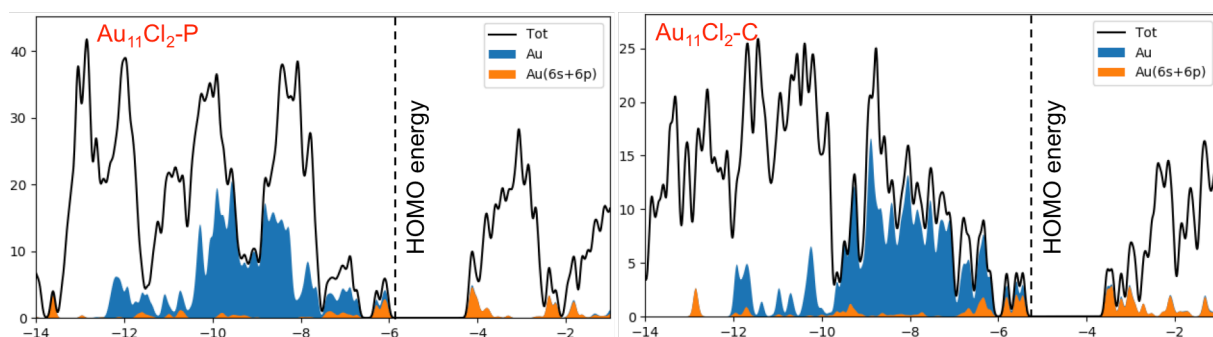


Figure S5. Density of states of $\text{Au}_{11}\text{Cl}_2\text{-X}$ ($X = \text{P}, \text{C}$).

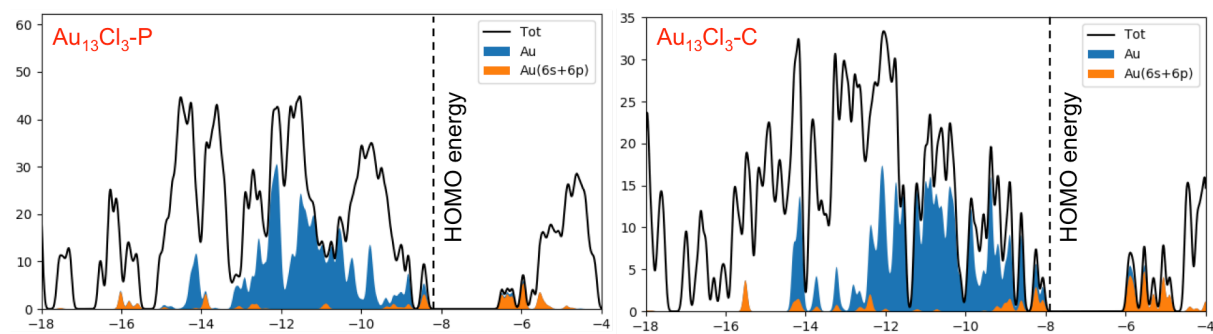


Figure S6. Density of states of $\text{Au}_{13}\text{Cl}_3\text{-X}$ ($X = \text{P}, \text{C}$).

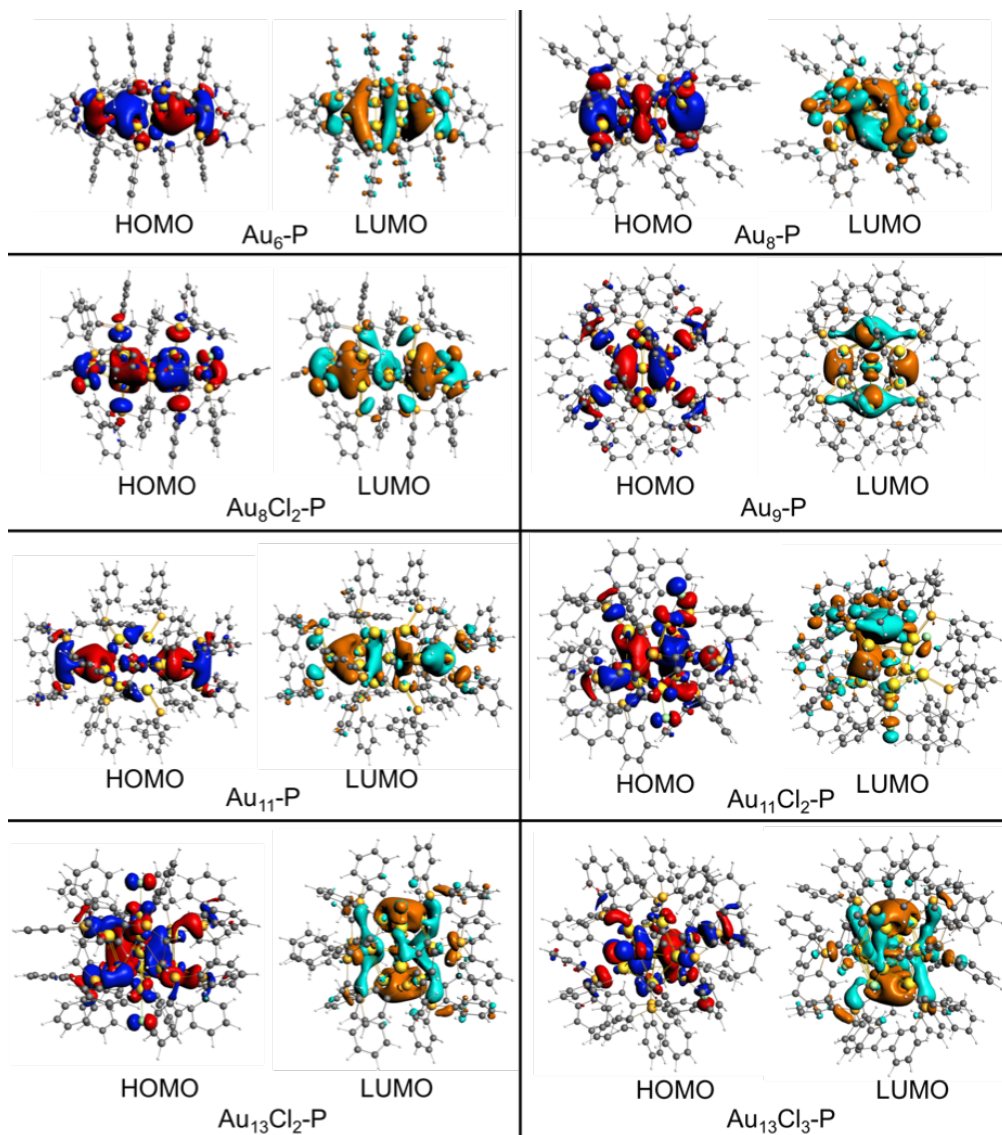


Figure S7. HOMOs and LUMOs of the computed phosphine-protected $\text{Au}_6\text{-P}$ species. Contour values are ± 0.02 (e/bohr^3)^{1/2}.

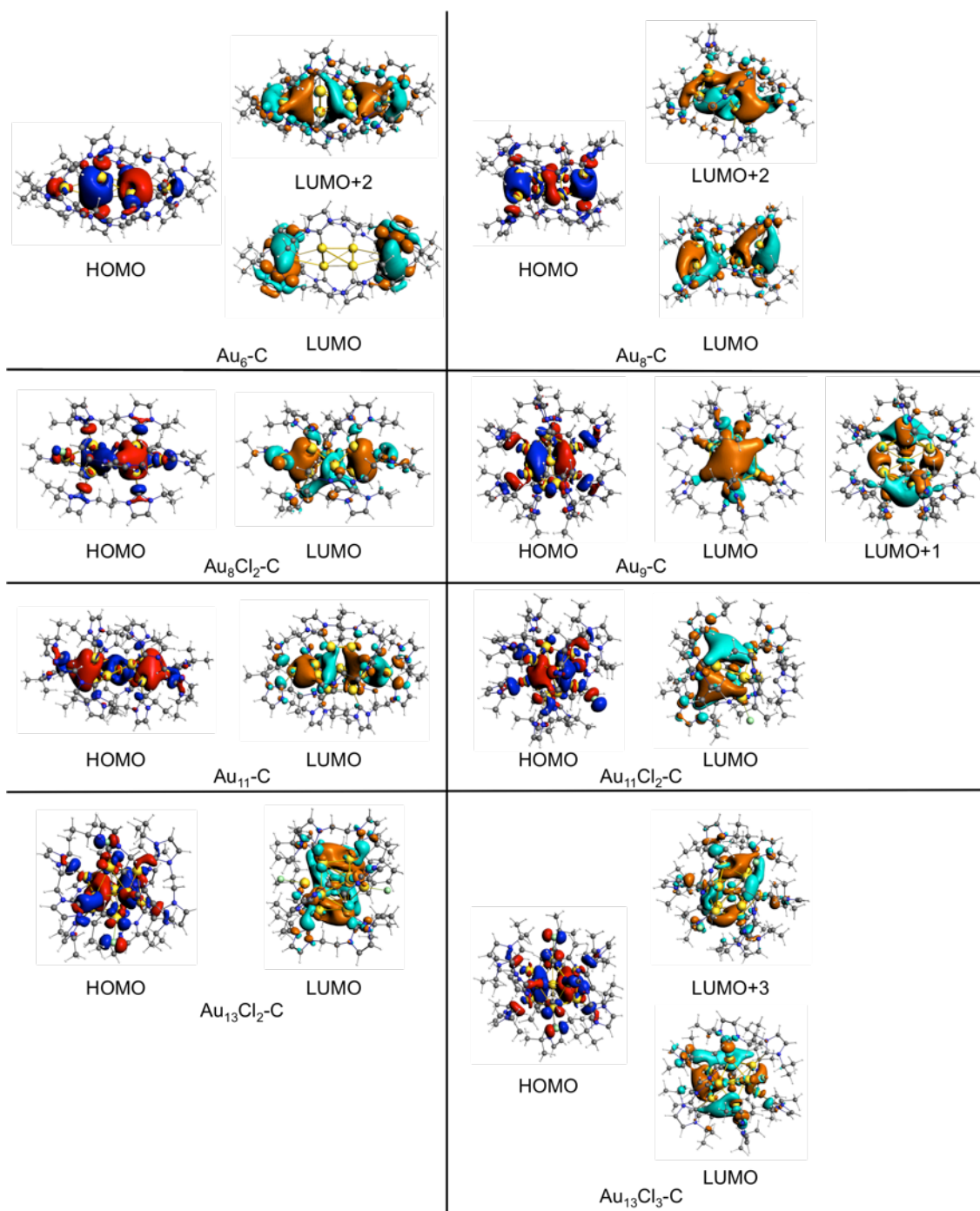


Figure S8. Some frontier orbitals of the computed phosphine-protected $\text{Au}_n\text{-C}$ species. Contour values are ± 0.02 (e/bohr^3)^{1/2}.

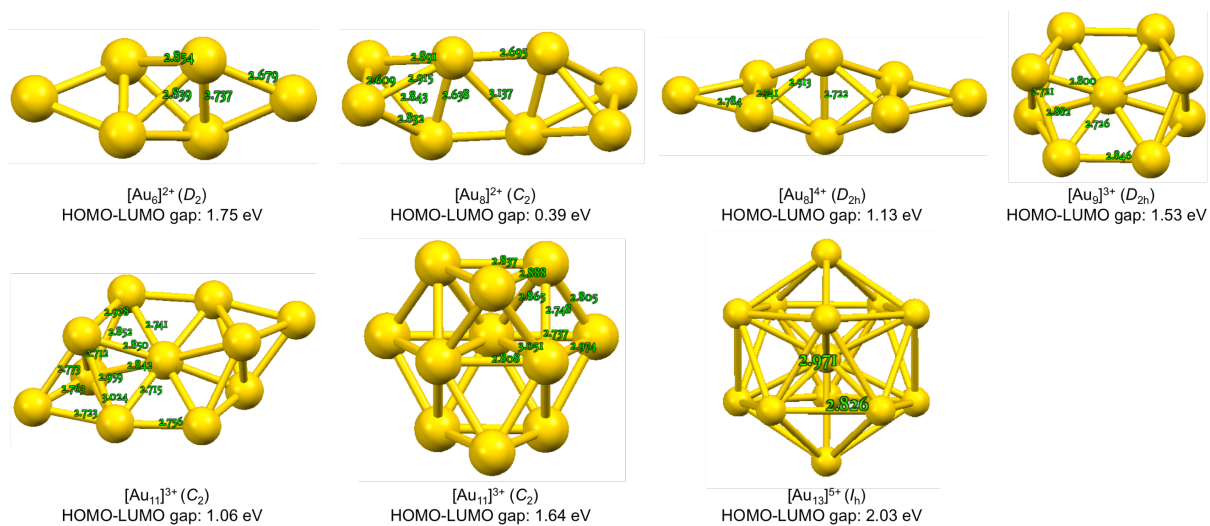


Figure S9. The optimized geometries of the $[\text{Au}_n]^{x+}$ systems obtained from starting from the cluster cores of the experimental structures of the $\text{Au}_n\text{-P}$ and $\text{Au}_n\text{Cl}_m\text{-P}$ listed in **Table 1**.

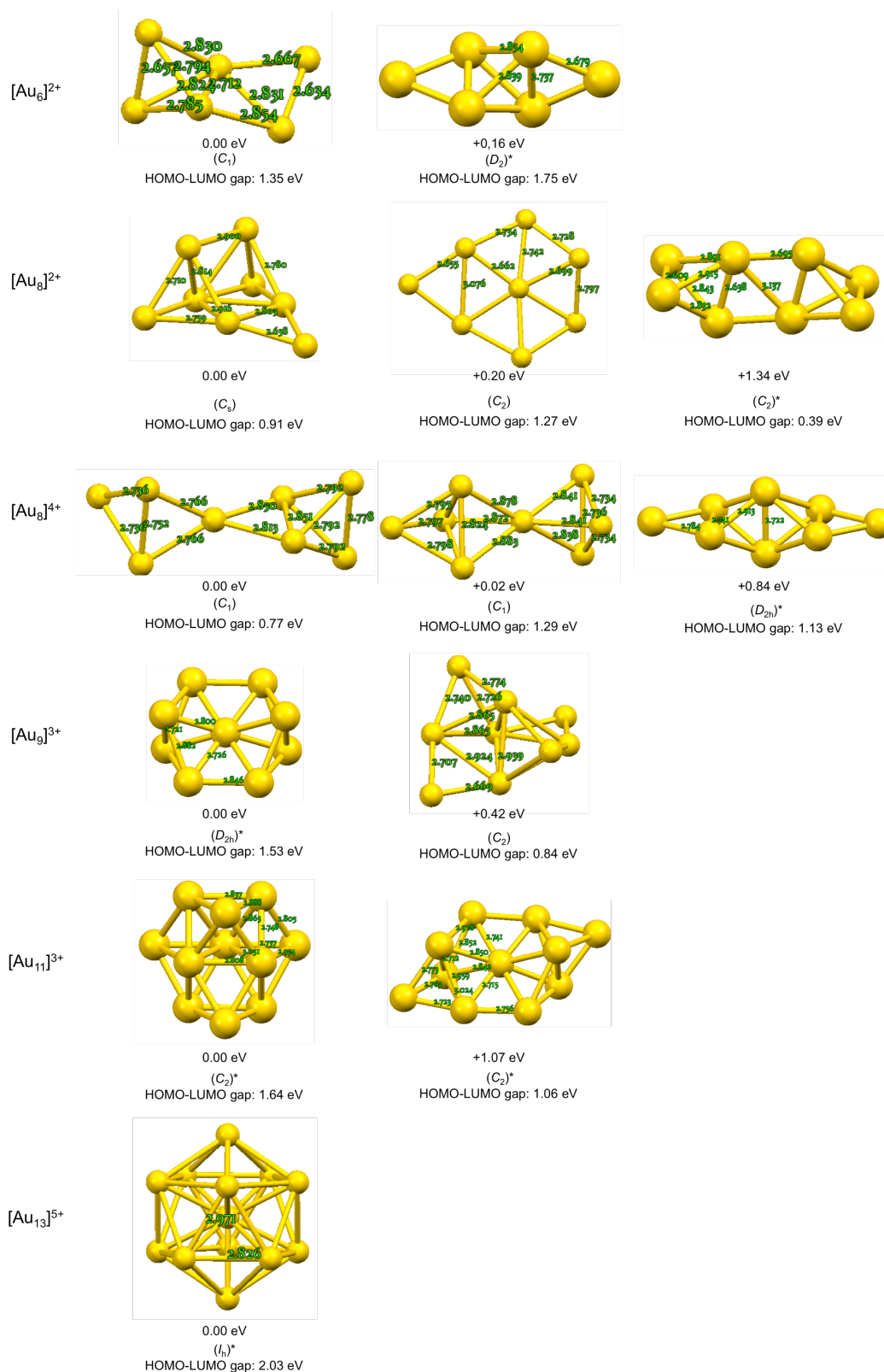


Figure S10. Structure and relative energies of $[\text{Au}_n]^{X+}$ isomers (non-exhaustive search). Starred structures are those shown in **Figure S9**.

Chapter 3

Insight into the Stability, Electronic and Optical Properties of N-Heterocyclic Carbene Analogues of Halogen/Phosphine Protected Au₁₃ *Superatomic* Clusters

3.1 Introduction

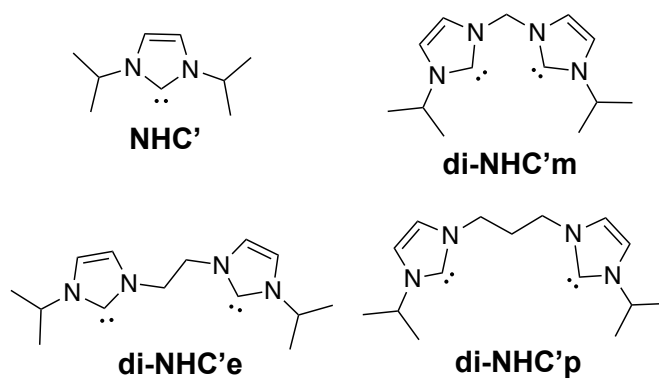
Atomically precise gold nanoclusters (AuNCs) have been the subject of intense research over the past decade^{1–6} owing to their potential use in emerging technological applications.^{7–15} Their unique molecule-like and size-dependent properties, as well as their rich structural diversity,^{1,16–23} provide the opportunity to design new species, opening new opportunities for tailorable applications.^{8,24,33–37,25–32} The AuNC structures are generally composed of a central metallic core, protected (passivated) by various ligands.^{29,38–41} The Au₁₃-centered icosahedron is one of the most recurrent core motifs. It was first characterized in [Au₁₃(PPhMe₂)₁₀Cl₂]³⁺ by Mingos and coworkers,⁴² and later in the extensive research on [Au₂₅(SR)₁₈][–] species.^{37,43–46}

The central metallic core exhibits particular electronic and structural features accounting for the stability of the overall cluster,^{47–52} with a specific number of bonding cluster electrons (*ce*), *i.e.*, electrons provided by the 6*s*(Au) orbitals. For example, the Au₁₃⁵⁺ core of [Au₁₃(PPhMe₂)₁₀Cl₂]³⁺ is an 8-*ce* species with a 1S² 1P⁶ electronic structure according to the *superatom* model.^{29,53,54} The highest occupied and lowest unoccupied molecular orbitals (HOMO and LUMO) correspond to the 1P⁶ and 1D⁰ shells, respectively.^{29,53,54} Furthermore, different synthetic strategies allow further exploration of the versatility of the cluster stability and properties by varying the number and nature of its attached ligands. For example, the classical [Au₁₃(dppe)₅Cl₂]³⁺ (dppe = 1,2-bis(diphenylphosphino)ethane) possesses enhanced optical, luminescent, and singlet-oxygen sensitization capabilities, as reported by Konishi and Li.^{55,56} Whereas this cluster is decorated with two Cl atoms, the number of chlorides can be increased to three or four.⁵⁶ In addition, the Au₁₃Cl₄ species has been shown to have related Au₁₃Br₄ and Au₁₃I₄ counterparts.⁵⁷

Moreover, the recent incorporation of N-heterocyclic carbenes (NHC) as neutral ligands of gold AuNCs,⁵⁸ as reported for the related [Au₁₃(NHC)₉Cl₃]²⁺ cluster by Crudden and coworkers,⁵⁹ and which displays a high emission quantum yield, allows further development of more versatile ligands owing to the central role of NHC ligands in organometallic chemistry.^{60–66} Hence, their evaluation and comparison to phosphines may encourage further ligand engineering efforts and synthetic exploration of such species,^{67,68,77–80,69–76} offering the opportunity of tuning nanocluster properties.

We have recently shown from density functional theory (DFT) calculations that NHCs are at least as efficient as phosphines for stabilizing AuNCs of small size and that they should

exhibit somewhat related optical properties (see chapter 2).⁸¹ In this chapter, we extend our investigations to the substitution of phosphine ligands by NHCs in a wide series of experimentally characterized halogen/phosphine-protected *δ-ce superatomic* Au₁₃ and M_nAu_{13-n} clusters (M = Cu, Ag, Pd). This work mainly focuses on the substitution-induced change of the stability, electronic structure, and optical (including emissive) properties. Meanwhile, the influence of changing of the type and number of halogen ligands is also investigated for both the phosphine- and NHC-protected analogues. The considered halogen/phosphine-protected Au₁₃ series are composed of the experimentally characterized compounds as follows, [Au₁₃(PPhMe₂)₁₀Cl₂]³⁺ (**Au₁₃Cl₂-P'**),⁴² [Au₁₃(dppe)₅Cl₂]³⁺ (**Au₁₃Cl₂-P'e**),⁵⁶ [Au₁₃(PMePh₂)₉Cl₃]²⁺ (**Au₁₃Cl₃-P'**),⁵⁷ [Au₁₃(PMePh₂)₈Cl₄]⁺ (**Au₁₃Cl₄-P'**),⁸² [Au₁₃(dppp)₄Cl₄]⁺ (**Au₁₃Cl₄-P'p**),^{83,84} [Cu₄Au₉(PMePh₂)₈Cl₄]⁺ (**Cu₄Au₉Cl₄-P'**),⁸² [Ag₄Au₉(PMePh₂)₈Cl₄]⁺ (**Ag₄Au₉Cl₄-P'**),⁸² [PdAu₁₂(dppe)(PPh₃)₆Cl₄]⁺ (**PdAu₁₂Cl₄-P'/P'e**),⁴⁴ [Au₁₃(PMePh₂)₈Br₄]⁺ (**Au₁₃Br₄-P'**),⁵⁷ and [Au₁₃(PMePh₂)₈I₄]⁺ (**Au₁₃I₄-P'**) (dppp = 1,3-bis(diphenylphosphino)propane).⁵⁷ To better understand the role of the halogen ligands, the homoleptic non-halogenated [Au₁₃(dppm)₆]⁵⁺ (**Au₁₃-P'm**) (dppm = 1,1-bis(diphenylphosphino)methane)^{85,86} clusters was also included for comparison. All the investigated compounds are *δ-ce superatoms*. Some of them contain di-phosphines (**P'm**, **P'e**, **P'p**), whereas others have simple phosphines (**P'**). Nevertheless, the X-ray and optical data are available for most of them. The hypothetical NHC homologues were designed by replacing the mono-phosphines by the mono-carbene N,N-diisopropylimidazolidene ligands (denoted as **NHC'** in the following), taken from the literature.^{58,87} The dppm, dppe, and dppp ligands were substituted by NHC counterparts, namely 1,3-bis(N-isopropylimidazolidenyl)methane (**di-NHC'm**), 1,3-bis(N-isopropylimidazolidenyl)ethane (**di-NHC'e**) and 1,3-bis(N-isopropylimidazolidenyl)propane (**di-NHC'p**), respectively (see Scheme 1). These carbenes are representative of standard NHCs and exhibit realistic steric volumes. Thus, the computed hypothetical NHC clusters are [Au₁₃(di-NHC'm)₆]⁵⁺ (**Au₁₃-C'm**), [Au₁₃(NHC')₁₀Cl₂]³⁺ (**Au₁₃Cl₂-C'**), [Au₁₃(di-NHC'e)₅Cl₂]³⁺ (**Au₁₃Cl₂-C'e**), [Au₁₃(NHC')₉Cl₃]²⁺ (**Au₁₃Cl₃-C'**), [Au₁₃(NHC')₈Cl₄]⁺ (**Au₁₃Cl₄-C'**), [Au₁₃(di-NHC'p)₄Cl₄]⁺ (**Au₁₃Cl₄-C'p**), [Cu₄Au₉(NHC')₈Cl₄]⁺ (**Cu₄Au₉Cl₄-C'**), [Ag₄Au₉(NHC')₈Cl₄]⁺ (**Ag₄Au₉Cl₄-C'**), [PdAu₁₂(di-NHC'e)(NHC')₆Cl₄]⁺ (**PdAu₁₂Cl₄-C'/C'e**), [Au₁₃(NHC')₈Br₄]⁺ (**Au₁₃Br₄-C'**) and [Au₁₃(NHC')₈I₄]⁺ (**Au₁₃I₄-C'**).



Scheme 1. The NHC ligands considered in this paper.

3.2 Computational Details

Geometry optimizations were performed at the DFT level using the Gaussian 16 package.⁸⁸ The Becke-Perdew exchange-correlation functional (BP86),^{89,90} together with the Def2-SVP basis set,⁹¹ which includes effective core potentials accounting for scalar relativistic effects, were used. Grimme's D3 empirical corrections⁹² were included in order to take into account dispersion effects. All the optimized singlet ground states structures were confirmed as genuine minima on their potential energy surface by vibrational frequency calculations. The natural atomic orbital (NAO) populations and Wiberg bond indices (WBIs) were calculated using the NBO 6.0 program,⁹³ with the help of Amsterdam Density Functional code (ADF2017).^{94,95} UV-vis optical transitions were computed using the time-dependent DFT (TD-DFT) method, at the B3LYP⁹⁶/Def2-SVP level, which provided a good quantitative agreement with the experimental spectra, the deviations between the computed transitions and their corresponding experimental values being always less than 80 nm. The UV-vis spectra were simulated from the computed TD-DFT transition energies and their oscillator strengths by using the SWizard program,⁹⁷ with each transition being associated with a Gaussian function of half-height width equal to 2000 cm^{-1} . All the computed UV-vis transition wavelengths reported below correspond to individual computed transitions. To calculate the fluorescence emission wavelengths, the geometry of the excited singlet states were optimized by TD-DFT at the PBE0⁹⁸/Def2-SVP level with the Gaussian16 program. To calculate the phosphorescence emission wavelengths, the triplet state geometries were firstly optimized by DFT calculations at the BP86/Def2-SVP level, and their energies, as well as those of their corresponding singlets, were recalculated by single point calculations at the PBE0⁹⁸/Def2-SVP level, which delivers better agreement to the experimentally available phosphorescence data.

Assuming that **M** designates any metal, **Y** any halogen ligand and **X** the whole neutral ligand (phosphine or NHC) shell, E_{Prep} and E_{Bond} energies discussed below are defined as follows: E_{Prep} .

is the energy cost afforded by the bare 8-electron $[\mathbf{M}_{13}]^{x+}$ metal core to go from its equilibrium structure to that it adopts in the equilibrium structure of the ligated $\mathbf{M}_{13}\text{-X}$ or $\mathbf{M}_{13}\mathbf{Y}_n\text{-X}$ clusters. E_{Bond} is calculated according to the following equations in which all of the considered (frozen) fragment structures are taken from the $\mathbf{M}_{13}\text{-X}$ and $\mathbf{M}_{13}\mathbf{Y}_n\text{-X}$ optimized geometries. $E_{\text{Bond}} = E(\mathbf{M}_{13}\text{-X}) - E([\mathbf{M}_{13}]^{x+}) - E(\text{X})$ or $E_{\text{Bond}} = E(\mathbf{M}_{13}\mathbf{Y}_n\text{-X}) - E([\mathbf{M}_{13}\mathbf{Y}_n]^{(x-n)+}) - E(\text{X})$.

3.3 Results and Discussion

The optimized geometries of the phosphine-protected clusters and of their NHC analogues are shown in Figure 1, where for sake of simplicity, \mathbf{M}_{13} denotes both monometallic Au_{13} and heterometallic cluster cores. The atomic bond distances of the $\mathbf{M}_{13}\text{-P}$ were found to be in good agreement with their corresponding X-ray structure data (Tables S1-S7, Annex). All the calculated compounds are isoelectronic, with a closed shell *8-cc* $1\text{S}^2 1\text{P}^6$ *superatom* configuration. The HOMO-LUMO gaps of the $\mathbf{M}_{13}\text{-P}$ series are found in the range of 1.4–2.2 eV (Tables S1-S7, Annex), which is consistent with the chemical stability of this kind of compound. Interestingly, the $\mathbf{M}_{13}\text{-C}$ compounds show HOMO-LUMO gaps that are slightly larger than that of their $\mathbf{M}_{13}\text{-P}$ counterparts, indicating rather similar stability. The Kohn-Sham frontier molecular orbital diagrams of both $\mathbf{M}_{13}\text{-P}$ and $\mathbf{M}_{13}\text{-C}$ series are shown in Figure 2. The HOMO and LUMO levels are all of 1P and 1D nature, respectively. Unsurprisingly, the frontier orbitals of both the $\mathbf{M}_{13}\text{-P}$ (Figure 2a) and $\mathbf{M}_{13}\text{-C}$ species (Figure 2b) are shifted up in energy when the cluster cationic charge decreases from +5 ($\mathbf{M}_{13}\text{-X}$) to 0 ($\text{PdAu}_{12}\text{Cl}_4\text{-X}'/\text{X}'\text{e}$). As a consequence, this energy upshift follows the increase of the number of chloride ligands. As a whole, the related electronic structures along with the series, suggest that the hypothetical NHC species should have similar properties as their phosphine relatives, allowing further experimental exploration.

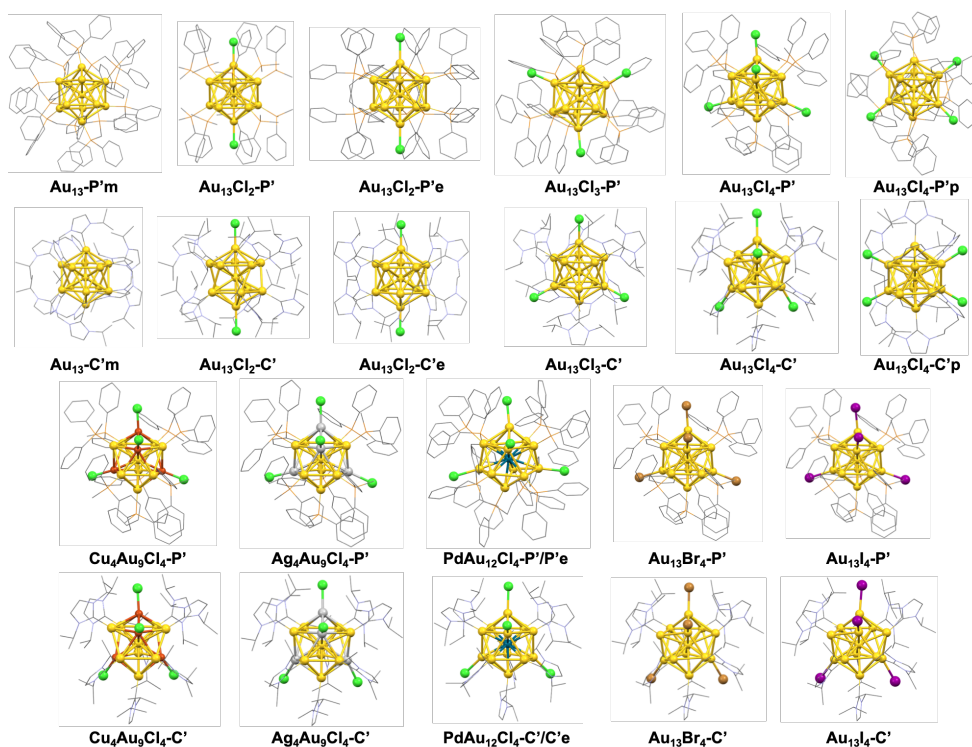


Figure 1. Optimized structures of $M_{13}Y_n-X$ ($M = Au, Cu, Ag, Pd$; $Y = Cl, Br, I$; $n = 0, 2-4$; $X = P, C$). The golden, green, reddish brown, light grey, dark blue, brown and purple spheres are Au, Cl, Cu, Ag, Pd, Br and I atoms, respectively.

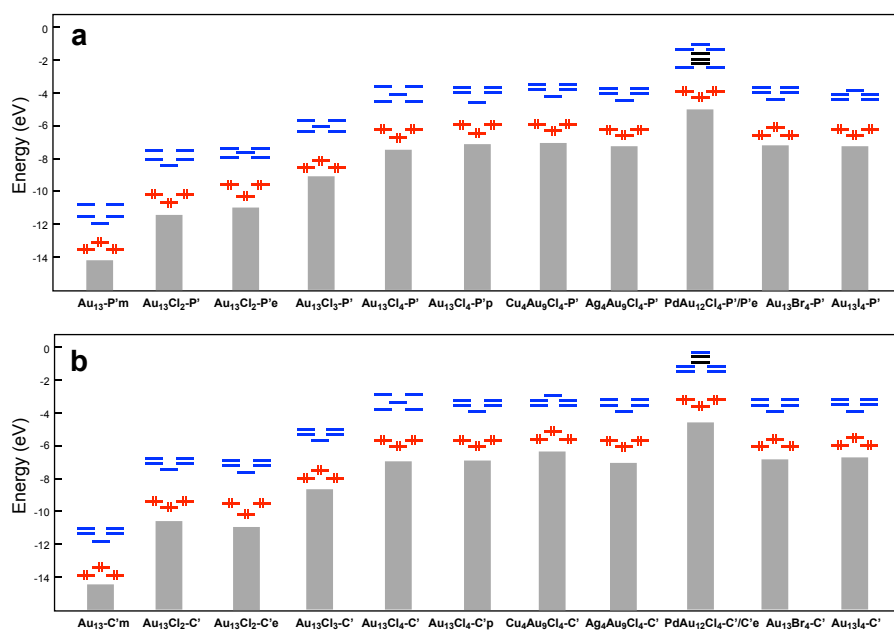


Figure 2. Kohn-Sham frontier molecular orbital diagrams of a) $M_{13}Y_n-P$ and b) $M_{13}Y_n-C$ ($Y = Cl, Br, I$; $n = 0, 2-4$). The grey boxes represent the $5d(Au)$ -block, the red and blue levels correspond to the *superatomic* 1P and 1D orbitals, respectively.

Thus, the energies of the HOMOs and LUMOs can be tuned by varying the composition of the ligand shell and/or that of the metal core. This capability enables to include such well-defined molecular devices into heterojunction, with more positive or more negative frontier orbital energies with respect to that of the valence band of a semiconductor in a heterojunction array,⁹⁹ allowing the control of the location of both electrons and holes in charge transfer mechanisms.

In order to evaluate the stabilizing role of the different ligand shells in the **M₁₃-P** and **M₁₃-C** series, a bonding energy analysis was carried out, not only for the comparison of the energies of interaction between the ligands and metal core, but also for an evaluation of the energy cost associated with the distortion afforded by the metal core upon ligand complexation. To this end, the corresponding bare metal cores were optimized. The energy cost afforded by the bare metal cores to prepare their structure to bond with the ligands (E_{Prep} , see Computational Details Section) is given in Table 1. The computed E_{Prep} values range between 0.10–0.33 eV, for the gold-halide cores and tend to increase for the doped $M_4\text{Au}_9\text{Cl}_4\text{-X}'$ ($M = \text{Cu}, \text{Ag}$) species. It is clear that the evaluated E_{Prep} in the **M₁₃-C** series is smaller than those of **M₁₃-P**, which means that the metal cores in **M₁₃-C** species cost less energy to reach their equilibrium states, suggesting that NHC-derivatives exhibit a less rigid ligand-shell, introducing more flexibility to the resulting cluster. This can be useful for studies on cluster core fluxionality, as explored for $\text{Au}_{25}(\text{SR})_{18}$ and $\text{Au}_{38}(\text{SR})_{24}$ species group.^{100,101}

The ligand-core interaction energies for the series evaluated by the computed bonding energies (E_{Bond} , see Computational Details Section) for the neutral phosphine and NHC ligand shell (Table 1) show that NHCs are slightly more strongly bonded than the phosphine analogues in all the investigated cases, suggesting that NHC-protected gold and gold-rich M_{13} clusters should exhibit a somewhat enhanced thermodynamic stability, which can be useful as ligand-engineering strategy to achieve more stable building-blocks. Interestingly, the **M₁₃-C** cluster cores bear more positive charges than their **M₁₃-P** counterparts (Table 1), as the result of the enhanced core-ligand back-bonding.¹⁰² This is in line with the fact that the frontier orbital energies of the former species are slightly higher than that of the latter (Figure 2). On the other hand, no clear relationship between the core charges and the number of chloride ligands could be traced.

The optical properties of AuNCs have been widely explored, owing to their potential use as optical devices,^{4,103} which can be tuned by involving different ligands.^{48,104–107} In this sense, the variation of the optical properties of the investigated compounds was evaluated with respect to the nature of the cluster core and the different ligand shell. The TD-DFT simulated UV-vis

spectra of **M₁₃-P** and **M₁₃-C** series are gathered in Figure 3, and the major computed electronic transition energies associated with them are given in Table 2, together with the corresponding experimental λ_{\max} values taken from the literature, where available.

Table 1. Energetic data associated with cluster bonding denoting the cluster core preparation energy (E_{Prep}) and ligand-core interaction (E_{Bond}) (values in eV), and the natural bond order (NBO) charges of the **M₁₃** core (q_{core} , in a.u.).

Compound	Corresponding optimized bare metal core	X = P E_{Prep}	X = C E_{Prep}	X = P E_{Bond}	X = C E_{Bond}	X = P q_{core}	X = C q_{core}
Au₁₃-X'm	[Au₁₃] ⁵⁺ (<i>I_h</i>)	0.19	0.16	-57.79	-62.78	1.35	2.35
Au₁₃Cl₂-X'		0.20	0.10	-39.48	-45.44	1.22	2.34
Au₁₃Cl₂-X'e		0.32	0.19	-40.50	-44.87	1.47	2.21
Au₁₃Cl₃-X'		0.24	0.14	-33.26	-38.61	1.49	2.25
Au₁₃Cl₄-X'		0.32	0.21	-27.75	-32.02	1.33	2.21
Au₁₃Cl₄-X'p		0.33	0.18	-27.82	-30.87	1.58	2.19
Au₁₃Br₄-X'		0.33	0.19	-27.54	-31.58	1.34	2.10
Au₁₃I₄-X'		0.31	0.16	-27.13	-30.93	1.11	1.99
Cu₄Au₉Cl₄-X'	[Cu₄Au₉] ⁵⁺ (<i>C_{2v}</i>)	0.41	0.21	-27.45	-30.80	1.96	2.77
Ag₄Au₉Cl₄-X'	[Ag₄Au₉] ⁵⁺ (<i>C_{2v}</i>)	0.51	0.40	-27.76	-31.65	1.75	2.59
PdAu₁₂Cl₄-X'/X'e	[PdAu₁₂] ⁴⁺ (<i>I_h</i>)	0.28	0.09	-23.36	-27.44	1.45	1.90

The shapes of the computed UV-vis spectra for the **M₁₃-P** series were found to have a good match with that of the experimental spectra. In all the cases, the lowest energy band is mainly associated with the HOMO → LUMO transition and in any case is of 1P → 1D metal-to-metal charge transfer (MMCT) nature. Figure S1 (Annex) illustrates the energy shift of the lowest energy transition wavelength when going from the phosphine species to their NHC homologues.

For the homometallic chlorinated **Au₁₃Cl_n-P** series, the lowest energy band is red-shifted when increasing the number of Cl atoms from 2 to 4 in both the mono-phosphine (**Au₁₃Cl₂-P'**, **Au₁₃Cl₃-P'**, **Au₁₃Cl₄-P'**) (Figure 3a) and di-phosphine (**Au₁₃Cl₂-P'e**, **Au₁₃Cl₄-P'p**) (Figure 3b) **Au₁₃Cl_n-P** series. The same trend is also found for the **Au₁₃Cl_n-C** species (**Au₁₃Cl₃-C'**, **Au₁₃Cl₄-C'**, **Au₁₃Cl₂-C'e**, **Au₁₃Cl₄-C'p**), except in the case of **Au₁₃Cl₂-C'**. When switching the ligands from mono-phosphines to di-phosphines, the lowest energy band is red-shifted in the **Au₁₃Cl_n-P** ($n = 2, 4$) series, but blue-shifted in the **Au₁₃Cl_n-C** ($n = 2, 4$) series (Figure 3b).

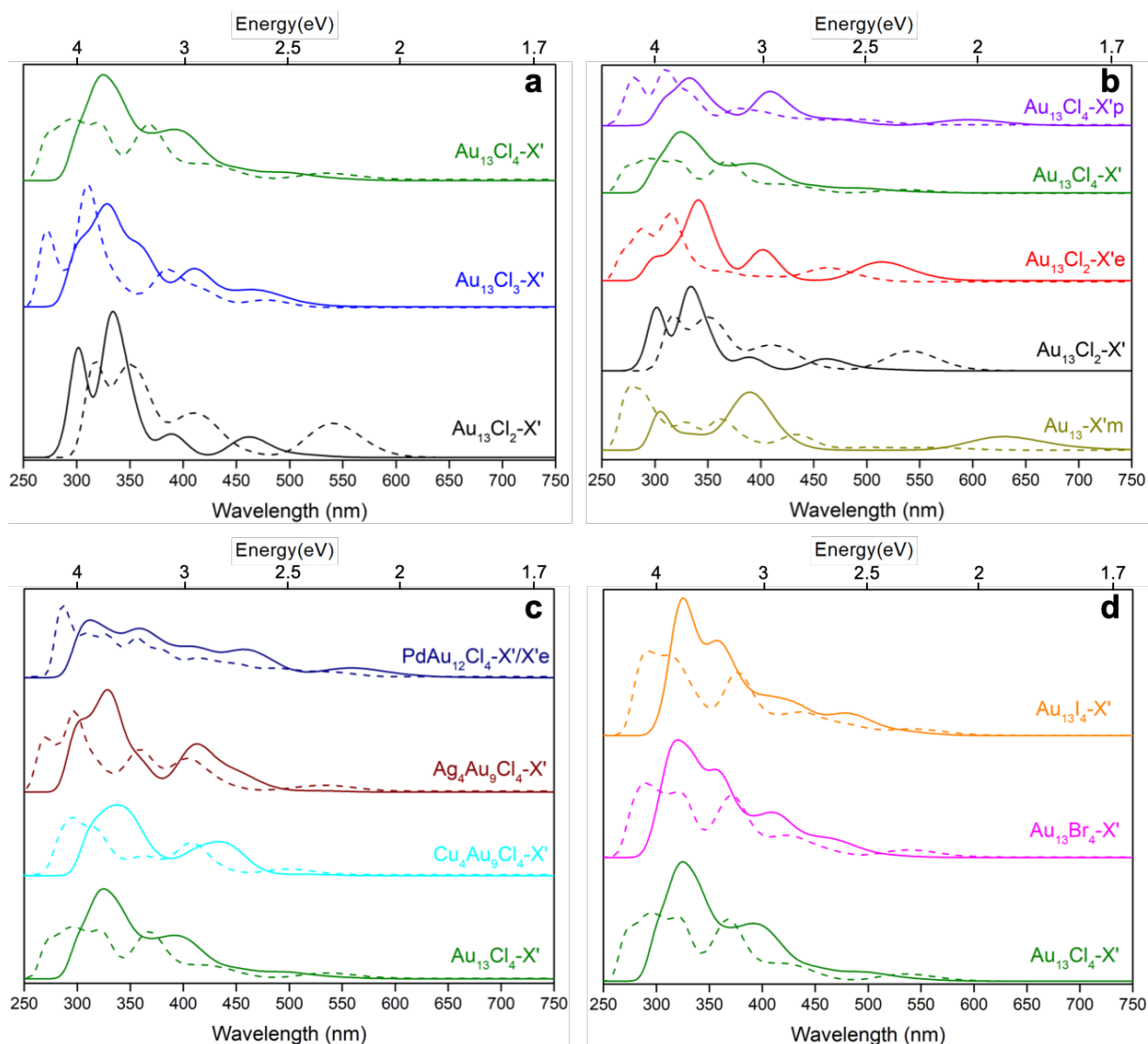


Figure 3. Simulated UV-vis absorption spectra for the computed phosphine derivatives (solid line) and NHC derivatives (dotted line) clusters.

When going from the mono-phosphine-protected $\text{Au}_{13}\text{Cl}_n\text{-P}$ ($\text{Au}_{13}\text{Cl}_3\text{-P}'$, $\text{Au}_{13}\text{Cl}_4\text{-P}'$) to the mono-NHC-protected $\text{Au}_{13}\text{Cl}_n\text{-C}$ ($\text{Au}_{13}\text{Cl}_3\text{-C}'$, $\text{Au}_{13}\text{Cl}_4\text{-C}'$), the lowest energy band is slightly red-shifted, whereas the highest energy band shows a blue-shift tendency (Figure 3a), except in the case of $\text{Au}_{13}\text{Cl}_2\text{-X}'$ ($X = \text{P}, \text{C}$), in which the whole UV-vis spectra is red-shifted. This trend was also found for the other two halide $\text{Au}_{13}\text{Y}_4\text{-X}'$ ($Y = \text{Br}, \text{I}; X = \text{P}, \text{C}$) (Figure 3d) and alloyed $\text{M}_4\text{Au}_9\text{-X}'$ ($M = \text{Cu}, \text{Ag}; X = \text{P}, \text{C}$) series, but not for the case of the palladium-doped species ($\text{PdAu}_{12}\text{-P}'/\text{P}'\text{e}$ and $\text{PdAu}_{12}\text{-C}'/\text{C}'\text{e}$), where the whole UV-vis spectra are blue-shifted (Figure 3c). From the di-phosphine-protected $\text{Au}_{13}\text{Cl}_n\text{-P}$ ($\text{Au}_{13}\text{Cl}_2\text{-P}'\text{e}$, $\text{Au}_{13}\text{Cl}_4\text{-P}'\text{p}$) to the di-NHC-protected $\text{Au}_{13}\text{Cl}_n\text{-C}$ ($\text{Au}_{13}\text{Cl}_2\text{-C}'\text{e}$, $\text{Au}_{13}\text{Cl}_4\text{-C}'\text{p}$), the whole UV-vis spectrum exhibits a systematic blue-shift tendency, and the same trend is also found for the homoleptic

$[\text{Au}_{13}(\text{dppm})_6]^{5+}$ ($\text{Au}_{13}\text{-P}'\text{m}$) clusters (Figure 3b). Such features depict the possibility to achieve a fine-tuning of optical absorption properties of the isoelectronic species. Moreover, for the chloride/phosphine protected alloy clusters $\text{M}_4\text{Au}_9\text{Cl}_4\text{-P}'$ ($\text{M} = \text{Au}, \text{Cu}, \text{Ag}$), the magnitude of the lowest energy band blue-shift follows the order $\text{Ag}_4\text{Au}_9\text{Cl}_4\text{-P}' < \text{Cu}_4\text{Au}_9\text{Cl}_4\text{-P}' < \text{Au}_{13}\text{Cl}_4\text{-P}'$, whereas the order within the NHC analogues, $\text{Ag}_4\text{Au}_9\text{Cl}_4\text{-C}'$ and $\text{Cu}_4\text{Au}_9\text{Cl}_4\text{-C}'$, is inverted (Figure 3c).

Table 2. Major TD-DFT-Computed UV-Vis excitation energies. Experimental values are also reported, when available in the literature. The Experimental values correspond to the phosphine protected clusters, except for $\text{Au}_{13}\text{Cl}_3\text{-C}'$.

Compound	Absorption (nm)			Major character of the low-energy band (X = P, C)
	Exp.	X = P	X = C	
$\text{Au}_{13}\text{-X}'\text{m}$	700, 440, 300-350(multiple) ^a	625, 387, 304	561(sh [⊥]), 434, 363, 328, 278	1P→1D
$\text{Au}_{13}\text{Cl}_2\text{-X}'$	428, 338, 296 ^b	460, 387, 335, 303	540, 409, 352, 319	1P→1D
$\text{Au}_{13}\text{Cl}_2\text{-X}'\text{e}$	493, 359, 304 (sh [⊥]) ^c	507, 402, 342, 299 (sh [⊥])	462, 366, 314, 288	1P→1D
$\text{Au}_{13}\text{Cl}_3\text{-X}'$	490, 420, 330 (X = C) ^d	469, 411, 328	480, 386, 310, 271	1P→1D
$\text{Au}_{13}\text{Cl}_4\text{-X}'$	440, 350, 290 (sh [⊥]) ^e	480, 393, 324	534, 422, 367, 295	1P→1D
$\text{Au}_{13}\text{Cl}_4\text{-X}'\text{p}$	430, 340 ^f	591, 406, 332	495, 380, 311, 280	1P→1D
$\text{Cu}_4\text{Au}_9\text{Cl}_4\text{-X}'$	450, 355, 325 (sh [⊥]) ^e	431, 334	497, 408, 362, 294	1P→1D
$\text{Ag}_4\text{Au}_9\text{Cl}_4\text{-X}'$	420, 330, 285 (sh [⊥]) ^e	414, 327, 304 (sh [⊥])	531, 403, 357, 296, 271(sh [⊥])	1P→1D
$\text{PdAu}_{12}\text{Cl}_4\text{-X}'/\text{X}'\text{e}$	–	558, 460, 404 (sh [⊥]), 357, 314	540, 411, 354, 327(sh [⊥]), 308(sh [⊥]) 287	1P→1D
$\text{Au}_{13}\text{Br}_4\text{-X}'$	425, 340, 296 (sh [⊥]) ^g	483, 409, 355, 318	540, 423, 371, 289	1P→1D
$\text{Au}_{13}\text{I}_4\text{-X}'$	–	492, 413, 354, 325	546, 436, 374, 292	1P→1D

Experimental data taken from reference: a) ⁸⁶; b) ⁴²; c) ⁵⁶; d) ⁵⁹; e) ⁸²; f) ⁸⁴; g) ⁵⁷. ⊥ sh = shoulder.

Finally, for the three different halogen protected $\text{Au}_{13}\text{Y}_4\text{-X}'$ ($\text{Y} = \text{Cl}, \text{Br}, \text{I}; \text{X} = \text{P}, \text{C}$) species, the lowest energy band shows a small systematic red-shift from Cl to Br to I for both phosphine and NHC analogues, which is consistent with the previous experimental observation on $[\text{Au}_{13}(\text{dppe}_5)\text{Y}_2]^{3+}$ ($\text{Y} = \text{Cl}, \text{Br}, \text{I}$) clusters.¹⁰⁸ Thus, it could be assumed that this red-shift in the lowest energy band is turned to occur in any halogen-protected Au_{13} *superatomic* cluster system, independently from the number of halogenide ligands.

In a subsequent step, owing to the relevant photoluminescent properties of $[\text{Au}_{13}(\text{dppe})_5\text{Cl}_2]^{3+}$,^{55,56} ascribed to a phosphorescent emission originating from the $T_1 \rightarrow S_0$ decay,⁵⁵ we have also explored the potential phosphorescent emission of all the investigated species. The $T_1 \rightarrow S_0$ emission⁵⁵ exhibits a mixed $1P \rightarrow 1D$ and $5d(\text{Au}) \rightarrow 1D$ character, thus mainly centered on the metal core. The reported emission for $[\text{Au}_{13}(\text{dppe})_5\text{Cl}_2]^{3+}$ is observed at 1.26 eV (982 nm),⁵⁵ which is calculated at 1.47 eV (Table 3). Along with the phosphine-protected series, the calculated values range from 0.67 eV (1850 nm) to 1.61 eV (770 nm), in the Au_{13}Y_n species, and from 1.31 eV (946 nm) to 1.53 eV (810 nm) in the doped clusters. In the case of their NHC counterparts, the emission is, in general, blue-shifted, with marked exceptions given by alloyed species and the Br- and I-ligated clusters ($\text{Au}_{13}\text{Br}_4$ and Au_{13}I_4 cores).

In the $\text{Au}_{13}\text{Y}_4\text{-P}'$ series ($\text{Y} = \text{Cl}, \text{Br}, \text{I}$), a blue-shift is suggested from 1.12 eV (1107 nm) to 1.61 eV (770 nm) when phosphine ligands are involved, and a red-shift for carbene species, from 1.22 eV (1016 nm) to 1.09 eV (1137 nm) (Table 3). Thus, the effect of ligand replacement may be evaluated for each species, suggesting that despite being isolobal ligands,¹⁰⁹ fine modifications and variations can be found between phosphine- and carbene-protected clusters. For the homometallic clusters, a blue-shift of the emission is observed when phosphine-based ligands are replaced by carbenes. However, a red-shift is generally found for the doped species ($\text{M}_4\text{Au}_9\text{Cl}_4$ cores, $\text{M} = \text{Cu}$ and Ag). Figure S2 (Annex) illustrates the shift of the phosphorescence emission wavelength when going from the phosphine species to their NHC homologues.

Table 3. DFT-computed hypothetical phosphorescence emissions.

Compound	E_{emission}	Compound	E_{emission}
$\text{Au}_{13}\text{-P}'\text{m}$	0.92 eV (1347 nm)	$\text{Au}_{13}\text{-C}'\text{m}$	1.72 eV (721 nm)
$\text{Au}_{13}\text{Cl}_2\text{-P}'$	1.33 eV (932 nm)	$\text{Au}_{13}\text{Cl}_2\text{-C}'$	1.54 eV (805 nm)
$\text{Au}_{13}\text{Cl}_2\text{-P}'\text{e}$	1.47 eV (843 nm)	$\text{Au}_{13}\text{Cl}_2\text{-C}'\text{e}$	1.43 eV (867 nm)
$\text{Au}_{13}\text{Cl}_3\text{-P}'$	1.39 eV (892 nm)	$\text{Au}_{13}\text{Cl}_3\text{-C}'$	1.79 eV (693 nm)
$\text{Au}_{13}\text{Cl}_4\text{-P}'$	1.12 eV (1107 nm)	$\text{Au}_{13}\text{Cl}_4\text{-C}'$	1.22 eV (1016 nm)
$\text{Au}_{13}\text{Cl}_4\text{-P}'\text{p}$	0.67 eV (1850 nm)	$\text{Au}_{13}\text{Cl}_4\text{-C}'\text{p}$	1.26 eV (984 nm)
$\text{Cu}_4\text{Au}_9\text{Cl}_4\text{-P}'$	1.53 eV (810 nm)	$\text{Cu}_4\text{Au}_9\text{Cl}_4\text{-C}'$	1.14 eV (1087 nm)
$\text{Ag}_4\text{Au}_9\text{Cl}_4\text{-P}'$	1.37 eV (905 nm)	$\text{Ag}_4\text{Au}_9\text{Cl}_4\text{-C}'$	1.34 eV (925 nm)
$\text{PdAu}_{12}\text{Cl}_4\text{-P}$	1.31 eV (946 nm)	$\text{PdAu}_{12}\text{Cl}_4\text{-C}$	1.13 eV (1097 nm)
$\text{Au}_{13}\text{Br}_4\text{-P}'$	1.56 eV (795 nm)	$\text{Au}_{13}\text{Br}_4\text{-C}'$	1.17 eV (1059 nm)
$\text{Au}_{13}\text{I}_4\text{-P}'$	1.61 eV (770 nm)	$\text{Au}_{13}\text{I}_4\text{-C}'$	1.09 eV (1137 nm)

The fluorescence emission of these phosphine- and NHC- species were also investigated (Table 4). For both series, the computed fluorescence emission energies are in the near-infrared region. The NHC series shows comparable emission wavelengths with their phosphine derivatives, except the $\text{Au}_{13}\text{-P}'\text{m}$, $\text{Au}_{13}\text{Cl}_2\text{-P}'$ and $\text{Au}_{13}\text{Cl}_4\text{-P}'\text{p}$. For the di-phosphine protected $\text{Au}_{13}\text{-P}'\text{m}$ and $\text{Au}_{13}\text{Cl}_2\text{-P}'$ clusters, an obvious blue-shift of the emission wavelength is observed when replacing phosphines by NHCs. However, a big red-shift of the emission wavelength was found when going from $\text{Au}_{13}\text{Cl}_2\text{-P}'$ to $\text{Au}_{13}\text{Cl}_2\text{-C}'$. In the $\text{Au}_{13}\text{Y}_4\text{-P}'$ series (Y = Cl, Br, I), a blue-shift of the fluorescence emission was found when going from Cl to Br to I, but their corresponding NHC species show an opposite trend. Figure S3 (Annex) illustrates the shift of the fluorescence emission wavelength when going from the phosphine species to their NHC homologues.

Table 4. DFT-computed hypothetical fluorescence emissions.

Compound	E_{emission}	Compound	E_{emission}
$\text{Au}_{13}\text{-P}'\text{m}$	0.89 eV (1387 nm)	$\text{Au}_{13}\text{-C}'\text{m}$	1.25 eV (988 nm)
$\text{Au}_{13}\text{Cl}_2\text{-P}'$	1.52eV (814 nm)	$\text{Au}_{13}\text{Cl}_2\text{-C}'$	0.98 eV (1258 nm)
$\text{Au}_{13}\text{Cl}_2\text{-P}'\text{e}$	1.44eV (863 nm)	$\text{Au}_{13}\text{Cl}_2\text{-C}'\text{e}$	1.60eV (773 nm)
$\text{Au}_{13}\text{Cl}_3\text{-P}'$	1.72 eV (720 nm)	$\text{Au}_{13}\text{Cl}_3\text{-C}'$	1.59eV (779 nm)
$\text{Au}_{13}\text{Cl}_4\text{-P}'$	1.15 eV (1075 nm)	$\text{Au}_{13}\text{Cl}_4\text{-C}'$	1.16 eV (1069 nm)
$\text{Au}_{13}\text{Cl}_4\text{-P}'\text{p}$	0.86 eV (1444 nm)	$\text{Au}_{13}\text{Cl}_4\text{-C}'\text{p}$	1.27 eV (974 nm)
$\text{Cu}_4\text{Au}_9\text{Cl}_4\text{-P}'$	1.53 eV (807 nm)	$\text{Cu}_4\text{Au}_9\text{Cl}_4\text{-C}'$	1.36 eV (911 nm)
$\text{Ag}_4\text{Au}_9\text{Cl}_4\text{-P}'$	1.24 eV (996 nm)	$\text{Ag}_4\text{Au}_9\text{Cl}_4\text{-C}'$	1.30 eV (954 nm)
$\text{PdAu}_{12}\text{Cl}_4\text{-P}$	1.25 eV (989 nm)	$\text{PdAu}_{12}\text{Cl}_4\text{-C}$	1.55 eV (798 nm)
$\text{Au}_{13}\text{Br}_4\text{-P}'$	1.29 eV (959 nm)	$\text{Au}_{13}\text{Br}_4\text{-C}'$	1.09 eV (1128 nm)
$\text{Au}_{13}\text{I}_4\text{-P}'$	1.55 eV (802 nm)	$\text{Au}_{13}\text{I}_4\text{-C}'$	1.03 eV (1208 nm)

3.4 Conclusions

The similar bonding features of phosphines and N-heterocyclic carbene (NHC) ligands in atomically precise gold nanoclusters (AuNCs) allow to further estimate their role in the modification of the molecular properties of different cluster cores. Based on a wide range of experimentally characterized *8-ce* superatoms, with Au_{13} and M_4Au_9 cores (M = Cu, Ag) decorated with phosphine or halogen and phosphine ligands, the substitution of phosphines by NHCs only marginally perturb the electronic structure, leading to roughly similar optical and luminescent properties, but with interesting modifications. For example, with monodentate ligands, the lowest energy emission wavelength is red-shifted when going from phosphines to NHCs (see Figure S1, Annex). This is the consequence of slightly lower HOMO-LUMO gaps in the NHC series, due to some π^* (carbene) stabilizing admixture in the 1D LUMO's. With

bidentate ligands, the opposite effect, *i.e.*, a blue shift occurs when going from phosphines to NHCs, which is related to the stronger chelating (distorting) effect of diphosphines on the metal core. These wavelength shifts are retained for the chelated species in the emission wavelengths (Figures S2 and S3, Annex), but somewhat blurred in the case of the non-chelated ones.

Our results allow us to propose medium-sized species based on gold or gold-rich M_{13} icosahedral core, supporting the feasible obtention of novel targets for explorative synthetic efforts featuring NHC-ligands. Moreover, the addition of successive halogen ligands to the cluster core, leads to a more electron-deficient core, enabling further modification of the frontier orbital energies useful in the design of devices in heterojunction arrays.

3.5 References

- 1 Jin, R.; Zeng, C.; Zhou, M.; Chen, Y. Atomically Precise Colloidal Metal Nanoclusters and Nanoparticles: Fundamentals and Opportunities. *Chem. Rev.* **2016**, *116* (18), 10346–10413.
- 2 Du, Y.; Sheng, H.; Astruc, D.; Zhu, M. Atomically Precise Noble Metal Nanoclusters as Efficient Catalysts: A Bridge between Structure and Properties. *Chem. Rev.* **2020**, *120*, 526–622.
- 3 Du, X.; Jin, R. Atomically Precise Metal Nanoclusters for Catalysis. *ACS Nano* **2019**, *13*, 7383–7387.
- 4 Jin, R. Atomically Precise Metal Nanoclusters: Stable Sizes and Optical Properties. *Nanoscale* **2015**, *7*, 1549–1565.
- 5 Kang, X.; Li, Y.; Zhu, M.; Jin, R. Atomically Precise Alloy Nanoclusters: Syntheses, Structures, and Properties. *Chem. Soc. Rev.* **2020**, *49*, 6443–6514.
- 6 Mingos, D. M. P. Electron Counting Rules for Gold Clusters Which Are Stereochemically Non-Rigid and Exhibit Skeletal Isomerism. *Struct. Bond.* **2021**, *188*, 1–67.
- 7 Hirai, H.; Ito, S.; Takano, S.; Koyasu, K.; Tsukuda, T. Ligand-Protected Gold/Silver Superatoms: Current Status and Emerging Trends. *Chem. Sci.* **2020**, *11*, 12233–12248.
- 8 Reber, A. C.; Khanna, S. N. Superatoms: Electronic and Geometric Effects on Reactivity. *Acc. Chem. Res.* **2017**, *50*, 255–263.
- 9 Hirata, K.; Tomihara, R.; Kim, K.; Koyasu, K.; Tsukuda, T. Characterization of Chemically Modified Gold and Silver Clusters in Gas Phase. *Phys. Chem. Chem. Phys.* **2019**, *21*, 17463–17474.
- 10 Hasegawa, S.; Takano, S.; Yamazoe, S.; Tsukuda, T. Prominent Hydrogenation

- Catalysis of a PVP-Stabilized Au₃₄ Superatom Provided by Doping a Single Rh Atom. *Chem. Commun.* **2018**, *54*, 5915–5918.
- 11 Sharma, S.; Yamazoe, S.; Ono, T.; Kurashige, W.; Niihori, Y.; Nobusada, K.; Tsukuda, T.; Negishi, Y. Tuning the Electronic Structure of Thiolate-Protected 25-Atom Clusters by Co-Substitution with Metals Having Different Preferential Sites. *Dalton Trans.* **2016**, *45*, 18064–18068.
- 12 Negishi, Y.; Kurashige, W.; Niihori, Y.; Nobusada, K. Toward the Creation of Stable, Functionalized Metal Clusters. *Phys. Chem. Chem. Phys.* **2013**, *15*, 18736.
- 13 Yamazoe, S.; Tsukuda, T. Metal Clusters in Catalysis. In *Functional Nanometer-Sized Clusters of Transition Metals: Synthesis, Properties and Applications*; Chen, W., Chen, S., Eds.; **2014**; pp 291–322.
- 14 Yuan, X.; Yao, Q.; Yu, Y.; Luo, Z.; Xie, J. Novel Synthetic Strategies for Thiolate-Protected Au and Ag Nanoclusters: Towards Atomic Precision and Strong Luminescence. In *Functional Nanometer-Sized Clusters of Transition Metals: Synthesis, Properties and Applications*; Chen, W., Chen, S., Eds.; **2014**; pp 131–168.
- 15 Kawawaki, T.; Kataoka, Y.; Ozaki, S.; Kawachi, M.; Hirata, M.; Negishi, Y. Creation of Active Water-Splitting Photocatalysts by Controlling Cocatalysts Using Atomically Precise Metal Nanoclusters. *Chem. Commun.* **2021**, *57*, 417–440.
- 16 Rao, C. N. R.; Müller, A.; Cheetham, A. K. *The Chemistry of Nanomaterials*; Rao, C. N. R., Müller, A., Cheetham, A. K., Eds.; Wiley-VCH Verlag GmbH & Co. KGaA: Weinheim, FRG, **2004**.
- 17 Sun, Y. Shape-Controlled Synthesis of Gold and Silver Nanoparticles. *Science* **2002**, *298*, 2176–2179.
- 18 Yin, Y.; Talapin, D. The Chemistry of Functional Nanomaterials. *Chem. Soc. Rev.* **2013**, *42*, 2484–2487.
- 19 Kurashige, W.; Niihori, Y.; Sharma, S.; Negishi, Y. Precise Synthesis, Functionalization and Application of Thiolate-Protected Gold Clusters. *Coord. Chem. Rev.* **2016**, *320–321*, 238–250.
- 20 Fernando, A.; Weerawardene, K. L. D. M.; Karimova, N. V.; Aikens, C. M. Quantum Mechanical Studies of Large Metal, Metal Oxide, and Metal Chalcogenide Nanoparticles and Clusters. *Chem. Rev.* **2015**, *115*, 6112–6216.
- 21 Stoll, T.; Sgrò, E.; Jarrett, J. W.; Réhault, J.; Oriana, A.; Sala, L.; Branchi, F.; Cerullo, G.; Knappenberger, K. L. Superatom State-Resolved Dynamics of the Au₂₅(SC₈H₉)₁₈⁻ Cluster from Two-Dimensional Electronic Spectroscopy. *J. Am. Chem. Soc.* **2016**, *138*,

- 1788–1791.
- 22 Costi, R.; Saunders, A. E.; Banin, U. Colloidal Hybrid Nanostructures: A New Type of Functional Materials. *Angew. Chem. Int. Ed.* **2010**, *49*, 4878–4897.
- 23 Cowan, M. J.; Nagarajan, A. V.; Mpourmpakis, G. Correlating Structural Rules with Electronic Properties of Ligand-Protected Alloy Nanoclusters. *J. Chem. Phys.* **2021**, *155*, 024303.
- 24 Qian, H.; Zhu, Y.; Jin, R. Size-Focusing Synthesis, Optical and Electrochemical Properties of Monodisperse Au₃₈(SC₂H₄Ph)₂₄ Nanoclusters. *ACS Nano* **2009**, *3*, 3795–3803.
- 25 Whetten, R. L.; Khoury, J. T.; Alvarez, M. M.; Murthy, S.; Vezmar, I.; Wang, Z. L.; Stephens, P. W.; Cleveland, C. L.; Luedtke, W. D.; Landman, U. Nanocrystal Gold Molecules. *Adv. Mater.* **1996**, *8*, 428–433.
- 26 Oro, L. A.; Braunstein, P.; Raithby, P. R. *Metal Clusters in Chemistry*; Wiley-vch Weinheim, Germany, **1999**; Vol. 3.
- 27 Daniel, M.-C.; Astruc, D. Gold Nanoparticles: Assembly, Supramolecular Chemistry, Quantum-Size-Related Properties, and Applications toward Biology, Catalysis, and Nanotechnology. *Chem. Rev.* **2004**, *104*, 293–346.
- 28 Heaven, M. W.; Dass, A.; White, P. S.; Holt, K. M.; Murray, R. W. Crystal Structure of the Gold Nanoparticle [N(C₈H₁₇)₄][Au₂₅(SCH₂CH₂Ph)₁₈]. *J. Am. Chem. Soc.* **2008**, *130*, 3754–3755.
- 29 Walter, M.; Akola, J.; Lopez-Acevedo, O.; Jadzinsky, P. D.; Calero, G.; Ackerson, C. J.; Whetten, R. L.; Grönbeck, H.; Häkkinen, H. A Unified View of Ligand-Protected Gold Clusters as Superatom Complexes. *Proc. Natl. Acad. Sci.* **2008**, *105*, 9157–9162.
- 30 Jena, P. Beyond the Periodic Table of Elements: The Role of Superatoms. *J. Phys. Chem. Lett.* **2013**, *4*, 1432–1442.
- 31 Knoppe, S.; Dolamic, I.; Bürgi, T. Racemization of a Chiral Nanoparticle Evidences the Flexibility of the Gold-Thiolate Interface. *J. Am. Chem. Soc.* **2012**, *134*, 13114–13120.
- 32 Levi-Kalisman, Y.; Jadzinsky, P. D.; Kalisman, N.; Tsunoyama, H.; Tsukuda, T.; Bushnell, D. A.; Kornberg, R. D. Synthesis and Characterization of Au₁₀₂(*p*-MBA)₄₄ Nanoparticles. *J. Am. Chem. Soc.* **2011**, *133*, 2976–2982.
- 33 Galloway, J. M.; Bramble, J. P.; Rawlings, A. E.; Burnell, G.; Evans, S. D.; Staniland, S. S. Biotemplated Magnetic Nanoparticle Arrays. *Small* **2012**, *8*, 204–208.
- 34 Zeng, C.; Chen, Y.; Das, A.; Jin, R. Transformation Chemistry of Gold Nanoclusters: From One Stable Size to Another. *J. Phys. Chem. Lett.* **2015**, *6*, 2976–2986.

- 35 Gao, Y.; Bulusu, S.; Zeng, X. C. A Global Search of Highly Stable Gold-Covered Bimetallic Clusters $M@Au_n$ ($n = 8-17$): Endohedral Gold Clusters. *ChemPhysChem* **2006**, *7*, 2275–2278.
- 36 Pembere, A. M. S.; Cui, C.; Wu, H.; Luo, Z. Small Gold Clusters Catalyzing Oxidant-Free Dehydrogenation of Glycerol Initiated by Methene Hydrogen Atom Transfer. *Chinese Chem. Lett.* **2019**, *30*, 1000–1004.
- 37 Ding, W.; Huang, C.; Guan, L.; Liu, X.; Luo, Z.; Li, W. Water-Soluble Au_{13} Clusters Protected by Binary Thiolates: Structural Accommodation and the Use for Chemosensing. *Chem. Phys. Lett.* **2017**, *676*, 18–24.
- 38 Castleman, A. W.; Khanna, S. N. Clusters, Superatoms, and Building Blocks of New Materials. *J. Phys. Chem. C* **2009**, *113*, 2664–2675.
- 39 Jadzinsky, P. D.; Calero, G.; Ackerson, C. J.; Bushnell, D. A.; Kornberg, R. D. Structure of a Thiol Monolayer-Protected Gold Nanoparticle at 1.1 Å Resolution. *Science* **2007**, *318*, 430–433.
- 40 Claridge, S. A.; Castleman, A. W.; Khanna, S. N.; Murray, C. B.; Sen, A.; Weiss, P. S. Cluster-Assembled Materials. *ACS Nano* **2009**, *3*, 244–255.
- 41 Bürgi, T. Properties of the Gold-Sulphur Interface: From Self-Assembled Monolayers to Clusters. *Nanoscale* **2015**, *7*, 15553–15567.
- 42 Briant, C. E.; Theobald, B. R. C.; White, J. W.; Bell, L. K.; Mingos, D. M. P.; Welch, A. J. Synthesis and X-Ray Structural Characterization of the Centred Icosahedral Gold Cluster Compound $[Au_{13}(PMe_2Ph)_{10}Cl_2](PF_6)_3$; the Realization of a Theoretical Prediction. *J. Chem. Soc. Chem. Commun.* **1981**, 201–202.
- 43 Sheong, F. K.; Zhang, J.-X.; Lin, Z. An $[Au_{13}]^{5+}$ Approach to the Study of Gold Nanoclusters. *Inorg. Chem.* **2016**, *55*, 11348–11353.
- 44 Laupp, M.; Strähle, J. $[(Ph_3PAu)_6(DppeAu_2)(AuCl)_4Pd]$, an Icosahedral Au_{12} Cluster with a Central Pd Atom. *Angew. Chem. Int. Ed.* **1994**, *33*, 207–209.
- 45 Kang, X.; Chong, H.; Zhu, M. $Au_{25}(SR)_{18}$: The Captain of the Great Nanocluster Ship. *Nanoscale* **2018**, *10*, 10758–10834.
- 46 Jin, S.; Zhou, M.; Kang, X.; Li, X.; Du, W.; Wei, X.; Chen, S.; Wang, S.; Zhu, M. Three-dimensional Octameric Assembly of Icosahedral M_{13} Units in $[Au_8Ag_{57}(Dppp)_4(C_6H_{11}S)_{32}Cl_2]Cl$ and Its $[Au_8Ag_{55}(Dppp)_4(C_6H_{11}S)_{34}][BPh_4]_2$ Derivative. *Angew. Chem. Int. Ed.* **2020**, *59*, 3891–3895.
- 47 Gam, F.; Paez-Hernandez, D.; Arratia-Perez, R.; Liu, C. W. W.; Kahlal, S.; Saillard, J.-Y.; Muñoz-Castro, A. Coinage Metal Superatomic Cores: Insights into Their Intrinsic

- Stability and Optical Properties from Relativistic DFT Calculations. *Chem. Eur. J.* **2017**, *23*, 11330–11337.
- 48 Tsukuda, T.; Häkkinen, H. *Protected Metal Clusters: From Fundamentals to Applications*; Elsevier, **2015**.
- 49 Saillard, J.-Y.; Halet, J.-F. Structure and Bonding Patterns in Large Molecular Ligated Metal Clusters. *Struct. Bond.* **2016**, *169*, 157–179.
- 50 Fehner, T.; Halet, J.-F.; Saillard, J.-Y. *Molecular Clusters. A Bridge to Solid State Chemistry*. Cambridge Univ. Press. Cambridge, UK. **2007**.
- 51 Häkkinen, H. Atomic and Electronic Structure of Gold Clusters: Understanding Flakes, Cages and Superatoms from Simple Concepts. *Chem. Soc. Rev.* **2008**, *37*, 1847–1859.
- 52 Mäkinen, V.; Koskinen, P.; Häkkinen, H. Modeling Thiolate-Protected Gold Clusters with Density-Functional Tight-Binding. *Eur. Phys. J. D* **2013**, *67*, 38.
- 53 Häkkinen, H. Electronic Structure: Shell Structure and the Superatom Concept. In *Protected Metal Clusters: From Fundamentals to Applications*; Häkkinen, H., Tsukuda, T., Eds.; Elsevier Science, **2015**; pp 189–222.
- 54 Lopez-Acevedo, O.; Akola, J.; Whetten, R. L.; Grönbeck, H.; Häkkinen, H. Structure and Bonding in the Ubiquitous Icosahedral Metallic Gold Cluster Au₁₄₄(SR)₆₀. *J. Phys. Chem. C* **2009**, *113*, 5035–5038.
- 55 Zhang, J.; Zhou, Y.; Zheng, K.; Abroshan, H.; Kauffman, D. R.; Sun, J.; Li, G. Diphosphine-Induced Chiral Propeller Arrangement of Gold Nanoclusters for Singlet Oxygen Photogeneration. *Nano Res.* **2017**, 1–12.
- 56 Shichibu, Y.; Konishi, K. HCl-Induced Nuclearity Convergence in Diphosphine-Protected Ultrasmall Gold Clusters: A Novel Synthetic Route to “Magic-Number” Au₁₃ Clusters. *Small* **2010**, *6*, 1216–1220.
- 57 Hall, K. P.; Mingos, D. M. P. Homo- and Heteronuclear Cluster Compounds of Gold. In *Progress in Inorganic Chemistry*; **1984**; pp 237–325.
- 58 Ube, H.; Zhang, Q.; Shionoya, M. A Carbon-Centered Hexagold(I) Cluster Supported by N-Heterocyclic Carbene Ligands. *Organometallics* **2018**, *37*, 2007–2009.
- 59 Narouz, M. R.; Takano, S.; Lummis, P. A.; Levchenko, T. I.; Nazemi, A.; Kaappa, S.; Malola, S.; Yousefalizadeh, G.; Calhoun, L. A.; Stampelcoskie, K. G.; et al. Robust, Highly Luminescent Au₁₃ Superatoms Protected by N-Heterocyclic Carbenes. *J. Am. Chem. Soc.* **2019**, *141*, 14997–15002.
- 60 Munz, D. Pushing Electrons-Which Carbene Ligand for Which Application? *Organometallics* **2018**, *37*, 275–289.

- 61 Liske, A.; Verlinden, K.; Buhl, H.; Schaper, K.; Ganter, C. Determining the π -Acceptor Properties of N-Heterocyclic Carbenes by Measuring the ^{77}Se NMR Chemical Shifts of Their Selenium Adducts. *Organometallics* **2013**, *32*, 5269–5272.
- 62 Huynh, H. V.; Han, Y.; Jothibas, R.; Yang, J. A. ^{13}C NMR Spectroscopic Determination of Ligand Donor Strengths Using N-Heterocyclic Carbene Complexes of Palladium(II). *Organometallics* **2009**, *28*, 5395–5404.
- 63 Gusev, D. G.; Peris, E. The Tolman Electronic Parameter (TEP) and the Metal–Metal Electronic Communication in Ditopic NHC Complexes. *Dalton Trans.* **2013**, *42*, 7359–7364.
- 64 Arduengo, A. J.; Bertrand, G. Carbenes Introduction. *Chem. Rev.* **2009**, *109*, 3209–3210.
- 65 Nelson, D. J.; Nolan, S. P. Quantifying and Understanding the Electronic Properties of N-Heterocyclic Carbenes. *Chem. Soc. Rev.* **2013**, *42*, 6723–6753.
- 66 Muñoz-Castro, A. Potential of N-Heterocyclic Carbene Derivatives from $\text{Au}_{13}(\text{Dppe})_5\text{Cl}_2$ Gold Superatoms. Evaluation of Electronic, Optical and Chiroptical Properties from Relativistic DFT. *Inorg. Chem. Front.* **2019**, *6*, 2349–2358.
- 67 Li, G.; Abroshan, H.; Liu, C.; Zhuo, S.; Li, Z.; Xie, Y.; Kim, H. J.; Rosi, N. L.; Jin, R. Tailoring the Electronic and Catalytic Properties of Au_{25} Nanoclusters via Ligand Engineering. *ACS Nano* **2016**, *10*, 7998–8005.
- 68 Yang, H.; Wang, Y.; Lei, J.; Shi, L.; Wu, X.; Mäkinen, V.; Lin, S.; Tang, Z.; He, J.; Häkkinen, H.; et al. Ligand-Stabilized $\text{Au}_{13}\text{Cu}_x$ ($x = 2, 4, 8$) Bimetallic Nanoclusters: Ligand Engineering to Control the Exposure of Metal Sites. *J. Am. Chem. Soc.* **2013**, *135*, 9568–9571.
- 69 Yuan, X.; Goswami, N.; Mathews, I.; Yu, Y.; Xie, J. Enhancing Stability through Ligand-Shell Engineering: A Case Study with $\text{Au}_{25}(\text{SR})_{18}$ Nanoclusters. *Nano Res.* **2015**, *8*, 3488–3495.
- 70 Wan, X.-K.; Wang, J.-Q.; Nan, Z.-A.; Wang, Q.-M. Ligand Effects in Catalysis by Atomically Precise Gold Nanoclusters. *Sci. Adv.* **2017**, *3*, e1701823.
- 71 Karimova, N. V.; Aikens, C. M. Chiroptical Activity in BINAP- and DIOP-Stabilized Octa- and Undecagold Clusters. *J. Phys. Chem. C* **2018**, *122*, 11051–11065.
- 72 Yang, Y.; Xu, H.; Cao, D.; Zeng, X. C.; Cheng, D. Hydrogen Production via Efficient Formic Acid Decomposition: Engineering the Surface Structure of Pd-Based Alloy Catalysts by Design. *ACS Catal.* **2019**, *9*, 781–790.
- 73 Xu, H.; Cheng, D.; Gao, Y.; Zeng, X. C. Assessment of Catalytic Activities of Gold Nanoclusters with Simple Structure Descriptors. *ACS Catal.* **2018**, *8*, 9702–9710.

- 74 Danopoulos, A. A.; Simler, T.; Braunstein, P. N-Heterocyclic Carbene Complexes of Copper, Nickel, and Cobalt. *Chem. Rev.* **2019**, *119*, 3730–3961.
- 75 Ai, P.; Mauro, M.; Gourlaouen, C.; Carrara, S.; De Cola, L.; Tobon, Y.; Giovanella, U.; Botta, C.; Danopoulos, A. A.; Braunstein, P. Bonding, Luminescence, Metallophilicity in Linear Au₃ and Au₂Ag Chains Stabilized by Rigid Diphosphanil NHC Ligands. *Inorg. Chem.* **2016**, *55*, 8527–8542.
- 76 Ai, P.; Danopoulos, A. A.; Braunstein, P. Auophilicity-Triggered Assembly of Novel Cyclic Penta- and Hexanuclear Gold(I) Complexes with Rigid Anionic NHC-Type Ligands. *Inorg. Chem.* **2015**, *54*, 3722–3724.
- 77 Hirano, K.; Takano, S.; Tsukuda, T. Ligand Effects on the Structures of [Au₂₃L₆(C≡CPh)₉]²⁺ (L = N-Heterocyclic Carbene vs Phosphine) with Au₁₇ Superatomic Cores. *J. Phys. Chem. C* **2021**, *125*, 9930–9936.
- 78 Qi, S.; Ma, Q.; He, X.; Tang, Y. Self-Assembled Monolayers of N-Heterocyclic Carbene on Gold: Stability under Ultrasonic Circumstance and Computational Study. *Colloids Surfaces A Physicochem. Eng. Asp.* **2018**, *538*, 488–493.
- 79 Sun, F.; Tang, Q. The Ligand Effect on the Interface Structures and Electrocatalytic Applications of Atomically Precise Metal Nanoclusters. *Nanotechnology* **2021**, *32*, 352001.
- 80 Deng, C.; Chen, J.; Tang, Q. Theoretical Investigation on the Adsorption and Interface Bonding between N-Heterocyclic Carbenes and Metal Surfaces. *J. Phys. Chem. C* **2021**, *125*, 4489–4497.
- 81 Wei, J.; Halet, J.-F.; Kahlal, S.; Saillard, J.-Y.; Muñoz-Castro, A. Toward the Formation of N-Heterocyclic-Carbene-Protected Gold Clusters of Various Nuclearities. A Comparison with Their Phosphine-Protected Analogues from Density Functional Theory Calculations. *Inorg. Chem.* **2020**, *59*, 15240–15249.
- 82 Copley, R. C. B.; Mingos, D. M. P. Synthesis and Characterization of the Centred Icosahedral Cluster Series [Au₉M^{IB}₄Cl₄(PMePh₂)₈][C₂B₉H₁₂], Where M^{IB} = Au, Ag or Cu. *J. Chem. Soc. Dalton Trans.* **1996**, 491–500.
- 83 Shichibu, Y.; Suzuki, K.; Konishi, K. Facile Synthesis and Optical Properties of Magic-Number Au₁₃ Clusters. *Nanoscale* **2012**, *4*, 4125–4129.
- 84 Yang, L.; Cheng, H.; Jiang, Y.; Huang, T.; Bao, J.; Sun, Z.; Jiang, Z.; Ma, J.; Sun, F.; Liu, Q.; et al. In Situ Studies on Controlling an Atomically-Accurate Formation Process of Gold Nanoclusters. *Nanoscale* **2015**, *7*, 14452–14459.
- 85 van der Velden, J. W. A.; Vollenbroek, F. A.; Bour, J. J.; Beurskens, P. T.; Smits, J. M.

- M.; Bosnian, W. P. Gold Clusters Containing Bidentate Phosphine Ligands. Preparation and X-Ray Structure Investigation of $[\text{Au}_5(\text{DppmH})_3(\text{Dppm})](\text{NO}_3)_2$ and $[\text{Au}_{13}(\text{DppmH})_6](\text{NO}_3)_n$. *Recl. des Trav. Chim. des Pays-Bas* **1981**, *100*, 148–152.
- 86 Zhang, S.-S.; Feng, L.; Senanayake, R. D.; Aikens, C. M.; Wang, X.-P.; Zhao, Q.-Q.; Tung, C.-H.; Sun, D. Diphosphine-Protected Ultrasmall Gold Nanoclusters: Opened Icosahedral Au_{13} and Heart-Shaped Au_8 Clusters. *Chem. Sci.* **2018**, *9*, 1251–1258.
- 87 Lei, Z.; Pei, X.-L.; Ube, H.; Shionoya, M. Reconstituting C-Centered Hexagold(I) Clusters with N-Heterocyclic Carbene Ligands. *Bull. Chem. Soc. Jpn.* **2021**, *94*, 1324–1330.
- 88 Frisch, M. J.; Trucks, G. W.; Schlegel, H. B.; Scuseria, G. E.; Robb, M. A.; Cheeseman, J. R.; Scalmani, G.; Barone, V.; Petersson, G. A.; Nakatsuji, H.; et al. Gaussian 16 Revision A.03. 2016.
- 89 Becke, A. D. Density-Functional Exchange-Energy Approximation with Correct Asymptotic Behavior. *Phys. Rev. A* **1988**, *38*, 3098–3100.
- 90 Perdew, J. P. Density-Functional Approximation for the Correlation Energy of the Inhomogeneous Electron Gas. *Phys. Rev. B* **1986**, *33*, 8822.
- 91 Weigend, F.; Ahlrichs, R. Balanced Basis Sets of Split Valence, Triple Zeta Valence and Quadruple Zeta Valence Quality for H to Rn: Design and Assessment of Accuracy. *Phys. Chem. Chem. Phys.* **2005**, *7*, 3297–3305.
- 92 Grimme, S. Semiempirical GGA-Type Density Functional Constructed with a Long-Range Dispersion Correction. *J. Comput. Chem.* **2006**, *27*, 1787–1799.
- 93 Glendening, E. D.; Badenhoop, J. K.; Reed, A. E.; Carpenter, J. E.; Bohmann, J. A.; Morales, C. M.; Landis, C. R.; Weinhold, F. NBO 6.0 Theoretical Chemistry Institute, University of Wisconsin, Madison. **2013**.
- 94 Te Velde, G.; Bickelhaupt, F. M.; Baerends, E. J.; Fonseca Guerra, C.; van Gisbergen, S. J. a.; Snijders, J. G.; Ziegler, T.; Velde, G. T. E.; Guerra, C. F.; Gisbergen, S. J. A. Chemistry with ADF. *J. Comput. Chem.* **2001**, *22*, 931–967.
- 95 ADF2016, SCM, Theoretical Chemistry, Vrije Universiteit, Amsterdam, The Netherlands. ADF2016, SCM, Theoretical Chemistry, Vrije Universiteit, Amsterdam, The Netherlands.
- 96 Stephens, P. J.; Devlin, F. J.; Chabalowski, C. F.; Frisch, M. J. Ab Initio Calculation of Vibrational Absorption and Circular Dichroism Spectra Using Density Functional Force Fields. *J. Phys. Chem.* **1994**, *98*, 11623–11627.
- 97 Gorelsky, S. I. SWizard Program.

- 98 Adamo, C.; Barone, V. Toward Reliable Density Functional Methods without Adjustable Parameters: The PBE0 Model. *J. Chem. Phys.* **1999**, *110*, 6158–6170.
- 99 Marschall, R. Semiconductor Composites: Strategies for Enhancing Charge Carrier Separation to Improve Photocatalytic Activity. *Adv. Funct. Mater.* **2014**, *24*, 2421–2440.
- 100 Pihlajamäki, A.; Hämäläinen, J.; Linja, J.; Nieminen, P.; Malola, S.; Kärkkäinen, T.; Häkkinen, H. Monte Carlo Simulations of Au₃₈(SCH₃)₂₄ Nanocluster Using Distance-Based Machine Learning Methods. *J. Phys. Chem. A* **2020**, *124*, 4827–4836.
- 101 Matus, M. F.; Malola, S.; Kinder Bonilla, E.; Barngrover, B. M.; Aikens, C. M.; Häkkinen, H. A Topological Isomer of the Au₂₅(SR)₁₈⁻ Nanocluster. *Chem. Commun.* **2020**, *56*, 8087–8090.
- 102 MacLeod Carey, D.; Muñoz-Castro, A. Evaluation of N-Heterocyclic Carbene Counterparts of Classical Gold Clusters; Bonding Properties of Octahedral CAu₆, Icosahedral Au₁₃Cl₂, and Bi-Icosahedral Au₂₅Cl₂ Cores from Relativistic DFT Calcula. *J. Phys. Chem. C* **2019**, *123*, 12466–12473.
- 103 Jung, J.; Kang, S.; Han, Y.-K. Ligand Effects on the Stability of Thiol-Stabilized Gold Nanoclusters: Au₂₅(SR)₁₈⁻, Au₃₈(SR)₂₄, and Au₁₀₂(SR)₄₄. *Nanoscale* **2012**, *4*, 4206–4210.
- 104 Aikens, C. M. Electronic and Geometric Structure, Optical Properties, and Excited State Behavior in Atomically Precise Thiolate-Stabilized Noble Metal Nanoclusters. *Acc. Chem. Res.* **2018**, *51*, 3065–3073.
- 105 Weerawardene, K. L. D. M.; Aikens, C. M. Effect of Aliphatic versus Aromatic Ligands on the Structure and Optical Absorption of Au₂₀(SR)₁₆. *J. Phys. Chem. C* **2016**, *120*, 8354–8363.
- 106 Aikens, C. M. Electronic Structure of Ligand-Passivated Gold and Silver Nanoclusters. *J. Phys. Chem. Lett.* **2011**, *2*, 99–104.
- 107 Aikens, C. M. Geometric and Electronic Structure of Au₂₅(SPhX)₁₈⁻ (X = H, F, Cl, Br, CH₃, and OCH₃). *J. Phys. Chem. Lett.* **2010**, *1*, 2594–2599.
- 108 Gao, Z.-H.; Dong, J.; Zhang, Q.-F.; Wang, L.-S. Halogen Effects on the Electronic and Optical Properties of Au₁₃ Nanoclusters. *Nanoscale Adv.* **2020**, *2*, 4902–4907.
- 109 Hoffmann, R. Building Bridges Between Inorganic and Organic Chemistry (Nobel Lecture). *Angew. Chem. Int. Ed.* **1982**, *21*, 711–724.

3.6 Annex

Table S1. Relevant computed data for $[\text{Au}_{13}\text{L}_6]^{5+}$ clusters (L = dppm ($\text{Au}_{13}\text{-P}'\text{m}$) and di-NHC'm ($\text{Au}_{13}\text{-C}'\text{m}$))^a.

		$\text{Au}_{13}\text{-X}$	
		X = dppm (C_1)	X = NHC'm (C_1)
Average Distance (Å) [WBI] ^b	$\text{Au}_c\text{-Au}_{\text{ico}}$	2.813 [0.1103] Exp. 2.786	2.814 [0.1255]
	$\text{Au}_{\text{ico}}\text{-Au}_{\text{ico}}$	2.958 [0.0655] Exp. 2.938	2.959 [0.0642]
	$\text{Au}_{\text{ico}}\text{-X}$	2.328 [0.4297] Exp. 2.460	2.046 [0.4476]
HOMO-LUMO gap (eV)		1.43 eV	1.81 eV
NAO ^c Charge (Av.)	Au_c	-0.33	-0.29
	Au_{ico}	+0.14	+0.22
	X	+0.61	+0.44

^a Au_c and Au_{ico} designate the centered and sphere Au atoms of the centered-icosahedral cluster kernel. ^bWiberg bond index. ^cNatural atomic orbital.

Table S2. Relevant computed data for $[\text{Au}_{13}\text{Cl}_2\text{L}_{10}]^{3+}$ (L = PMe_2Ph ($\text{Au}_{13}\text{Cl}_2\text{-P}'$) and NHC' ($\text{Au}_{13}\text{Cl}_2\text{-C}'$)) and $[\text{Au}_{13}\text{Cl}_2\text{L}_5]^{3+}$ (L = dppe ($\text{Au}_{13}\text{Cl}_2\text{-P}'\text{e}$) and NHC'e ($\text{Au}_{13}\text{Cl}_2\text{-C}'\text{e}$)) clusters.

		$\text{Au}_{13}\text{Cl}_2\text{-X}$			
		X = PMe_2Ph (C_1)	X = NHC' (C_1)	X = dppe (D_5)	X = di-NHC'e (C_1)
Average Distance (Å) [WBI]	$\text{Au}_c\text{-Au}_{\text{ico}}$	2.798 [0.1235] Exp. 2.769	2.846 [0.1298]	2.785 [0.1213] Exp. 2.764	2.801 [0.1332]
	$\text{Au}_{\text{ico}}\text{-Au}_{\text{ico}}$	2.943 [0.0607] Exp. 2.912	2.998 [0.0651]	2.928 [0.0628] Exp. 2.906	2.946 [0.0637]
	$\text{Au}_{\text{ico}}\text{-Cl}$	2.366 [0.3799] Exp. 2.297	2.374 [0.3522]	2.376 [0.3600] Exp. 2.351	2.378 [0.3687]
	$\text{Au}_{\text{ico}}\text{-X}$	2.316 [0.4514] Exp. 2.286	2.065 [0.4354]	2.302 [0.4402] Exp. 2.289	2.037 [0.4471]
HOMO-LUMO gap (eV)		2.02	2.09	1.81	1.99
NAO Charge (Av.)	Au_c	-0.34	-0.30	-0.33	-0.31
	Au_{ico}	+0.13	+0.22	+0.15	+0.21
	Cl	-0.54	-0.59	-0.56	-0.58
	X	+0.29	+0.18	+0.53	+0.39

Table S3. Relevant computed data for $[\text{Au}_{13}\text{Cl}_3\text{L}_9]^{2+}$ (L = PPh₂Me (Au₁₃Cl₃-P') and NHC' (Au₁₃Cl₃-C')) clusters.

		Au ₁₃ Cl ₃ -X	
		X = PMePh ₂ (C ₁)	X = NHC' (C ₁)
Average Distance (Å) [WBI]	Au _c -Au _{ico}	2.800 [0.1211]	2.811 [0.1294] Exp. 2.768
	Au _{ico} -Au _{ico}	2.945 [0.0647]	2.956 [0.0666] Exp. 2.911
	Au _{ico} -Cl	2.386 [0.3472]	2.416 [0.3100] Exp. 2.352
	Au _{ico} -X	2.315 [0.4380]	2.044 [0.4452] Exp. 2.051
HOMO-LUMO gap (eV)		1.97	2.13
NAO Charge (Av.)	Au _c	-0.31	-0.27
	Au _{ico}	+0.15	+0.21
	Cl	-0.57	-0.60
	X	+0.25	+0.17

Table S4. Relevant computed data for $[\text{Au}_{13}\text{Cl}_4\text{L}_8]^+$ (L = PPh₂Me (Au₁₃Cl₄-P') and NHC' (Au₁₃Cl₄-C')) and $[\text{Au}_{13}\text{Cl}_4\text{L}_4]^+$ (L = dppp (Au₁₃Cl₄-P'p) and NHC'p (Au₁₃Cl₄-C'p)) clusters.

		Au ₁₃ Cl ₄ -X			
		X = PMePh ₂ (C ₁)	X = NHC' (C ₂)	X = dppp (C ₂)	X = di-NHC'p (D ₂)
Average Distance (Å) [WBI]	Au _c -Au _{ico}	2.787 [0.1273]	2.821 [0.1303]	2.790 [0.1254]	2.821 [0.1372]
	Au _{ico} -Au _{ico}	2.931 [0.0650]	2.975 [0.0726]	2.935 [0.0678]	2.975 [0.0688]
	Au _{ico} -Cl	2.393 [0.3425]	2.442 [0.2801]	2.398 [0.3493]	2.395 [0.3602]
	Au _{ico} -X	2.297 [0.4515]	2.035 [0.4624]	2.298 [0.4266]	2.044 [0.4371]
HOMO-LUMO gap (eV)		1.88	1.84	1.44	1.87
NAO Charge (Av.)	Au _c	-0.35	-0.31	-0.34	-0.33
	Au _{ico}	+0.14	+0.21	+0.16	+0.21
	Cl	-0.59	-0.62	-0.57	-0.58
	X	+0.25	+0.16	+0.43	+0.28

Table S5. Relevant computed data for $[M_4Au_9Cl_4L_8]^+$ ($M = Cu, Ag; L = PPh_2Me (M_4Au_9Cl_4-P')$) and NHC' ($M_4Au_9Cl_4-C'$)) clusters.

		$M_4Au_9Cl_4-X (M = Cu)$		$M_4Au_9Cl_4-X (M = Ag)$	
		$X = PPh_2Me (C_2)$	$X = NHC' (C_1)$	$X = PPh_2Me (C_1)$	$X = NHC' (C_2)$
Average Distance (Å) [WBI]	Au_c-Au_{ico}	2.738 [0.1336] Exp. 2.737	2.795 [0.1453]	2.750 [0.1374] Exp. 2.746	2.807 [0.1422]
	Au_c-M_{ico}	2.575 [0.1385] Exp. 2.584	2.551 [0.1473]	2.830 [0.1179] Exp. 2.828	2.793 [0.1335]
	$Au_{ico}-Au_{ico}$	2.908 [0.0657] Exp. 2.899	2.960 [0.0618]	2.910 [0.0636] Exp. 2.904	2.940 [0.0667]
	$Au_{ico}-M_{ico}$	2.782 [0.0874] Exp. 2.790	2.808 [0.0895]	2.926 [0.0669] Exp. 2.924	2.955 [0.0739]
	$M_{ico}-Cl$	2.186 [0.2817] Exp. 2.134	2.226 [0.2389]	2.395 [0.3124] Exp. 2.378	2.445 [0.2482]
	$Au_{ico}-X$	2.301 [0.4071] Exp. 2.290	2.047 [0.4106]	2.303 [0.4189] Exp. 2.299	2.047 [0.4229]
HOMO-LUMO gap (eV)		1.87 eV	1.88	1.97	1.90
NAO Charge (Av.)	Au_c	-0.52	-0.55	-0.45	-0.45
	Au_{ico}	+0.04	+0.14	+0.09	+0.20
	M_{ico}	+0.54	+0.55	+0.37	+0.36
	Cl	-0.68	-0.70	-0.67	-0.69
	X	+0.22	+0.13	+0.24	+0.15

Table S6. Relevant computed data for $[PdAu_{12}Cl_4L_6L'e]$ ($L = PPh_3, L'e = dppe (PdAu_{12}Cl_4-P)$ and $L = NHC', L'e = di-NHC'e (PdAu_{12}Cl_4-C)$) clusters.

		$PdAu_{12}Cl_4-X$	
		$X = dppe/PPh_3 (C_1)$	$X = di-NHC'e/NHC' (C_2)$
Average Distance (Å) [WBI]	Pd_c-Au_{ico}	2.780 [0.1281] Exp. 2.748	2.777 [0.1379]
	$Au_{ico}-Au_{ico}$	2.933 [0.0715] Exp. 2.889	2.920 [0.0696]
	$Au_{ico}-Cl$	2.421 [0.3177] Exp. 2.385	2.374 [0.2566]
	$Au_{ico}-X$	2.316 [0.3932] Exp. 2.294	2.043 [0.4486]
HOMO-LUMO gap (eV)		1.63	1.92
NAO Charge (Av.)	Pd_c	-0.59	-0.62
	Au_{ico}	+0.17	+0.21
	Cl	-0.60	-0.65
	X	+0.12	+0.09

Table S7. Relevant computed data for $[\text{Au}_{13}\text{Y}_4\text{L}_8]^+$ ($\text{Y} = \text{Br}, \text{I}$) ($\text{L} = \text{PPh}_2\text{Me}$ ($\text{Au}_{13}\text{Y}_4\text{-P}'$) and NHC' ($\text{Au}_{13}\text{Y}_4\text{-C}'$)) clusters.

		$\text{Au}_{13}\text{Y}_4\text{-X}$ ($\text{Y} = \text{Br}$)		$\text{Au}_{13}\text{Y}_4\text{-X}$ ($\text{Y} = \text{I}$)	
		$\text{X} = \text{PMePh}_2$ (C_1)	$\text{X} = \text{NHC}'$ (C_2)	$\text{X} = \text{PMePh}_2$ (C_1)	$\text{X} = \text{NHC}'$ (C_2)
Average Distance (\AA) [WBI]	$\text{Au}_c\text{-Au}_{\text{ico}}$	2.787 [0.1248]	2.826 [0.1282]	2.789 [0.1213]	2.830 [0.1252]
	$\text{Au}_{\text{ico}}\text{-Au}_{\text{ico}}$	2.931 [0.0644]	2.979 [0.0686]	2.933 [0.0634]	2.983 [0.0676]
	$\text{Au}_{\text{ico}}\text{-Y}$	2.500 [0.3517]	2.547 [0.2884]	2.653 [0.3761]	2.694 [0.3129]
	$\text{Au}_{\text{ico}}\text{-X}$	2.294 [0.4494]	2.038 [0.4616]	2.296 [0.4467]	2.043 [0.4575]
HOMO-LUMO gap (eV)		1.96	1.78	1.91	1.67
NAO Charge (Av.)	Au_c	-0.34	-0.30	-0.33	-0.29
	Au_{ico}	+0.14	+0.20	+0.12	+0.19
	Y	-0.58	-0.61	-0.54	-0.59
	X	+0.25	+0.17	+0.26	+0.17

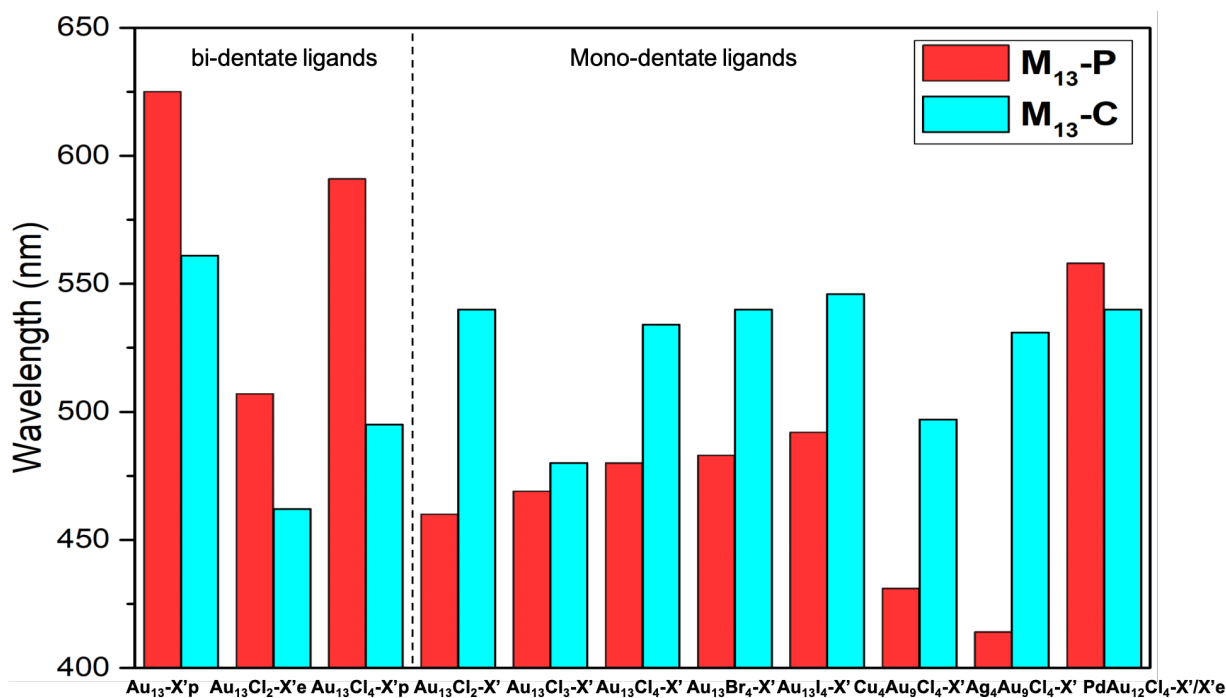


Figure S1. Comparison of the simulated UV-Vis transition wavelength associated with the lowest energy band of the $\text{M}_{13}\text{-X}$ ($\text{X} = \text{P}, \text{C}$) species.

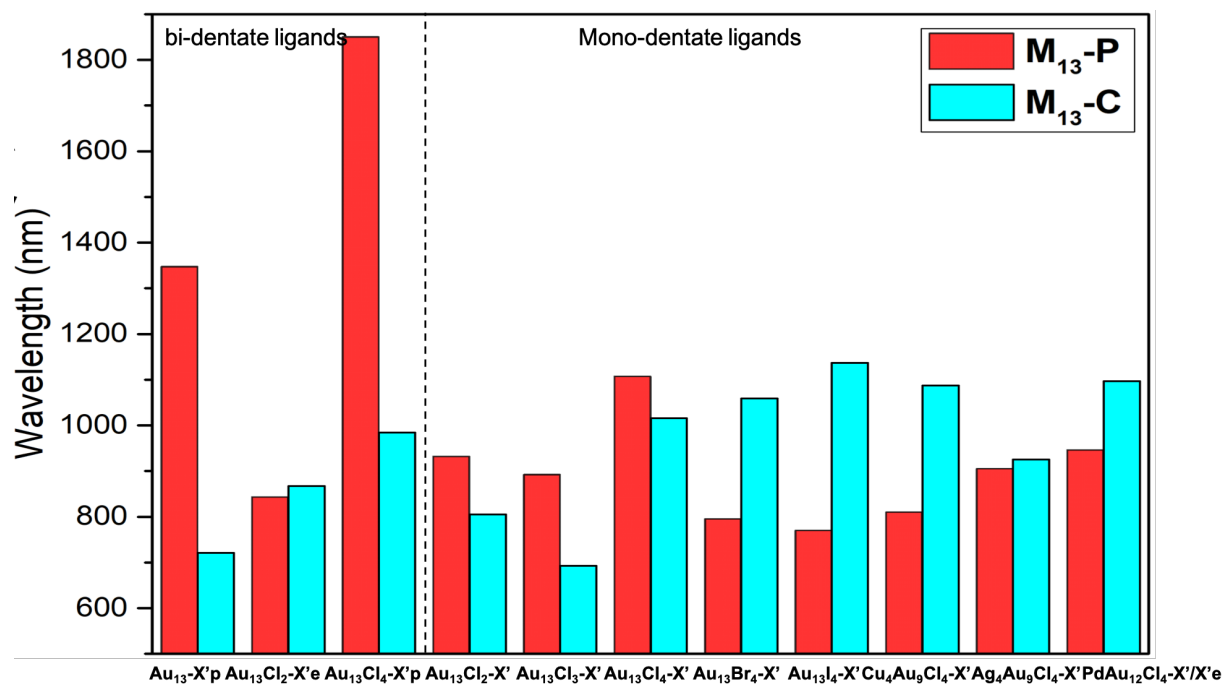


Figure S2. Comparison of the simulated hypothetical phosphorescence emission wavelength of the $M_{13}-X$ ($X = P, C$) species.

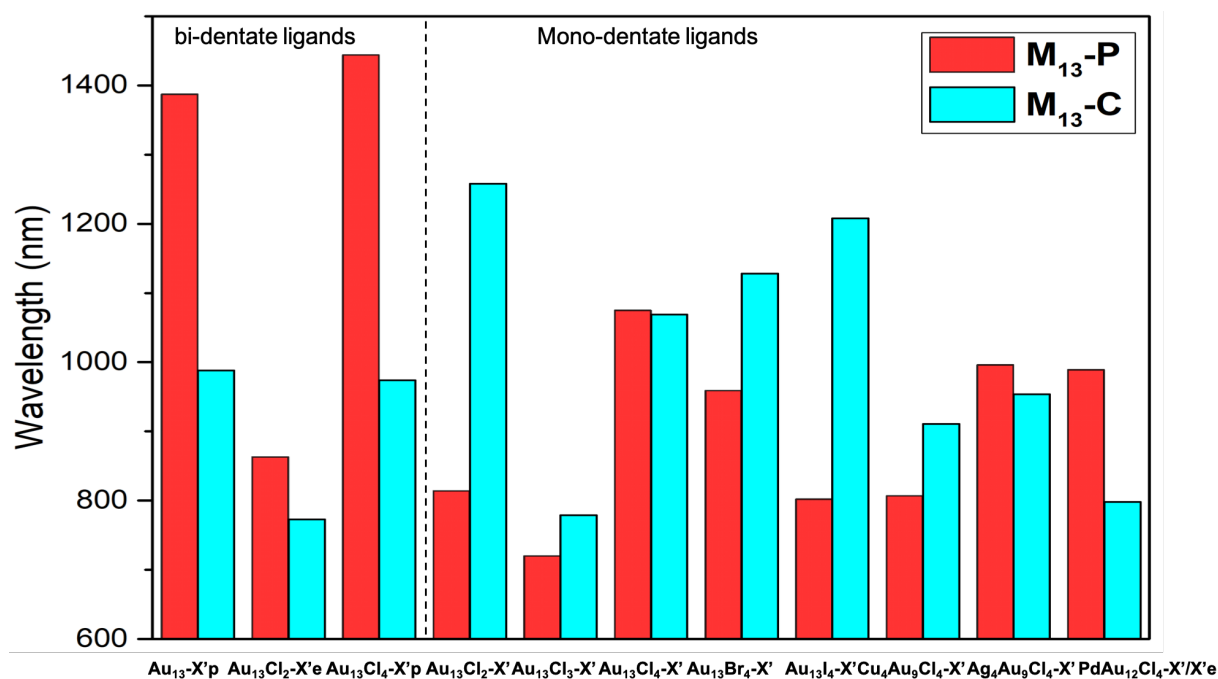


Figure S3. Comparison of the simulated hypothetical fluorescence emission wavelength of the $M_{13}-X$ ($X = P, C$) species.

Chapter 4

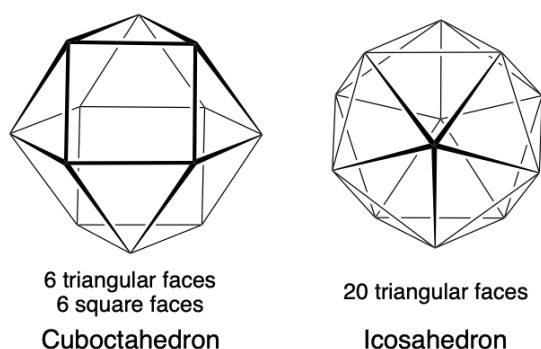
Ligand-Induced Cuboctahedral versus Icosahedral Core Isomerism within Eight-Electron Heterocyclic-Carbene- Protected Gold Nanoclusters

4.1 Introduction

Since the beginning of this century, the field of ligated gold nanoclusters (AuNCs) has been the subject of a tremendous development, owing to the many potential applications of these species, associated with their atom-precise nature, allowing accurate chemical control of their properties.¹⁻³ Such AuNCs can be viewed as fully delocalized mixed-valent compounds, with an averaged Au oxidation state comprised between +I and 0 ($5d^{10} 6s^x$ ($0 < x < 1$) average configuration). The bonding in these clusters is associated with the 6s electrons. In the most common cases of clusters having a pseudo-spherical cluster core, the total number of 6s electrons tend to equal a so-called “magic” number (2, 8, 18, 20, 34, 40, 58...), which provides the cluster with closed-shell stability. These specific closed-shell electron counts are rationalized within the concept of *superatom*,⁴⁻⁶ itself derived from the *spherical jellium approximation*⁷ that considers the cluster core as a homogeneous medium in which the electrons in question are subject to a spherical homogeneous potential. It is of critical importance to note that such an approximation assumes that the cluster core should be both spherical and compact enough. The Au@Au₁₂ centered icosahedral arrangement is by far the most pseudo-spherical compact motif encountered in ligated AuNC chemistry, as exemplified by the very first AuNC characterized by Mingos and colls., namely [Au₁₃(PMe₂Ph)₁₀Cl₂]³⁺,⁸ and the currently extensively studied [Au₂₅(SR)₁₈] family of compounds, which are described as Au@Au₁₂ centered icosahedra decorated with 18 thiolates and 12 peripheral Au(I) centers.^{9,10} All these compounds can be considered as *superatoms* with an 8-electron [Au₁₃]⁵⁺ core of I_h symmetry and 1S² 1P⁶ 1D⁰ *superatomic* configuration. Assuming that these 8 electrons are hosted in molecular orbitals (MOs) expressed as 6s(Au) combinations and using simple 3D Hückel theory, one is lead to a favorable situation in which the bonding *a_g* and *t_{1u}* combinations (1S and 1P within the *spherical jellium approximation*) are occupied, whereas the antibonding combinations are left vacant. The corresponding total bonding Hückel energy is $|26.96 \beta|$.

Although it can be viewed as a piece of *fcc* bulk, the alternative M@M₁₂ centered cuboctahedral arrangement is only slightly less compact than its icosahedral counterpart (Scheme 1). Using again simple 3D Hückel theory for a regular cuboctahedron (*O_h* symmetry), one is lead to occupied *a_{1g}* (1S) and *t_{1u}* (1P) combinations which are slightly less bonding than their icosahedral counterparts, and consequently the cuboctahedron possesses a slightly lower total bonding Hückel energy of $|24.00 \beta|$. Consistently, the possibility of existence of both

cuboctahedral and icosahedral structures for 8-electron clusters has been discussed since a long time.¹¹⁻¹³ In fact, M_{13} centered cuboctahedral *superatoms* exist, as exemplified by the Cu-rich clusters $[(M@Cu_{12})(dithiolate)_6(CCR)_4]^+$ ($M = Cu, Ag, Au$),¹⁴⁻¹⁶ but they are 2-electron *superatoms* ($1S^2 1P^0$). In contrast to copper, all known examples of centered gold clusters with 13 atoms have icosahedral geometries, but a few larger AuNCs that contain a distorted Au_{13} cuboctahedral core also exist, as for instance $[Au_{22}(CCR)_{18}]$,^{17,18} $[Au_{40}(SR)_{24}]$,¹⁹ $[AuAg_{28}(SR)_{18}(PPh_3)_4]$,²⁰ and $[Au_{23}(SR)_{16}]$.²¹ Only the latter is an 8-electron species.



Scheme 1. Comparative views of the cuboctahedral and icosahedral polyhedra.

It turns out that, within the framework of our general investigations on the stabilization of AuNCs by NHCs (NHC = N-heterocyclic carbene),¹²⁻²⁴ we found that some NHCs can, in certain circumstances, stabilize cuboctahedral cluster cores, suggesting rational control of the core structure with respect to the nature of the ligand shell. NHCs have been recently introduced in AuNC chemistry as alternative neutral 2-electron ligands of phosphines and appear to favor promising photo-emissive properties.²⁵⁻³⁸ This is why we recently investigated, by means of density-functional theory (DFT) calculations (chapter 2 and chapter 3), hypothetical NHC analogues of the 8-electron phosphine/halogenide heteroleptic clusters $[Au_{13}(PR_3)_nX_{12-n}]^{(n-7)+}$ ($X = \text{halogen}$).^{8,39-42} Interestingly, our calculations show that at least in the tetrabromide case, the cuboctahedral $[Au_{13}(NHC)_8Br_4]^+$ species can be stabilized, as described in this chapter.

4.2 Computational Details

Geometry optimizations were performed at the density-functional theory (DFT) level using the *Amsterdam Density Functional* code (ADF2018).⁴³ The BP86 exchange-correlation functional^{44,45} and a triple- ξ Slater basis set plus two polarization functions (STO-TZ2P) were employed.⁴⁶ The relativistic scalar corrections *via* the ZORA⁴⁷ Hamiltonian were considered. Dispersion effects were also considered by addition of Grimme's DFT-D3 empirical

corrections.⁴⁸ An energy convergence criterion of 5×10^{-5} Hartree and a radial convergence criterion of 5×10^{-3} Å were employed. Analytical vibrational frequency calculations were carried out to confirm that all of the optimized singlet ground state structures were genuine minima on their potential energy surface. The UV-Vis optical electronic transitions were calculated *via* time-dependent DFT (TD-DFT)⁴⁹ calculations, using the *Gaussian16* package⁵⁰ with the B3LYP hybrid functional⁵¹ and a Def2-SVP basis set⁵² which include effective core potentials accounting for scalar relativistic effects. This approach was used in previous similar studies, showing a good agreement to the available experimental absorption spectra.^{23,24} The UV-Vis spectra were simulated from the computed TD-DFT transition energies and their oscillator strengths using the SWizard program,⁵³ with each transition being associated with a Gaussian function of half-height width equal to 2000 cm⁻¹. To compute the phosphorescence emission wavelengths, the triplet state geometries were firstly optimized at the BP86/TZ2P level, and their energies, as well as those of their corresponding singlets, were recalculated *via* single point calculations at the B3LYP/TZ2P level. The *Gaussian16* package was used to calculate natural atomic orbital (NAO) populations by using the ADF-optimized geometries with its NBO6.0 module,⁵⁴ with the Def2-SVP basis set and the BP86 functional.

4.3 Results and Discussion

Six different NHC ligands of different size and shape were considered, MeIm, EtIm, *i*PrIm, *t*BuIm, *i*PrBzIm and BzBzIm (see top of Figure 1). The assumed starting structure considered in the geometry optimizations is that of the structurally characterized $[\text{Au}_{13}(\text{PR}_3)_8\text{X}_4]^+$ ($\text{X} = \text{Cl}, \text{Br}, \text{I}$),^{39,40} *i.e.*, a centered icosahedral core and the four bromide positions describing a tetrahedral-like arrangement. In fact, two bromide ligands are connected to one icosahedral edge and the two others to the opposite vertices of two edge-sharing triangular faces, in such a way that the ideal symmetry of the $\text{Au}_{13}\text{Br}_4$ skeleton is D_{2d} . When the smaller N,N'-dimethylimidazolidene (MeIm) and N,N'-diethylimidazolidene (EtIm) NHC ligands are considered, the centered icosahedral arrangement is conserved (Figure 1). With the medium-sized N,N'-diisopropylimidazolidene (*i*PrIm) ligand, two geometrical isomers fully characterized as true energy minima are found, with an icosahedral and a cuboctahedral core and different orientations of the ligands (Figure 1). The cuboctahedral isomer lies 0.33 eV lower in energy (0.71 eV in free energy) than the icosahedral isomer. This is an interesting result since both isomers are isoelectronic. In general, the icosahedral and cuboctahedral structures differ by their electron count with the latter being more electron-rich than the former. Similar results were also found for the related chloro- and iodo- species $[\text{Au}_{13}(\text{iPrIm})_8\text{X}_4]^+$ ($\text{X} = \text{Cl}, \text{I}$) (Figure

S1, Annex). With the bulkier ligand *N,N'*-ditertbutylimidazolidene (*t*BuIm), two more open-core structures are computed to be stable that can be viewed as highly distorted icosahedral and cuboctahedral arrangements, due to the excessive steric effect of *t*BuIm (Figure 1). The loss of compacity is accompanied by a reduction of the HOMO-LUMO gap (0.85 eV in the most stable cuboctahedral form), suggesting these species are unlikely to be isolated. By replacing the imidazolidine group of *i*PrIm with benzoimidazolidene, a larger sized ligand, *N,N'*-diisopropylbenzoimidazolidene (*i*PrBzIm), was designed, which led to solely the cuboctahedral structure (Figure 1). Surprisingly, replacing the isopropyl group of *i*PrBzIm with benzyl generates the *N,N'*-dibenzylbenzoimidazolidene (BzBzIm) ligand, which, despite its still more important size, led to only the icosahedral structure. These results suggest that both the size and shape of the NHC ligands play a crucial role for the icosahedral vs. cuboctahedral core arrangement of $[\text{Au}_{13}(\text{NHC})_8\text{Br}_4]^+$ species, where the use of *i*PrBzIm ensures an effective structural isomerism.

The experimentally characterized phosphine-protected $[\text{Au}_{13}(\text{PMePh}_2)_8\text{Br}_4]^+$ analogue³⁹ was also calculated for comparison (Figure S2, Annex). Its optimized structure conserves the experimentally observed icosahedral arrangement and no high-energy cuboctahedral isomer could be found. This gives confidence in the results which were found with the different NHC ligands. To evaluate the steric effect of the phosphine ligands, the larger triphenylphosphine ligand was considered (Figure S2, Annex). The optimized structure of $[\text{Au}_{13}(\text{PPh}_3)_8\text{Br}_4]^+$ is comparable to that of the icosahedral species $[\text{Au}_{13}(\text{PMePh}_2)_8\text{Br}_4]^+$. These results indicate that the Au_{13} core isomerization is more likely to occur within NHC-protected species. The Au_{13} core of $[\text{Au}_{13}(\text{PMePh}_2)_8\text{Br}_4]^+$ is more compact than that of the icosahedral form of $[\text{Au}_{13}(\text{iPrIm})_8\text{Br}_4]^+$ (ico), with a shorter average distance between the centered Au and the peripheral Au_{12} shell (Tables S1 and S2, Annex).

To further evaluate the influence of the bromide distribution on the Au_{13} core, a model cluster $[\text{Au}_{13}(\text{iPrBzIm})_8\text{Br}_4]^+$ derived from $[\text{Au}_{13}(\text{dppp})_4\text{Cl}_4]^+$,^{41,42} in which the four bromide positions describe a rectangle (ideal symmetry of the $\text{Au}_{13}\text{Br}_4$ skeleton: D_{2h}), was considered. Its optimized structure maintains the icosahedral arrangement (Figure S3, Annex), but lies 0.18 eV above the low-energy cuboctahedral isomer.

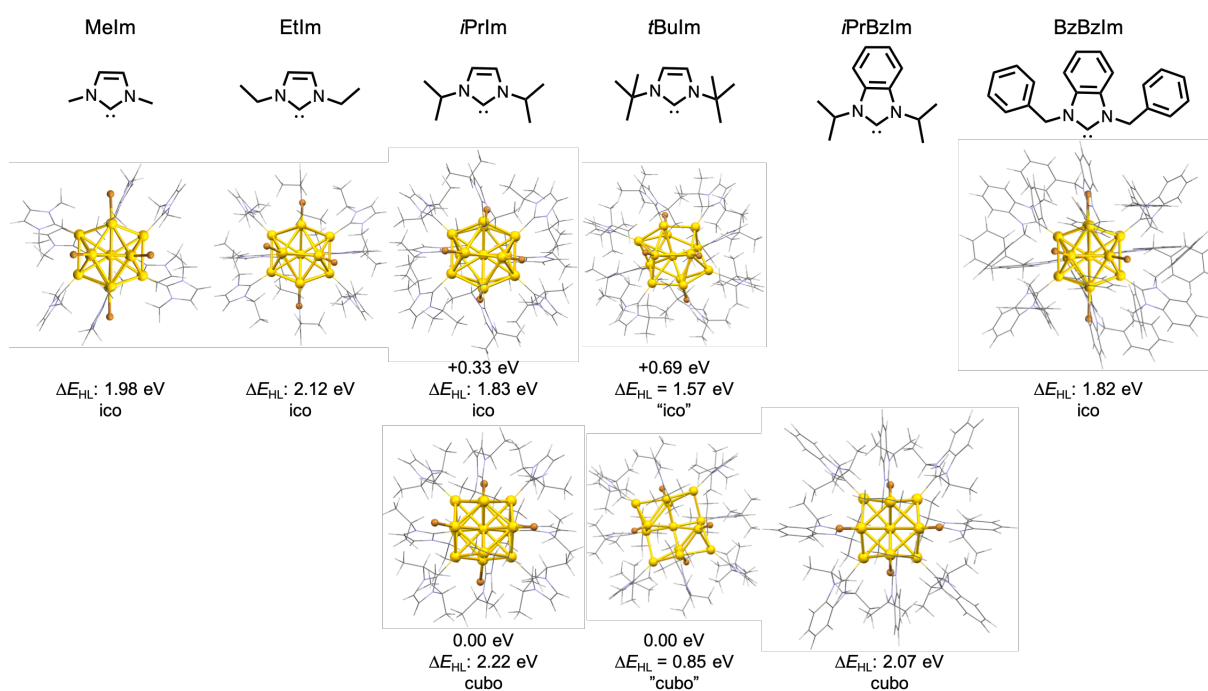


Figure 1. Optimized structures of the investigated $[\text{Au}_{13}(\text{NHC})_8\text{Br}_4]^+$ clusters, with relative energies between isomers. ΔE_{HL} is the HOMO-LUMO gap.

The Kohn-Sham molecular orbital diagrams of the two isomers of $[\text{Au}_{13}(\text{iPrIm})_8\text{Br}_4]^+$ are shown in Figure 2. They reflect an 8-electron *superatomic* configuration in both cases. In spite of the fact that the $\text{Au}_c\text{-Au}_p$ distances in the icosahedral isomer (av. 2.796 Å) are shorter than those in its cuboctahedral counterpart (av. 2.830 Å), a larger HOMO-LUMO gap is found for the cuboctahedral isomer (Table S1, Annex). This counterintuitive result, which is not reproduced in the corresponding bare $[\text{Au}_{13}]^{5+}$ fragments, originates from a ligand effect that tends to lower the energy of the LUMOs of the icosahedral isomer. This effect is to be related to a more important ligand steric congestion in the icosahedral form. Examination of the Au-C bond distances (Table S4, Annex) and of the corresponding Au and C natural atomic orbital (NAO) charges (Table S3, Annex) indicate similar metal-ligand bonding in both isomers of $[\text{Au}_{13}(\text{iPrIm})_8\text{Br}_4]^+$.

The optical properties of both phosphine- and NHC-protected Au_{13} *superatomic* clusters have been widely explored, owing to their potential use as optical devices.^{55,56} It is easily assumed that the tuned kernel structure of a ligated Au_{13} *superatomic* cluster will lead to tailored optical properties. The time-dependent (TD)-DFT simulated UV-Vis spectra of the $[\text{Au}_{13}(\text{NHC})_8\text{Br}_4]^+$ species, as well as that of the experimentally characterized $[\text{Au}_{13}(\text{PMePh}_2)_8\text{Br}_4]^+$ analogue, are gathered in Figure 3a. The shape of the calculated UV-Vis spectra of $[\text{Au}_{13}(\text{PMePh}_2)_8\text{Br}_4]^+$ is in a good agreement with the available experimental

spectra.^{39,40} The computed lowest absorption energy wavelength (427 nm) is close to the corresponding experimental value (440 nm). The absorption spectrum of its related NHC counterpart, $[\text{Au}_{13}(\text{iPrIm})_8\text{Br}_4]^+$ (ico), exhibits a red-shifted lowest energy band (518 nm) but a blue-shifted highest energy band, which is in line with our previous studies.²⁴ As expected, the $[\text{Au}_{13}(\text{iPrIm})_8\text{Br}_4]^+$ (cubo) isomer shows an intrinsically different UV-Vis spectrum. In comparison to its icosahedral isomer, its lowest energy band is blue-shifted to 425 nm, which is in agreement with its larger HOMO-LUMO gap. The absorption spectrum of the cuboctahedral $[\text{Au}_{13}(\text{iPrBzIm})_8\text{Br}_4]^+$ (cubo) shows similar features as those of $[\text{Au}_{13}(\text{iPrIm})_8\text{Br}_4]^+$ (cubo), suggesting that the differences in the UV-Vis spectra between these $[\text{Au}_{13}(\text{NHC})_8\text{Br}_4]^+$ series are mainly dominated by the Au_{13} core structure, and less affected by the nature of the protecting ligands.

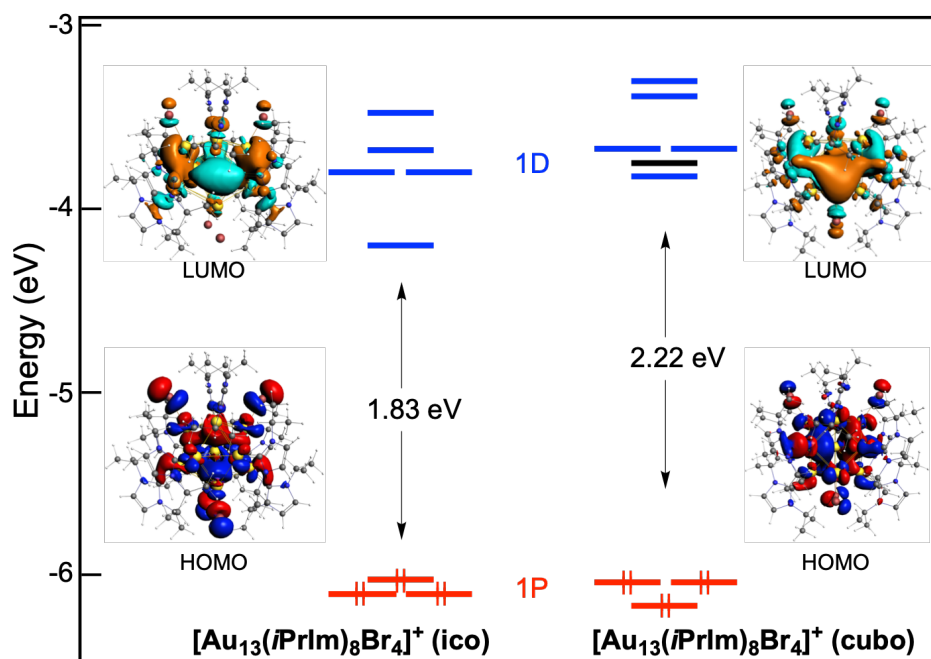


Figure 2. Kohn-Sham molecular orbital diagrams of the $[\text{Au}_{13}(\text{iPrIm})_8\text{Br}_4]^+$ (ico) and $[\text{Au}_{13}(\text{iPrIm})_8\text{Br}_4]^+$ (cubo) isomers. Red, blue and black stick correspond to *superatomic* 1P, 1D and 1F levels, respectively.

A more detailed analysis of the differences in the optical properties of the icosahedral and cuboctahedral forms of $[\text{Au}_{13}(\text{iPrIm})_8\text{Br}_4]^+$ can be traced from the MO diagrams shown in Figure 3b. In the case of the icosahedral isomer, the transitions associated to the main absorption band at 518 nm are from the three 1P levels to the $1\text{D}_{x^2-y^2}$ LUMO level. For the cuboctahedral isomer, the transitions associated to the main absorption band at 425 nm are from two of the

three 1P levels ($1P_x$ and $1P_y$) to the $1D_x^2 - y^2$ type LUMO, $1D_{yz}$ type LUMO+2 and $1D_{xz}$ type LUMO+3 levels.

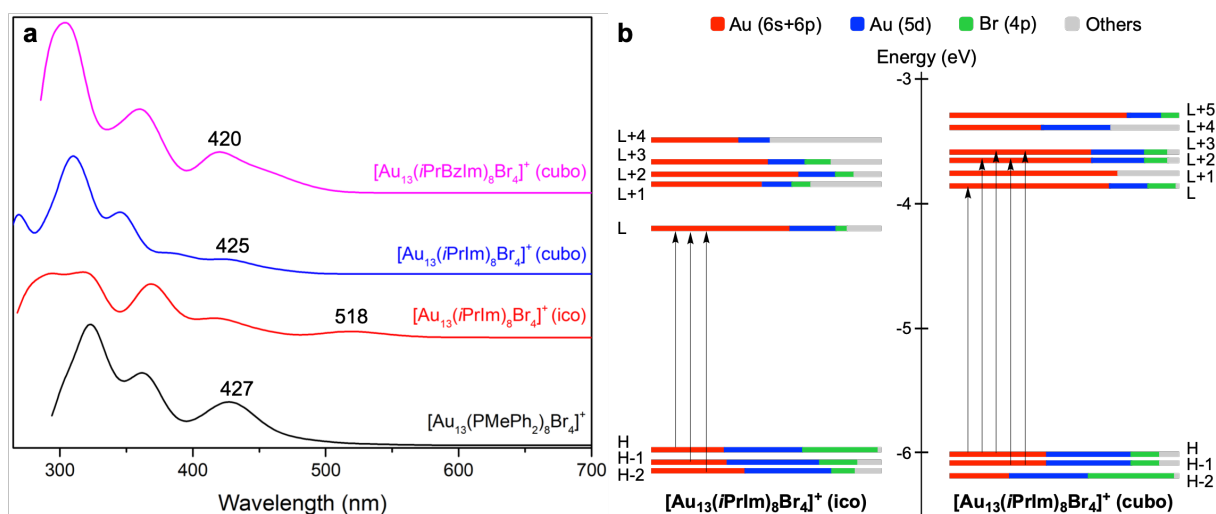


Figure 3. (a) TD-DFT simulated UV-Vis spectra of the $[\text{Au}_{13}(\text{NHC})_8\text{Br}_4]^+$ species as well as the experimentally characterized $[\text{Au}_{13}(\text{PMePh}_2)_8\text{Br}_4]^+$ analogous. (b) The frontier molecular orbitals composition and the transitions associated to the main absorption band for $[\text{Au}_{13}(\text{iPrIm})_8\text{Br}_4]^+$ (ico) and $[\text{Au}_{13}(\text{iPrIm})_8\text{Br}_4]^+$ (cubo) isomers.

Finally, owing to the relevant photoluminescent properties reported for the experimentally characterized NHC-protected AuNCs series²⁵⁻³⁸ ascribed to a phosphorescent emission originating from the $T_1 \rightarrow S_0$ decay, it is also interesting to see the difference in phosphorescent emissions induced by the core isomerization in the investigated $[\text{Au}_{13}(\text{iPrIm})_8\text{Br}_4]^+$ isomers. As for most of the known 8-electron *superatoms*, the T_1 states of both isomers can be viewed as the result of a HOMO ($1P$) \rightarrow LUMO ($1D$) excitation (see Figures S5 and S6, Annex). Unsurprisingly, their optimized structures are more expanded than their corresponding S_0 state, the effect being somewhat larger in the case of the cubo isomer (Table S4 and Figure S4, Annex). The phosphorescent emission wavelength of $[\text{Au}_{13}(\text{iPrIm})_8\text{Br}_4]^+$ (ico) is calculated at 1.14 eV (1087 nm), and the value of the $[\text{Au}_{13}(\text{iPrIm})_8\text{Br}_4]^+$ (cubo) isomer is 1.62 eV (765 nm). Such a blue shift of the emission wavelength from the *ico*-isomer to the *cubo*-isomer is in line with the increased HOMO-LUMO gap of the latter one. The low emission energy of the icosahedral form results mainly from the low energy of its S_0 LUMO, due to ligand mixing (see above). These results show that it is possible to design *superatomic* clusters with fine-tuned absorption and emission properties through ligand-induced core isomerization.

4.4 Conclusion

In summary, following previous reports on other systems,⁵⁷⁻⁶² we have shown that AuNC core isomerization can be ligand-controlled. Our DFT calculations on the hypothetical NHC-protected clusters $[\text{Au}_{13}(\text{NHC})_8\text{X}_4]^+$ ($X = \text{Cl}, \text{Br}, \text{I}$) show that isomerization can be achieved by simply tuning the size and shape of the NHC ligands. When the smaller MeIm and EtIm ligands are considered, the core structure conserves an icosahedral arrangement. With the medium-size *i*PrIm ligand, two isomers with both of icosahedral and (very rare) cuboctahedral core structures are found. Increasing the ligand size to $\text{NHC} = i\text{PrBzIm}$ leads to the sole cuboctahedral structure. The differences of two $[\text{Au}_{13}(i\text{PrIm})_8\text{Br}_4]^+$ (ico/cubo) isomers in their geometries, electronic structures and optical properties (including emissive properties) were further investigated. In comparison with the icosahedral $[\text{Au}_{13}(i\text{PrIm})_8\text{Br}_4]^+$ isomer, its cuboctahedral variation shows a larger HOMO-LUMO gap, inducing differences in their absorption and emission properties. Our results provide a rational approach to achieve the controllable core isomerization in the widely studied Au_{13} *superatomic* clusters which encourages further exploration on core isomerizations that could induce controlled differences in chemical and physical properties in ligated gold cluster chemistry. Beside of modulating properties through isomerization, the mechanistic isomer interchange pathways, that could be investigated by using variable temperature NMR studies,^{13,63,64} might also deserve interest. The above reported results strongly encourage further experimental work in this direction.

4.5 References

- 1 Jin, R.; Zeng, C.; Zhou, M.; Chen, Y. Atomically Precise Colloidal Metal Nanoclusters and Nanoparticles: Fundamentals and Opportunities. *Chem. Rev.* **2016**, *116*, 10346–10413.
- 2 Kang, X.; Li, Y.; Zhu, M.; Jin, R. Atomically Precise Alloy Nanoclusters: Syntheses, Structures, and Properties. *Chem. Soc. Rev.* **2020**, *49*, 6443–6514.
- 3 Zhou, M.; Jin, R. Optical Properties and Excited-State Dynamics of Atomically Precise Gold Nanoclusters. *Annu. Rev. Phys. Chem.* **2021**, *72*, 121–142.
- 4 Walter, M.; Akola, J.; Lopez-Acevedo, O.; Jadzinsky, P. D.; Calero, G.; Ackerson, C. J.; Whetten, R. L.; Grönbeck, H.; Häkkinen, H. A Unified View of Ligand-protected Gold Clusters as Superatom Complexes. *Proc. Natl. Acad. Sci. USA* **2008**, *105*, 9157–9162.
- 5 Häkkinen, H. Atomic and Electronic Structure of Gold Clusters: Understanding Flakes, Cages and Superatoms from Simple Concepts. *Chem. Soc. Rev.* **2008**, *37*, 1847–1859.

- 6 Jena, P.; Sun, Q. *Superatoms: Principles, Synthesis and Applications*, John Wiley & Sons Ltd, **2022**.
- 7 Knight, W. D.; Clemenger, K.; de Heer, W. A.; Saunders, W. A.; Chou, M. Y.; Cohen, M. L. Electronic Shell Structure and Abundances of Sodium Clusters. *Phys. Rev. Lett.* **1984**, *52*, 2141.
- 8 Briant, C. E.; Theobald, B. R.; White, J. W.; Bell, L. K.; Mingos, D. M. P.; Welch, A. J. Synthesis and X-ray Structural Characterization of The Centred Icosahedral Gold Cluster Compound $[\text{Au}_{13}(\text{PMe}_2\text{Ph})_{10}\text{Cl}_2](\text{PF}_6)_3$; The Realization of a Theoretical Prediction. *J. Chem. Soc. Chem. Commun.* **1981**, 201–202.
- 9 Zhu, M.; Aikens, C. M.; Hollander, F. J.; Schatz, G. C., Jin, R. Correlating the Crystal Structure of a Thiol-Protected Au_{25} Cluster and Optical Properties. *J. Am. Chem. Soc.* **2008**, *130*, 5883–5885.
- 10 Kang, X.; Chong, H., Zhu, M. $\text{Au}_{25}(\text{SR})_{18}$: The Captain of the Great Nanocluster Ship. *Nanoscale* **2018**, *10*, 10758–10834.
- 11 Mingos, D.M.P. Structural and Bonding Issues in Clusters and Nano-clusters. *Struct. Bond.* **2014**, *162*, 1–65.
- 12 Mingos, D.M.P. Structural and bonding patterns in gold clusters. *Dalton Trans.* **2015**, *44*, 6680–6695.
- 13 Mingos, D.M.P. Electron Counting Rules for Gold Clusters Which Are Stereochemically Non-rigid and Exhibit Skeletal Isomerism. *Struct. Bond.* **2021**, *188*, 1–67.
- 14 Chakrahari, K. K.; Liao, J.-H.; Kahlal, S.; Liu, Y.-C.; Chiang, M.-H.; Saillard, J. -Y.; Liu, C. W. $[\text{Cu}_{13}\{\text{S}_2\text{CN}^n\text{Bu}_2\}_6(\text{acetylide})_4]^+$: A Two-Electron Superatom. *Angew. Chem. Int. Ed.* **2016**, *128*, 14924–14928.
- 15 Silalahi, R.P.B.; Chakrahari, K.K.; Liao, J.-H.; Kahlal, S.; Liu, Y.-C.; Chiang, M. H.; Saillard, J.-Y.; Liu, C.W. Synthesis of Two-Electron Bimetallic Cu–Ag and Cu–Au Clusters by using $[\text{Cu}_{13}(\text{S}_2\text{CN}^n\text{Bu}_2)_6(\text{C}\equiv\text{CPh})_4]^+$ as a Template. *Chem. Asian J.* **2018**, *13*, 500–504.
- 16 Silalahi, R. P. B.; Chiu, T.-H.; Kao, J.-H.; Wu, C.-Y.; Yin, C.-W.; Liu, Y.-C.; Chen, Y. J.; Saillard, J.-Y.; Chiang, M.-H.; Liu, C. W. Synthesis and Luminescence Properties of Two-Electron Bimetallic Cu–Ag and Cu–Au Nanoclusters via Copper Hydride Precursors. *Inorg. Chem.* **2021**, *60*, 10799–10807.
- 17 Ito, S.; Takano, S.; Tsukuda, T. Alkynyl-Protected $\text{Au}_{22}(\text{C}\equiv\text{CR})_{18}$ Clusters Featuring New Interfacial Motifs and R-Dependent Photoluminescence. *J. Phys. Chem. Lett.* **2019**, *10*, 6892–6896.

- 18 Han, X.; Luan, X.; Su, H.; Li, J.; Yuan, S.; Lei, Z.; Pei, Y.; Wang, Q. M. Structure Determination of Alkynyl-Protected Gold Nanocluster $\text{Au}_{22}(\text{tBuC}\equiv\text{C})_{18}$ and Its Thermochemical Luminescence. *Angew. Chem. Int. Ed.* **2020**, *132*, 2329–2332.
- 19 Zeng, C.; Chen, Y.; Liu, C.; Nobusada, K.; Rosi, N.L.; Jin, R. Gold Tetrahedra Coil up: Kekulé-like and Double Helical Superstructures. *Sci. Adv.* **2015**, *1*, 1500425.
- 20 Kang, X.; Wei, X.; Jin, S.; Yuan, Q.; Luan, X.; Pei, Y.; Wang, S.; Zhu, M.; Jin, R. Rational Construction of a Library of M_{29} Nanoclusters from Monometallic to Tetrametallic. *Proc. Natl. Acad. Sci. USA* **2019**, *116*, 18834–18840.
- 21 Das, A.; Li, T.; Nobusada, K.; Zeng, C.; Rosi, N.L.; Jin, R. Nonsuperatomic $[\text{Au}_{23}(\text{SC}_6\text{H}_{11})_{16}]^-$ Nanocluster Featuring Bipyramidal Au_{15} Kernel and Trimeric $\text{Au}_3(\text{SR})_4$ Motif. *J. Am. Chem. Soc.* **2013**, *135*, 18264–18267.
- 22 Muñoz-Castro, A. Potential of N-heterocyclic Carbene Derivatives from $\text{Au}_{13}(\text{dppe})_5\text{Cl}_2$ Gold Superatoms. Evaluation of Electronic, Optical and Chiroptical Properties from Relativistic DFT. *Inorg. Chem. Front.* **2019**, *6*, 2349–2358.
- 23 Wei, J.; Halet, J.-F.; Kahlal, S.; Saillard, J.-Y.; Muñoz-Castro, A. Toward the Formation of N-Heterocyclic-Carbene-Protected Gold Clusters of Various Nuclearities. A Comparison with Their Phosphine-Protected Analogues from Density Functional Theory Calculations. *Inorg. Chem.* **2020**, *59*, 15240–15249.
- 24 Wei, J.; Kahlal, S.; Halet, J.-F.; Saillard, J.-Y.; Muñoz-Castro, A. Insight into the Stability and Electronic and Optical Properties of N-Heterocyclic Carbene Analogues of Halogen/Phosphine-Protected Au_{13} Superatomic Clusters. *J. Phys. Chem. A* **2022**, *126*, 536–545.
- 25 Ube, H.; Zhang, Q.; Shionoya, M. A Carbon-Centered Hexagold(I) Cluster Supported by N-Heterocyclic Carbene Ligands. *Organometallics* **2018**, *37*, 2007–2009.
- 26 Narouz, M. R.; Osten, K. M.; Unsworth, P. J.; Man, R. W. Y.; Salorinne, K.; Takano, S.; Tomihara, R.; Kaappa, S.; Malola, S.; Dinh, C.-T.; Padmos, J. D.; Ayoo, K.; Garrett, P. J.; Nambo, M.; Horton, J. H.; Sargent, E. H.; Häkkinen, H.; Tsukuda, T.; Crudden, C. M. N-heterocyclic Carbene-functionalized Magic-number Gold Nanoclusters. *Nat. Chem.* **2019**, *11*, 419–425.
- 27 Narouz, M. R.; Takano, S.; Lummis, P. A.; Levchenko, T. I.; Nazemi, A.; Kaappa, S.; Malola, S.; Yousefalizadeh, G.; Calhoun, L. A.; Stampelcoskie, K. G.; Häkkinen, H.; Tsukuda, T.; Crudden, C. M. Robust, Highly Luminescent Au_{13} Superatoms Protected by N-Heterocyclic Carbenes. *J. Am. Chem. Soc.* **2019**, *141*, 14997–15002.

- 28 Shen, H.; Deng, G.; Kaappa, S.; Tan, T.; Han, Y.; Malola, S.; Lin, S.; Teo, B. K.; Häkkinen, H.; Zheng, N. Highly Robust but Surface-Active: An N-Heterocyclic Carbene-Stabilized Au₂₅ Nanocluster. *Angew. Chem., Int. Ed.* **2019**, *58*, 17731–17735.
- 29 Shen, H.; Xiang, S.; Xu, Z.; Liu, C.; Li, X.; Sun, C.; Lin, S.; Teo, B. K.; Zheng, N. Superatomic Au₁₃ Clusters Ligated by Different N-heterocyclic Carbenes and Their Ligand-dependent Catalysis, Photoluminescence, and Proton Sensitivity. *Nano Res.* **2020**, *13*, 1908–1911.
- 30 Salorinne, K.; Man, R.W.; Lummis, P.A.; Hazer, M.S.A.; Malola, S.; Yim, J.C.H.; Veinot, A.J.; Zhou, W.; Häkkinen, H.; Nambo, M.; Crudden, C.M. Synthesis and Properties of an Au₆ Cluster Supported by a Mixed N-heterocyclic Carbene–thiolate Ligand. *Chem. Commun.* **2020**, *56*, 6102–6105.
- 31 Yi, H.; Osten, K. M.; Levchenko, T. I.; Veinot, A. J.; Aramaki, Y.; Ooi, T.; Nambo, M.; Crudden, C. M. Synthesis and Enantioseparation of Chiral Au₁₃ Nanoclusters Protected by bis-N-heterocyclic Carbene Ligands. *Chem. Sci.* **2021**, *12*, 10436–10440.
- 32 Lei, Z.; Pei, X.; Ube, H.; Shionoya, M. Reconstituting C-Centered Hexagold(I) Clusters with N-Heterocyclic Carbene Ligands. *Bull. Chem. Soc. Jpn.* **2021**, *94*, 1324–1330.
- 33 Hirano, K.; Takano, S.; Tsukuda, T. Ligand Effects on the Structures of [Au₂₃L₆(C≡CPh)₉]²⁺ (L = N-Heterocyclic Carbene vs Phosphine) with Au₁₇ Superatomic Cores. *J. Phys. Chem. C* **2021**, *125*, 9930–9936.
- 34 Luo, P.; Bai, S.; Wang, X.; Zhao, J.; Yan, Z.; Han, Y.; Zang, S.; Mak, T. C. W. Tuning the Magic Sizes and Optical Properties of Atomically Precise Bidentate N-Heterocyclic Carbene-Protected Gold Nanoclusters via Subtle Change of N-Substituents. *Adv. Opt. Mater.* **2021**, *9*, 2001936.
- 35 Pei, X.; Zhao, P.; Ube, H.; Lei, Z.; Nagata, K.; Ehara, M.; Shionoya, M. Asymmetric Twisting of C-Centered Octahedral Gold(I) Clusters by Chiral N-Heterocyclic Carbene Ligation. *J. Am. Chem. Soc.* **2022**, *144*, 2156–2163.
- 36 Man, R. W. Y.; Yi, H.; Malola, S.; Takano, S.; Tsukuda, T.; Häkkinen, H.; Nambo, M.; Crudden, C. M. Synthesis and Characterization of Enantiopure Chiral Bis NHC-Stabilized Edge-Shared Au₁₀ Nanocluster with Unique Prolate Shape. *J. Am. Chem. Soc.* **2022**, *144*, 2056–2061.
- 37 Shen, H.; Tian, G.; Xu, Z.; Wang, L.; Wu, Q.; Zhang, Y.; Teo, B. K.; Zheng, N. N-heterocyclic Carbene Coordinated Metal Nanoparticles and Nanoclusters. *Coord. Chem. Rev.* **2022**, *458*, 214425.

- 38 Hazer, M.S.A.; Malola, S.; Hakkinen, H. Isomer Dynamics of the $[\text{Au}_6(\text{NHC-S})_4]^{2+}$ Nanocluster. *Chem. Commun.* **2022**, *58*, 3218–3221.
- 39 Hall, K. P.; Mingos, D. M. P. Homo- and Heteronuclear Cluster Compounds of Gold. *Prog. Inorg. Chem.* **1984**, *32*, 237–325.
- 40 Copley, R. C. B.; Mingos, D. M. P. Synthesis and Characterization of The Centred Icosahedral Cluster Series $[\text{Au}_9\text{M}^{\text{IB}}_4\text{Cl}_4(\text{PMePh}_2)^8][\text{C}_2\text{B}_9\text{H}_{12}]$, Where $\text{M}^{\text{IB}} = \text{Au}, \text{Ag}$ or Cu . *J. Chem. Soc. Dalton Trans.* **1996**, *4*, 491–500.
- 41 Shichibu, Y.; Suzuki, K.; Konishi, K. Facile Synthesis and Optical Properties of Magic-number Au_{13} Clusters. *Nanoscale* **2012**, *4*, 4125–4129.
- 42 Yang, L.; Cheng, H.; Jiang, Y.; Huang, T.; Bao, J.; Sun, Z.; Jiang, Z.; Ma, J.; Sun, F.; Liu, Q.; Yao, T.; Deng, H.; Wang, S.; Zhu, M.; Wei, S. *In situ* Studies on Controlling An Atomically-accurate Formation Process of Gold Nanoclusters. *Nanoscale* **2015**, *7*, 14452–14459.
- 43 a) te Velde, G.; Bickelhaupt, F. M.; van Gisbergen, S. J. A.; Guerra, C. F.; Baerends, E. J.; Snijders, J. G.; Ziegler, T. Chemistry with ADF. *J. Comput. Chem.* **2001**, *22*, 931–967; b) ADF2016, SCM, Theoretical Chemistry, Vrije Universiteit: Amsterdam, The Netherlands; <http://www.scm.com>.
- 44 Becke, A. D. Density-functional exchange-energy approximation with correct asymptotic behavior. *Phys. Rev. A* **1988**, *38*, 3098–3100.
- 45 Perdew, J. P. Density-functional approximation for the correlation energy of the inhomogeneous electron gas. *Phys. Rev. B* **1986**, *33*, 8822–8824.
- 46 Lenthe, E. V.; Baerends, E. J. Optimized Slater-type basis sets for the elements 1-118. *J. Comput. Chem.* **2003**, *24*, 1142–1156.
- 47 van Lenthe, E.; Baerends, E. J.; Snijders, J. G. Relativistic total energy using regular approximations. *J. Chem. Phys.* **1994**, *101*, 9783–9792.
- 48 Grimme, S. Semiempirical GGA-type density functional constructed with a long-range dispersion correction. *J. Comput. Chem.* **2006**, *27*, 1787–1799.
- 49 Runge, E.; Gross, E. K. U. Density-functional theory for time-dependent systems. *Phys. Rev. Lett.* **1984**, *52*, 997–1000.
- 50 Frisch, M. J.; Trucks, G. W.; Schlegel, H. B.; Scuseria, G. E.; Robb, M. A.; Cheeseman, J. R.; Scalmani, G.; Barone, V.; Petersson, G. A.; Nakatsuji, H.; Li, X.; Caricato, M.; Marenich, A. V.; Bloino, J.; Janesko, B. G.; Gomperts, R.; Mennucci, B.; Hratchian, H. P.; Ortiz, J. V.; Izmaylov, A. F.; Sonnenberg, J. L.; Williams-Young, D.; Ding, F.; Lipparini, F.; Egidi, F.; Goings, J.; Peng, B.; Petrone, A.; Henderson, T.; Ranasinghe, D.; Zakrzewski,

- V. G.; Gao, J.; Rega, N.; Zheng, G.; Liang, W.; Hada, M.; Ehara, M.; Toyota, K.; Fukuda, R.; Hasegawa, J.; Ishida, M.; Nakajima, T.; Honda, Y.; Kitao, O.; Nakai, H.; Vreven, T.; Throssell, K.; Montgomery, J. A., Jr.; Peralta, J. E.; Ogliaro, F.; Bearpark, M. J.; Heyd, J. J.; Brothers, E. N.; Kudin, K. N.; Staroverov, V. N.; Keith, T. A.; Kobayashi, R.; Normand, J.; Raghavachari, K.; Rendell, A. P.; Burant, J. C.; Iyengar, S. S.; Tomasi, J.; Cossi, M.; Millam, J. M.; Klene, M.; Adamo, C.; Cammi, R.; Ochterski, J. W.; Martin, R. L.; Morokuma, K.; Farkas, O.; Foresman, J. B.; Fox, D. J. *Gaussian16*, Gaussian, Inc.: Wallingford, CT, **2016**.
- 51 Stephens, P. J.; Devlin, F. J.; Chabalowski, C. F.; Frisch, M. J. Ab Initio calculation of vibrational absorption and circular dichroism spectra using density functional force fields. *J. Phys. Chem.* **1994**, *98*, 11623–11626.
- 52 Weigend F.; Ahlrichs, R. Balanced basis sets of split valence, triple zeta valence and quadruple zeta valence quality for H to Rn: Design and assessment of accuracy. *Phys. Chem. Chem. Phys.* **2005**, *7*, 3297–3305.
- 53 Gorelsky, S. I. *SWizard* program. Revision 4.5, <http://www.sg-chem.net>.
- 54 Glendening, E. D.; Badenhoop, J. K.; Reed, A. E.; Carpenter, J. E.; Bohmann, J. A.; Morales, C. M.; Weinhold, F. NBO 6.0. Theoretical Chemistry Institute, University of Wisconsin (Madison, WI, 2001, <http://nbo6.chem.wisc.edu>).
- 55 Konishi, K. Phosphine-Coordinated Pure-Gold Clusters: Diverse Geometrical Structures and Unique Optical Properties/Responses. *Struct. Bond.* **2014**, *161*, 49–86.
- 56 Konishi, K.; Iwasaki, M.; Shichibu, Y. Phosphine-ligated gold clusters with core+ exo geometries: Unique properties and interactions at the ligand–cluster interface. *Acc. Chem. Res.* **2018**, *51*, 3125–3133.
- 57 Chen, Y.; Liu, C.; Tang, Q.; Zeng, C.; Higaki, T.; Das, A.; Jiang, D.; Rosi, N. L.; Jin, R. Isomerism in Au₂₈(SR)₂₀ nanocluster and stable structures. *J. Am. Chem. Soc.* **2016**, *138*, 1482–1485.
- 58 Kang, X.; Huang, L.; Liu, W.; Xiong, L.; Pei, Y.; Sun, Z.; Wang, S.; Wei, S.; Zhu, M. Reversible nanocluster structure transformation between face-centered cubic and icosahedral isomers. *Chem. Sci.* **2019**, *10*, 8685–8693.
- 59 Higaki, T.; Zeng, C.; Chen, Y.; Hussain, E.; Jin, R. Controlling the crystalline phases (FCC, HCP and BCC) of thiolate-protected gold nanoclusters by ligand-based strategies. *CrystEngComm* **2016**, *18*, 6979–6986.
- 60 Weerawardene, K. D. M.; Aikens, C. M. Effect of aliphatic versus aromatic ligands on the structure and optical absorption of Au₂₀(SR)₁₆. *J. Phys. Chem. C* **2016**, *120*, 8354–8363.

- 61 Tang, Q.; Ouyang, R.; Tian, Z.; Jiang, D. The ligand effect on the isomer stability of Au₂₄(SR)₂₀ clusters. *Nanoscale* **2015**, *7*, 2225–2229.
- 62 Nasaruddin, R. R.; Chen, T.; Yan, N.; Xie, J. Roles of thiolate ligands in the synthesis, properties and catalytic application of gold nanoclusters. *Coord. Chem. Rev.* **2018**, *368*, 60–79.
- 63 Briant, C. E.; Hall, K. P.; Mingos, D. M. P. Structural characterisation of two crystalline modifications of [Au₉{P(C₆H₄OMe-*p*)₃}₈](NO₃)₃: the first example of skeletal isomerism in metal cluster chemistry. *J. Chem. Soc., Chem. Commun.* **1984**, 290–291.
- 64 Mingos, D. M. P.; Watson, M. J. Recent developments in the homo- and hetero-metallic cluster compounds of gold. *Transition Met. Chem.* **1991**, *16*, 285–287.

4.6 Annex

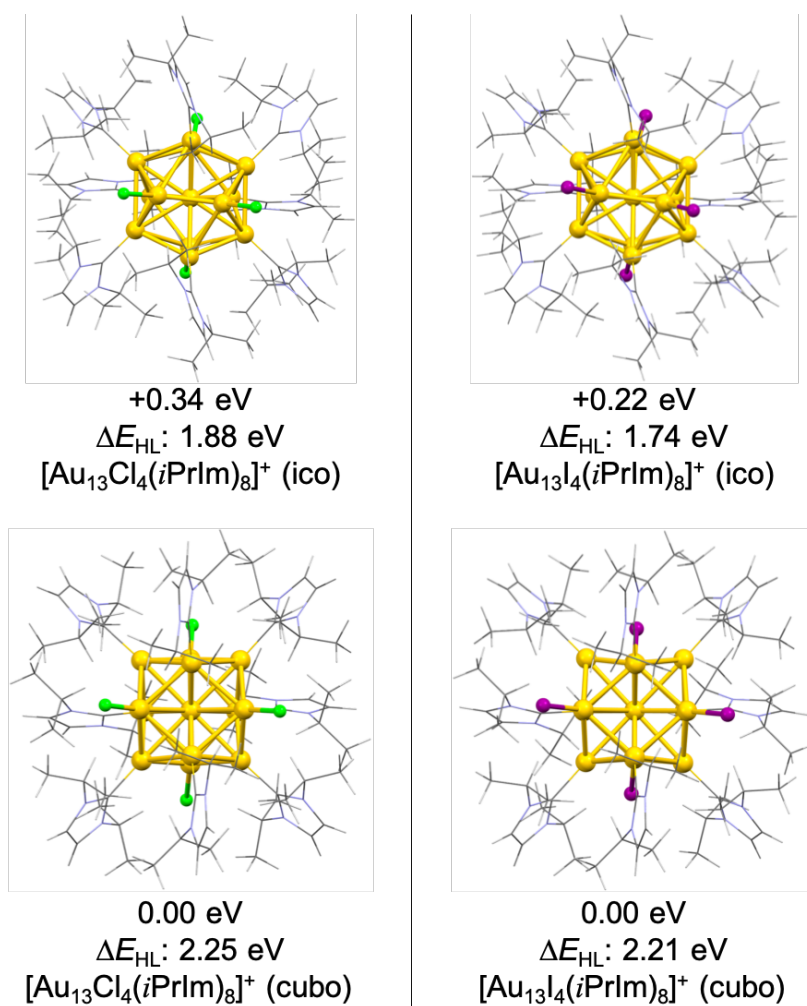


Figure S1. Optimized structure of $[\text{Au}_{13}\text{X}_4(\text{iPrIm})_8]^+$ (X = Cl, I) species.

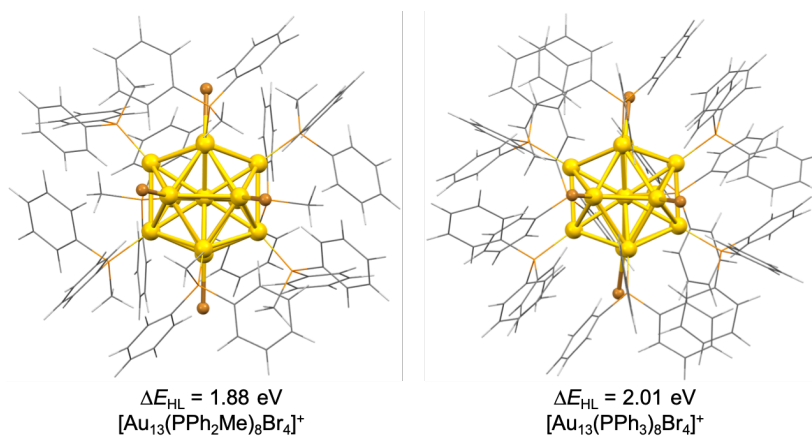


Figure S2. Optimized structure of $[\text{Au}_{13}(\text{PR})_8\text{Br}_4]^+$ (R = Ph₂Me, Ph₃) species.

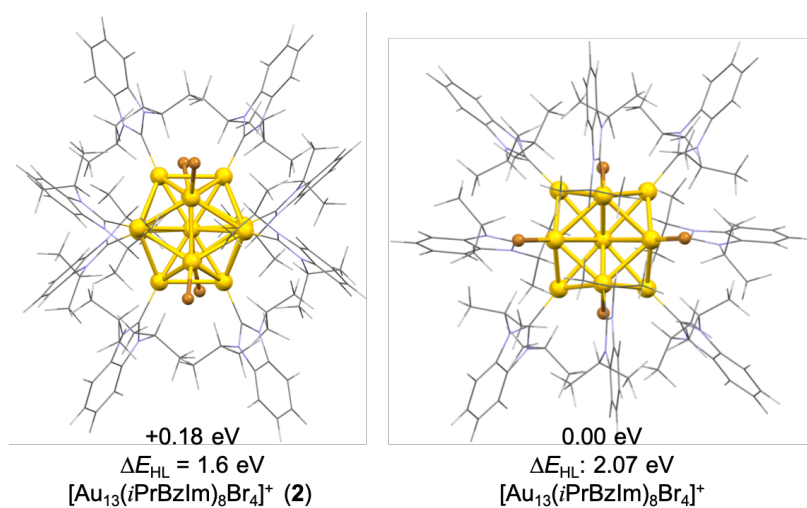


Figure S3. Optimized structure of [Au₁₃(iPrIm)₈Br₄]⁺ (**2**) and [Au₁₃(iPrIm)₈Br₄]⁺.

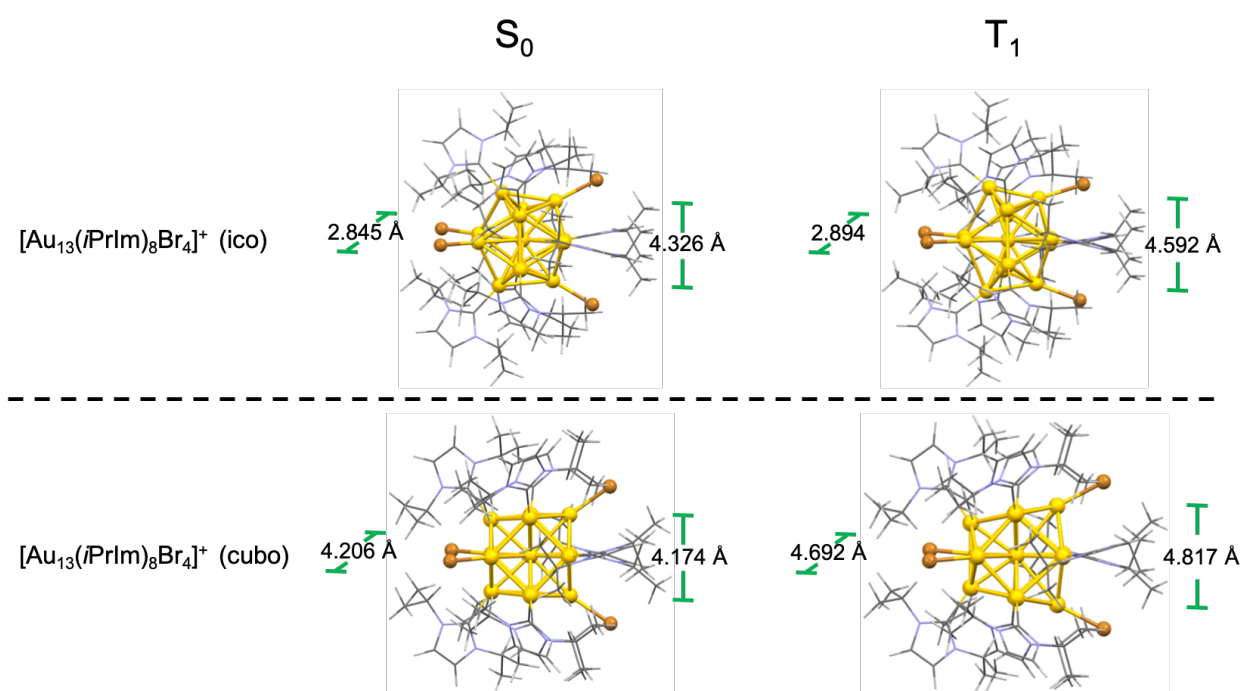


Figure S4. Optimized structures of the singlet ground state (S₀) and triplet excited state (T₁) of [Au₁₃(iPrIm)₈Br₄]⁺ (ico/cubo) isomers. The Br...Br separations are indicated for information.

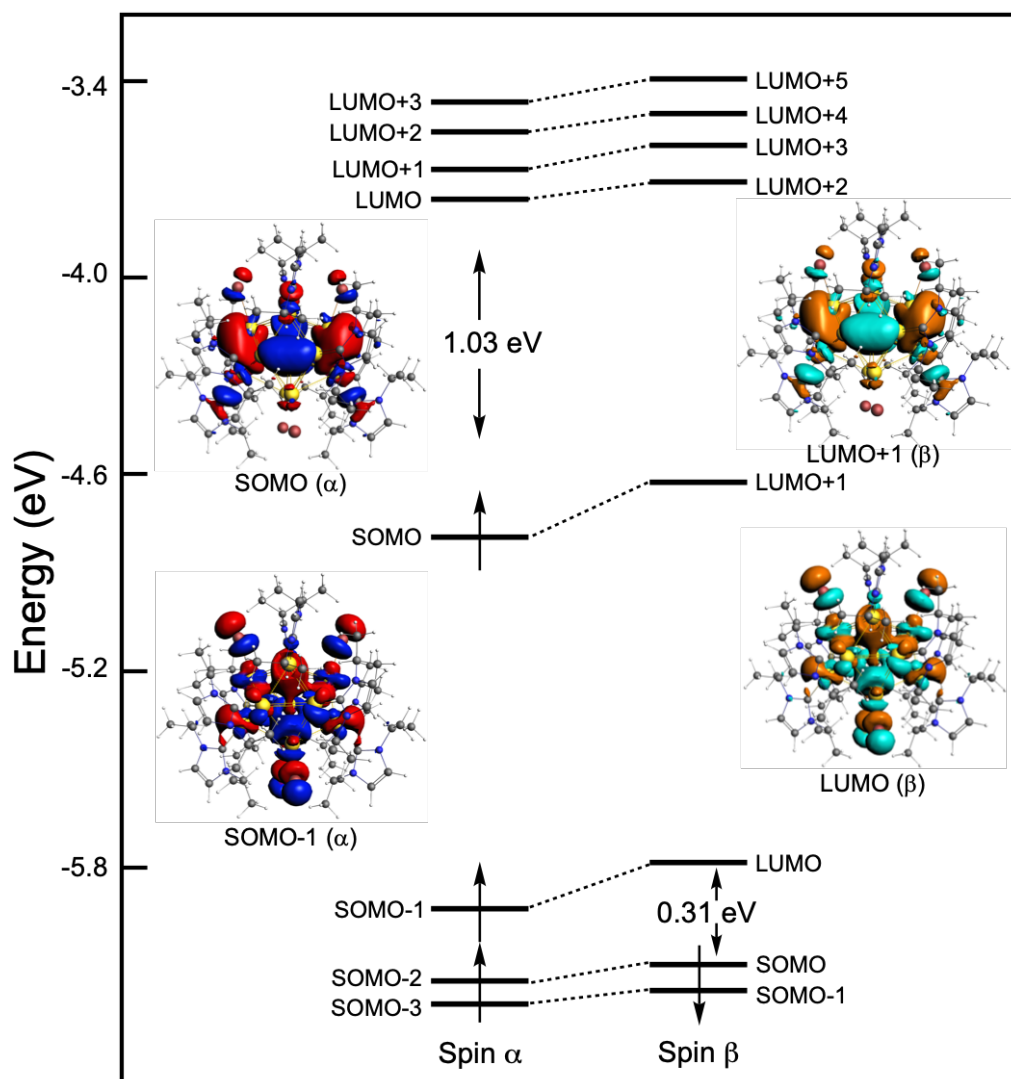


Figure S5. Kohn-Sham frontier orbital diagram of the T_1 state of $[\text{Au}_{13}(\text{iPrIm})_8\text{Br}_4]^+$ (ico).

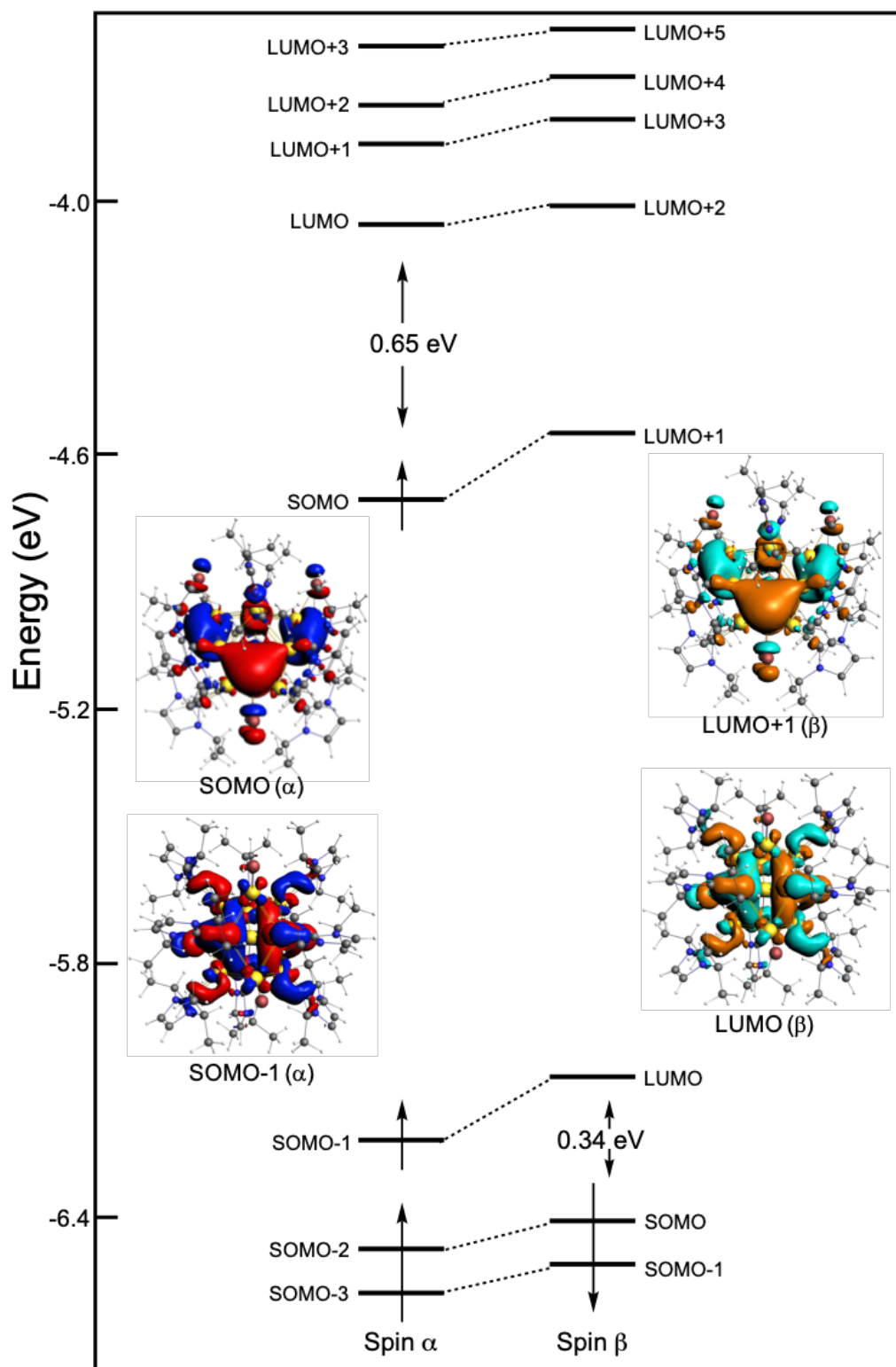


Figure S6. Kohn-Sham frontier orbital diagram of the T_1 state of $[\text{Au}_{13}(\text{iPrIm})_8\text{Br}_4]^+$ (cubo).

Table S1. Relevant computed data for $[\text{Au}_{13}(\text{NHC})_8\text{Br}_4]^+$ species. Au_c and Au_p represent central Au and peripheral Au atoms, respectively.

		$[\text{Au}_{13}(\text{MeIm})_8\text{Br}_4]^+$	$[\text{Au}_{13}(\text{EtIm})_8\text{Br}_4]^+$	$[\text{Au}_{13}(i\text{PrIm})_8\text{Br}_4]^+$ (ico)	$[\text{Au}_{13}(i\text{PrIm})_8\text{Br}_4]^+$ (cubo)	$[\text{Au}_{13}(i\text{PrBzIm})_8\text{Br}_4]^+$ (cubo)	$[\text{Au}_{13}(\text{BzBzIm})_8\text{Br}_4]^+$
ΔE_{HL} (eV)		1.98	2.12	1.83	2.22	2.07	1.82
Average Distance (Å)	$\text{Au}_c\text{--Au}_p$	2.771	2.779	2.796	2.830	2.826	2.787
	$\text{Au}_p\text{--Au}_p$	2.972	2.924	2.949	2.832	2.832	2.930
	Au--C	2.028	2.033	2.034	2.032	2.030	2.034
	Au--Br	2.508	2.513	2.532	2.545	2.522	2.514

Table S2. Relevant computed data for $[\text{Au}_{13}(\text{PR})_8\text{Br}_4]^+$ ($\text{R} = \text{PPh}_2\text{Me}, \text{PPh}_3$) species. Au_c and Au_p represent central Au and peripheral Au atoms, respectively.

		$[\text{Au}_{13}(\text{PPh}_2\text{Me})_8\text{Br}_4]^+$	$[\text{Au}_{13}(\text{PPh}_3)_8\text{Br}_4]^+$
ΔE_{HL} (eV)		1.88	2.01
Average Distance (Å)	$\text{Au}_c\text{--Au}_p$	2.763	2.778
	$\text{Au}_p\text{--Au}_p$	2.906	2.922
	Au--P	2.270	2.289
	Au--Br	2.497	2.500

Table S3. Natural atomic orbital (NAO) charges of $[\text{Au}_{13}(\text{PPh}_2\text{Me})_8\text{Br}_4]^+$ and the $[\text{Au}_{13}(\text{NHC})_8\text{Br}_4]^+$ species.

		$[\text{Au}_{13}(\text{PPh}_2\text{Me})_8\text{Br}_4]^+$	$[\text{Au}_{13}(i\text{PrIm})_8\text{Br}_4]^+$ (ico)	$[\text{Au}_{13}(i\text{PrIm})_8\text{Br}_4]^+$ (cubo)	$[\text{Au}_{13}(i\text{PrBzIm})_8\text{Br}_4]^+$ (cubo)
NAO Charge (Average)	Au_c	-0.43	-0.41	-0.34	-0.36
	$\text{Au}_p(\text{P})/\text{Au}_p(\text{C})$	+0.17	+0.27	+0.28	+0.28
	$\text{Au}_p(\text{Br})$	+0.15	+0.13	+0.11	+0.13
	$\text{P}(\text{Phosphine})/\text{C}(\text{NHC})$	+0.88	+0.06	+0.05	+0.10
	Br	-0.62	-0.66	-0.65	-0.64

Table S4. Relevant computed data for the S₀ and T₁ states of the [Au₁₃(*i*PrIm)₈Br₄]⁺ (ico/cubo) isomers. Au_c and Au_p are the central Au and peripheral Au atoms, respectively.

		[Au ₁₃ (<i>i</i> PrIm) ₈ Br ₄] ⁺ (ico)		[Au ₁₃ (<i>i</i> PrIm) ₈ Br ₄] ⁺ (cubo)	
		S ₀	T ₁	S ₀	T ₁
Average Distance (Å)	Au _c -Au _p	2.796	2.816	2.830	2.851
	Au _p -Au _p	2.949	2.970	2.832	2.893
	Au-C	2.034	2.045	2.032	2.042
	Au-Br	2.532	2.522	2.545	2.568

Chapter 5

On Heteronuclear Isoelectronic Alternatives to [Au₁₃(dppe)₅Cl₂]³⁺: Electronic and Optical Properties of the 18-electron Os@[Au₁₂(dppe)₅Cl₂] Cluster from DFT Computations

5.1 Introduction

The fastly developing chemistry of gold nanoclusters (AuNCs) is currently of huge topical interest owing to their many potential interdisciplinary applications,¹⁻²⁰ Numerous theoretical and experimental research efforts have contributed to the rationalization of their structure and the viability of novel noble-metal nanostructures.²¹⁻³⁸ The most recent developments of this field encompass the design of doped AuNCs,³⁹⁻⁴⁸ an efficient strategy to tune the properties of the parent homonuclear clusters.^{24,25,44,49-57}

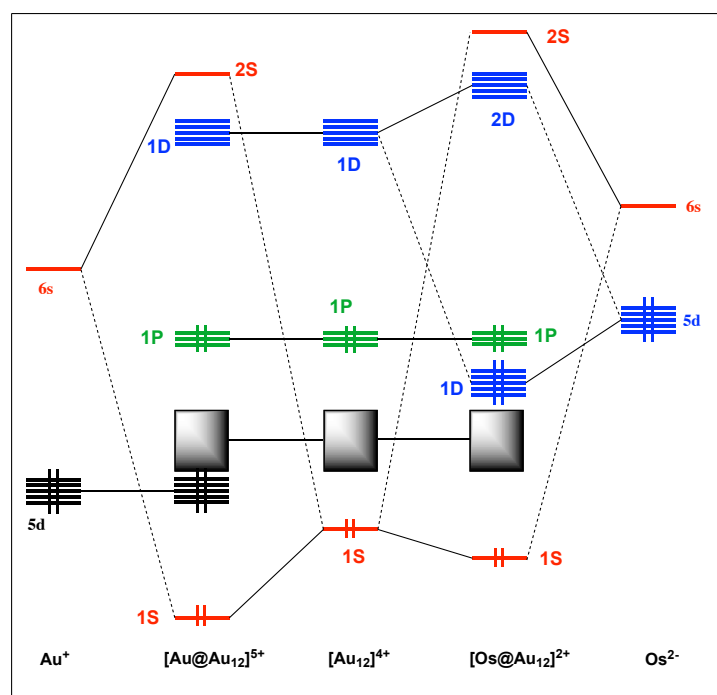
AuNCs consist of atomically precise metallic cores further passivated by a protecting shell of ligand, to which in some cases are added additional Au(I) centers.⁵⁸⁻⁶² The Au₁₃ icosahedron is one of their most recognizable motifs as earlier characterized in the very first phosphine derivatives [Au₁₃(PMe₂Ph)₁₀Cl₂]³⁺ by Mingos and coworkers⁶³ and later in [Au₁₃(dppe)₅Cl₂]³⁺ (**1**),^{64,65} precluding the most recent extensive research on [Au₂₅(SR)₁₈]⁻,⁶⁶⁻⁷⁰ which have been extended to other related clusters.^{53,71-75}

In the last decade compound **1** has been further explored revealing its interesting optical and chiroptical properties as investigated separately by Konishi⁶⁴ and Li,^{64,65} showing an enhanced behavior compared to other phosphine-protected clusters.⁷⁶⁻⁷⁸ In addition, the high quantum yield of the lowest triplet state (T₁) leads to promising singlet-oxygen (¹O₂) photogeneration capabilities in comparison to organic dyes such as by anthracene, as well as related Au₂₅(SR)₁₈ and Au₃₈(SR)₂₄ clusters.^{79,80}

Within the *superatom* model,^{53,58,74} **1** is described as a 8-cluster-electron (8-*ce*) species. Indeed, only the electrons significantly involved in metal-metal bonding, that is the 6s(Au) valence electrons of the [Au₁₃]⁵⁺ core, are included in the *superatom ce* count. The 5d(Au) electrons are not considered for they have been recognized a long time ago to play a negligible role.⁸¹ The highest occupied orbitals of **1** correspond to the 1P shell^{58,82,83} and the lowest unoccupied levels to the 1D manifold. The 1P→1D electronic transitions account for the character of the low-energy UV/Vis spectrum and the related luminescent properties. In this context, the exploration of 18-*ce* related counterparts allows further understanding of the role of electron counts in the optical properties, based on heteroatom doping of the cluster-core,^{24,84-88} as earlier theoretically proposed and experimentally demonstrated by the bare W@Au₁₂ cluster by Pyykkö and Li, respectively.^{89,90}

A proper candidate is given by doping the parent cluster **1** by Os resulting in a neutral 18-*ce* $[\text{OsAu}_{12}(\text{dppe})_5\text{Cl}_2]$ (**2**) species (assuming that Os lies at the cluster center, see below). It is important at this stage to note that although $[\text{Au}_{13}(\text{dppe})_5\text{Cl}_2]^{3+}$ (**1**) and 18-*ce* (**2**) are isoelectronic in terms of their total and valence number of electrons, within the *superatom* model, we suggest considering them as respectively 8-*ce* and 18-*ce* species. This difference originates in the fact that the fully occupied 5*d*(Au) orbitals are low-lying and contracted, whereas the 5*d*(Os) ones are higher in energy and more diffuse. Therefore, contrarily to the former, the latter can participate to cluster bonding. This is why we include the 5*d* electrons of Os into the *ce* count of (**1**), whereas in (**2**) we do not include that of the encapsulated Au. Likewise, the naked W@Au_{12} cluster is also commonly considered as a 18-*ce* species.^{89,90} We thus consider **2** as having the $1\text{S}^2 1\text{P}^6 1\text{D}^{10}$ configuration, with 1D HOMOs (or near HOMOs) of large 5*d*(Os) nature, giving rise to optical properties different from that of **1**, whose configuration is $1\text{S}^2 1\text{P}^6$. These different situations are sketched in Scheme 1, where the *superatomic* electronic structures of M@Au_{12} (M = Au, Os) cores are shown on the basis of the interaction of M with its M_{12} icosahedral cage.

Obviously, the two situations crudely illustrated in Scheme 1 should be considered as two limit cases and there should be a gradual transition between them, *i.e.* when going from W to Au. Thus, the description of a $[\text{M@Au}_{12}]^{n+}$ (M = W, Au; n = 0, +5) cluster core as a 18-*ce* rather than a 8-*ce* species (or conversely) is somewhat formal. From the relativistic density functional (DFT) calculations described below, we suggest placing the formal 18-*ce*/8-*ce* borderline on the right side of Os. In this chapter, the stability and bonding patterns of the hypothetical cluster **2** are explored and its electronic, optical, chiroptical and potential luminescent properties are analysed, with systematic comparison with its homonuclear parent **1**. The isoelectronic clusters $[\text{MAu}_{12}(\text{dppe})_5\text{Cl}_2]$ (M = Fe, Ru) are also discussed. As we were working on these hypothetical species, the isolation and full characterization of $[\text{IrAu}_{12}(\text{dppe})_5\text{Cl}_2]^+$ and $[\text{PtAu}_{12}(\text{dppe})_5\text{Cl}_2]^{2+}$ were published by Tsukuda and coworkers,⁹¹ thus supporting the fact that the hypothetical title Os species is feasible.



Scheme 1. Interaction of a formally d^{10} encapsulated metal atom M with an icosahedral $[\text{Au}_{12}]^{4+}$ icosahedral cage. Left: M = gold; right: M = osmium. Note that the $[\text{Os@Au}_{12}]^{2+}$ case is similar to that of $[\text{W@Au}_{12}]$.^{81,82}

5.2 Computational Details

Calculations were carried within the Density Functional Theory⁹² (DFT) formalism using the ADF2019 code.⁹³ Scalar relativistic corrections via the ZORA Hamiltonian were considered⁹⁴ together with the generalized gradient approximation (GGA) Perdew-Burke-Ernzerhof (PBE) exchange-correlation (xc) functional,^{95,96} owing to its reliable performance at reasonable computational cost on AuNCs.^{83,97–100,89} Dispersion forces were considered via the empirical pairwise corrections of Grimme (DFT-D3).¹⁰¹ Basis sets of triple-zeta Slater quality, plus two polarization functions (STO-TZ2P) were employed for valence electrons. The frozen core approximation was applied to the $[1s^2-4f^{14}]$ shells for Au and Os, $[1s^2-4p^6]$ Ru, $[1s^2-3p^6]$ Fe, $[1s^2]$ for C, and $[1s^2-2s^2]$ for P and Cl, leaving the remaining electrons to be treated variationally. Ground and excited states geometry optimizations were performed without any symmetry constraint, via the analytical energy gradient method implemented by Versluis and Ziegler,¹⁰² with energy convergence criteria set at 10^{-4} Hartree, gradient convergence at 10^{-3} Hartree/Å and radial convergence of 10^{-2} Å. Electronic excitation energies were calculated via time-dependent-DFT (TD-DFT) considering the van Leeuwen–Baerends (LB94) xc-functional as in previous similar studies.^{46,100,103} The current approach was tested on the description of

dual photoluminescence properties of a ligand-supported hexanuclear Au(I) framework, with good agreement to experimental emission and absorption energies.¹⁰⁴

5.3 Results and Discussion

The question of the location of heteroatoms in doped group 11 metal clusters has been first addressed in 1989.¹⁰⁵ In the case of **1**, doping it by formally replacing one Au atom by Os (keeping constant the total electron number) results in three possible configurations for **2**. One with Os on the central site (isomer **I**), another one with Os bonded to a dppe ligand (isomer **II**) and the third one when bonded to chlorine (isomer **III**). The resulting optimized structures (Figure 1) indicate a large preference for isomer **I**, being largely favored by +99.1 and +101.0 kcal.mol⁻¹ with respect to isomers **II** and **III**, respectively. This is consistent with the fact that only isomer **I** can be described as a *superatom* with *18-ce* count (see above). This observation agrees with the recently published structures of the closely related compound [IrAu₁₂(dppe)₅Cl₂]⁺.⁹¹ Thus, hereafter, we refer our results to isomer **I** for **2**. The relaxed structures of **1** and **2** exhibit similar M_(center)-Au_(ligand) distances of 2.622 and 2.612 Å, respectively, which compares well to experimental data available (2.552 Å) for **1** (Table 1).⁶⁴ The calculated M_(center)-Au_(Cl) distance in **2** (2.596 Å) is slightly enlarged in comparison to those in **1** (from 2.548 to 2.596 Å). Similar Au-Cl separations (from 2.201 to 2.288 Å) are computed for **1** and **2**, denoting that the Au₁₂Cl₂ cage remains similar upon osmium doping.

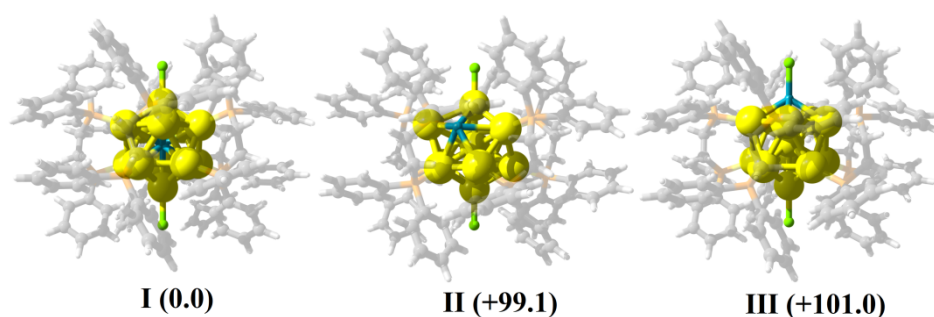


Figure 1. Relaxed structures of the three isomers **I-III** of [OsAu₁₂Cl₂(dppe)₅] (**2**). Relative energies are given in brackets (kcal.mol⁻¹). Os atom is in blue.

The electronic structures of **1** and **2** are illustrated in Figure 2. The occupied 1D shell of **2** is intercalated between the 1P_{x,y} HOMOs and 1P_z *superatomic* orbitals (shell splitting allowed by symmetry). In average, the 1D shell of **2** is composed of 52% 5d(Os) character mixed in a bonding way with 21% 6s/6p(Au), and 27% from protecting ligands. Such an occupied

$5d(M_{\text{center}})$ shell does also exist in **1**. However, these low-lying combinations are fully non-bonding, with no significant $6s/6p(\text{Au}_{\text{ico}})$ admixture and thus cannot be considered as the *superatomic* 1D shell. Rather, the true 1D orbitals of **1** are its five lowest vacant ones, which are of dominant $6s/6p(\text{Au})$ composition, with $\text{Au}_{\text{center}}-\text{Au}_{\text{ico}}$ bonding character (Figure 2). On the other hand, the lowest vacant levels of **2** are not of *superatomic* character, but π^* -ligand centered orbitals.

Table 1. Structural parameters for $[\text{M}@\text{Au}_{12}(\text{dppe})\text{Cl}_2]^{n+}$ species ($\text{M} = \text{Au}, n = 3; \text{M} = \text{Os}, \text{Ru}, \text{Fe}, n = 0$).

	Exp Au ^a	Au (1)	Os (2)	Ru	Fe
$\text{M}_{\text{(center)}}-\text{Au}_{\text{(ligand)}}$	2.552	2.622	2.612	2.623	2.624
$\text{M}_{\text{(center)}}-\text{Au}_{\text{(Cl)}}$	2.486	2.548	2.596	2.608	2.483
Au-Cl	2.169	2.201	2.288	2.307	2.331

^aExperimental data from ref.⁶⁴

The singlet state of **2** is largely favored in comparison to the triplet and quintet states (by 53.2 kcal.mol⁻¹ and 91.9 kcal.mol⁻¹, respectively). Consistently, its HOMO-LUMO is large (1.53 eV) and similar to that of **1** (1.96 eV). The $[\text{Ru}@\text{Au}_{12}(\text{dppe})_5\text{Cl}_2]$ and $[\text{Fe}@\text{Au}_{12}(\text{dppe})_5\text{Cl}_2]$ relatives have also a substantial preference for isomer **I** (+88.7 and +128.4 kcal.mol⁻¹ from the next isomer, respectively, see Annex). They also have significant HOMO-LUMO gaps (1.52 and 1.09 eV, respectively) and show similar frontier orbitals.

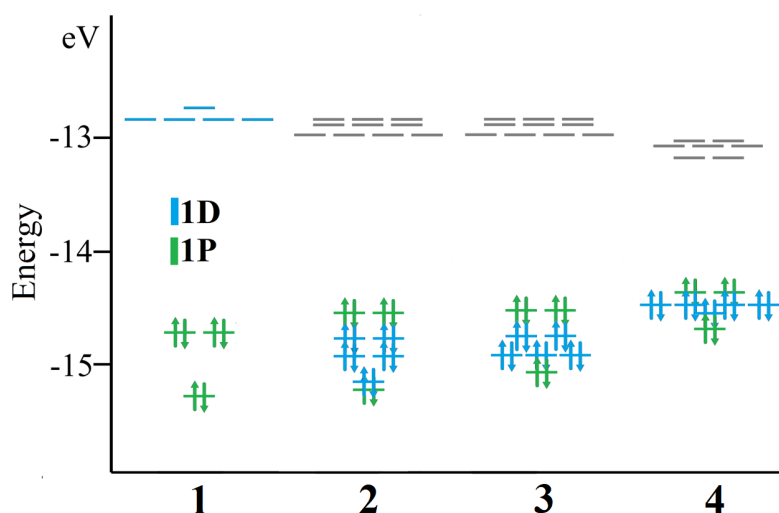


Figure 2. Electronic structure of $[\text{Au}_{13}\text{Cl}_2(\text{dppe})_5]^{3+}$ (**1**), $[\text{Os}@\text{Au}_{12}\text{Cl}_2(\text{dppe})_5]$ (**2**), $[\text{Ru}@\text{Au}_{12}\text{Cl}_2(\text{dppe})_5]$ (**3**) and $[\text{Fe}@\text{Au}_{12}\text{Cl}_2(\text{dppe})_5]$ (**4**), showing 1P and 1D *superatomic* shells.

In order to evaluate the variation of the interaction between the dppe ligands and the rest of the molecule, we computed the overall interaction energy (ΔE_{int}) between the [(dppe)₅] phosphine shell and the [M@Au₁₂Cl₂]ⁿ⁺ (M = Au, n = 3; M = Os, n = 0) fragment. It amounts to $-160.7 \text{ kcal.mol}^{-1}$ for **1** and $-96.5 \text{ kcal.mol}^{-1}$ for **2** (per dppe unit). Values similar to **2** were found for the M = Ru and Fe relatives, i.e., -96.0 and $-91.7 \text{ kcal.mol}^{-1}$, respectively. The origin of the difference in interaction energy ΔE_{int} between the homonuclear Au cluster and its heteronuclear congeners can be interpreted within the Energy Decomposition Analysis (EDA) framework given by Ziegler and Rauk,^{106–108} according to:

$$\Delta E_{\text{int}} = \Delta E_{\text{Pauli}} + \Delta E_{\text{elstat}} + \Delta E_{\text{orb}} + \Delta E_{\text{disp}}$$

leading to different chemically meaningful quantities accounting for the destabilizing character of the interaction given by the repulsion between occupied orbitals (ΔE_{Pauli}), and for the stabilizing electrostatic, covalent and dispersion (charge transfer) characters, ΔE_{elstat} , ΔE_{orb} and ΔE_{disp} . The character of the interaction is mainly electrostatic, similar to other phosphine protected gold clusters.¹⁰⁹

The EDA analysis shows that the stabilizing ligand-core interaction, involving one dppe ligand from [Au₁₃Cl₂(dppe)₅]³⁺ to [Os@Au₁₂(dppe)₅Cl₂], varies mostly by the decrease in the orbital interaction term (ΔE_{orb}) from -190.4 to $-146.6 \text{ kcal.mol}^{-1}$, retaining a smaller variation from the electrostatic character of the interaction (-336.9 to $-343.5 \text{ kcal.mol}^{-1}$, respectively), which accounts for the variation in the ligand-core interaction. In the Ru and Fe counterparts, a similar variation is found with ΔE_{orb} amounting to -144.0 and $-144.8 \text{ kcal.mol}^{-1}$, respectively. The proposed 18-*ce* phosphine-protected clusters are thus structurally related to the parent [Au₁₃Cl₂(dppe)₅]³⁺, with weaker ligand-core interaction energy indicating the smaller role of the protecting ligands to achieve stable species with sizable HOMO-LUMO gap, owing to the extra 1D¹⁰ electrons in the cluster core of the former. Analysis of the overall interaction energy of the [M@Au₁₂]ⁿ⁺ metallic core with the whole protecting ligands shell leads to a similar trend (see Annex).

Optical properties were also addressed in order to investigate the expected differences between **1** (8-*ce*) and **2** (18-*ce*). The experimental UV/Vis spectrum of **1** (Figure 3) features a moderate shoulder between 620 and 520 nm, followed by a more intense signal at 488 nm.⁶⁴ The calculated spectrum of **1** exhibits peaks at 590 and 473 nm accounting nicely for the experimental observation,¹¹⁰ with $1P_{x,y} \rightarrow \pi^*$ -ligand and $1P_z \rightarrow 1D$ transition character, respectively. In the case of **2**, several peaks appear in the calculated spectrum (Figure 3). That of lowest energy (801 nm) is associated with a $1P_{x,y} \rightarrow \pi^*$ -ligand transition. It is substantially

red-shifted with respect to the parent cluster **1** (590 nm). The next peak manifold is composed of five signals at 672, 642, 603, 577, and 541 nm, accounting for different $1D \rightarrow \pi^*$ -ligand transitions, which are not found in the 8-*ce* parent **1**. Another peak at 499 nm is found of mixed $1D \rightarrow \pi^*$ -ligand and $1P_z \rightarrow \pi^*$ -ligand character, resembling the peak of **1** at 473 nm (488 nm experimentally⁶⁴). Thus, the existence of an occupied $1D$ shell in **2** gives rise to a manifold peak pattern expected from the UV/Vis spectrum characterized mainly by metal $\rightarrow \pi^*$ -ligand transitions, which are desired for photo-induced electron injection over surfaces from anchored gold nanoclusters.¹¹¹

Table 2. Energy decomposition analysis between the [(dppe)₅] phosphine shell and the [M@Au₁₂Cl₂]ⁿ⁺ (M = Au, *n* = 3; M = Os, Ru, Fe, *n* = 0). Values in kcal.mol⁻¹.

	1 (Au)		2 (Os)		3 (Ru)		4 (Fe)	
ΔE_{Pauli}	390.2		416.5		400.5		389.1	
ΔE_{elstat}	-336.9	61.1%	-343.1	66.9%	-329.5	66.4%	-311.9	64.9%
ΔE_{orb}	-190.4	34.6%	-146.6	28.6%	-144.0	29.0%	-144.8	30.1%
ΔE_{disp}	-23.6	4.3%	-23.3	4.5%	-23.0	4.6%	-24.1	5.0%
ΔE_{int}	-160.7		-96.5		-96.0		-91.7	

A quite similar simulated UV/Vis behaviour is obtained for the Ru relative, with the first peak at 796 nm of $1P_{x,y} \rightarrow \pi^*$ -ligand nature followed by a 671–542 nm manifold of $1D \rightarrow \pi^*$ -ligand character with mixed $1D \rightarrow \pi^*$ -ligand and $1P_z \rightarrow \pi^*$ -ligand transition at 490 nm. In the case of the Fe species, the simulated spectrum exhibits a weak low-energy peak at 796 nm ($1P_{x,y} \rightarrow \pi^*$ -ligand) followed by a 663–526 nm peak manifold of $1D \rightarrow \pi^*$ -ligand character, with the appearance of the related $1P_z \rightarrow \pi^*$ -ligand transition at 450 nm.

The stereochemical constraints of the dppe ligands in **1** induce a substantial distortion of the icosahedral Au₁₃ core^{63–65} and their helical orientation induces some chirality, resulting in two possible enantiomers insphering circular dichroism (CD) properties. The CD spectra were computed for the right-handed enantiomers (Figure 4). That of [Au₁₃Cl₂(dppe)₅]³⁺ (**1**) reproduces well its experimental CD spectrum,⁶⁴ with a positive peak at 560 nm (563 nm experimental) and a negative peak at 462 nm (472 nm experimental). That of [Os@Au₁₂(dppe)₅Cl₂] (**2**) shows similar amplitudes but different shape. Its peak at 801 nm appears as a positive band, followed by another positive band peaking at 642 nm. The next peak manifold shows a negative and positive band, resulting in a pattern fingerprint different than for **1**. A pattern quite similar to that of **2** is found for its Ru and Fe counterparts, with the exception of a negative band around 800 nm for the Fe species. A comparison of the strength

of the CD signal, suggest a slightly more pronounced for heterometallic species, which can be of interest for further studies.

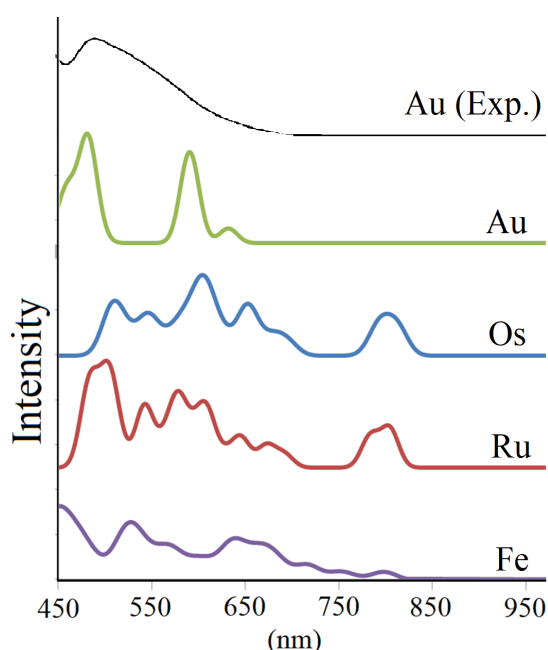


Figure 3. Calculated UV/Vis absorption spectra of $[\text{Au}_{13}\text{Cl}_2(\text{dppe})_5]^{3+}$, and $[\text{M}@\text{Au}_{12}\text{Cl}_2(\text{dppe})_5]$ ($\text{M} = \text{Os}, \text{Ru}, \text{Fe}$). The experimental spectrum of $[\text{Au}_{13}\text{Cl}_2(\text{dppe})_5]^{3+}$ ⁶⁴ is also shown for comparison.

The remarkable photoluminescent properties reported for **1**^{64,65} are ascribed to a $T_1 \rightarrow S_0$ decay⁶⁴ process, providing interesting singlet-oxygen sensitization applications. For a comparison, they were also evaluated for the 18-*ce* cluster counterparts and are discussed here. The emission wavelength of **1** was found experimentally at 766 nm (1.61 eV) by Konishi and Shichibu.⁶⁵ Computations indicate a transition between the related $T_1 \rightarrow S_0$ states at the T_1 geometry at 809 nm (1.53 eV),¹¹⁰ which corresponds to a $1D \rightarrow 1P$ decay. The excited state affords an increase of the axial AuCl–AuCl distance from 5.096 (S_0) to 5.184 Å (T_1). For $[\text{Os}@\text{Au}_{12}(\text{dppe})_5\text{Cl}_2]$ (**2**) the computed emission wavelength is red-shifted to the NIR at 1045 nm (1.19 eV). This time the T_1 states retain an axial ClAu–AuCl distance (5.18 Å) similar to that in S_0 , but affords a particular equatorial PAu–AuP change from 5.22 (S_0) to 5.43 Å (T_1), in contrast to the structural rearrangements at the excited state from **1**.

The calculated emission energies of the Ru and Fe counterparts are similar, amounting to 1076 nm (1.15 eV) and 1210 nm (1.02 eV), respectively. In the case of Ru, the T_1 states exhibits also a similar axial ClAu–AuCl distance (5.180 Å) than its S_0 ground-state, (5.217 Å) but

affords a particular equatorial PAu–AuP change from 5.245 (S_0) to 5.536 Å (T_1). In the case of Fe, the S_0 and T_1 states retain similar ClAu–AuCl distance (4.967 and 4.886 Å, respectively), but show a decrease of the PAu–AuP distance from S_0 (5.248 Å) to T_1 (5.164 Å).

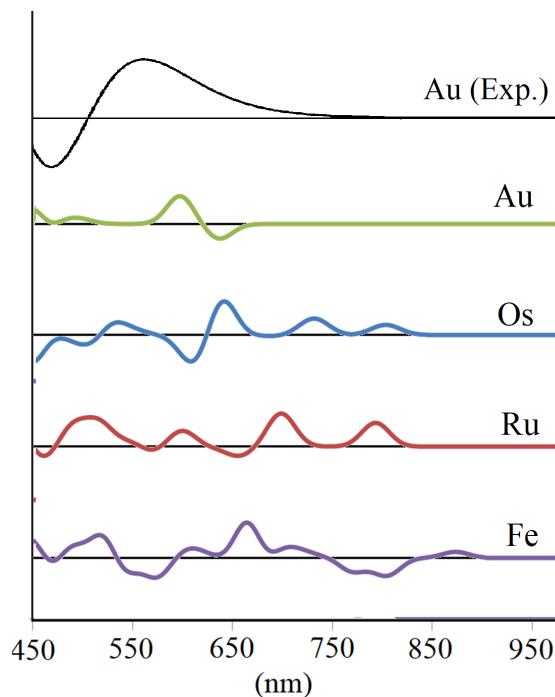


Figure 4. Calculated circular dichroism spectra for right-handed isomers of $[\text{Au}_{13}\text{Cl}_2(\text{dppe})_5]^{3+}$, and $[\text{M}@\text{Au}_{12}\text{Cl}_2(\text{dppe})_5]$ ($\text{M} = \text{Os}, \text{Ru}, \text{Fe}$). A broadening of 0.2 eV was employed. Values centered between $\pm 500 \times 10^{-40} \text{ esu}^2 \cdot \text{cm}^2$. The experimental spectrum of $[\text{Au}_{13}\text{Cl}_2(\text{dppe})_5]^{3+}$ ⁶⁴ is also shown for comparison.

Analysis of related Hg-doped species given by $[\text{Hg}@\text{Au}_{12}\text{Cl}_2(\text{dppe})_5]^{4+}$ species, leads to the preference for isomer **III**, i.e. Hg located at the M–Cl site, suggesting the possible extension to other doped species at different sites of the MAu_{12} core, besides the central position (see Annex).

We would like at this stage to come back to the fact that **1** and **2** are both isoelectronic and have different *superatom* electron counts (18-*ce* and 8-*ce*, respectively). They have the same total number of cluster valence electrons (162 including the ligand lone pairs and all the 5*d* electrons). This electron count satisfy the rule established by Mingos in the 1980s for spherical high-nuclearity gold phosphine clusters ($12 \times n_s + 18$, where n_s = number of surface gold atoms).^{112,113}

On the other hand, **1** and **2** are 18-*ce* and 8-*ce* *superatoms*, respectively. This difference originates from the fact that the 5*d*($\text{M}_{(\text{center})}$) orbitals (and electrons) participate to the bonding

in the former but do not participate significantly in the later (Scheme 1). As discussed in the introduction, there should be a continuum with intermediate situations when going from Os to Au, with the 10 $5d(M_{\text{center}})$ electrons participating in an intermediate fashion to the bonding. The very recently published compounds $[\text{IrAu}_{12}(\text{dppe})_5\text{Cl}_2]^+$ and $[\text{PtAu}_{12}(\text{dppe})_5\text{Cl}_2]^{2+}$ are now elegantly completing the continuum series.⁹¹ They were described by Tsukuda and coworkers as 8-*ce* species, but differing from $[\text{Au}_{13}(\text{dppe})_5\text{Cl}_2]^{3+}$ in that when doping the central position by Pt or Ir (keeping the total electron number constant), the *jellium* core potential which controls the *superatomic* electron configuration becomes shallower at the central position.⁹¹ Although different, this rationalizing approach is equivalent to ours, but would be less useful for interpreting optical properties.

Finally, we would like to mention that the isoelectronic substitution of one Au atom in $[\text{Au}_{13}\text{Cl}_2(\text{dppe})_5]^{3+}$ by Hg^+ substantially disfavors configuration **I** (Figure 1). Indeed, the even lesser availability of the $5d(\text{Hg})$ orbitals, as compared to $5d(\text{Au})$, for bonding with the Au_{12} cage, leads to an energetic preference by 27 kcal/mol for isomer **III**, i.e. Hg located at the M–Cl site, suggesting the possible extension to other doped species at different sites of the MAu_{12} core, besides the central position (see Annex).

5.4 Conclusion

Here we predict the stabilization of 18-*ce superatoms* based on the central doping of the $\text{M@Au}_{12}\text{Cl}_2$ core, showing characteristic patterns for both UV/Vis and CD spectra. The optical properties are dominated by core-to-ligand charge transfer in contrast to the 8-*ce* cluster **1**, showing $1D \rightarrow \pi^*$ -ligand and $1P \rightarrow \pi^*$ -ligand character transitions. Such differences are also noted in the calculated CD spectra with a peak manifold between 950 and 650 nm, not observed for the parent Au_{13} cluster. The emission properties derived from the $T_1 \rightarrow S_1$ decay exhibit a red-shift from 809 nm calculated for **1** to 1045 nm for $[\text{Os@Au}_{12}(\text{dppe})_5\text{Cl}_2]$, which involves an equatorial distortion of the $\text{Au}_{12}\text{Cl}_2$ core for the emissive excited state, rather than the axial distortion observed for **1**. The proposed neutral 18-*ce* $[\text{M@Au}_{12}(\text{dppe})_5\text{Cl}_2]$ ($M = \text{Os, Ru, Fe}$) clusters exhibit weaker ligand-core interaction energy owing to a decrease in the ligand-core bonding interaction due to the extra $1D^{10}$ shell, denoting the smaller role of the protecting ligands to achieve stable species. The resulting sizable HOMO-LUMO gaps computed for these species indicate substantial stability. As already explored extensively for $\text{MAu}_{24}(\text{SR})_{18}$ clusters, similar structural features are found for 8-*ce* and 18-*ce* species. This suggests further exploration of different doped species derived from the ligand-protected $\text{Au}_{12}\text{Cl}_2$ core that

would allow to tuning molecular properties, and further designing novel building blocks for nanostructured materials under the *superatom* approach.

5.5 References

- 1 Levi-Kalisman, Y.; Jadzinsky, P. D.; Kalisman, N.; Tsunoyama, H.; Tsukuda, T.; Bushnell, D. A.; Kornberg, R. D. Synthesis and Characterization of Au₁₀₂(p-MBA)₄₄ Nanoparticles. *J. Am. Chem. Soc.* **2011**, *133*, 2976–2982.
- 2 Tsukuda, T.; Tsunoyama, H.; Sakurai, H. Aerobic Oxidations Catalyzed by Colloidal Nanogold. *Chem. Asian J.* **2011**, *6*, 736–748.
- 3 Zhao, P.; Li, N.; Astruc, D. State of the Art in Gold Nanoparticle Synthesis. *Coord. Chem. Rev.* **2013**, *257*, 638–665.
- 4 Wuthschick, M.; Birnbaum, A.; Witte, S.; Sztucki, M.; Vainio, U.; Pinna, N.; Rademann, K.; Emmerling, F.; Kraehnert, R.; Polte, J. Turkevich in New Robes: Key Questions Answered for the Most Common Gold Nanoparticle Synthesis. *ACS Nano* **2015**, *9*, 7052–7071.
- 5 Jin, R.; Zeng, C.; Zhou, M.; Chen, Y. Atomically Precise Colloidal Metal Nanoclusters and Nanoparticles: Fundamentals and Opportunities. *Chem. Rev.* **2016**, *116*, 10346–10413.
- 6 Weerawardene, K. L. D. M.; Aikens, C. M. Origin of Photoluminescence of Ag₂₅(SR)₁₈⁻ Nanoparticles: Ligand and Doping Effect. *J. Phys. Chem. C* **2018**, *122*, 2440–2447.
- 7 Zhao, J.; Du, Q.; Zhou, S.; Kumar, V. Endohedrally Doped Cage Clusters. *Chem. Rev.* **2020**, *120*, 9021–9163.
- 8 Luo, Z.; Castleman, A. W.; Khanna, S. N. Reactivity of Metal Clusters. *Chem. Rev.* **2016**, *116*, 14456–14492.
- 9 *Gold Clusters, Colloids and Nanoparticles I*; Mingos, D. M. P., Ed.; Struct. Bond. **2014**; Vol. 161. <https://doi.org/10.1007/978-3-319-07848-9>.
- 10 *Gold Clusters, Colloids and Nanoparticles II*; Mingos, D. M. P., Ed.; Struct. Bond. **2014**; Vol. 162. <https://doi.org/10.1007/978-3-319-07845-8>.
- 11 Gao, Z.-H.; Dong, J.; Zhang, Q.-F.; Wang, L.-S. Halogen Effects on the Electronic and Optical Properties of Au₁₃ Nanoclusters. *Nanoscale Adv.* **2020**, *2*, 4902–4907.
- 12 Kamei, Y.; Shichibu, Y.; Konishi, K. Generation of Small Gold Clusters with Unique Geometries through Cluster-to-Cluster Transformations: Octanuclear Clusters with Edge-Sharing Gold Tetrahedron Motifs. *Angew. Chem. Int. Ed.* **2011**, *50*, 7442–7445.
- 13 Zhu, Y.; Qian, H.; Jin, R. Catalysis Opportunities of Atomically Precise Gold Nanoclusters. *J. Mater. Chem.* **2011**, *21*, 6793.

- 14 Kwak, K.; Kumar, S. S.; Lee, D. Selective Determination of Dopamine Using Quantum-Sized Gold Nanoparticles Protected with Charge Selective Ligands. *Nanoscale* **2012**, *4*, 4240–4246.
- 15 Sakai, N.; Tatsuma, T. Photovoltaic Properties of Glutathione-Protected Gold Clusters Adsorbed on TiO₂ Electrodes. *Adv. Mater.* **2010**, *22*, 3185–3188.
- 16 Wu, Z.; Wang, M.; Yang, J.; Zheng, X.; Cai, W.; Meng, G.; Qian, H.; Wang, H.; Jin, R. Well-Defined Nanoclusters as Fluorescent Nanosensors: A Case Study on Au₂₅(SG)₁₈. *Small* **2012**, *8*, 2028–2035.
- 17 Murray, R. W. Nanoelectrochemistry: Metal Nanoparticles, Nanoelectrodes, and Nanopores. *Chem. Rev.* **2008**, *108*, 2688–2720.
- 18 Galloway, J. M.; Bramble, J. P.; Rawlings, A. E.; Burnell, G.; Evans, S. D.; Staniland, S. S. Biotemplated Magnetic Nanoparticle Arrays. *Small* **2012**, *8*, 204–208.
- 19 Du, Y.; Sheng, H.; Astruc, D.; Zhu, M. Atomically Precise Noble Metal Nanoclusters as Efficient Catalysts: A Bridge between Structure and Properties. *Chem. Rev.* **2020**, *120*, 526–622.
- 20 Ebina, A.; Hossain, S.; Horihata, H.; Ozaki, S.; Kato, S.; Kawawaki, T.; Negishi, Y. One-, Two-, and Three-Dimensional Self-Assembly of Atomically Precise Metal Nanoclusters. *Nanomaterials* **2020**, *106*, 1105.
- 21 Yao, Q.; Chen, T.; Yuan, X.; Xie, J. Toward Total Synthesis of Thiolate-Protected Metal Nanoclusters. *Acc. Chem. Res.* **2018**, *51*, 1338–1348.
- 22 Sakthivel, N. A.; Dass, A. Aromatic Thiolate-Protected Series of Gold Nanomolecules and a Contrary Structural Trend in Size Evolution. *Acc. Chem. Res.* **2018**, *51*, 1774–1783.
- 23 Aikens, C. M. Electronic and Geometric Structure, Optical Properties, and Excited State Behavior in Atomically Precise Thiolate-Stabilized Noble Metal Nanoclusters. *Acc. Chem. Res.* **2018**, *51*, 3065–3073.
- 24 Ghosh, A.; Mohammed, O. F.; Bakr, O. M. Atomic-Level Doping of Metal Clusters. *Acc. Chem. Res.* **2018**, *51*, 3094–3103.
- 25 Hossain, S.; Niihori, Y.; Nair, L. V.; Kumar, B.; Kurashige, W.; Negishi, Y. Alloy Clusters: Precise Synthesis and Mixing Effects. *Acc. Chem. Res.* **2018**, *51*, 3114–3124.
- 26 Bhattarai, B.; Zaker, Y.; Atmagulov, A.; Yoon, B.; Landman, U.; Bigioni, T. P. Chemistry and Structure of Silver Molecular Nanoparticles. *Acc. Chem. Res.* **2018**, *51*, 3104–3113.
- 27 Harb, M.; Rabilloud, F.; Simon, D. Structural, Electronic, Magnetic and Optical Properties of Icosahedral Silver–Nickel Nanoclusters. *Phys. Chem. Chem. Phys.* **2010**, *12*, 4246.
- 28 Yu, C.; Schira, R.; Brune, H.; von Issendorff, B.; Rabilloud, F.; Harbich, W. Optical

- Properties of Size Selected Neutral Ag Clusters: Electronic Shell Structures and the Surface Plasmon Resonance. *Nanoscale* **2018**, *10*, 20821–20827.
- 29 Hossain, S.; Suzuki, D.; Iwasa, T.; Kaneko, R.; Suzuki, T.; Miyajima, S.; Iwamatsu, Y.; Pollitt, S.; Kawawaki, T.; Barrabés, N.; et al. Determining and Controlling Cu-Substitution Sites in Thiolate-Protected Gold-Based 25-Atom Alloy Nanoclusters. *J. Phys. Chem. C* **2020**, *124*, 22304–22313.
- 30 Xavier, P. L.; Chaudhari, K.; Baksi, A.; Pradeep, T. Protein-Protected Luminescent Noble Metal Quantum Clusters: An Emerging Trend in Atomic Cluster Nanoscience. *Nano Rev.* **2012**, *3*, 14767.
- 31 Zhang, Q.-F.; Chen, X.; Wang, L.-S. Toward Solution Syntheses of the Tetrahedral Au₂₀ Pyramid and Atomically Precise Gold Nanoclusters with Uncoordinated Sites. *Acc. Chem. Res.* **2018**, *51*, 2159–2168.
- 32 Cook, A. W.; Hayton, T. W. Case Studies in Nanocluster Synthesis and Characterization: Challenges and Opportunities. *Acc. Chem. Res.* **2018**, *51*, 2456–2464.
- 33 Lei, Z.; Wan, X.-K.; Yuan, S.-F.; Guan, Z.-J.; Wang, Q.-M. Alkynyl Approach toward the Protection of Metal Nanoclusters. *Acc. Chem. Res.* **2018**, *51*, 2465–2474.
- 34 Sharma, S.; Chakrahari, K. K.; Saillard, J.-Y.; Liu, C. W. Structurally Precise Dichalcogenolate-Protected Copper and Silver Superatomic Nanoclusters and Their Alloys. *Acc. Chem. Res.* **2018**, *51*, 2475–2483.
- 35 Higaki, T.; Li, Q.; Zhou, M.; Zhao, S.; Li, Y.; Li, S.; Jin, R. Toward the Tailoring Chemistry of Metal Nanoclusters for Enhancing Functionalities. *Acc. Chem. Res.* **2018**, *51*, 2764–2773.
- 36 Tang, Q.; Hu, G.; Fung, V.; Jiang, D. Insights into Interfaces, Stability, Electronic Properties, and Catalytic Activities of Atomically Precise Metal Nanoclusters from First Principles. *Acc. Chem. Res.* **2018**, *51*, 2793–2802.
- 37 Konishi, K.; Iwasaki, M.; Shichibu, Y. Phosphine-Ligated Gold Clusters with Core+exo Geometries: Unique Properties and Interactions at the Ligand–Cluster Interface. *Acc. Chem. Res.* **2018**, *51*, 3125–3133.
- 38 Yan, J.; Teo, B. K.; Zheng, N. Surface Chemistry of Atomically Precise Coinage–Metal Nanoclusters: From Structural Control to Surface Reactivity and Catalysis. *Acc. Chem. Res.* **2018**, *51*, 3084–3093.
- 39 Jin, R. Atomically Precise Metal Nanoclusters: Stable Sizes and Optical Properties. *Nanoscale* **2015**, *7*, 1549–1565.
- 40 Zhu, M.; Aikens, C. M.; Hollander, F. J.; Schatz, G. C.; Jin, R. Correlating the Crystal

- Structure of A Thiol-Protected Au₂₅ Cluster and Optical Properties. *J. Am. Chem. Soc.* **2008**, *130*, 5883–5885.
- 41 Yuan, X.; Zhang, B.; Luo, Z.; Yao, Q.; Leong, D. T.; Yan, N.; Xie, J. Balancing the Rate of Cluster Growth and Etching for Gram-Scale Synthesis of Thiolate-Protected Au₂₅ Nanoclusters with Atomic Precision. *Angew. Chem. Int. Ed.* **2014**, *53*, 4623–4627.
- 42 Kurashige, W.; Niihori, Y.; Sharma, S.; Negishi, Y. Precise Synthesis, Functionalization and Application of Thiolate-Protected Gold Clusters. *Coord. Chem. Rev.* **2016**, *320–321*, 238–250.
- 43 Chakraborty, I.; Pradeep, T. Atomically Precise Clusters of Noble Metals: Emerging Link between Atoms and Nanoparticles. *Chem. Rev.* **2017**, *117*, 8208–8271.
- 44 Kawawaki, T.; Imai, Y.; Suzuki, D.; Kato, S.; Kobayashi, I.; Suzuki, T.; Kaneko, R.; Hossain, S.; Negishi, Y. Atomically Precise Alloy Nanoclusters. *Chem. – A Eur. J.* **2020**, *26*, 16150–16193.
- 45 Negishi, Y.; Hashimoto, S.; Ebina, A.; Hamada, K.; Hossain, S.; Kawawaki, T. Atomic-Level Separation of Thiolate-Protected Metal Clusters. *Nanoscale* **2020**, *12*, 8017–8039.
- 46 Alkan, F.; Muñoz-Castro, A.; Aikens, C. M. C. M. Relativistic DFT Investigation of Electronic Structure Effects Arising from Doping the Au₂₅ Nanocluster with Transition Metals. *Nanoscale* **2017**, *9*, 15825–15834.
- 47 Ito, E.; Takano, S.; Nakamura, T.; Tsukuda, T. Controlled Dimerization and Bonding Scheme of Icosahedral M@Au₁₂ (M=Pd, Pt) Superatoms. *Angew. Chem. Int. Ed.* **2021**, *60*, 645–649.
- 48 Qin, Z.; Sharma, S.; Wan, C.; Malola, S.; Xu, W.; Häkkinen, H.; Li, G. A Homoleptic Alkynyl-Ligated [Au₁₃Ag₁₆L₂₄]³⁻ Cluster as a Catalytically Active Eight-Electron Superatom. *Angew. Chem. Int. Ed.* **2021**, *60*, 970–975.
- 49 Negishi, Y.; Kurashige, W.; Kobayashi, Y.; Yamazoe, S.; Kojima, N.; Seto, M.; Tsukuda, T. Formation of a Pd@Au₁₂ Superatomic Core in Au₂₄Pd₁(SC₁₂H₂₅)₁₈ Probed by ¹⁹⁷Au Mössbauer and Pd K-Edge EXAFS Spectroscopy. *J. Phys. Chem. Lett.* **2013**, *4*, 3579–3583.
- 50 Kwak, K.; Tang, Q.; Kim, M.; Jiang, D. E.; Lee, D. Interconversion between Superatomic 6-Electron and 8-Electron Configurations of M@Au₂₄(SR)₁₈ Clusters (M = Pd, Pt). *J. Am. Chem. Soc.* **2015**, *137*, 10833–10840.
- 51 Juarez-Mosqueda, R.; Malola, S.; Häkkinen, H. Stability, Electronic Structure, and Optical Properties of Protected Gold-Doped Silver Ag_{29-x}Au_x (x = 0–5) Nanoclusters. *Phys. Chem. Chem. Phys.* **2017**, *19*, 13868–13874.

- 52 Alkan, F.; Pandeya, P.; Aikens, C. M. Understanding the Effect of Doping on Energetics and Electronic Structure for Au₂₅, Ag₂₅, and Au₃₈ Clusters. *J. Phys. Chem. C* **2019**, *123*, 9516–9527.
- 53 Tsukuda, T.; Häkkinen, H. *Protected Metal Clusters: From Fundamentals to Applications*; Elsevier, **2015**.
- 54 Jin, R.; Nobusada, K. Doping and Alloying in Atomically Precise Gold Nanoparticles. *Nano Res.* **2014**, *7*, 285–300.
- 55 Bhat, S.; Bakshi, A.; Mudedla, S. K.; Natarajan, G.; Subramanian, V.; Pradeep, T. Au₂₂Ir₃(PET)₁₈: An Unusual Alloy Cluster through Intercluster Reaction. *J. Phys. Chem. Lett.* **2017**, 2787–2793.
- 56 Chai, J.; Lv, Y.; Yang, S.; Song, Y.; Zan, X.; Li, Q.; Yu, H.; Wu, M.; Zhu, M. X-Ray Crystal Structure and Optical Properties of Au_{38-x}Cu_x (2,4-(CH₃)₂C₆H₃S)₂₄ (x = 0–6) Alloy Nanocluster. *J. Phys. Chem. C* **2017**, *121*, 21665–21669.
- 57 Omoda, T.; Takano, S.; Tsukuda, T. Toward Controlling the Electronic Structures of Chemically Modified Superatoms of Gold and Silver. *Small* **2020**, 2001439.
- 58 Walter, M.; Akola, J.; Lopez-Acevedo, O.; Jadzinsky, P. D.; Calero, G.; Ackerson, C. J.; Whetten, R. L.; Grönbeck, H.; Häkkinen, H.; Gronbeck, H.; et al. A Unified View of Ligand-Protected Gold Clusters as Superatom Complexes. *Proc. Natl. Acad. Sci.* **2008**, *105*, 9157–9162.
- 59 Castleman, A. W.; Khanna, S. N. Clusters, Superatoms, and Building Blocks of New Materials. *J. Phys. Chem. C* **2009**, *113*, 2664–2675.
- 60 Jadzinsky, P. D.; Calero, G.; Ackerson, C. J.; Bushnell, D. A.; Kornberg, R. D. Structure of a Thiol Monolayer-Protected Gold Nanoparticle at 1.1 Å Resolution. *Science* **2007**, *318*, 430–433.
- 61 Claridge, S. A.; Castleman, A. W.; Khanna, S. N.; Murray, C. B.; Sen, A.; Weiss, P. S. Cluster-Assembled Materials. *ACS Nano* **2009**, *3*, 244–255.
- 62 Bürgi, T. Properties of the Gold-Sulphur Interface: From Self-Assembled Monolayers to Clusters. *Nanoscale* **2015**, *7*, 15553–15567.
- 63 Briant, C. E.; Theobald, B. R. C.; White, J. W.; Bell, L. K.; Mingos, D. M. P.; Welch, A. J. Synthesis and X-Ray Structural Characterization of the Centred Icosahedral Gold Cluster Compound [Au₁₃(PMe₂Ph)₁₀Cl₂](PF₆)₃; the Realization of a Theoretical Prediction. *J. Chem. Soc. Chem. Commun.* **1981**, *5*, 201–202.
- 64 Zhang, J.; Zhou, Y.; Zheng, K.; Abroshan, H.; Kauffman, D. R.; Sun, J.; Li, G. Diphosphine-Induced Chiral Propeller Arrangement of Gold Nanoclusters for Singlet

- Oxygen Photogeneration. *Nano Res.* **2017**, 1–12.
- 65 Shichibu, Y.; Konishi, K. HCl-Induced Nuclearity Convergence in Diphosphine-Protected Ultrasmall Gold Clusters: A Novel Synthetic Route to “Magic-Number” Au₁₃ Clusters. *Small* **2010**, *6*, 1216–1220.
- 66 Ding, W.; Huang, C.; Guan, L.; Liu, X.; Luo, Z.; Li, W. Water-Soluble Au₁₃ Clusters Protected by Binary Thiolates: Structural Accommodation and the Use for Chemosensing. *Chem. Phys. Lett.* **2017**, *676*, 18–24.
- 67 Sheong, F. K.; Zhang, J.-X.; Lin, Z. An [Au₁₃]⁵⁺ Approach to the Study of Gold Nanoclusters. *Inorg. Chem.* **2016**, *55*, 11348–11353.
- 68 Laupp, M.; Strähle, J. [(Ph₃PAu)₆(DppeAu₂)(AuCl)₄Pd], an Icosahedral Au₁₂ Cluster with a Central Pd Atom. *Angew. Chem. Int. Ed.* **1994**, *33*, 207–209.
- 69 Kang, X.; Chong, H.; Zhu, M. Au₂₅(SR)₁₈: The Captain of the Great Nanocluster Ship. *Nanoscale* **2018**, *10*, 10758–10834.
- 70 Zhu, M.; Aikens, C. M.; Hendrich, M. P.; Gupta, R.; Qian, H.; Schatz, G. C.; Jin, R. Reversible Switching of Magnetism in Thiolate-Protected Au₂₅ Superatoms. *J. Am. Chem. Soc.* **2009**, *131*, 2490–2492.
- 71 Gam, F.; Paez-Hernandez, D.; Arratia-Perez, R.; Liu, C. W. W.; Kahlal, S.; Saillard, J.-Y. J.-Y.; Muñoz-Castro, A.; Gam, F.; Paez-Hernandez, D.; Arratia-Perez, R.; et al. Coinage Metal Superatomic Cores: Insights into Their Intrinsic Stability and Optical Properties from Relativistic DFT Calculations. *Chem. Eur. J.* **2017**, *23*, 11330–11337.
- 72 Saillard, J.-Y.; Halet, J.-F. Structure and Bonding Patterns in Large Molecular Ligated Metal Clusters. *Struct. Bond.* **2016**, *169*, 157–179.
- 73 Fehlner, T.; Halet, J.-F.; Saillard, J.-Y. Molecular Clusters. A Bridge to Solid State Chemistry. *Cambridge Univ. Press. Cambridge, UK* **2007**.
- 74 Häkkinen, H. Atomic and Electronic Structure of Gold Clusters: Understanding Flakes, Cages and Superatoms from Simple Concepts. *Chem. Soc. Rev.* **2008**, *37*, 1847–1859.
- 75 Mäkinen, V.; Koskinen, P.; Häkkinen, H. Modeling Thiolate-Protected Gold Clusters with Density-Functional Tight-Binding. *Eur. Phys. J. D* **2013**, *67*, 38.
- 76 Wen, F.; Englert, U.; Gutrath, B.; Simon, U. Crystal Structure, Electrochemical and Optical Properties of [Au₉(PPh₃)₈](NO₃)₃. *Eur. J. Inorg. Chem.* **2008**, *2008*, 106–111.
- 77 Woehrle, G. H.; Warner, M. G.; Hutchison, J. E. Ligand Exchange Reactions Yield Subnanometer, Thiol-Stabilized Gold Particles with Defined Optical Transitions. *J. Phys. Chem. B* **2002**, *106*, 9979–9981.
- 78 Schmid, G.; Pfeil, R.; Boese, R.; Bandermann, F.; Meyer, S.; Calis, G. H. M.; van der

- Velden, J. W. A. Au₅₅[P(C₆H₅)₃]₁₂Cl₆⁻ Ein Goldcluster Ungewöhnlicher Größe. *Chem. Ber.* **1981**, *114*, 3634–3642.
- 79 Ashen-Garry, D.; Selke, M. Singlet Oxygen Generation by Cyclometalated Complexes and Applications. *Photochem. Photobiol.* **2014**, *90*, 257–274.
- 80 DeRosa, M. Photosensitized Singlet Oxygen and Its Applications. *Coord. Chem. Rev.* **2002**, *233–234*, 351–371.
- 81 Mingos, D. M. P. Molecular-Orbital Calculations on Cluster Compounds of Gold. *J. Chem. Soc. Dalton Trans.* **1976**, *13*, 1163–1169.
- 82 Häkkinen, H. Electronic Structure: Shell Structure and the Superatom Concept. In *Protected Metal Clusters: From Fundamentals to Applications*; Häkkinen, H., Tsukuda, T., Eds.; Elsevier Science, 2015; 189–222.
- 83 Lopez-Acevedo, O.; Akola, J.; Whetten, R. L.; Grönbeck, H.; Häkkinen, H.; Grönbeck, H.; Häkkinen, H. Structure and Bonding in the Ubiquitous Icosahedral Metallic Gold Cluster Au₁₄₄(SR)₆₀. *J. Phys. Chem. C* **2009**, *113*, 5035–5038.
- 84 Kurashige, W.; Hayashi, R.; Wakamatsu, K.; Kataoka, Y.; Hossain, S.; Iwase, A.; Kudo, A.; Yamazoe, S.; Negishi, Y. Atomic-Level Understanding of the Effect of Heteroatom Doping of the Cocatalyst on Water-Splitting Activity in AuPd or AuPt Alloy Cluster-Loaded BaLa₄Ti₄O₁₅. *ACS Appl. Energy Mater.* **2019**, *2*, 4175–4187.
- 85 Kumar, B.; Kawawaki, T.; Shimizu, N.; Imai, Y.; Suzuki, D.; Hossain, S.; Nair, L. V.; Negishi, Y. Gold Nanoclusters as Electrocatalysts: Size, Ligands, Heteroatom Doping, and Charge Dependences. *Nanoscale* **2020**, *12*, 9969–9979.
- 86 Puls, A.; Jerabek, P.; Kurashige, W.; Förster, M.; Molon, M.; Bollermann, T.; Winter, M.; Gemel, C.; Negishi, Y.; Frenking, G.; et al. A Novel Concept for the Synthesis of Multiply Doped Gold Clusters [(M@AunM'm)Lk]^{Q+}. *Angew. Chem. Int. Ed.* **2014**, *53*, 4327–4331.
- 87 Negishi, Y.; Munakata, K.; Ohgake, W.; Nobusada, K. Effect of Copper Doping on Electronic Structure, Geometric Structure, and Stability of Thiolate-Protected Au₂₅ Nanoclusters. *J. Phys. Chem. Lett.* **2012**, *3*, 2209–2214.
- 88 Negishi, Y.; Igarashi, K.; Munakata, K.; Ohgake, W.; Nobusada, K. Palladium Doping of Magic Gold Cluster Au₃₈(SC₂H₄Ph)₂₄: Formation of Pd₂Au₃₆(SC₂H₄Ph)₂₄ with Higher Stability than Au₃₈(SC₂H₄Ph)₂₄. *Chem. Commun.* **2012**, *48*, 660–662.
- 89 Pyykkö, P.; Runeberg, N. Icosahedral WAu₁₂: A Predicted Closed-Shell Species, Stabilized by Auophilic Attraction and Relativity and in Accord with the 18-Electron Rule. *Angew. Chem. Int. Ed.* **2002**, *41*, 2174–2176.
- 90 Li, X.; Kiran, B.; Li, J.; Zhai, H.-J.; Wang, L.-S. Experimental Observation and

- Confirmation of Icosahedral $W@Au_{12}$ and $Mo@Au_{12}$ Molecules. *Angew. Chem. Int. Ed.* **2002**, *41*, 4786–4789.
- 91 Hirai, H.; Takano, S.; Nakamura, T.; Tsukuda, T. Understanding Doping Effects on Electronic Structures of Gold Superatoms: A Case Study of Diphosphine-Protected $M@Au_{12}$ ($M = Au, Pt, Ir$). *Inorg. Chem.* **2020**, *59*, 17889–17895.
- 92 Dylla, K. G.; Fægri, K. *Introduction to Relativistic Quantum Chemistry*; Oxford University Press, New York, **2007**.
- 93 Amsterdam Density Functional (ADF) Code, Vrije Universiteit: Amsterdam, The Netherlands. [Http://Www.Scm.Com](http://www.scm.com).
- 94 van Lenthe, E.; Baerends, E.-J. J.; Snijders, J. G. Relativistic Total Energy Using Regular Approximations. *J. Chem. Phys.* **1994**, *101*, 9783.
- 95 Perdew, J. P.; Burke, K.; Wang, Y. Generalized Gradient Approximation for the Exchange-Correlation Hole of a Many-Electron System. *Phys. Rev. B* **1996**, *54*, 16533–16539.
- 96 Perdew, J. P.; Burke, K.; Ernzerhof, M. Generalized Gradient Approximation Made Simple. *Phys. Rev. Lett.* **1997**, *78*, 1396–1396.
- 97 Akola, J.; Walter, M.; Whetten, R. L.; Häkkinen, H.; Grönbeck, H. On the Structure of Thiolate-Protected Au_{25} . *J. Am. Chem. Soc.* **2008**, *130*, 3756–3757.
- 98 Jiang, D. The Expanding Universe of Thiolated Gold Nanoclusters and Beyond. *Nanoscale* **2013**, *5*, 7149–7160.
- 99 Akola, J.; Kacprzak, K. A.; Lopez-Acevedo, O.; Walter, M.; Grönbeck, H.; Häkkinen, H. Thiolate-Protected Au_{25} Superatoms as Building Blocks: Dimers and Crystals. *J. Phys. Chem. C* **2010**, *114*, 15986–15994.
- 100 Jiang, D.; Kühn, M.; Tang, Q.; Weigend, F. Superatomic Orbitals under Spin-Orbit Coupling. *J. Phys. Chem. Lett.* **2014**, *5*, 3286–3289.
- 101 Grimme, S. Density Functional Theory with London Dispersion Corrections. *Wiley Interdiscip. Rev. Comput. Mol. Sci.* **2011**, *1*, 211–228.
- 102 Versluis, L.; Ziegler, T. The Determination of Molecular Structures by Density Functional Theory. The Evaluation of Analytical Energy Gradients by Numerical Integration. *J. Chem. Phys.* **1988**, *88*, 322–328.
- 103 Lopez-Acevedo, O.; Tsunoyama, H.; Tsukuda, T.; Häkkinen, H.; Aikens, C. M.; Häkkinen, H.; Aikens, C. M. Chirality and Electronic Structure of the Thiolate-Protected Au_{38} Nanocluster. *J. Am. Chem. Soc.* **2010**, *132*, 8210–8218.
- 104 Ai, P.; Mauro, M.; Danopoulos, A. A. A. A.; Muñoz-Castro, A.; Braunstein, P. Dual

- Emission of a Cyclic Hexanuclear Gold(I) Complex. Interplay between Au₃ and Au₂ Ligand-Supported Luminophores. *J. Phys. Chem. C* **2019**, *123*, 915–921.
- 105 Mingos, D. M. P.; Lin, Z. Site Preference Effects in Heterometallic Clusters. *Comments Inorg. Chem.* **1989**, *9*, 95–122.
- 106 Morokuma, K. Molecular Orbital Studies of Hydrogen Bonds. III. C=O···H–O Hydrogen Bond in H₂CO···H₂O and H₂CO···2H₂O. *J. Chem. Phys.* **1971**, *55*, 1236–1244.
- 107 Ziegler, T.; Rauk, A. Calculation of Bonding Energies by Hartree-Fock Slater Method. 1. Transition-State Method. *Theor. Chim. Acta* **1977**, *46*, 1–10.
- 108 Hopffgarten, M. von; Frenking, G.; von Hopffgarten, M.; Frenking, G. Energy Decomposition Analysis. *Wiley Interdiscip. Rev. Comput. Mol. Sci.* **2012**, *2*, 43–62.
- 109 MacLeod Carey, D.; Muñoz-Castro, A. Evaluation of N-Heterocyclic Carbene Counterparts of Classical Gold Clusters; Bonding Properties of Octahedral CAu₆, Icosahedral Au₁₃Cl₂, and Bi-Icosahedral Au₂₅Cl₂ Cores from Relativistic DFT Calcula. *J. Phys. Chem. C* **2019**, *123*, 12466–12473.
- 110 Muñoz-Castro, A. Potential of N-Heterocyclic Carbene Derivatives from Au₁₃(Dppe)₅Cl₂ Gold Superatoms. Evaluation of Electronic, Optical and Chiroptical Properties from Relativistic DFT. *Inorg. Chem. Front.* **2019**, *6*, 2349–2358.
- 111 Du, L.; Furube, A.; Hara, K.; Katoh, R.; Tachiya, M. Ultrafast Plasmon Induced Electron Injection Mechanism in Gold–TiO₂ Nanoparticle System. *J. Photochem. Photobiol. C Photochem. Rev.* **2013**, *15*, 21–30.
- 112 Mingos, D. M. P.; Lewis, J.; Green, M. L. H. Some Theoretical and Structural Aspects of Gold Cluster Chemistry. *Philos. Trans. R. Soc. London. Ser. A, Math. Phys. Sci.* **1982**, *308*, 75–83.
- 113 Hall, K. P.; Mingos, D. M. P. Homo- and Heteronuclear Cluster Compounds of Gold. *Prog. Inorg. Chem.*, **1984**, *32*, 237–325.

5.6 Annex

Table S1. Energy decomposition analysis between the $[\text{Cl}_2(\text{dppe})_5]^{2-}$ ligand shell and the $[\text{M}@\text{Au}_{12}]^{n+}$ ($\text{M} = \text{Au}, n = 5$; $\text{M} = \text{Os}, \text{Ru}, \text{Fe}, n = 2$) fragment. Values in kcal.mol^{-1} .

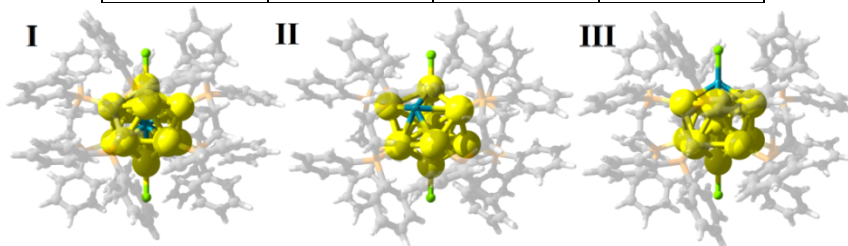
	1 (Au)		2 (Os)		3 (Ru)		4 (Fe)	
ΔE_{Pauli}	2005.8		2099.7		2005.2		1911.5	
ΔE_{elstat}	-2218.2	61.4%	-1911.8	66.3%	-1834.3	65.8%	-1725.7	64.7%
ΔE_{orb}	-1278.6	35.4%	-861.5	29.9%	-842.2	30.2%	-827.0	31.0%
ΔE_{disp}	-113.1	3.1%	-111.2	3.9%	-109.6	3.9%	-114.4	4.3%
ΔE_{int}	-1604.1		-784.8		-780.9		-755.7	

Table S2. Energy decomposition analysis between a single Cl^- anion and the $[\text{M}@\text{Au}_{12}\text{Cl}(\text{dppe})_5]^{n+}$ fragment ($\text{M} = \text{Au}, n = 4$; $\text{M} = \text{Os}, \text{Ru}, \text{Fe}, n = 1$). Values in kcal.mol^{-1} .

	1 (Au)		2 (Os)		3 (Ru)		4 (Fe)	
ΔE_{Pauli}	157.1		119.1		116.7		110.9	
ΔE_{elstat}	-286.0	72.0%	-130.0	59.0%	-127.4	59.5%	-119.5	59.2%
ΔE_{orb}	-104.7	26.4%	-83.9	38.1%	-80.1	37.5%	-76.1	37.7%
ΔE_{disp}	-6.7	1.7%	-6.3	2.9%	-6.4	3.0%	-6.3	3.1%
ΔE_{int}	-240.3		-101.1		-97.3		-91.0	

Table S3. Relative energy of isomers **I**, **II**, and **III**, for $[\text{Fe}@\text{Au}_{12}(\text{dppe})_5\text{Cl}_2]$, $[\text{Ru}@\text{Au}_{12}(\text{dppe})_5\text{Cl}_2]$, and $[\text{Os}@\text{Au}_{12}(\text{dppe})_5\text{Cl}_2]$. Values in kcal.mol^{-1} .

	Fe	Ru	Os
Isomer I	0.0	0.0	0.0
Isomer II	+253.5	+129.8	+99.1
Isomer III	+128.4	+88.7	+101.0



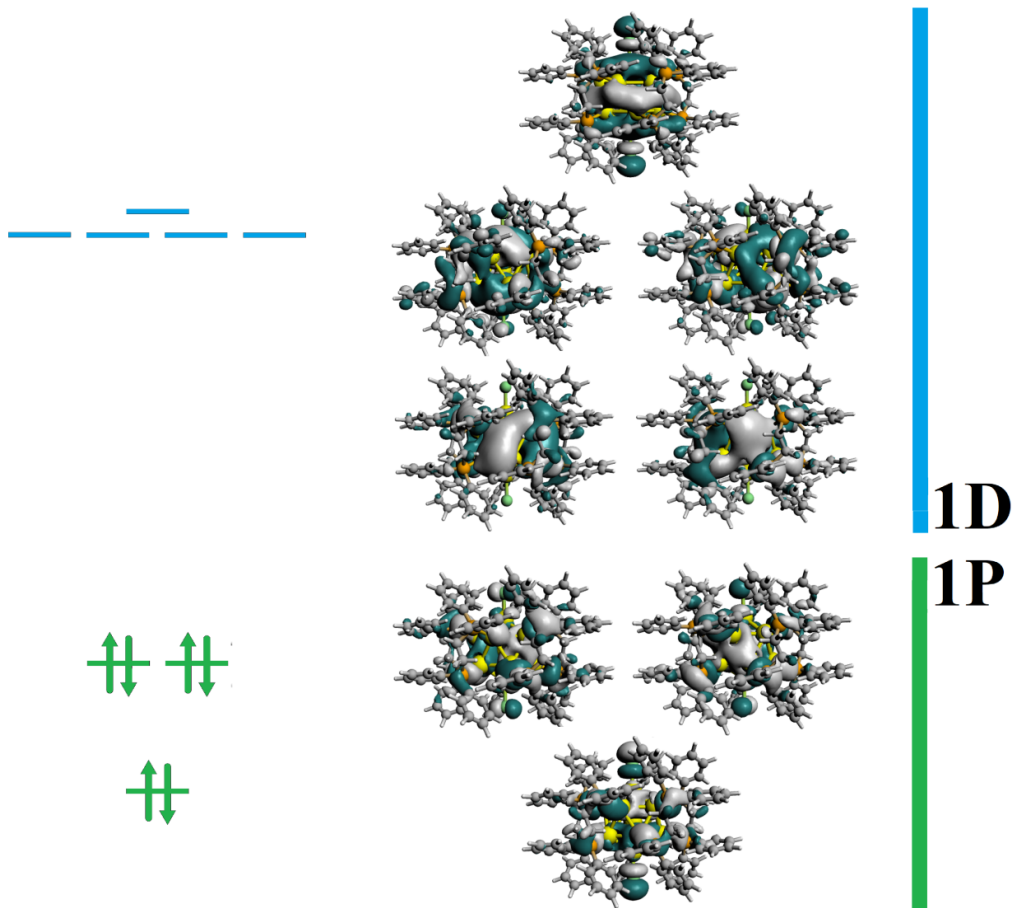


Figure S1. Isosurface for the 1P and 1D levels of $[\text{Au}_{13}\text{Cl}_2(\text{dppe})_5]^{3+}$.

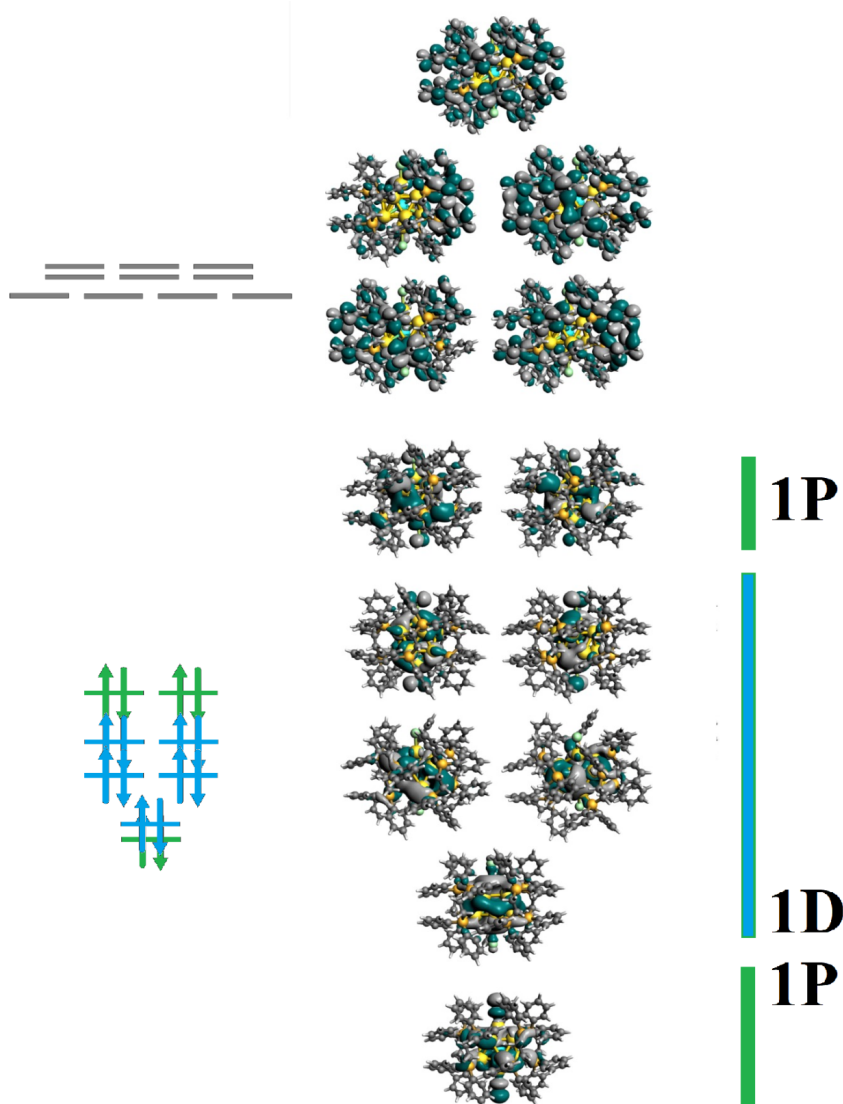


Figure S2 Isosurface for the 1P and 1D occupied levels of [Os@Au₁₂Cl₂(dppe)₅], as well as the lowest unoccupied levels, which are of ligand character.

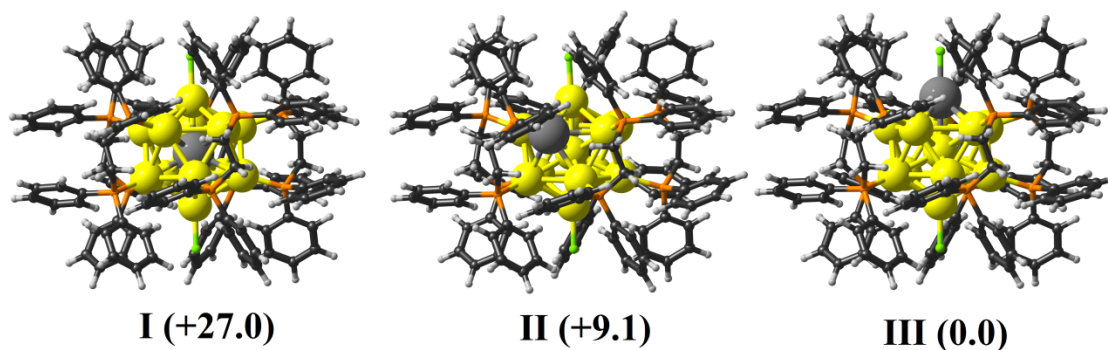


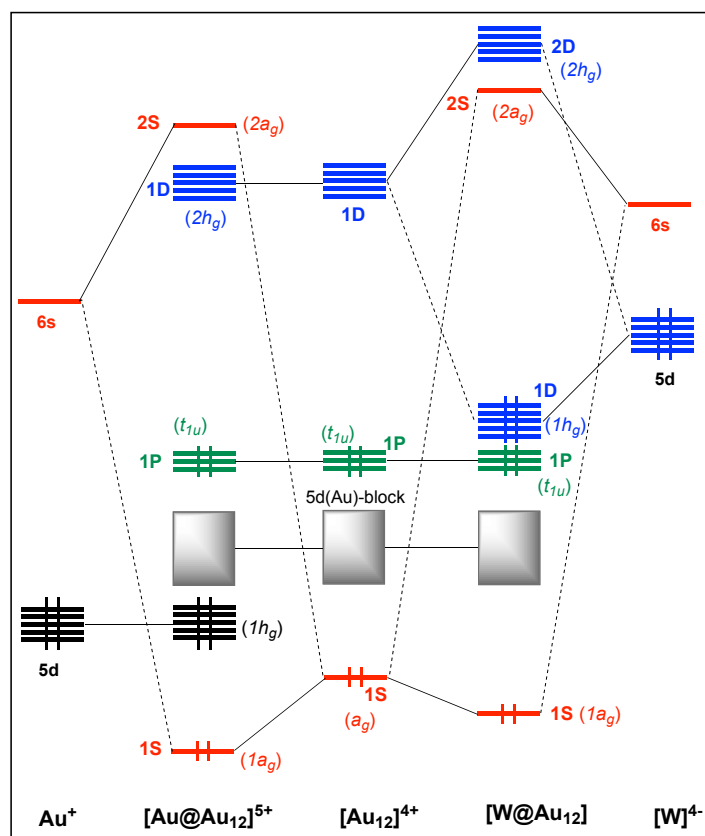
Figure S3. Relative energy for isomers I, II, and III, of [Hg@Au₁₂(dppe)₅Cl₂]⁴⁺. Values in kcal.mol⁻¹.

Chapter 6

From 8- to 18-cluster electrons Superatoms. Investigation of the Ligand-Protected $W@Au_{12}(dppe)_6$ Cluster Displaying Distinctive Electronic and Optical Properties

6.1 Introduction

Gold nanoparticles (AuNP) continue to attract the interest of the scientific community owing to their peculiar structural and optical properties leading to a wide range of applications in different fields, such as biotechnology,^{1,2} sensors,^{3,4} catalysis,⁵⁻⁷ among others.⁸ Further exploration and advances in the synthesis of nanoparticles provide control of ultra-small NP's with atomic precision,⁹⁻¹⁵ achieving prototypical architectures serving as stable frameworks to gain more insights in the structure-property relationship based on size, composition, and electron counting considerations.¹⁶⁻²⁰ Furthermore, doping of metal clusters has been considered as an efficient strategy to deliver related counterparts to homometallic templates,^{21,22} enabling tuning their molecular properties in terms of variation of their electronic structures.²³⁻³⁶ Among the different cluster motifs, the recursive Au₁₃ atom-centered icosahedron has been observed in thiolate-protected [Au₂₅(SR)₁₈]⁻ derivatives, for instance,³⁷⁻⁴³ as a representative of an 8-electron cluster *superatom*.⁴⁴⁻⁴⁶ In contrast, although fully phosphine-protected gold clusters have been studied in earlier years,⁴⁷⁻⁵⁰ they have been somewhat neglected thereafter and only in the last years they aroused a renewed interest, owing to their role as synthetic intermediates in high-yield synthesis of AuNPs,¹² or ligand-exchange reactions,^{51,52} and for their previously unreported properties.⁵³⁻⁵⁶ The homoleptic [Au₁₃(dppm)₆]⁵⁺ (**1**) (dppm = 1,1-bis(diphenylphosphino)methane is a simple representative of this type of clusters, featuring an icosahedral [Au@Au₁₂]⁵⁺ core surrounded by neutral diphosphine ligands.^{47,54} Within the framework of the *superatom* model,^{57,58} **1** is a 8-cluster electron (8-*ce*) *superatom*. Indeed, in the context of this electron counting model, the bonding within the [Au@Au₁₂]⁵⁺ core is assumed to be primarily ensured by the 6s electrons and orbitals. This situation is sketched by the simplified interaction MO diagram on the left side of Scheme 1, where the 9 lowest 6s combinations (among a total of 13) of [Au@Au₁₂]⁵⁺ correspond to the 1S, 1P and 1D levels, of which the two former are bonding and the later antibonding. The combinations of the 5d AOs (including those of the encapsulated Au) are considered non-bonding. It results that the best closed-shell electron count is 8-*ce*, with the bonding 1S and 1P levels occupied (1S² 1P⁶ 1D⁰ *superatomic* configuration). The next closed-shell electron count, 18, would require the filling of the 1D level, which is highly unfavorable owing to its substantial antibonding nature.



Scheme 1. Simplified MO interaction diagrams of the centered icosahedral $[\text{Au}@\text{Au}_{12}]^{5+}$ and $[\text{W}@\text{Au}_{12}]$ clusters illustrating the fact that although isoelectronic, they should be considered as 8- and 18-electron *superatoms*, respectively.

To our knowledge, there is no report of the bare (non-ligated) $[\text{Au}@\text{Au}_{12}]^{5+}$ cluster, so far. On the other hand, the notorious $[\text{W}@\text{Au}_{12}]$ was experimentally observed in 2002 by Wang and collaborators⁵⁹ after having first been elegantly predicted by Pyykkö and coworkers.^{60,61} This bare cluster, which is also icosahedral, is obviously isoelectronic to $[\text{Au}@\text{Au}_{12}]^{5+}$, in the meaning that both species possess the same total number of (valence) electrons. Nevertheless, $[\text{W}@\text{Au}_{12}]$ was shown by Pyykkö to be an 18-*ce* (not an 8-*ce* as $[\text{Au}@\text{Au}_{12}]^{5+}$) species. This apparent contradiction can be rationalized within the framework of the *superatom* model, as sketched on the right side of Scheme 1. Contrarily to the case of the encapsulated Au atom on the left side of the Scheme 1, The 5*d* AOs of W are more diffuse and lie higher in energy. As a consequence, they interact significantly with the 1*D* orbitals (6*s* combinations) of its Au_{12} cage, generating one bonding (new 1*D* level) and one antibonding (new 2*D* level) combinations. Thus, contrarily to $[\text{Au}@\text{Au}_{12}]^{5+}$, the 5*d* AOs of the encapsulated atom are not non-bonding, but they constitute, after mixing with the 6*s* AOs of the cage, the occupied *superatomic* 1*D* bonding level, leading to the $1\text{S}^2 1\text{P}^6 1\text{D}^{10}$ configuration.

We have shown recently that a rather similar situation occurs in the hypothetical $[\text{Os}@Au_{12}(\text{dppe})_5\text{Cl}_2]$, featuring an 18-*ce* $[\text{Os}@Au_{12}]^{2+}$ core.⁶² (see Chapter 5) We investigate in this chapter, on the basis of relativistic density functional theory (DFT) calculations, the potential stability and optical properties of an 18-*ce* fully phosphine-protected neutral cluster containing the $[\text{W}@Au_{12}]$ core that would be “isoelectronic” to the 8-*ce* cluster **1**, namely $[\text{W}@Au_{12}(\text{dppm})_6]$ (**2**). The obtained results provide reliable models to establish the electron count–property relationship from ultra-small clusters regime, contributing from fundamental aspects towards larger clusters.

6.2 Computational Details

Density functional theory calculations⁶³ were carried out by using the ADF code,⁶⁴ incorporating scalar relativistic corrections via the ZORA Hamiltonian.⁶⁵ All calculations were performed employing triple-zeta Slater quality basis set, plus two polarization functions (STO-TZ2P), within the generalized gradient approximation (GGA) according to the Perdew-Burke-Ernzerhof (PBE) exchange-correlation functional.^{66,67} This functional was chosen because of its performance on the description of similar clusters, allowing a direct comparison with other computational studies of related gold clusters.^{35,68-71} In addition, empirical corrections for dispersion interactions related to London forces were considered through the pairwise correction of Grimme (DFT-D3).⁷² Geometry optimizations were performed without any symmetry constraint via the analytical energy gradient method implemented by Versluis and Ziegler.⁷³ The frozen core approximation was applied to the $[1s^2-4f^{14}]$ shells for Au and W, $[1s^2]$ for C, and $[2s^2]$ for P, leaving the remaining electrons to be treated variationally. The optical properties were simulated by using the Van Leeuwen and Baerends functional (LB94),⁷⁴ known for its good performance in the study of excitation in ligand-protected clusters.⁷⁵⁻⁷⁹ Solvation effects were taken into account via a continuum solvation scheme given by the COSMO module from ADF to describe the screening effects from solvation, considering dichloromethane as the solvent.⁸⁰

6.3 Results and Discussion

The structure of the parent $[Au_{13}(\text{dppm})_6]^{5+}$ (**1**)⁴⁷ is of D_3 symmetry.⁵⁴ On the other hand, the isoelectronic clusters $[\text{M}@Au_{12}(\text{dppm})_6]^{q+}$ ($\text{M} = \text{Ru}$, $q = 3$; $\text{M} = \text{Rh}$, Ir , $q = 4$), recently characterized by Tsukuda and collaborators,⁸¹ feature a pseudo- T_h symmetry. Such a structural difference between strongly related clusters originates from the particular decorations of the dppm ligands. In the case of **1**, the D_3 structure is more favorable by 11.5 kcal/mol in

comparison to the pseudo- T_h arrangement. Interestingly, calculations on the $[M@Au_{12}(dppm)_6]^{q+}$ ($M = Ru, q = 3; M = Rh, Ir; q = 4$), species,⁸¹ found also a more favorable D_3 structure by 11.3, 17.8, and, 17.4 kcal/mol for $M = Ru, Rh$ and Ir , respectively, suggesting that the ligand arrangement can be modified by the nature of the counterions or in the course of the synthetic routes.

Our hypothetical neutral species **2** consists in a $W@Au_{12}$ core (the classical Pyykkö cluster), which is protected by six dppm units in such a way that twelve Au–P bonds are created, similarly as in the related homometallic **1**.⁴⁷ The D_3 structure is favored by 8.4 kcal/mol over pseudo- T_h one. Hence, hereafter we focus our discussion on the former arrangement. Two doped isomers can be obtained, namely isomer **I** and **II** (Figure 1), where the W atom occupies the center or one vertex of the icosahedron, respectively. Unsurprisingly, the hypothetical isomer **II** of **2** with the dopant atom located at the cage surface, namely $[Au@WAu_{11}(dppm)_6]$ (**2'**), is computed to be 118.2 kcal/mol higher in energy than isomer **I**, indicating that W largely prefers being placed at the center of the icosahedron, thus retaining the structural feature of the bare $[W@Au_{12}]$ parent cluster, for which the W-centered isomer is favored by 122.6 kcal/mol.^{59,60}

Table 1. Selected average metrical values of **1** and **2** (isomers I and II. Data for the T_1 excited states are also given.

		1 $M = Au$	1 Exp. ^a	2 I ^b $M = W$	2' II ^b $M = Au$	1 T_1 $M = Au$	2 T_1 $M = W$
$M_{cent-Au_{ico}}$	Average	2.869	2.832	2.806	2.855	2.899	2.801
	Standard Dev.	0.055	0.114	0.063	0.128	0.168	0.028
	<i>CShM</i>	0.315	0.568	0.207	0.668	1.096	0.052
Au_{ico-P}	Average	2.334	2.314	2.336	2.312	2.336	2.345
	Standard Dev.	0.009	0.033	0.022	0.023	0.014	0.011

^aExperimental results from reference ⁴⁷. ^bIsomers I and II.

Selected structural data for **1**, **2** and **2'** are summarized in Table 1. The calculated W– Au_{ico} distances range from 2.728 to 2.885 Å, with an average of 2.806 Å, similar to the average in **1** (calc. 2.869 Å; exp. 2.832 Å).⁴⁷ The Au_{ico} –P distances range between 2.314 to 2.368 Å, averaging to 2.336 Å, a value in line with that of **1** (calc. 2.334; exp. 2.314 Å). Structural deviations from a fully symmetric $M@Au_{12}$ icosahedron (I_h) were evaluated via the continuous-shape-measure (*CShM*) approach developed by Alvarez and coworkers.⁸²⁻⁸⁴ The X-ray structure of **1**, shows an Au_{13} core with a *CShM* value of 0.568. The corresponding value of the calculated structure is 0.315. These non-zero measures account for the I_h to D_3 lowering of symmetry

(Table S1, Annex). Interestingly, the CS_{hM} value of **2** is lower (0.207) indicative of a more symmetrical core than **1**.

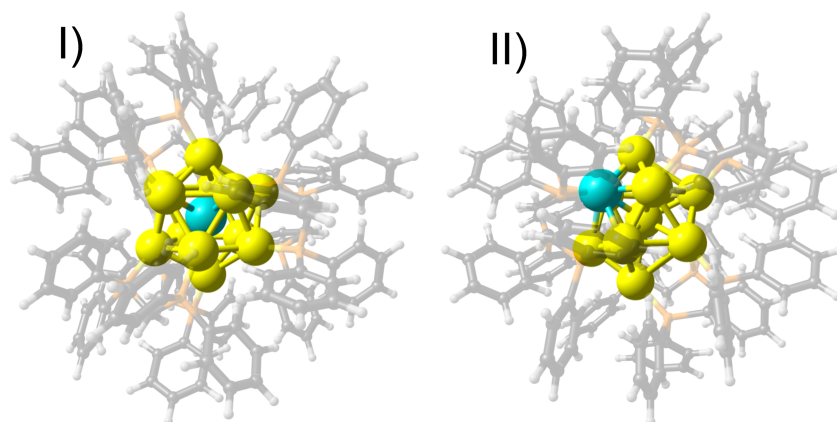


Figure 1. Optimized structures of **2** and **2'**, as endohedral- (I) and cage-doped (II) isomers of $[W@Au_{13}(dppm)_6]$. Color code: yellow Au, magenta W, orange P, black C, white H.

The computed HOMO-LUMO gap of **2** (1.24 eV) is somewhat smaller than that of the bare $[W@Au_{12}]$ cluster (1.87 eV),⁸⁵ as well as that of **1** (1.53 eV). The Kohn-Sham MO diagram of their metal cores (Figure 2) denotes the formation of 1P and 1D *superatomic* shells,^{86,87} of which the isosurfaces are plotted in Figure S1 (Annex). Consistently, **1** exhibits an 8-*ce* $1S^2 1P^6$ electronic configuration, with the 1P shell as the HOMOs, and the 1D shell as the LUMOs. In contrast, **2** exhibits an 18-*ce* $1S^2 1P^6 1D^{10}$ configuration, with the 1D shell as the HOMOs, except for the $1D_{22}$ orbital which lies within the 1P shell. In average, the 1D shell of **2** is made of 46.3% from W, 40.2% from the Au_{12} cage, and 12.5% from phosphine orbitals. The LUMO of **2** is a ligand-based orbital, the 2D orbitals lying at much higher energy. This situation is at variance with that in the 8-*ce* **1**, suggesting that the electronic excitation characteristics are of 1D→Ligand charge transfer nature in **2**, instead of 1P→1D in **1** and related clusters.^{75,88,89}

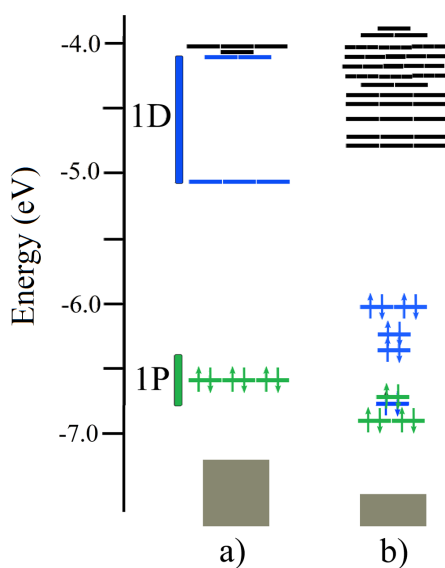


Figure 2. Kohn-Sham frontier orbital diagrams of **1** (a) and **2** (b). The 1P and 1D orbitals are in green and blue, respectively. Ligand-based orbitals are in black. Grey boxes represent the tops of the 5d(Au) blocks.

To further evaluate the bonding between the overall phosphine ligand shell and the [W@Au₁₂] core in **2**, the related interaction energy (ΔE_{int}) was calculated within the Morokuma–Ziegler energy decomposition analysis (EDA) scheme.⁹⁰⁻⁹² It amounts to -397.3 kcal/mol (Table 2). In comparison with **1** ($\Delta E_{\text{int}} = -1168.2$ kcal/mol), the interaction energy is sizably smaller. For a deeper bonding analysis, ΔE_{int} can be further decomposed in several contributions as follows:

$$\Delta E_{\text{disp}} = \Delta E_{\text{Pauli}} + \Delta E_{\text{elstat}} + \Delta E_{\text{orb}} + \Delta E_{\text{disp}}$$

The stabilizing terms are given by ΔE_{elstat} and ΔE_{orb} , which account for both the electrostatic and covalent character of the interaction. The repulsive ΔE_{Pauli} term accounts for the four-electron two-orbital interactions between occupied orbitals, which includes steric hindrance effects. In addition, the ΔE_{disp} term accounts for dispersion forces. In order to overcome basis set superposition error (BSSE) in the EDA analysis, the counterpoise method was employed. The various ΔE_{disp} components of **1** and **2** are given in Table 2).

In both clusters, the main character of the stabilizing interaction is electrostatic (55.8% and 67.0% for **1** and **2**, respectively). Whereas the electrostatic interaction is stronger in the case of **2** ($\Delta\Delta E_{\text{elstat}} = -136.1$ kcal/mol), the covalent interaction is significantly weaker ($\Delta\Delta E_{\text{orb}} = 453.0$ kcal/mol). In addition, the sizable increase of the steric repulsion in **2** with respect to **1** ($\Delta\Delta E_{\text{Pauli}} = 459.9$ kcal/mol), leads to a weaker metal-ligand bonding in the case of **2**.

Table 2. Energy decomposition analysis for the core-ligand interaction in **1** and **2**, and the relative difference between each term ($\Delta\Delta E$). Values in kcal/mol.

	1	2	$\Delta\Delta E$
ΔE_{Pauli}	1917.6	2377.5	459.9
ΔE_{elstat}	-1722.1 (55.8%)	-1858.2 (67.0%)	-136.1
ΔE_{orb}	-1254.3 (40.6%)	-801.3 (28.9%)	453.0
ΔE_{disp}	-109.4 (3.6%)	-115.2 (4.1%)	-5.8
ΔE_{int}	-1168.2	-397.27	770.9

The bonding scheme associated with the contribution of ΔE_{orb} was next evaluated by the Natural Orbitals for Chemical Valence extension of the EDA method (EDA-NOCV),⁹²⁻⁹⁵ revealing in- and out-flow of charges owing to bonding interaction. The relevant deformation densities obtained from the NOCV analysis exhibit a set of $\sigma(\text{P}) \rightarrow \text{W}@\text{Au}_{12}$ donation of **2** (Figure S2, Annex), leading to a net charge transfer of 0.79 e towards the core, as obtained from Hirshfeld charge analysis. For **1** parent the net charge transfer to the core is evaluated to 2.83 e, in line with the more relevant ΔE_{orb} component in this case. Moreover, in the case of the hypothetical isoelectronic dichloro $[\text{Os}@\text{Au}_{12}(\text{dppe})_5\text{Cl}_2]$ cluster,⁶² the core receives 0.23 e from the dppe shell, suggesting that 18-ce species are less prone to receive charge from the protecting layer. The weaker metal-ligand bonding in the case of 18-ce species is to be related to the lower accepting availability of the 6s peripheral AOs, due to their stronger involvement in the bonding with the encapsulated central atom. On the other hand, in the 8-ce cluster **1**, for instance, the vacant 1D orbitals of the metal core (left side of Scheme 1) are available to participate (to some extent) to the bonding with the phosphines, whereas in **2** (right side of Scheme 1) they participate to the W-Au bonding.

Optical properties were also computed to investigate the differences between the 8- and 18-ce species in order to evaluate the possible role in photoinduction applications. The simulated optical spectrum of **1** (Figure 3) is in agreement with a previous analysis.⁵⁴ It shows a strong absorption band at 437 nm, resulting from $1\text{P} \rightarrow \text{ligand}$ and $5d(\text{Au})\text{-block} \rightarrow 1\text{D}$ transitions, and a few weak absorptions ranging between 500–750 nm due to $1\text{P} \rightarrow 1\text{D}$ transitions, thus associated with charge transfers within the metal core.

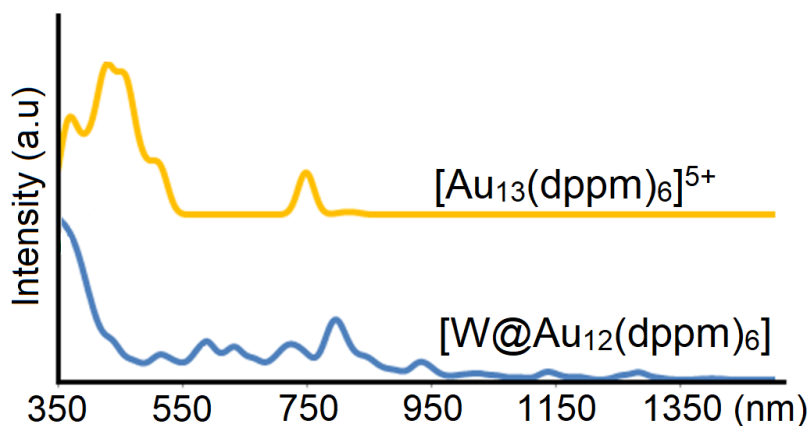


Figure 3. Simulated optical absorption spectra for $[\text{Au}_{13}(\text{dppm})_6]^{5+}$ (**1**), and $[\text{W}@\text{Au}_{12}(\text{dppm})_6]$ (**2**).

A different pattern is found in the simulated spectrum of **2** (Figure 3), which is composed of bands involving a manifold of core-to-ligand transitions in a wide range between 500–1350 nm, and not observed in **1**. This resulting wide absorption pattern suggests a useful approach for designing black absorbers, with the potential to enhance the efficiency of thin-film solar cells.⁹⁶⁻¹⁰⁰

Furthermore, the observed photoluminescence properties of the related cluster $[\text{Au}_{13}\text{Cl}_2(\text{dppe})_5]^{3+}$,^{53,56} encourage the evaluation those of the related clusters **1** and **2**. The emission of $[\text{Au}_{13}\text{Cl}_2(\text{dppe})_5]^{3+}$ is characterized as a triplet-singlet decay ($T_1 \rightarrow S_0$),⁵³ enabled upon excitation from two different excitation bands located at 490 and 360 nm, respectively,⁵⁶ and involving $1P \rightarrow 1D$ and $5d(\text{Au}) \rightarrow 1D$ character. Owing to these features, potential applications of $[\text{Au}_{13}\text{Cl}_2(\text{dppe})_5]^{3+}$ in singlet-oxygen sensitization have been suggested.⁵³ The calculated T_1 state of $[\text{Au}_{13}\text{Cl}_2(\text{dppe})_5]^{3+}$ ¹⁰¹ exhibits interesting geometrical changes denoted by the increase of the $\text{Au}_{\text{cent}}-\text{Au}(\text{Cl})$ distance from 2.534 to 2.592 Å (Figure 5), leading to a $T_1 \rightarrow S_0$ emission calculated at 809 nm (1.533 eV) in line to the value of 766 nm (1.619 eV) measured experimentally in acetonitrile by Konishi and Shichibu.⁵⁶ A larger distortion of the T_1 state is found in the case of **1** (Table 1 and Figure 4), which exhibits an elongated icosahedron with two particularly long $\text{Au}_{\text{cent}}-\text{Au}_{\text{ico}}$ distances (3.108 and 3.330 Å, respectively), leading to a large $CShM$ value of 1.096. This distortion induces a stabilization of some of the of 1D components and a destabilization of one 1P orbital (Figure 5), leading to a very low energy $T_1 \rightarrow S_0$ emission obtained at 3115 nm (0.398 eV). Note that **1** has been ascribed as a non-luminescent species,⁵⁴ suggesting that the very low energy of the calculated transition is the reason for this non-luminescent behaviour.

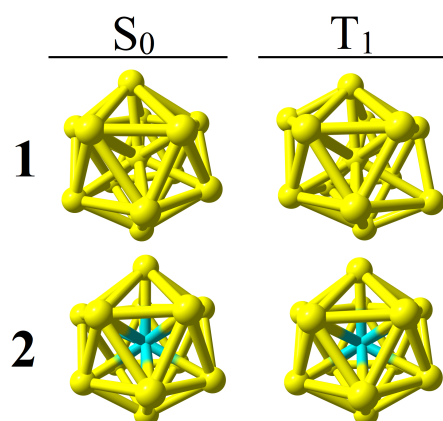


Figure 4. Relaxed structures of S_0 and T_1 states of **1** and **2**, denoting the core structure by removing ligands for clarity.

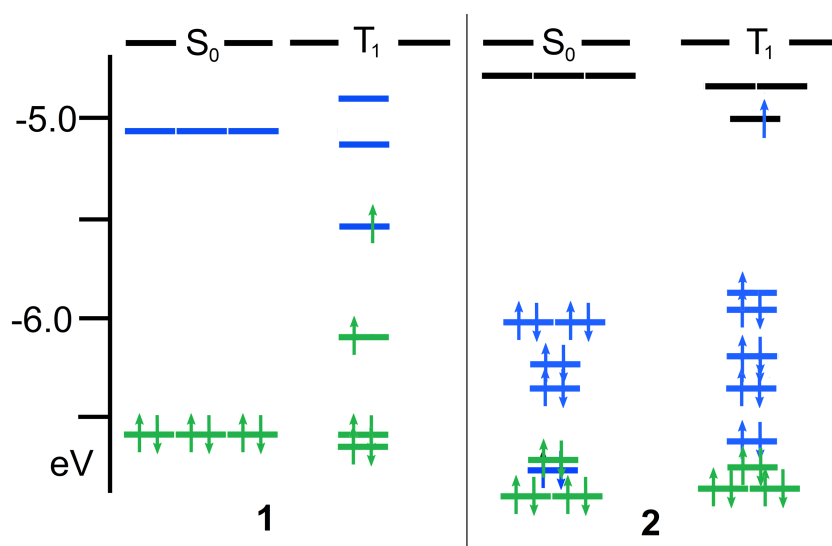


Figure 5. Electronic structures at S_0 and T_1 states of **1** and **2**. 1P and 1D shells are in green and blue, respectively.

Conversely, the T_1 state of **2** exhibits a much more symmetrical cage ($CShM = 0.052$), with $Au_{cent}-Au_{ico}$ distances that are similar to that in the S_0 ground state (S_0) (Table 1 and Figure 4). For example, the average $Au_{cent}-Au_{ico}$ distances in T_1 (2.801 Å) are similar to those computed in S_0 (2.806 Å). Thus, the 1D \rightarrow ligand transitions change to a lesser extent the geometry of the metal core in the 18-*ce* species **2**, in contrast to the 1P \rightarrow 1D transitions in the 8-*ce* cluster **1**. The resulting electronic structure of the T_1 state of **2** involves a slight stabilization of some ligand-based orbitals and a destabilization of the 1D shell, leading to a calculated $T_1\rightarrow S_0$ emission at 1884 nm (0.657 eV). Let us remind that the evaluation of the $Au_{25}(SR)_{18}^-$ emission processes also involves structural distortions and subsequent electronic structure variations at the

emissive states.^{102,103} The current approach for calculating emission energies has been employed in related species leading to a good agreement with experimental data.^{79,104,105}

Going back to the two simplified diagrams sketched in Scheme 1, obviously they describe two different situations that should be considered as two limit cases to which **1** and **2** are approaching, respectively, and there should be a continuum between these two cases. We have explored this continuum by comparing the whole series $[M@Au_{12}(dppm)_6]^{q+}$ ($M = Au, Pt, Ir, Os, Re$ and W , with $q = 5, 4, 3, 2, 1, 0$, respectively). It was first checked that all these species are global energy minima with the heteroatom at the center of cluster and the D_3 ligand arrangement (Table S2, Annex). The corresponding MO diagrams of the series of clusters are shown in Figure 6.

In order to get a more quantitative view of the involvement of the nd AOs of M within the series, we have calculated the nd NBO population of M in both the bare $[M@Au_{12}]^{q+}$ and ligated $[M@Au_{12}(dppm)_6]^{q+}$ clusters (Table 3). Looking first at the bare cluster series, one can see that it is close to 10 for $M = Au$, illustrating the limit case on the right side of Scheme 1. When going from $M = Au$ to $M = W$, it decreases monotonically from 9.90 (Au) to 7.97 (W), the later value indicating substantial mixing of the nd AOs of W with the 1D level of the empty cage (right side of Scheme 1). A similar trend is found for the ligated $[M@Au_{12}(dppm)_6]^{q+}$ series (Table 3), in which the nd NBO population decreases monotonically from 9.75 (Au) to 7.34 (W).

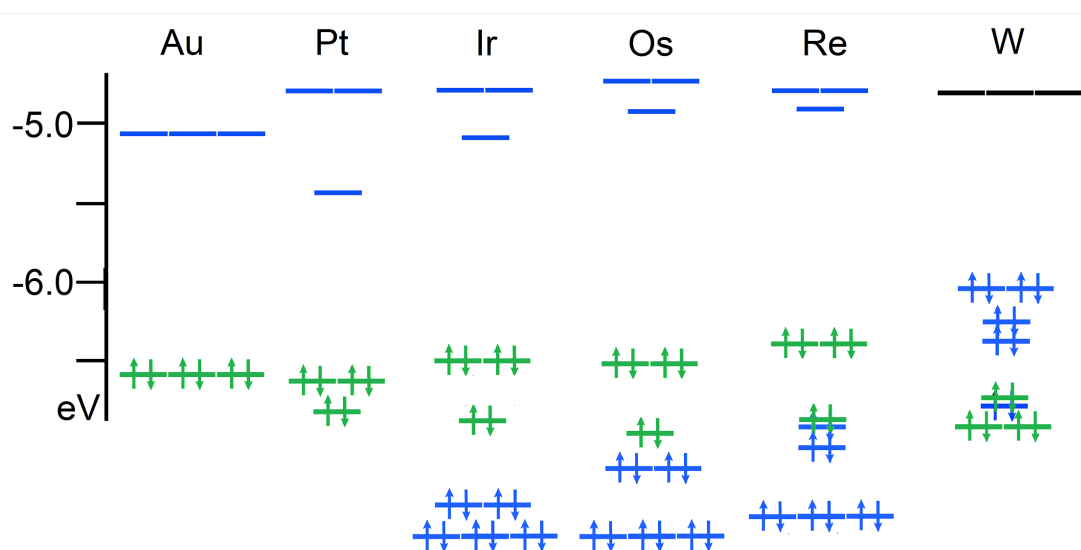


Figure 6. Electronic structures for $[Au_{13}(dppm)_6]^{5+}$ (Au), and $[M@Au_{13}(dppm)_6]^{q+}$ with $M = Pt, Ir, Os, Re,$ and W . 1P and 1D shells are in green and blue, respectively.

Table 3. Computed *nd* NBO population of M in the $[\text{MAu}_{12}]^{q+}$ and $[\text{MAu}_{12}\text{dppm}_6]^{q+}$ series. M = Au (q = 5), Pt (q = 4), Ir (q = 3), Os (q = 2), Re (q = 1), W (q = 0).

$[\text{MAu}_{12}]^{q+}$						
M	Au	Pt	Ir	Os	Re	W
	9.90	9.65	9.31	8.92	8.48	7.97
$[\text{MAu}_{12}\text{dppm}_6]^{q+}$						
M	Au	Pt	Ir	Os	Re	W
	9.75	9.50	8.89	8.31	7.88	7.34

6.4 Conclusions

In summary, we have explored in this chapter the possible existence of the 18-cluster electron species $[\text{W@Au}_{12}(\text{dppm})_6]$ based on the central doping of the 8-*ce* $[\text{Au}_{13}(\text{dppm})_6]^{5+}$ parent species, with an endohedral early transition-metal atom providing available extra electrons. The proposed structure is strongly related to the seminal W@Au_{12} bare cluster, with a closed-shell electronic configuration $1\text{S}^2 1\text{P}^6 1\text{D}^{10}$, leading to different properties and behaviours in comparison to the $1\text{S}^2 1\text{P}^6 1\text{D}^0$ parent. Though the role of the ligand-protected shell in the proposed heterometallic cluster is not so prominent in comparison to the homometallic parent cluster, it contributes to the stabilization of the structure. Moreover, the 18-*ce* count favors the inclusion of W at the center of the icosahedron, displaying a frontier orbital character of 1D (HOMOs) and ligand-based orbitals (LUMOs), contrasting to the 8-*ce* parent. This implies that the electronic excitation characteristics involve $1\text{D} \rightarrow \text{ligand}$ charge transfer rather than $1\text{P} \rightarrow 1\text{D}$ charge transfer for the latter.

A characteristic pattern is found for the calculated optical spectrum of $[\text{W@Au}_{12}(\text{dppm})_6]$, showing several absorption peaks in a wide range between 500–1350 nm, which involve a manifold of core-to-ligand transitions as a result of the 1D^{10} -ligand-frontier orbital characteristics of its electronic structure. Particularly, the wide absorption from 300 to 950 nm is of interest for envisaging further black absorbers enabling light to be absorbed in a wide range. Further evaluation of related species involving group 11 to 6 metals denotes a continuum between Au and W, with a breaking point that could be tentatively situated between M = Pt (8-*ce*) and M = Ir.⁶² This should encourage further synthetic exploration for this class of *superatoms* in fully phosphine-protected structures.

6.5 References

- 1 Yeh, Y. -C.; Creran, B.; Rotello, V. M. Gold nanoparticles: preparation, properties, and applications in bionanotechnology. *Nanoscale* **2012**, *4*, 1871–1880.
- 2 Xu, L.; Cao, Y.; Hong, S.; Kuang, Y.; Liu, M.; Liu, A.; Zhang, Y.; Pei, R. Facile

- Synthesis of Water-Dispersed Photoluminescent Gold (I)-Alkanethiolate Nanoparticles via Aggregation-Induced Emission and Their Application in Cell Imaging. *ACS Appl. Nano Mater.* **2018**, *1*, 6641–6648.
- 3 Mathew, M. S.; Joseph, K. Green synthesis of gluten-stabilized fluorescent gold quantum clusters: application as turn-on sensing of human blood creatinine. *ACS Sustain. Chem. Eng.* **2017**, *5*, 4837–4845.
 - 4 Chen, L.-Y.; Wang, C. -W.; Yuan, Z.; Chang, H. -T. Fluorescent gold nanoclusters: recent advances in sensing and imaging. *Anal. Chem.* **2015**, *87*, 216–229.
 - 5 Corma, A.; Garcia, H. Supported gold nanoparticles as catalysts for organic reactions. *Chem. Soc. Rev.* **2008**, *37*, 2096–2126
 - 6 Yamazoe, S.; Koyasu, K.; Tsukuda, T. Nonscalable oxidation catalysis of gold clusters. *Acc. Chem. Res.* **2014**, *47*, 816–824.
 - 7 Xu, H.; Cheng, D.; Gao, Y.; Zeng, X. C. Assessment of catalytic activities of gold nanoclusters with simple structure descriptors. *ACS Catal.* **2018**, *8*, 9702–9710.
 - 8 Deepak, F. L. *Metal Nanoparticles and Clusters*, Springer International Publishing, Cham, **2018**.
 - 9 Zhang, J.; Li, Z.; Zheng, K.; Li, G. Synthesis and characterization of size-controlled atomically precise gold clusters. *Phys. Sci. Rev.* **2018**, *3*, 20170083.
 - 10 Rus, Y. B.; Bosmi, M.; Maisonneuve, S.; Guérineau, V.; Noël, V.; Courty, A.; Miomandre, F. Versatile one-pot synthesis of gold nanoclusters and nanoparticles using 3, 6-(dipyridin-2-yl)-(1, 2, 4, 5)-tetrazine. *RSC Adv.* **2021**, *11*, 7043–7050.
 - 11 Huang, Z.; Ishida, Y.; Yonezawa, T. Basic $[\text{Au}_{25}(\text{SCH}_2\text{CH}_2\text{Py})_{18}]^- \cdot \text{Na}^+$ Clusters: Synthesis, Layered Crystallographic Arrangement, and Unique Surface Protonation. *Angew. Chem. Int. Ed.* **2019**, *58*, 13411–13415.
 - 12 Lei, Z.; Li, J.; Nan, Z.; Jiang, Z.; Wang, Q.; Cluster From Cluster: A Quantitative Approach to Magic Gold Nanoclusters $[\text{Au}_{25}(\text{SR})_{18}]^-$. *Angew. Chem. Int. Ed.* **2021**, *60*, 14415–14419.
 - 13 Mingos, D. M. P. Gold Clusters, Colloids and Nanoparticles I. *Struct. Bond.* **2014**, *161*, 1–278.
 - 14 Chakraborty, I.; Pradeep, T. Atomically precise clusters of noble metals: emerging link between atoms and nanoparticles. *Chem. Rev.* **2017**, *117*, 8208–8271.
 - 15 Khatun, E.; Pradeep, T. New routes for multicomponent atomically precise metal nanoclusters. *ACS Omega* **2021**, *6*, 1–16.
 - 16 Gam, F.; Wei, J.; Kahlal, S.; Saillard, J. -Y.; Halet, J. -F. Electron Counting in Ligated

- High Nuclearity Late Transition Metal Clusters. In: 50th Anniversary of Electron Counting Paradigms for Polyhedral Molecules – Historical and Recent Developments. *Struct. Bond.* **2021**, *188*, 69–102.
- 17 Burda, C.; Chen, X.; Narayanan, R.; El-Sayed, M. A. Chemistry and properties of nanocrystals of different shapes. *Chem. Rev.* **2005**, *105*, 1025–1102.
- 18 Kundu, S.; Patra, A. Nanoscale strategies for light harvesting. *Chem. Rev.* **2017**, *117*, 712–757.
- 19 Jin, R.; Zeng, C.; Zhou, M.; Chen, Y. Atomically precise colloidal metal nanoclusters and nanoparticles: fundamentals and opportunities. *Chem. Rev.* **2016**, *116*, 10346–10413.
- 20 Suchomel, P.; Kvitek, L.; Prucek, R.; Panacek, A.; Halder, A.; Vajda, S.; Zboril, R. Simple size-controlled synthesis of Au nanoparticles and their size-dependent catalytic activity. *Sci. Rep.* **2018**, *8*, 4589.
- 21 Wang, S.; Meng, X.; Das, A.; Li, T.; Song, Y.; Cao, T.; Zhu, X.; Zhu, M.; Jin, R. A 200-fold Quantum Yield Boost in the Photoluminescence of Silver-Doped $\text{Ag}_x\text{Au}_{25-x}$ Nanoclusters: The 13 th Silver Atom Matters. *Angew. Chem. Int. Ed.* **2014**, *126*, 2408–2412.
- 22 Niihori, Y.; Matsuzaki, M.; Pradeep, T.; Negishi, Y. Separation of precise compositions of noble metal clusters protected with mixed ligands. *J. Am. Chem. Soc.* **2013**, *135*, 4946–4949.
- 23 Jin, R.; Nobusada, K. Doping and alloying in atomically precise gold nanoparticles. *Nano Res.* **2014**, *7*, 285–300.
- 24 Liao, L.; Zhou, S.; Dai, Y.; Liu, L.; Yao, C.; Fu, C.; Yang, J.; Wu, Z. Mono-Mercury Doping of Au_{25} and the HOMO/LUMO Energies Evaluation Employing Differential Pulse Voltammetry. *J. Am. Chem. Soc.* **2015**, *137*, 9511–9514.
- 25 Jiang, D.; Whetten, R. L. Magnetic doping of a thiolated-gold superatom: First-principles density functional theory calculations. *Phys. Rev. B* **2009**, *80*, 115402.
- 26 Zhu, M.; Aikens, C. M.; Hendrich, M. P.; Gupta, R.; Qian, H.; Schatz, G. C.; Jin, R. Reversible Switching of Magnetism in Thiolate-Protected Au_{25} Superatoms. *J. Am. Chem. Soc.* **2009**, *131*, 2490–2492.
- 27 Hirai, H.; Takano, S.; Nakamura, T.; Tsukuda, T. Understanding Doping Effects on Electronic Structures of Gold Superatoms: A Case Study of Diphosphine-Protected $\text{M}@\text{Au}_{12}$ ($\text{M} = \text{Au}, \text{Pt}, \text{Ir}$). *Inorg. Chem.* **2020**, *59*, 17889–17895.
- 28 Jiang, D.; Dai, S. From Superatomic $\text{Au}_{25}(\text{SR})_{18}^-$ to Superatomic $\text{M}@\text{Au}_{24}(\text{SR})_{18}^q$ Core–Shell Clusters. *Inorg. Chem.* **2009**, *48*, 2720–2722.

- 29 Zhou, M.; Qian, H.; Sfeir, M. Y.; Nobusada, K.; Jin, R. Effects of single atom doping on the ultrafast electron dynamics of $M_1Au_{24}(SR)_{18}$ ($M = Pd, Pt$) nanoclusters. *Nanoscale* **2016**, *8*, 7163–7171.
- 30 Beletskaya, A. V.; Pichugina, D. A.; Shestakov, A. F.; Kuz'menko, N. E. Formation of H_2O_2 on Au_{20} and $Au_{19}Pd$ Clusters: Understanding the Structure Effect on the Atomic Level. *J. Phys. Chem. A* **2013**, *117*, 6817–6826.
- 31 Polynskaya, Y. G.; Pichugina, D. A.; Kuz'menko, N. E. Correlation between electronic properties and reactivity toward oxygen of tetrahedral gold–silver clusters. *Comput. Theor. Chem.* **2015**, *1055*, 61–67.
- 32 Cortés-Arriagada, D.; Toro-Labbé, A. Insights into the use of $Au_{19}Cu$ and $Au_{19}Pd$ clusters for adsorption of trivalent arsenic. *Theor. Chem. Acc.* **2016**, *135*, 52.
- 33 Cortés-Arriagada, D.; Oyarzún, M. P.; Sanhueza, L.; Toro-Labbé, A. Binding of Trivalent Arsenic onto the Tetrahedral Au_{20} and $Au_{19}Pt$ Clusters: Implications in Adsorption and Sensing. *J. Phys. Chem. A* **2015**, *119*, 6909–6918.
- 34 Gam, F.; Chantrenne, I.; Kahlal, S.; Chiu, T. H.; Liao, J. H.; Liu, C. W.; Saillard, J. -Y. Alloying dichalcogenolate-protected Ag_{21} eight-electron nanoclusters: a DFT investigation. *Nanoscale* **2022**, *14*, 196–203.
- 35 Jiang, D. The expanding universe of thiolated gold nanoclusters and beyond. *Nanoscale* **2013**, *5*, 7149–7160.
- 36 Qian, H.; Jiang, D.; Li, G.; Gayathri, C.; Das, A.; Gil, R. R.; Jin, R. Monoplatinum doping of gold nanoclusters and catalytic application. *J. Am. Chem. Soc.* **2012**, *134*, 16159–16162.
- 37 Oro, L. A.; Braunstein, P.; Raithby, P. R. *Metal clusters in chemistry*, Wiley-vch Weinheim, Germany, **1999**, vol. 3.
- 38 Daniel, M. -C.; Astruc, D. Gold nanoparticles: assembly, supramolecular chemistry, quantum-size-related properties, and applications toward biology, catalysis, and nanotechnology. *Chem. Rev.* **2004**, *104*, 293–346.
- 39 Bergeron, D. E. Al cluster superatoms as halogens in polyhalides and as alkaline earths in iodide salts. *Science* **2005**, *307*, 231–235.
- 40 Homberger, M.; Simon, U. On the application potential of gold nanoparticles in nanoelectronics and biomedicine. *Philos. Trans. A. Math. Phys. Eng. Sci.* **2010**, *368*, 1405–1453.
- 41 Yang, Y.; Chen, S. Surface manipulation of the electronic energy of subnanometer-sized gold clusters: an electrochemical and spectroscopic investigation. *Nano Lett.* **2003**, *3*,

- 75–79.
- 42 Zhu, Y.; Qian, H.; Jin, R. Catalysis opportunities of atomically precise gold nanoclusters. *J. Mater. Chem.* **2011**, *21*, 6793–6799.
- 43 Jin, R. Atomically precise metal nanoclusters: stable sizes and optical properties. *Nanoscale* **2015**, *7*, 1549–1565.
- 44 Li, G.; Jin, R. Atomically precise gold nanoclusters as new model catalysts. *Acc. Chem. Res.* **2013**, *46*, 1749–1758.
- 45 Raut, S.; Chib, R.; Rich, R.; Shumilov, D.; Gryczynski, Z.; Gryczynski, I. Polarization properties of fluorescent BSA protected Au₂₅ nanoclusters. *Nanoscale* **2013**, *5*, 3441–3446.
- 46 Russier-Antoine, I.; Bertorelle, F.; Vojkovic, M.; Rayane, D.; Salmon, E.; Jonin, C.; Dugourd, P.; Antoine, R.; Brevet, P. -F. Non-linear optical properties of gold quantum clusters. The smaller the better. *Nanoscale* **2014**, *6*, 13572–13578.
- 47 van der Velden, J. W. A.; Vollenbroek, F. A.; Bour, J. J.; Beurskens, P. T.; Smits, J. M. M.; Bosnian, W. P. Gold clusters containing bidentate phosphine ligands. Preparation and X-Ray structure investigation of [Au₅(dppmH)₃(dppm)](NO₃)₂ and [Au₁₃(dppmH)₆](NO₃)_n. *Recl. des Trav. Chim. des Pays-Bas* **1981**, *100*, 148–152.
- 48 Teo, B. K.; Zhang, H. Cluster of clusters. Structure of a new cluster [(*p*-Tol₃P)₁₀Au₁₃Ag₁₂Cl₇](SbF₆)₂ containing a nearly staggered-eclipsed-staggered metal configuration and five doubly-bridging ligands. *Inorg. Chem.* **1991**, *30*, 3115–3116.
- 49 Mingos, D. M. P.; Historical Introduction to Gold Colloids, Clusters and Nanoparticles. *Struct. Bond.* **2014**, *161*, 1–47.
- 50 Briant, C. E.; Theobald, B. R.; White, J. W.; Bell, L. K.; Mingos, D. M. P.; Welch, A. J. Synthesis and X-ray Structural Characterization of The Centred Icosahedral Gold Cluster Compound [Au₁₃(PMe₂Ph)₁₀Cl₂](PF₆)₃; The Realization of a Theoretical Prediction. *J. Chem. Soc. Chem. Commun.* **1981**, 201–202.
- 51 Wang, W.; Murray, R. W. Reaction of Triphenylphosphine with Phenylethanethiolate-Protected Au₃₈ Nanoparticles. *Langmuir* **2005**, *21*, 7015–7022.
- 52 McKenzie, L. C.; Zaikova, T. O.; Hutchison, J. E. Structurally Similar Triphenylphosphine-Stabilized Undecagolds, Au₁₁(PPh₃)₇Cl₃ and [Au₁₁(PPh₃)₈Cl₂]Cl, Exhibit Distinct Ligand Exchange Pathways with Glutathione. *J. Am. Chem. Soc.* **2014**, *136*, 13426–13435.
- 53 Zhang, J.; Zhou, Y.; Zheng, K.; Abroshan, H.; Kauffman, D. R.; Sun, J.; Li, G. Diphosphine-Induced Chiral Propeller Arrangement of Gold Nanoclusters for Singlet

- Oxygen Photogeneration. *Nano Res.* **2017**, 1–12.
- 54 Zhang, S.-S.; Feng, L.; Senanayake, R. D.; Aikens, C. M.; Wang, X.-P.; Zhao, Q.-Q.; Tung, C.-H.; Sun, D. Diphosphine-Protected Ultrasmall Gold Nanoclusters: Opened Icosahedral Au₁₃ and Heart-Shaped Au₈ Clusters. *Chem. Sci.* **2018**, *9*, 1251–1258.
- 55 Jin, S.; Du, W.; Wang, S.; Kang, X.; Chen, M.; Hu, D.; Chen, S.; Zou, X.; Sun, G.; Zhu, M. Thiol-induced synthesis of phosphine-protected gold nanoclusters with atomic precision and controlling the structure by ligand/metal engineering. *Inorg. Chem.* **2017**, *56*, 11151–11159.
- 56 Shichibu, Y.; Konishi, K. HCl-Induced Nuclearity Convergence in Diphosphine-Protected Ultrasmall Gold Clusters: A Novel Synthetic Route to “Magic-Number” Au₁₃ Clusters. *Small* **2010**, *6*, 1216–1220.
- 57 Walter, M.; Akola, J.; Lopez-Acevedo, O.; Jadzinsky, P. D.; Calero, G.; Ackerson, C. J. Whetten, R. L.; Grönbeck, H.; Häkkinen, H. A Unified View of Ligand-protected Gold Clusters as Superatom Complexes. *Proc. Natl. Acad. Sci. USA* **2008**, *105*, 9157–9162.
- 58 Häkkinen, H. Atomic and electronic structure of gold clusters: understanding flakes, cages and superatoms from simple concepts. *Chem. Soc. Rev.* **2008**, *37*, 1847–1859.
- 59 Li, X.; Kiran, B.; Li, J.; Zhai, H. -J.; Wang, L. -S. Experimental Observation and Confirmation of Icosahedral W@Au₁₂ and Mo@Au₁₂ Molecules. *Angew. Chem. Int. Ed.* **2002**, *41*, 4786–4789.
- 60 Autschbach, J.; Hess, B. A.; Johansson, M. P.; Neugebauer, J.; Patzschke, M.; Pyykkö, P.; Reiher, M.; Sundholm, D. Properties of WAu₁₂. *Phys. Chem. Chem. Phys.* **2004**, *6*, 11–22.
- 61 Pyykkö, P.; Runeberg, N. Icosahedral WAu₁₂: A Predicted Closed-Shell Species, Stabilized by Auophilic Attraction and Relativity and in Accord with the 18-Electron Rule. *Angew. Chem. Int. Ed.* **2002**, *41*, 2174–2176.
- 62 Wei, J.; Rodríguez-Kessler, P. L.; Halet, J. -F.; Kahlal, S.; Saillard, J. -Y.; Muñoz-Castro, A. On Heteronuclear Isoelectronic Alternatives to [Au₁₃(dppe)₅Cl₂]³⁺: Electronic and Optical Properties of the 18-Electron Os@[Au₁₂(dppe)₅Cl₂] Cluster from Relativistic Density Functional Theory Computations. *Inorg. Chem.* **2021**, *60*, 8173–8180.
- 63 Dyllal, K. G.; Fægri, K. *Introduction to Relativistic Quantum Chemistry*, Oxford University Press, New York, **2007**.
- 64 Amsterdam Density Functional (ADF) Code, Vrije Universiteit: Amsterdam, The Netherlands. <http://www.scm.com>.
- 65 van Lenthe, E.; Baerends, E. -J. J.; Snijders, J. G. Relativistic total energy using regular

- approximations. *J. Chem. Phys.* **1994**, *101*, 9783.
- 66 Perdew, J. P.; Burke, K.; Wang, Y. Generalized gradient approximation for the exchange-correlation hole of a many-electron system. *Phys. Rev. B* **1996**, *54*, 16533–16539.
- 67 Perdew, J. P.; Burke, K.; Ernzerhof, M. Generalized gradient approximation made simple. *Phys. Rev. Lett.* **1997**, *78*, 1396–1396.
- 68 Lopez-Acevedo, O.; Akola, J.; Whetten, R. L.; Grönbeck, H.; Häkkinen, H. Structure and Bonding in the Ubiquitous Icosahedral Metallic Gold Cluster Au₁₄₄(SR)₆₀. *J. Phys. Chem. C* **2009**, *113*, 5035–5038.
- 69 Akola, J.; Walter, M.; Whetten, R. L.; Häkkinen, H.; Grönbeck, H. On the Structure of Thiolate-Protected Au₂₅. *J. Am. Chem. Soc.* **2008**, *130*, 3756–3757.
- 70 Akola, J.; Kacprzak, K. A.; Lopez-Acevedo, O.; Walter, M.; Grönbeck, H.; Häkkinen, H. Thiolate-Protected Au₂₅ Superatoms as Building Blocks: Dimers and Crystals. *J. Phys. Chem. C* **2010**, *114*, 15986–15994.
- 71 Jiang, D.; Kühn, M.; Tang, Q.; Weigend, F. Superatomic orbitals under spin–orbit coupling. *J. Phys. Chem. Lett.* **2014**, *5*, 3286–3289.
- 72 Grimme, S. Density functional theory with London dispersion corrections. *Wiley Interdiscip. Rev. Comput. Mol. Sci.* **2011**, *1*, 211–228.
- 73 Versluis, L.; Ziegler, T. The determination of molecular structures by density functional theory. The evaluation of analytical energy gradients by numerical integration. *J. Chem. Phys.* **1988**, *88*, 322–328.
- 74 van Leeuwen, R.; Baerends, E. J. Exchange-correlation potential with correct asymptotic behavior. *Phys. Rev. A* **1994**, *49*, 2421–2431.
- 75 Aikens, C. M. Effects of Core Distances, Solvent, Ligand, and Level of Theory on the TDDFT Optical Absorption Spectrum of the Thiolate-Protected Au₂₅ Nanoparticle. *J. Phys. Chem. A* **2009**, *113*, 10811–10817.
- 76 Guidez, E. B.; Aikens, C. M. Quantum mechanical origin of the plasmon: from molecular systems to nanoparticles. *Nanoscale* **2014**, *6*, 11512–11527.
- 77 Durante, N.; Fortunelli, A.; Broyer, M.; Stener, M. Optical properties of Au nanoclusters from TD-DFT calculations. *J. Phys. Chem. C* **2011**, *115*, 6277–6282.
- 78 Bae, G.-T.; Aikens, C. M. Time-dependent density functional theory studies of optical properties of Au nanoparticles: Octahedra, truncated octahedra, and icosahedra. *J. Phys. Chem. C* **2015**, *119*, 23127–23137.
- 79 Mauro, P. Ai, M.; Danopoulos, A. A.; Muñoz-Castro, A.; Braunstein, P. Dual Emission

- of a Cyclic Hexanuclear Gold(I) Complex. Interplay between Au₃ and Au₂ Ligand-Supported Luminophores. *J. Phys. Chem. C* **2019**, *123*, 915–921.
- 80 Klamt, A.; Jonas, V. Treatment of the outlying charge in continuum solvation models. *J. Chem. Phys.* **1996**, *105*, 9972.
- 81 Takano, S.; Hirai, H.; Nakashima, T.; Iwasa, T.; Taketsugu, T.; Tsukuda, T. Photoluminescence of Doped Superatoms M@Au₁₂ (M = Ru, Rh, Ir) Homoleptically Capped by (Ph₂)PCH₂P(Ph₂): Efficient Room-Temperature Phosphorescence from Ru@Au₁₂. *J. Am. Chem. Soc.* **2021**, *143*, 10560–10564.
- 82 Ruiz-Martínez, A.; Casanova, D.; Alvarez, S. Polyhedral Structures with an Odd Number of Vertices: Nine-Coordinate Metal Compounds. *Chem. Eur. J.* **2008**, *14*, 1291–1303.
- 83 Alvarez, S.; Alemany, P.; Casanova, D.; Cirera, J.; Llunell, M.; Avnir, D. Shape maps and polyhedral interconversion paths in transition metal chemistry. *Coord. Chem. Rev.* **2005**, *249*, 1693–1708.
- 84 Cirera, J.; Ruiz, E.; Alvarez, S. Continuous shape measures as a stereochemical tool in organometallic chemistry. *Organometallics* **2005**, *24*, 1556–1562.
- 85 Muñoz-Castro, A. Golden Endohedral Main-Group Clusters, [E@Au₁₂]^{q-}: Theoretical Insights Into the 20-e Principle. *J. Phys. Chem. Lett.* **2013**, *4*, 3363–3366.
- 86 Akola, J.; Kacprzak, K. A.; Lopez-Acevedo, O.; Walter, M.; Grönbeck, H.; Häkkinen, H. Thiolate-Protected Au₂₅ Superatoms as Building Blocks: Dimers and Crystals. *J. Phys. Chem. C* **2010**, *114*, 15986–15994.
- 87 *Superatoms: Principles, Synthesis and Applications*, Jena, P.; Sun, Q., Eds., John Wiley & Sons, **2022**.
- 88 Kang, X.; Chong, H.; Zhu, M. Au₂₅(SR)¹⁸⁻: The Captain of The Great Nanocluster Ship. *Nanoscale* **2018**, *10*, 10758–10834.
- 89 Zhu, M.; Aikens, C. M.; Hollander, F. J.; Schatz, G. C., Jin, R. Correlating the Crystal Structure of A Thiol-Protected Au₂₅ Cluster and Optical Properties. *J. Am. Chem. Soc.* **2008**, *130*, 5883–5885.
- 90 Morokuma, K. Molecular Orbital Studies of Hydrogen Bonds. III. C=O···H–O Hydrogen Bond in H₂CO···H₂O and H₂CO···₂H₂O. *J. Chem. Phys.* **1971**, *55*, 1236–1244.
- 91 te Velde, G.; Bickelhaupt, F. M.; van Gisbergen, S. J. A.; Guerra, C. F.; Baerends, E. J.; Snijders, J. G.; Ziegler, T. Chemistry with ADF. *J. Comput. Chem.* **2001**, *22*, 931–967.
- 92 Ziegler, T.; Rauk, A. On the calculation of bonding energies by the Hartree Fock Slater method. *Theor. Chim. Acta* **1977**, *46*, 1–10.

- 93 Frenking, G.; Bickelhaupt, M.; Matthias Bickelhaupt, F. in *The Chemical Bond*, Wiley-VCH Verlag GmbH & Co. KGaA, Weinheim, Germany, **2014**, pp. 121–157.
- 94 Michalak, A.; DeKock, R. L.; Ziegler, T. Bond multiplicity in transition-metal complexes: applications of two-electron valence indices. *J. Phys. Chem. A* **2008**, *112*, 7256–7263.
- 95 Nalewajski, R. F.; Mrozek, J.; Michalak, A. Two-electron valence indices from the Kohn-Sham orbitals. *Int. J. Quantum Chem.* **1997**, *61*, 589–601.
- 96 Hao, Y.; Yang, S.; Li, Z.; Wang, X.; Zhang, J.; Liao, Y.; Li, D. Ultrabroadband metal-black absorbers and the performance simulations based on a three-dimensional cluster-structure model. *Opt. Express* **2021**, *29*, 8510.
- 97 Browning, C.; Hudson, J. M.; Reinheimer, E. W.; Kuo, F. -L.; McDougald, R. N.; Raba , H.; Pan, H.; Bacs , J.; Wang, X.; Dunbar, K. R.; Shepherd, N. D.; Omary, M. A. Synthesis, Spectroscopic Properties, and Photoconductivity of Black Absorbers Consisting of Pt(Bipyridine)(Dithiolate) Charge Transfer Complexes in the Presence and Absence of Nitrofluorenone Acceptors. *J. Am. Chem. Soc.* **2014**, *136*, 16185–16200.
- 98 Kinoshita, T.; Fujisawa, J.; Nakazaki, J.; Uchida, S.; Kubo, T.; Segawa, H. Enhancement of near-IR photoelectric conversion in dye-sensitized solar cells using an osmium sensitizer with strong spin-forbidden transition. *J. Phys. Chem. Lett.* **2012**, *3*, 394–398.
- 99 Altobello, S.; Argazzi, R.; Caramori, S.; Contado, C.; Da Fr , S.; Rubino, P.; Chon , C.; Larramona, G.; Bignozzi, C. A. Sensitization of Nanocrystalline TiO₂ with Black Absorbers Based on Os and Ru Polypyridine Complexes. *J. Am. Chem. Soc.* **2005**, *127*, 15342–15343.
- 100 Kinoshita, T.; Nonomura, K.; Joong Jeon, N.; Giordano, F.; Abate, A.; Uchida, S.; Kubo, T.; Il Seok, S.; Nazeeruddin, M. K.; Hagfeldt, A.; Gr tzel, M.; Segawa, H. Spectral splitting photovoltaics using perovskite and wideband dye-sensitized solar cells. *Nat. Commun.* **2015**, *6*, 8834.
- 101 Mu oz-Castro, A. Potential of N-heterocyclic Carbene Derivatives from Au₁₃(dppe)₅Cl₂ Gold Superatoms. Evaluation of Electronic, Optical and Chiroptical Properties from Relativistic DFT. *Inorg. Chem. Front.* **2019**, *6*, 2349–2358.
- 102 Weerawardene, K. L. D. M.; Aikens, C. M. Theoretical Insights into the Origin of Photoluminescence of Au₂₅(SR)₁₈[−] Nanoparticles. *J. Am. Chem. Soc.* **2016**, *138*, 11202–11210.
- 103 Mu oz-Castro, A. On the ligand–core interaction in ligand-protected gold superatoms. Insights from Au₂₅(XR)₁₈(X= S, Se, Te) via relativistic DFT calculations. *Phys. Chem.*

- Chem. Phys.* **2019**, *21*, 13022–13029.
- 104 Muñoz-Castro, A.; Macleod Carey, D.; Arratia-Pérez, R. Calculated molecular properties of triangular tribenzo and perfluoro-tribenzo trimercuronin macrocycles. *J. Phys. Chem. A* **2010**, *114*, 666–672.
- 105 Rabaâ, H.; Omary, M. A.; Taubert, S.; Sundholm, D. Insights into Molecular Structures and Optical Properties of Stacked $[\text{Au}_3(\text{RN}=\text{CR}')_3]_n$ Complexes. *Inorg. Chem.* **2018**, *57*, 718–730.

6.6 Annex

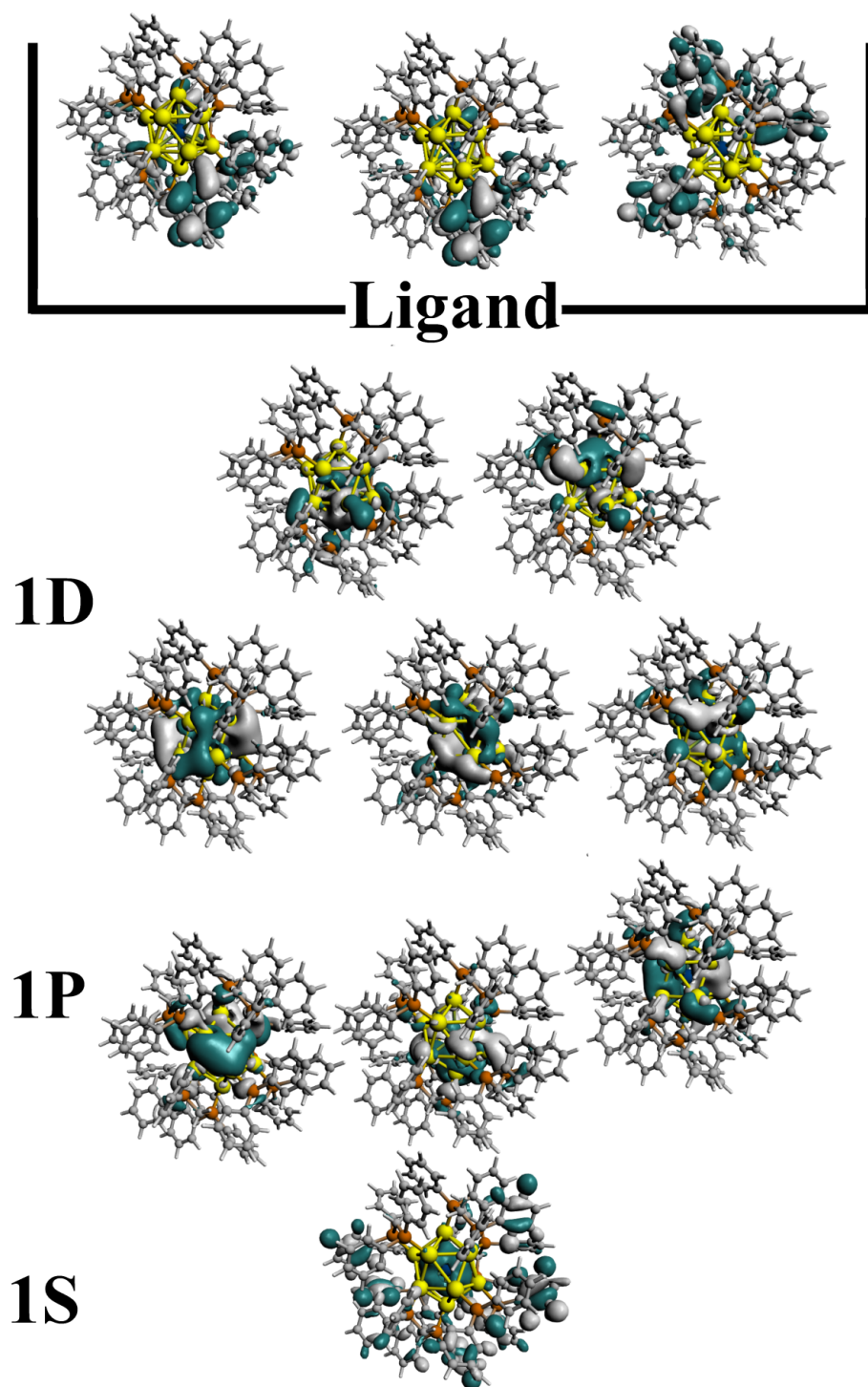


Figure S1. Isosurface plots of *superatomic* shells for $[\text{W}@\text{Au}_{12}(\text{dppm})_6]$ (**2**). Isosurface value set at 0.01 a.u.

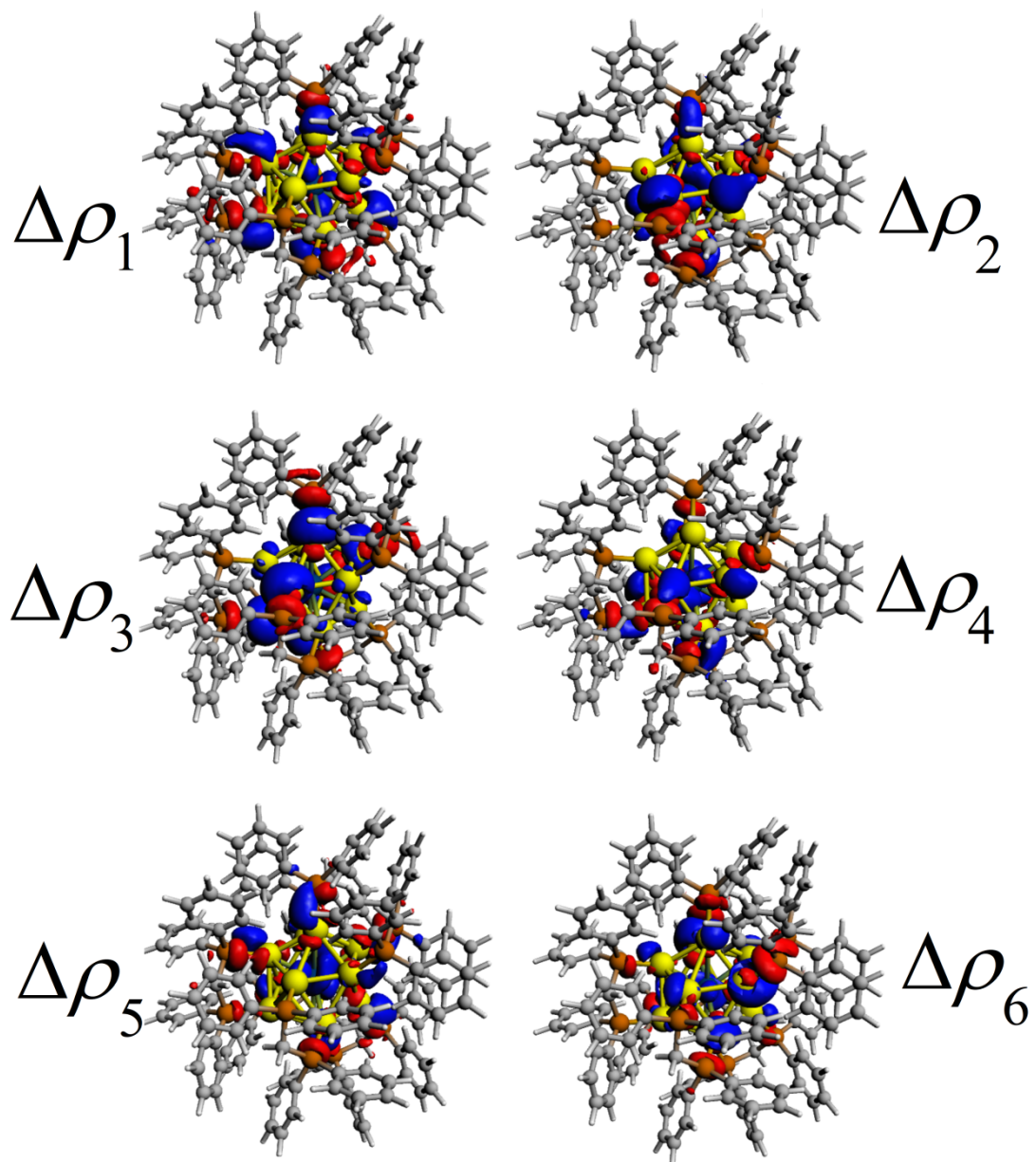


Figure S2. Isosurface plots (0.001 a.u.) for relevant deformation density channels ($\Delta\rho_n$), contributing to ΔE_{orb} , from NOCV-EDA analysis of $[\text{W}@\text{Au}_{12}(\text{dppm})_6]$ (**2**). Charge transfer flow from red to blue isosurfaces.

Table S1. Distances for $M_{\text{cent-Au}_{\text{ico}}}$ for the studied clusters. Values in Å. *CShM* values for the icosahedral core are provided. Geometries of T_1 excited states are given.

	1	1 exp.^a	2 I^b	2 II^b	1 T₁	2 T₁
	Au ₁₃ -Calc	Au ₁₃ -Exp	WAu ₁₂ -Calc	WAu ₁₂ -IsoII	Au ₁₃ -Calc	WAu ₁₂ -Calc
$M_{\text{cent-Au}_{\text{ico}}}$	2.802	2.702	2.728	2.678	2.753	2.752
	2.807	2.702	2.728	2.706	2.774	2.759
	2.807	2.702	2.740	2.768	2.788	2.765
	2.827	2.703	2.740	2.775	2.789	2.795
	2.827	2.703	2.775	2.801	2.800	2.800
	2.829	2.923	2.775	2.810	2.827	2.815
	2.912	2.923	2.852	2.876	2.868	2.818
	2.914	2.924	2.852	2.877	2.897	2.818
	2.916	2.924	2.853	2.913	2.915	2.818
	2.922	2.924	2.853	2.917	2.937	2.821
	2.929	2.925	2.885	3.004	3.108	2.826
	2.930	2.925	2.885	3.131	3.330	2.830
Average	2.869	2.832	2.806	2.855	2.899	2.801
<i>CShM</i>	0.315	0.568	0.207	0.668	1.096	0.052
Standard Dev.	0.055	0.114	0.063	0.128	0.168	0.028
Au _{ico} -P	2.320	2.282	2.314	2.273	2.311	2.349
	2.320	2.282	2.314	2.283	2.345	2.333
	2.320	2.282	2.315	2.293	2.340	2.330
	2.332	2.282	2.315	2.295	2.348	2.356
	2.334	2.282	2.318	2.300	2.344	2.337
	2.334	2.282	2.318	2.308	2.345	2.342
	2.340	2.346	2.346	2.309	2.334	2.360
	2.340	2.346	2.346	2.314	2.338	2.346
	2.341	2.346	2.358	2.329	2.343	2.364
	2.341	2.346	2.358	2.343	2.307	2.355
	2.342	2.346	2.368	2.345	2.332	2.345
	2.342	2.346	2.368	2.347	2.348	2.322
Average	2.334	2.314	2.336	2.312	2.336	2.345
Standard Dev.	0.009	0.033	0.022	0.023	0.014	0.011

Table S2. Relative energies in kcal/mol for isomers **I** and **II**, in both D_3 - and pseudo T_h symmetries for groups 6 to 11 doping atoms. “ D_3 -symmetry” “pseudo T_h -symmetry”.

	“ D_3 -symmetry”		“pseudo T_h -symmetry”	
	Isomer I	Isomer II	Isomer I	Isomer II
$[\text{Au}_{13}(\text{dppm})_6]^{5+}$	0.0		+11.5	
$[\text{PtAu}_{12}(\text{dppm})_6]^{4+}$	0.0	+28.0	+16.0	+49.4
$[\text{IrAu}_{12}(\text{dppm})_6]^{3+}$	0.0	+64.2	+17.4	+83.1
$[\text{OsAu}_{12}(\text{dppm})_6]^{2+}$	0.0	+117.3	+9.5	+107.8
$[\text{ReAu}_{12}(\text{dppm})_6]^{1+}$	0.0	+108.4	+8.3	+156.1
$[\text{WAu}_{12}(\text{dppm})_6]$	0.0	+118.2	+8.4	+164.1

Chapter 7

Elucidating the Electronic Structure of the Ligated Cuboctahedral Palladium Cluster $[\text{Pd}_{13}(\mu_4\text{-C}_7\text{H}_7)_6]^{2+}$

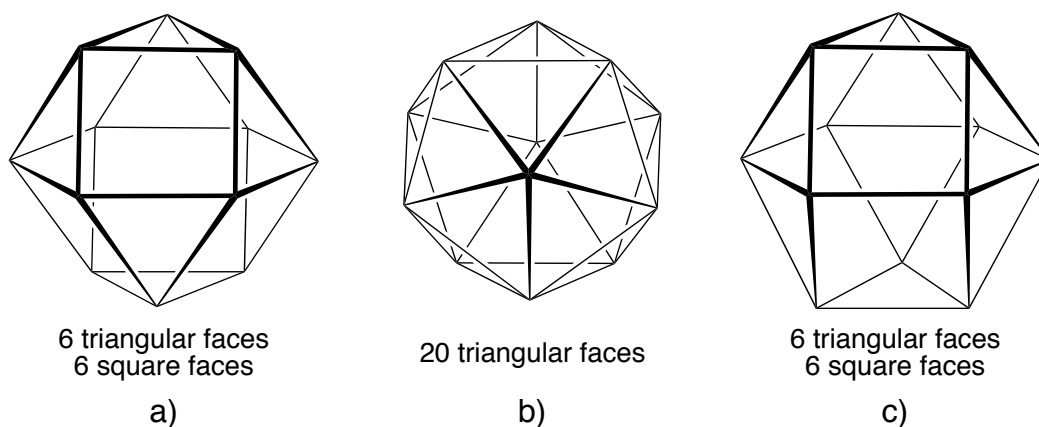
7.1 Introduction

In 1869 Mendeleev published his Periodic Table.¹ Discovered in 1803, palladium element is then mentioned among the 60 elements reported in the table. 150 years later, palladium is a key chemical element largely used in catalysis but also in electronics, dentistry, medicine, hydrogen purification, chemical applications, groundwater treatment, jewelry, etc. Over the last decades, it became apparent that palladium in its zero-valent state, forms unique highly condensed nano-sized carbonyl-ligated clusters,^{2,3} distinguishing itself from other elements, including the other two Group-10 congeneric Ni and Pt metals.⁴⁻⁶ Indeed, relatively weak metal–metal and metal–carbonyl (and/or phosphine) connectivity must be responsible for the rich variety of structural arrangements reported for these high-nuclearity ligated clusters, which can extend up to 165 atoms (so far).⁷ Most of them features a compact (pseudo) spherical metallic kernel, with a mixed carbonyl and phosphine ligands shell, which were mainly developed in the group of Dahl in USA.⁷⁻¹⁷ More recently, some Pd nanoclusters which do not contain CO or phosphine ligands have also been reported.¹⁸⁻²⁰ A substantial number of them have been crystallographically identified,³ and theoretically investigated.²¹⁻²³ Interestingly, they adopt various shapes, ranging from “bulk-like” cubic closed packed and/or hexagonal closed packed architectures to, also compact but “molecular” icosahedral shapes. Surprisingly, the bonding properties of these ligated Group-10 metal clusters do not parallel those of the coinage metal Cu, Ag or Au ligated clusters. Whereas the cluster architecture of the latter species can generally be rationalized within the *superatom* paradigm based on the spherical *jellium* model^{22,24-31} that of palladium still lacks general rationalization rules.

Ligands certainly play an important role in stabilizing the metallic cluster cores of these species. Despite similar bonding properties of σ -donating CO and phosphine ligands with cyclic hydrocarbon ligands,³² palladium clusters ligated with the latter are very scarce. The fascinating compound recently synthesized and characterized by Teramoto *et al.*, namely $[\text{Pd}_{13}(\mu_4\text{-Tr})_6][\text{B}(\text{Ar}^{\text{F}})_4]_2$ ($\text{Tr} = \text{C}_7\text{H}_7$, $\text{Ar}^{\text{F}} = 3,5\text{-(CF}_3)_2\text{C}_6\text{H}_3$) constitutes one example.³³ Its uniqueness comes not only from the nature of the fairly “exotic” cyclic hydrocarbon tropylium ligands (formally C_7H_7^+), but also from the structural arrangement of its Pd_{13} core (Figure 1). Indeed, contrarily to many M_{13} clusters which adopt either a centered icosahedral arrangement³⁴⁻³⁹ or a centered anticuboctahedral geometry,⁴⁰⁻⁴² the metal atoms in $[\text{Pd}_{13}\text{Tr}_6]^{2+}$ are forming a centered cuboctahedron, a scarcely encountered architecture in transition-metal chemistry^{43, 44} (Scheme

1). Indeed, although the centered cuboctahedron can be seen as a chunk of face centered cubic bulk metal, it is less compact than the M_{13} centered icosahedron. On the other hand, a cuboctahedral core provides to the tropylium ligands with six size-adapted square faces to cap. Its electron count, 170 cluster valence electrons (cve) if the Tr^+ ligands are assumed to give 6 electrons to the cluster, is also puzzling, since, assuming cationic tropylium ligands, the resulting putative $[\text{Pd}_{13}]^{4-}$ core is in a negative oxidation state. This is in contrast with the Pd^0 oxidation state found ordinarily in the carbonyl- or phosphine-protected clusters.³ In fact, we will show below that the metal core is best described, as in a formal $[\text{Pd}_{13}]^{4-}$ state, at least before interaction with the ligands. Interestingly also, 170 cve is also the electron count for the anticuboctahedral cluster $[\text{H}_2\text{Rh}_{13}(\text{CO})_{24}]^{3-}$,⁴⁰⁻⁴² or for the icosahedral species $[\text{Rh}_{12}(\mu\text{-}_{12}\text{S})(\text{CO})_{27}]^{3-}$,^{45,46} for instance. All these three structures share a common valence electron count obeying the $14n_s + 2$ cve rule proposed by Mingos for spherical high nuclearity ligated clusters,⁴⁷⁻⁴⁹ despite a different number of triangular and square faces (Scheme 1).

Although Moller-Plesset (MP2) computations on $[\text{Pd}_{13}(\mu_4\text{-Tr})_6]^{2+}$ were reported by Teramoto *et al.*,³³ no clear rationalization of its peculiar structure on the basis of its valence electron count has been provided yet. This prompted us to undertake a detailed analysis of its electronic structure by means of density functional theory (DFT) calculations, in order to provide an orbital interpretation of its bonding, structure and stability. The main results are discussed in this chapter.



Scheme 1. Different twelve-vertex geometrical isomeric cluster cores: a) cuboctahedral, b) icosahedral, and c) anticuboctahedral.

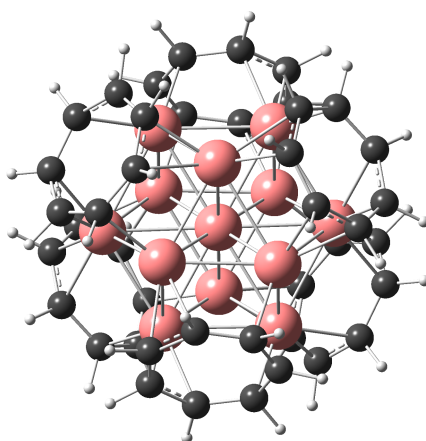


Figure 1. The molecular structure of $[\text{Pd}_{13}(\mu_4\text{-C}_7\text{H}_7^+)_6]^{2+}$ characterized by Teramoto *et al.*³³

7.2 Computational Details

Geometry optimizations were carried out with the Gaussian 09 package⁵⁰ at the DFT level of theory. The BP86 functional^{51,52} and the general triple- ξ -polarized Def2-TZVP basis set were used to perform all-electron calculations. The optimized geometries were characterized as true minima on their potential energy surface by harmonic vibrational analysis. Wiberg indices and natural orbital populations analyses were computed by using NBO 5.0 program.⁵³ The compositions of the molecular orbitals were calculated with the AOMix Program.⁵⁴ The bonding analysis was performed by carrying out a fragment decomposition analysis with the help of the ADF2016 program,⁵⁵ using the BP86 functional^{51,52} and an STO all-electron TZP basis set.⁵⁶ This fragment decomposition analysis was based on single-point calculations using the Gaussian-optimized geometries.

7.3 Results and Discussion

The optimized structure of $[\text{Pd}_{13}\text{Tr}_6]^{2+}$ was found to be of C_{2h} symmetry, the C_2 axis passing through two opposite vertices. A similar optimized geometry was found at the MP2 level of theory.³³ Its Kohn-Sham molecular orbital (MO) diagram is shown in Figure 2. The reasonably large HOMO-LUMO gap computed at the GGA level of theory (0.72 eV) is consistent with the cluster stability and experimental diamagnetic behavior. The two lowest unoccupied orbitals (LUMO) are similar to those shown by Teramoto *et al.*,³³ being evenly distributed on the metallic core and the ligand shell. On the other hand, the highest occupied orbitals (HOMO) are mostly localized on the cuboctahedral Pd_{12} core and to a lesser extent on the ligand envelope. They hardly show any character on the interstitial Pd atom.

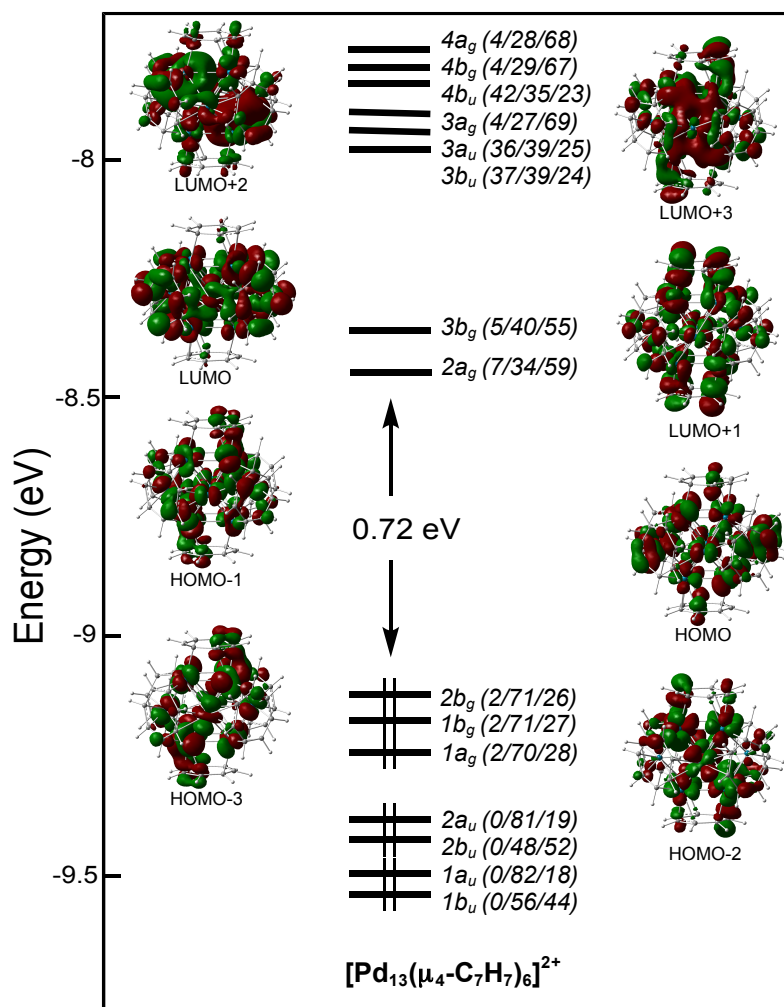


Figure 2. Kohn-Sham orbital diagram of the $[\text{Pd}_{13}\text{Tr}_6]^{2+}$ cluster (C_{2h} symmetry). Values in parentheses are the orbital localization (in %) on the interstitial Pd atom, Pd_{12} cuboctahedral core and Tr_6 ligand shell, respectively.

The major computed metrical data are given in Table 1, together with their corresponding experimental ones.³³ The optimized Pd–Pd distances are $\sim 3\%$ larger than those measured experimentally, as often found for late transition-metal-containing molecules using with GGA functionals. As a whole however, the agreement between the optimized and X-ray structure is fairly good. The metal cuboctahedron does not depart importantly from the ideal O_h symmetry. The computed Pd–Pd Wiberg indices (avg. 0.095) are indicative of moderate metal-metal bonding interactions. The natural atomic orbital (NAO) charges (Table 1) correspond to $[\text{Pd}_{13}]^{+3.80}$ and $[\text{Tr}_6]^{-1.80}$ (note that atomic charges are not oxidation states), indicating significant electron transfer from the metal core to the tropylium ligands. As expected, the interstitial Pd atom (Pd_i , charge = -0.70) is largely more electron-rich than the peripheral metal atoms

(average charge = +0.38). The charge distribution on the Pd atoms and Tr ligands is consistent with a pseudo- O_h symmetry of the whole cluster.

Table 1. Relevant computed data for $[\text{Pd}_{13}\text{Tr}_6]^{2+}$ and $[\text{Pd}_{13}\text{Tr}_6]^{4+}$. Interatomic distances are given in Å. The corresponding Wiberg indices are given in brackets. Experimental bond distances are also given for comparison.

		$[\text{Pd}_{13}\text{Tr}_6]^{2+}$
HOMO-LUMO gap (eV)		0.72 eV
$\text{Pd}_i\text{-Pd}_{\text{cubo}}$		4 x 2.808 [0.109] 2 x 2.808 [0.107] 4 x 2.793 [0.111] 2 x 2.813 [0.108] Avg.: 2.804 [0.1090] (exp: 2.720)
$\text{Pd}_{\text{cubo}}\text{-Pd}_{\text{cubo}}$		2 x 2.900 [0.071] 2 x 2.718 [0.102] 4 x 2.808 [0.082] 4 x 2.770 [0.089] 4 x 2.835 [0.078] 4 x 2.749 [0.096] 4 x 2.856 [0.076] Avg.: 2.808 [0.085] (exp. 2.720)
$\text{Pd}_{\text{cubo}}\text{-C}$		Range: 2.189-2.556 (exp: 2.084-2.607) Avg.: 2.300 [0.191] (exp: 2.302)
NAO charges	Pd_i	-0.70
	Pd_{cubo}	4 x 0.377
		4 x 0.378
		2 x 0.356 2 x 0.384
Tr	2 x -0.307 4 x -0.297	

In order to get a deeper understanding of the electronic structure of $[\text{Pd}_{13}\text{Tr}_6]^{2+}$, with the help of the ADF program (see computational details above), its molecular one-electron orbitals were expressed as linear combinations of the orbitals of two fragments (assumed to be in singlet states), namely the metal Pd_{13} core and the Tr_6 octahedral envelope. Then, the question of fragment charge partitioning arises. The tropylium ligand being known to be stable in its aromatic cationic form, the *a priori* most obvious fragmentation is $[\text{Pd}_{13}]^{4+}$ and $[\text{Tr}_6]^{6+}$. Unfortunately, the $[\text{Pd}_{13}]^{4+}$ fragment could not be converged in a singlet ground state, but rather in an “excited” singlet state. A singlet ground state could be obtained only for a neutral $[\text{Pd}_{13}]^0$ fragment, but on the other hand, the $[\text{Tr}_6]^{2+}$ counterpart converged in an excited singlet state. Obviously, regardless of the charge partitioning, a Kohn-Sham description of the two fragments

in singlet ground states appears to be only approximate. However, independently of the charge partitioning, the qualitative description of the bonding picture, which arises from a fragment analysis is the same. In particular, the occupations of the fragment orbitals in the whole cluster are rather stable with respect to the choice of fragment charges. The values discussed below correspond to $[\text{Pd}_{13}]^0$ and $[\text{Tr}_6]^{2+}$. The qualitative interaction MO diagram is shown below, but before investigating it in detail, we would like to first analyze the electronic structure of a centered cuboctahedral $[\text{Pd}_{13}]$ bare cluster. This should indirectly provide us some information about the role of the “protective” ligand environment.

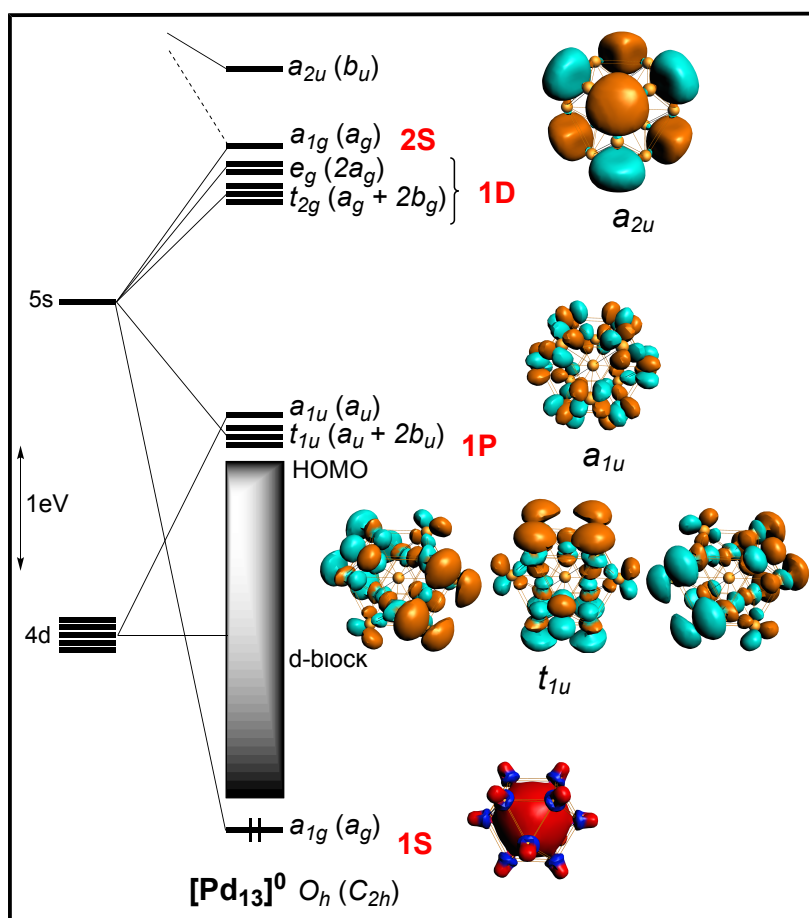


Figure 3. Kohn-Sham orbital diagram of a neutral centered cuboctahedral $[\text{Pd}_{13}]$ unit of O_h symmetry. The irreducible representations expressed in C_{2h} symmetry are given in parenthesis.

Figure 3 illustrates the Kohn-Sham orbital diagram obtained by a single-point calculation on a regular $[\text{Pd}_{13}]^0$ species of O_h symmetry ($\text{Pd-Pd} = 2.80 \text{ \AA}$). The $13 \times 5 = 65$ weakly bonding/antibonding combinations of the $4d(\text{Pd})$ atomic orbitals (AO) constitute the so-called d -block. However, the more antibonding one, of a_{1u} symmetry, lies slightly above the other 64 closely energetically spaced combinations and is therefore unoccupied (see Figure 2). Because

of substantial overlap, the 5s(Pd) combinations split within a huge range of energy. In particular, the in-phase combination (a_{1g}) is so importantly stabilized that it lies just below the d -block bottom. Within the *spherical jellium* model, this level is associated with the 1S *superatomic* orbital. The next 5s(Pd) bonding combinations are of t_{1u} symmetry and correspond to the 1P *superatomic* shell. They are situated just below the highest a_{1u} 4d(Pd) level. The next 5s(Pd) combinations (1D and 2S *superatomic* levels) lie above this a_{1u} orbital. Above them, one finds the lowest combination of dominant 5p(Pd) character, which is of a_{2u} symmetry. Owing to its small HOMO-LUMO gap, such a neutral cuboctahedral architecture is not a stable species.

The qualitative MO diagram of $[\text{Pd}_{13}\text{Tr}_6]^{2+}$ built as the result of the interaction between the metal core and its ligand envelope is sketched in Figure 4. The charge distribution $[\text{Pd}_{13}]^{2-}$ and $[\text{Tr}_6]^{4+}$ was assumed (see below for its justification). Owing to the fact that the cluster symmetry does not depart that much from the ideal O_h symmetry, the orbital diagram of the Pd_{13} fragment (left side of Figure 4) is not very different from that shown in Figure 3. Its orbitals are labelled in the actual C_{2h} cluster symmetry (see Figure 3). The π MO level energy ordering of an isolated tropylium ion of D_{7h} symmetry (far right-hand side of Figure 4) is $a''_2 < e''_1 < e''_2 < e''_3$, of which a''_2 and e''_1 are bonding and contain the six π -electrons of Tr^+ . Owing to the electrophilic character of the ligand, its antibonding e''_2 LUMOs are rather low-lying in energy. In the pseudo-octahedral Tr_6 fragment, each individual Tr orbital generates six combinations. The occupied π -combinations are somewhat stabilized by vacant 5s/5p(Pd) combinations of the Pd_{13} fragment, including the t_{1u} (1P) level, which is in turn destabilized. The corresponding ligand-to-metal electron donation is ~ 1.6 e. On the other hand, the π^* Tr_6 combinations interact importantly with occupied 4d(Pd) levels, in particular those deriving from the e''_2 level. However, one of these combinations of b_u symmetry behaves differently. Indeed, it interacts particularly strongly with the vacant b_u 5p(Pd) level labelled a_{2u} (O_h symmetry) in Figure 3, in such a way it generates a bonding combination, which is sufficiently low-lying in energy to be occupied in the cluster. The occupation in $[\text{Pd}_{13}\text{Tr}_6]^{2+}$ of this e''_2 -derived b_u fragment orbital is 1.7 e. This indicates that, from the point of view of oxidation states, it is formally occupied. Thus, the ligand fragment, being formally $[\text{Tr}_6]^{4+}$, is reduced by the metal core. The metal-to-ligand electron-transfer involving all the other formally vacant ligand π^* combinations is also substantial, ~ 7.1 e, and concerns mainly the 11 formally vacant e''_2 combinations. This very large electron transfer is the footprint of the substantial metal-ligand mixing in the orbitals shown in Figure 2.

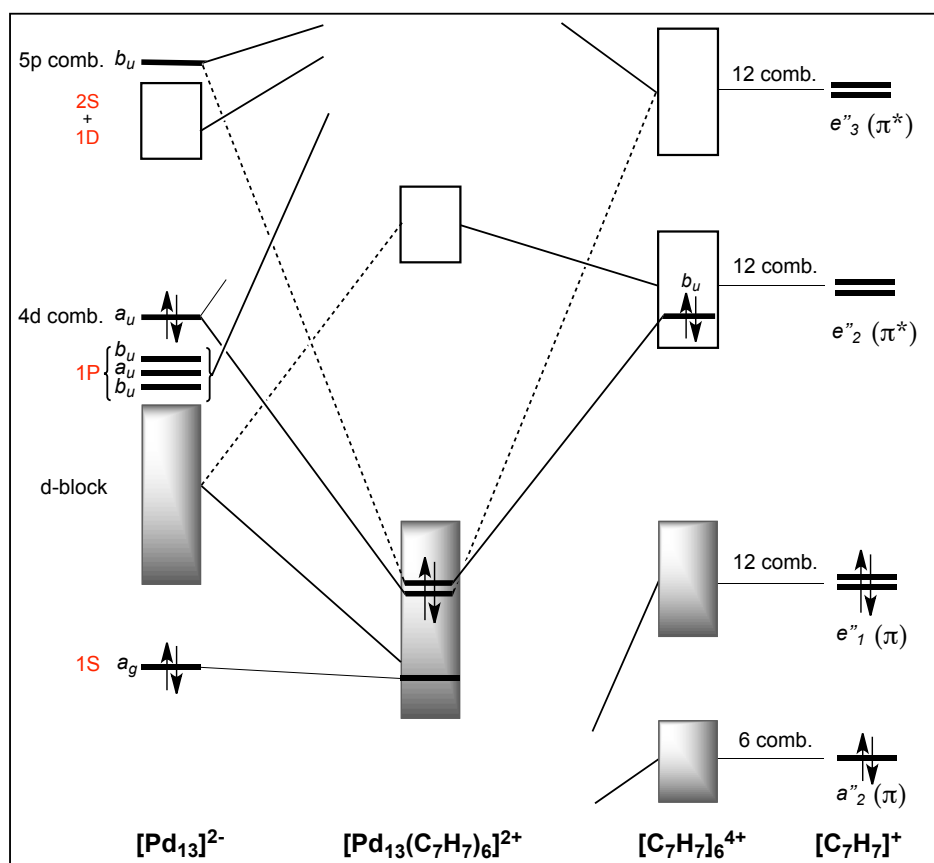


Figure 4. Qualitative MO diagram illustrating the interaction between the centered cubocathedral cage $[\text{Pd}_{13}]^{2-}$ and the $[\text{Tr}_6]^{4+}$ ligand envelope in $[\text{Pd}_{13}\text{Tr}_6]^{2+}$ of C_{2h} symmetry.

Assuming the charged $[\text{Tr}_6]^{4+}$ fragment implies an anionic $[\text{Pd}_{13}]^{2-}$ core. Actually, all the $4d(\text{Pd})$ levels are formally occupied in $[\text{Pd}_{13}\text{Tr}_6]^{2+}$, including the highest a_u combination. Indeed, this orbital interacts strongly with ligand $\pi^*(a_u)$ combinations and is in turn stabilized below the HOMO after interaction (occupation 1.8 e). Thus, the full d -block is occupied in the complex, as well as the additional strongly bonding *jellium* $1S$ level (in-phase combination of the $5s(\text{Pd})$ AOs), which is responsible for a large part of the Pd–Pd bonding character in $[\text{Pd}_{13}\text{Tr}_6]^{2+}$. Another significant contribution to Pd–Pd bonding comes from the mixing of the metal-metal bonding orbitals ($1P$ and $a_u(5p)$, occupations 1.3 and 0.3 e, respectively) into occupied levels through their mixing with ligand orbitals.

Cyclic voltammetry experiments of $[\text{Pd}_{13}\text{Tr}_6]^{2+}$ indicated two reversible one-electron oxidations and one reversible one-electron reduction.³³ The paramagnetic tricationic cluster was chemically prepared and X-ray characterized. Our calculations indicate that the one-electron oxidation of $[\text{Pd}_{13}\text{Tr}_6]^{2+}$ corresponds to an electron removal from the HOMO (see Figure S1, Annex), without any significant structural change (see Table S1, Annex). The spin density of $[\text{Pd}_{13}\text{Tr}_6]^{3+}$ is concentrated on the metal core (see Figure S2, Annex), thus allowing

kinetic protection from the ligand shell envelope. Calculations on the mono-reduced species $[\text{Pd}_{13}\text{Tr}_6]^+$ indicate occupation of the LUMO (see Figure S3, Annex), again without little structural change (see Table S1, Annex).

7.4 Conclusion

The bonding in the cluster $[\text{Pd}_{13}\text{Tr}_6]^{2+}$ can be formally described as resulting from the interaction between a $[\text{Pd}_{13}]^{2-}$ core and a partly reduced $[\text{Tr}_6]^{4+}$ ligand shell. The orbital interactions between the two fragments are strong, owing in particular to the strong π -accepting ability of the ligands. As a consequence, a very important charge transfer occurs between the two fragments, which in fact reverses their charge polarity. Nevertheless, in the full $[\text{Pd}_{13}\text{Tr}_6]^{2+}$ cluster, the Pd_{13} core has an electron configuration corresponding to the formal occupation of all its $4d$ combinations, plus the in-phase combination of the $5s(\text{Pd})$ orbitals (the $1S$ *jellium* level). The (moderate) Pd–Pd covalent bonding character is in part due to the occupation of this strongly bonding $1S$ orbital and for another part from through-bond interactions, in particular from the partial occupation of other bonding $5s/5p(\text{Pd})$ combinations (of t_{1u} ($1P$ level) and a_{2u} symmetry).

A question which arises from the above discussion is why the $[\text{Pd}_{13}\text{Tr}_6]^{4+}$ tetracation, formally made of $[\text{Pd}_{13}]^{2-}$ and six aromatic $(\text{C}_7\text{H}_7)^+$ ligands was not chemically isolated? Our calculations on $[\text{Pd}_{13}\text{Tr}_6]^{4+}$ found a very small HOMO ($1b_g$)–LUMO ($2b_g$) gap of 0.24 eV for this charge, (see Figure S4, Annex). Thus, the tetracation is likely not to be stable. Moreover, the expected electron configurations for the tetracation should be that which corresponds to the depopulation of a ligand-based b_u level from the parent dianion, restoring full aromaticity to the ligands. One of the possible reasons for such a situation could be the particularly large electrophilicity of tropylium beside of the (relative) basicity of the palladium core.

The peculiar centered cuboctahedral architecture is probably favored, as originally suggested by Teramoto *et al.*,³³ by the size of the tropylium ligands, which are particularly suited for capping Pd_4 square faces. It is noteworthy that centered cuboctahedral copper clusters of the type $[\text{Cu}_{13}\{\text{S}_2\text{CNR}_2\}_6(\text{CCR}')_4]^+$ have also been suggested to be stabilized because of the preference of the dithiocarbamate ligands to cap square faces.^{43, 57} Interestingly, such copper species are also 2-electron *superatomic* species with $1S^2$ *jellium* configuration. However, the comparison between palladium clusters such as $[\text{Pd}_{13}\text{Tr}_6]^{2+}$ and *superatomic* clusters of Group-11 metals should not be pushed too far. Indeed, they usually have different electron counts and moreover, contrarily to a large number of Au and Ag clusters, their metal cores do not retain their closed-shell *superatom* electron configuration when their ligands are removed.

7.5 References

- 1 Mendeleev, D. On the relationship of the properties of the elements to their atomic weights. *Z. Chem.* **1869**, *12*, 405–406.
- 2 Mednikov, E. G.; Dahl, L. F. Palladium: It Forms Unique Nano-Sized Carbonyl Clusters. *J. Chem. Educ.* **2009**, *86*, 1135–1135.
- 3 Mednikov, E. G.; Dahl, L. F. Syntheses, structures and properties of primarily nanosized homo/heterometallic palladium CO/PR₃-ligated clusters. *Philos. Trans. R. Soc. A* **2010**, *368*, 1301–1332.
- 4 Belyakova, O.; Slovokhotov, Y. Structures of large transition metal clusters. *Russ. Chem. Bull.* **2003**, *52*, 2299–2327.
- 5 Femoni, C.; Iapalucci, M. C.; Kaswalder, F.; Longoni, G.; Zacchini, S. The possible role of metal carbonyl clusters in nanoscience and nanotechnologies. *Coord. Chem. Rev.* **2006**, *250*, 1580–1640.
- 6 Ciabatti, I.; Femoni, C.; Iapalucci, M. C.; Longoni, G.; Zacchini, S. Platinum carbonyl clusters chemistry: four decades of challenging nanoscience. *J. Clust. Sci.* **2014**, *25*, 115–146.
- 7 Mednikov, E. G.; Jewell, M. C.; Dahl, L. F. Nanosized (μ_{12} -Pt)Pd_{164-x}Pt_x(CO)₇₂(PPh₃)₂₀ ($x \approx 7$) Containing Pt-Centered Four-Shell 165-Atom Pd–Pt Core with Unprecedented Intershell Bridging Carbonyl Ligands: Comparative Analysis of Icosahedral Shell-Growth Patterns with Geometrically Related Pd₁₄₅(CO)_x(PEt₃)₃₀ ($x \approx 60$) Containing Capped Three-Shell Pd₁₄₅ Core. *J. Am. Chem. Soc.* **2007**, *129*, 11619–11630.
- 8 Moiseev, I. I.; Stromnova, T. A.; Vargaftig, M. N.; Mazo, G. J.; Kuz'Mina, L. G.; Struchkov, Y. T. New palladium carbonyl clusters: X-ray crystal structure of [Pd₄(CO)₄(OAc)₄]⁻(AcOH)₂. *J. Chem. Soc., Chem. Commun.* **1978**, 27–28.
- 9 Mednikov, E. G.; Eremenko, N. K.; Mikhailov, V. A.; Gubin, S. P.; Slovokhotov, Y. L.; Struchkov, Y. T. New palladium cluster compounds. X-Ray crystal structure of Pd₁₀(CO)₁₂(PⁿBu₃)₆. *J. Chem. Soc., Chem. Commun.* **1981**, 989–990.
- 10 Mednikov, E. G.; Wittayakun, J.; Dahl, L. F. Synthesis and Stereochemical/Electrochemical Analyses of Cuboctahedral-Based Pd₂₃(CO)_x(PR₃)₁₀ Clusters ($x = 20$ with R₃ = ⁿBu₃, Me₂Ph; $x = 20, 21, 22$ with R₃ = Et₃): Geometrically Analogous Pd₂₃(PEt₃)₁₀ Fragments with Variable Carbonyl Ligations and Resulting Implications. *J. Cluster Sci.* **2005**, *16*, 429–454.

- 11 Mednikov, E. G.; Ivanov, S. A.; Dahl, L. F. [Pd₃₀(CO)₂₆(PEt₃)₁₀] and [Pd₅₄(CO)₄₀(PEt₃)₁₄]: Generation of Nanosized Pd₃₀-and Pd₅₄-Core Geometries Containing Interpenetrating Cuboctahedral-Based Metal Polyhedra. *Angew. Chem. Int. Ed.* **2003**, *42*, 323–327.
- 12 Tran, N. T.; Kawano, M.; Dahl, L. F. High-nuclearity palladium carbonyl trimethylphosphine clusters containing unprecedented face-condensed icosahedral-based transition-metal core geometries: proposed growth patterns from a centered Pd₁₃ icosahedron. *J. Chem. Soc. Dalton Trans.* **2001**, *19*, 2731–2748.
- 13 Mednikov, E. G.; Dahl, L. F. Nanosized Pd₃₇(CO)₂₈{P(*p*-Tolyl)₃}₁₂ containing geometrically unprecedented central 23-atom interpenetrating tri-icosahedral palladium kernel of double icosahedral units: Its postulated metal-core evolution and resulting stereochemical implications. *J. Am. Chem. Soc.* **2008**, *130*, 14813–14821.
- 14 Mednikov, E. G.; Eremenko, N. K.; Slovokhotov, Y. L.; Struchkov, Y. T. Synthesis of high-nuclearity carbonyl–phosphine clusters of palladium under mild conditions and X-ray crystal structure of Pd₃₈(μ₃-CO)₄(μ₂-CO)₂₄(PEt₃)₁₂. *J. Chem. Soc. Chem. Commun.* **1987**, *3*, 218–219.
- 15 Mednikov, E. G.; Ivanov, S. A.; Slovokhotova, I.V.; Dahl, L. F. Nanosized [Pd₅₂(CO)₃₆(PEt₃)₁₄] and [Pd₆₆(CO)₄₅(PEt₃)₁₆] Clusters Based on a Hypothetical Pd₃₈ Vertex-Truncated *v*3 Octahedron. *Angew. Chem. Int. Ed.* **2005**, *44*, 6848–6854.
- 16 Tran, N. T.; Dahl, L. F. Nanosized [Pd₆₉(CO)₃₆(PEt₃)₁₈]: Metal-Core Geometry Containing a Linear Assembly of Three Face-Sharing Centered Pd₃₃ Icosahedra Inside of a Hexagonal-Shaped Pd₃₀ Tube. *Angew. Chem. Int. Ed.* **2003**, *42*, 3533–3537.
- 17 Tran, N. T.; Powell, D. R.; Dahl, L. F. Nanosized Pd₁₄₅(CO)_x(PEt₃)₃₀ Containing a Capped Three-Shell 145-Atom Metal-Core Geometry of Pseudo Icosahedral Symmetry. *Angew. Chem. Int. Ed.* **2000**, *39*, 4121–4125.
- 18 Murahashi, T.; Fujimoto, M.; Oka, M.-a.; Hashimoto, Y.; Uemura, T.; Tatsumi, Y.; Nakao, Y.; Ikeda, A.; Sakaki, S.; Kurosawa, H. Discrete Sandwich Compounds of Monolayer Palladium Sheets. *Science* **2006**, *313*, 1104–1107.
- 19 Koizumi, T.-a.; Tanaka, K.; Tsuchido, Y.; Tanabe, M.; Ide, T.; Osakada, K. Bimolecular fusion of [Pd₃(μ-CN-C₆H₃Me₂-2,6)₃(CN-C₆H₃Me₂-2,6)₃] induced by Ph₂GeH₂: formation of the redox-active Pd₆Ge₂ complex. *Dalton Trans.* **2019**, *48*, 7541–7545.
- 20 Cook, A. W.; Hrobárik, P.; Damon, P. L.; Wu, G.; Hayton, T. W. A Ketimide-Stabilized Palladium Nanocluster with a Hexagonal Aromatic Pd₇ Core. *Inorg. Chem.* **2020**, *59*, 1471–1480.

- 21 Marchal, R.; Manca, G.; Furet, E.; Kahlal, S.; Saillard, J.-Y.; Halet, J.-F. On the Electronic Structure of Organometallic Palladium Clusters of Medium and Large Size: A Theoretical Study. *J. Cluster Sci.* **2015**, *26*, 41–51.
- 22 Saillard, J.-Y.; Halet, J.-F. Structure and bonding patterns in large molecular ligated metal clusters. *Struct. Bond.* **2016**, *169*, 157–179.
- 23 Frapper, G.; Halet, J.-F. in *Computational Materials Discovery* (A. R. Oganov, A. G. Kvashnin, G. Saleh, eds.), Royal Society of Chemistry, London, **2019**, pp. 320–351.
- 24 Knight, W. D.; Clemenger, K.; de Heer, W. A.; Saunders, W. A.; Chou, M. Y.; Cohen, M. L. Electronic shell structure and abundances of sodium clusters. *Phys. Rev. Lett.* **1984**, *52*, 2141–2143.
- 25 Lin, Z.; Slee, T.; Mingos, D. M. P. A structural jellium model of cluster electronic structure. *Chem. Phys.* **1990**, *142*, 321–334.
- 26 de Heer, W. A. The physics of simple metal clusters: experimental aspects and simple models. *Rev. Mod. Phys.* **1993**, *65*, 611–676.
- 27 Mingos, D. M. P. in *Structural and Electronic Paradigms in Cluster Chemistry*; Springer; Berlin, Heidelberg, **1997**.
- 28 Jena, P.; Khanna, S. N.; Rao, B. K. in *Clusters and Nano-Assemblies: Physical and Biological Systems*, World Scientific, **2005**.
- 29 Khanna, S. N.; Jena, P. Atomic clusters: Building blocks for a class of solids. *Phys. Rev. Lett.* **2008**, *51*, 13705–13716.
- 30 Häkkinen, H. Atomic and electronic structure of gold clusters: understanding flakes, cages and superatoms from simple concepts. *Chem. Soc. Rev.* **2008**, *37*, 1847–1859.
- 31 Walter, M.; Akola, J.; Lopez-Acevedo, O.; Jadzinsky, P. D.; Calero, G.; Ackerson, C. J.; Whetten, R. L.; Grönbeck, H.; Häkkinen, H. A Unified View of Ligand-protected Gold Clusters as Superatom Complexes. *Proc. Natl. Acad. Sci. USA* **2008**, *105*, 9157–9162.
- 32 Elian, M.; Chen, M. M.-L.; Mingos, D. M. P.; Hoffmann, R. Comparative bonding study of conical fragments. *Inorg. Chem.* **1976**, *15*, 1148–1155.
- 33 Teramoto, M.; Iwata, K.; Yamaura, H.; Kurashima, K.; Miyazawa, K.; Kurashige, Y.; Yamamoto, K.; Murahashi, T. Three-dimensional sandwich nanocubes composed of 13-atom Palladium core and hexakis-carbocycle shell. *J. Am. Chem. Soc.* **2018**, *140*, 12682–12686.
- 34 Briant, C. E.; Theobald, B. R.; White, J. W.; Bell, L. K.; Mingos, D. M. P.; Welch, A. J. Synthesis and X-ray Structural Characterization of The Centred Icosahedral Gold Cluster

- Compound $[\text{Au}_{13}(\text{PMe}_2\text{Ph})_{10}\text{Cl}_2](\text{PF}_6)_3$; The Realization of a Theoretical Prediction. *J. Chem. Soc. Chem. Commun.* **1981**, 5, 201–202.
- 35 Heaven, M. W.; Dass, A.; White, P. S.; Holt, K. M.; Murray, R. W. Crystal Structure of the Gold Nanoparticle $[\text{N}(\text{C}_8\text{H}_{17})_4][\text{Au}_{25}(\text{SCH}_2\text{CH}_2\text{Ph})_{18}]$. *J. Am. Chem. Soc.* **2008**, 130, 3754–3755.
- 36 Zhu, M.; Aikens, C. M.; Hollander, F. J.; Schatz, G. C., Jin, R. Correlating the Crystal Structure of a Thiol-Protected Au_{25} Cluster and Optical Properties. *J. Am. Chem. Soc.* **2008**, 130, 5883–5885.
- 37 Negishi, Y.; Nobusada, K.; Tsukuda, T. Glutathione-protected gold clusters revisited: bridging the gap between gold (I)–thiolate complexes and thiolate-protected gold nanocrystals. *J. Am. Chem. Soc.* **2005**, 127, 5261–5270.
- 38 Femoni, C.; Iapalucci, M. C.; Longoni, G.; Zacchini, S.; Zarra, S. Icosahedral Pt-Centered Pt_{13} and Pt_{19} Carbonyl Clusters Decorated by $[\text{Cd}_5(\mu\text{-Br})_5\text{Br}_{5-x}(\text{solvent})_x]^{x+}$ Rings Reminiscent of the Decoration of Au–Fe–CO and Au–Thiolate Nanoclusters: A Unifying Approach to Their Electron Counts. *J. Am. Chem. Soc.* **2011**, 133, 2406–2409.
- 39 Ciabatti, I.; Femoni, C.; Iapalucci, M. C.; Longoni, G.; Zacchini, S.; Zarra, S. Surface decorated platinum carbonyl clusters. *Nanoscale* **2012**, 4, 4166–4177.
- 40 Albano, V. G.; Ceriotti, A.; Chini, P.; Ciani, G.; Martinengo, S.; Anker, W. M. Hexagonal close packing of metal atoms in the new polynuclear anions $[\text{Rh}_{13}(\text{CO})_{24}\text{H}_{5-n}]^{n-}$ ($n = 2$ or 3); X-ray structure of $[(\text{Ph}_3\text{P})_2\text{N}]_2[\text{Rh}_{13}(\text{CO})_{24}\text{H}_3]$. *J. Chem. Soc., Chem. Commun.* **1975**, 859–860.
- 41 Bau, R.; Drabnis, M. H.; Garlaschelli, L.; Klooster, W. T.; Xie, Z.; Koetzle, T. F.; Martinengo, S. Five-Coordinate Hydrogen: Neutron Diffraction Analysis of the Hydrido Cluster Complex $[\text{H}_2\text{Rh}_{13}(\text{CO})_{24}]^{3-}$. *Science* **1997**, 275, 1099–1102.
- 42 Gautier, R.; Halet, J.-F. Five-coordinate hydrogen in hydrido rhodium cluster compounds: A theoretical analysis. *J. Organomet. Chem.* **1998**, 565, 217–224.
- 43 Silalahi, R. P. B.; Chakrahari, K. K.; Liao, J.-H.; Kahlal, S.; Liu, Y.-C.; Chiang, M. H.; Saillard, J.-Y.; Liu, C. W. Synthesis of Two-Electron Bimetallic Cu–Ag and Cu–Au Clusters by using $[\text{Cu}_{13}(\text{S}_2\text{CN}^n\text{Bu}_2)_6(\text{C}\equiv\text{CPh})_4]^+$ as a Template. *Chem. Asian J.* **2018**, 13, 500–504.
- 44 Kahlal, S.; Liu, C. W.; Saillard, J.-Y. Ag_{13} -Centered Cuboctahedral Architecture in Inorganic Cluster Chemistry: A DFT Investigation. *Inorg. Chem.* **2017**, 56, 1209–1215.
- 45 Vidal, J. L. $[\text{Rh}_{12}\text{Sb}(\text{CO})_{27}]^{3-}$. An example of encapsulation of antimony by a transition metal carbonyl cluster. *J. Organomet. Chem.* **1981**, 213, 351–363.

- 46 Femoni, C.; Ciabatti, I.; Iapalucci, M. C.; Ruggieri, S.; Zacchini, S. Alternative synthetic route for the heterometallic CO-releasing $[\text{Sb}@\text{Rh}_{12}(\text{CO})_{27}]^{3-}$ icosahedral carbonyl cluster and synthesis of its new unsaturated $[\text{Sb}@\text{Rh}_{12}(\text{CO})_{24}]^{4-}$ and dimeric $[\{\text{Sb}@\text{Rh}_{12}\text{Sb}(\text{CO})_{25}\}_2\text{Rh}(\text{CO})_2\text{PPh}_3]^{7-}$ derivatives. *Prog. Nat. Sci.: Mater. Inter.* **2016**, *26*, 461–428.
- 47 Mingos, D. M. P. Theoretical analyses and electron counting rules for high nuclearity clusters. *J. Chem. Soc. Chem. Commun.* **1985**, 1352–1354.
- 48 Johnston, R. L.; Mingos, D. M. P. General theoretical analysis of four-connected polyhedral molecules. *J. Organomet. Chem.* **1985**, *280*, 419–428.
- 49 Johnston, R. L.; Mingos, D. M. P. Theoretical models of cluster bonding. *Struc. Bond.* **1987**, *68*, 29–87.
- 50 Gaussian 09, Revision A.1, M. J. Frisch, G. W. Trucks, H. B. Schlegel, G. E. Scuseria, M. A. Robb, J. R. Cheeseman, G. Scalmani, V. Barone, B. Mennucci, G. A. Petersson, H. Nakatsuji, M. Caricato, X. Li, H. P. Hratchian, A. F. Izmaylov, J. Bloino, G. Zheng, J. L. Sonnenberg, M. Hada, M. Ehara, K. Toyota, R. Fukuda, J. Hasegawa, M. Ishida, T. Nakajima, Y. Honda, O. Kitao, H. Nakai, T. Vreven, J. A. Montgomery, Jr., J. E. Peralta, F. Ogliaro, M. Bearpark, J. J. Heyd, E. Brothers, K. N. Kudin, V. N. Staroverov, R. Kobayashi, J. Normand, K. Raghavachari, A. Rendell, J. C. Burant, S. S. Iyengar, J. Tomasi, M. Cossi, N. Rega, J. M. Millam, M. Klene, J. E. Knox, J. B. Cross, V. Bakken, C. Adamo, J. Jaramillo, R. Gomperts, R. E. Stratmann, O. Yazyev, A. J. Austin, R. Cammi, C. Pomelli, J. W. Ochterski, R. L. Martin, K. Morokuma, V. G. Zakrzewski, G. A. Voth, P. Salvador, J. J. Dannenberg, S. Dapprich, A. D. Daniels, O. Farkas, J. B. Foresman, J. V. Ortiz, J. Cioslowski, and D. J. Fox (Gaussian, Inc., Wallingford CT, 2009M).
- 51 Becke, A. D. Density-functional exchange-energy approximation with correct asymptotic behavior. *Phys. Rev. A* **1988**, *38*, 3098–3100.
- 52 Perdew, J. P. Density-functional approximation for the correlation energy of the inhomogeneous electron gas. *Phys. Rev. B* **1986**, *33*, 8822–8824.
- 53 Glendening, E. D.; Badenhoop, J. K.; Reed, A. E.; Carpenter, J. E.; Bohmann, J. A.; Morales, C. M.; Weinhold, F. NBO 5.0; Theoretical Chemistry Institute, University of Wisconsin (Madison, WI, **2001**, <http://www.chem.wisc.edu/nbo5>).
- 54 Gorelsky, S. I. AOMix program; <http://www.sg-chem.net>.
- 55 a) te Velde, G.; Bickelhaupt, F. M.; van Gisbergen, S. J. A.; Guerra, C. F.; Baerends, E. J.; Snijders, J. G.; Ziegler, T. Chemistry with ADF. *J. Comput. Chem.* **2001**, *22*, 931–967; b)

ADF2016, SCM, Theoretical Chemistry, Vrije Universiteit: Amsterdam, The Netherlands;
<http://www.scm.com>.

- 56 Lenthe, E. V.; Baerends, E. J. Optimized Slater-type basis sets for the elements 1-118. *J. Comput. Chem.* **2003**, *24*, 1142–1156.
- 57 Sharma, S.; Chakrahari, K. K.; Saillard, J.-Y.; Liu, C. W. Structurally precise dichalcogenolate-protected copper and silver superatomic nanoclusters and their alloys. *Acc. Chem. Res.* **2018**, *51*, 2475–2483.

7.6 Annex

Table S1. Relevant computed data for $[\text{Pd}_{13}\text{Tr}_6]^{n+}$ ($n = 1-3$). Interatomic distances are given in Å

	$[\text{Pd}_{13}\text{Tr}_6]^{2+}$	$[\text{Pd}_{13}\text{Tr}_6]^+$	$[\text{Pd}_{13}\text{Tr}_6]^{3+}$	$[\text{Pd}_{13}\text{Tr}_6]^{4+}$
HOMO-LUMO gap (eV)	0.72 eV	α -electron: 0.16 eV β -electron: 0.66 eV	α -electron: 0.77 eV β -electron: 0.15 eV	0.24 eV
$\text{Pd}_i\text{-Pd}_{\text{cubo}}$	4 x 2.808 [0.109] 2 x 2.808 [0.107] 4 x 2.793 [0.111] 2 x 2.813 [0.108] Avg: 2.804 [0.109] (exp: 2.720)	4 x 2.807 [0.113] 2 x 2.820 [0.105] 4 x 2.799 [0.107] 2 x 2.818 [0.102] Avg: 2.808 [0.108]	4 x 2.818 [0.101] 2 x 2.795 [0.105] 4 x 2.775 [0.112] 2 x 2.802 [0.104] Avg: 2.797 [0.106]	2 x 2.910 [0.088] 2 x 2.779 [0.108] 2 x 2.743 [0.112] 2 x 2.783 [0.116] 2 x 2.768 [0.107] 1 x 2.895 [0.090] 1 x 2.739 [0.119] Avg: 2.800 [0.091]
$\text{Pd}_{\text{cubo}}\text{-Pd}_{\text{cubo}}$	2 x 2.900 [0.071] 2 x 2.718 [0.102] 4 x 2.808 [0.082] 4 x 2.770 [0.089] 4 x 2.835 [0.078] 4 x 2.749 [0.096] 4 x 2.856 [0.076] Avg: 2.808 [0.085] (exp. 2.720)	2 x 2.720 [0.102] 2 x 2.848 [0.075] 4 x 2.790 [0.086] 4 x 2.759 [0.090] 4 x 2.878 [0.075] 4 x 2.856 [0.076] 4 x 2.785 [0.090] Avg: 2.809 [0.084]	2 x 2.708 [0.108] 2 x 2.830 [0.082] 4 x 2.817 [0.079] 4 x 2.757 [0.093] 4 x 2.815 [0.080] 4 x 2.864 [0.075] 4 x 2.761 [0.094] Avg: 2.797 [0.086]	2 x 2.729 [0.000] 2 x 2.839 [0.082] 2 x 2.843 [0.081] 2 x 2.796 [0.094] 2 x 2.718 [0.106] 2 x 2.926 [0.071] 2 x 2.842 [0.077] 2 x 2.738 [0.103] 2 x 2.715 [0.109] 2 x 2.818 [0.078] 2 x 2.809 [0.088] 2 x 2.848 [0.081]

					Avg: 2.802 [0.081]
$\text{Pd}_{\text{cubo-C}}$		Range: 2.189-2.556 (exp: 2.084- 2.607) Avg: 2.300 [0.191] (exp: 2.302)	Range: 2.201-2.561 Avg: 2.295 [0.188]	Range: 2.197-2.566 Avg: 2.306 [0.191]	Range: 2.206-2.444 Avg: 2.297 [0.202]
NAO charges	Pd_i	-0.70	-0.70	-0.70	-0.72
	Pd_{cubo}	4 x 0.377	4 x 0.387	4 x 0.380	4 x 0.376
		4 x 0.378	4 x 0.362	4 x 0.393	2 x 0.404
		2 x 0.356	2 x 0.364	2 x 0.374	2 x 0.391
2 x 0.384		2 x 0.392	2 x 0.386	2 x 0.383	
Tr	2 x -0.307	2 x -0.428	2 x -0.151	2 x 0.006	
	4 x -0.297	4 x -0.489	4 x -0.153	2 x 0.009	
				2 x 0.015	

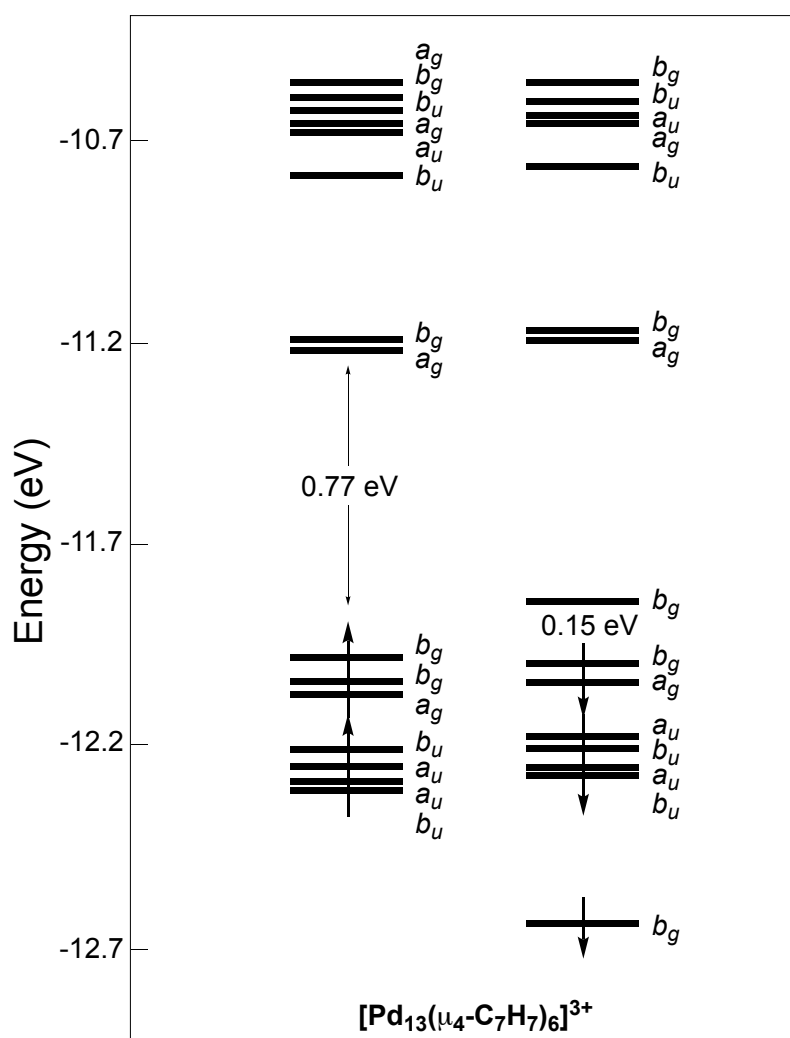


Figure S1. Kohn-Sham spin-orbital diagram of the $[\text{Pd}_{13}\text{Tr}_6]^{3+}$ cluster (C_{2h} symmetry).

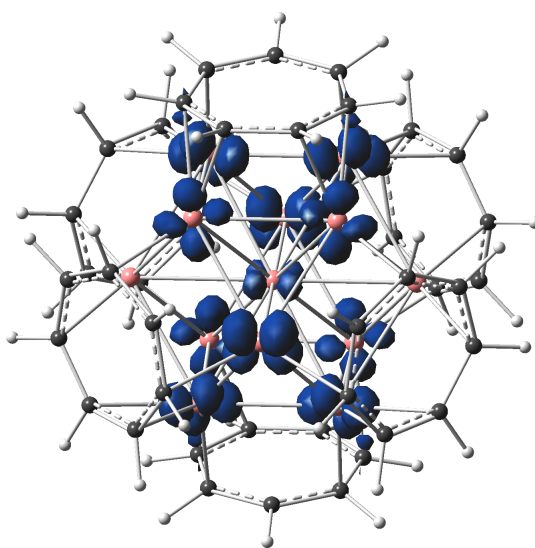


Figure S2. Spin density of the $[\text{Pd}_{13}\text{Tr}_6]^{3+}$ cluster (C_{2h} symmetry).

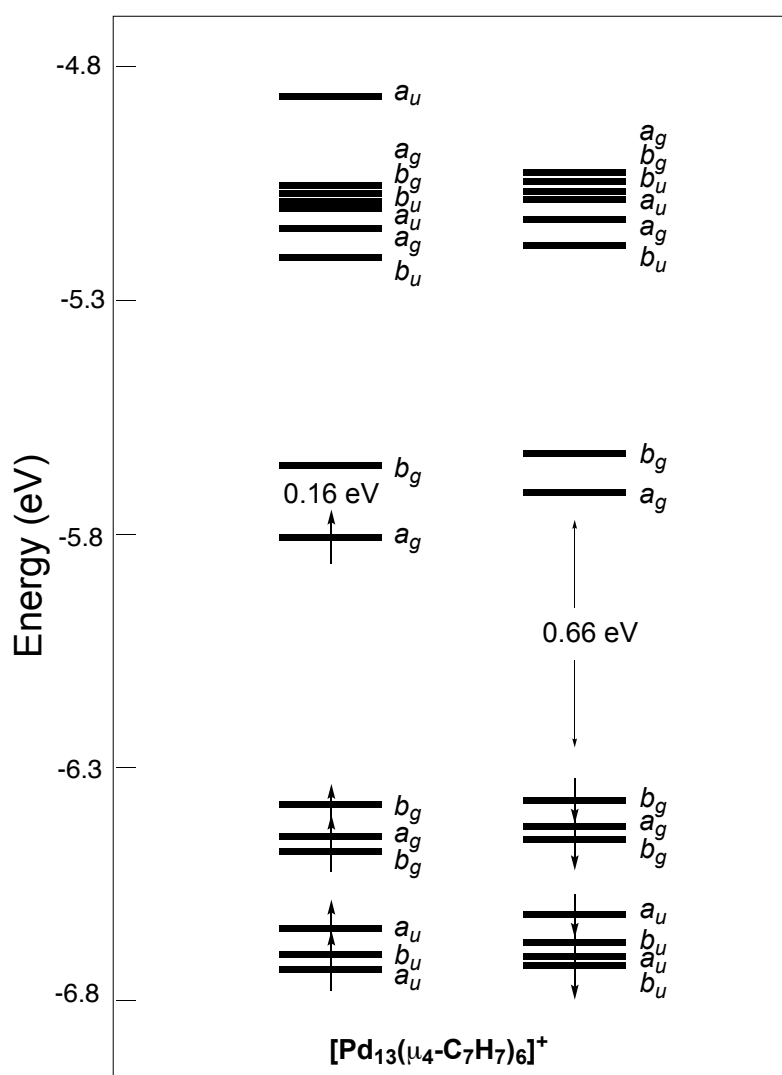


Figure S3. Kohn-Sham spin-orbital diagram of the $[\text{Pd}_{13}\text{Tr}_6]^+$ cluster (C_{2h} symmetry).

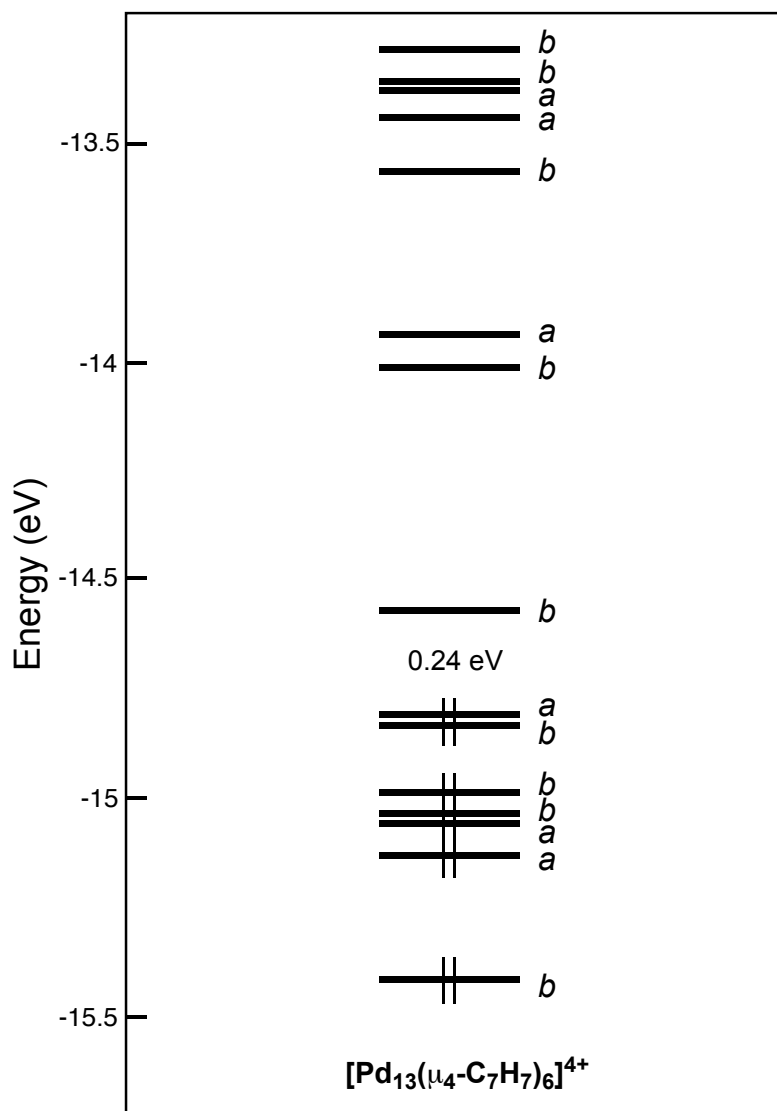


Figure S4. Kohn-Sham spin-orbital diagram of the $[\text{Pd}_{13}\text{Tr}_6]^{4+}$ cluster (C_2 symmetry).

Chapter 8

Theoretical Analysis of the Mackay Icosahedral Cluster

$\text{Pd}_{55}(\text{P}^i\text{Pr}_3)_{12}(\mu_3\text{-CO})_{20}$: An Open-shell 20-electron

Superatom

8.1 Introduction

In 2016, the first isolation of the crystalline icosahedral Mackay $\text{Pd}_{55}(\text{P}^i\text{Pr}_3)_{12}(\mu_3\text{-CO})_{20}$ (**1**) cluster was reported.¹ This fascinating compound that ideally conforms to I_h symmetry (without isopropyl substituents) is somewhat unique. The Matryoshka doll-like 55-metal-atom two-shell cluster architecture consists of a centered Pd_{13} icosahedron encapsulated within a Pd_{42} icosahedron. In I_h symmetry, the outer icosahedron is made of two different types of symmetry equivalent vertices, of 12 and 30 degeneracy, respectively. The whole $\text{Pd}@Pd_{12}@Pd_{42}$ metal kernel corresponds to a so-called Mackay “hard-sphere” model.² Mackay icosahedra are densely packed assemblies of equal-sized spheres which are characterized by specific numbers of spheres (atoms), 13, 55, 147, 309, etc. forming concentric shells, 1, 2, 3, 4, etc., respectively.² The Pd_{55} kernel of **1** is the first crystallographically documented molecular example of a Mackay icosahedron.¹ The 12 outer Pd atoms that are located on the C_5 axis are coordinated by a phosphine ligand, whereas 20 symmetry-equivalent triangular faces of the Pd_{42} outer shell (metal atoms not attached to the 12 phosphine ligands) are capped by carbonyl ligands. The icosahedral two-shell Pd architecture of $\text{Pd}_{55}(\text{P}^i\text{Pr}_3)_{12}(\mu_3\text{-CO})_{20}$ is shown in Figure 1.

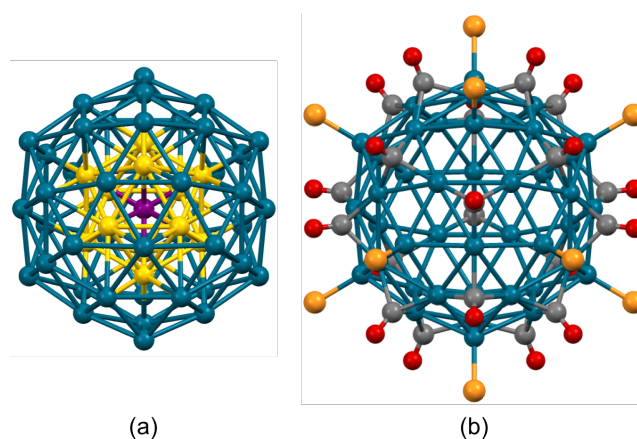


Figure 1. Structural arrangement of $\text{Pd}_{55}(\text{P}^i\text{Pr}_3)_{12}(\mu_3\text{-CO})_{20}$: a) “Matryoshka doll sequence” of the $\text{Pd}@Pd_{12}@Pd_{42}$ metal kernel, and b) outer Pd_{42} shell with surrounding ligands (isopropyl groups not shown for clarity). The purple, yellow, dark blue, orange, grey, and red spheres are central Pd (Pd'), inner Pd (Pd''), outer Pd (Pd'''), P, C, and O atoms, respectively.¹

The structure and bonding properties of stable (viable³) inorganic clusters, are usually governed by their number of valence electrons. Indeed, as for any stable molecular compound,

there are strong relationships between the structure and the electron count of clusters. Such relationships are based on the closed-shell principle and assume that no antibonding orbital is occupied. In the case of organometallic transition-metal clusters, these relationships are issued from the polyhedral skeletal electron pair (PSEP) theory,⁴ of which the Wade-Mingos electron-counting rules⁵⁻⁹ are the most popularized. These rules generally apply well to hollow clusters made of metal atoms, the valence *d* orbitals of which participate to the bonding. This is not the case for group 11 metal clusters, for example, which have their (localized) valence *d* shell filled and then can be ignored in the count of bonding electrons.¹⁰ Thus, group 11 metals participate to the bonding mainly with their valence *s* orbitals. They usually tend to aggregate in a compact (non-hollow) and often spherical way. To understand their structure and composition, the concept of *superatom*,⁸⁻²⁴ based on the spherical *jellium* model,²⁵⁻²⁷ is used. This qualitative model considers electrons within a radial phenomenological potential supposed to describe the average electrostatic potential associated with the cluster atom nuclei. Thus, the spherical *jellium* model does not consider explicitly the atom nuclei. On the other side, it allows describing the cluster electronic structure in terms of *superatomic* orbitals, somewhat similar to atomic orbitals, but extending over the whole cluster sphere. Their shell ordering is largely independent from the cluster composition and spans as $1S < 1P < 1D < 2S < 1F$, etc. As for atomic systems, closed-shell (noble gas) stability will be achieved for specific (“magic”) electron counts, i.e., 2, 8, 18, 20, 34, etc. It is of note that the *superatom* approach considers only the delocalized electrons that are responsible for the bonding within the cluster kernel. In a regular LCAO-MO DFT calculations on group 11 clusters, these electrons are identified as those occupying the Kohn-Sham orbitals of dominant valence *s* character.^{10,14-18,20} It turns out that most of the coinage metal clusters isolated so far obey the above-mentioned closed-shell *superatomic* rule.¹⁴⁻¹⁹ It is also noteworthy that in the case of group 11 clusters, both the whole cluster and its metal *superatomic* kernel possess a HOMO-LUMO gap for the considered “magic” electron count. Thus, the external “passivating” shell (the ligands and possibly additional outer metal atoms, all in their actual oxidation states) does not participate to the *superatom* (*jellium*) electron count.

Group-10 clusters of a certain size also tend to aggregate in a compact fashion.²⁸⁻³³ However, no general electron-counting rules developed for high nuclearity spherical clusters^{4,33} seem to apply to these species in a comprehensive manner. On one side, they often do not obey the classical Wade-Mingos rules. On the other side, the metal oxidation state being generally zero (or close to zero), their *superatomic* electron number is, at least at first sight, also zero (no valence *s* electrons). Dahl’s unique atom-precise $\text{Pd}_{55}(\text{P}^i\text{Pr}_3)_{12}(\mu_3\text{-CO})_{20}$ with a total of 614

valence electrons and zero 5s electron (assuming Pd(0) $4d^{10} 5s^0$ configuration) is a typical example. Several questions arise from its structure and composition: (i) Are both the whole cluster and its isolated Pd₅₅ kernel closed-shell entities? (ii) Is the number of 2-electron ligands, i.e., 32, imposed by electronic stability or can it be varied without substantial stability and structural change? (iii) To what extent are the 4d and 5s metallic orbitals involved in the Pd-Pd and Pd-ligand bonding? And finally, (iv) is the electronic structure of Pd₅₅(P^{*i*}Pr₃)₁₂(μ₃-CO)₂₀ somewhat related to that of group-11 *superatoms*? Density functional theory (DFT) calculations were carried out on the title compound, aiming at providing some answers to these questions. The main results are discussed in this chapter.

8.2 Computational Details

Density functional theory (DFT) calculations³⁴ were performed using the Amsterdam Density Functional (ADF2016) code.³⁵ Scalar relativistic effects were taken into account via the Zeroth Order Regular Approximation (ZORA).³⁶ The Vosko-Wilke-Nusair functional (VWN)³⁷ for the Local Density Approximation (LDA) and gradient corrections for exchange and correlation of Becke and Perdew (BP86 functional),^{38,39} together with Grimme's empirical DFT-D3 corrections,⁴⁰ were used for geometry optimization and analytical vibrational frequency computation. A triple-zeta basis set, augmented with a polarization function (STO-TZP)⁴¹ for palladium was used. Similar results were obtained with other functionals (see Annex). Natural atomic orbital (NAO) populations and Wiberg bond indices (WBIs) were computed using ADF optimized geometries with the natural bond orbital (NBO) 6.0 program,⁴² implemented in the Gaussain16 package,⁴³ at the BP86/Def2-SVP⁴⁴ level.

8.3 Results and Discussion

Three different Pd₅₅L₁₂(μ₃-CO)₂₀ model clusters were considered in the calculations. The P^{*i*}Pr₃ ligands of Dahl's compound were first modeled by simple PH₃ phosphines to reduce computational efforts. However, because of the mismatch of the phosphine three-fold symmetry with the five-fold icosahedral symmetry axes, the exact symmetry of the computed cluster was reduced to C_{2h}. Linear L = CO and CNH – the latter possesses electronic properties similar to those of phosphines and allows a higher symmetry of the molecule – ligands were also considered, for which the highest possible cluster symmetry is I_h. The three computed models provided similar results in terms of both their electronic structures and geometries overall. In the following, the L = CO case is analyzed in more details. Since the ADF program does not work with the I_h symmetry group, models with L = CO and CNH were treated in D_{5d} symmetry

instead, although the optimized structures were found to be very close to I_h . This is why they are most often described below assuming ideal I_h symmetry.

The three $\text{Pd}_{55}\text{L}_{12}(\mu_3\text{-CO})_{20}$ ($\text{L} = \text{PH}_3, \text{CO}, \text{CNH}$) models were found to have a triplet ground state (Table 1). The lowest singlet states were found to lie 0.83, 0.45 and 0.13 eV above the triplet for $\text{L} = \text{Ph}_3, \text{CO}$ and CNH , respectively. The ground state optimized geometrical data are in a good agreement with the X-ray data of $\text{Pd}_{55}(\text{P}^i\text{Pr}_3)_{12}(\mu_3\text{-CO})_{20}$.¹ A careful analysis of the Kohn-Sham frontier orbitals suggests that a closed-shell ground state configuration should be achieved with two additional electrons accompanied with minor structural differences with respect to their neutral states, i.e., pseudo- I_h symmetry. Calculations on the $[\text{Pd}_{55}\text{L}_{12}(\mu_3\text{-CO})_{20}]^{2-}$ dianionic species confirmed this hypothesis, with significant HOMO-LUMO energy gaps of the order of 0.5-0.6 eV (Table 2). As expected, the addition of two electrons hardly affects the interatomic distances of the cluster. The computed Pd–Pd Wiberg indices reflect the interatomic distances and are indicative of moderate metal–metal bonding interactions (Table 2). A glance at the computed natural atomic orbital (NAO) charges reveals some electron transfer from the Pd_{42} *outer* metal shell to the ligand envelope via $d\pi(\text{Pd})-\pi^*(\text{CO})$ back-bonding, as well as to the *inner* Pd_{12} shell and central Pd atom (Table 2).¹

Table 1. Relevant atomic distances computed for the three optimized neutral models $\text{Pd}_{55}\text{L}_{12}(\mu_3\text{-CO})_{20}$ ($\text{L} = \text{PH}_3, \text{CO}, \text{CNH}$) in their triplet ground state configuration. The metal atom labelling corresponds to $\text{Pd}'@_{12}\text{Pd}''@_{42}$. X-ray experimental distances of $\text{Pd}_{55}(\text{P}^i\text{Pr}_3)_{12}(\mu_3\text{-CO})_{20}$ are given for comparison.¹

$[\text{Pd}_{55}\text{L}_{12}(\mu_3\text{-CO})_{20}]$ ($\text{L} = \text{PH}_3, \text{CO}, \text{CNH}$)					
L		PH_3	CO	CNH	Exp. ¹
Average Distances (Å)	$\text{Pd}'-\text{Pd}''$	2.636	2.649	2.645	2.63
	$\text{Pd}''-\text{Pd}''$	2.772	2.785	2.782	2.76
	$\text{Pd}''-\text{Pd}'''$	2.800	2.802	2.800	2.77
	$\text{Pd}'''-\text{Pd}'''$	2.845	2.857	2.853	2.83
	$\text{Pd}'''-\text{L}$	2.229	1.907	1.918	2.24
	$\text{Pd}'''-\text{CO}$	2.092	2.096	2.092	2.07

We discuss below the electronic structure of the $[\text{Pd}_{55}(\text{CO}_{12})(\mu_3\text{-CO})_{20}]^{2-}$ dianion in more detail, before returning to that of the neutral clusters. Its density of states (DOS), plotted in Figure 2, is consistent with a unique favored closed-shell electron count of 616, corresponding to a dianionic species (similar DOS are computed for $[\text{Pd}_{55}(\text{PH}_3)_{12}(\mu_3\text{-CO})_{20}]^{2-}$ and $[\text{Pd}_{55}(\text{CNH})_{12}(\mu_3\text{-CO})_{20}]^{2-}$, see Figure S1 and S2 in Annex). A Kohn-Sham diagram of the

frontier orbitals of $[\text{Pd}_{55}(\text{CO}_{12})(\mu_3\text{-CO})_{20}]^{2-}$ is also provided in Figure 3. Unsurprisingly, the highest occupied states are of dominant $4d$ metal character, while the lowest unoccupied ones have also some $\pi^*(\text{CO})$ admixture.

Table 2. Relevant data computed for the three optimized dianionic models $[\text{Pd}_{55}\text{L}_{12}(\mu_3\text{-CO})_{20}]^{2-}$ ($\text{L} = \text{PH}_3, \text{CO}, \text{CNH}$) in their ground state (singlet) configuration. The metal atom labelling corresponds to $\text{Pd}'@_{12}\text{Pd}''@_{12}\text{Pd}'''$. The two different symmetry types of Pd''' atoms are labelled Pd_a''' and Pd_b''' .

$[\text{Pd}_{55}\text{L}_{12}(\mu_3\text{-CO})_{20}]^{2-}$ ($\text{L} = \text{PH}_3, \text{CO}, \text{CNH}$)				
L		PH_3	CO	CNH
HOMO-LUMO gap (eV)		0.54	0.58	0.62
Average Distances (Å) [Wiberg indices]	$\text{Pd}'\text{-Pd}''$	2.644 [0.078]	2.658 [0.075]	2.655 [0.074]
	$\text{Pd}''\text{-Pd}''$	2.781 [0.092]	2.795 [0.092]	2.792 [0.092]
	$\text{Pd}''\text{-Pd}'''$	2.798 [0.115]	2.799 [0.112]	2.798 [0.111]
	$\text{Pd}'''\text{-Pd}'''$	2.846 [0.069]	2.858 [0.065]	2.855 [0.067]
	$\text{Pd}'''\text{-L}$	2.222 [0.475]	1.898 [0.796]	1.902 [0.766]
	$\text{Pd}'''\text{-CO}$	2.089 [0.405]	2.092 [0.398]	2.091 [0.402]
Average NAO populations and atomic charges	1 x Pd'	$4d^{9.33} 5s^{0.92} 5p^{0.04}$ -0.31	$4d^{9.35} 5s^{0.95} 5p^{0.05}$ -0.37	$4d^{9.35} 5s^{0.95} 5p^{0.05}$ -0.37
	12 x Pd''	$4d^{9.48} 5s^{0.63} 5p^{0.03}$ -0.17	$4d^{9.48} 5s^{0.65} 5p^{0.03}$ -0.20	$4d^{9.49} 5s^{0.65} 5p^{0.03}$ -0.20
	30 x Pd_a'''	$4d^{9.32} 5s^{0.45} 5p^{0.01}$ +0.21	$4d^{9.32} 5s^{0.45} 5p^{0.01}$ +0.21	$4d^{9.32} 5s^{0.45} 5p^{0.01}$ +0.22
	12 x Pd_b'''	$4d^{9.46} 5s^{0.65} 5p^{0.02}$ -0.15	$4d^{9.29} 5s^{0.69} 5p^{0.02}$ -0.01	$4d^{9.27} 5s^{0.68} 5p^{0.02}$ +0.02
	42 x Pd''' (av.)	+0.11	+0.15	+0.16
	L	+0.20	+0.01	+0.02
	CO	-0.33	-0.28	-0.31

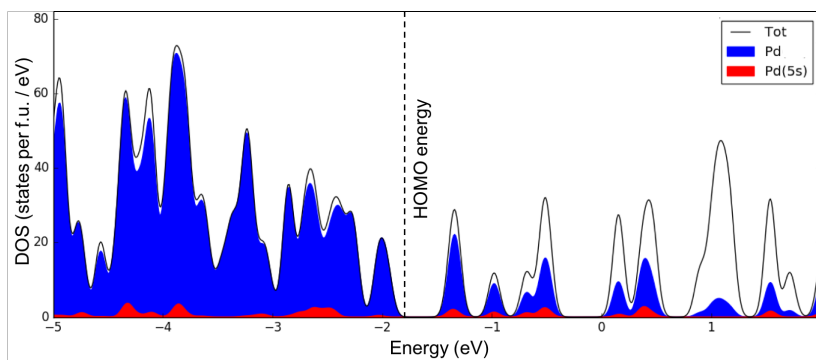


Figure 2. Total, Pd, and Pd(5s) projected DOS of $[\text{Pd}_{55}(\text{CO})_{12}(\mu_3\text{-CO})_{20}]^{2-}$ (Gaussian full width at half maximum = 0.1 eV). The dotted line corresponds to the energy of the HOMO.

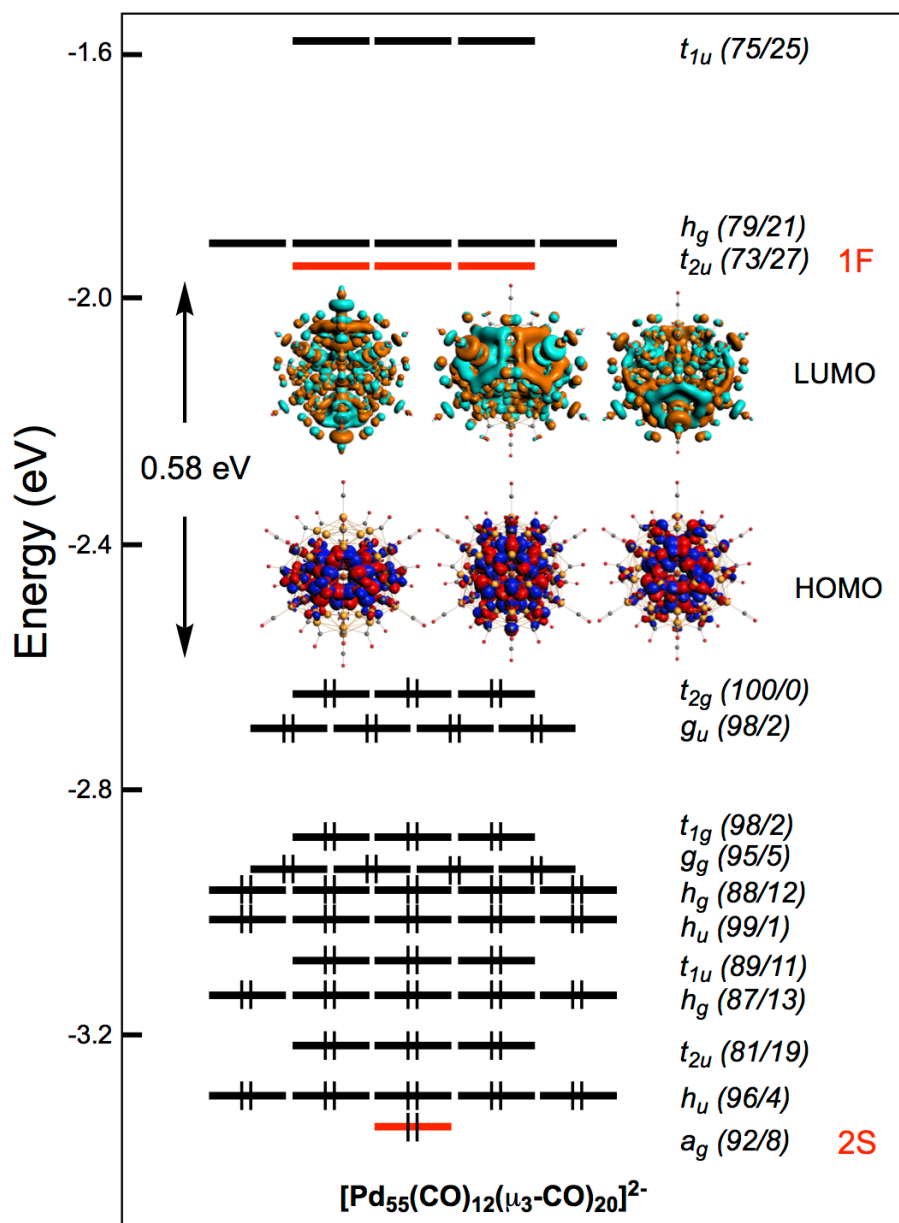


Figure 3. Kohn-Sham molecular orbital (MO) diagram of $[\text{Pd}_{55}(\text{CO})_{12}(\mu_3\text{-CO})_{20}]^{2-}$ (I_h symmetry assumed). Values in parenthesis indicate metal/ligand composition (in %). Levels shown in red correspond to *jellium* levels. In I_h symmetry, the vacant 1F level is split into t_{2u} (LUMO) and g_u (lying at higher energy and not shown).

A detailed analysis of the occupied orbital compositions reveals that ten of them are also of major 5s (Pd) character. These orbitals are plotted in Figure 4. They can be easily identified as the 1S, 1P, 1D and 2S *superatomic* (“*jellium*”) orbitals. The lowest one (1S) is strongly bonding and lies below the whole block of the 4d states. The highest one (2S) is still significantly bonding and situated 0.79 eV below the HOMO. Thus, with a $1S^2 1P^6 1D^{10} 2S^2$ *superatom* configuration, $[\text{Pd}_{55}(\text{CO})_{12}(\mu_3\text{-CO})_{20}]^{2-}$ is a 20-electron *superatom*. Assuming that Pd(0) is

$4d^{10}5s^0$, one should expect only one of the $5s$ combinations occupied by the two electrons associated with the $2-$ charge. Since ten $5s$ combinations are actually occupied in the dianionic clusters, it means that nine $4d$ -type combinations have formally transferred their electrons to nine of the $5s$ combinations. In order to get a deeper understanding on this MO level crossing, we used the opportunity given by the ADF program suite to express the molecular orbitals as linear combinations of the orbitals of two fragments, that we chose to be $[\text{Pd}_{55}]^{2-}$ metal kernel and its complete $[(\text{CO})_{32}]$ ligand shell, respectively. Unsurprisingly, single-point spin-restricted calculations (as required by the ADF program) on the $[\text{Pd}_{55}]^{2-}$ fragment could not converge in a reasonable ground state. Excited states were obtained instead. Just to mention, the same situation occurred for the neutral I_h fragment. These results are in line with calculations previously carried out on Pt_{55} .⁴⁵ Nevertheless, these results were sufficient for extracting the qualitative bonding picture sketched in Figure 5. For the sake of simplicity, the $\pi^*(\text{CO})$ orbitals are not considered in this diagram, although they play a substantial role in stabilizing the occupied $4d$ -block. The unstable $[\text{Pd}_{55}]^{2-}$ fragment has $275 (4d) + 10 (5s) = 285$ low-lying combinations, of which $275 + 1 = 276$ are occupied.

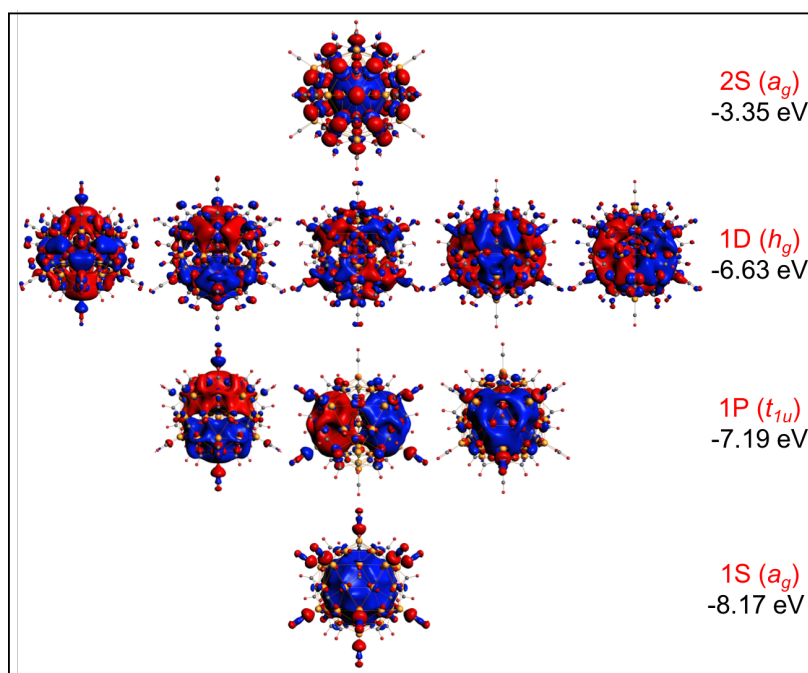


Figure 4. The ten occupied *superatomic* orbitals of $[\text{Pd}_{55}(\text{CO})_{12}(\mu_3\text{-CO})_{20}]^{2-}$.

Assuming formally that nine among the ten $5s$ combinations are unoccupied, one is left with the $[\text{Pd}_{55}]^{2-}$ MO picture shown on the left of Figure 5. The combinations of the ligand lone pair orbitals interact with the high-lying accepting orbitals on the metal-outer shell (sp -type), but also with the $4d$ -block. This later interaction results in the destabilization of nine $4d$

combinations, which in turn transfer their electrons to the mainly unperturbed 1P, 1D and 2S orbitals. This creates a not-very-large but significant HOMO-LUMO gap which provides $[\text{Pd}_{55}(\text{CO}_{12})(\mu_3\text{-CO})_{20}]^{2-}$ with a closed-shell configuration for the count of 20 *superatom* electrons. Unfortunately, because of important mixing with $\pi^*(\text{CO})$ orbitals, it was not possible to individually identify the nine vacant 4d combinations. However, a detailed orbital counting allows to determine their symmetry ($a_g + t_{1u} + h_g$), which is the same as that of the nine *superatomic* orbitals to which they transfer their electrons (Figure 5). To conclude this section, it is noteworthy that the two other computed models $[\text{Pd}_{55}\text{L}_{12}(\mu_3\text{-CO})_{20}]^{2-}$ (L = PH_3 , CNH) provided the same electronic structure as $[\text{Pd}_{55}(\text{CO}_{12})(\mu_3\text{-CO})_{20}]^{2-}$.

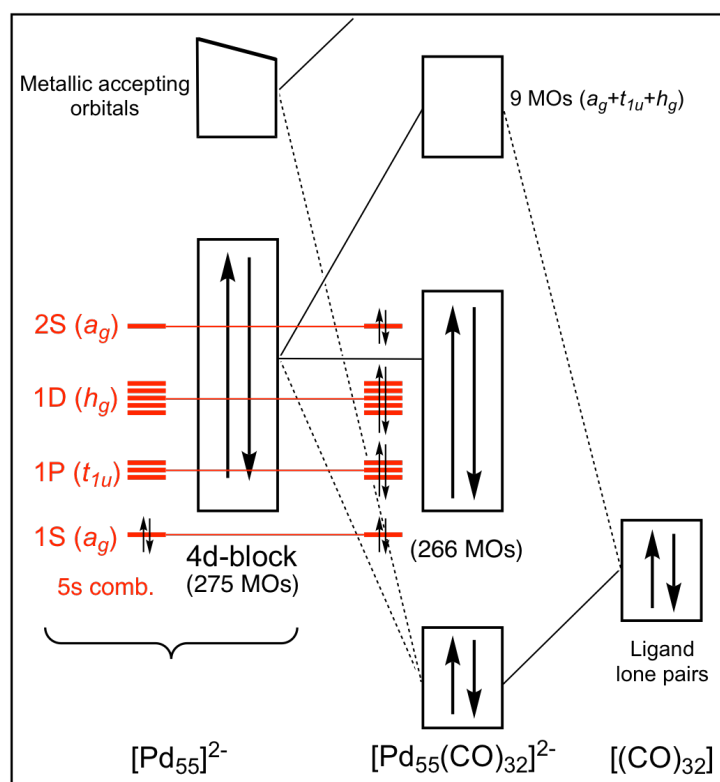


Figure 5. Simplified MO diagram of $[\text{Pd}_{55}(\text{CO})_{12}(\mu_3\text{-CO})_{20}]^{2-}$ obtained on the basis of the interaction between the $[\text{Pd}_{55}]^{2-}$ and $[(\text{CO})_{32}]$ fragments.

A peculiarity of these $[\text{Pd}_{55}\text{L}_{12}(\mu_3\text{-CO})_{20}]^{2-}$ clusters is that their (unstable) icosahedral Pd_{55} metal kernel needs its ligand outer shell for reaching a closed-shell configuration associated with a “magic” *superatom* electron count. A similar situation was found for another Pd cluster, namely the two-electron *superatomic* cuboctahedral species $[\text{Pd}_{13}(\mu_4\text{-C}_7\text{H}_7)_6]^{2+}$ (see Chapter 7 of this thesis).^{46,47} Our calculations on the $[\text{Pd}_{55}\text{L}_{12}(\mu_3\text{-CO})_{20}]^{2-}$ models indicate that this closed-shell configuration is retained when the 12 terminal L ligands are removed, but with a very

small HOMO-LUMO gap. Further adding of these 12 ligands results in a substantial destabilization of the LUMOs, leading to the HOMO-LUMO gaps given in Table 2. We believe that the fact that some metal *d*-type orbitals participate to the bonding with the ligands (i.e., are destabilized and depopulated to the benefit of *superatomic* orbitals) is likely not to be uncommon in Pd or Pt cluster chemistry. Indeed, group-10 metals are at the borderline between middle transition-metal and group-11 elements that tend to keep their d-block fully occupied and non-bonding. Indeed, the general MO interacting diagram for a closed-shell Au, Ag or Cu *superatom* sketched in Figure 6 can be compared to that of Figure 5.

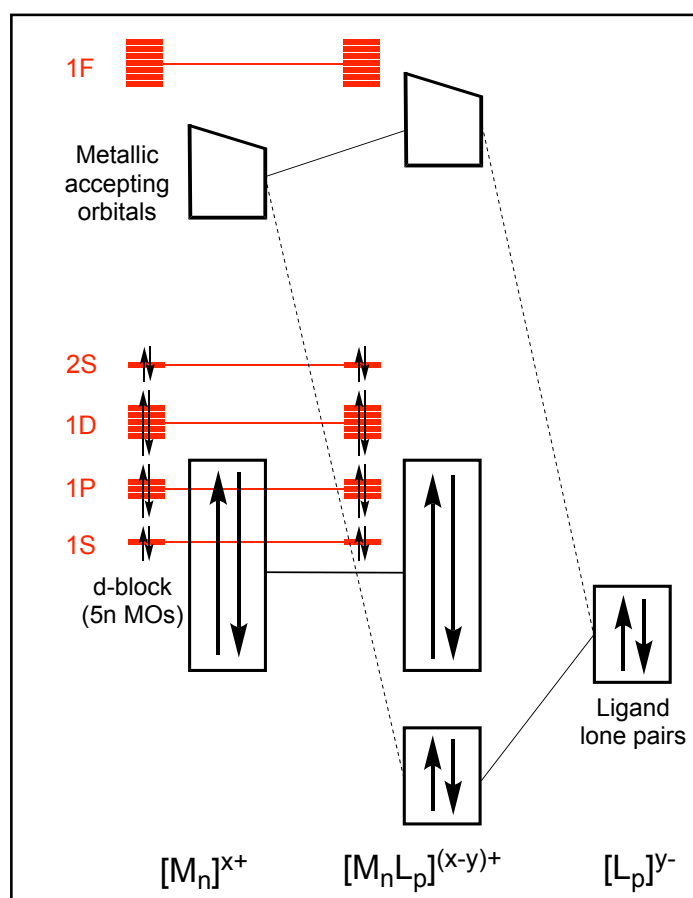


Figure 6. Simplified general MO diagram for a ligated group-11 closed-shell $[M_n L_p]^{(x-y)+}$ *superatom* with an arbitrarily chosen 20-electron “magic” count for a direct comparison with the case of figure 5. Ligands are considered as two-electron donors, with their formal charges adjusted accordingly (for example, neutral phosphines but anionic thiolates or halogenides).

We now return to the discussion on the real charge of Dahl’s cluster which is not a di-anion, but a neutral species. Removing two electrons from the dianion does not modify the *superatom* electron count since the depopulated orbitals are 4*d*-type combinations (Figure 3). As said

above, our computed species were found to have triplet ground state configurations. Unfortunately, no explicit mention of the spin state is provided in Dahl's paper for $\text{Pd}_{55}(\text{P}^i\text{Pr}_3)_{12}(\mu_3\text{-CO})_{20}$.¹ No paramagnetic behavior can be traced from the reported ^{31}P NMR spectrum and unfortunately no NMR ^1H or ^{13}C measurements were reported. In any case, regardless of the considered spin state, Jahn-Teller instability is virtually cancelled by the very high cluster compactness of the cluster. Kinetic stability is also expected from the spin density plots of the computed $\text{Pd}_{55}\text{L}_{12}(\mu_3\text{-CO})_{20}$ neutral models (Figure 7), which indicate that most of the spin density is confined in the heart of the metallic kernel, with negligible participation of the cluster surface shell (less than 6 %). Thus, low radical reactivity is expected for such species. In fact, another fully characterized example of a 55-atom Mackay *superatom* is known, namely the paramagnetic cluster $[\text{Cu}_{43}\text{Al}_{12}](\text{Cp}^*)_{12}$ ($\text{Cp}^* = \text{C}_5\text{Me}_5$) with an open-shell 67-electron *superatom* configuration.⁴⁸ The kinetic stability of the latter originates from the steric protection of a compact Cp^* outer shell. The not yet fully characterized Schmid's cluster (Nanogold®)⁴⁹⁻⁵³ $\text{Au}_{55}(\text{PPh}_3)_{12}\text{Cl}_6$ is also (as well as its monoanion) an open-shell species with the $1\text{S}^2 1\text{P}^6 1\text{D}^{10} 2\text{S}^2 2\text{P}^6 1\text{F}^{14} 1\text{G}^9$ *superatomic* configuration.⁵⁴ However, its chemical composition and electron count have been debated.⁵⁵ Obviously, Mackay compact kernel structures of 55 atoms reaches a size where it starts to behave (somewhat) as a nanoparticle, allowing not a single but a (small) range of electron counts. The upper limit of this range corresponds to the best closed-shell favored electron count, i.e., the "molecular" favored count. Such a situation is not so uncommon in transition-metal cluster chemistry. For example, it has been observed in the case of much smaller cobalt-carbonyl clusters.^{56,57} The fact that the neutral form of Dahl's cluster was isolated and not its closed-shell dianion is likely to result from the balance of several factors, among which the method of synthesis is one of the most determinant. In any case, $[\text{Pd}_{55}\text{L}_{12}(\mu_3\text{-CO})_{20}]$ should be easily be reduced.

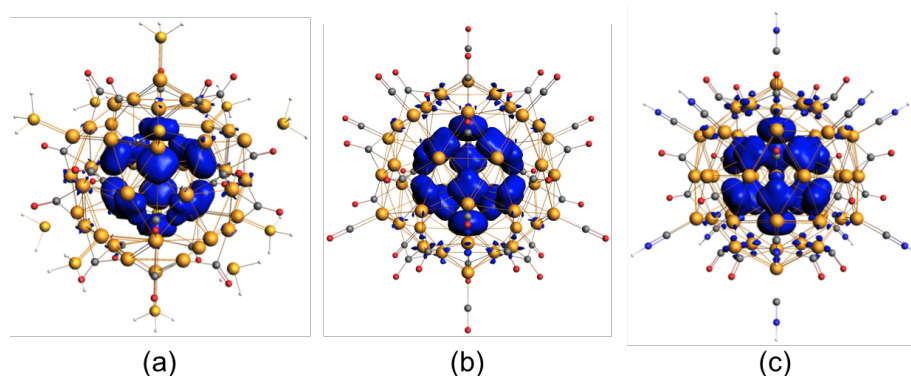


Figure 7. Spin density plots of $\text{Pd}_{55}\text{L}_{12}(\mu_3\text{-CO})_{20}$ with $\text{L} = \text{PH}_3$ (a), CO (b), CNH (c).

8.4 Conclusion

We have shown for the first time that the structure of the spherical nanosized cluster $[\text{Pd}_{55}\text{L}_{12}(\mu_3\text{-CO})_{20}]$ can be interpreted using the *jellium* model as a regular *superatom*, characterized by the “magic” 20-electron count ($1\text{S}^2 1\text{P}^6 1\text{D}^{10} 2\text{S}^2$ configuration). Its open shell nature is associated with 4*d*-type single electrons located deeply on the metal kernel, so that the stability of the cluster is not affected. A favored closed-shell situation occurs with two additional electrons (dianionic state). This does not modify the *superatomic* 20-electron count. These 20 electrons are located in bonding combinations of 5*s* AOs, which means that, considering the closed-shell dianion, nine 4*d*-type combinations have formally transferred their electrons in nine of the 5*s* MO combinations. This level crossing does not occur on the bare $[\text{Pd}_{55}]^{2-}$ kernel. It necessitates the presence of the ligands, which destabilize the nine 4*d*-type MOs and open a HOMO-LUMO gap. This is at variance with group-11 ligated clusters for which no *d*-type to *s*-type electron transfer occurs. The need for the ligand envelope for inducing a closed-shell situation has already been noted in the case of the two-electron *superatom* species $[\text{Pd}_{13}(\mu_4\text{-C}_7\text{H}_7)_6]^{2+}$ (Chapter 7).^{46,47}

Interestingly, among the flurry of extraordinary diverse nanosized CO/PR₃-ligated icosahedral and ccp/hcp-based (homo/hetero) Pd_n clusters reported over the last 20 years,^{28,29} only three conform to the icosahedral Mackay model, namely the title compound, the three-shell 145-metal-atom $\text{Pd}_{145}(\text{CO})_x(\text{PEt}_3)_{30}$ ($x \approx 60$) cluster compound,⁵⁸ and the Pd-Pt four-shell 165-metal-atom $\text{Pd}_{164-x}\text{Pt}_x(\mu_{12}\text{-Pt})(\text{CO})_{72}(\text{PPh}_3)_{20}$ ($x \approx 7$) cluster compound.⁵⁹ It is likely that the *superatom* feature observed for $\text{Pd}_{55}\text{L}_{12}(\mu_3\text{-CO})_{20}$ is a general rule that can be applicable to group-10 spherical or nearly spherical ligated clusters such as the Pd₁₄₅ and Pd/Pt₁₆₅ species that contain interior two-shell icosahedral Mackay-type geometries.^{58,59} Following this line, we suggest that these palladium spherical clusters are indeed *superatoms* characterized by (at least approximately) “magic” electron counts, these electrons occupying 5*s* (Pd) or 6*s* (Pt) states and resulting from electron transfer from 4*d* (Pd) or 5*d* (Pt) states. We think that such electron transfers are likely to govern the metal-metal bonding in the whole chemistry of these group-10 clusters. Finally, note that the present study is also relevant to catalysis as Pd₅₅ clusters are close to the optimal cluster size for maximum catalytic activity of Pd clusters and small nanoparticle catalysts.⁶⁰⁻⁶²

8.5 References

- 1 Erickson, J. D.; Mednikov, E. G.; Ivanov, S. A.; Dahl, L. F. Isolation and Structural Characterization of a Mackay 55-Metal-Atom Two-Shell Icosahedron of Pseudo- I_h Symmetry, $\text{Pd}_{55}\text{L}_{12}(\mu_3\text{-CO})_{20}$ (L = PR_3 , R = Isopropyl): Comparative Analysis with Interior Two-Shell Icosahedral Geometries in Capped Three-Shell Pd_{145} , Pt-Centered Four-Shell Pd–Pt M_{165} , and Four-Shell Au_{133} Nanoclusters. *J. Am. Chem. Soc.* **2016**, *138*, 1502–1505.
- 2 Mackay, A. L. A dense non-crystallographic packing of equal spheres. *Acta Crystallogr.* **1962**, *15*, 916–918.
- 3 Hoffmann, R.; Schleyer, P. v. R.; Schaefer III, H. F. Predicting molecules—more realism, please! *Angew. Chem. Int. Ed.* **2008**, *47*, 7164–7167.
- 4 Mingos, D. M. P.; Wales, D. J. Introduction to Cluster Chemistry, Prentice-Hall, Englewood Cliffs, **1990**.
- 5 Mason, R.; Thomas, K. M.; Mingos, D. M. P. Stereochemistry of octadecacarbonylhexaosmium (0). Novel hexanuclear complex based on a bicapped tetrahedron of metal atoms. *J. Am. Chem. Soc.* **1973**, *95*, 3802–3804.
- 6 Johnston, R. L.; Mingos, D. M. P. Theoretical models of cluster bonding. *Struc. Bond.* **1987**, *68*, 29–87.
- 7 Mingos, D. M. P. Theoretical aspects of metal cluster chemistry. *Pure. Appl. Chem.* **1991**, *63*, 807–812.
- 8 Saillard, J.-Y.; Halet, J.-F. Structure and bonding patterns in large molecular ligated metal clusters. *Struct. Bond.* **2016**, *169*, 157–179.
- 9 Frapper, G.; Halet, J.-F.; Oganov, A. R.; Kvashnin, A. G.; Saleh, G. in Computational Materials Discovery (Royal Society of Chemistry), London, **2019**, pp. 320–351.
- 10 Mingos, D. M. P. Structural and bonding patterns in gold clusters. *Dalton Trans.* **2015**, *44*, 6680–6695.
- 11 Lin, Z.; Slee, T.; Mingos, D. M. P. A structural jellium model of cluster electronic structure. *Chem. Phys.* **1990**, *142*, 321–334.
- 12 Jena, P.; Khanna, S. N.; Rao, B. K. in *Clusters and Nano-Assemblies: Physical and Biological Systems*, World Scientific, **2005**.
- 13 Khanna, S. N.; Jena, P. Atomic clusters: Building blocks for a class of solids. *Phys. Rev. Lett.* **2008**, *51*, 13705–13716.

- 14 Walter, M.; Akola, J.; Lopez-Acevedo, O.; Jadzinsky, P. D.; Calero, G.; Ackerson, C. J. Whetten, R. L.; Grönbeck, H.; Häkkinen, H. A Unified View of Ligand-protected Gold Clusters as Superatom Complexes. *Proc. Natl. Acad. Sci. USA* **2008**, *105*, 9157–9162.
- 15 Häkkinen, H. Atomic and electronic structure of gold clusters: understanding flakes, cages and superatoms from simple concepts. *Chem. Soc. Rev.* **2008**, *37*, 1847–1859.
- 16 Akola, J.; Walter, M.; Whetten, R. L.; Hakkinen, H.; Gronbeck, H. On the Structure of Thiolate-Protected Au₂₅. *J. Am. Chem. Soc.* **2008**, *130*, 3756–3757.
- 17 Häkkinen, H. in: *Front. Nanosci.* **2015**, *9*, (Chap. 8) Tsukuda, T.; Häkkinen, H. Eds. Elsevier, Oxford, UK.
- 18 Wang, S.; Li, Q.; Kang, X.; Zhu, M. Customizing the structure, composition, and properties of alloy nanoclusters by metal exchange. *Acc. Chem. Res.* **2018**, *51*, 2784–2792.
- 19 Muñoz-Castro, A. On the ligand–core interaction in ligand-protected gold superatoms. Insights from Au₂₅(XR)₁₈ (X = S, Se, Te) via relativistic DFT calculations. *Phys. Chem. Chem. Phys.* **2019**, *21*, 13022–13029.
- 20 Roduner, E.; Superatom chemistry: promising properties of near-spherical noble metal clusters. *Phys. Chem. Chem. Phys.* **2018**, *20*, 23812–23826.
- 21 Khanna, S. N.; Jena, P. Assembling crystals from clusters. *Phys. Rev. Lett.* **1992**, *69*, 1664–1667.
- 22 Reveles, J. U.; Khanna, S. N.; Roach, P. J.; Castleman, A. W. Multiple valence superatoms. *Proc. Natl. Acad. Sci.*, **2006**, *103*, 18405–18410.
- 23 Castleman, A. W.; Khanna, S. N. Clusters, superatoms, and building blocks of new materials. *J. Phys. Chem. C* **2009**, *113*, 2664–2675.
- 24 Claridge, S. A.; Castleman, A. W.; Khanna, S. N.; Murray, C. B.; Sen, A.; Weiss, P. S.; Cluster-assembled materials. *ACS Nano* **2009**, *3*, 244–255.
- 25 de Heer, W. A. The physics of simple metal clusters: experimental aspects and simple models. *Rev. Mod. Phys.* **1993**, *65*, 611–676.
- 26 Knight, W. D.; Clemenger, K.; de Heer, W. A.; Saunders, W. A.; Chou, M. Y.; Cohen, M. L. Electronic shell structure and abundances of sodium clusters. *Phys. Rev. Lett.* **1984**, *52*, 2141–2143.
- 27 Mingos, D. M. P.; Slee, T.; Lin, Z. Bonding models for ligated and bare clusters. *Chem. Rev.* **1990**, *90*, 383–402.
- 28 Mednikov, E. G.; Dahl, L. F. Palladium: It Forms Unique Nano-Sized Carbonyl Clusters. *J. Chem. Educ.* **2009**, *86*, 1135–1135.

- 29 Mednikov, E. G.; Dahl, L. F. Syntheses, structures and properties of primarily nanosized homo/heterometallic palladium CO/PR₃-ligated clusters. *Philos. Trans. R. Soc. A* **2010**, *368*, 1301–1332.
- 30 Belyakova, O.; Slovokhotov, Y. Structures of large transition metal clusters. *Russ. Chem. Bull.* **2003**, *52*, 2299–2327.
- 31 Femoni, C.; Iapalucci, M. C.; Kaswalder, F.; Longoni, G.; Zacchini, S. The possible role of metal carbonyl clusters in nanoscience and nanotechnologies. *Coord. Chem. Rev.* **2006**, *250*, 1580–1640.
- 32 Ciabatti, I.; Femoni, C.; Iapalucci, M. C.; Longoni, G.; Zacchini, S. Platinum carbonyl clusters chemistry: four decades of challenging nanoscience. *J. Clust. Sci.* **2014**, *25*, 115–146.
- 33 Gam, F.; Wei, J.; Kahlal, S.; Saillard, J.-Y.; Halet, J.-F. Electron Counting in Ligated High Nuclearity Late Transition Metal Clusters. In: 50th Anniversary of Electron Counting Paradigms for Polyhedral Molecules – Historical and Recent Developments. D. M. P. Mingos (ed.), *Structure and Bonding* (Springer, Berlin, Heidelberg), **2021**, *188*, 69–102.
- 34 Dyllal, K.G.; Fægri, Jr., K. Introduction to Relativistic Quantum Chemistry, Oxford University Press, New York, **2007**.
- 35 a) te Velde, G.; Bickelhaupt, F. M.; van Gisbergen, S. J. A.; Guerra, C. F.; Baerends, E. J.; Snijders, J. G.; Ziegler, T. Chemistry with ADF. *J. Comput. Chem.* **2001**, *22*, 931–967; b) ADF2016, SCM, Theoretical Chemistry, Vrije Universiteit: Amsterdam, The Netherlands; <http://www.scm.com>.
- 36 van Lenthe, E.; Baerends, E. J.; Snijders, J. G. Relativistic total energy using regular approximations. *J. Chem. Phys.* **1994**, *101*, 9783–9792.
- 37 Vosko, S. D.; Wilk, L.; Nusair, M. Accurate spin-dependent electron liquid correlation energies for local spin density calculations: a critical analysis. *Can. J. Chem.* **1980**, *58*, 1200–1211.
- 38 Becke, A. D. Density-functional exchange-energy approximation with correct asymptotic behavior. *Phys. Rev. A* **1988**, *38*, 3098–3100.
- 39 Perdew, J. P. Density-functional approximation for the correlation energy of the inhomogeneous electron gas. *Phys. Rev. B* **1986**, *33*, 8822–8824.
- 40 Grimme, S. Semiempirical GGA-type density functional constructed with a long-range dispersion correction. *J. Comput. Chem.* **2006**, *27*, 1787–1799.
- 41 Lenthe, E. V.; Baerends, E. J. Optimized Slater-type basis sets for the elements 1-118. *J. Comput. Chem.* **2003**, *24*, 1142–1156.

- 42 Glendening, E. D.; Badenhop, J. K.; Reed, A. E.; Carpenter, J. E.; Bohmann, J. A.; Morales, C. M.; Weinhold, F. NBO 6.0, Theoretical Chemistry Institute, University of Wisconsin (Madison, WI, **2001**, <http://nbo6.chem.wisc.edu>).
- 43 Frisch, M. J.; Trucks, G. W.; Schlegel, H. B.; Scuseria, G. E.; Robb, M. A.; Cheeseman, J. R.; Scalmani, G.; Barone, V.; Petersson, G. A.; Nakatsuji, H.; Li, X.; Caricato, M.; Marenich, A. V.; Bloino, J.; Janesko, B. G.; Gomperts, R.; Mennucci, B.; Hratchian, H. P.; Ortiz, J. V.; Izmaylov, A. F.; Sonnenberg, J. L.; Williams-Young, D.; Ding, F.; Lipparini, F.; Egidi, F.; Goings, J.; Peng, B.; Petrone, A.; Henderson, T.; Ranasinghe, D.; Zakrzewski, V. G.; Gao, J.; Rega, N.; Zheng, G.; Liang, W.; Hada, M.; Ehara, M.; Toyota, K.; Fukuda, R.; Hasegawa, J.; Ishida, M.; Nakajima, T.; Honda, Y.; Kitao, O.; Nakai, H.; Vreven, T.; Throssell, K.; Montgomery, J. A., Jr.; Peralta, J. E.; Ogliaro, F.; Bearpark, M. J.; Heyd, J. J.; Brothers, E. N.; Kudin, K. N.; Staroverov, V. N.; Keith, T. A.; Kobayashi, R.; Normand, J.; Raghavachari, K.; Rendell, A. P.; Burant, J. C.; Iyengar, S. S.; Tomasi, J.; Cossi, M.; Millam, J. M.; Klene, M.; Adamo, C.; Cammi, R.; Ochterski, J. W.; Martin, R. L.; Morokuma, K.; Farkas, O.; Foresman, J. B.; Fox, D. J. *Gaussian16*, Gaussian, Inc.: Wallingford, CT, **2016**.
- 44 Weigend, F.; Ahlrichs, R. Balanced basis sets of split valence, triple zeta valence and quadruple zeta valence quality for H to Rn: Design and assessment of accuracy. *Phys. Chem. Chem. Phys.* **2005**, *7*, 3297–3305.
- 45 Da Silva, J. L. F.; Kim, H. G.; Piotrowski, M. J.; Prieto, M. J.; Tremiliosi-Filho, G. Reconstruction of core and surface nanoparticles: The example of Pt₅₅ and Au₅₅. *Phys. Rev. B* **2010**, *82*, 205424.
- 46 Wei, J.; Kahlal, S.; Halet J.-F.; Saillard, J.-Y. Elucidating the electronic structure of the ligated cuboctahedral palladium cluster [Pd₁₃(μ₄-C₇H₇)₆]²⁺. *J. Clust. Sci.* **2019**, *30*, 1227–1233.
- 47 Teramoto, M.; Iwata, K.; Yamaura, H.; Kurashima, K.; Miyazawa, K.; Kurashige, Y.; Yamamoto, K.; Murahashi, T. Three-dimensional sandwich nanocubes composed of 13-atom Palladium core and hexakis-carbocycle shell. *J. Am. Chem. Soc.* **2018**, *140*, 12682–12686.
- 48 Weßing, J.; Ganesamoorthy, C.; Kahlal, S.; Marchal, R.; Gemel, C.; Cador, O.; Da Silva, A. C. H.; Da Silva, J. L. F.; Saillard, J.-Y.; Fischer, R. A. The Mackay-Type Cluster [Cu₄₃Al₁₂](Cp*)₁₂: Open-Shell 67-Electron Superatom with Emerging Metal-Like Electronic Structure. *Angew. Chem. Int. Ed.* **2018**, *57*, 14630–14634.

- 49 Schmid, G.; Pfeil, R.; Boese, R.; Bandermann, F.; Meyer, S.; Calis, G. H. M.; van der Velden, J. W. A. $\text{Au}_{55}[\text{P}(\text{C}_6\text{H}_5)_3]_{12}\text{Cl}_6$ —ein Goldcluster ungewöhnlicher Größe. *Chem. Ber.* **1981**, *114*, 3634–3642.
- 50 Schmid, G. The relevance of shape and size of Au_{55} clusters. *Chem. Soc. Rev.* **2008**, *37*, 1909–1930.
- 51 Schmid, G. Large clusters and colloids. Metals in the embryonic state. *Chem. Rev.* **1992**, *92*, 1709–1727.
- 52 Schmid, G. In *Physics and Chemistry of Metal Cluster Compounds*; de Jongh, L. J., Ed.; Kluwer Academic Publ.: Dordrecht/Boston/London, **1994**, Chap. 3, pp 107–134.
- 53 Schmid, G. In *Clusters and Colloids: From Theory to Applications*; Schmid, G., Ed.; VCH Publ. Inc.: New York, **1994**, pp 178–211.
- 54 Muñoz-Castro, A. personal communication, **2019**.
- 55 Walter, M.; Moseler, M.; Whettende, R. L.; Häkkinen, H. A 58-electron superatom-complex model for the magic phosphine-protected gold clusters (Schmid-gold, Nanogold®) of 1.4-nm dimension. *Chem. Sci.* **2011**, *2*, 1583–1587.
- 56 Bencharif, M.; Cador, O.; Cattey, H.; Ebner, A.; Halet, J.-F.; Kahlal, S.; Meier, W.; Mugnier, Y.; Saillard, J.-Y.; Schwarz, P.; Trodi, F. Z.; Wachter, J.; Zabel, M. Electron-Sponge Behavior, Reactivity and Electronic Structures of Cobalt-Centered Cubic $\text{Co}_9\text{Te}_6(\text{CO})_8$ Clusters. *Eur. J. Inorg. Chem.* **2008**, *12*, 1959–1968.
- 57 Cador, O.; Cattey, H.; Halet, J.-F.; Meier, W.; Mugnier, Y.; Wachter, J.; Saillard, J.-Y.; Zouhoune, B.; Zabel, M. Electron-Sponge Behavior and Electronic Structures in Cobalt-Centered Pentagonal Prismatic $\text{Co}_{11}\text{Te}_7(\text{CO})_{10}$ and $\text{Co}_{11}\text{Te}_5(\text{CO})_{15}$ Cluster Anions. *Inorg. Chem.* **2007**, *46*, 501–509.
- 58 Tran, N. T.; Powell, D. R.; Dahl, L. F. Nanosized $\text{Pd}_{145}(\text{CO})_x(\text{PEt}_3)_{30}$ Containing a Capped Three-Shell 145-Atom Metal-Core Geometry of Pseudo Icosahedral Symmetry. *Angew. Chem. Int. Ed.* **2000**, *39*, 4121–4125.
- 59 Mednikov, E. G.; Jewell, M. C.; Dahl, L. F. Nanosized $(\mu_{12}\text{-Pt})_{\text{Pd}164-x}\text{Pt}_x(\text{CO})_{72}(\text{PPh}_3)_{20}$ ($x \approx 7$) Containing Pt-Centered Four-Shell 165-Atom Pd–Pt Core with Unprecedented Intershell Bridging Carbonyl Ligands: Comparative Analysis of Icosahedral Shell-Growth Patterns with Geometrically Related $\text{Pd}_{145}(\text{CO})_x(\text{PEt}_3)_{30}$ ($x \approx 60$) Containing Capped Three-Shell Pd_{145} Core. *J. Am. Chem. Soc.* **2007**, *129*, 11619–11630.
- 60 Astruc, D. Palladium catalysis using dendrimers: molecular catalysts versus nanoparticles. *Tetrahedron Asym.* **2010**, *21*, 1041–1054.

- 61 Du, Y.; Sheng, H.; Astruc, D.; Zhu, M. Atomically precise noble metal nanoclusters as efficient catalysts: a bridge between structure and properties. *Chem. Rev.* **2020**, *120*, 526–622.
- 62 Yamamoto, K.; Imaoka, T.; Tanabe, M.; Kambe, T. New horizon of nanoparticle and cluster catalysis with dendrimers. *Chem. Rev.* **2020**, *120*, 1397–1437.

8.6 Annex

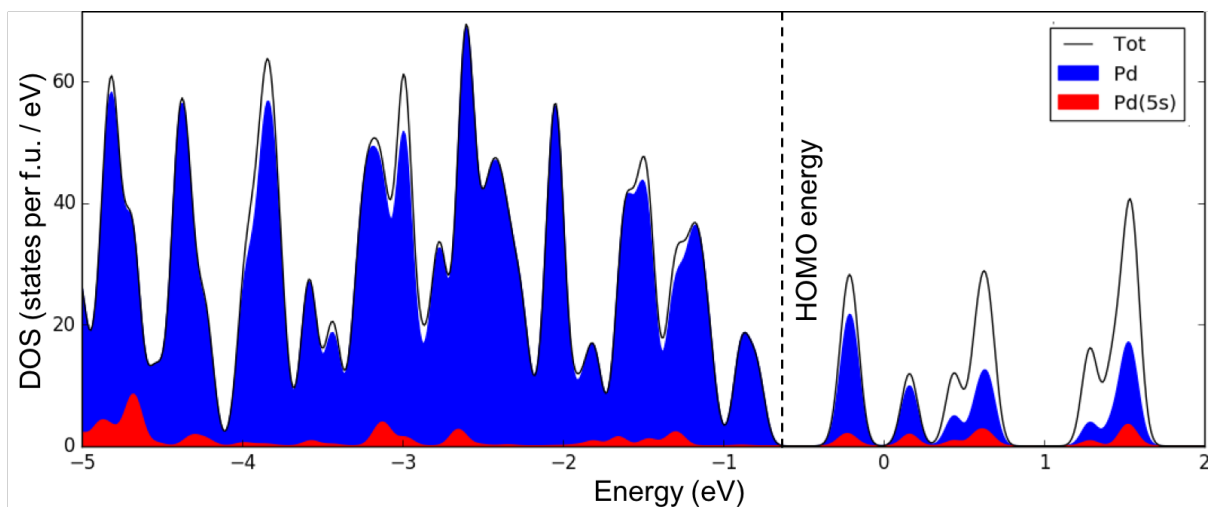


Figure S1. Total, Pd, and Pd(5s) projected DOS of $[\text{Pd}_{55}(\text{PH}_3)_{12}(\mu_3\text{-CO})_{20}]^{2-}$. The dotted line corresponds to the energy of the HOMO.

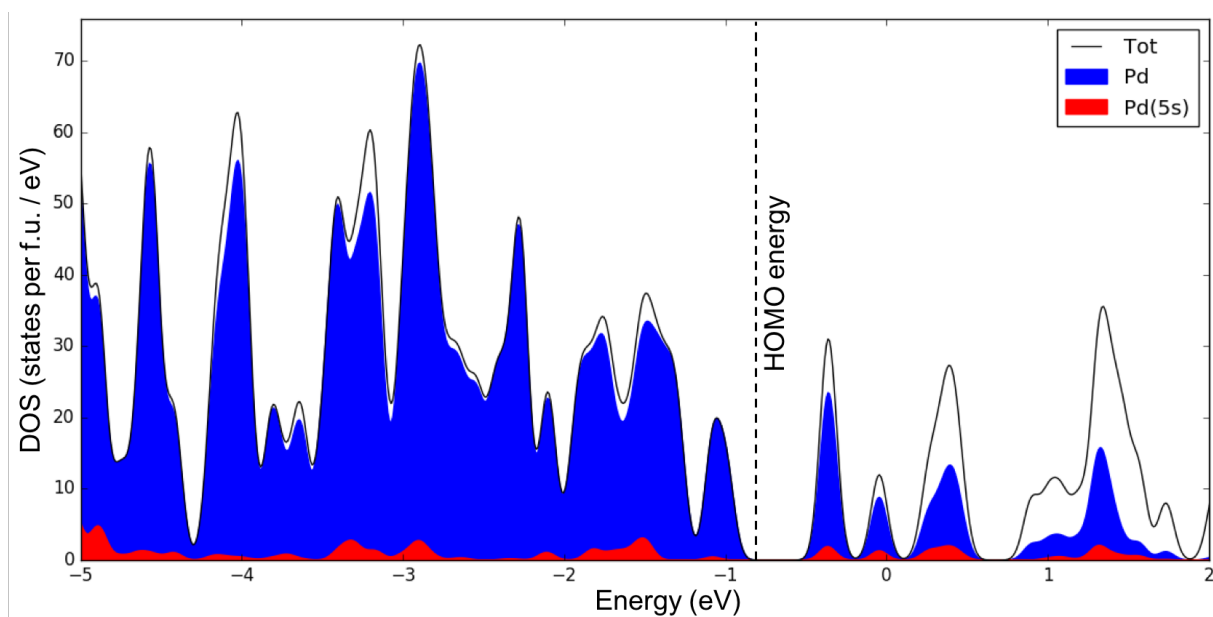


Figure S2. Total, Pd, and Pd(5s) projected DOS of $[\text{Pd}_{55}(\text{CNH})_{12}(\mu_3\text{-CO})_{20}]^{2-}$. The dotted line corresponds to the energy of the HOMO.

Table S1. Calculated metrical data of $\text{Pd}_{55}(\text{PH}_3)_{12}(\mu_3\text{-CO})_{20}$ with different functionals.

$\text{Pd}_{55}(\text{PH}_3)_{12}(\mu_3\text{-CO})_{20}$					
L		BP86	PBE	B3LYP	Exp.
Average Distances (Å)	Pd'–Pd''	2.636	2.677	2.702	2.63
	Pd''–Pd''	2.772	2.775	2.841	2.76
	Pd''–Pd'''	2.800	2.821	2.874	2.77
	Pd'''–Pd'''	2.845	2.880	2.917	2.83
	Pd'''–L	2.229	2.253	2.271	2.24
	Pd'''–CO	2.092	2.095	2.126	2.07

Table S2. Calculated metrical data of $[\text{Pd}_{55}(\text{PH}_3)_{12}(\mu_3\text{-CO})_{20}]^{2-}$ with different functionals.

$[\text{Pd}_{55}(\text{PH}_3)_{12}(\mu_3\text{-CO})_{20}]^{2-}$				
L		BP86	PBE	B3LYP
HOMO – LUMO gap (eV)		0.54	0.48	1.07
Average Distances (Å)	Pd'–Pd''	2.644	2.686	2.714
	Pd''–Pd''	2.781	2.824	2.854
	Pd''–Pd'''	2.798	2.812	2.869
	Pd'''–Pd'''	2.846	2.872	2.918
	Pd'''–L	2.222	2.245	2.265
	Pd'''–CO	2.089	2.093	2.124

Chapter 9

Looking at Platinum Carbonyl Nanoclusters as *Superatoms*

9.1 Introduction

The design and synthesis of atomically precise ligated nanoclusters is currently a very hot topic in nanoscience.¹⁻¹⁸ As part of this large family, that of gold nanoclusters is the most renowned one, but that of platinum nanoclusters, the exploration of which dates back to the late sixties,¹⁹ is still widely investigated,²⁰⁻²² owing to their various properties and their use as models for size-controlled metallic platinum nanoparticles. Interestingly, whereas the structure, bonding and stability of ligated gold (and other group-11 metals) nanoclusters is nowadays well understood, thanks to the concept of *superatom*,²³⁻³⁰ that of their group 10 homologues is not.³¹⁻³⁴

As said in previous chapters of this manuscript, the qualitative *superatom* model is based on the spherical *jellium* approximation,³⁵ which considers the electrons lying within a radial phenomenological potential supposed to describe the average electrostatic potential associated with the cluster atom nuclei. Replacing the dense spherical cloud of nuclei point-charges by such a smoothed radial potential allows describing the cluster electronic structure in terms of *superatomic* orbitals, resembling atomic orbitals (AOs), but extending over the whole cluster sphere.²³⁻³⁰ Their shell ordering is largely independent from the cluster nature and spans as $1S < 1P < 1D < 2S < 1F$, etc. As for atomic systems, closed-shell stability is achieved for specific (“*magic*”) electron counts, i.e., 2, 8, 18, 20, 34, etc. In the case of ligated nanoclusters of coinage metals (Cu, Ag, Au), the electrons that have to be considered in this count are those (and only those) coming from the valence $(n + 1)s$ orbitals (see chapters 1-6).^{36,37} Indeed, in such species the mixed-valent metal atoms are in an average oxidation state comprised between 0 and +I, i.e., in an $nd^{10}(n + 1)s^x$ ($0 < x < 1$) configuration, thus with a fully occupied nd shell, implying that valence d electrons cannot significantly participate to metal–metal bonding. Thus, in first approximation, the *superatom* orbitals can be identified as the combinations of the $(n + 1)s$ AOs. In the literature, the electrons they contain are called either *jellium*, *superatomic*, free, nearly free or delocalized electrons. In the followings, we choose to call them *free electrons* (*fe*) and their number nfe . This simple electron counting scheme works perfectly in the case of ligated group-11 metal clusters and indeed, most of them can be described as closed-shell *superatoms*³⁸⁻⁴⁵ or closed-shell assemblies of *superatoms* (*supermolecules*).^{33,46-54}

In the case of group-10 ligated nanoclusters, it turns out that the above methodology for counting electrons does not apply so straightforwardly. Thus, this sizeable structural chemistry

appears to stand outside the *superatom* concept and remains mostly unexplained. Indeed, in the majority of the structurally characterized Ni, Pd or Pt ligated nanoclusters, the average metal oxidation state is zero (valence $nd^{10} (n + 1)s^0$ metal configuration), or close to zero ($nd^{10} (n + 1)s^x, x \approx 0$), and one is driven to an apparent *superatom* electron count equal or close to zero. In other words, within the concept of *superatoms*, there are no (or not enough) electrons to ensure the metal-metal bonding within these clusters, which obviously contradicts the fact they exist.

We have shown that, in the case of ligated palladium nanoclusters, this mechanical electron counting is not appropriate (see Chapters 7 and 8). In fact, in such species, due to the peripheral ligand shell, some bonding combinations of the “empty” $(n + 1)s$ AOs are stabilized at sufficiently low energy for being occupied in the cluster, to the detriment of the same number of nd combinations of higher energy that are destabilized by the ligand lone pairs, and then get depopulated. In other words, the Pd average electron configuration in these species is $nd^{10-x} (n + 1)s^x$. This is what happens in $[\text{Pd}_{13}(\mu_4\text{-C}_7\text{H}_7)_6]^{2+}$ ($nfe = 2, 1S^2$ configuration)^{55,56} and $\text{Pd}_{55}(\text{PR}_3)_{12}(\mu_3\text{-CO})_{20}$ ($nfe = 20, 1S^2 1P^6 1D^{10} 2S^2$ configuration) for instance.^{57,58} In this chapter, we move to platinum, which is also remarkable in its propensity to form high nuclearity carbonyl clusters, in particular the so-called family of “platinum browns”,³¹ which were mainly developed in the past in the group of Longoni and now that of Zacchini in Italy,^{31,59-66} and to a lesser extent, in that of Dahl in the USA.^{67,68} So, we explore a large series of this platinum nanocluster family and we demonstrate that, most of the time, it can also be rationalized within the concepts of *superatoms* and *supermolecules*. The specific and well-known branch of columnar $\{[\text{Pt}_3(\text{CO})_6]_n\}^{2-}$ clusters^{69,70} will not be considered here, as it has been fully rationalized in the past by Hoffmann and collaborators.^{32,71} These high-nuclearity clusters resulting from different close-packed arrangements were tentatively rationalized via the so-called polyhedral skeletal electron pair theory (PSEPT) and its condensation principle extension^{32,72,73} but as the cluster size increases, the energy differences between alternative arrangements become smaller and it is no longer possible to associate a particular cluster electron count with a specific cluster geometry.^{32,73,74}

9.2 Computational Details

Geometry optimizations were carried out at the density functional theory (DFT) level by using the ADF2018 code,⁷⁵ incorporating the relativistic Zeroth Order Regular Approximation (ZORA).⁷⁶ The Becke and Perdew (BP86) functional,^{77,78} together with a triple zeta basis set augmented with a polarization function (STO-TZP). Grimme's empirical DFT-D3 dispersion corrections⁷⁹ were included for taking into account of the van der Waals interactions. An energy

convergence criterion of 5×10^{-5} Hartree and a radial convergence criterion of 5×10^{-3} Å were employed. The optimized structures were confirmed as genuine minima on their potential energy surface by analytical vibrational frequency calculations. Natural atomic orbital (NAO) populations⁸⁰ and Wiberg bond indices (WBI) were computed with the Gaussian 16 program⁸¹ at the BP86/Def2-SVP⁸² level using the ADF-optimized structures. For each cluster, *nfe* was obtained from the detailed analysis of its Kohn-Sham orbitals by detecting the occupied molecular orbitals of major Pt 6s character and identifying them as the cluster *superatomic* or *supermolecular* orbitals that contain the *fe*'s. Consistency with the nature of the lowest unoccupied combinations of large Pt 6s character, as well as the number of occupied and vacant combinations of major Pt 5d contribution was systematically controlled, allowing to safely treat the cases where 6s/5d mixing is significant. Unless specified in the figure captions, the orbitals are plotted with density isovalues of ± 0.01 (e/bohr³)^{1/2}. For the sake of comparison, some of them are also plotted with a different isovalue in Figure S2, S6 and S9, see Annex).

9.3 Results and Discussion

9.3.1 Decorated 8-electron *Superatoms* and Related Species

9.3.1.1 Experimentally Characterized Species

The compound $[\text{NBu}_4]_2[\text{Pt}_{13}(\text{CO})_{12}\{\text{Cd}_5(\mu\text{-Br})_5\text{Br}_2(\text{dmf})_3\}_2]$ (dmf = dimethylformamide), isolated in 2011 by Zacchini and coworkers,^{59,60} contains the complex anion $[\text{Pt}_{13}(\text{CO})_{12}\{\text{Cd}_5(\mu\text{-Br})_5\text{Br}_2(\text{dmf})_3\}_2]^{2-}$ that can be described as a centred icosahedral $[\text{Pt}_{13}(\text{CO})_{12}]^{8-}$ polyanion decorated with 10 Cd^{2+} cations, 14 Br^- anions, and 6 solvent molecules. The 12 carbonyl ligands being terminal, the idealized symmetry of $[\text{Pt}_{13}(\text{CO})_{12}]^{8-}$ is I_h (Figure 1 and Figure S1, Annex). The cluster anion is isoelectronic with $[\text{Au}_{13}(\text{PMe}_2\text{Ph})_{10}\text{Cl}_2]^{3+}$ synthesized a long time ago by Mingos and coworkers.⁴⁵ The latter is a *superatom* with *nfe* = 13 (Au_{13}) – 2 (Cl_2) – 3 (charge) = 8 and $1\text{S}^2 1\text{P}^6$ closed-shell configuration. It is easy to predict that the 8– charge of $[\text{Pt}_{13}(\text{CO})_{12}]^{8-}$ provides the 8 electrons that will occupy the four 6s(Pt) bonding combinations that can be identified as the 1S and 1P *superatomic* orbitals. This is confirmed by analyzing the Kohn-Sham orbital diagram of $[\text{Pt}_{13}(\text{CO})_{12}]^{8-}$ (Figure 2 and Figure S2, Annex), which shows that the 1S (a_g) and 1P (t_{1u}) orbitals lie at the bottom of the fully occupied 5d block, whereas the vacant 1D (h_g) level is situated above the $\pi^*(\text{CO})$ combinations. Thus, in $[\text{Pt}_{13}(\text{CO})_{12}]^{8-}$, the Pt average configuration is $5d^{10} 6s^{0.62}$ ($0.62 = 8/13$). The substantial computed HOMO-LUMO gap of $[\text{Pt}_{13}(\text{CO})_{12}]^{8-}$ should be related to the complete filling of the 5d block. Whereas in this simple case the metal 5d AOs are not involved in the bonding, the radial 6p orbitals of the

peripheral Pt atoms are to some extent. Indeed, these atoms are somewhat *sp*-hybridized. The outward-pointing hybrid (of *6p* major character) is used for Pt–CO bonding, whereas the inward-pointing hybrid (of *6s* major character) participates to the *superatomic* orbitals. Relevant computed data are given in Table S1 (Annex). Calculations on the fully decorated anion $[\text{Pt}_{13}(\text{CO})_{12}\{\text{Cd}_5(\mu\text{-Br})_5\text{Br}_2(\text{dmf})_3\}_2]^{2-}$ provided similar results that found for the isolated cluster $[\text{Pt}_{13}(\text{CO})_{12}]^{8-}$ (Table S2, Annex). One can notice the agreement with the experimental structure.⁶⁰ This result was expected owing to the electrostatic nature of the interaction between the various $[\text{Pt}_{13}(\text{CO})_{12}]^{8-}$, Cd^{2+} and Br^- ions.

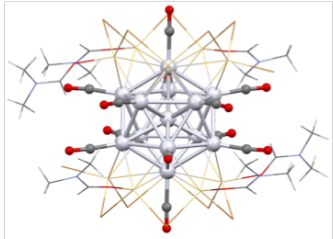
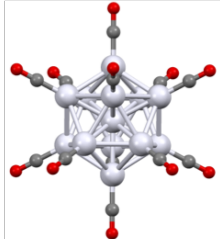
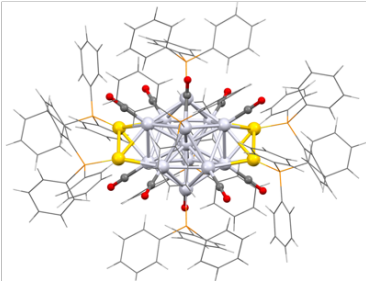
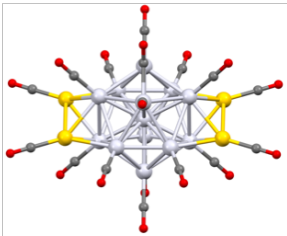
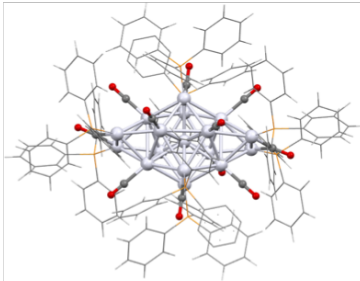
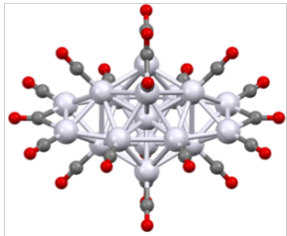
Computed model	Experimental structure	Optimized structure	
$[\text{Pt}_{13}(\text{CO})_{12}]^{8-}$	 $[\text{Pt}_{13}(\text{CO})_{12}\{\text{Cd}_5(\mu\text{-Br})_5\text{Br}_2(\text{dmf})_3\}_2]^{2-}$ ⁶⁰	 $[\text{Pt}_{13}(\text{CO})_{12}]^{8-} (I_h)$	$\Delta E_{\text{HL}} = 1.41 \text{ eV}$ $nfe = 8$
$[\text{Pt}_{13}\text{Au}_4(\mu\text{-CO})_2(\text{CO})_{16}]$	 $[\text{Pt}_{13}\text{Au}_4(\mu\text{-CO})_2\text{CO}_8(\text{PPh}_3)_8]^{83}$	 $[\text{Pt}_{13}\text{Au}_4(\mu\text{-CO})_2(\text{CO})_{16}] (D_{2h})$	$\Delta E_{\text{HL}} = 0.96 \text{ eV}$ $nfe = 8$
$[\text{Pt}_{17}(\mu\text{-CO})_4(\text{CO})_{16}]$	 $[\text{Pt}_{17}(\mu\text{-CO})_4\text{CO}_8(\text{PPh}_3)_8]^{85}$	 $[\text{Pt}_{17}(\mu\text{-CO})_4(\text{CO})_{16}] (D_{2h})$	$\Delta E_{\text{HL}} = 0.3 \text{ eV}$ $nfe = 8$

Figure 1. Optimized structures (right) of decorated icosahedral 8-electron *superatomic* models. EHL is the HOMO-LUMO gap. The corresponding experimental structures (left) are shown for comparison.

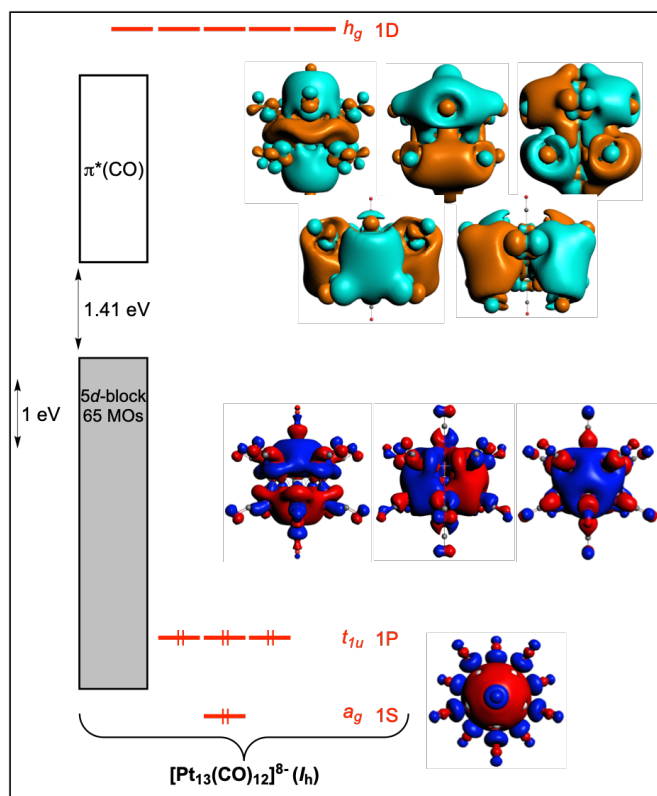


Figure 2. Kohn-Sham MO diagram of $[\text{Pt}_{13}(\text{CO})_{12}]^{8-}$.

Two strongly related clusters that can also be described as made of a decorated $\text{Pt}_{13}\text{L}_{12}$ centred icosahedral unit, namely compounds $\text{Pt}_{13}[\text{Au}_2(\text{PPh}_3)_2]_2(\mu\text{-CO})_2(\text{CO})_8(\text{PPh}_3)_4$ ⁸³ and $\text{Pt}_{13}[\text{Pt}_2(\text{PR}_3)_2(\mu\text{-CO})]_2(\mu\text{-CO})_2(\text{CO})_8(\text{PR}_3)_4$ ($\text{R} = \text{Et}, \text{Ph}$),^{84,85} which have been also reported. Both clusters contain a central $\text{Pt}_{13}(\text{CO})_8(\text{PR}_3)_4$ icosahedral unit, in which the 12 two-electron ligands are terminal, in a similar way as the CO ligands in $[\text{Pt}_{13}(\text{CO})_{12}]^{8-}$. In $\text{Pt}_{13}[\text{Au}_2(\text{PPh}_3)_2]_2(\mu\text{-CO})_2(\text{CO})_8(\text{PPh}_3)_4$, the central unit is decorated with two supplementary CO ligands that bridge opposite edges of the icosahedron, and two bidentate $\text{Ph}_3\text{PAu-AuPPh}_3$ fragments that cap two opposite pairs of adjacent icosahedral faces (Figure 1 and Figure S1, Annex). The ideal symmetry of the latter is D_{2h} . $\text{Pt}_{13}[\text{Pt}_2(\text{PR}_3)_2(\mu\text{-CO})]_2(\mu\text{-CO})_2(\text{CO})_8(\text{PR}_3)_4$ has the same structure and symmetry, except that the $\text{Ph}_3\text{PAu-AuPPh}_3$ fragment is now replaced by an isoelectronic $(\text{PR}_3)\text{Pt-Pt}(\text{PR}_3)(\mu\text{-CO})$ fragment. Considering the $\text{Ph}_3\text{PAu-AuPPh}_3$ and $(\text{PR}_3)\text{Pt-Pt}(\text{PR}_3)(\mu\text{-CO})$ fragments as two-electron M_2L_n organometallic ligands, both $\text{Pt}_{13}[\text{Au}_2(\text{PPh}_3)_2]_2(\mu\text{-CO})_2(\text{CO})_8(\text{PPh}_3)_4$ and $\text{Pt}_{13}[\text{Pt}_2(\text{PR}_3)_2(\mu\text{-CO})]_2(\mu\text{-CO})_2(\text{CO})_8(\text{PR}_3)_4$ can be viewed as Pt_{13} clusters having a total of 162 cluster valence electrons (CVEs), i.e., 13×10 (Pt) + 14×2 ($\text{L} = \text{CO}, \text{PR}_3$) + 2×2 (M_2L_n).⁸³ Not surprisingly, this is also the CVE count of $[\text{Pt}_{13}(\text{CO})_{12}]^{8-}$ ($13 \times 10 + 12 \times 2 + 8$). This means that the two $\mu\text{-CO}$ and the two M_2L_n ligands

have their 4 occupied frontier orbitals interacting with 4 combinations of the 5*d* block of the central Pt₁₃(CO)₈(PR₃)₄ icosahedral unit, thus making bonding and antibonding combinations, as sketched in Figure 3 in the case of the model Pt₁₃[Au₂(CO)₂]₂(μ-CO)₂(CO)₁₂. The computed Kohn-Sham orbital diagram of this model is given in Figure S3 (Annex) and that of Pt₁₃[Pt₂(CO)₂(μ-CO)]₂(μ-CO)₂(CO)₁₂ in Figure S4 (Annex). DFT calculations on the simplified PH₃-substituted models Pt₁₃[Au₂(PH₃)₂]₂(μ-CO)₂(CO)₈(PH₃)₄ and Pt₁₃[Pt₂(PH₃)₂(μ-CO)]₂(μ-CO)₂(CO)₈(PH₃)₄ are fully consistent with this qualitative description, as illustrated in Tables S3 and S4 (Annex). Thus, the occupied *superatomic* orbitals of the central Pt₁₃L₁₂ icosahedral unit are retained in Pt₁₃[Au₂(PPh₃)₂]₂(μ-CO)₂(CO)₈(PPh₃)₄ and Pt₁₃[Pt₂(PR₃)₂(μ-CO)]₂(μ-CO)₂(CO)₈(PR₃)₄, which thus can also be viewed as 8-*fe superatoms*, in a similar way as [Pt₁₃(CO)₁₂]⁸⁻ (*vide supra*). The involvement of some of the valence 5*d* orbitals in the bonding with “supplementary” ligands in these platinum *superatoms* is at variance with [Pt₁₃(CO)₁₂]⁸⁻ and group 11 *superatoms*, in which all the valence *nd* combinations are fully non-bonding and occupied, *i.e.*, in which the ligands interact only with metal (*n* + 1)*p* or outward-pointing (*n* + 1)*sp* AOs. Since there are four 5*d* antibonding combinations that are unoccupied in their MO diagram, Pt₁₃[Au₂(PPh₃)₂]₂(μ-CO)₂(CO)₈(PPh₃)₄ and Pt₁₃[Pt₂(PR₃)₂(μ-CO)]₂(μ-CO)₂(CO)₈(PR₃)₄ have lower HOMO-LUMO gaps than [Pt₁₃(CO)₁₂]⁸⁻ (Table S1, Annex).

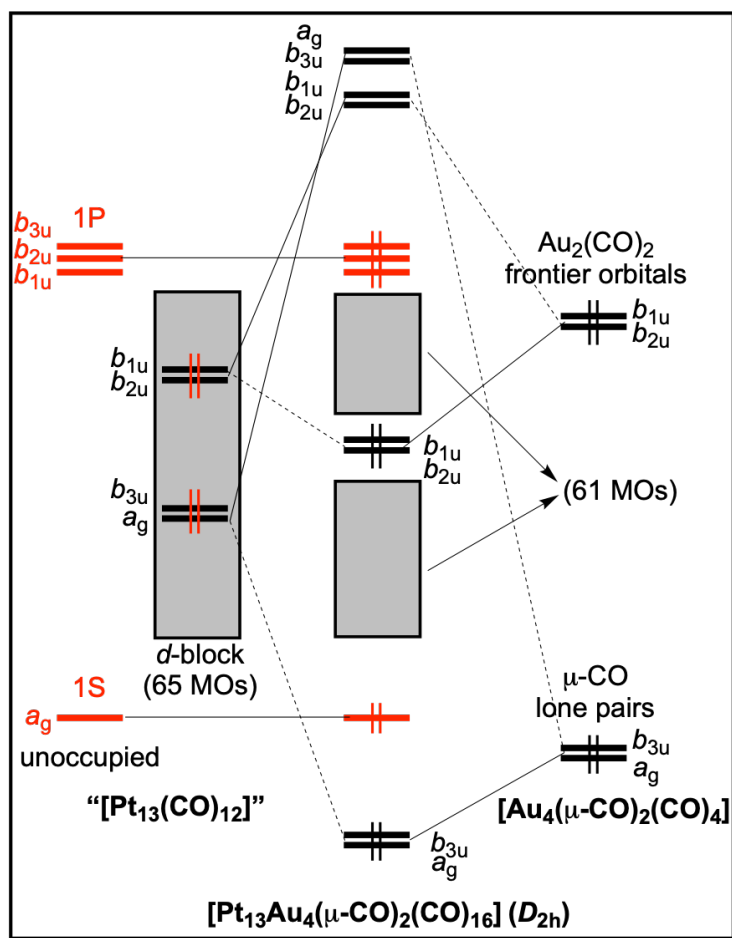


Figure 3. Qualitative MO interaction diagram between the icosahedral Pt₁₃(CO)₁₂ fragment and its two -CO and two Au₂(CO)₂ capping units in the [Pt₁₃Au₄(μ-CO)₂(CO)₁₆] model. Note that (i) the first fragment is formally in an excited state and (ii) the total number of occupied MOs (69) remains the same before and after interaction.

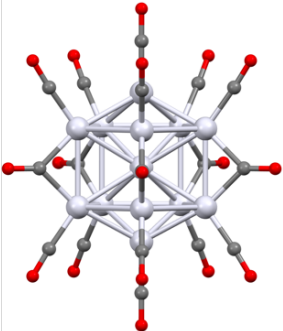
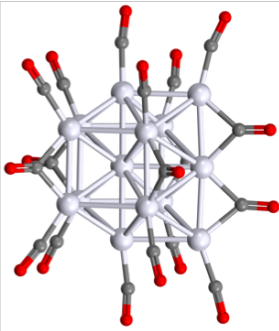
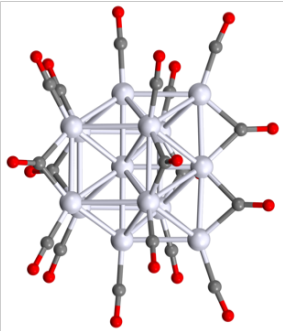
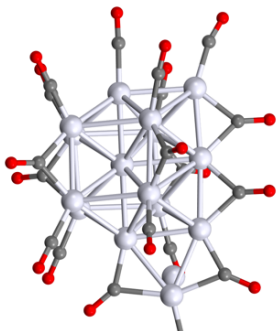
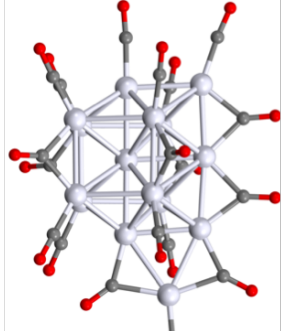
Computed model	Experimental structure	Optimized structure	
$[\text{Pt}_{13}(\mu\text{-CO})_5(\text{CO})_{12}]^{2-}$	Hypothetical compound		$\Delta E_{\text{HL}} = 1.12 \text{ eV}$ $nfe = 8$
		$[\text{Pt}_{13}(\mu\text{-CO})_5(\text{CO})_{12}]^{2-} (D_{5h})$	
$[\text{Pt}_{14}(\mu\text{-CO})_6(\text{CO})_{12}]^{4-}$			$\Delta E_{\text{HL}} = 1.00 \text{ eV}$ $nfe = 10$
	$[\text{Pt}_{14}(\mu\text{-CO})_6(\text{CO})_{12}]^{4-31}$	$[\text{Pt}_{14}(\mu\text{-CO})_6(\text{CO})_{12}]^{4-} (C_2)$	
$[\text{Pt}_{15}(\mu\text{-CO})_8(\text{CO})_{11}]^{4-}$			$\Delta E_{\text{HL}} = 1.09 \text{ eV}$ $nfe = 10$
	$[\text{Pt}_{15}(\mu\text{-CO})_8(\text{CO})_{11}]^{4-61}$	$[\text{Pt}_{15}(\mu\text{-CO})_8(\text{CO})_{11}]^{4-} (C_s)$	

Figure 4. Optimized structures (right) of $[\text{Pt}_{13}(\mu\text{-CO})_5(\text{CO})_{12}]^{2-}$, $[\text{Pt}_{14}(\mu\text{-CO})_6(\text{CO})_{12}]^{4-}$ and $[\text{Pt}_{15}(\mu\text{-CO})_8(\text{CO})_{11}]^{4-}$. ΔE_{HL} is the HOMO-LUMO gap. The corresponding experimental structures (left) are shown for comparison where available.

9.3.1.2 The Hypothetical D_{5h} $[\text{Pt}_{13}(\mu\text{-CO})_5(\text{CO})_{12}]^{2-}$ Model: The Versatile Role of “Additional” Bridging Ligands

As discussed just above, the $\text{Pt}_{13}[\text{Au}_2(\text{PPh}_3)_2]_2(\mu\text{-CO})_2(\text{CO})_8(\text{PPh}_3)_4$ and $\text{Pt}_{13}[\text{Pt}_2(\text{PR}_3)_2(\mu\text{-CO})]_2(\mu\text{-CO})_2(\text{CO})_8(\text{PR}_3)_4$ clusters can be described as made of an icosahedral $\text{Pt}_{13}(\text{CO})_{12}$ central unit, decorated by four “additional” ligands, namely two $\mu\text{-CO}$ and two $\eta^6\text{:}\mu_3, \mu_3\text{-M}_2\text{L}_n$ units. The four orbitals containing the four electron pairs provided by these four ligands interact

with $5d(\text{Pt})$ combinations in such a way that a significant HOMO-LUMO gap is created for the magic $8\text{-}fe$ count (see Figure 4, Figure S5, Annex). As regard to “additional” carbonyls, one could expect that the lone-pair of any of them would destabilize one $5d(\text{Pt})$ combination above the HOMO, as in regular “Wade-Mingos” organometallic clusters.³² Therefore, assuming such one-to-one orbital interaction scheme, the number of destabilized (thus depopulated) $5d(\text{Pt})$ combinations should be equal to the number of “additional” carbonyls. It turns out that this is not always the case. It can happen that the number of $5d(\text{Pt})$ combinations destabilized above the HOMO is lower than the number of “additional” carbonyls. This is exemplified by the hypothetical D_{5h} $[\text{Pt}_{13}(\mu\text{-CO})_5(\text{CO})_{12}]^{2-}$ model, which exhibits a bicapped centred pentagonal prismatic Pt_{13} core, a structure somewhat less compact and spherical than the icosahedron, but which offers five edges to be easily bridged by “additional” carbonyls (Figure 4, top). Whereas the destabilization of five $5d(\text{Pt})$ combinations (of $a'_1 + e'_1 + e'_2$ symmetry) by the five $\mu\text{-CO}$ lone-pair combinations is expected, only three of them (of $a'_1 + e'_2$ symmetry) actually are. This situation is sketched on the left side of Figure 5 (see also Figure S6, Annex). The large computed HOMO-LUMO gap (1.12 eV) undoubtedly indicates stability. This dianion is likely to be isolated as its salt in the future. On the other hand, the corresponding dication was not found to be stable. Although not very spherical, $[\text{Pt}_{13}(\mu\text{-CO})_5(\text{CO})_{12}]^{2-}$ has occupied pseudo-spherical *superatomic* orbitals of 1S and 1P nature (see Figure 5 and Figure S6, Annex), making it an $8\text{-}fe$ *superatom*.

9.3.1.3 Non-spherical Clusters Related to the D_{5h} $[\text{Pt}_{13}(\mu\text{-CO})_5(\text{CO})_{12}]^{2-}$ Model: $[\text{Pt}_{14}(\mu\text{-CO})_6(\text{CO})_{12}]^{4-}$ and $[\text{Pt}_{15}(\mu\text{-CO})_8(\text{CO})_{11}]^{4-}$

The two relatively small and non-spherical clusters $[\text{Pt}_{14}(\mu\text{-CO})_6(\text{CO})_{12}]^{4-}$ and $[\text{Pt}_{15}(\mu\text{-CO})_8(\text{CO})_{11}]^{4-}$ experimentally reported^{31,61} (Figure 4 and Figure S5, Annex) are both structurally related to the hypothetical D_{5h} $[\text{Pt}_{13}(\mu\text{-CO})_5(\text{CO})_{12}]^{2-}$ model discussed just above. Going from the latter to $[\text{Pt}_{14}(\mu\text{-CO})_6(\text{CO})_{12}]^{4-}$ corresponds formally to the insertion of a supplementary Pt atom in one of the edges connecting the two pentagons, together with the addition of a $\mu\text{-CO}$ ligand attached to this Pt atom. Note also the cluster charge variation. The idealized geometry of $[\text{Pt}_{14}(\mu\text{-CO})_6(\text{CO})_{12}]^{4-}$ is of C_{2v} symmetry, but the optimized structure was found slightly distorted to C_2 . Analysis of its electronic structure indicates that the cluster has one more occupied $6s(\text{Pt})$ combination than $[\text{Pt}_{13}(\mu\text{-CO})_5(\text{CO})_{12}]^{2-}$, which is located around the “additional” Pt atom (Figure 4). The number of unoccupied $5d(\text{Pt})$ combinations is unchanged, so the two “additional” electrons are used for filling this supplementary $6s(\text{Pt})$

combination (Figure 5) leading to a count of 10 fe 's and the $1S^2 1P^6 2S^2$ closed-shell configuration. Going now from $[\text{Pt}_{14}(\mu\text{-CO})_6(\text{CO})_{12}]^{4-}$ to $[\text{Pt}_{15}(\mu\text{-CO})_8(\text{CO})_{11}]^{4-}$ consists in the formal insertion of a linear $\text{Pt}(\text{CO})$ unit on a $\text{Pt}\text{-Pt}$ edge (Figure 4). Such a $\text{Pt}(\text{CO})$ unit formally donates two electrons to the $\text{Pt}\text{-Pt}$ edge it bridges and receives two electrons from its carbonyl neighbors, which move from terminal to bridging upon $\text{Pt}(\text{CO})$ insertion. Thus, the number of cluster electrons does not change upon insertion of this $\text{Pt}(\text{CO})$ ligand. It follows that the electronic structures of $[\text{Pt}_{14}(\mu\text{-CO})_6(\text{CO})_{12}]^{4-}$ and $[\text{Pt}_{15}(\mu\text{-CO})_8(\text{CO})_{11}]^{4-}$ are basically the same, corresponding to non-spherical species with $nfe = 10$ (Figure 5). Their occupied $6s(\text{Pt})$ combination are plotted in Figure S7 (Annex). Selected computed data are provided in Table S5 (Annex).

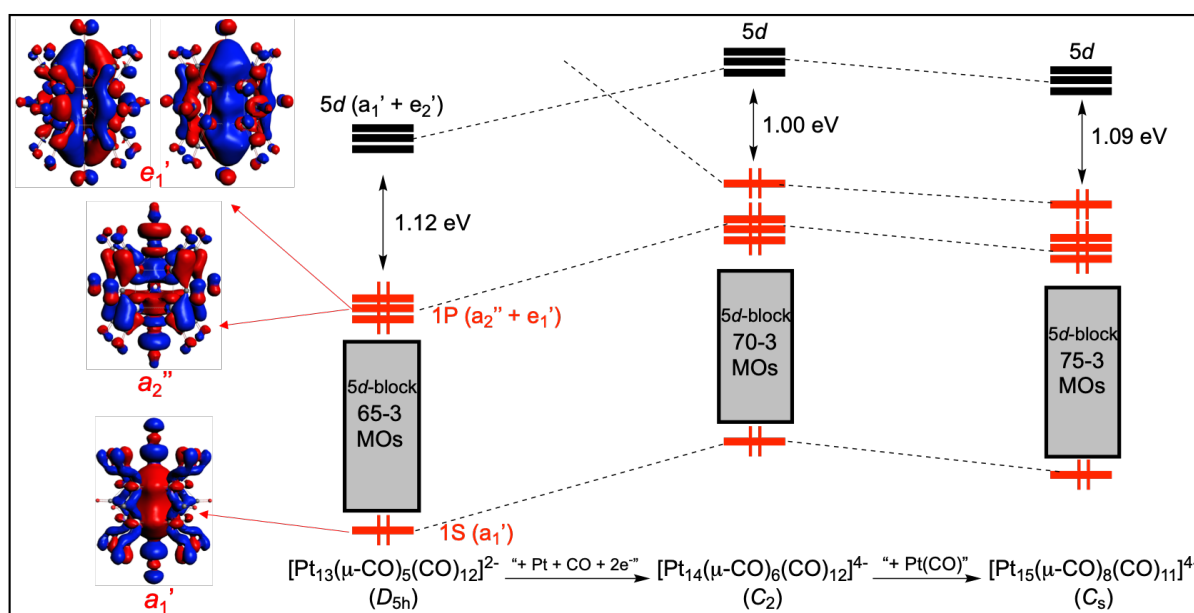


Figure 5. Kohn-Sham orbital diagram of $[\text{Pt}_{13}(\mu\text{-CO})_5(\text{CO})_{12}]^{2-}$ (left), $[\text{Pt}_{14}(\mu\text{-CO})_6(\text{CO})_{12}]^{4-}$ (middle) and $[\text{Pt}_{15}(\mu\text{-CO})_8(\text{CO})_{11}]^{4-}$ (right).

9.3.2 Assemblies of Individual Superatoms

9.3.2.1 Experimentally Characterized Species

Non-spherical metal group-11 nanoclusters, the structure of which can be described as resulting from the assembly of several pseudo-spherical individual units (most often icosahedral) are becoming quite common.^{33,51,52,86-90} In such assemblies, the icosahedral units share either a vertex, a triangular face or are interpenetrated in such a way they share a pentagonal face and its two capping atoms. Such assemblies of individual *superatomic* units can be viewed as

“*supermolecules*”, with *supermolecular* orbitals looking like molecular orbitals, and electron counts related to that of simple main-group molecules, depending on their fusion extent, in the same way as molecule electron counts depend on bond orders (BOs).^{52,91,92} Concerning group-11 nanoclusters made of two fused centred icosahedra, vertex-sharing systems have favored *superatomic* closed-shell electron counts of 16 or 14, i.e., equivalent to Ne₂ (BO = 0) or F₂ (BO = 1), respectively.^{90,93} Face-sharing icosahedra can also have a favored count of 14⁹³ whereas interpenetrated icosahedra can display a favored count of 10, i.e., equivalent to N₂ (BO = 3).⁹⁴

It turns out that a platinum cluster made of two interpenetrated icosahedra, namely [Pt₁₉(CO)₁₇]⁸⁻ (Figure 6 and Figure S8, Annex), was shown to exist as a decorated polyanion in the solid state compound [PPh₃Me]₂[Pt₁₉(CO)₁₇{Cd₅(μ-Br)₅Br₃(Me₂CO)₂}{Cd₅(μ-Br)₅Br(Me₂CO)₄}] isolated some years ago by Zacchini and coworkers.^{59,60} In this cluster of ideal D_{5h} symmetry, the 17 CO ligands are terminally bonded to the 17 peripheral Pt atoms. Assuming an average Pt 5d¹⁰ 6s^{0.42} (0.42 = 8/19) configuration ends up with the apparent *superatomic* count *nfe* = 8. DFT calculations indicated that in fact this number is 10, occupying five *supermolecular* orbitals of large 6s(Pt) character having similar nodal properties as the 1σ_g, 1σ_u, 1π_u and 2σ_g molecular orbitals of N₂. Vacant orbitals analogues to the 1π_g* and 2σ_u* combinations can be found at higher energies. Moreover, [Pt₁₉(CO)₁₇]⁸⁻ is found to have a triplet ground-state, with a half-filled e' HOMO of large 5d(Pt) character. With two more electrons, [Pt₁₉(CO)₁₇]¹⁰⁻ has a closed-shell configuration, with a significant, although moderate, HOMO-LUMO gap (0.37 eV). Its Kohn-Sham molecular diagram is shown in Figure 7 (see also Figure S9, Annex). Thus, in spite of their different charges, both [Pt₁₉(CO)₁₇]⁸⁻ and [Pt₁₉(CO)₁₇]¹⁰⁻ are 10-*nfe* *supermolecules*. Indeed, they differ from their number of 5d electrons. In [Pt₁₉(CO)₁₇]¹⁰⁻ these ten electrons are coming from the overall 10- charge of the cluster, and occupy low-lying *supermolecular* orbitals. With two less electrons, [Pt₁₉(CO)₁₇]⁸⁻ turns to have a half-occupied 5d-based e' HOMO, making [Pt₁₉(CO)₁₇]⁸⁻ an unsaturated triplet. The thermodynamical stability of [Pt₁₉(CO)₁₇]⁸⁻ is to be related to the localization of its spin density on its Pt₁₉ kernel and its protection by the ligand shell (Figure S10, Annex), as well as its ionic decoration in the fully decorated [Pt₁₉(CO)₁₇{Cd₅(μ-Br)₅Br₃(Me₂CO)₂}{Cd₅(μ-Br)₅Br(Me₂CO)₄}]⁴⁻ (Figure S11, Annex). The electronic situation of [Pt₁₉(CO)₁₇]⁸⁻ is reminiscent of that of the icosahedral Pd₅₅(PR₃)₁₂(μ₃-CO)₂₀ *superatom*, which also has a triplet ground state configuration with a “magic” *nfe* count of 20 (*superatomic* 1S² 1P⁶ 1D¹⁰ 2S² configuration).⁵⁸ The calculated metrical data of [Pt₁₉(CO)₁₇]⁸⁻ are in good agreement with their

experimental counterparts,⁶⁰ as well as that of the fully decorated $[\text{Pt}_{19}(\text{CO})_{17}\{\text{Cd}_5(\mu\text{-Br})_5\text{Br}_3(\text{Me}_2\text{CO})_2\}\{\text{Cd}_5(\mu\text{-Br})_5\text{Br}(\text{Me}_2\text{CO})_4\}]^{2-}$ (Tables S6 and S7, Annex).

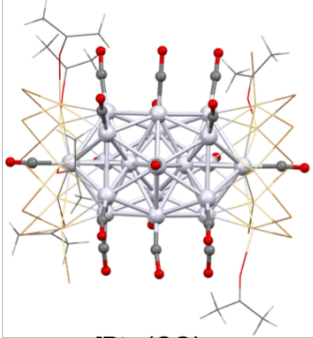
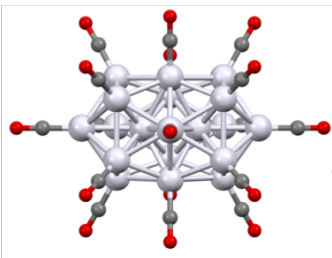
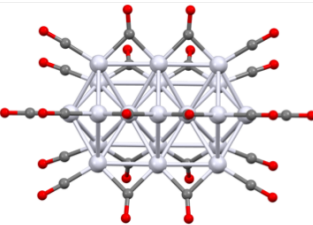
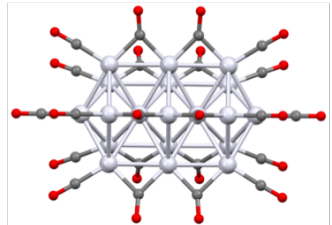
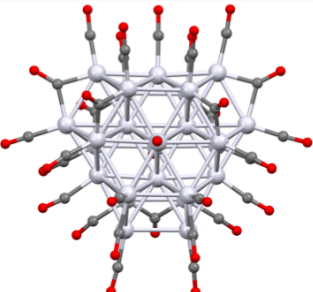
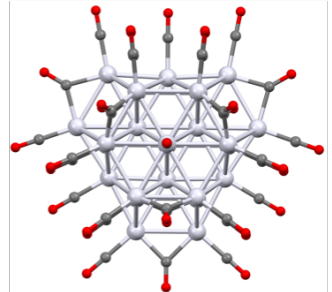
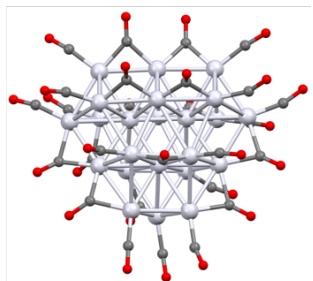
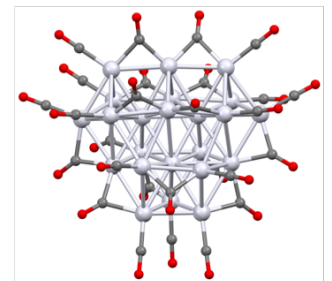
Computed model	Experimental structure	Optimized structure	
$[\text{Pt}_{19}(\text{CO})_{17}]^{8-/10-}$			$\Delta E_{\text{HL}} = 0.37 \text{ eV}$ $n_{\text{fe}} = 10$ (analogous to N_2)
	$[\text{Pt}_{19}(\text{CO})_{17}\{\text{Cd}_5(\mu\text{-Br})_5\text{Br}_3(\text{Me}_2\text{CO})_2\}\{\text{Cd}_5(\mu\text{-Br})_5\text{Br}(\text{Me}_2\text{CO})_4\}]^{2-}$ ⁶⁰	$[\text{Pt}_{19}(\text{CO})_{17}]^{8-/10-} (D_{5h})$	
$[\text{Pt}_{19}(\mu\text{-CO})_{10}(\text{CO})_{12}]^{4-}$			$\Delta E_{\text{HL}} = 0.80 \text{ eV}$ $n_{\text{fe}} = 14$ (analogous to F_2)
	$[\text{Pt}_{19}(\mu\text{-CO})_{10}(\text{CO})_{12}]^{4-}$ ⁶⁸	$[\text{Pt}_{19}(\mu\text{-CO})_{10}(\text{CO})_{12}]^{4-} (D_{5h})$	
$[\text{Pt}_{26}(\mu\text{-CO})_9(\text{CO})_{23}]^{2-}$			$\Delta E_{\text{HL}} = 0.57 \text{ eV}$ $n_{\text{fe}} = 18$ (analogous to Cyclic O_3)
	$[\text{Pt}_{26}(\mu\text{-CO})_9(\text{CO})_{23}]^{2-}$ ^{31,67}	$[\text{Pt}_{26}(\mu\text{-CO})_9(\text{CO})_{23}]^{2-} (D_{3h})$	
$[\text{Pt}_{23}(\mu\text{-CO})_{13}(\text{CO})_{14}]^{2-}$			$\Delta E_{\text{HL}} = 0.42 \text{ eV}$ $n_{\text{fe}} = 18$ (analogous to Cyclic O_3)
	$[\text{Pt}_{23}(\mu\text{-CO})_{13}(\text{CO})_{14}]^{2-}$ ³¹	$[\text{Pt}_{23}(\mu\text{-CO})_{13}(\text{CO})_{14}]^{2-} (C_1)$	

Figure 6. Optimized structures (right) of experimentally characterized clusters that can be viewed as linear assemblies of individual *superatoms*. ΔE_{HL} is the HOMO-LUMO gap. The corresponding experimental structures (left) are shown for comparison.

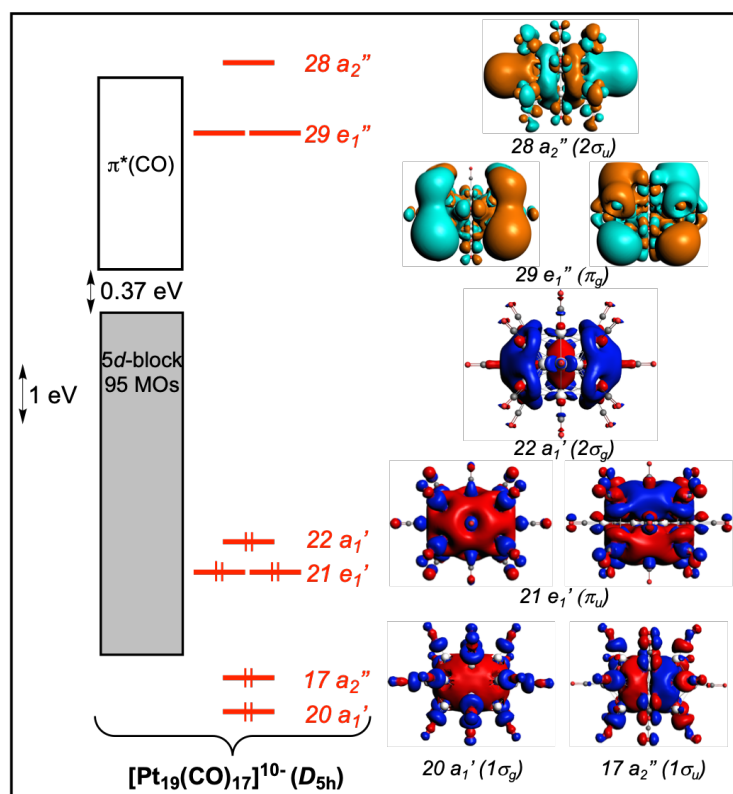


Figure 7. Kohn-Sham orbital diagram of $[\text{Pt}_{19}(\text{CO})_{17}]^{10-}$. The *supermolecular* orbitals plotted on the right side are reminiscent of the valence orbitals of N_2 .

The metal core of $[\text{Pt}_{19}(\mu\text{-CO})_{10}(\text{CO})_{12}]^{4-}$ ⁶⁸ is related to that of $[\text{Pt}_{19}(\text{CO})_{17}]^{8-}$ in that it derives from the latter through a 36° rotation of its middle Pt_5 ring (Figure 6 and Figure S8, Annex). In other words, whereas the cluster core of $[\text{Pt}_{19}(\text{CO})_{17}]^{8-}$ results from the interpenetration of two centred icosahedra, that of $[\text{Pt}_{19}(\mu\text{-CO})_{10}(\text{CO})_{12}]^{4-}$ is made of two interpenetrated bi-capped centred pentagonal prisms. This moderate rotational change slightly lowers the cluster compactness, and makes additional space for allowing 10 additional $\mu\text{-CO}$ ligands. The whole cluster symmetry is D_{5h} (Table S8, Annex). Analysis of its Kohn-Sham orbital diagram (Figure 8) allows identifying 14 occupied *supermolecular* orbitals, making $[\text{Pt}_{19}(\mu\text{-CO})_{10}(\text{CO})_{12}]^{4-}$ a closed-shell *supermolecule* with $n_{fe} = 14$, analogous to F_2 with the $1\sigma_g^2 1\sigma_u^2 \pi_u^4 2\sigma_g^2 \pi_g^4 2\sigma_u^0$ electron configuration. Considering the tetra-anionic charge of the cluster, a level crossing occurs between five $6s(\text{Pt})$ and five $5d(\text{Pt})$ combinations, the latter transferring their 10 electrons into the former. Thus, in this particular case, the number of destabilized $5d(\text{Pt})$ combinations is equal to that of the “additional” CO ligands ($5 = 22$ (total of COs) – 17 (total of surface Pt atoms)).

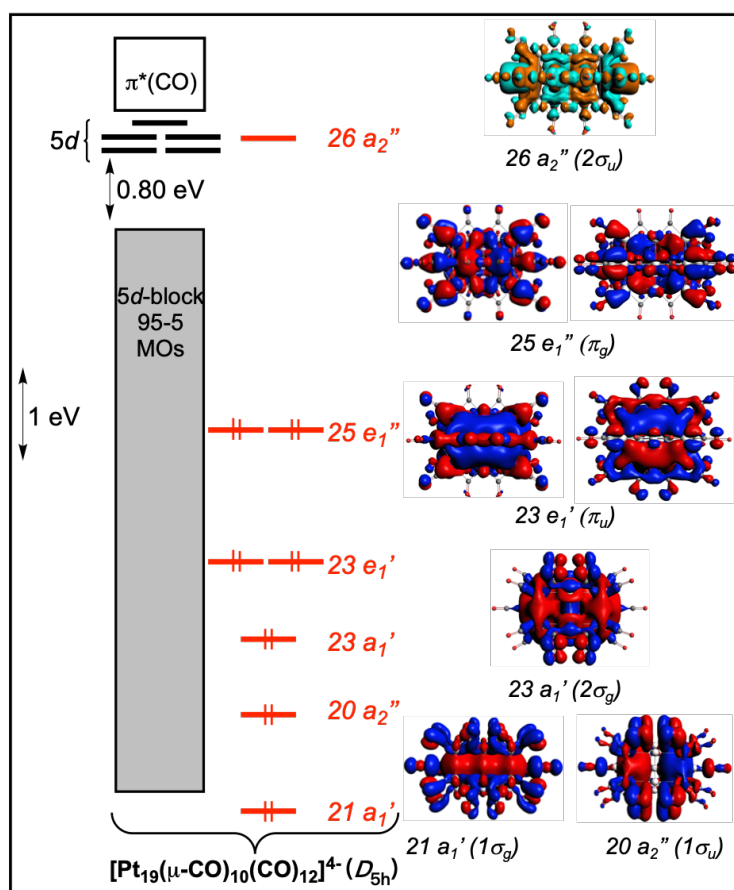


Figure 8. Kohn-Sham orbital diagram of $[\text{Pt}_{19}(\mu\text{-CO})_{10}(\text{CO})_{12}]^{4-}$. The *supermolecular* orbitals plotted on the right side are reminiscent of the valence orbitals of F_2 .

It is noteworthy that $[\text{Pt}_{19}(\text{CO})_{17}]^{8-/10-}$ and $[\text{Pt}_{19}(\mu\text{-CO})_{10}(\text{CO})_{12}]^{4-}$ differ by their number of *supermolecular* electrons ($n_{fe} = 10$ and 14, respectively). The total cluster valence electron (CVE) counts (232/234 and 238, respectively) follow the same trend, and is consistent with the fact that the metallic core of the more electron-rich prismatic cluster $[\text{Pt}_{19}(\mu\text{-CO})_{10}(\text{CO})_{12}]^{4-}$ is less compact than that of the antiprismatic cluster $[\text{Pt}_{19}(\text{CO})_{17}]^{8-/10-}$.

Cyclic assemblies of platinum *superatoms* can also exist as exemplified by $[\text{Pt}_{26}(\mu\text{-CO})_9(\text{CO})_{23}]^{2-}$.^{31,67} This cluster possesses a non-pseudo-spherical core of ideal D_{3h} symmetry that can be described as a piece of *hcp* metal made of the *ABA* stacking of *hc* layers of 7, 12 and 7 atoms, respectively (Figure 6 and Figure S8, Annex).^{31,67} It can be also viewed as a flattened (oblate) 2-shell $\text{Pt}_3@Pt_{23}$ system. Alternatively, one can look at it as made of three interpenetrated centred anti-cuboctahedra, their three centers constituting the encapsulated triangle of the $\text{Pt}_3@Pt_{23}$ system. Six vertices are shared between two centred anti-cuboctahedra and four are common to the three of them. There is a terminal carbonyl on each of the outer metals and 9 additional bridging ones. Its computed HOMO-LUMO gap (0.57 eV) is consistent

with closed-shell stability. Examination of its electronic structure (Figure S12 and Table S9, Annex) indicates that it is an 18-electron species, which is best described as a *supermolecule* made of the triangular assembly of three interpenetrating centred anti-cuboctahedral *superatoms*. It is equivalent to the hypothetical triangular isomer of ozone (18 valence electrons),⁹⁵⁻⁹⁹ as exemplified by the correspondence between the *supermolecular* orbitals of $[\text{Pt}_{26}(\mu\text{-CO})_9(\text{CO})_{23}]^{2-}$ and the molecular orbitals of cyclic O_3 . In this particular case, the nine “additional” CO ligands induce the level crossing of only eight $5d(\text{Pt})$ with eight $6s(\text{Pt})$ combinations, inducing the transfer of 16 electrons into the latter. The cluster anionic charge provides 2 supplementary electrons.

The metal core arrangement of $[\text{Pt}_{23}(\mu\text{-CO})_{13}(\text{CO})_{14}]^{2-}$ ³¹ can be described as a defect structure of that of $[\text{Pt}_{26}(\mu\text{-CO})_9(\text{CO})_{23}]^{2-}$ with *ABA* stacking of 5, 12 and 6 atoms, respectively ($\text{Pt}_3@Pt_{20}$ (Figure 6 and Figure S8, Annex). Nevertheless, in this molecule of low symmetry it is still possible to identify three 11-vertex incomplete (and distorted) anti-cuboctahedra interpenetrating each other. Its computed HOMO-LUMO gap of 0.45 eV (Table S10, Annex) and its electronic structure are also consistent with a description of an 18-electron *supermolecule* equivalent to cyclic O_3 .

9.3.2.2 Hypothetical Models

Starting from two interpenetrating centred icosahedra like in $[\text{Pt}_{19}(\text{CO})_{17}]^{8-}$ (see above) it is possible to build linear oligomeric structures made of the interpenetration of several centred icosahedra. With three of them and assuming terminal ligands on every peripheral metal, the $\text{Pt}_{25}(\text{CO})_{22}$ structure of D_{5d} symmetry was designed (Figure 9 and Figure S13, Annex). Calculations found the corresponding $[\text{Pt}_{25}(\text{CO})_{22}]^{12-}$ anion to be a thermodynamically stable closed-shell species with a significant HOMO-LUMO gap of 0.63 eV, (Table S11, Annex). Examination of its electronic structure (Figure S14, Annex) indicates that this 3-*superatom* model species is a 16-electron *supermolecule*. Within the $D_{\infty h}$ pseudosymmetry, the 16 electrons occupy *supermolecular* orbitals of σ_g (two), σ_u (two), π_g (one) and π_u (one) nature, thus making cluster $[\text{Pt}_{25}(\text{CO})_{22}]^{12-}$ equivalent to CO_2 . The 16 electrons are provided in part by the anionic charge and in part by the transfer of 4 electrons from two $5d$ -type combinations into two $6s$ combinations.

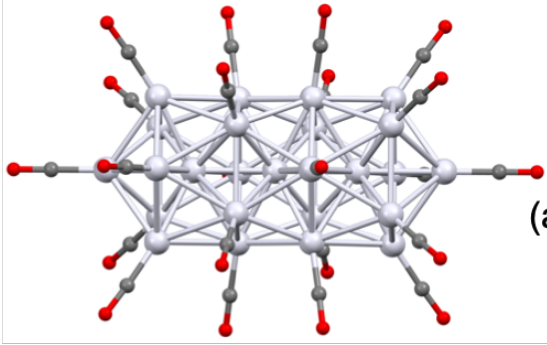
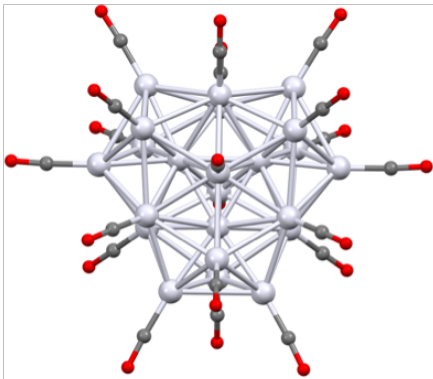
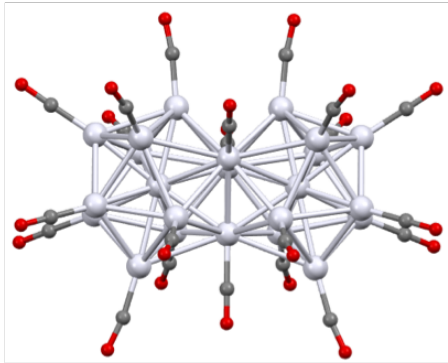
Computed model	Optimized structure
$[\text{Pt}_{25}(\text{CO})_{22}]^{12-}$ (D_{5d})	 <p>$\Delta E_{\text{HL}} = 0.63 \text{ eV}$ $n_{\text{fe}} = 16$ (analogous to CO_2)</p>
$[\text{Pt}_{23}(\text{CO})_{20}]^{12-}$ (D_{3h})	 <p>$\Delta E_{\text{HL}} = 0.57 \text{ eV}$ $n_{\text{fe}} = 20$</p>
$[\text{Pt}_{23}(\text{CO})_{21}]^{10-}$ (D_{3h})	 <p>$\Delta E_{\text{HL}} = 0.51 \text{ eV}$ $n_{\text{fe}} = 14$ (analogous to F_2)</p>

Figure 9. Optimized structures of linear assemblies of individual icosahedral *superatoms* (hypothetical models). ΔE_{HL} is the HOMO-LUMO gap.

One can also build an equilateral assembly of three interpenetrating icosahedra, resulting in a D_{3h} $\text{Pt}_3@Pt_{20}$ core. Assuming the existence of 20 terminal ligands, the structure is found thermodynamically stable for the unique 20- n_{fe} count, i.e., $[\text{Pt}_{23}(\text{CO})_{20}]^{12-}$ (Figure 9 and Figure S13, Annex), with a HOMO-LUMO gap of 0.57 eV (Figure S15 and Table S12, Annex). This unexpected electron count was also previously predicted for related Ag-rich structures.⁵²

It is of course possible to imagine various types of linear assemblies made of several fused *superatomic* units. For example, assuming the Pt_{23} core made of two face-sharing centred icosahedra, with terminal carbonyls on each of the 21 peripheral metal atoms (Figure 9 and

Figure S13, Annex), leads to the D_{3h} $\text{Pt}_{23}(\text{CO})_{21}$ framework, for which a closed-shell ground state was found for a charge of 10^- . Examination of its electronic structure (Figure S16 and Table S13, Annex) leads to describe it as a species with an $nfe = 14$, equivalent of F_2 (two vacant $5d$ combinations).

Of course, one can argue that such highly charged hypothetical anions are unlikely to be isolated. One may however remark that real anionic clusters, such as $[\text{Pt}_{13}(\text{CO})_{12}]^{8-}$, $[\text{Pt}_{19}(\text{CO})_{17}]^{8-}$ and $[\text{Pt}_{19}(\mu\text{-CO})_{10}(\text{CO})_{12}]^{4-}$ for instance, exist (see above), being stabilized by a more or less complex cationic decorating shell.^{59,60} Moreover, the presence of additional bridging ligands such as in $\text{Pt}_{13}[\text{Au}_2(\text{PPh}_3)_2]_2(\mu\text{-CO})_2(\text{CO})_8(\text{PPh}_3)_4$ and $\text{Pt}_{13}[\text{Pt}_2(\text{PR}_3)_2(\mu\text{-CO})]_2(\mu\text{-CO})_2(\text{CO})_8(\text{PR}_3)_4$ ⁸³⁻⁸⁵ (and not considered in our models) could also help reducing the cluster charge by bringing supplementary electrons to the structure (see above). It seems thus likely that new Pt (or Pd) *supermolecular* clusters made of the linear (or cyclic) assembly of fused centred icosahedra (and/or centred bicapped pentagonal prisms) will be characterized in the future.

9.3.3 Other Clusters with 3D Architectures

9.3.3.1 Pseudo-spherical Species

Any pseudo-spherical species should be described as a regular *superatom*, providing its metal core is sufficiently compact. This is the case of $[\text{Pt}_{38}(\mu\text{-CO})_{12}(\text{CO})_{32}]^{2-}$,^{63,67} which exhibits an O_h metal core that is a piece of *fcc* metal resulting from the *ABBA* stacking of *hc* layers of 7, 12, 12 and 7 atoms, respectively (Figure 10 and Figure S17, Annex). Alternatively, it can be viewed as made of two concentric O_h polyhedra ($\text{Pt}_6@Pt_{32}$). This metal core is passivated by a shell of 44 CO ligands, reducing the ideal symmetry to D_{2d} . Examination of the cluster electronic structure (Figure S18, Annex) indicates that it is a *superatom* with $1S^2 1P^6 1D^{10}$ configuration ($nfe = 18$). These 18 electrons located in MOs of large $6s(\text{Pt})$ character are originating in part from the cluster anionic charge and in the other part from the destabilization of eight $5d$ combinations, which in turn get depopulated. This 8-level block lies 0.45 eV above the HOMO (Figure S18 and Table S14, Annex). The structure of the related species $[\text{Pt}_{36}(\mu\text{-CO})_{18}(\text{CO})_{26}]^{2-}$ (Figure 10 and Figure S17, Annex)³¹ can be conceptually derived from that of $[\text{Pt}_{38}(\mu\text{-CO})_{12}(\text{CO})_{32}]^{2-}$ by the removal of two Pt atoms from one of the 7-atom layer and a reorganization of the ligand shell. Its optimized geometry (Table S15, Annex) is of C_{2v} symmetry, and its HOMO-LUMO gap is rather small (0.24 eV). Nevertheless, it is still possible

to identify in its orbital spectrum 9 occupied levels of large $6s(\text{Pt})$ character that attributes to $[\text{Pt}_{36}(\mu\text{-CO})_{18}(\text{CO})_{26}]^{2-}$ the character of 18-electron *superatom* (Figure S19, Annex).

9.3.3.2 Non-pseudo-spherical Species

Superatoms can move away from sphericity through oblate (flattening) or prolate (elongating) deformations that can be described as Jahn-Teller distortions associated with degeneracy splitting of *superatomic* electron shells, thus inducing electron counts that deviate from the *magic* numbers. This is the case of the isoelectronic clusters $[\text{Pt}_{19}(\mu_3\text{-CO})_3(\mu\text{-CO})_3(\text{CO})_{18}(\mu_4\text{-AuPPh}_3)_3]^-$ and $[\text{Pt}_{19}(\mu_3\text{-CO})(\mu\text{-CO})_5(\text{CO})_{18}\{\mu_4\text{-Au}_2(\text{PPh}_3)_2\}_2]^{100}$ which can be described as prolate species. They exhibit similar Pt_{19} core made of the *fcc ABCA* packing of *hc* layers of 3, 7, 6 and 3 atoms (Figure 10 and Figure S17, Annex). The computed HOMO-LUMO gaps of their PH_3 -substituted models, respectively 1.06 eV and 0.94 eV, are large (Tables S16 and S17, Annex). In the D_{3h} pseudo-symmetry of their metal core the five-fold 1D level is split into three-below-two *superatomic* orbitals, generating the $1S^2 1P^6 1D^6$ configuration (14-*fe* species).

In the same vein, the unique large platinum cluster with a *bcc* metal core, namely $[\text{Pt}_{40}(\mu\text{-CO})_{16}(\text{CO})_{24}]^{6-}$ (Figure 10, Figure S17 and Table S18, Annex),⁶² has an elongated shape that can be viewed as a distorted sphere. It can be associated with an *nfe* count of 28 with the $1S^2 1P^6 1D^{10} 2S^2 1F^8$ configuration resulting from a degeneracy splitting of the 1F shell in D_{2h} symmetry, although the small computed HOMO-LUMO gap leaves some doubts about this cluster description.

There are also clusters the shape of which cannot be derived from that of a sphere nor can be described as resulting from the condensation of smaller spherical units. Although such species cannot be rationalized within the concepts of *superatoms* or *supermolecules*, it remains nonetheless that their bonding is achieved through the population of $6s(\text{Pt})$ combinations, providing their metal core remains compact enough. For example, the far from spheroidal cluster $[\text{Pt}_{24}(\mu\text{-CO})_8(\text{CO})_{22}]^{2-}$ ^{31,67} (Figure 10, Figure S17 and Table S19, Annex) adopts a Pt *fcc ABCA* packing of 10-, 9- and 5-atom *hc* layers. Seven orbitals with large $6s$ participation could be identified below the non-negligible HOMO-LUMO gap (0.66 eV), securing a 14-*fe* count. Similarly, the *fcc* core of $[\text{Pt}_{33}(\mu\text{-CO})_{10}(\text{CO})_{28}]^{2-}$ ⁶² (Figure 10, Figure S17 and Table S20, Annex) resulting from the packing of compact layers made of 8, 12, 9 and 4 atoms can be identified as an 18-*fe* cluster.

Computed model	Experimental structure	Optimized structure	
$[\text{Pt}_{38}(\mu\text{-CO})_{12}(\text{CO})_{32}]^{2-}$			$\Delta E_{\text{HL}} = 0.45 \text{ eV}$ $nfe = 18$
	$[\text{Pt}_{38}(\mu\text{-CO})_{12}(\text{CO})_{32}]^{2-63,67}$	$[\text{Pt}_{38}(\mu\text{-CO})_{12}(\text{CO})_{32}]^{2-} (D_{2d})$	
$[\text{Pt}_{36}(\mu\text{-CO})_{18}(\text{CO})_{26}]^{2-}$			$\Delta E_{\text{HL}} = 0.24 \text{ eV}$ $nfe = 18$
	$[\text{Pt}_{36}(\mu\text{-CO})_{18}(\text{CO})_{26}]^{2-31}$	$[\text{Pt}_{36}(\mu\text{-CO})_{18}(\text{CO})_{26}]^{2-} (C_{2v})$	
$[\text{Pt}_{19}(\mu_3\text{-CO})_3(\mu\text{-CO})_3(\text{CO})_{18}(\mu_4\text{-AuPPh}_3)_3]^-$			$\Delta E_{\text{HL}} = 1.06 \text{ eV}$ $nfe = 14$
	$[\text{Pt}_{19}(\mu_3\text{-CO})_3(\mu\text{-CO})_3(\text{CO})_{18}(\mu_4\text{-AuPPh}_3)_3]^{-100}$	$[\text{Pt}_{19}(\mu_3\text{-CO})_3(\mu\text{-CO})_3(\text{CO})_{18}(\mu_4\text{-AuPPh}_3)_3]^- (C_1)$	
$[\text{Pt}_{19}(\mu_3\text{-CO})(\mu\text{-CO})_5(\text{CO})_{18}\{\mu_4\text{-Au}_2(\text{PPh}_3)_2\}_2]$			$\Delta E_{\text{HL}}: 0.94 \text{ eV}$ $nfe = 14$
	$[\text{Pt}_{19}(\mu_3\text{-CO})(\mu\text{-CO})_5(\text{CO})_{18}\{\mu_4\text{-Au}_2(\text{PPh}_3)_2\}_2]^{100}$	$[\text{Pt}_{19}(\mu_3\text{-CO})(\mu\text{-CO})_5(\text{CO})_{18}\{\mu_4\text{-Au}_2(\text{PPh}_3)_2\}_2] (C_1)$	
$[\text{Pt}_{24}(\mu\text{-CO})_8(\text{CO})_{22}]^{2-}$			$\Delta E_{\text{HL}} = 0.66 \text{ eV}$ $nfe = 14$
	$[\text{Pt}_{24}(\mu\text{-CO})_8(\text{CO})_{22}]^{2-31,67}$	$[\text{Pt}_{24}(\mu\text{-CO})_8(\text{CO})_{22}]^{2-} (C_2)$	
$[\text{Pt}_{33}(\mu\text{-CO})_{10}(\text{CO})_{28}]^{2-}$			$\Delta E_{\text{HL}} = 0.49 \text{ eV}$ $nfe = 18$
	$[\text{Pt}_{33}(\mu\text{-CO})_{10}(\text{CO})_{28}]^{2-62}$	$[\text{Pt}_{33}(\mu\text{-CO})_{10}(\text{CO})_{28}]^{2-} (C_1)$	
$[\text{Pt}_{40}(\mu\text{-CO})_{16}(\text{CO})_{24}]^{6-}$			$\Delta E_{\text{HL}} = 0.25 \text{ eV}$ $nfe = 28$
	$[\text{Pt}_{40}(\mu\text{-CO})_{16}(\text{CO})_{24}]^{6-62}$	$[\text{Pt}_{40}(\mu\text{-CO})_{16}(\text{CO})_{24}]^{6-} (D_{2d})$	

Figure 10. Optimized structures (right) of various clusters with non-spheroidal 3D architectures. ΔE_{HL} is the HOMO-LUMO gap. The corresponding experimental structures (left) are shown for comparison.

9.4 Conclusion

Compact platinum clusters in which the average metal configuration is $5d^{10} 6s^0$ (or very close to) cannot exist, due to their incapacity to form (enough) occupied bonding MOs with their antibonding counterparts being vacant. To compensate for this incapacity, partial average occupation of the 6s Pt AO would allow occupying strongly bonding 6s combinations. There are two ways to achieve this condition:

(i) One is simply making highly charged anionic clusters in which the Pt atoms are in a sufficiently negative average oxidation state, such as in the experimental observed icosahedral $[\text{Pt}_{13}(\text{CO})_{12}]^{8-}$ species ($5d^{10} 6s^{0.62}$).

(ii) The other way is realized by electron transfer (thus level crossing) between occupied $5d$ combinations and vacant $6s$ bonding combinations, thus achieving an “excited” $5d^{10-x} 6s^x$ average configuration. This level crossing does not occur (or is not fully completed) in the (hypothetical) bare Pt_n fragments, which are computed to be metallic (most often high-spin) systems. In fact, the level crossing is induced by the presence of the ligands which are bonded to the surface of the cluster metal core. In most of the cases, there is a terminal ligand on each of the peripheral (surface) Pt atoms, as well as additional edge- or face-bridging ligands. Whereas one may expect that n bridging ligands induce the destabilization of n $5d$ -type combinations, calculations showed that this is true only when n is small. In most of the cases the number of destabilized $5d$ combinations is lower than n . The reason lies in the fact that the surface metal atoms use only their valence sp_σ AOs (in first approximation) for M–M and M– $\text{CO}_{\text{terminal}}$ bonding, the latter being of localized two-center/two-electron nature. Thus, their $6p_\pi$ AOs are available for bonding with bridging ligands, in addition to the $5d$ ones. Anticipating the nature ($6p_\pi$ vs. $5d$) and the respective number of the involved metal combinations is a particularly difficult task, for it depends on several individual topological parameters. In any case, the number of “supplementary” ligands is not simply related to the number of occupied $6s$ combinations ($nfe/2$), unfortunately. A general situation is sketched in Figure S20 (Annex), which shows the MO interaction diagram of a neutral $[\text{Pt}_n(\text{CO})_n(\mu\text{-CO})_m]$ species having $2m_1 < 2m$ fe 's.

Assuming compact ligated platinum clusters with $5d^{10-x} 6s^x$ average configuration, their bonding can be rationalized with the same tools as for their gold counterparts, which are of $5d^{10} 6s^x$ average configuration. In other words, spherical clusters can be described as *superatoms* and assemblies of spherical units as *supermolecules*. All these species have closed-shell configurations associated with *magic nfe* counts. It is however noticeable that several platinum

carbonyl clusters exhibit shapes which do not allow them to be described as *superatoms*, Jahn-Teller distorted *superatoms* or *supermolecules*. In any case, the metal–metal bonding within these species is provided by the 6s orbitals. In such cases, non-spherical *jellium* models, such as for instance the *box-shaped* model,^{101,102} could be useful. Observing that all the large 3D platinum clusters characterized so far have *fcc* or *hcp* metal core, a qualitative Hückel-type description of their 6s-derived electronic structure might also be useful.

Finally, it should be noted that the 5d/6s level crossing discussed above is most of the time a formally avoided level crossing. It means that substantial 5d/6s mixing occurs in the crucial bonding orbitals and pure 6s combinations do not exist. 5d orbitals also contribute to Pt–Pt bonding from the depopulation of some of their antibonding combinations. However, such a contribution does not change the number of free electrons, nor the contribution of the 6p AOs.

9.5 References

- 1 Qian, H.; Zhu, M.; Wu, Z.; Jin, R. Quantum sized gold nanoclusters with atomic precision *Acc. Chem. Res.*, **2012**, *45*, 1470–1479.
- 2 Tsukuda, T. Optical properties of ultra-small gold nanostructures. *Springer Series in Chemical Physics (Progress in Photon Science)*. **2017**, *115*, 205–218.
- 3 Kang, X.; Chong, H.; Zhu, M. Au₂₅(SR)₁₈: the captain of the great nanocluster ship, *Nanoscale*, **2018**, *10*, 10758–10834.
- 4 Tang, Q.; Hu, G.; Fung, V.; Jiang, D. Insights into interfaces, stability, electronic properties, and catalytic activities of atomically precise metal nanoclusters from first principles. *Acc. Chem. Res.* **2018**, *51*, 2793–2802.
- 5 Pei, Y.; Wang, P.; Ma, Z.; Xiong, L. Growth-rule-guided structural exploration of thiolate-protected gold nanoclusters. *Acc. Chem. Res.* **2019**, *52*, 23–33.
- 6 Higaki, T.; Li, Q.; Zhou, M.; Zhao, S.; Li, Y.; Li, S.; Jin, R. Toward the tailoring chemistry of metal nanoclusters for enhancing functionalities. *Acc. Chem. Res.* **2018**, *51*, 2764–2773.
- 7 Yao, Q.; Chen, T.; Yuan, X.; Xie, J. Toward total synthesis of thiolate-protected metal nanoclusters. *Acc. Chem. Res.* **2018**, *51*, 1338–1348.
- 8 Sakthivel, N. A.; Dass, A. Aromatic thiolate-protected series of gold nanomolecules and a contrary structural trend in size evolution. *Acc. Chem. Res.* **2018**, *51*, 1774–1783.
- 9 Aikens, C. M. Electronic and geometric structure, optical properties, and excited state behavior in atomically precise thiolate-stabilized noble metal nanoclusters. *Acc. Chem. Res.* **2018**, *51*, 3065–3073.

- 10 Ghosh, A.; Mohammed, O. F.; Bakr, O. M. Atomic-level doping of metal clusters. *Acc. Chem. Res.* **2018**, *51*, 3094–3103.
- 11 Hossain, S.; Niihori, Y.; Nair, L. V.; Kumar, B.; Kurashige, W.; Negishi, Y. Alloy clusters: Precise synthesis and mixing effects. *Acc. Chem. Res.* **2018**, *51*, 3114–3124.
- 12 Cook, A. W.; Hayton, T. W. Case studies in nanocluster synthesis and characterization: Challenges and opportunities. *Acc. Chem. Res.* **2018**, *51*, 2456–2464.
- 13 Lei, Z.; Wan, X.-K.; Yuan, S. F.; Guan, Z.-J.; Wang, Q. M. Alkynyl approach toward the protection of metal nanoclusters. *Acc. Chem. Res.* **2018**, *51*, 2465–2474.
- 14 Sharma, S.; Chakrahari, K. K.; Saillard, J.-Y.; Liu, C. W. Structurally precise dichalcogenolate-protected copper and silver superatomic nanoclusters and their alloys. *Acc. Chem. Res.* **2018**, *51*, 2475–2483.
- 15 Konishi, K.; Iwasaki, M.; Shichibu, Y. Phosphine-ligated gold clusters with core+exo geometries: Unique properties and interactions at the ligand-cluster interface. *Acc. Chem. Res.* **2018**, *51*, 3125–3133.
- 16 Yan, J.; Teo, B. K.; Zheng, N. Surface chemistry of atomically precise coinage–metal nanoclusters: from structural control to surface reactivity and catalysis. *Acc. Chem. Res.* **2018**, *51*, 3084–3093.
- 17 Femoni, C.; Iapalucci, M. C.; Ruggieri, S.; Zacchini, S. From Mononuclear Complexes to Molecular Nanoparticles: The Buildup of Atomically Precise Heterometallic Rhodium Carbonyl Nanoclusters *Acc. Chem. Res.*, **2018**, *51*, 2748–2755.
- 18 Du, Y.; Sheng, H.; Astruc, D.; Zhu, M. Atomically precise noble metal nanoclusters as efficient catalysts: A bridge between structure and properties. *Chem. Rev.* **2020**, *120*, 526–622.
- 19 Longoni, G. Thesis, University of Milano, **1967**.
- 20 Femoni, C.; Iapalucci, M. C.; Kaswalder, F.; Longoni, G.; Zacchini, S. The possible role of metal carbonyl clusters in nanoscience and nanotechnologies. *Coord. Chem. Rev.* **2006**, *250*, 1580–1640.
- 21 Ciabatti, I.; Femoni, C.; Iapalucci, M. C.; Longoni, G.; Zacchini, S. Platinum carbonyl clusters chemistry: four decades of challenging nanoscience. *J. Clust. Sci.* **2014**, *25*, 115–146.
- 22 Cesari, C.; Shon, J. H.; Zacchini, S.; Berben, L. A. Metal carbonyl clusters of groups 8–10: synthesis and catalysis. *Chem. Soc. Rev.* **2021**, *50*, 9503–9539.

- 23 Leuchtner, R. E.; Harms, A. C.; Castleman Jr, A. W. Thermal metal cluster anion reactions: Behavior of aluminum clusters with oxygen. *J Chem. Phys.* **1989**, *91*, 2753–2754.
- 24 Khanna, S. N.; Jena, P. Assembling crystals from clusters. *Phys. Rev. Lett.* **1992**, *69*, 1664–1667.
- 25 Khanna, S. N.; Jena, P. Atomic clusters: Building blocks for a class of solids. *Phys. Rev. B*, **1995**, *51*, 13705–13716.
- 26 Jena, P.; Khanna, S. W.; Rao, B. K. Designing clusters as superelements. *Surf. Rev. Lett.* **1996**, *3*, 993–999.
- 27 Bergeron, D. E.; Roach, P. J.; Castleman Jr, A. W.; Jones, N. O.; Khanna, S. N. Al cluster superatoms as halogens in polyhalides and as alkaline earths in iodide salts. *Science* **2005**, *307*, 231–235.
- 28 Castleman Jr, A. W.; Khanna, S. N. Clusters, superatoms, and building blocks of new materials. *J. Phys. Chem. C* **2009**, *113*, 2664–2675.
- 29 Luo, Z.; Castleman Jr, A. W. Special and general superatoms, *Acc. Chem. Res.* **2014**, *47*, 2931–2940.
- 30 Jena, P.; Sun, Q. *Superatoms: Principles, Synthesis and Applications*, John Wiley & Sons Ltd, **2022**.
- 31 Cattabriga, E.; Ciabatti, I.; Femoni, C.; Iapalucci, M. C.; Longoni, G.; Zacchini, S. Globular molecular platinum carbonyl nanoclusters: Synthesis and molecular structures of the $[\text{Pt}_{26}(\text{CO})_{32}]^-$ and $[\text{Pt}_{14+x}(\text{CO})_{18+x}]^{4-}$ anions and their comparison to related platinum “browns”. *Inorg. Chim. Acta* **2018**, *470*, 238–249.
- 32 Mingos, D. M. P.; Wales, D. J. *Introduction to cluster chemistry*. Prentice-Hall, Englewood Cliffs, **1990**.
- 33 Gam, F.; Wei, J.; Kahlal, S.; Saillard, J.-Y.; Halet, J.-F. Electron Counting in Ligated High Nuclearity Late Transition Metal Clusters. In: 50th Anniversary of Electron Counting Paradigms for Polyhedral Molecules – Historical and Recent Developments. *Struct. Bond.* **2021**, *188*, 69–102.
- 34 Saillard, J.-Y.; Halet, J.-F. Structure and Bonding Patterns in Large Molecular Ligated Metal Clusters. In: The Chemical Bond I – 100 Years Old and Getting Stronger, D. M. P. Mingos (ed.), *Structure and Bonding* (Springer, Berlin, Heidelberg) **2016**, *169*, 157–180, DOI: 10.1007/430_2015_210.
- 35 Woods, R. D.; Saxon D. S. Diffuse surface optical model for nucleon-nuclei scattering. *Phys. Rev.* **1954**, *95*, 577–578.

- 36 Walter, M.; Akola, J.; Lopez-Acevedo, O.; Jadzinsky, P. D.; Calero, G.; Ackerson, C. J. Whetten, R. L.; Grönbeck, H.; Häkkinen, H. A Unified View of Ligand-protected Gold Clusters as Superatom Complexes. *Proc. Natl. Acad. Sci. USA* **2008**, *105*, 9157–9162.
- 37 Häkkinen, H. Atomic and electronic structure of gold clusters: understanding flakes, cages and superatoms from simple concepts. *Chem. Soc. Rev.* **2008**, *37*, 1847–1859.
- 38 Zhu, M.; Aikens, C. M.; Hollander, F. J.; Schatz, G. C.; Jin, R. Correlating the crystal structure of a thiol-protected Au₂₅ cluster and optical properties. *J. Am. Chem. Soc.* **2008**, *130*, 5883–5885.
- 39 Dhayal, R. S.; Liao, J. H.; Liu, Y. C.; Chiang, M. H.; Kahlal, S.; Saillard, J.-Y.; Liu, C. W. [Ag₂₁ {S₂P(O^{*i*}Pr)₂}₁₂]⁺: An Eight-Electron Superatom. *Angew. Chem. Int. Ed.*, **2015**, *127*, 3773–3777.
- 40 Dhayal, R.S.; Lin, Y.R.; Liao, J.H.; Chen, Y.J.; Liu, Y.C.; Chiang, M.H.; Kahlal, S.; Saillard, J.-Y.; Liu, C. W. [Ag₂₀{S₂P(OR)₂}₁₂]: a superatom complex with a chiral metallic core and high potential for isomerism. *Chem. Eur. J.* **2016**, *22*, 9943–9947.
- 41 Yang, H.; Wang, Y.; Lei, J.; Shi, L.; Wu, X.; Mäkinen, V.; Lin, S.; Tang, Z.; He, J.; Häkkinen, H.; Zheng, L.; Zheng, N. Ligand-Stabilized Au₁₃Cu_x (x = 2, 4, 8) Bimetallic Nanoclusters: Ligand Engineering to Control the Exposure of Metal Sites. *J. Am. Chem. Soc.* **2013**, *135*, 9568–9571.
- 42 Heaven, M. W.; Dass, A.; White, P. S.; Holt, K. M.; Murray, R. W. Crystal structure of the gold nanoparticle [N(C₈H₁₇)₄][Au₂₅(SCH₂CH₂Ph)₁₈]. *J. Am. Chem. Soc.* **2008**, *130*, 3754–3755.
- 43 Akola, J.; Walter, M.; Whetten, R. L.; Häkkinen, H.; Grönbeck, H. On the structure of thiolate-protected Au₂₅. *J. Am. Chem. Soc.* **2008**, *130*, 3756–3757.
- 44 Shichibu, Y.; Konishi, K. HCl-Induced nuclearity convergence in diphosphine-protected ultrasmall gold clusters: A novel synthetic route to “Magic-Number” Au₁₃ clusters. *Small* **2010**, *6*, 1216–1220.
- 45 Briant, C. E.; Theobald, B. R.; White, J. W.; Bell, L. K.; Mingos, D. M. P.; Welch, A. J. Synthesis and X-ray structural characterization of the centred icosahedral gold cluster compound [Au₁₃(PMe₂Ph)₁₀Cl₂](PF₆)₃; the realization of a theoretical prediction. *J. Chem. Soc. Chem. Commun.* **1981**, *5*, 201–202.
- 46 Saito, S.; Ohnishi, S. Stable (Na₁₉)₂ as a giant alkali-metal–atom dimer. *Phys. Rev. Lett.* **1987**, *59*, 190–193.
- 47 Cheng, L.; Yang, J. Communication: New insight into electronic shells of metal clusters: Analogues of simple molecules. *J. Chem. Phys.* **2013**, *138*, 141101.

- 48 Goicoechea, J. M.; Sevov, S. C. [(Pd–Pd)@Ge₁₈]⁴⁺: A Palladium Dimer Inside the Largest Single-Cage Deltahedron. *J. Am. Chem. Soc.* **2005**, *127*, 7676–7677.
- 49 Sun, Z. M.; Xiao, H.; Li, J.; Wang, L. S. Pd₂@Sn₁₈⁴⁺: Fusion of two endohedral stannaspherenes. *J. Am. Chem. Soc.* **2007**, *129*, 9560–9561.
- 50 Chakraborty, I.; Pradeep, T. Atomically precise clusters of noble metals: emerging link between atoms and nanoparticles. *Chem. Rev.* **2017**, *117*, 8208–8271.
- 51 Chiu, T. H.; Liao, J. H.; Gam, F.; Chantrenne, I.; Kahlal, S.; Saillard, J.-Y.; Liu, C. W. Homoleptic Platinum/Silver Superatoms Protected by Dithiolates: Linear Assemblies of Two and Three Centered Icosahedra Isolobal to Ne₂ and I₃⁻. *J. Am. Chem. Soc.* **2019**, *141*, 12957–12961.
- 52 Gam, F.; Liu, C. W.; Kahlal, S.; Saillard, J.-Y. Electron counting and bonding patterns in assemblies of three and more silver-rich superatoms. *Nanoscale*, **2020**, *12*, 20308–20316.
- 53 Lin, Z.; Kanters, R. P. F.; Mingos, D. M. P. Closed-shell electronic requirements for condensed clusters of the group 11 elements. *Inorg. Chem.* **1991**, *30*, 91–95.
- 54 Sheong, F. K.; Zhang, J. X.; Lin, Z. An [Au₁₃]⁵⁺ Approach to the Study of Gold Nanoclusters. *Inorg. Chem.* **2016**, *55*, 11348–11353.
- 55 Teramoto, M.; Iwata, K.; Yamaura, H.; Kurashima, K.; Miyazawa, K.; Kurashige, Y.; Yamamoto, K.; Murahashi, T. Three-dimensional sandwich nanocubes composed of 13-atom palladium core and hexakis-carbocycle shell. *J. Am. Chem. Soc.* **2018**, *140*, 12682–12686.
- 56 Wei, J.; Kahlal, S.; Halet, J.-F.; Saillard, J.-Y. Elucidating the electronic structure of the ligated cuboctahedral palladium cluster [Pd₁₃(μ₄-C₇H₇)₆]²⁺. *J. Clust. Sci.* **2019**, *30*, 1227–1233.
- 57 Erickson, J. D.; Mednikov, E. G.; Ivanov, S. A.; Dahl, L. F.; Isolation and Structural Characterization of a Mackay 55-Metal-Atom Two-Shell Icosahedron of Pseudo-*I_h* Symmetry, Pd₅₅L₁₂(μ₃-CO)₂₀ (L= PR₃, R = Isopropyl): Comparative Analysis with Interior Two-Shell Icosahedral Geometries in Capped Three-Shell Pd₁₄₅, Pt-Centered Four-Shell Pd–Pt M₁₆₅, and Four-Shell Au₁₃₃ Nanoclusters. *J. Am. Chem. Soc.* **2016**, *138*, 1502–1505.
- 58 Wei, J.; Marchal, R.; Astruc, D.; Saillard, J.-Y.; Halet, J.-F.; Kahlal, S. Theoretical Analysis of the Mackay Icosahedral Cluster Pd₅₅(PⁱPr₃)₁₂(μ₃-CO)₂₀: An open-shell 20-electron superatom. *Chem. Eur. J.* **2020**, *26*, 5508–5514.
- 59 Ciabatti, I.; Femoni, C.; Iapalucci, M. C.; Longoni, G.; Zacchini, S.; Zarra, S. Surface decorated platinum carbonyl clusters. *Nanoscale*, **2012**, *4*, 4166–4177.

- 60 Femoni, C.; Iapalucci, M. C.; Longoni, G.; Zacchini, S.; Zarra, S. Icosahedral Pt-Centered Pt₁₃ and Pt₁₉ Carbonyl Clusters Decorated by [Cd₅(μ-Br)₅Br_{5-x}(solvent)_x]^{x+} Rings Reminiscent of the Decoration of Au-Fe-CO and Au-Thiolate Nanoclusters: A Unifying Approach to Their Electron Counts. *J. Am. Chem. Soc.* **2011**, *133*, 2406–2409.
- 61 Gao, F.; Li, C.; Heaton, B. T.; Zacchini, S.; Zarra, S.; Longoni, G.; Garland, M. The inter-conversions of platinum carbonyl dianionic clusters, [Pt₃(CO)₆]_n²⁻ (n = 2–5), in THF and acetonitrile. A combined in situ FTIR spectroscopic and BTEM study leading to the characterization of the new [H_{4-x}Pt₁₅(CO)₁₉]^{x-} (x = 2–4) clusters. *Dalton Trans.* **2011**, *40*, 5002–5008.
- 62 Cattabriga, E.; Ciabatti, I.; Femoni, C.; Funaioli, T.; Iapalucci, M. C.; Zacchini, S. Syntheses, Structures, and Electrochemistry of the Defective ccp [Pt₃₃(CO)₃₈]²⁻ and the bcc [Pt₄₀(CO)₄₀]⁶⁻ Molecular Nanoclusters. *Inorg. Chem.* **2016**, *55*, 6068–6079.
- 63 Ceriotti, A.; Masciocchi, N.; Macchi, P.; Longoni, G. [Pt₁₉(CO)₂₁(NO)]³⁻ and [Pt₃₈(CO)₄₄]²⁻: Nitrosyl Bending through Intramolecular Electron Transfer as an Intermediate Step in the Nucleation Process from Polydecker to ccp Platinum Carbonyl Clusters. *Angew. Chem. Int. Ed.* **1999**, *38*, 3724–3727.
- 64 Fabrizi De Biani, F.; Femoni, C.; Iapalucci, M. C.; Longoni, G.; Zanello, P.; Ceriotti, A. Redox Behavior of [H_{6-n}Ni₃₈Pt₆(CO)₄₈]ⁿ⁻ (n = 4–6) Anions: A Series of Metal Carbonyl Clusters Displaying Electron-Sink Features. *Inorg. Chem.* **1999**, *38*, 3721–3724.
- 65 Ceriotti, A.; Demartin, F.; Longoni, G.; Manassero, M.; Marchionna, M.; Piva, G.; Sansoni, M. Synthesis and Structure of the [Ni₃₈Pt₆(CO)₄₈H_{6-n}]ⁿ⁻ (n = 5, 4) Ions: Ni-Pt Clusters as Models for “Cherry” Crystallites. *Angew. Chem. Int. Ed.* **1985**, *24*, 697–698.
- 66 Zacchini, S. Using metal carbonyl clusters to develop a molecular approach towards metal nanoparticles. *Eur. J. Inorg. Chem.* **2011**, *27*, 4125–4145.
- 67 Roth, J. D.; Lewis, G. J.; Safford, L. K.; Jiang, X.; Dahl, L. F.; Weaver, M. J. Exploration of the ionizable metal cluster-electrode surface analogy: infrared spectroelectrochemistry of [Pt₂₄(CO)₃₀]ⁿ, [Pt₂₆(CO)₃₂]ⁿ, and [Pt₃₈(CO)₄₄]ⁿ (n = 0 to -10) and comparisons with potential-dependent spectra of carbon monoxide adlayers on platinum surfaces. *J. Am. Chem. Soc.* **1992**, *114*, 6159–6169.
- 68 Washecheck, D. M.; Wucherer, E. J.; Dahl, L. F.; Ceriotti, A.; Longoni, G.; Manassero, M.; Sansoni, M.; Chini, P. Synthesis, structure, and stereochemical implication of the [Pt₁₉(CO)₁₂(μ₂-CO)₁₀]⁴⁻ tetraanion: a bicapped triple-decker all-metal sandwich of idealized fivefold (D_{5h}) geometry. *J. Am. Chem. Soc.* **1979**, *101*, 6110–6112.

- 69 Longoni, G.; Chini, P. Synthesis and chemical characterization of platinum carbonyl dianions $[\text{Pt}_3(\text{CO})_6]_n^{2-}$ ($n = \text{apprx. } 10, 6, 5, 4, 3, 2, 1$). A new series of inorganic oligomers. *J. Am. Chem. Soc.* **1976**, *98*, 7225–7231.
- 70 Calabrese, J. C.; Dahl, L. F.; Chini, P.; Longoni, G.; Martinengo, S. Synthesis and structural characterization of platinum carbonyl cluster dianions bis, tris, tetrakis, or pentakis (μ_3 -carbonyl-tricarbonyltriplatinum)(2-). New series of inorganic oligomers. *J. Am. Chem. Soc.* **1974**, *96*, 2614–2616.
- 71 Underwood, D. J.; Hoffmann, R.; Tatsumi, K.; Nakamura, A.; Yamamoto, Y. Triangular Platinum and Nickel Clusters: The “Tinker-Toy” Construction of Chains with High Nuclearity. *J. Am. Chem. Soc.* **1985**, *107*, 5968–5980.
- 72 Mingos, D. M. P. A general theory for cluster and ring compounds of the main group and transition elements. *Nat. Phys. Sci.* **1972**, *236*, 99–102.
- 73 Fehner, T. P.; Halet, J.-F.; Saillard, J.-Y. Molecular clusters. A bridge to solid state chemistry. Cambridge University Press, Cambridge, **2007**.
- 74 Frapper, G.; Halet, J.-F. Rationalising and Predicting the Structure and Bonding of Bare and Ligated Transition Metal Clusters and Nanoparticles. In: Computational Materials Discovery (Oganov, A. R.; Kvashnin, A. G.; Saleh, G. eds.), Royal Society of Chemistry, London, **2019**, pp. 320–351.
- 75 a) te Velde, G.; Bickelhaupt, F. M.; van Gisbergen, S. J. A.; Guerra, C. F.; Baerends, E. J.; Snijders, J. G.; Ziegler, T. Chemistry with ADF. *J. Comput. Chem.* **2001**, *22*, 931–967; b) ADF2018, SCM, Theoretical Chemistry, Vrije Universiteit: Amsterdam, The Netherlands; <http://www.scm.com>.
- 76 Van Lenthe, E.; Baerends, E. J.; Snijders, J. G. Relativistic total energy using regular approximations. *J. Chem. Phys.* **1994**, *101*, 9783–9792.
- 77 Becke, A. D. Density-functional exchange-energy approximation with correct asymptotic behavior. *Phys. Rev. A* **1988**, *38*, 3098–3100.
- 78 Perdew, J. P. Density-functional approximation for the correlation energy of the inhomogeneous electron gas. *Phys. Rev. B* **1986**, *33*, 8822–8824.
- 79 Grimme, S. Semiempirical GGA-type density functional constructed with a long-range dispersion correction. *J. Comput. Chem.* **2006**, *27*, 1787–1799.
- 80 Glendening, E. D.; Badenhoop, J. K.; Reed, A. E.; Carpenter, J. E.; Bohmann, J. A.; Morales, C. M.; Weinhold, F. NBO 6.0. Theoretical Chemistry Institute, University of Wisconsin (Madison, WI, **2001**, <http://nbo6.chem.wisc.edu>).

- 81 Frisch, M. J.; Trucks, G. W.; Schlegel, H. B.; Scuseria, G. E.; Robb, M. A.; Cheeseman, J. R.; Scalmani, G.; Barone, V.; Petersson, G. A.; Nakatsuji, H.; Li, X.; Caricato, M.; Marenich, A. V.; Bloino, J.; Janesko, B. G.; Gomperts, R.; Mennucci, B.; Hratchian, H. P.; Ortiz, J. V.; Izmaylov, A. F.; Sonnenberg, J. L.; Williams-Young, D.; Ding, F.; Lipparini, F.; Egidi, F.; Goings, J.; Peng, B.; Petrone, A.; Henderson, T.; Ranasinghe, D.; Zakrzewski, V. G.; Gao, J.; Rega, N.; Zheng, G.; Liang, W.; Hada, M.; Ehara, M.; Toyota, K.; Fukuda, R.; Hasegawa, J.; Ishida, M.; Nakajima, T.; Honda, Y.; Kitao, O.; Nakai, H.; Vreven, T.; Throssell, K.; Montgomery, J. A., Jr.; Peralta, J. E.; Ogliaro, F.; Bearpark, M. J.; Heyd, J. J.; Brothers, E. N.; Kudin, K. N.; Staroverov, V. N.; Keith, T. A.; Kobayashi, R.; Normand, J.; Raghavachari, K.; Rendell, A. P.; Burant, J. C.; Iyengar, S. S.; Tomasi, J.; Cossi, M.; Millam, J. M.; Klene, M.; Adamo, C.; Cammi, R.; Ochterski, J. W.; Martin, R. L.; Morokuma, K.; Farkas, O.; Foresman, J. B.; Fox, D. J. *Gaussian16*, Gaussian, Inc.: Wallingford, CT, **2016**.
- 82 Weigend F.; Ahlrichs, R. Balanced basis sets of split valence, triple zeta valence and quadruple zeta valence quality for H to Rn: Design and assessment of accuracy. *Phys. Chem. Chem. Phys.* **2005**, *7*, 3297–3305.
- 83 de Silva, N.; Dahl, L.F. Synthesis and Structural Analysis of the First Nanosized Platinum–Gold Carbonyl/Phosphine Cluster, Pt₁₃[Au₂(PPh₃)₂]₂(CO)₁₀(PPh₃)₄, Containing a Pt-Centered [Ph₃PAu–AuPPh₃]-Capped Icosahedral Pt₁₂ Cage. *Inorg. Chem.* **2005**, *44*, 9604–9606.
- 84 Kurasov, S. S.; Eremenko, N. K.; Slovokhotov, Y. L.; Struchkov, Y. T. High-nuclearity icosahedral carbonylphosphineplatinum clusters: synthesis and crystal structure of Pt₁₇(μ₂-CO)₄(CO)₈(PEt₃)₈. *J. Organomet. Chem.* **1989**, *361*, 405–408.
- 85 Nair, L.V.; Hossain, S.; Wakayama, S.; Takagi, S.; Yoshioka, M.; Maekawa, J.; Harasawa, A.; Kumar, B.; Niihori, Y.; Kurashige, W.; Negishi, Y. [Pt₁₇(CO)₁₂(PPh₃)₈]ⁿ⁺ (n = 1, 2): Synthesis and Geometric and Electronic Structures. *J. Phys. Chem. C* **2017**, *121*, 11002–11009.
- 86 Nobusada, K.; Iwasa, T. Oligomeric gold clusters with vertex-sharing bi- and triicosahedral structures. *J. Phys. Chem. C* **2007**, *111*, 14279–14282.
- 87 Jin, R.; Liu, C.; Zhao, S.; Das, A.; Xing, H.; Gayathri, C.; Xing, Y.; Rosi, N.L.; Gil, R. R.; Jin, R. Tri-icosahedral gold nanocluster [Au₃₇(PPh₃)₁₀(SC₂H₄Ph)₁₀X₂]⁺: Linear assembly of icosahedral building blocks. *ACS Nano* **2015**, *9*, 8530–8536.
- 88 Teo, B. K.; Shi, X.; Zhang, H. Cluster of clusters. Structure of a novel gold-silver cluster [(Ph₃P)₁₀Au₁₃Ag₁₂Br₈](SbF₆) containing an exact staggered-eclipsed-staggered metal

- configuration. Evidence of icosahedral units as building blocks. *J. Am. Chem. Soc.* **1991**, *113*, 4329–4331.
- 89 Teo, B. K.; Zhang, H.; Shi, X. Cluster of clusters: a modular approach to large metal clusters. Structural characterization of a 38-atom cluster $[(p\text{-Tol}_3\text{P})_{12}\text{Au}_{18}\text{Ag}_{20}\text{Cl}_{14}]$ based on vertex-sharing triicosahedra. *J. Am. Chem. Soc.* **1990**, *112*, 8552–8562.
- 90 Teo, B. K.; Keating, K. Novel triicosahedral structure of the largest metal alloy cluster: hexachlorododecakis (triphenylphosphine)-gold-silver cluster $[(\text{Ph}_3\text{P})_{12}\text{Au}_{13}\text{Ag}_{12}\text{Cl}_6]^{m+}$. *J. Am. Chem. Soc.* **1984**, *106*, 2224–2226.
- 91 Hoffmann, R. Building bridges between inorganic and organic chemistry (Nobel Lecture). *Angew. Chem. Int. Ed.* **1982**, *21*, 711–724.
- 92 Mingos, D. M. P. Structural and bonding patterns in gold clusters. *Dalton Trans.* **2015**, *44*, 6680–6695.
- 93 Qian, H.; Eckenhoff, W. T.; Zhu, Y.; Pintauer, T.; Jin, R. Total structure determination of thiolate-protected Au_{38} nanoparticles. *J. Am. Chem. Soc.* **2010**, *132*, 8280–8281.
- 94 Nunokawa, K.; Ito, M.; Sunahara, T.; Onaka, S.; Ozeki, T.; Chiba, H.; Funahashi, Y.; Masuda, H.; Yonezawa, T.; Nishihara, H.; Nakamoto, M. A new 19-metal-atom cluster $[(\text{Me}_2\text{PhP})_{10}\text{Au}_{12}\text{Ag}_7(\text{NO}_3)_9]$ with a nearly staggered–staggered M_5 ring configuration. *Dalton Trans.* **2005**, *16*, 2726–2730.
- 95 Wright, J. S. Theoretical evidence for a stable form of cyclic ozone, and its chemical consequences. *Can. J. Chem.* **1973**, *51*, 139–146.
- 96 Burton, P. G.; Harvey, M. D. Theoretical evidence for metastable cyclic ozone. *Nature* **1977**, *266*, 826–827.
- 97 Harding, L. B.; Goddard III, W. A. Ab initio theoretical results on the stability of cyclic ozone. *J. Chem. Phys.* **1977**, *67*, 2377–2379.
- 98 Flemmig, B.; Wolczanski, P. T.; Hoffmann, R. Transition metal complexes of cyclic and open ozone and thiozone. *J. Am. Chem. Soc.* **2005**, *127*, 1278–1285.
- 99 Sabirov, D. S.; Shepelevich, I. S. Information entropy of oxygen allotropes. A still open discussion about the closed form of ozone. *Comput. Theor. Chem.* **2015**, *1073*, 61–66.
- 100 Ceriotti, A.; Macchi, P.; Sironi, A.; El Afefey, S.; Daghetta, M.; Fedi, S.; Fabrizi de Biani, F.; Della Pergola, R. Cooperative Effects of Electron Donors and Acceptors for the Stabilization of Elusive Metal Cluster Frameworks: Synthesis and Solid-State Structures of $[\text{Pt}_{19}(\text{CO})_{24}(\mu_4\text{-AuPPh}_3)_3]^-$ and $[\text{Pt}_{19}(\text{CO})_{24}\{\mu_4\text{-Au}_2(\text{PPh}_3)_2\}_2]$. *Inorg. Chem.* **2013**, *52*, 1960–1964.

- 101 Alhilaly, M. J.; Bootharaju, M. S.; Joshi, C. P.; Besong, T. M.; Emwas, A. H.; Juarez-Mosqueda, R.; Kaappa, S.; Malola, S.; Adil, K.; Shkurenko, A.; Häkkinen, H.; Eddaoudi M.; Bakr O. M. $[\text{Ag}_{67}(\text{SPhMe}_2)_{32}(\text{PPh}_3)_8]^{3+}$: Synthesis, total structure, and optical properties of a large box-shaped silver nanocluster. *J. Am. Chem. Soc.* **2016**, *138*, 14727–14732.
- 102 Juarez-Mosqueda, R.; Kaappa, S.; Malola, S.; Häkkinen, H. Analysis of the Electronic Structure of Non-Spherical Ligand-Protected Metal Nanoclusters: The Case of a Box-Like Ag_{67} . *J. Phys. Chem. C* **2017**, *121*, 10698–10705.

9.6 Annex

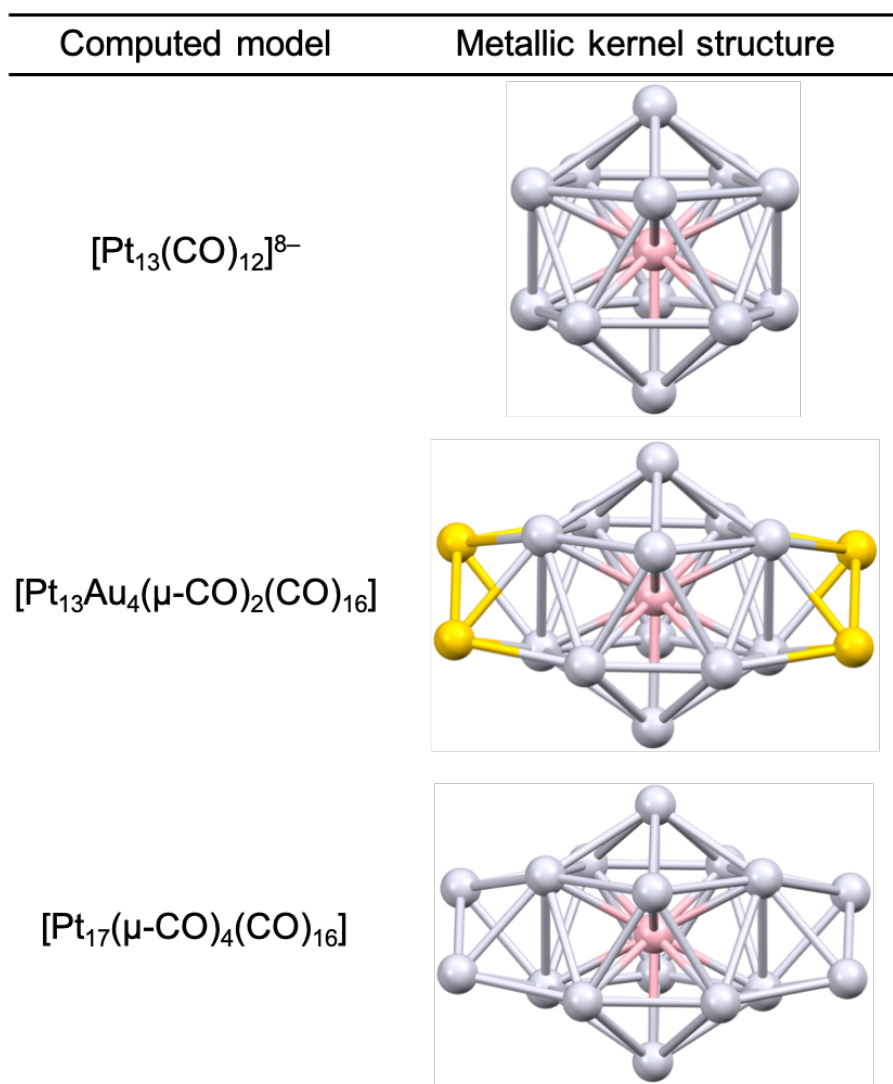


Figure S1. Metallic kernel structure of the icosahedral 8-electron *superatom* models. Light-grey, pink and golden-yellow spheres are outer Pt, central Pt and Au atoms, respectively.

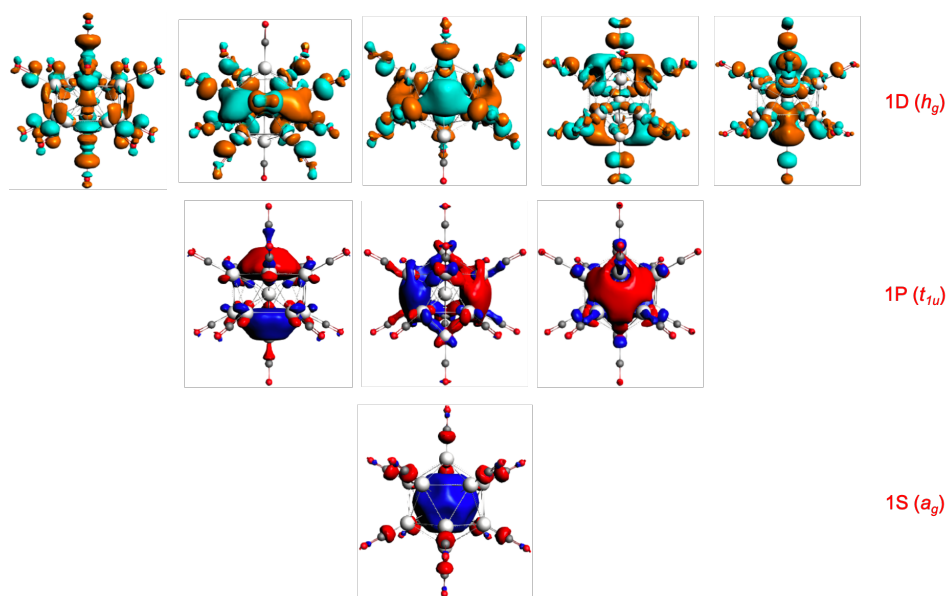


Figure S2. Plots of the *superatomic* orbitals of $[\text{Pt}_{13}(\text{CO})_{12}]^{8-}$ (I_h) with the surface isovalue of ± 0.02 (e/bohr^3) $^{1/2}$.

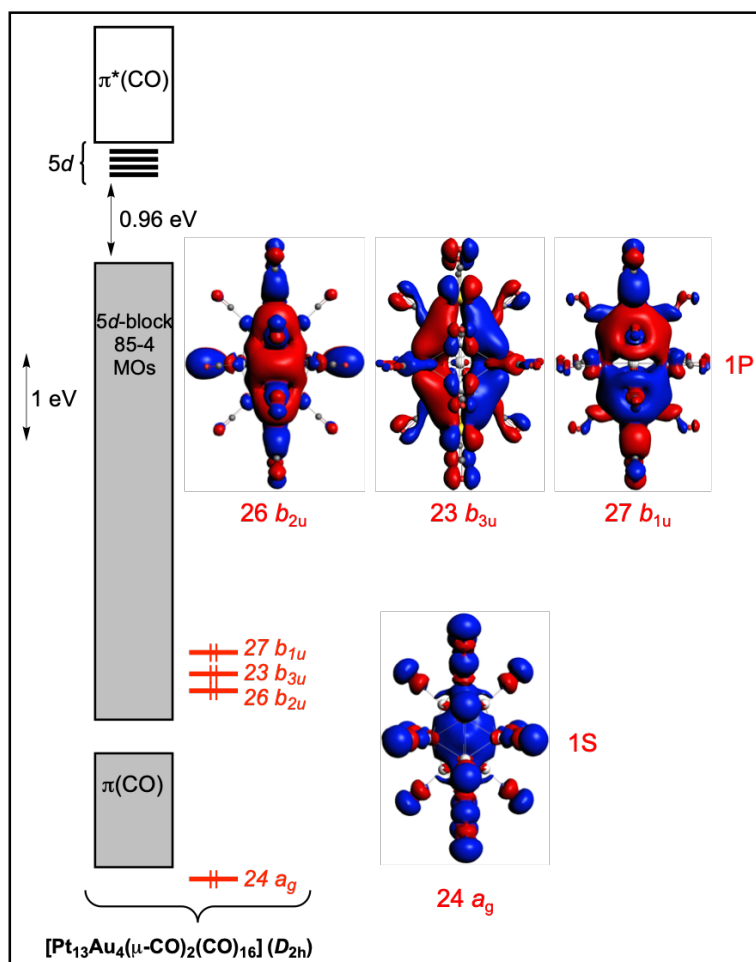


Figure S3. Kohn-Sham orbital diagram of $\text{Pt}_{13}\text{Au}_4(\mu_2\text{-CO})_2(\text{CO})_{16}$. The $5d$ block contains all Pt and Au contributions.

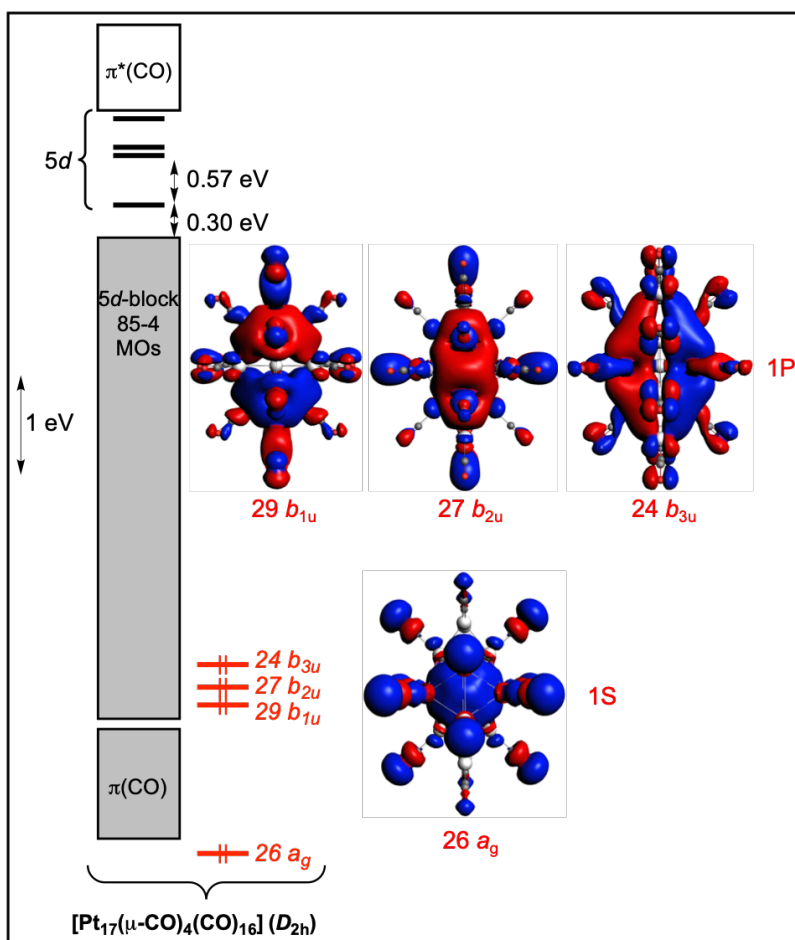


Figure S4. Kohn-Sham orbital diagram of $\text{Pt}_{17}(\mu_2\text{-CO})_4(\text{CO})_{16}$. The $5d$ block contains all Pt contributions.

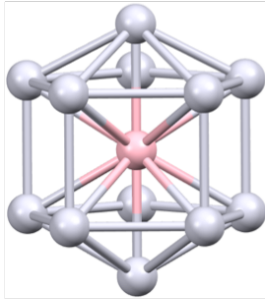
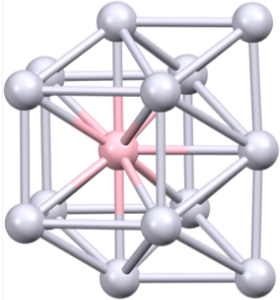
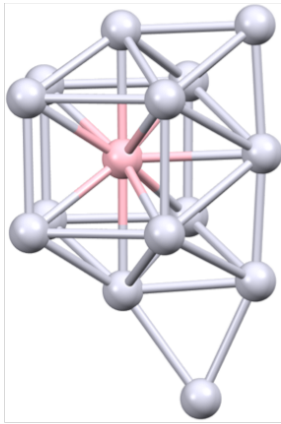
Computed model	Metallic kernel structure
$[\text{Pt}_{13}(\mu\text{-CO})_5(\text{CO})_{12}]^{2-}$	
$[\text{Pt}_{14}(\mu\text{-CO})_6(\text{CO})_{12}]^{4-}$	
$[\text{Pt}_{15}(\mu\text{-CO})_8(\text{CO})_{11}]^{4-}$	

Figure S5. Metallic kernel structure of $[\text{Pt}_{13}(\text{CO})_{12}(\mu\text{-CO})_5]^{2-}$, $[\text{Pt}_{14}(\text{CO})_{12}(\mu\text{-CO})_6]^{4-}$ and $[\text{Pt}_{15}(\text{CO})_{11}(\mu\text{-CO})_8]^{4-}$. Light-grey and pink spheres are outer Pt and central Pt, respectively.

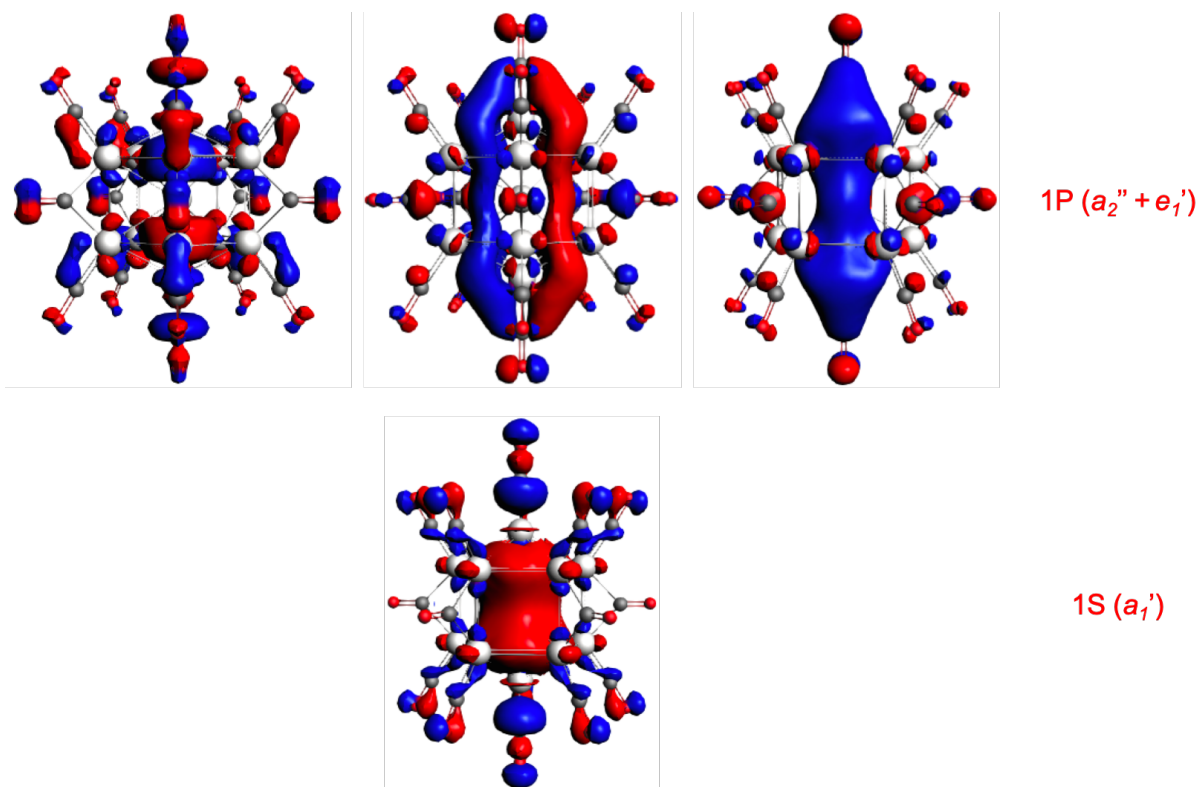


Figure S6. Plots of the *superatomic* orbitals of $[\text{Pt}_{13}(\text{CO})_{12}(\mu\text{-CO})_5]^{2-}$ (D_{5h}) with the surface isovalue of ± 0.02 (e/bohr^3)^{1/2}.

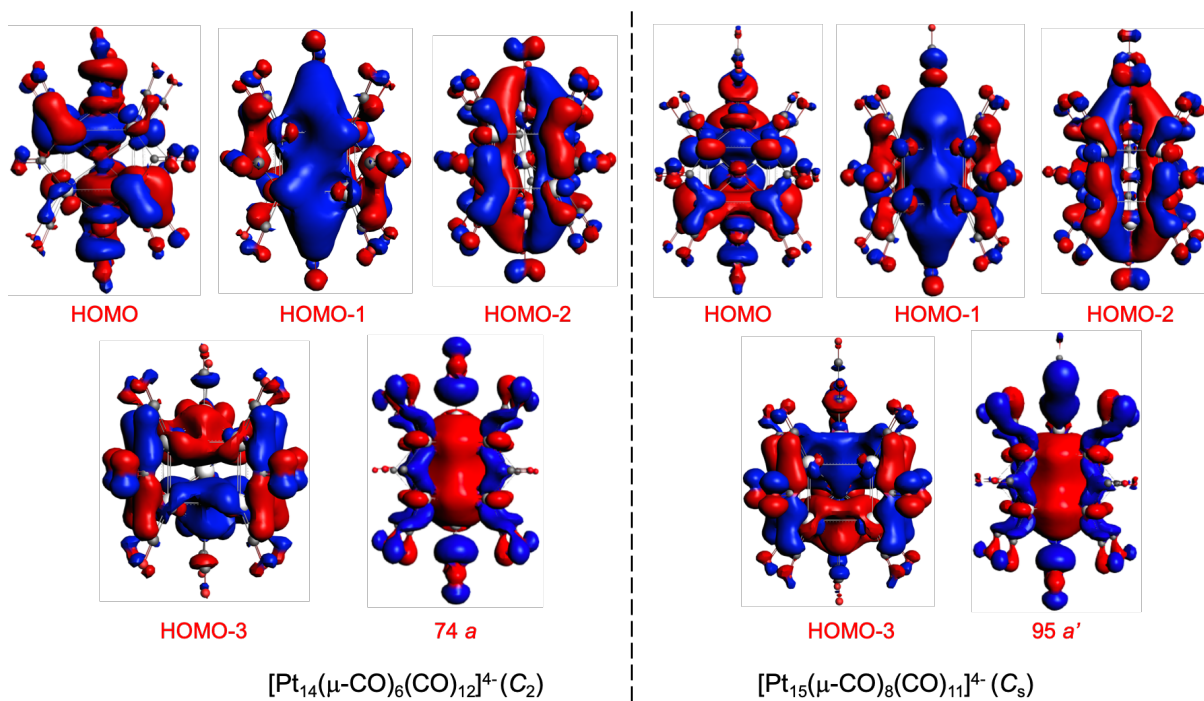


Figure S7. The occupied $6s(\text{Pt})$ combinations of $[\text{Pt}_{14}(\mu\text{-CO})_6(\text{CO})_{12}]^{4-}$ and $[\text{Pt}_{15}(\mu\text{-CO})_8(\text{CO})_{11}]^{4-}$.

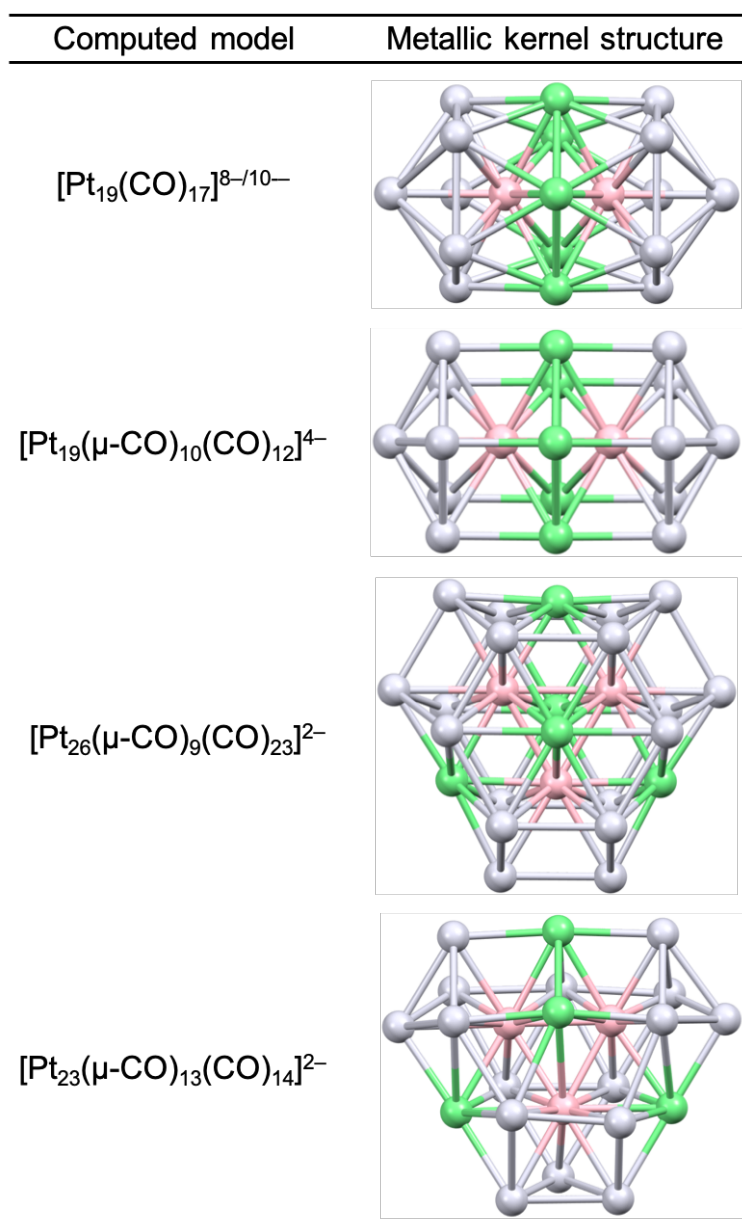


Figure S8. Metallic kernel structure of the clusters that can be viewed as assemblies of individual *superatoms*. Light-grey, pink and green spheres are outer Pt, central Pt and the Pt that shared between two or three *superatoms*, respectively.

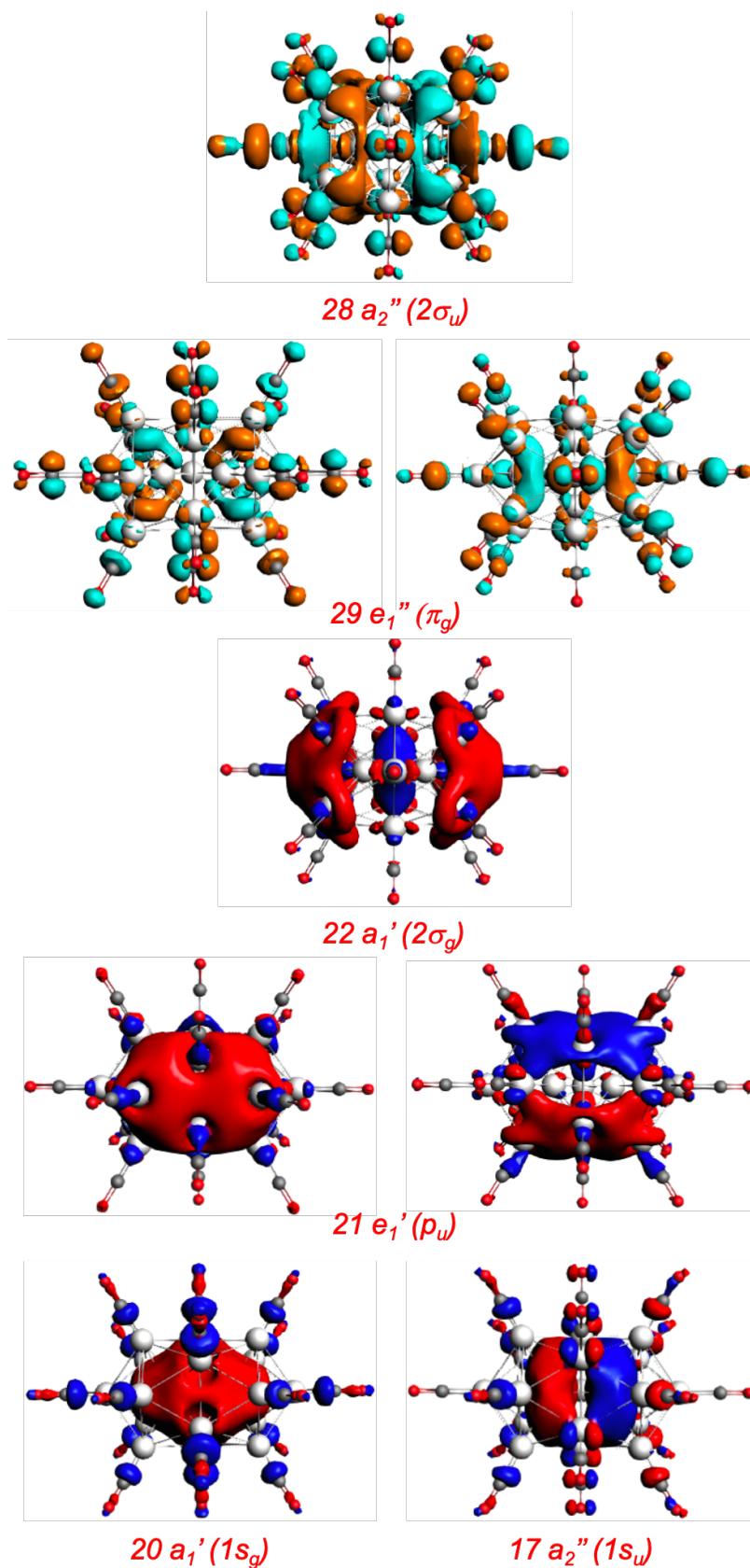


Figure S9. Plots of the *supermolecular* orbitals of $[\text{Pt}_{19}(\text{CO})_{17}]^{10-}$ (D_{5h}) with the surface isovalue of ± 0.02 (e/bohr^3)^{1/2}.

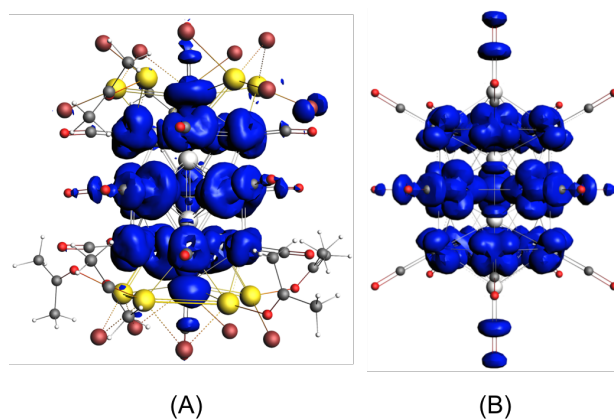


Figure S10. Spin density plots of $[\text{Pt}_{19}(\text{CO})_{17}\{\text{Cd}_5(\mu\text{-Br})_5\text{Br}_3(\text{Me}_2\text{CO})_2\}\{\text{Cd}_5(\mu\text{-Br})_5\text{Br}(\text{Me}_2\text{CO})_4\}]^{2-}$ (A) and $[\text{Pt}_{19}\text{CO}_{17}]^{8-}$ (D_{5h}) (B).

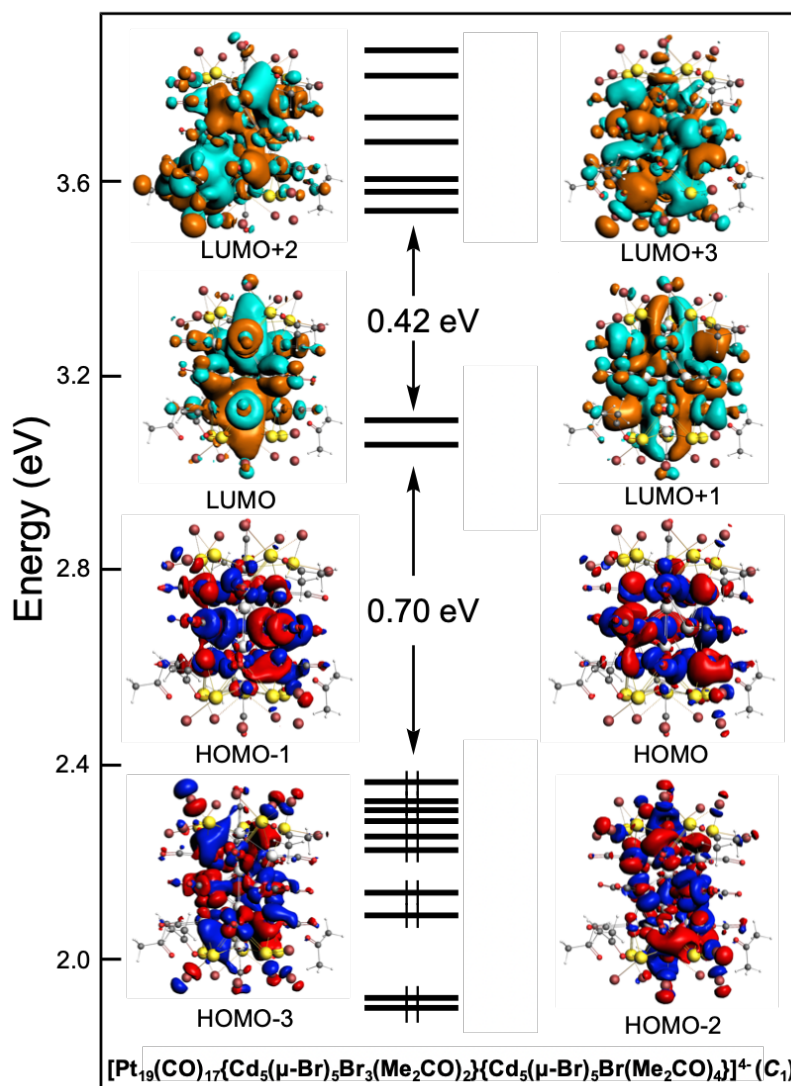


Figure S11. Kohn-Sham orbital diagram of the fully decorated $[\text{Pt}_{19}(\text{CO})_{17}\{\text{Cd}_5(\mu\text{-Br})_5\text{Br}_3(\text{Me}_2\text{CO})_2\}\{\text{Cd}_5(\mu\text{-Br})_5\text{Br}(\text{Me}_2\text{CO})_4\}]^{4-}$.

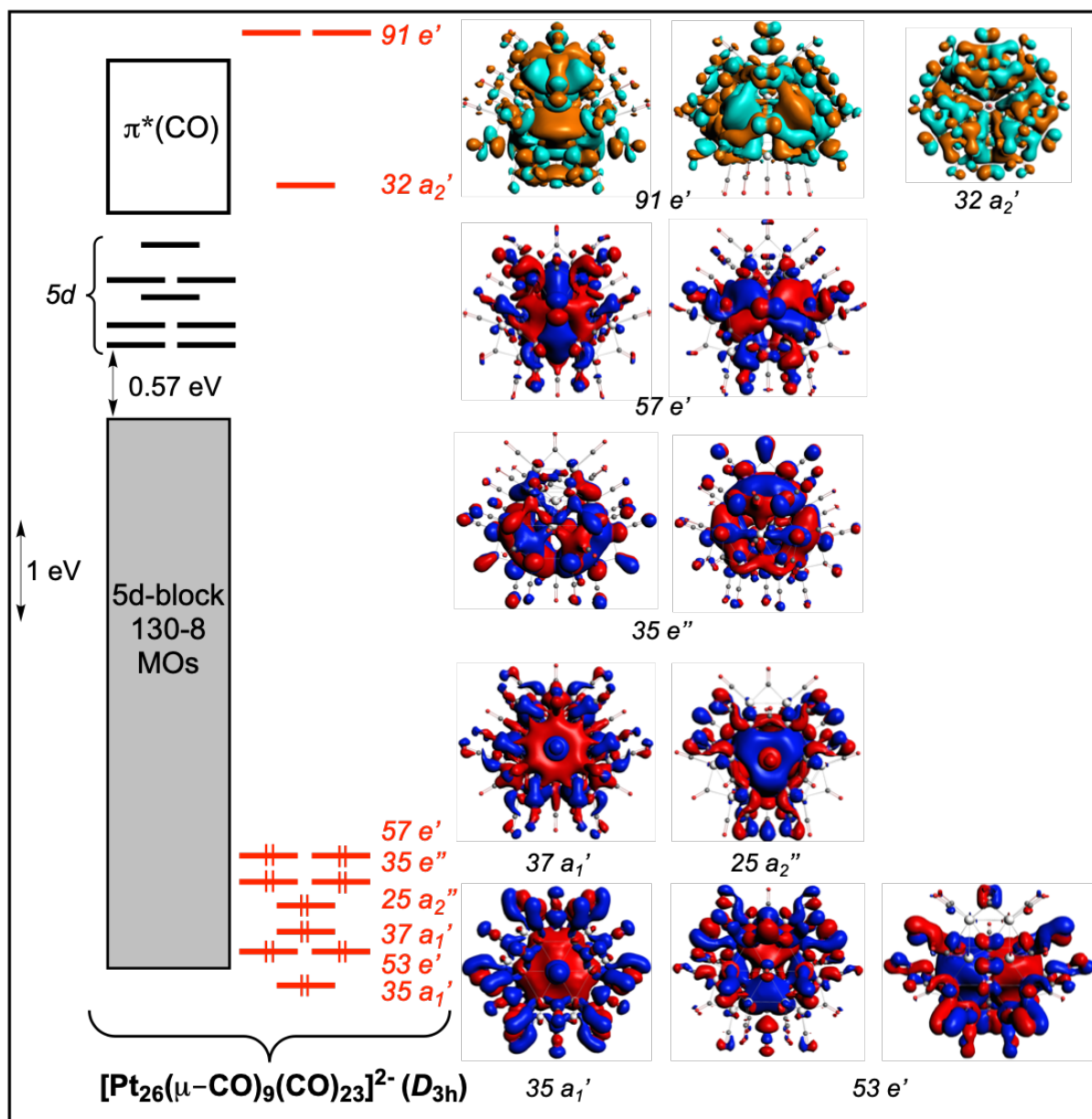


Figure S12. Kohn-Sham orbital diagram of $[\text{Pt}_{26}(\mu_2\text{-CO})_9(\text{CO})_{23}]^{2-}$. The *supermolecular* orbitals plotted on the right side are reminiscent of the valence orbitals of the hypothetical triangular isomer of O_3 .

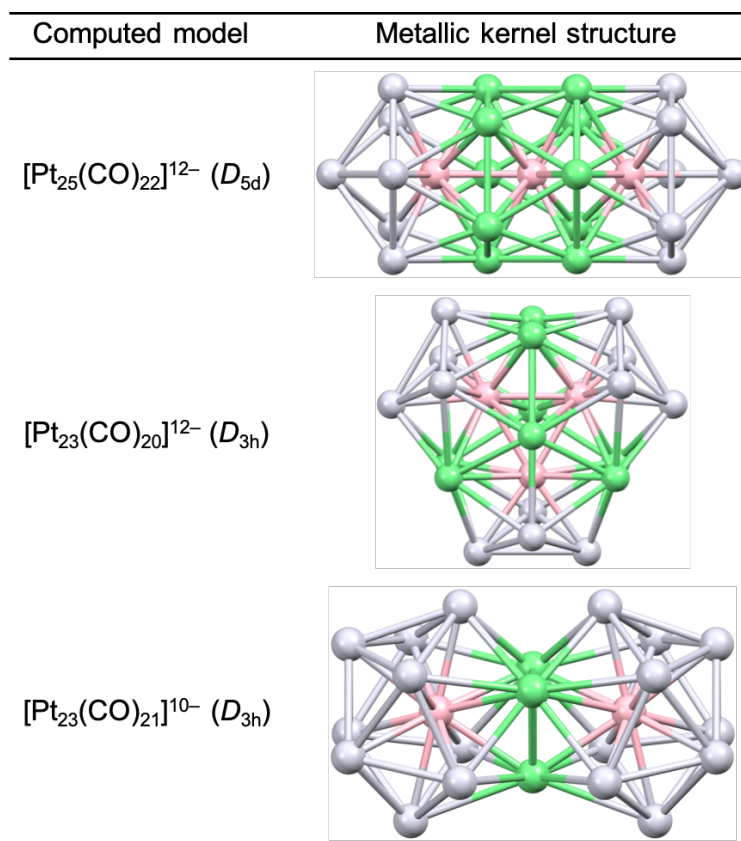


Figure S13. Metallic kernel structure of the linear assemblies of individual icosahedral *superatoms* (hypothetical models). Light-grey, pink and green spheres are outer Pt, central Pt and the Pt that shared between two or three *superatoms*, respectively.

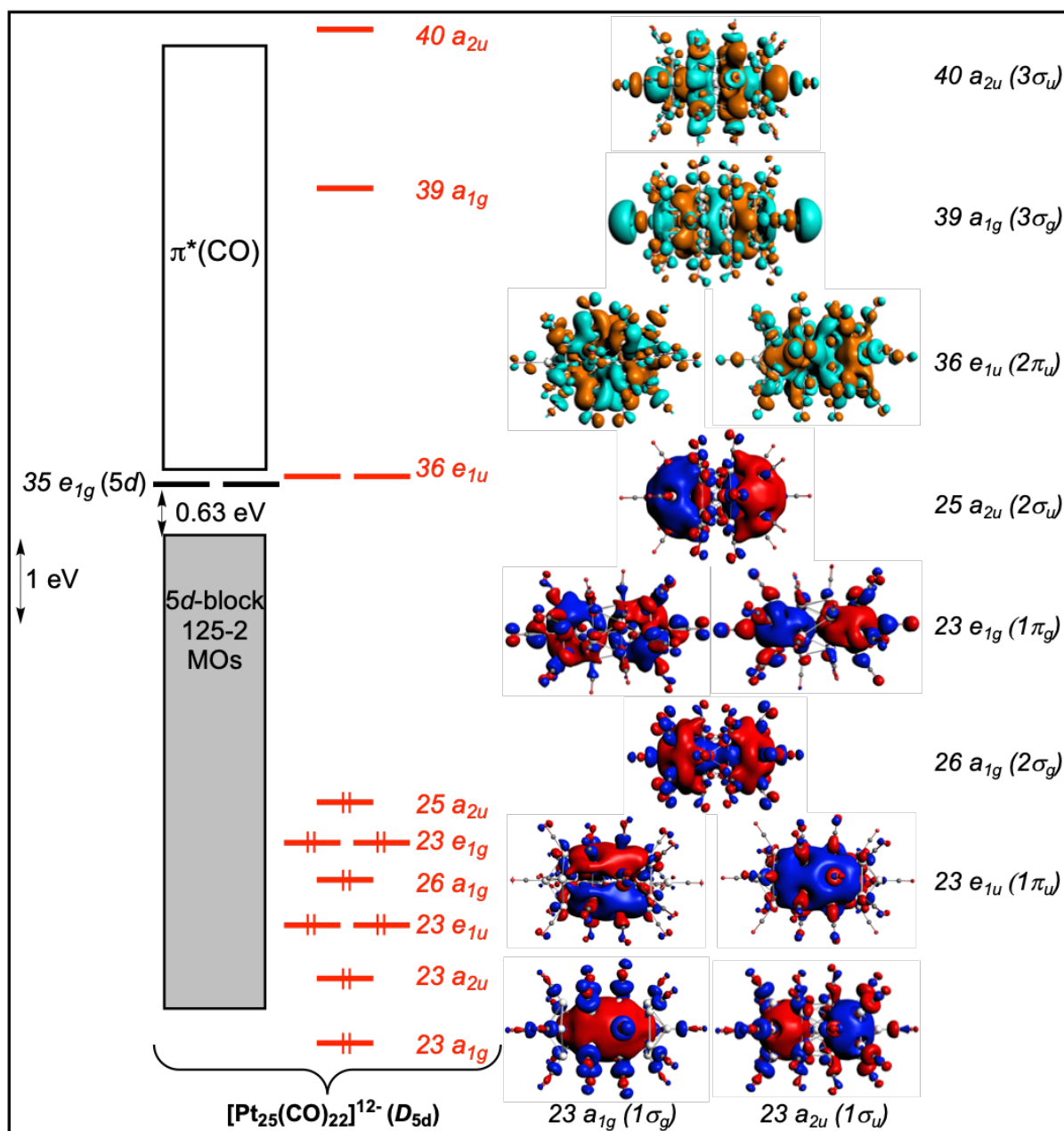


Figure S14. Kohn-Sham orbital diagram of the hypothetical $[\text{Pt}_{25}(\text{CO})_{22}]^{12-}$, the core of which is made of three interpenetrating centered icosahedra. The *supermolecular* orbitals plotted on the right side are reminiscent of the valence orbitals of CO_2 .

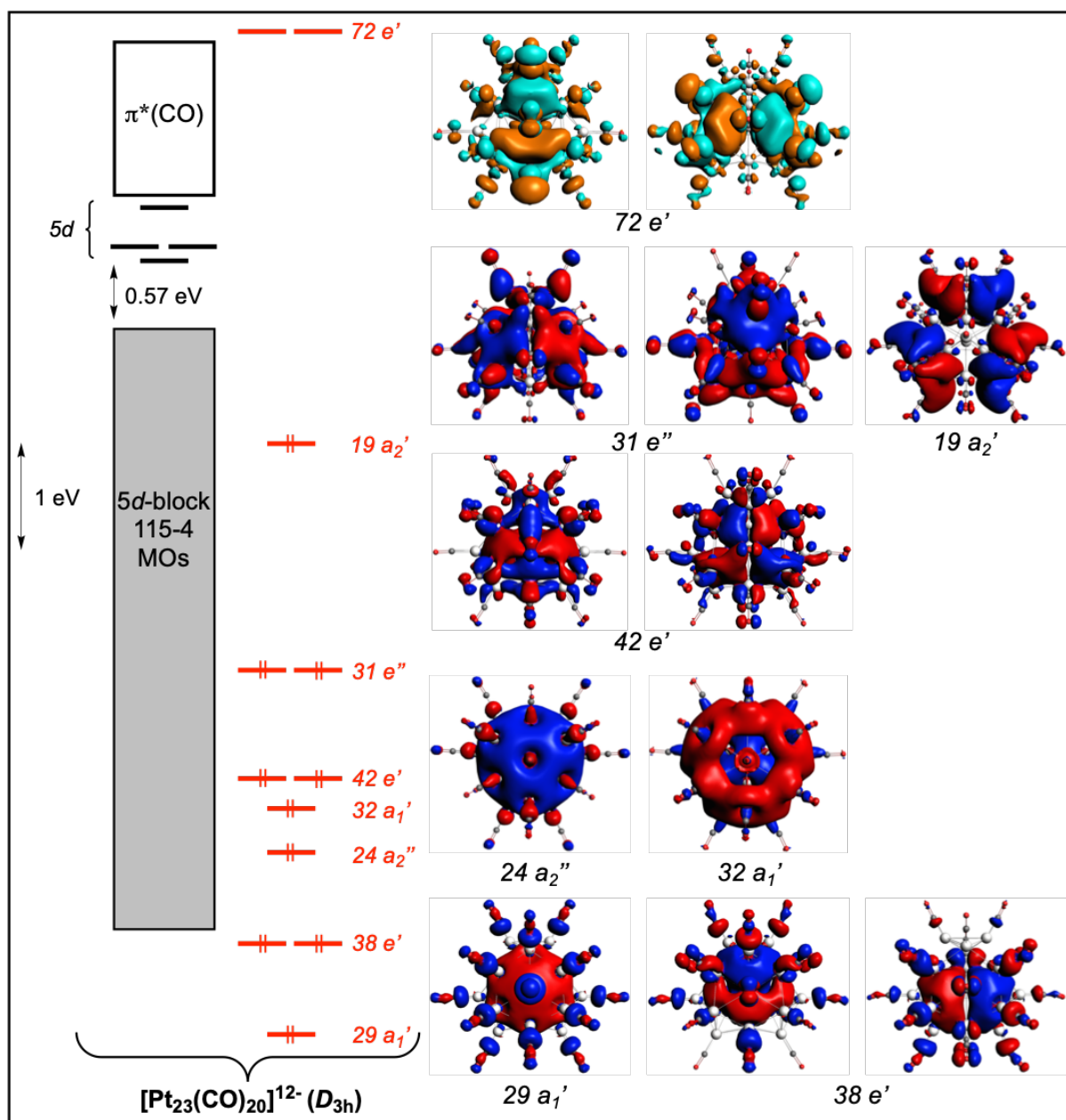


Figure S15. Kohn-Sham orbital diagram of the hypothetical $[\text{Pt}_{23}(\text{CO})_{20}]^{12-}$, the core of which is made of three interpenetrated icosahedra. The *supermolecular* orbitals are plotted on the right side.

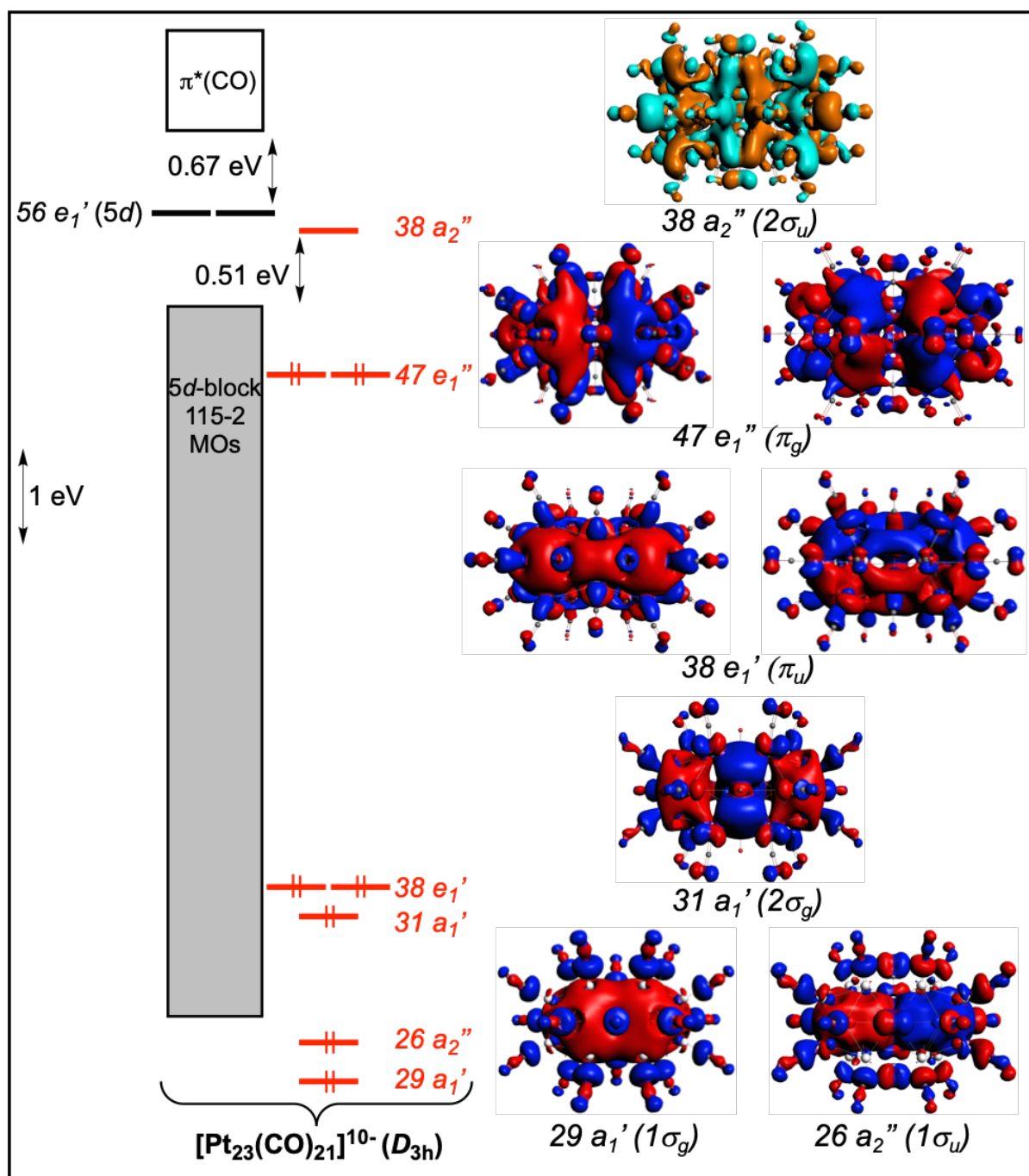


Figure S16. Kohn-Sham orbital diagram of the hypothetical $[\text{Pt}_{23}(\text{CO})_{21}]^{10-}$, the core of which is made of two face-sharing centered icosahedra. The *supermolecular* orbitals, plotted on the right side, are reminiscent of the valence orbitals of F_2 .

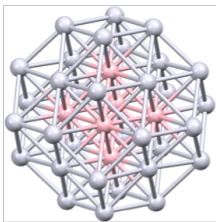
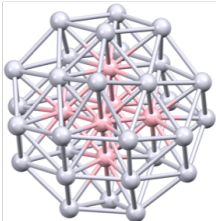
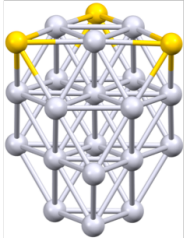
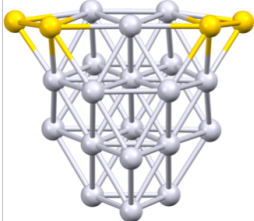
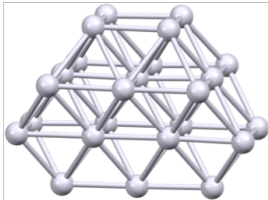
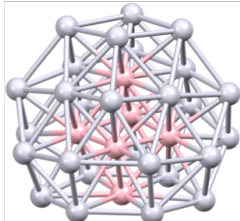
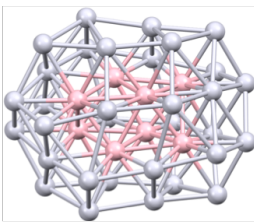
Computed model	Metallic kernel structure
$[\text{Pt}_{38}(\mu\text{-CO})_{12}(\text{CO})_{32}]^{2-}$	
$[\text{Pt}_{36}(\mu\text{-CO})_{18}(\text{CO})_{26}]^{2-}$	
$[\text{Pt}_{19}(\mu_3\text{-CO})_3(\mu\text{-CO})_3(\text{CO})_{18}(\mu_4\text{-AuPH}_3)_3]^{-}$	
$[\text{Pt}_{19}(\mu_3\text{-CO})(\mu\text{-CO})_5(\text{CO})_{18}\{\mu_4\text{-Au}_2(\text{PH}_3)_2\}_2]^{-}$	
$[\text{Pt}_{24}(\mu\text{-CO})_8(\text{CO})_{22}]^{2-}$	
$[\text{Pt}_{33}(\mu\text{-CO})_{10}(\text{CO})_{28}]^{2-}$	
$[\text{Pt}_{40}(\mu\text{-CO})_{16}(\text{CO})_{24}]^{6-}$	

Figure S17. Metallic kernel structure of various clusters with non-spherical 3D structure. Light-grey, pink and golden-yellow spheres are outer Pt, inner Pt that belonging to the encapsulated polyhedron and Au atoms, respectively.

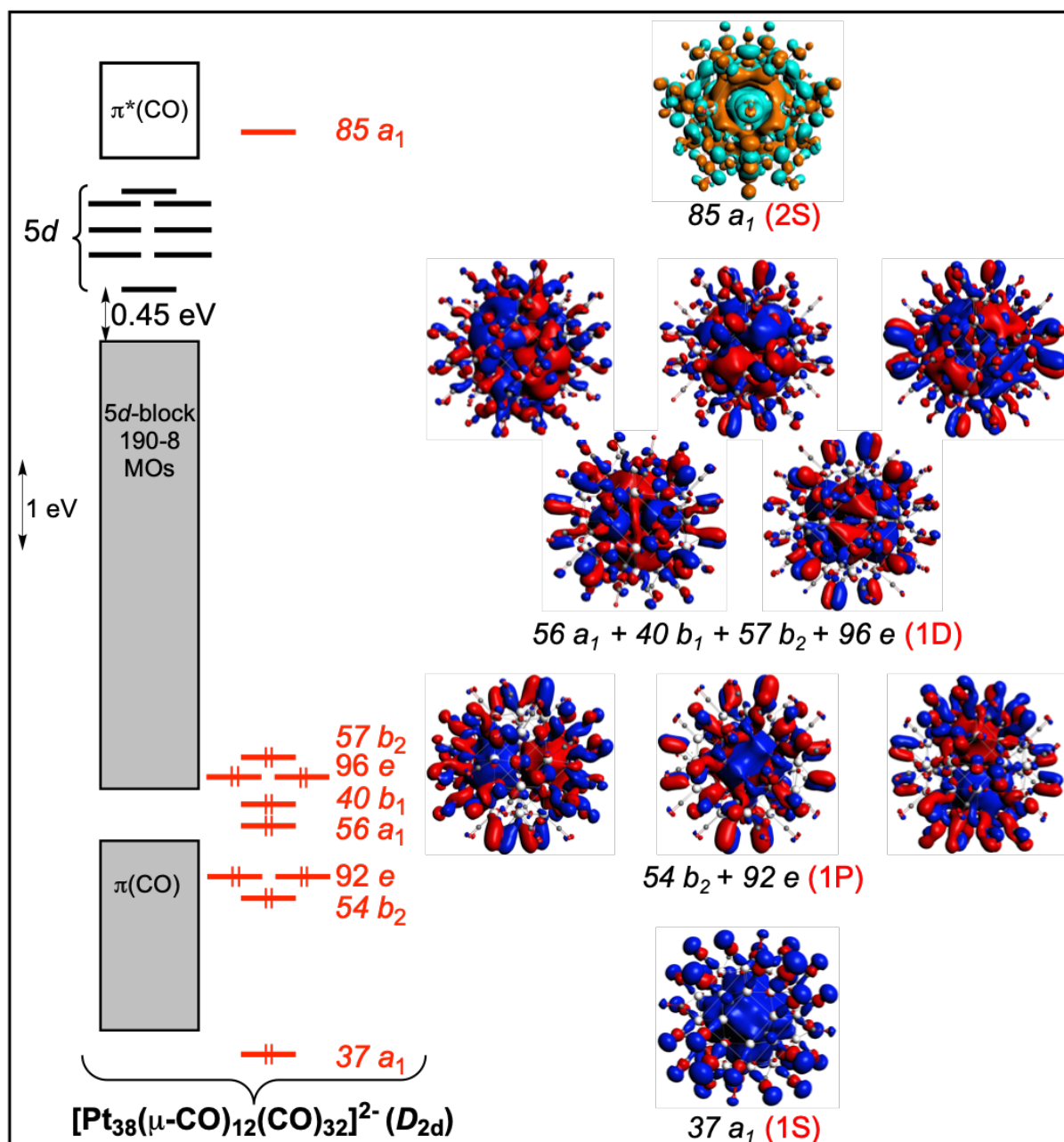


Figure S18. Kohn-Sham orbital diagram of the pseudo-spherical $[\text{Pt}_{38}(\mu_2\text{-CO})_{12}(\text{CO})_{32}]^{2-}$ ($\text{Pt}_6@Pt_{32}$). The *supermolecular* orbitals, plotted on the right side, are consistent with the $1S^2 1P^8 1D^{10}$ configuration.

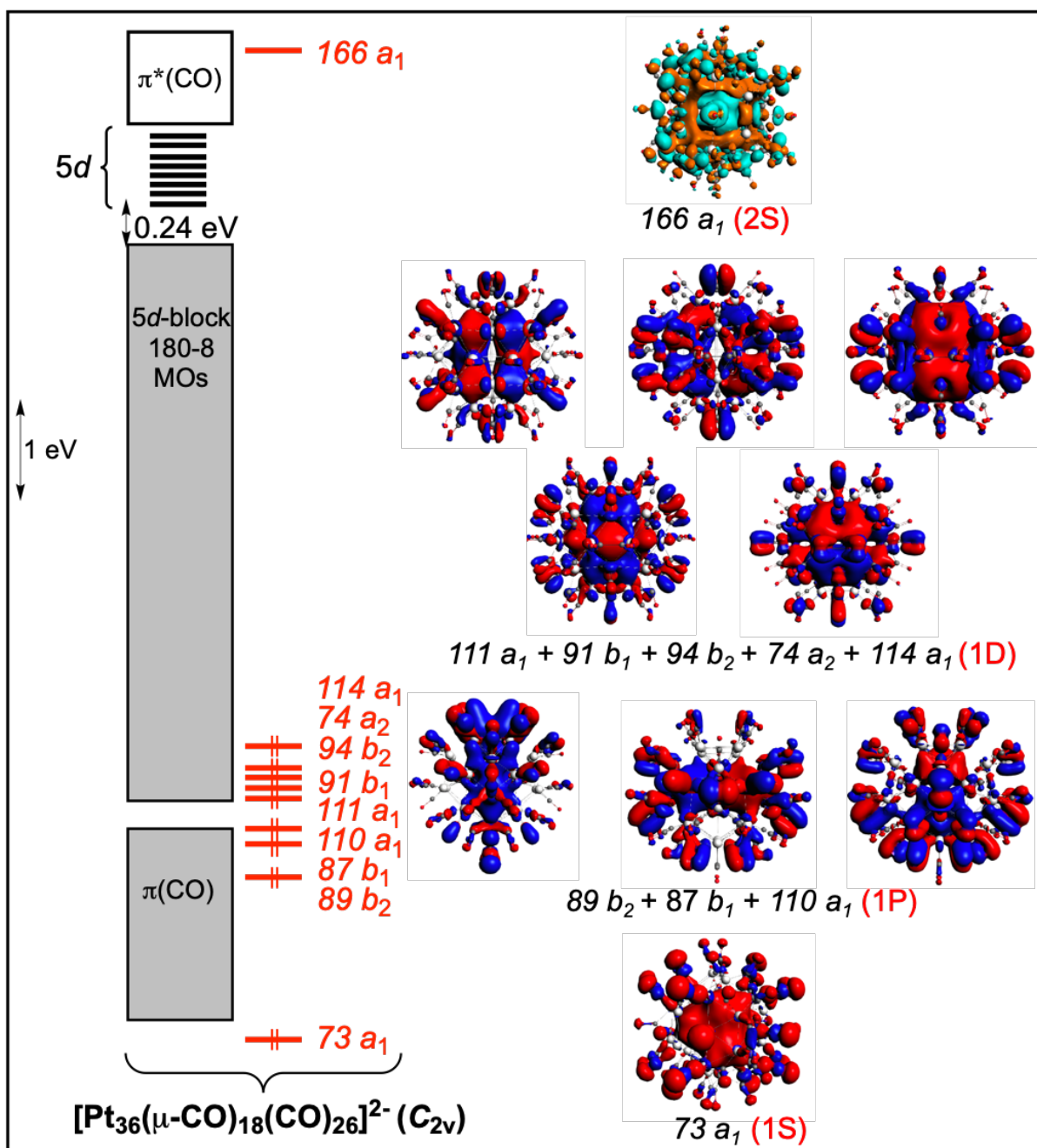


Figure S19. Kohn-Sham MO diagram of $[\text{Pt}_{36}(\mu\text{-CO})_{18}(\text{CO})_{26}]^{2-}$.

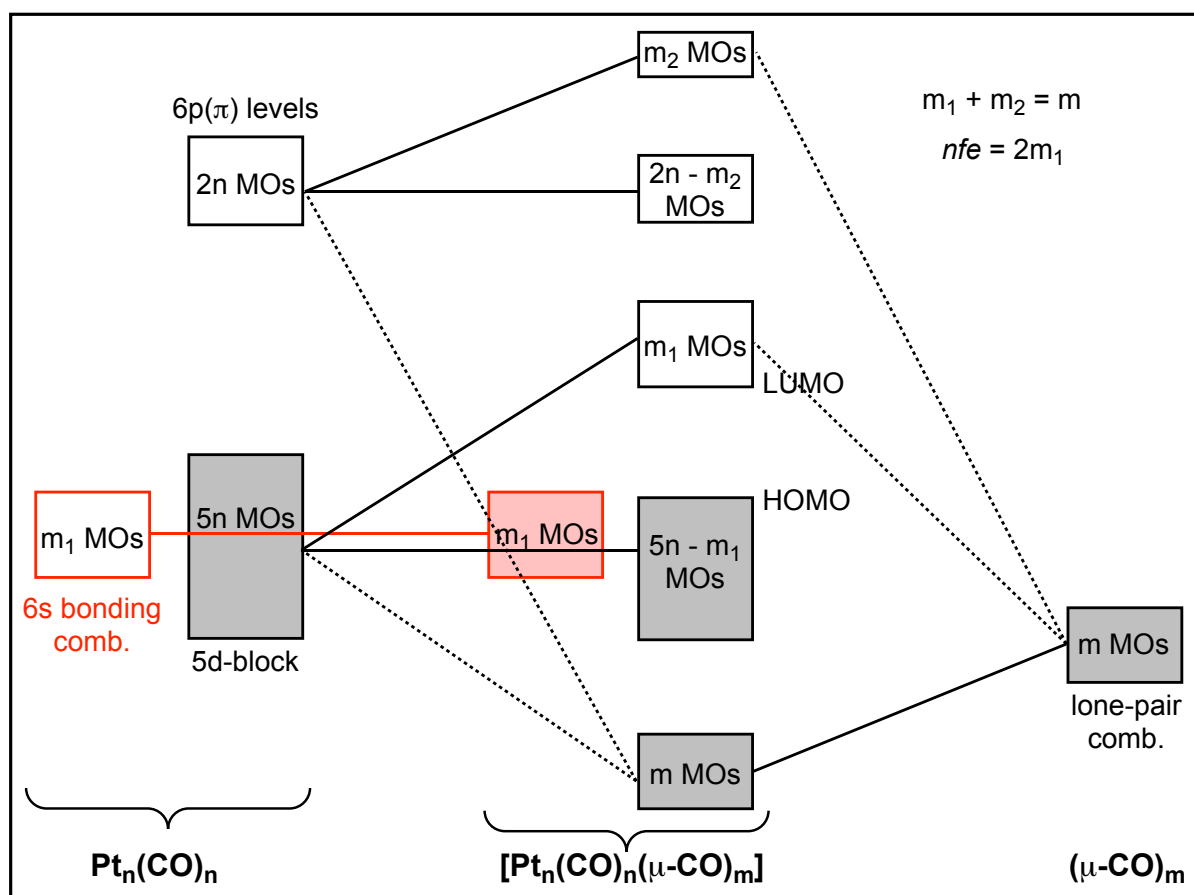


Figure S20. Simplified MO interaction diagram between the $\text{Pt}_n(\text{CO})_n$ and $(\mu\text{-CO})_m$ fragments in a neutral $[\text{Pt}_n(\text{CO})_n(\mu\text{-CO})_m]$ nanocluster with n terminal and m bridging carbonyls (no qualitative change if $\mu_3\text{-CO}$ s in the place of $\mu\text{-CO}$ s). Both the $\pi^*(\text{CO})$ levels and the antibonding $6s(\text{Pt})$ combinations (all vacant orbitals) are not shown, as well as the n occupied low-lying bonding MOs associated with the n Pt-CO terminal bonds. In the case of a dianionic $[\text{Pt}_n(\text{CO})_n(\mu\text{-CO})_m]^{2-}$ species, for example, then the number of $6s$ bonding (occupied) combinations would be $m_1 + 1$ and $nfe = 2m_1 + 2$. The bridging COs are necessary to get a closed-shell configuration with the $6s$ bonding combinations filled but their total number m and the m_1/m_2 ratio are difficult to predict owing to their dependence on complex topological parameters.

Table S1. Relevant computed data for $[\text{Pt}_{13}(\text{CO})_{12}]^{8-}$.

		$[\text{Pt}_{13}(\text{CO})_{12}]^{8-}$
HOMO-LUMO gap		1.41 eV
Distances (Å) [Wiberg indices]	Pt _c -Pt _p	av. 2.781 [0.1518]
	Pt _p -Pt _p	av. 2.923 [0.0688]
	Pt _p -C	av. 1.829 [1.1925]
NAO Charges (av.)	Pt _c	-0.96
	Pt _p	-0.12
	CO	-0.48

Table S2. Relevant computed data for $[\text{Pt}_{13}(\text{CO})_{12}\{\text{Cd}_5(\mu\text{-Br})_5\text{Br}_2(\text{dmf})_3\}_2]^{2-}$. The atomic distances are given in Å, Wiberg indices are given in brackets. Experimental bond distances are reported for comparison.⁶⁰

		$[\text{Pt}_{13}(\text{CO})_{12}\{\text{Cd}_5(\mu\text{-Br})_5\text{Br}_2(\text{dmf})_3\}_2]^{2-}$	
		Calc.	Exp.
HOMO-LUMO gap		1.19 eV	-
Pt _{cent.} -Pt _{vert.}		2.727-2.757 av. 2.742 [0.1052]	2.696-2.718 av. 2.707
Pt _{vert.} -Pt _{vert.}		2.765-2.988 av. 2.882 [0.0650]	2.765-2.912 av. 2.850
Cd _{Br} -Pt _{5 ring}		2.868-2.891 av. 2.877 [0.0741]	av. 2.826
Cd _{Br} -Pt _{apical}		3.308-3.321 av. 3.315 [0.0229]	av. 3.262
Cd _{dmf} -Pt _{5 ring}		2.821-2.865 av. 2.843 [0.0954]	av. 2.807
Cd _{dmf} -Pt _{apical}		3.006-3.051 av. 3.022 [0.0536]	av. 3.031
Cd-Br _{br}		2.704-2.822 av. 2.756 [0.2111]	av. 2.711
Cd-Br _{terminal}		2.649-2.663 av. 2.656 [0.2975]	av. 2.567
Cd-O		2.388-2.408 av. 2.396 [0.0742]	av. 2.231
Pt-C (Carbonyl)		1.858-1.897 av. 1.873 [0.8318]	av. 1.84
C-O (Carbonyl)		1.156-1.168 av. 1.162 [2.0157]	av. 1.14
NAO charges (av.)	Pt ₁	-0.54	-
	Pt ₁₂	-0.29	-
	CO	-0.15	-
	L	+1.91	-

Table S3. Relevant computed data for the $\text{Pt}_{13}(\text{Au}_2\text{L}_2)_2(\mu\text{-CO})_2(\text{CO})_8(\text{L})_4$ ($\text{L} = \text{CO}, \text{PH}_3$) clusters. Experimental bond distances are reported for comparison.⁸³

		$\text{Pt}_{13}(\text{Au}_2(\text{X})_2)_2(\mu\text{-CO})_2(\text{CO})_8(\text{X})_4$		
		L = CO	L = PH ₃	Exp.
HOMO-LUMO gap		0.96 eV	0.93 eV	
Distances (Å) [Wiberg indices]	Pt _c -Pt _p	av. 2.729 [0.1461]	av. 2.726 [0.1458]	av. 2.707
	Pt _p -Pt _p	av. 2.869 [0.0766]	av. 2.866 [0.0681]	av. 2.846
	Pt _p -Au _b	av. 2.775 [0.1281]	av. 2.779 [0.1316]	av. 2.783
	Au _b -Au _b	av. 3.202 [0.0184]	av. 3.151 [0.0237]	av. 3.131
	Pt _p -CO _t	av. 1.873 [0.8488]	av. 1.864 [0.8887]	av. 1.877
	Pt _p -CO _b	av. 2.048 [0.5759]	av. 2.025 [0.6167]	av. 2.007
	Pt _p -L	av. 1.893 [0.7598]	av. 2.242 [0.4516]	av. 2.260
	Au _b -L	av. 1.928 [0.7622]	av. 2.261 [0.5201]	av. 2.247
NAO Charges (av.)	Pt _c	-0.75	-0.65	
	Pt _p	-0.06	-0.10	
	Au _b	+0.48	+0.31	

Table S4. Relevant computed data for the $\text{Pt}_{13}(\text{Pt}_2(\mu\text{-CO})(\text{L})_2)_2(\mu\text{-CO})_2(\text{CO})_8(\text{L})_4$ ($\text{L} = \text{CO}, \text{PH}_3$) clusters. Experimental bond distances are reported for comparison.⁸⁵

		$\text{Pt}_{13}(\text{Pt}_2(\mu\text{-CO})(\text{L})_2)_2(\text{CO})_{10}(\text{L})_4$		
		L = CO	L = PH ₃	Exp.
HOMO-LUMO gap		0.30 eV	0.35 eV	
Distances (Å) [Wiberg indices]	Pt _c -Pt _p	av. 2.728 [0.1452]	av. 2.724 [0.1439]	av. 2.698
	Pt _p -Pt _p	av. 2.869 [0.0804]	av. 2.862 [0.0816]	av. 2.837
	Pt _p -Pt _b	av. 2.768 [0.1316]	av. 2.776 [0.1337]	av. 2.780
	Pt _b -Pt _b	av. 2.936 [0.0964]	av. 2.891 [0.1096]	av. 2.860
	Pt _p -CO _t	av. 1.871 [0.8336]	av. 1.861 [0.8747]	1.64 – 1.83
	Pt _p -CO _b	av. 2.057 [0.5653]	av. 2.030 [0.6086]	1.94 – 2.13
	Pt _p -L	av. 1.896 [0.7534]	av. 2.245 [0.4509]	2.20 – 2.26
	Pt _b -CO _b	av. 2.035 [0.6224]	av. 2.007 [0.6727]	1.94 – 2.13
	Pt _b -L	av. 1.872 [0.9068]	av. 2.219 [0.5774]	2.20 – 2.26
NAO Charges (av.)	Pt _c	-0.76	-0.66	
	Pt _p	-0.02	-0.06	
	Pt _b	+0.28	+0.12	

Table S5. Relevant computed data for the $[\text{Pt}_{14}(\mu\text{-CO})_6(\text{CO})_{12}]^{4-}$ and $[\text{Pt}_{15}(\mu\text{-CO})_8(\text{CO})_{11}]^{4-}$ clusters. Experimental bond distances are reported for comparison.³¹

		$[\text{Pt}_{14}(\mu\text{-CO})_6(\text{CO})_{12}]^{4-}$	$[\text{Pt}_{15}(\mu\text{-CO})_8(\text{CO})_{11}]^{4-}$
HOMO-LUMO gap		1.00 eV	1.09 eV
Distances (Å)	Pt _c -Pt _p	av. 2.777 exp. 2.730	av. 2.775 exp. 2.731
	Pt _p -Pt _p	av. 2.867 exp. 2.821	av. 2.874 exp. 2.827
	Pt _p -Pt _b	-	av. 2.753 exp. 2.681
	Pt _p -C _t	av. 1.862 exp. 1.844	av. 1.860 exp. 1.858
	Pt _p -C _b	av. 2.033 exp. 2.004	av. 2.037 exp. 2.011

Table S6. Relevant computed data for the $[\text{Pt}_{19}(\text{CO})_{17}]^{8-/10-}$ clusters. Experimental bond distances are reported for comparison.⁶⁰

		$[\text{Pt}_{19}(\text{CO})_{17}]^{10-}$	$[\text{Pt}_{19}(\text{CO})_{17}]^{8-}$	Exp.
HOMO-LUMO or SOMO-LUMO gap		0.37 eV	Spin- α : 0.47 eV Spin- β : 0.09 eV	
Distances (Å) [Wiberg indices]	Pt _c -Pt _{c'}	av. 2.611 [0.0984]	av. 2.571	av. 2.557
	Pt _c -Pt _p	av. 2.813 [0.1298]	av. 2.782	av. 2.730
	Pt _p -Pt _p	av. 2.960 [0.0604]	av. 2.922	av. 2.866
	Pt _p -C	av. 1.829 [1.1851]	av. 1.832	av. 1.800
NAO Charges (av.)	Pt _c	-0.80		
	Pt _p	-0.07		
	CO	-0.43		

Table S7. Computed data for $[\text{Pt}_{19}(\text{CO})_{17}\{\text{Cd}_5(\mu\text{-Br})_5\text{Br}_3(\text{Me}_2\text{CO})_2\}\{\text{Cd}_5(\mu\text{-Br})_5\text{Br}(\text{Me}_2\text{CO})_4\}]^{x-}$ ($x = 2, 4$). The atomic distances are given in Å. Wiberg indices are given in brackets. Experimental bond distances are given for comparison.⁶⁰

	$[\text{Pt}_{19}(\text{CO})_{17}\{\text{Cd}_5(\mu\text{-Br})_5\text{Br}_3(\text{Me}_2\text{CO})_2\}\{\text{Cd}_5(\mu\text{-Br})_5\text{Br}(\text{Me}_2\text{CO})_4\}]^{2-}$	$[\text{Pt}_{19}(\text{CO})_{17}\{\text{Cd}_5(\mu\text{-Br})_5\text{Br}_3(\text{Me}_2\text{CO})_2\}\{\text{Cd}_5(\mu\text{-Br})_5\text{Br}(\text{Me}_2\text{CO})_4\}]^{4-}$	Exp.
HOMO-LUMO or SOMO-LUMO gap (eV)	α -electron: 0.72 eV β -electron: 0.08 eV	0.70 eV	-
Pt _c -Pt _c '	2.594	2.590 [0.1161]	2.557
Pt _c -Pt _p	2.683–2.859 av. 2.761	2.688–2.852 av. 2.770 [0.1184]	2.663–2.793 av. 2.730
Pt _p -Pt _p	2.755–3.043 av. 2.894	2.778–3.112 av. 2.903 [0.0630]	2.775–2.976 av. 2.866
Cd-Pt _{5 ring}	2.789–2.911 av. 2.856	2.774–2.911 av. 2.841 [0.1113]	av. 2.790
Cd-Pt _{apical}	2.939–3.410 av. 3.093	2.911–3.394 av. 3.074 [0.0526]	av. 3.019
Cd-Br _{br}	2.692–2.855 av. 2.765	2.693–3.026 av. 2.812 [0.1775]	av. 2.741
Cd-Br _{terminal}	2.621–2.629 av. 2.625	2.650–2.662 av. 2.657 [0.2989]	av. 2.637
Cd-O	2.458–2.488 av. 2.475	2.517–2.555 av. 2.540 [0.0670]	av. 2.350
Pt-C (Carbonyl)	1.848–1.900 av. 1.865	1.841–1.897 av. 1.861 [0.8762]	av. 1.800
C-O (Carbonyl)	1.153–1.169 av. 1.160	1.155–1.174 av. 1.164 [2.0414]	av. 1.170
NAO charges	Pt _{cent}	–	-0.55
	Pt _{apical}	–	-0.46
	Pt _{outer}	–	-0.21
	CO	–	-0.08
	Cd ₅ ($\mu\text{-Br}$) ₅ Br ₃ (Me ₂ CO) ₂	–	+0.62
	Cd ₅ ($\mu\text{-Br}$) ₅ Br(Me ₂ CO) ₄	–	+1.91

Table S8. Relevant computed data for $[\text{Pt}_{19}(\mu\text{-CO})_{10}(\text{CO})_{12}]^{4-}$. Experimental bond distances are given for comparison.⁶⁸

		$[\text{Pt}_{19}(\mu\text{-CO})_{10}(\text{CO})_{12}]^{4-}$	Exp.
HOMO-LUMO gap		0.80 eV	
Distances (Å) [Wiberg indices]	Pt _c -Pt _{c'}	av. 2.710 [0.1309]	av. 2.641
	Pt _c -Pt _p	av. 2.813 [0.1183]	av. 2.794
	Pt _p -Pt _p	av. 2.821 [0.0928]	av. 2.797
	Pt _p -C _t	av. 1.857 [0.9237]	–
	Pt _p -C _b	av. 2.025 [0.5576]	–
NAO Charges (av.)	Pt _c	-0.66	
	Pt _p	+0.13	
	CO	-0.22	

Table S9. Relevant computed data for $[\text{Pt}_{26}(\mu\text{-CO})_9(\text{CO})_{23}]^{2-}$. Experimental bond distances are given for comparison.³¹

		$[\text{Pt}_{26}(\mu\text{-CO})_9(\text{CO})_{23}]^{2-}$	Exp.
HOMO-LUMO gap		0.57 eV	
Distances (Å) [Wiberg indices]	Pt ₃ -Pt ₃	av. 2.813 [0.0630]	av. 2.803
	Pt ₃ -Pt _p	av. 2.823 [0.1072]	av. 2.801
	Pt _p -Pt _p	av. 2.827 [0.0809]	av. 2.804
	Pt _p -C _t	av. 1.875 [0.8001]	av. 1.840
	Pt _p -C _b	av. 2.029 [0.5536]	av. 1.960
NAO Charges (av.)	Centered Pt ₃	-0.63	
	μ ₆ -Pt _p	-0.07	
	Pt _p	+0.20	
	Pt _{capping}	+0.22	
	CO	-0.11	

Table S10. Relevant computed data for $[\text{Pt}_{23}(\mu\text{-CO})_{13}(\text{CO})_{14}]^{2-}$. Experimental bond distances are given for comparison.³¹

		$[\text{Pt}_{23}(\mu\text{-CO})_{13}(\text{CO})_{14}]^{2-}$	Exp.
HOMO-LUMO gap		0.42 eV	
Distances (Å)	Pt ₃ -Pt ₃	av. 2.679	av. 2.655
	Pt ₃ -Pt _p	av. 2.878	av. 2.808
	Pt _p -Pt _p	av. 2.966	av. 2.936
	Pt _p -C _t	av. 1.874	av. 1.821
	Pt _p -C _b	av. 2.037	av. 2.001

Table S11. Relevant computed data for the hypothetical cluster $[\text{Pt}_{25}(\text{CO})_{22}]^{12-}$.

		$[\text{Pt}_{25}(\text{CO})_{22}]^{12-}$
HOMO-LUMO gap		0.63 eV
Distances (Å) [Wiberg indices]	Pt _c -Pt _{c'}	av. 2.710 [0.0766]
	Pt _c -Pt _p	av. 2.782 [0.1336]
	Pt _{c'} -Pt _p	av. 2.831 [0.1178]
	Pt _p -Pt _p	av. 2.988 [0.0596]
	Pt _p -C _t	av. 1.829 [1.1733]
	Pt _p -C _b	-
NAO Charges (av.)	Pt _c	-0.71
	Pt _{c'}	-0.79
	Pt _p	-0.04
	CO	+0.40

Table S12. Relevant computed data for the hypothetical cluster $[\text{Pt}_{23}\text{CO}_{20}]^{12-}$.

		$[\text{Pt}_{23}(\text{CO})_{20}]^{12-}$
HOMO-LUMO gap		0.57 eV
Distances (Å)	Pt ₃ -Pt ₃	2.752
	Pt ₃ -Pt _p	av. 2.822
	Pt _p -Pt _p	av. 3.001
	Pt _p -C	av. 1.831

Table S13. Relevant computed data for the hypothetical cluster $[\text{Pt}_{23}\text{CO}_{21}]^{10-}$.

		$[\text{Pt}_{23}(\text{CO})_{21}]^{10-}$
HOMO-LUMO gap		0.51 eV
Distances (Å)	Pt _c -Pt _p	av. 2.781
	Pt _p -Pt _p	av. 2.951
	Pt _p -C _t	av. 1.843

Table S14. Relevant computed data for $[\text{Pt}_{38}(\mu\text{-CO})_{12}(\text{CO})_{32}]^{2-}$. Experimental bond distances are given for comparison.⁶³

		$[\text{Pt}_{38}(\mu\text{-CO})_{12}(\text{CO})_{32}]^{2-}$	Exp.
HOMO-LUMO gap		0.45 eV	
Distances (Å) [Wiberg indices]	Pt ₆	av. 2.822 [0.0566]	av. 2.811
	Pt ₆ -Pt _p	av. 2.838 [0.1141]	av. 2.822
	Pt _p -Pt _p	av. 2.857 [0.0761]	av. 2.845
	Pt _p -C _t	av. 1.880 [0.7805]	av. 1.857
	Pt _p -C _b	av. 2.021 [0.5574]	av. 1.973
NAO Charges (av.)	Centered Pt ₆	-0.55	
	Pt _p	+0.17	
	CO	-0.05	

Table S15. Relevant computed data for $[\text{Pt}_{36}(\mu\text{-CO})_{18}(\text{CO})_{26}]^{2-}$. Experimental bond distances are given for comparison.³¹

		$[\text{Pt}_{36}(\mu\text{-CO})_{18}(\text{CO})_{26}]^{2-}$	Exp.
HOMO-LUMO gap		0.24 eV	
Distances (Å)	Pt ₆	av. 2.769	av. 2.770
	Pt ₆ -Pt _p	av. 2.830	av. 2.784
	Pt _p -Pt _p	av. 2.898	av. 2.855
	Pt _p -C _t	av. 1.880	av. 1.833
	Pt _p -C _b	av. 2.050	av. 2.011

Table S16. Relevant computed data for $[\text{Pt}_{19}(\mu_3\text{-CO})_3(\mu\text{-CO})_3(\text{CO})_{18}(\mu_4\text{-AuPH}_3)_3]^-$. Experimental bond distances are given for comparison.¹⁰⁰

		$[\text{Pt}_{19}(\mu_3\text{-CO})_3(\mu\text{-CO})_3(\text{CO})_{18}(\mu_4\text{-AuPH}_3)_3]^-$	Exp.
HOMO-LUMO gap		1.06 eV	
Distances (Å)	Pt ₃ -Pt ₃	av. 2.835	av. 2.816
	Pt ₃ -Pt ₇	av. 2.844	av. 2.782
	Pt ₇ -Pt ₇	av. 2.828	av. 2.796
	Pt ₇ -Pt ₆	av. 2.820	av. 2.796
	Pt ₆ -Pt ₆	av. 2.846	av. 2.833
	Pt ₆ -Pt _{3'}	av. 2.835	av. 2.804
	Pt _{3'} -Pt _{3'}	av. 2.856	av. 2.859
	Pt-(μ ₄ -Au)	av. 2.832	av. 2.859
	Pt-C _t	av. 1.882	av. 1.905
	Pt-C _b	av. 2.030	av. 2.072
	Pt-(μ ₃ -C)	av. 2.158	av. 2.187

Table S17. Relevant computed data for $[\text{Pt}_{19}(\mu_3\text{-CO})(\mu\text{-CO})_5(\text{CO})_{18}\{\mu_4\text{-Au}_2(\text{PH}_3)_2\}_2]$. Experimental bond distances are given for comparison.¹⁰⁰

		$[\text{Pt}_{19}(\mu_3\text{-CO})(\mu\text{-CO})_5(\text{CO})_{18}\{\mu_4\text{-Au}_2(\text{PH}_3)_2\}_2]$	Exp.
HOMO-LUMO gap		0.94 eV	
Distances (Å)	Pt ₃ -Pt ₃	av. 2.823	av. 2.808
	Pt ₃ -Pt ₇	av. 2.851	av. 2.799
	Pt ₇ -Pt ₇	av. 2.842	av. 2.795
	Pt ₇ -Pt ₆	av. 2.802	av. 2.786
	Pt ₆ -Pt ₆	av. 2.859	av. 2.823
	Pt ₆ -Pt _{3'}	av. 2.840	av. 2.799
	Pt _{3'} -Pt _{3'}	av. 2.835	av. 2.823
	Pt-(μ ₄ -Au)	av. 2.828	av. 2.838
	Pt-C _t	av. 1.886	av. 1.885
	Pt-C _b	av. 2.037	av. 1.983
	Pt-(μ ₃ -C)	av. 2.150	av. 2.146

Table S18. Relevant computed data for $[\text{Pt}_{40}(\mu\text{-CO})_{16}(\text{CO})_{24}]^{6-}$. Experimental bond distances are given for comparison.⁶²

		$[\text{Pt}_{40}(\mu\text{-CO})_{16}(\text{CO})_{24}]^{6-}$	Exp.
HOMO-LUMO gap		0.25 eV	
Distances (Å)	Pt ₈	av. 2.762	av. 2.745
	Pt ₈ -Pt _p	av. 2.773	av. 2.737
	Pt _p -Pt _p	av. 2.874	av. 2.883
	Pt _p -C _t	av. 1.860	av. 1.851
	Pt _p -C _b	av. 2.023	av. 1.978

Table S19. Relevant computed data for $[\text{Pt}_{24}(\mu\text{-CO})_8(\text{CO})_{22}]^{2-}$. Experimental bond distances are given for comparison.³¹

		$[\text{Pt}_{24}(\mu\text{-CO})_8(\text{CO})_{22}]^{2-}$	Exp.
HOMO-LUMO gap		0.66 eV	
Distances (Å)	Pt ₁₀ -Pt ₁₀	av. 2.826	av. 2.803
	Pt ₁₀ -Pt ₉	av. 2.850	av. 2.826
	Pt ₉ -Pt ₉	av. 2.819	av. 2.797
	Pt ₉ -Pt ₅	av. 2.843	av. 2.819
	Pt ₅ -Pt ₅	av. 2.824	av. 2.796
	Pt-C _t	av. 1.878	av. 1.860
	Pt-C _b	av. 2.033	av. 1.996

Table S20. Relevant computed data for $[\text{Pt}_{33}(\mu\text{-CO})_{10}(\text{CO})_{28}]^{2-}$. Experimental bond distances are given for comparison.⁶²

		$[\text{Pt}_{33}(\mu\text{-CO})_{10}(\text{CO})_{28}]^{2-}$	Exp.
HOMO-LUMO gap		0.49 eV	
Distances (Å)	Pt ₈ -Pt ₈	av. 2.858	av. 2.828
	Pt ₈ -Pt ₁₂	av. 2.838	av. 2.815
	Pt ₁₂ -Pt ₁₂	av. 2.824	av. 2.827
	Pt ₁₂ -Pt ₉	av. 2.850	av. 2.818
	Pt ₉ -Pt ₉	av. 2.823	av. 2.796
	Pt ₉ -Pt ₄	av. 2.856	av. 2.829
	Pt ₄ -Pt ₄	av. 2.882	av. 2.837
	Pt-C _t	av. 1.876	av. 1.857
	Pt-C _b	av. 2.028	av. 1.996

Chapter 10

Synthesis and Characterizations of

Ferrocenylalkylthiolates Protected Gold Nanoparticles

10.1 Introduction

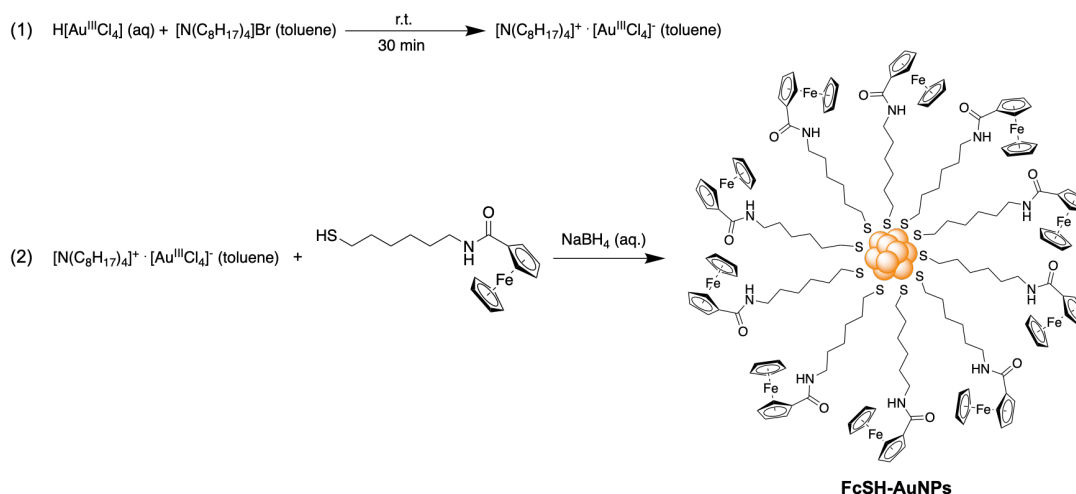
Gold nanoparticles (AuNPs), with average size between 1-100 nm, have been attracted broad research interests in nanoscience since 19th century.¹⁻⁸ On one hand, AuNPs with controlled structure can be used as building block for the construction of large 3D nanomaterials. On the other hand, AuNPs also have their own intrinsic interest due to their distinct physical and chemical properties which make them as potential candidates for multiple applications, in particular for the research field of optical devices,⁹ biomedicines,¹⁰ sensors¹¹ and catalysis.⁷ In AuNPs synthesis, surface ligands play crucial role for the stabilization of the very high active AuNP surface, which can prevent the AuNPs aggregation. Indeed, ligands can also have a significant influence on the AuNP size, structure and properties.¹²⁻¹⁶ Therefore, introducing new ligands in the synthetic AuNPs chemistry is considered as one of the most efficient strategies for tuning the structure and properties of AuNPs and AuNPs based nanomaterials.

In 1994, Brust and co-workers firstly shown a “two-phase-liquid-liquid” method for synthesis of thiolate protected AuNPs with average size of 1-3 nm.¹⁷ The synthesized AuNPs exhibit excellent dispersity and stability. Based on Brust’s methods, various synthetic systems with different kind of ligands were developed.^{2, 18-21} Among them, the ligands which contain ferrocenyl group can certainly modify AuNPs with their reversible cyclic voltammetry and redox properties.²²⁻³⁹ Our group have been shown in 2002 that AuNPs protected by a mixed of alkylthiolate and ferrocenyl terminated alkylthiolate ligands can be used as an electrochemical sensor for the redox recognition of oxoanions.³³ This AuNPs sensor shown highly stability and selectivity toward a series of oxoanions compounds. However, the ligand-exchange method used in the previous work gave a content never higher than 38% ferrocenylalkylthiolate ligands in the mixed AuNPs, which may limit the redox properties of the whole AuNPs system. As a continuation of our former work, we developed a one-pot “two phase” method to prepare the all ferrocenylalkylthiolate ligands protected AuNPs, its associated properties were also studied.

In this chapter, the synthesis of 6-(amidoferrocenyl)hexanethiol (**FcSH**) ligands as well as **FcSH** stabilized AuNPs (**FcSH-AuNPs**) is presented. The synthesized **FcSH-AuNPs** were characterized by UV-Vis spectra and transmission electron microscopy. Indeed, the redox properties of **FcSH-AuNPs** were also investigated by cyclic voltammetry technique.

10.2 Results and Discussion

The “two-phase” synthesis of **FcSH-AuNPs** was described in Scheme 1. Briefly, an aqueous solution of tetrachloroaurate acid (30 mL, 30 mM) was mixed with a toluene solution of tetraoctylammonium bromide (80 mL, 50 mM). The two-phase mixture was vigorously stirred for 30 min until all the tetrachloroaurate transferred into the organic layer. Then, the aqueous phase was removed by a syringe. 290 mg 6-(amidoferrocenyl)hexanethiol ligand (details in Experimental Section) was added rapidly into the reaction mixture, and a freshly prepared aqueous solution of sodium borohydride (20 mL, 0.4 M) was slowly added under vigorous stirring. After further stirring for 3 hour the organic phase was collected and evaporated with rotary evaporator. The residues were dissolved into 10 mL dichloromethane. The final product **FcSH-AuNPs** was precipitated as black powder from diethyl ether.



Scheme 1. Synthesis of **FcSH-AuNPs**.

The synthesized **FcSH-AuNPs** was firstly characterized by TEM (Figure 1a). It indicates that the **FcSH-AuNPs** was very fine and mono-dispersed with an average size of 2 nm. The size distribution analysis of the nanoparticle was shown in Figure 1b. It shows that the size of the obtained nanoparticles was distributed in a narrow range (1 – 3 nm), suggesting that FcSH ligand could be a good stabilizer for gold nanoparticles. Indeed, the average atoms number (*N*) of the **FcSH-AuNPs** was calculated to be 190, in which its surface atoms number (*N_s*) was calculated to be 132 (see Experimental Section). In comparison with the previous work in 2002,³³ all ferrocenylalkylthiolate ligands protected gold nanoparticle exhibits smaller particle size than the mixed ligated one, which may due to the larger steric effect caused by the ferrocenyl group inhibits the growth of the metallic kernel.

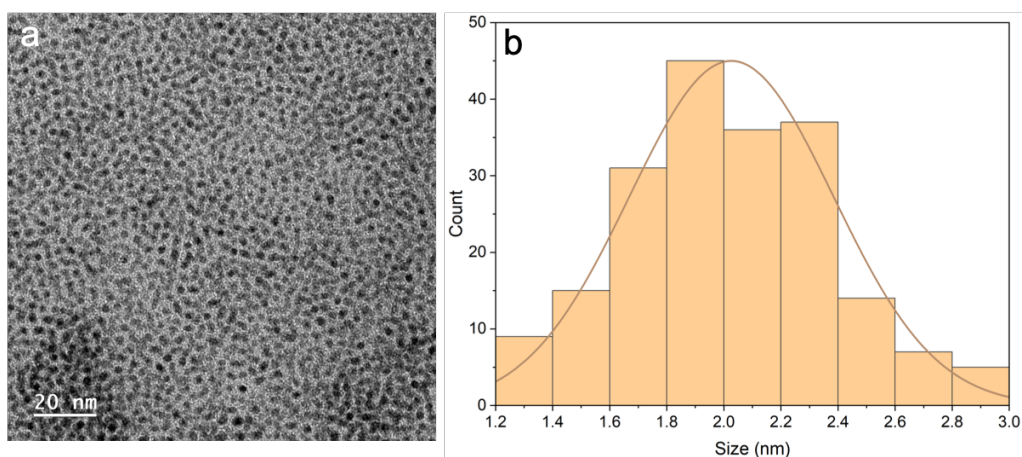


Figure 1. TEM image (a) and size distribution (b) of **FcSH-AuNPs**.

The UV-Vis spectra of **FcSH-AuNPs** exhibits a broad plasmon band at 500 nm (Figure 2). This broad absorption band is resulted from the short distances between each particle (Figure 1a). **FcSH-AuNPs** also shows superior stability. The solid powder of **FcSH-AuNPs** could be stable within 2 month without any degradation. It could also be stable in organic solvent such as dichloromethane within 1 month without any aggregation.

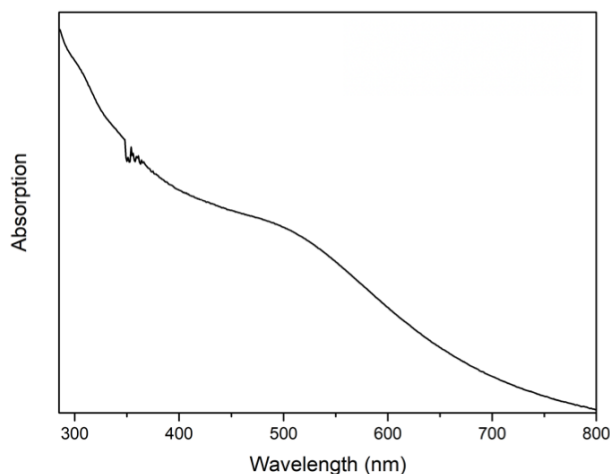


Figure 2 UV-Vis spectra of **FcSH-AuNPs** in dichloromethane.

Ultrasmall gold nanoparticles sometimes show photo-luminescence emission.⁴⁰ It is noteworthy to see if the ferrocenylalkylthiolate ligands influence the luminescence properties of AuNPs or not. Unfortunately, we do not record any fluorescent emission of **FcSH-AuNPs** (Figure 3), which may due to the number of gold atoms and free electrons in the particles should be high enough to diminish any energy spacing.

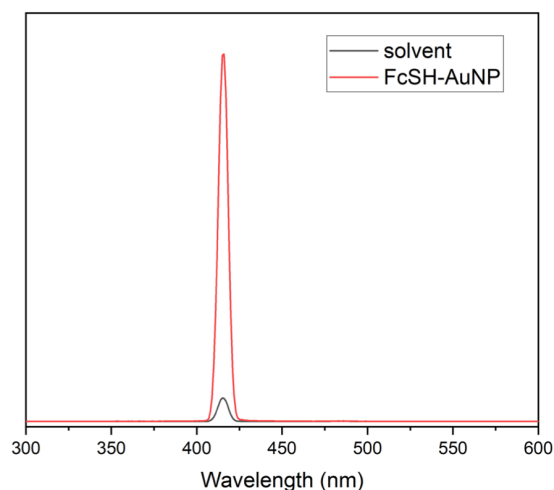


Figure 3. Fluorescence spectra of **FcSH-AuNPs** in DMF/H₂O ($v : v = 8 : 2$).

The cyclic voltammograms (CVs) of **FcSH-AuNPs** were recorded using classic conditions (Pt, CH₂Cl₂). As for previously reported nanoparticles bearing ferrocenyl termini, a single reversible ferrocene/ferrocenium wave was obtained with all the colloids bearing a proportion of thiol ligands with an amidoferrocenyl termini or one of its derivatives.^{33, 36, 41-46} The shape of this wave varies and depends on the exact nature of the ferrocene termini, but the following common features are observed. The cathodic return wave is, in general, higher and thinner than the anodic forward wave, which can be attributed to some adsorption of the colloids onto the electrode surface in the ferrocenium form.

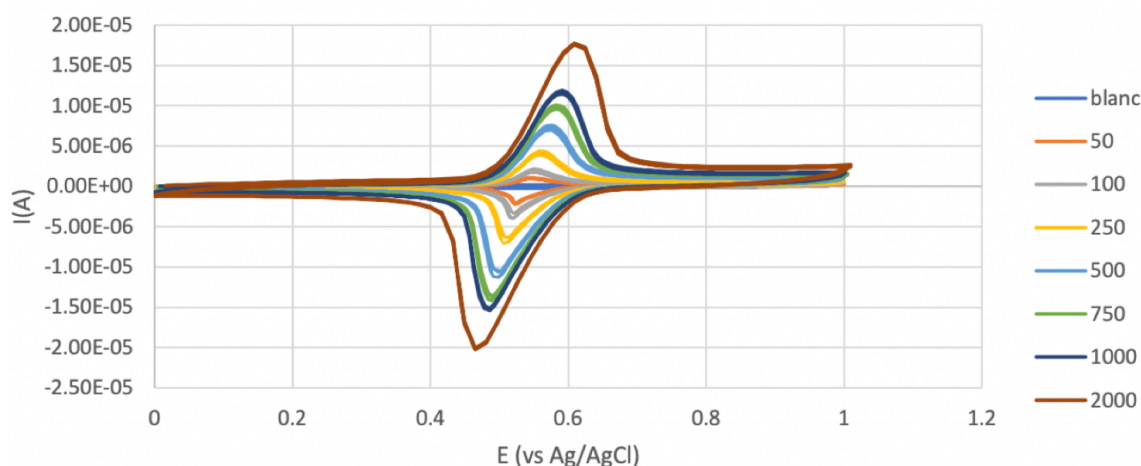


Figure 4. Cyclic voltammograms of **FcSH-AuNPs**. Solvent: CH₂Cl₂; reference electrode, Ag/AgCl; working electrode: graphite (d = 1mm); counter electrode: Pt; scan rate, 1 mV/s.

Recorded by Dr. Philippe Hapiot and his group (ISCR, UMR 6226, Université de Rennes, CNRS, Rennes, France).

10.3 Conclusion

In conclusion, the all ferrocenylalkylthiolate ligands protected gold nanoparticles **FcSH-AuNPs** were synthesized and characterized. The results show that the 6-(amidoferrocenyl)hexanethiol ligand could be stabilize ultrafine **AuNPs** with very good stability and mono-dispersity. The synthesized **FcSH-AuNPs** have an average size of 2 nm which smaller than the previous reported mixed alkylthiolate and ferrocenylalkylthiolate ligands protected AuNPs. The possible reason is that the large steric effect of the terminal ferrocenyl group inhibits the further growth of the gold metallic kernel. **FcSH-AuNPs** shows a broad plasmon band at 500 nm because of the short distance between each particle. A clear cyclic voltammograms signal of **FcSH-AuNPs** was observed in CH₂Cl₂ both with classical voltammetry and steady state on a microelectrode, encouraging this **FcSH-AuNPs** could be a derivatized electrode for sensing applications (for instance oxo anions, etc.).

10.4 Experimental Section

Materials

All chemicals used for the synthesis of ligand and NPs are commercially available. All flasks were washed with aqua regia (HCl: HNO₃ = 3:1) before usage to avoid the presence of metal residues. Milli-Q water (18.2 MΩ, Thermo Fischer Scientific Inc., USA) was used in the process of NP fabrication.

Calculations of the Average Atoms Number and Surface Atoms Number in Metal Nanoparticle

The average atoms number (N) was calculated by the following equations.² (eq. 1 to eq. 3)

$$N = V_{NP}/V_{atom} \text{ (eq. 1)}$$

$$V = 4/3\pi R^3 \text{ (eq. 2)}$$

Then, eq. 3 is obtained by combination of eq. 1 and eq. 2.

$$N = (R_{NP}/R_{atom})^3 \text{ (eq. 3)}$$

The surface atoms number (N_s) was calculated by the following equations.² (eq. 4 to eq. 6)

$$N_s = S_{NP}/\pi R_{atom}^2 \text{ (eq. 4)}$$

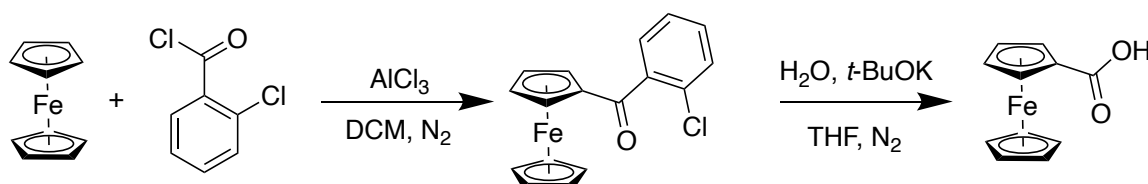
$$S_{NP} = 4\pi R_{NP}^2 \text{ (eq. 5)}$$

Thus, eq. 6 is obtained by combinations of eq. 4 and eq. 5.

$$N_s = 4(R_{NP}/R_{atom})^2 \text{ (eq. 6)}$$

Synthesis of Ferrocene Carboxylic Acid (Fe-COOH)

Ferrocene carboxylic acid was synthesized through a previous reported method (Scheme 2).⁴⁷ Ferrocene (1.86 g, 0.01 mol), 2-chlorobenzoyl chloride (1.3 mL, 0.01 mol) and 20 mL of dry dichloromethane (DCM) were placed in a two-necked round bottom flask under positive flow of nitrogen and continuous stirring at 0 °C (ice bath). Anhydrous aluminum chloride (1.4 g, 0.01 mol) was added to the reaction mixture in small portions. As the reaction proceeded, the appearance of a blue color was observed. Once the addition was finished the mixture was stirred at 0 °C for 30 min, and at room temperature for 2 h. Subsequently, the mixture was cooled in ice and 100 mL of water were added to the flask. The two-phase mixture was stirred vigorously for 30 min, and successively extracted with DCM. The DCM phase was reduced under vacuum and dried under air, to afford a red viscous slurry of 2-chlorobenzoyl ferrocene that was used in the next step without further purification. Potassium tert-butoxide (4.6 g, 0.04 mol) and 50.0 mL of tetrahydrofuran (THF) were added to the flask containing the 2-chlorobenzoyl ferrocene slurry with continuous stirring before it was placed under nitrogen flow, and equipped with a reflux condenser. Water (0.2 mL, 0.01 mol) was added to the mixture, and the reaction was refluxed for 1 h, undergoing a color change from yellow to tan. Once the reaction was cooled, 100 mL of water were added to the mixture and several extractions with diethyl ether were performed. The aqueous phase was isolated and acidified with concentrated hydrochloric acid (37 % HCl). The resultant yellow precipitate was filtered under vacuum and washed with water. The solid was dried overnight, affording pure **Fe-COOH** with 80% yield.



Scheme 2. Synthesis of **Fe-COOH**.

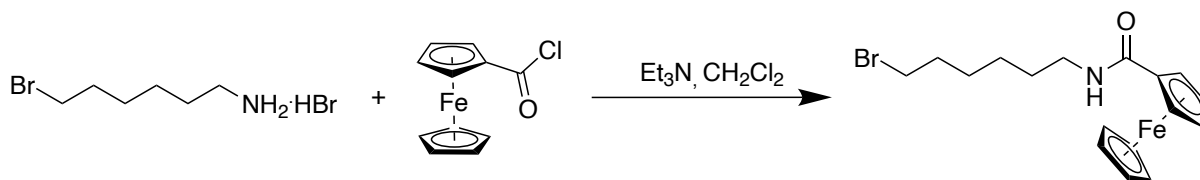
Synthesis of 6-Bromohexanamine Hydrobromide

6-bromohexanamine hydrobromide was synthesized by a previous reported method.⁴⁸ Aqueous hydrogen bromide solution (19.5 mL, 256 mmol, 62% wt, 33.4 g, 3.0 equiv.) was carefully

added to 6-aminohexan-1-ol (10.0 g, 85 mmol, 1.0 equiv) at 0 °C. The reaction mixture was stirred in an oil bath at 100 °C for 24 h. As far as possible, the solvent was removed under reduced pressure. In order to eliminate the remaining water, the residue was dissolved in acetone and the solvent was removed by rotary evaporation. The residue was precipitated in Et₂O, the colourless solid was obtained with 80% yield. ¹H NMR (300 MHz, CDCl₃): δ 3.49 (t, 3J = 7.5 Hz, 2H, H-6), 2.99 (t, 3J = 7.5 Hz, 2H, H-1), 1.90 (m, 2H, H-5), 1.68 (m, 2H, H-2), 1.59–1.50 (m, 2H, H-4), 1.47–1.42 (m, 2H, H-3) ppm.

Synthesis of 6-(amidoferrocenyl)bromohexane

The synthesis of 6-(amidoferrocenyl)bromohexane is illustrated in Scheme 3. Triethylamine (0.1 ml, 0.72 mmol) was added dropwise at room temperature (r. t.) under nitrogen (N₂) atmosphere to a suspension of **Fe-COOH** (0.4 g, 1.74 mmol) in dry CH₂Cl₂ (35 ml). Then, oxalyl chloride (0.75 ml, 8.7 mmol) was added dropwise at 0 °C. The obtained mixture was stirred overnight at r. t. and dried in vacuum. The residual red solid of crude chlorocarbonyl ferrocene (FcCOCl) was dissolved in dry CH₂Cl₂ (15 ml) and added dropwise to a CH₂Cl₂ solution (20 ml) of 6-bromohexanamine hydrobromide (0.2 g, 0.59 mmol) and triethylamine (1.5 ml, 10.7 mmol). The mixture was stirred overnight under N₂ atmosphere at r. t., then washed with saturated NaHCO₃ solution (1 × 100 ml) and distilled water (3 × 100 ml). The organic solution was dried over anhydrous Na₂SO₄, filtered, and the solvent was removed in vacuum. The product was purified by column chromatography with CH₂Cl₂/methanol (0% → 20%) as eluent and obtained as orange solid with 60 yeild. ¹H NMR (300 MHz, MeOD): δ 3.48 (t, 3J = 6.0 Hz, 2H, H-1), 1.91 (t, 3J = 6.0 Hz, 2H, H-6), 1.31-1.66 (m, 8H, H-2 to H-5), 4.81 (t, 2H, 3J = 6.0 Hz, H-7), 4.41 (t, 2H, 3J = 6.0 Hz, H-8), 4.21 (s, 5H, H-9) ppm.

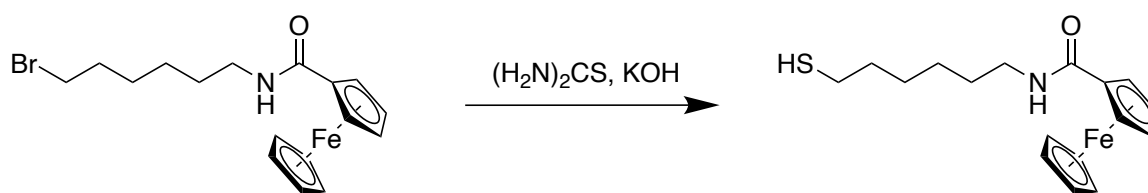


Scheme 3. Synthesis of 6-(amidoferrocenyl)bromohexane.

Synthesis of 6-(amidoferrocenyl)hexanethiol

The synthesis of 6-(amidoferrocenyl)hexanethiol was followed a previous reported method⁴⁹ and illustrated in Scheme 4. 6-(amidoferrocenyl)hexanebromide (1.25 g, 3.2 mmol) and thiourea (0.24 g, 3.5 mmol) were added to 20 ml of absolute ethanol and the resulting solution

refluxed under N₂ for 18 h. Following removal of solvent under vacuum, 20 ml of an aqueous solution of potassium hydroxide (0.20 g, 3.5 mmol) were added and the mixture further refluxed for 2 h under N₂. A yellow-orange oil settled to the bottom of the flask. This oil was extracted from the cooled reaction mixture with three 50 ml portions of dichloromethane and the combined extracts were evaporated and dried over anhydrous NaSO₄. Yellow solid was obtained with 50% yield. ¹H NMR (300 MHz, MeOD): δ 2.71 (t, 3J = 6.0 Hz, 2H, H-1), 1.73 (t, 3J = 7.5 Hz, 2H, H-6), 1.65-1.29 (m, 8H, H-2 to H-5), 4.82 (t, 2H, 3J = 3.0 Hz, H-7), 4.40 (t, 2H, 3J = 3.0 Hz, H-8), 4.21 (s, 5H, H-9), 1.26 (t, 3J = 4.5 Hz, H, H-10) ppm.



Scheme 4. Synthesis of 6-(amidoferrocenyl)hexanethiol.

NMR Analysis

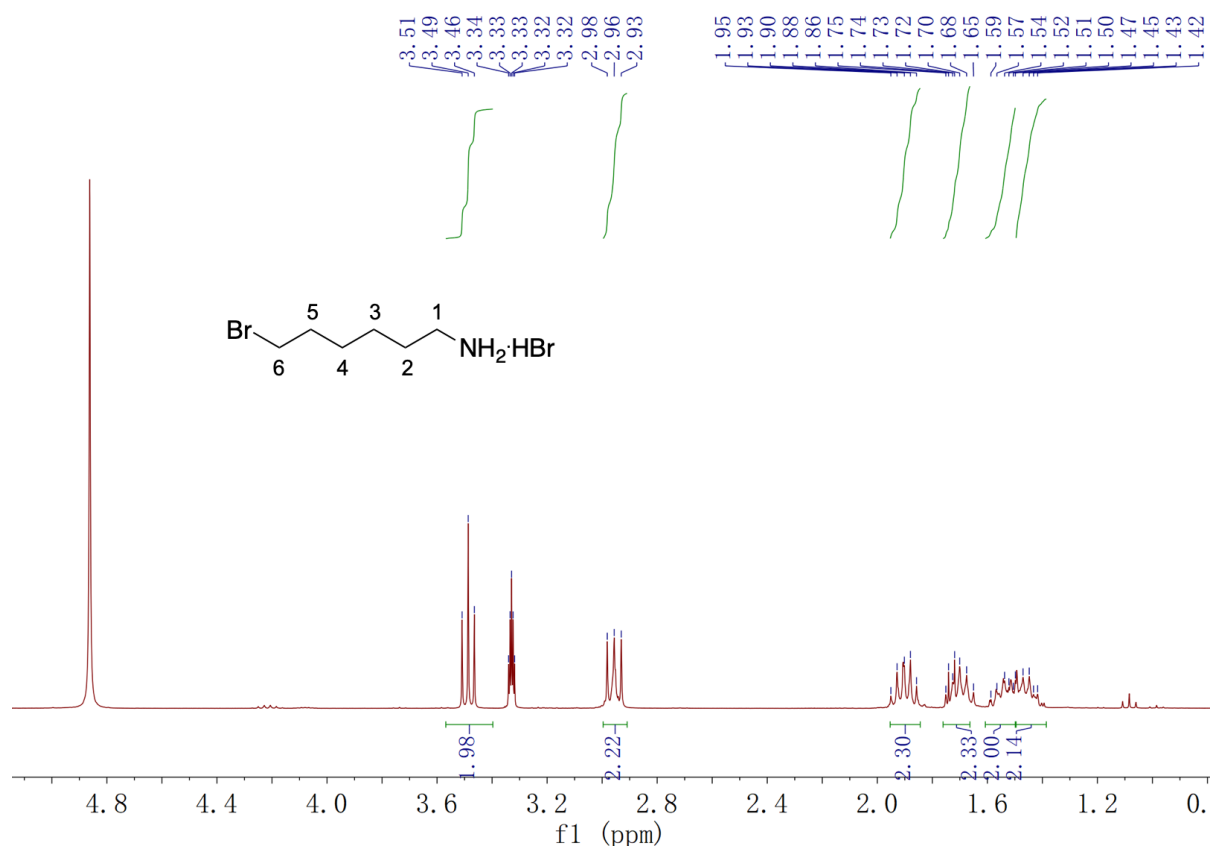


Figure 5. ¹H NMR of 6-bromohexanamine hydrobromide in CDCl₃.

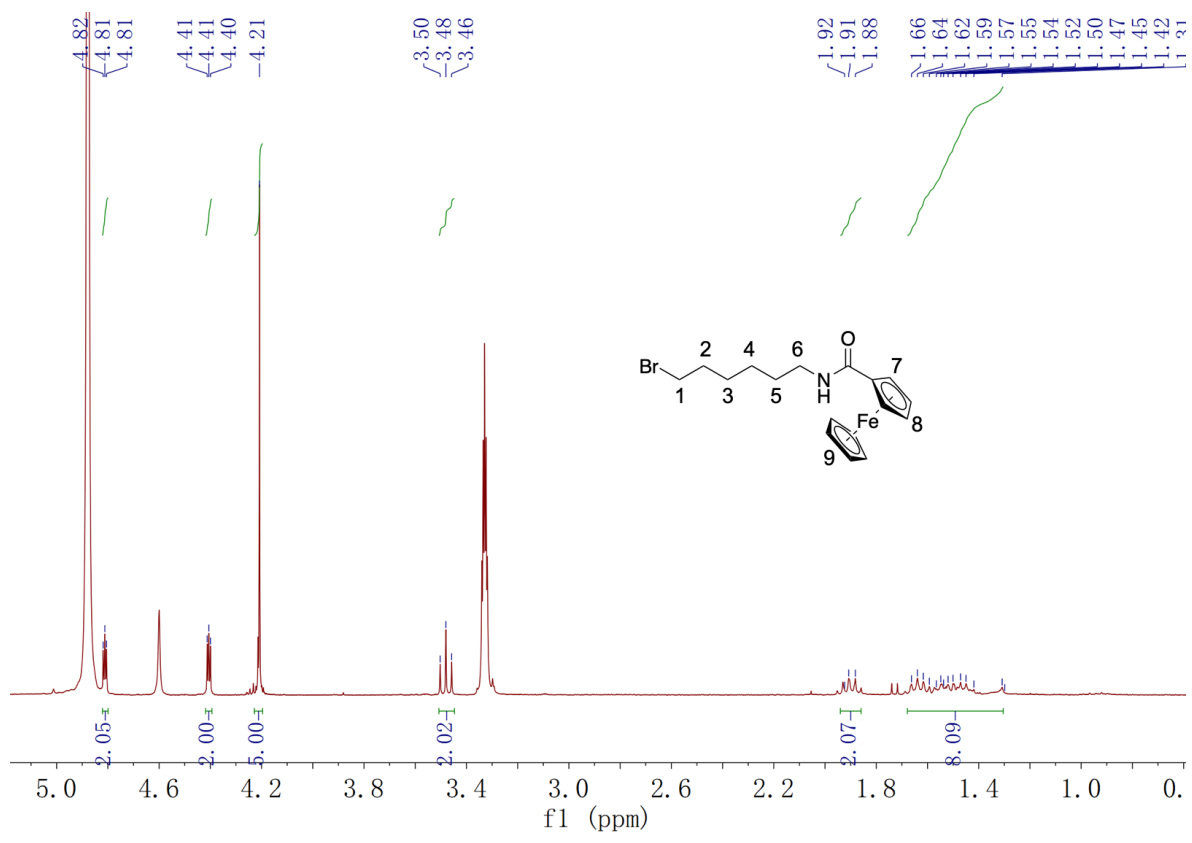


Figure 6. ¹H NMR of 6-(amidoferrocenyl)hexanebromide in MeOD.

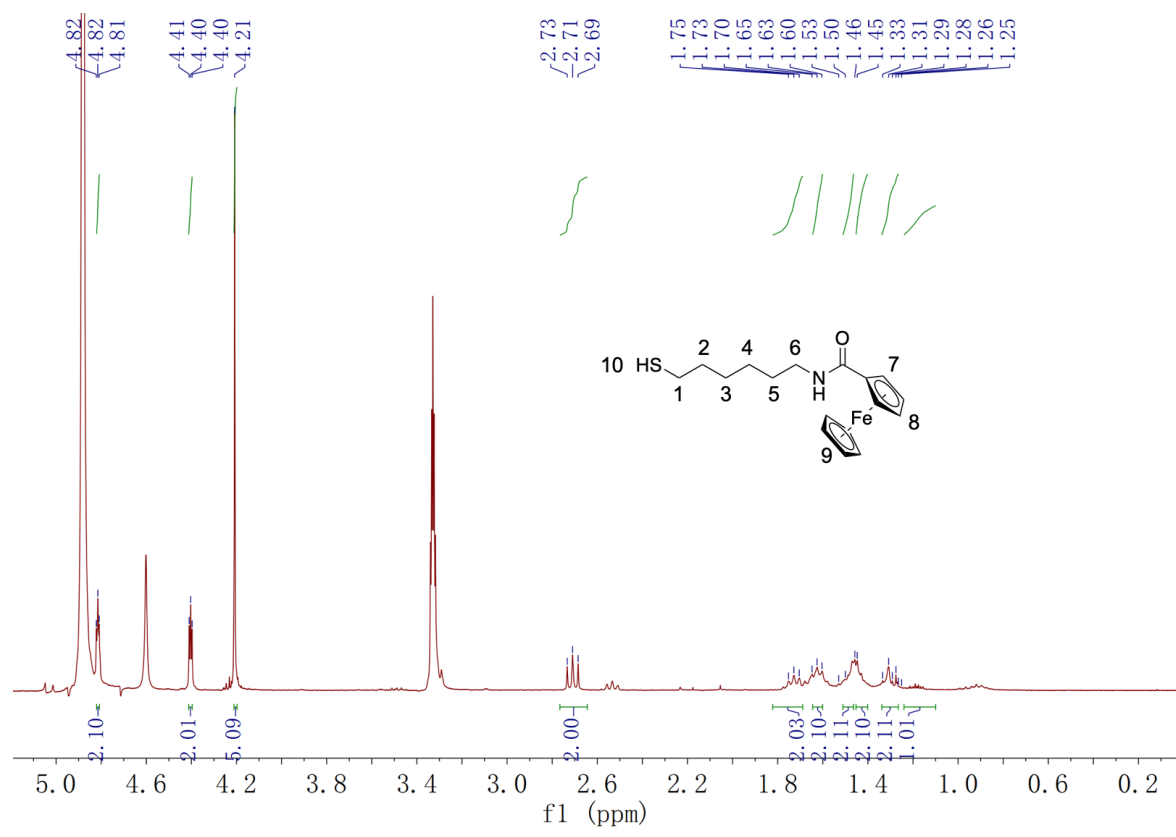


Figure 7. ¹H NMR of 6-(amidoferrocenyl)hexanethiol in MeOD.

10.5 References

- 1 Daniel, M.-C.; Astruc, D. Gold nanoparticles: assembly, supramolecular chemistry, quantum-size-related properties, and applications toward biology, catalysis, and nanotechnology. *Chem. Rev.* **2004**, *104*, 293–346.
- 2 Zhao, P.; Li, N.; Astruc, D. State of the art in gold nanoparticle synthesis. *Coord. Chem. Rev.* **2013**, *257*, 638–665.
- 3 Boisselier, E.; Astruc, D. Gold nanoparticles in nanomedicine: preparations, imaging, diagnostics, therapies and toxicity. *Chem. Soc. Rev.* **2009**, *38*, 1759–1782.
- 4 Kang, H.; Buchman, J. T.; Rodriguez, R. S.; Ring, H. L.; He, J.; Bantz, K. C.; Haynes, C. L. Stabilization of silver and gold nanoparticles: preservation and improvement of plasmonic functionalities. *Chem. Rev.* **2018**, *119*, 664–699.
- 5 Jin, R.; Zeng, C.; Zhou, M.; Chen, Y. Atomically precise colloidal metal nanoclusters and nanoparticles: fundamentals and opportunities. *Chem. Rev.* **2016**, *116*, 10346–10413.
- 6 Ishida, T.; Murayama, T.; Taketoshi, A.; Haruta, M. Importance of size and contact structure of gold nanoparticles for the genesis of unique catalytic processes. *Chem. Rev.* **2019**, *120*, 464–525.
- 7 Astruc, D. Introduction: Nanoparticles in catalysis. *Chem. Rev.* **2020**, *120*, 461–463.
- 8 Zare, I.; Yarak, M. T.; Speranza, G.; Najafabadi, A. H.; Haghighi, A. S.; Nik, A. B.; Manshian, B. B.; Saraiva, C.; Soenen, S. J.; Kogan, M. J. Gold nanostructures: synthesis, properties, and neurological applications. *Chem. Soc. Rev.* **2022**, *51*, 2601–2680.
- 9 Wu, Y.; Ali, M. R.; Chen, K.; Fang, N.; El-Sayed, M. A. Gold nanoparticles in biological optical imaging. *Nano Today* **2019**, *24*, 120–140.
- 10 Llevot, A.; Astruc, D. Applications of vectorized gold nanoparticles to the diagnosis and therapy of cancer. *Chem. Soc. Rev.* **2012**, *41*, 242–257.
- 11 Si, P.; Razmi, N.; Nur, O.; Solanki, S.; Pandey, C. M.; Gupta, R. K.; Malhotra, B. D.; Willander, M.; de la Zerda, A. Gold nanomaterials for optical biosensing and bioimaging. *Nanoscale Adv.* **2021**, *3*, 2679–2698.
- 12 Ong, Q.; Luo, Z.; Stellacci, F. Characterization of ligand shell for mixed-ligand coated gold nanoparticles. *Acc. Chem. Res.* **2017**, *50*, 1911–1919.
- 13 Zhang, B.; Chen, J.; Cao, Y.; Chai, O. J. H.; Xie, J. Ligand Design in Ligand-Protected Gold Nanoclusters. *Small* **2021**, *17*, 2004381.
- 14 Wan, X. -K.; Wang, J. -Q.; Nan, Z. -A.; Wang, Q. -M. Ligand effects in catalysis by

- atomically precise gold nanoclusters. *Sci. Adv.* **2017**, *3*, e1701823.
- 15 Zhang, J.; Huang, Z.; Xie, Y.; Jiang, X. Modulating the catalytic activity of gold nanoparticles using amine-terminated ligands. *Chem. Sci.* **2022**, *13*, 1080–1087.
- 16 Wei, J.; Kahlal, S.; Halet, J. -F.; Muñoz-Castro, A.; Saillard, J. -Y. Ligand-Induced Cuboctahedral versus Icosahedral Core Isomerism within Eight-Electron Heterocyclic-Carbene-Protected Gold Nanoclusters. *Inorg. Chem.* **2022**, *61*, 8623–8628.
- 17 Brust, M.; Walker, M.; Bethell, D.; Schiffrin, D. J.; Whyman, R. Synthesis of thiol-derivatised gold nanoparticles in a two-phase Liquid–Liquid system. *J. Chem. Soc. Chem. Commun.* **1994**, 801–802.
- 18 Mat Isa, S. Z.; Zainon, R.; Tamal, M. State of the Art in Gold Nanoparticle Synthesis via Pulsed Laser Ablation in Liquid and Its Characterisation for Molecular Imaging: A Review. *Materials* **2022**, *15*, 875.
- 19 Das, R. P.; Pradhan, A. K. An Introduction to Different Methods of Nanoparticles Synthesis. *Bio-Nano Interface* **2022**, 21–34.
- 20 Grzelczak, M.; Pérez-Juste, J.; Mulvaney, P.; Liz-Marzán, L. M. Shape control in gold nanoparticle synthesis. *Chem. Soc. Rev.* **2008**, *37*, 1783–1791.
- 21 Quintana, C.; Cifuentes, M. P.; Humphrey, M. G. Transition metal complex/gold nanoparticle hybrid materials. *Chem. Soc. Rev.* **2020**, *49*, 2316–2341.
- 22 Daniel, M.-C.; Aranzaes, J. R.; Nlate, S.; Astruc, D. Gold-nanoparticle-cored polyferrocenyl dendrimers: Modes of synthesis and functions as exoreceptors of biologically important anions and re-usable redox sensors. *J. Inorg. Organomet. Polym. Mater.* **2005**, *15*, 107–119.
- 23 Rapakousiou, A.; Djeda, R.; Grillaud, M.; Li, N.; Ruiz, J.; Astruc, D. “Click” assemblies and redox properties of arene-and gold-nanoparticle-cored triazolylbiferrocene-terminated dendrimers. *Organometallics* **2014**, *33*, 6953–6962.
- 24 Liu, L.; Du, J.; Li, S.; Yuan, B.; Han, H.; Jing, M.; Xia, N. Amplified voltammetric detection of dopamine using ferrocene-capped gold nanoparticle/streptavidin conjugates. *Biosens. Bioelectron.* **2013**, *41*, 730–735.
- 25 Chaicharoenwimolkul, L.; Munmai, A.; Chairam, S.; Tewasekson, U.; Sapudom, S.; Lakliang, Y.; Somsook, E. Effect of stabilizing ligands bearing ferrocene moieties on the gold nanoparticle-catalyzed reactions of arylboronic acids. *Tetrahedron Lett.* **2008**, *49*, 7299–7302.
- 26 Ciganda, R.; Irigoyen, J.; Gregurec, D.; Hernández, R.; Moya, S.; Wang, C.; Ruiz, J.; Astruc, D. Liquid–liquid interfacial electron transfer from ferrocene to gold (III): an

- ultrasimple and ultrafast gold nanoparticle synthesis in water under ambient conditions. *Inorg. Chem.* **2016**, *55*, 6361–6363.
- 27 Escorcia, A.; Dhirani, A.-A. Electrochemical properties of ferrocenylalkane dithiol-gold nanoparticle films prepared by layer-by-layer self-assembly. *J. Electroanal. Chem.* **2007**, *601*, 260–268.
- 28 Wang, W.; Ornelas, C.; Diallo, A. K.; Deraedt, C.; Wang, Y.; Lu, F.; Gu, H.; Astruc, D. Ferrocene-based dendritic macromolecules as efficient supports in nanocatalysis. *Polymer* **2022**, *246*, 124714.
- 29 Wang, C.; Brudo, A.; Ducrot, L.; Fu, F.; Ruiz, J.; Escobar, A.; Martinez-Villacorta, A.; Moya, S.; Astruc, D. Generation of catalytically active gold nanocrystals in water induced with ferrocene carboxylate. *Eur. J. Inorg. Chem.* **2021**, *2021*, 2471–2479.
- 30 Daniel, M.-C.; Ruiz, J.; Nlate, S.; Blais, J.-C.; Astruc, D. Nanoscopic assemblies between supramolecular redox active metallodendrons and gold nanoparticles: synthesis, characterization, and selective recognition of H_2PO_4^- , HSO_4^- , and adenosine-5'-triphosphate (ATP^{2-}) anions. *J. Am. Chem. Soc.* **2003**, *125*, 2617–2628.
- 31 Rapakousiou, A.; Deraedt, C.; Irigoyen, J.; Wang, Y.; Pinaud, N. I.; Salmon, L.; Ruiz, J.; Moya, S.; Astruc, D. Synthesis and redox activity of “clicked” triazolylbiferrocenyl polymers, network encapsulation of gold and silver nanoparticles and anion sensing. *Inorg. Chem.* **2015**, *54*, 2284–2299.
- 32 Li, N.; Zhao, P.; Igartua, M. E.; Rapakousiou, A.; Salmon, L.; Moya, S.; Ruiz, J.; Astruc, D. Stabilization of AuNPs by monofunctional triazole linked to ferrocene, ferricenium, or coumarin and applications to synthesis, sensing, and catalysis. *Inorg. Chem.* **2014**, *53*, 11802–11808.
- 33 Labande, A.; Ruiz, J.; Astruc, D. Supramolecular gold nanoparticles for the redox recognition of oxoanions: syntheses, titrations, stereoelectronic effects, and selectivity. *J. Am. Chem. Soc.* **2002**, *124*, 1782–1789.
- 34 Rapakousiou, A.; Deraedt, C.; Gu, H.; Salmon, L.; Belin, C.; Ruiz, J.; Astruc, D. Mixed-valent click intertwined polymer units containing biferrocenium chloride side chains form nanosnakes that encapsulate gold nanoparticles. *J. Am. Chem. Soc.* **2014**, *136*, 13995–13998.
- 35 Daniel, M. -C.; Ruiz, J.; Nlate, S.; Palumbo, J.; Blais, J. -C.; Astruc, D. Gold nanoparticles containing redox-active supramolecular dendrons that recognize H_2PO_4^- . *Chem. Commun.* **2001**, 2000–2001.

- 36 Horikoshi, T.; Itoh, M.; Kurihara, M.; Kubo, K.; Nishihara, H. Synthesis, redox behavior and electrodeposition of biferrocene-modified gold clusters. *J. Electroanal. Chem.* **1999**, *473*, 113–116.
- 37 Lee, L. Y. S.; Lennox, R. B. Ferrocenylalkylthiolate labeling of defects in alkylthiol self-assembled monolayers on gold. *Phys. Chem. Chem. Phys.* **2007**, *9*, 1013–1020.
- 38 Yamada, M.; Tadera, T.; Kubo, K.; Nishihara, H. Electroreductive deposition of anthraquinone derivative attached Au clusters: optical properties and scanning tunneling microscopy observation of the electrodeposited cluster film. *Langmuir* **2001**, *17*, 2363–2370.
- 39 Patel, D. A.; Chevalier, R. B.; Weller, A. M.; Shakespeare, C. C.; Soares, E. J.; Landis, E. C. Porosity Effects on the Ordering and Stability of Self-Assembled Monolayers on Nanoporous Gold. *J. Phys. Chem. C* **2020**, *124*, 26851–26863.
- 40 Kang, K. A.; Wang, J. Smart dual-mode fluorescent gold nanoparticle agents. *Wiley Interdiscip. Rev. Nanomed. Nanobiotechnol.* **2014**, *6*, 398–409.
- 41 Hostetler, M. J.; Green, S. J.; Stokes, J. J.; Murray, R. W. Monolayers in three dimensions: synthesis and electrochemistry of ω -functionalized alkanethiolate-stabilized gold cluster compounds. *J. Am. Chem. Soc.* **1996**, *118*, 4212–4213.
- 42 Ingram, R. S.; Hostetler, M. J.; Murray, R. W. Poly-hetero- ω -functionalized alkanethiolate-stabilized gold cluster compounds. *J. Am. Chem. Soc.* **1997**, *119*, 9175–9178.
- 43 Hostetler, M. J.; Templeton, A. C.; Murray, R. W. Dynamics of place-exchange reactions on monolayer-protected gold cluster molecules. *Langmuir* **1999**, *15*, 3782–3789.
- 44 Templeton, A. C.; Wuelfing, W. P.; Murray, R. W. Monolayer-protected cluster molecules. *Acc. Chem. Res.* **2000**, *33*, 27–36.
- 45 Yamada, M.; Quiros, I.; Mizutani, J.; Kubo, K.; Nishihara, H. Preparation of palladium nanoparticles functionalized with biferrocene thiol derivatives and their electro-oxidative deposition. *Phys. Chem. Chem. Phys.* **2001**, *3*, 3377–3381.
- 46 Men, Y.; Kubo, K.; Kurihara, M.; Nishihara, H. Redox behavior of biferrocene dithiol and disulfide derivatives in SAMs with and without gold clusters on the gold substrate. *Phys. Chem. Chem. Phys.* **2001**, *3*, 3427–3430.
- 47 Celis-Salazar, P. J.; Cai, M.; Cucinell, C. A.; Ahrenholtz, S. R.; Epley, C. C.; Usov, P. M.; Morris, A. J. Independent Quantification of Electron and Ion Diffusion in Metallocene-Doped Metal–Organic Frameworks Thin Films. *J. Am. Chem. Soc.* **2019**,

141, 11947–11953.

- 48 Wolf, N.; Kersting, L.; Herok, C.; Mihm, C.; Seibel, J. High-Yielding Water-Soluble Asymmetric Cyanine Dyes for Labeling Applications. *J. Org. Chem.* **2020**, *85*, 9751–9760.
- 49 Creager, S. E.; Rowe, G. K. Competitive self-assembly and electrochemistry of some ferrocenyl-n-alkanethiol derivatives on gold. *J. Electroanal. Chem.* **1994**, *370*, 203–211.

Conclusion and Perspectives

During my PhD work, I principally investigated by means of density functional theory (DFT) calculations of the bonding, stability, structure and optical properties of ligand-protected group-10 and group-11 stable nanoclusters.

In a first step, I have investigated a series of N-heterocyclic carbene (NHC) protected gold nanoclusters (AuNCs) with different nuclearity which derived from the well-known experimentally-characterized phosphine-stabilized AuNCs (Chapter 2). The results show that NHCs can stabilize variable-sized AuNCs with properties related to their parent phosphine-protected species. The similarities in the bond distances and Wiberg bond indices (WBIs) are indicative of analogous thermodynamic stability. This is confirmed by evaluation of the Au–P and Au–C bonding energies in these species, with the latter being even slightly stronger than the former by a few kilocalories per mole. Furthermore, by replacing phosphines by NHC ligands, the optical properties of the clusters can be modified, with a clear trend for UV-Vis band shifting.

Then, I extended the investigations to a series of 8-electron hypothetical Au_{13} and M_4Au_9 *superatomic* clusters decorated with phosphine or halogen and phosphine ligands (Chapter 3). The substitution of phosphines by NHCs only marginally perturb the electronic structure, leading to roughly similar optical and luminescent properties, but with interesting modifications. For example, with monodentate ligands, the lowest-energy absorption wavelength is red shifted when going from phosphines to NHCs. This is the consequence of a lesser HOMO \rightarrow LUMO contribution to this $1\text{P} \rightarrow 1\text{D}$ transition in the NHC series. With bidentate ligands, the opposite effect, i.e., a blue-shift occurs when going from phosphines to NHCs, which is related to the stronger chelating (distorting) effect of diphosphines on the metal core. These UV–vis wavelength shifts are retained for the chelated species in the emission wavelengths, but somewhat blurred in the case of the nonchelated ones.

Moreover, I also found that the structure of the metallic core of a ligated icosahedral Au_{13} cluster can be changed by tuning the size and shape of the NHC ligands (Chapter 4). DFT calculations on the hypothetical NHC-protected clusters $[\text{Au}_{13}(\text{NHC})_8\text{X}_4]^+$ ($\text{X} = \text{Cl}, \text{Br}, \text{I}$) show that isomerization can be achieved by simply tuning the size and shape of the NHC ligands. When the smaller MeIm and EtIm ligands are considered, the core structure conserves an icosahedral arrangement. With the medium-sized iPrIm ligand, two isomers with both icosahedral and (very rare) cuboctahedral core structures are found. Increasing the ligand size to $\text{NHC} = \text{iPrBzIm}$ leads to the sole cuboctahedral structure. The differences of two $[\text{Au}_{13}(\text{iPrIm})_8\text{Br}_4]^+$ (ico/cubo) isomers in their geometries, electronic structures, and optical properties (including emissive properties) were further investigated. In comparison with the

icosahedral $[\text{Au}_{13}(\text{iPrIm})_8\text{Br}_4]^+$ isomer, its cuboctahedral variation shows a larger HOMO–LUMO gap, inducing differences in their absorption and emission properties.

Our theoretical results related to the above mentioned NHC protected gold clusters strongly encourage further experimental work on the synthesis and exploration of the novel NHC-ligated gold nanoclusters and their coresponded properties. We believe that our investigations can also help experimental chemists to accelerate the discovery of new AuNCs based optical materials with different absorption and emission properties. Our future work, in this direction, will focus on the evaluation of the catalytic activity of NHC protected AuNCs since some NHC-protected AuNCs reported recently shown excellent catalytic performance towards various reactions.^{1,2} It is interesting to understand how these clusters driving a reaction and how the NHC ligands interact with the metal surface during reaction conditions.

In a subsequent step, I investigated the effect of doping Au_{13} NCs by a single transition-metal atom. Various ligated $\text{M}@\text{Au}_{12}$ *superatomic* clusters (M = group 11 to 6) were investigated. The results show that the isoelectronic doping induces a progressive change of the number of *superatomic* electrons from 8 ($1\text{S}^2 1\text{P}^6 1\text{D}^0$) to 18 ($1\text{S}^2 1\text{P}^6 1\text{D}^{10}$) when M varies from Au to W, associated with a variation in the bonding and properties of the cluster. Among them, two model clusters, namely $[\text{Os}@\text{Au}_{12}\text{dppe}_5\text{Cl}_2]$ (chapter 5) and $[\text{W}\text{Au}_{12}\text{dppm}_6]$ (Chapter 6), were analysed in details. Their corresponding homometallic analogues, namely $[\text{Au}_{13}\text{dppe}_5\text{Cl}_2]^{3+}$ and $[\text{Au}_{13}\text{dppm}_6]^{5+}$, were also calculated for comparison. The optical properties of $[\text{Os}@\text{Au}_{12}\text{dppe}_5\text{Cl}_2]$ are dominated by core-to-ligand charge transfer in contrast to the 8-*ce* cluster $[\text{Au}_{13}\text{dppe}_5\text{Cl}_2]^{3+}$, showing $1\text{D}\rightarrow\pi^*$ -ligand and $1\text{P}\rightarrow\pi^*$ -ligand character transitions. Such differences are also noted in the calculated CD spectra with a peak manifold between 950 and 650 nm, not observed for the parent Au_{13} cluster. The emission properties derived from the $\text{T1}\rightarrow\text{S1}$ decay exhibit a red shift from 809 nm calculated for $[\text{Au}_{13}\text{dppe}_5\text{Cl}_2]^{3+}$ to 1045 nm for $[\text{Os}@\text{Au}_{12}\text{dppe}_5\text{Cl}_2]$, which involves an equatorial distortion of the $\text{Au}_{12}\text{Cl}_2$ core for the emissive excited state, rather than the axial distortion observed for $[\text{Au}_{13}\text{dppe}_5\text{Cl}_2]^{3+}$. The $[\text{W}\text{Au}_{12}\text{dppm}_6]$ cluster shown a similar electronic configuration with $[\text{Os}@\text{Au}_{12}\text{dppe}_5\text{Cl}_2]$ but somewhat differences in HOMO-LUMO gap, absorption/emission spectra and CD spectra.

Our results on the doped cluster series strongly encourage further synthetic exploration for this class of *superatoms* in fully phosphine-protected structures. With the transition from 8-*ce* to 18-*ce* clusters, the bonding between centered atom, Au_{12} cage, and the phosphine ligand shells could be modified, which can raise distinct properties in its optical and catalytic properties. These have been shown in recently published experimental works from Tsukuda's group.^{3,4} In future studies, we are interested in exploring the new dopant elements for the parent

Au₁₂ system, such as the heavier homologues (Sg to Rg) of the current studied W to Au series. The bare Sg@Au₁₂ cluster has been theoretically studied by Li and colleagues in 2015.⁵ It shows the similar *superatomic* character as the well-known 18-electron W@Au₁₂ compound, with a significant 6d(Sg)–6s(Au) covalent-metallic interaction. According to these interesting results, it is worth to see whether these heavier homologue elements (Sg to Rg) can make stable ligated species M@Au₁₂.

I have also undertaken a complete DFT investigation of the Pd and Pt organometallic nanocluster structural chemistry (Chapters 7-9), for which no rationalization existed, so far. Our results show that these species can be considered as *superatoms* or assemblies of *superatoms* (*supermolecules*). In fact, in these nanoclusters the actual average configuration of Pd/Pt is $nd^{10-x}(n+1)s^x$, thus providing to the whole cluster a “magic” total number of 5s/6s electrons that ensures metal-metal bonding, as in a regular *superatom* or *supermolecule*. This “excited” $nd^{10-x}(n+1)s^x$ configuration results from a level crossing between *nd* combinations and $(n+1)s$ combinations, the former transferring their electrons to the latter. This level crossing is the result from the interaction of some metal *nd* combinations with the ligands. This interaction involving metal *nd* valence orbitals does not exist in group-11 nanoclusters. For instance, we show Dahl’s Mackay icosahedral cluster [Pd₅₅L₁₂(μ₃-CO)₂₀] (Chapter 8) can be interpreted using the *jellium* model as a regular *superatom*, characterized by the “magic” 20-electron count (1S² 1P⁶ 1D¹⁰ 2S² configuration). These 20 electrons are located in bonding combinations of 5s AOs, which means that, considering the closed-shell dianion, nine 4*d*-type combinations have formally transferred their electrons in nine of the 5s MO combinations. This level crossing does not occur on the bare [Pd₅₅]²⁻ kernel. It necessitates the presence of the ligands, which destabilize the nine 4*d*-type MOs and open a HOMO-LUMO gap. In this case the actual configuration of Pd in [Pd₅₅L₁₂(μ₃-CO)₂₀] is $4d^{9.64} 5s^{0.36}$ (0.36 = 20/55). We shown also some ligated platinum clusters can be described as *superatoms*, such as Zacchini’s [Pt₁₃(CO)₁₂]⁸⁻ (8-electron *superatom* with configuration of 1S² 1P⁶) and Longoni’s [Pt₃₈(CO)₄₄]²⁻ (18-electron *superatom* with configuration of 1S² 1P⁶ 1D¹⁰). Indeed, the assemblies of individual platinum *superatoms* (*supermolecules*) can also be achieved. These are the cases of Zacchini’s [Pt₁₉(CO)₁₇]⁸⁻ (10-electron *supermolecule* isoelectronic to molecular N₂) and Chini’s [Pt₁₉(CO)₂₂]⁴⁻ (14-electron *supermolecule* isoelectronic to molecular F₂). Our studies explored the frontier of the *superatom* concept, and certainly paved the road of the electron counting between the group-11 metal clusters to group-10 counterparts.

Our investigations on group-10 cluster chemistry provided the scientific community ideas to easily understand the structure, bonding pattern and electronic structure of ligated group-10 nanoclusters. We believe new *superatomic* and *supermolecular* Pd/Pt nanoclusters will be synthesized and isolated by synthetic chemists in the near future.

Based on the results I have obtained, the next work will be to focus on some larger group-10 nanoclusters, such as the three-shell 145-metal-atom $\text{Pd}_{145}(\text{CO})_x(\text{PEt}_3)_{30}$ ($x \approx 60$) cluster compound,⁶ and the Pd-Pt four-shell 165-metal-atom $\text{Pd}_{164-x}\text{Pt}_x(\mu_{12}\text{-Pt})(\text{CO})_{72}(\text{PPh}_3)_{20}$ ($x \approx 7$) cluster compound,⁷ which shows the same Pd_{55} metallic inner core as above mentioned $[\text{Pd}_{55}\text{L}_{12}(\mu_3\text{-CO})_{20}]$. We believe that these palladium spherical clusters are indeed *superatoms* characterized by (at least approximately) “magic” electron counts, these electrons occupying $5s(\text{Pd})$ or $6s(\text{Pt})$ states and resulting from electron transfer from $4d(\text{Pd})$ or $5d(\text{Pt})$ states. I have made some effort to compute these large compounds, unfortunately, no reliable results were obtained so far because of the computational limits. With the fast development of computer science, I believe that we can find a solution to handle this problem in the future – we currently study the possibility to use the large-scale and linear scaling density functional theory code CONQUEST, which shows excellent parallel scaling and can be applied to systems containing thousands of atoms with diagonalization and millions of atoms with linear scaling.⁸

The last part of this manuscript (Chapter 10) reports an experimental work on the synthesis and characterization of ferrocenylalkylthiolate protected Au nanoparticles (**FcSH-AuNPs**). The synthesized **FcSH-AuNPs** show an ultrafine average size of 2 nm which is smaller than the previously reported mixed alkylthiolate and ferrocenylalkylthiolate ligands protected AuNPs. The possible reason is that the large steric effect of the terminal ferrocenyl group inhibits the further growth of the gold metallic kernel. **FcSH-AuNPs** shows a broad plasmon band at 500 nm because of the short distance between each particle. A clear signal in their cyclic voltammograms could be recorded, encouraging the fact that **FcSH-AuNPs** could be used in the design of derivatized electrode for sensing applications.

References

- 1 Shen, H.; Wu, Q.; Hazer, M.S.A.; Tang, X.; Han, Y.Z.; Qin, R.; Ma, C.; Malola, S.; Teo, B.K.; Häkkinen, H.; Zheng, N. Regioselective hydrogenation of alkenes over atomically dispersed Pd sites on NHC-stabilized bimetallic nanoclusters. *Chem* **2022**, *8*, 2380-2392.
- 2 Kulkarni, V.K.; Khiarak, B.N.; Takano, S.; Malola, S.; Albright, E.L.; Levchenko, T.I.; Aloisio, M.D.; Dinh, C. T.; Tsukuda, T.; Häkkinen, H.; Crudden, C. M. N-Heterocyclic Carbene-Stabilized Hydrido Au_{24} Nanoclusters: Synthesis, Structure, and Electrocatalytic

- Reduction of CO₂. *J. Am. Chem. Soc.* **2022**, *144*, 9000–9006.
- 3 Hirai, H.; Takano, S.; Nakashima, T.; Iwasa, T.; Taketsugu, T.; Tsukuda, T. Doping-Mediated Energy-Level Engineering of M@Au₁₂ Superatoms (M= Pd, Pt, Rh, Ir) for Efficient Photoluminescence and Photocatalysis. *Angew. Chem. Int. Ed.* **2022**, *61*, e2022072.
 - 4 Takano, S.; Hirai, H.; Nakashima, T.; Iwasa, T.; Taketsugu, T.; Tsukuda, T. Photoluminescence of doped superatoms M@Au₁₂ (M = Ru, Rh, Ir) homoleptically capped by (Ph₂)PCH₂P(Ph₂): Efficient room-temperature phosphorescence from Ru@Au₁₂. *J. Am. Chem. Soc.* **2021**, *143*, 10560–10564.
 - 5 Cao, G.J.; Schwarz, W. E.; Li, J. An 18-electron system containing a superheavy element: theoretical studies of Sg@Au₁₂. *Inorg. Chem.* **2015**, *54*, 3695–3701.
 - 6 Tran, N. T.; Powell, D. R.; Dahl, L. F. Nanosized Pd₁₄₅(CO)_x(PEt₃)₃₀ Containing a Capped Three-Shell 145-Atom Metal-Core Geometry of Pseudo Icosahedral Symmetry. *Angew. Chem. Int. Ed.* **2000**, *39*, 4121–4125.
 - 7 Mednikov, E. G.; Jewell, M. C.; Dahl, L. F. Nanosized (μ₁₂-Pt)_{Pd_{164-x}Pt_x}(CO)₇₂(PPh₃)₂₀ (x ≈ 7) Containing Pt-Centered Four-Shell 165-Atom Pd–Pt Core with Unprecedented Intershell Bridging Carbonyl Ligands: Comparative Analysis of Icosahedral Shell-Growth Patterns with Geometrically Related Pd₁₄₅(CO)_x(PEt₃)₃₀ (x ≈ 60) Containing Capped Three-Shell Pd₁₄₅ Core. *J. Am. Chem. Soc.* **2007**, *129*, 11619–11630.
 - 8 Nakata, A.; Baker, J. S.; Mujahed, S. Y.; Poulton, J. T. L.; Lin, J.; Raza, Z.; Yadav, S.; Truflandier, L; Miyazaki, T.; Bowler, D. R. Large scale and linear scaling DFT with the CONQUEST code. *J. Chem. Phys.* **2020**, *152*, 164112.

Publications related to this work

A large part of my PhD work has been published in the following articles:

- 1 Wei, J.; Kahlal, S.; Halet, J.-F.; Saillard, J.-Y. Elucidating the electronic structure of the ligated cuboctahedral palladium cluster $[\text{Pd}_{13}(\mu_4\text{-C}_7\text{H}_7)_6]^{2+}$. *J. Clust. Sci.* **2019**, *30*, 1227–1233.
- 2 Wei, J.; Marchal, R.; Astruc, D.; Saillard, J.-Y.; Halet, J.-F.; Kahlal, S. Theoretical Analysis of the Mackay Icosahedral Cluster $\text{Pd}_{55}(\text{P}^i\text{Pr}_3)_{12}(\mu_3\text{-CO})_{20}$: An open-shell 20-electron superatom. *Chem. Eur. J.* **2020**, *26*, 5508–5514.
- 3 Wei, J.; Halet, J.-F.; Kahlal, S.; Saillard, J.-Y.; Muñoz-Castro, A. Toward the Formation of N-Heterocyclic-Carbene-Protected Gold Clusters of Various Nuclearities. A Comparison with Their Phosphine-Protected Analogues from Density Functional Theory Calculations. *Inorg. Chem.* **2020**, *59*, 15240–15249.
- 4 Wei, J.; Rodríguez-Kessler, P. L.; Halet, J.-F.; Kahlal, S.; Saillard, J.-Y.; Muñoz-Castro, A. On Heteronuclear Isoelectronic Alternatives to $[\text{Au}_{13}(\text{dppe})_5\text{Cl}_2]^{3+}$: Electronic and Optical Properties of the 18-Electron $\text{Os}@\text{[Au}_{12}(\text{dppe})_5\text{Cl}_2]$ Cluster from Relativistic Density Functional Theory Computations. *Inorg. Chem.* **2021**, *60*, 8173–8180.
- 5 Gam, F.; Wei, J.; Kahlal, S.; Saillard, J.-Y.; Halet, J.-F. Electron Counting in Ligated High Nuclearity Late Transition Metal Clusters. *Struct. Bond.* **2021**, *188*, 69–102.
- 6 Wei, J.; Kahlal, S.; Halet, J.-F.; Saillard, J.-Y.; Muñoz-Castro, A. Insight into the Stability and Electronic and Optical Properties of N-Heterocyclic Carbene Analogues of Halogen/Phosphine-Protected Au_{13} Superatomic Clusters. *J. Phys. Chem. A* **2022**, *126*, 536–545.
- 7 Wei, J.; Marchal, R.; Astruc, D.; Kahlal, S.; Halet, J.-F.; Saillard, J.-Y. Looking at platinum carbonyl nanoclusters as *superatoms*. *Nanoscale* **2022**, *14*, 3946–3957.
- 8 Wei, J.; Kahlal, S.; Halet, J.-F.; Muñoz-Castro, A.; Saillard, J.-Y. Ligand-Induced Cuboctahedral versus Icosahedral Core Isomerism within Eight-Electron Heterocyclic-Carbene-Protected Gold Nanoclusters. *Inorg. Chem.* **2022**, *61*, 8623–8628.
- 9 Wei, J.; MacLeod-Carey, D.; Halet, J.-F.; Kahlal, S.; Saillard, J.-Y.; Muñoz-Castro, A. From 8- to 18-cluster electrons *Superatoms*. Investigation of the Ligand-Protected $\text{W}@\text{Au}_{12}(\text{dppe})_6$ Cluster Displaying Distinctive Electronic and Optical Properties, **2022**, pending for submission.

Titre : Etude théorique et expérimentale de nanoclusters et nanoparticules organométalliques de métaux de transition

Mots clés : métaux de transition, nanoclusters, nanoparticules, structures électroniques, superatomes, théorie de la fonctionnelle de la densité

Résumé : Le travail décrit dans ce mémoire concerne principalement l'étude, par des calculs en théorie de la fonctionnelle de la densité (DFT), de la stabilité, de la structure et des propriétés optiques de nanoclusters stables des groupes 10 et 11, protégés par des ligands. Nous avons étudié dans un premier temps, une série de nanoclusters d'or hypothétiques stabilisés par des carbènes N-hétérocycliques (NHC) dérivés de nanoclusters d'or (AuNC) bien connus, stabilisés par des phosphines et caractérisés expérimentalement. Nos résultats montrent que les NHC sont aptes à stabiliser des AuNC de taille variable avec des propriétés comparables à leurs homologues protégés par des phosphines.

Nous nous sommes ensuite intéressés à l'effet du dopage de nanoclusters Au₁₃ par un atome de métal de transition. Divers clusters superatomiques M@Au₁₂ (M = groupe 6-10) protégés par des ligands ont été étudiés.

Nous avons également réalisé une investigation générale par la méthode DFT de la chimie structurale des nanoclusters organométalliques de Pd et Pt, pour laquelle aucune rationalisation n'a été proposée à ce jour. Nos résultats montrent que ces espèces peuvent être considérées comme des superatomes ou des assemblages de superatomes (supermolécules).

La dernière partie de ce mémoire décrit un travail expérimental sur la synthèse et la caractérisation de nanoparticules d'or protégées par des ferrocénylalkylthiolates (FcSH-AuNPs). Un signal clair présent dans leurs voltammogrammes cycliques laisse penser que les nanoparticules FcSH-AuNP pourraient être utilisées dans la conception d'électrodes dérivées pour des applications dans le domaine des capteurs.

Title: Theoretical and Experimental Study of Organometallic Transition Metal Nanoclusters and Nanoparticles

Keywords: density functional theory, electronic structures, nanoclusters, nanoparticles, *superatoms*, transition metals

Abstract: The work reported therein deals principally with the investigation by density functional theory (DFT) calculations of the stability, structure and optical properties of ligand-protected group 10 and 11 stable nanoclusters. In a first step we have investigated a series of N-heterocyclic carbene (NHC) protected gold nanoclusters (AuNCs) derived from the well-known experimentally-characterized phosphine-stabilized AuNCs. The results show that NHCs can stabilize variable-sized AuNCs with properties related to their parent phosphine-protected species.

In a subsequent step we investigated the effect of doping Au₁₃ NCs by a single transition-metal atom. Various ligated M@Au₁₂ *superatomic*

clusters (M = group 6-10) were investigated.

We have also undertaken a general DFT investigation of the Pd and Pt organometallic nanocluster structural chemistry, for which no rationalization existed so far. Our results show that these species can be considered as *superatoms* or assemblies of *superatoms* (*supermolecules*).

The last part of this manuscript reports an experimental work on the synthesis and characterization of ferrocénylalkylthiolate protected Au nanoparticles (FcSH-AuNPs). A clear signal in their cyclic voltammograms could be recorded, encouraging the fact that FcSH-AuNPs could be used in the design of derivatized electrode for sensing applications.